DOCTORAL THESIS

Mathematical modelling of brain tumour growth

Integrating mechanics, phenotypic evolution, and nutrient transport to describe anisotropic behaviour and personalised therapies

Author:
Francesca BALLATORE

Supervisor:
Chiara GIVERSO

Politecnico di Torino
Department of Mathematical Sciences "G. L. Lagrange"

Università di Torino
Department of Mathematics "G. Peano"

February 18, 2025

Declaration of Authorship

I, Francesca BALLATORE, declare that this thesis titled "Mathematical modelling of brain tumour growth. Integrating mechanics, phenotypic evolution, and nutrient transport to describe anisotropic behaviour and personalised therapies", submitted in fulfilment of the requirements for the Degree of Doctor of Philosophy in the Faculty of Mathematical Sciences at Politecnico di Torino, and the work presented in it, are my own. I confirm that:

- This work was done wholly while in candidature for a research degree at this University.
- No part of this thesis has previously been submitted for a degree or any other qualification at these Universities or any other institution.
- Where I have consulted the published work of others, this is always clearly attributed.
- Where I have quoted from the work of others, the source is always given. With the exception of such quotations, this thesis is entirely my own work.
- I have acknowledged all main sources of help.
- Where the thesis is based on work done by myself jointly with others, I have made clear exactly what was done by others and what I have contributed myself.

Date: February 18, 2025

Publications from this Thesis

1. **F. Ballatore**, G. Lucci, A. Borio, and C. Giverso.
   An imaging-informed mechanical framework to provide a quantitative description of brain tumour growth and the subsequent deformation of white matter tracts.
   In: G. Bretti, R. Natalini, P. Palumbo, L. Preziosi. *Mathematical Models and Computer Simulations for Biomedical Applications* (2023) SEMA SIMAI Springer Series, vol 33.
   DOI: 10.1007/978-3-031-35715-2_5

2. **F. Ballatore**, G. Lucci, and C. Giverso.
   Modelling and simulation of anisotropic growth in brain tumours through poroelasticity: A study of ventricular compression and therapeutic protocols.
   Computational Mechanics (2024)
   DOI: 10.1007/s00466-024-02471-7

3. **F. Ballatore**, C. Giverso, and R. Penta.
   Effective macroscopic equations for biological fluid and nutrients' transport in vascularized tumours growing via proliferation and chemotaxis.
   Submitted (2024)

4. G. Small, **F. Ballatore**, C. Giverso, and V. Balbi.
   Modelling the non-linear viscoelastic behaviour of brain tissue in torsion.
   Submitted (2025)

5. **F. Ballatore**, X. Ruan, C. Giverso, and T. Lorenzi.
   Non-local anisotropic reaction-diffusion modelling of phenotypic heterogeneity in growing brain tumours under spatially inhomogeneous oxygen gradients.
   In preparation

Abstract

This thesis introduces several mathematical models to explore the multifaceted dynamics of brain tumour growth. By integrating mechanical deformation, phenotypic heterogeneity, and fluid-nutrient transport, the study leverages multiscale and multiphase approaches to analyse tumour progression within anisotropic and heterogeneous environments. Patient-specific imaging data is employed to enhance the precision of simulations, paving the way for personalised therapeutic strategies.

Malignant brain tumours pose a significant challenge in modern medicine due to their aggressive behaviour, resistance to treatment, and unpredictable locations. Despite advancements in clinical research, recurrence remains the leading cause of mortality. The migration and invasion of tumours into brain tissue involve complex mechanisms that are not yet fully understood, underscoring the need to develop mathematical models to enhance our understanding of these processes.

Firstly, we address tumour-induced stresses and deformations by developing a multiphase mechanical model that incorporates anisotropic growth aligned with brain fibre architecture. Simulations performed on realistic brain geometries offer valuable insights into tumour-induced ventricular compression and its effects on surrounding healthy tissues. Validation through numerical simulations demonstrates the model's ability to replicate observed tumour mechanics and inform therapeutic planning. Subsequently, the viscoelastic behaviour of brain tissue is investigated through experimental studies and a modified quasi-linear viscoelastic model. Material parameters derived from cylindrical brain samples provide a robust foundation for simulating brain deformation under various conditions, with applications extending beyond tumour modelling to include studies on traumatic brain injury.

Moreover, we focus on developing therapeutic strategies, with particular emphasis on T-lymphocyte-based immunotherapies. We develop mathematical models based on reaction-advection-diffusion equations to study immune response dynamics, employing bifurcation analysis to identify critical thresholds for treatment efficacy. In a distinct approach, phenotypic heterogeneity in response to spatial oxygen gradients is examined using a reaction-diffusion integro-differential equation framework. By incorporating anisotropic diffusion and phenotypic dynamics, the model elucidates the intricate interplay between tumour growth, oxygen diffusion, and cellular proliferation mechanisms. Lastly, nutrient and fluid transport within the tumour micro-environment are investigated through a homogenisation-based approach. By integrating microvascular structures into a double porous medium framework, the model captures the complex interactions among vascular geometry, nutrient transport, and tumour progression.

This thesis bridges experimental, clinical, and computational approaches, providing innovative methodologies to advance the understanding of brain tumour growth and progression. The findings lay a foundation for future research and contribute to the development of mathematical models able to deal with patient-specific anisotropic data and personalised treatments, with the potential to significantly improve patient outcomes in oncology.

Contents

List of Figures

List of Tables

List of Abbreviations

ABM	**A**gent-**B**ased **M**odel
ADC	**A**pparent **D**iffusion **C**oefficient
ALT	**A**lternative **L**engthening of **T**elomeres
ARD	**A**dvection-**R**eaction-**D**iffusion equations
ATP	**A**denosine **Tri**phosphate
BBB	**B**lood-**B**rain **B**arrier
CA	**C**ellular **A**utomata
CAR-T	**C**himeric **A**ntigen **R**eceptor **T**-cell
CH	**C**ahn-**H**illiard model
CHT	**Ch**emo**t**herapy
CM	**C**ontinuum-**M**echanics-based model
CNS	**C**entral **N**ervous **S**ystem
CSF	**C**erebro**s**pinal **F**luid
CT	**C**omputed **T**omography
CTL	**C**ytotoxic **T**-**L**ymphocyte
DTI	**D**iffusion **T**ensor **I**maging
DWI	**D**iffusion-**w**eighted **I**maging
EC	**E**ndothelial **C**ells
ECM	**E**xtra**c**ellular **M**atrix
EMT	**E**pithelial-**M**esenchymal **T**ransition
FA	**F**ractional **A**nisotropy
FE	**F**inite **E**lement
FGF	**F**ibroblast **G**rowth **F**actor
FGS	**F**luorescence-**G**uided **S**urgery
FL	**Fl**uid
FW	**F**ree **W**ater
FWE-FA	**F**ree **W**ater **E**liminated **F**ractional **A**nisotropy
GB	**G**lio**b**lastoma
GBM	**G**lio**b**lastoma **M**ultiforme
GTV	**G**ross **T**umour **V**olume
HIF	**H**ypoxia-**I**nducible **F**actor
HYB	**Hyb**rid model
IL-8	**I**nter**l**eukin-**8**
IMRT	**I**ntensity-**M**odulated **R**adio**t**heraphy
KM	**K**inetic **M**odel
LE	**L**inear **E**lasticity
LITT	**L**aser **I**nterstitial **T**hermal **T**herapy
MMP	**M**atrix **M**etallo**p**roteinases
MQLV	**M**odified **Q**uasi-**L**inear **V**iscoelasticity
MRE	**M**agnetic **R**esonance **E**lastography
MRI	**M**agnetic **R**esonance **I**maging

MRS	**M**agnetic **R**esonance **S**pectroscopy
NFW	**N**on **F**ree **W**ater
NLE	**N**on**l**inear **E**lasticity
ODE	**O**rdinary **D**ifferential **E**quation
OVs	**O**ncolytic **V**irus**es**
PDE	**P**artial **D**ifferential **E**quation
PET	**P**ositron **E**mission **T**omography
PIDE	**P**artial **I**ntegro-**D**ifferential **E**quation
PTV	**P**lanning **T**reatment **V**olume
PWI	**P**erfusion-**W**eighted **I**maging
QLV	**Q**uasi-**L**inear **V**iscoelasticity
RD	**R**eaction-**D**iffusion equations
RT	**R**adio**t**heraphy
SASP	**S**enescence-**a**ssociated **S**ecretory **P**henotype
SGR	**S**pecific **G**rowth **R**ate
SRS	**S**tereotactic **R**adio**s**urgery
TMZ	**T**e**m**o**z**olomide
TTFs	**T**umour **T**reatment **F**ield**s**
VEGF	**V**ascular **E**ndothelial **G**rowth **F**actor
VRE	**V**elocity of **R**adial **E**xpansion
WHO	**W**orld **H**ealth **O**rganization

1 Introduction

Cancer is a multifactorial and multistage disease characterised by a range of structural, biochemical, molecular, and genetic alterations. These changes vary depending on the tissue and cancer subtype involved. In this dissertation, we focus on brain tumours, which allows us to delve deeper into the unique characteristics of this disease, develop specific models, and interpret results in the context of experimental data related to brain tissue, where applicable.

In Section 1.1, we delve into the biological characteristics that define tumours, with a particular emphasis on brain tumours. This includes a detailed discussion of the different grades of tumour progression and their distinguishing features. Regarding the mathematical aspects of this dissertation, our focus is on developing different modelling approaches for brain tumours. Consequently, in Section 1.2, we offer a general and introductory overview of the mathematical framework employed in this context.

1.1 Biological characteristics of tumours

The human body consists of billions of cells that coordinate and interact to form tissues and organs. In normal circumstances, these cells follow a tightly regulated cycle of growth, division, and replacement of damaged or dead cells. Cancer cells, however, deviate from this normal behaviour due to malfunctions in the regulation of cell division. Unlike healthy cells, cancer cells proliferate uncontrollably, grow indefinitely, and invade nearby tissues with the potential to metastasise to distant organs. This ability to sustain unchecked proliferation is one of the primary features that distinguish cancer cells from normal cells.

In 2000, Hanahan and Weinberg identified the capacity of cancer cells to sustain proliferative signalling as a defining *hallmark of cancer* in their seminal work [234]. Since then, they have expanded their framework to include a broader set of behaviours that are fundamental to cancer progression [232, 233]. These hallmarks include the ability to sustain proliferative signalling, evade growth suppressors, resist cell death, enable replicative immortality, induce angiogenesis, activate invasion and metastasis, reprogram energy metabolism, and evade immune destruction (see Figure 1.1).

The first four hallmarks primarily involve disruptions in the cell cycle and regulatory mechanisms of cell growth. For instance, cancer cells maintain continuous proliferative signalling by overexpressing growth factor receptors or producing their own growth factors to stimulate autocrine growth loops. Furthermore, they evade critical growth-suppressing mechanisms controlled by tumour suppressor genes such as RB and TP53, allowing them to bypass inhibitory signals and divide without restriction [449]. Another critical hallmark is their ability to resist apoptosis (programmed cell death), enabling cancer cells to survive despite genetic damage or other signals that would typically trigger cell death [336]. Additionally, cancer cells can achieve replicative immortality by circumventing the natural division limit through the activation of telomerase or alternative lengthening of telomeres (ALT) mechanisms [447].

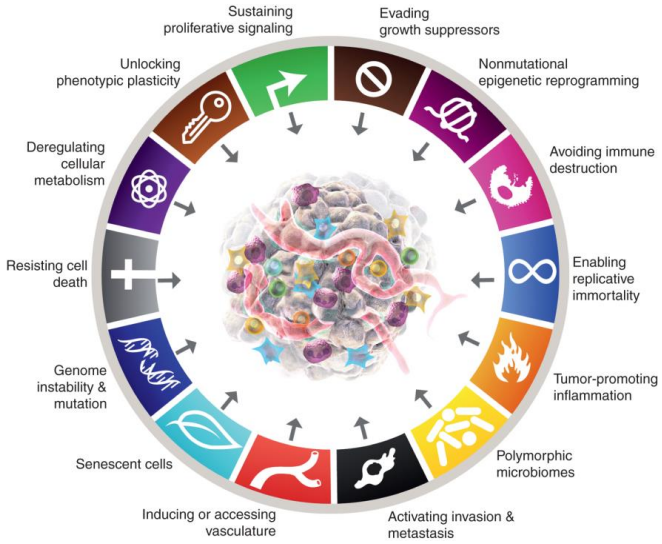

FIGURE 1.1: Schematic representation of the hallmarks of cancer, proposed by Hanahan and Weinberg. (Reprinted from [232] by permission from *Elsevier* and *Copyright Clearance Center*).

Cancer cells also modify their surrounding environment to further support tumour growth and dissemination. One such modification is angiogenesis, the formation of new blood vessels, which ensures a steady supply of oxygen and nutrients while facilitating the removal of waste products [90, 97]. Additionally, cancer cells can invade neighbouring tissues and metastasise to distant organs, often involving processes like the epithelial-mesenchymal transition (EMT), which grants them enhanced migratory and invasive capabilities [408].

The 2011 update to the hallmark framework introduced two additional enabling characteristics: genome instability and tumour-promoting inflammation. Genome instability, characterised by an increased mutation rate, provides the genetic diversity needed for tumour evolution and adaptation [174]. Moreover, inflammation within the tumour micro-environment, often driven by immune cell infiltration, can promote tumour growth by supplying bioactive molecules such as growth factors and mutagenic agents [228]. The update introduced also new hallmarks, such as the reprogramming of cellular metabolism in cancer cells. A key example is their frequent reliance on aerobic glycolysis, also known as the Warburg effect, which enables cancer cells to meet their energy demands even in oxygen-rich conditions, thereby supporting rapid proliferation and survival in the typically hypoxic tumour micro-environment [141, 509]. Additionally, the ability of cancer cells to evade immune surveillance has been shown to be a crucial mechanism that allows them to persist despite the body's natural defences.

In 2022, Hanahan expanded the framework further by introducing four new hallmarks that reflect the most recent advancements in cancer biology. These include unlocking phenotypic plasticity, whereby cancer cells can transition between different cell states, allowing them to adapt to various environmental conditions [525]. Another addition is non-mutational epigenetic reprogramming, wherein tumour cells use epigenetic modifications to alter gene expression without changing the underlying DNA sequence, promoting cancer progression and resistance to therapy [137, 262]. The 2022 update also introduced two new enabling characteristics: polymorphic microbiomes and senescent cells. Polymorphic microbiomes refer to the complex and dynamic communities of microorganisms within the tumour micro-environment, which can influence cancer progression through their interactions with the immune system [160, 243]. Senescent cells,

on the other hand, enter a state of irreversible growth arrest but continue secreting inflammatory factors, which can promote tumour growth and therapy resistance [297, 311, 504].

Brain tumours occur when abnormal cells form within the brain, disrupting its normal functions. Brain and central nervous system cancers represent a significant global public health concern due to their high mortality rates, substantial economic burden, low survival rates, and profound impact on patients' quality of life [452]. They account for approximately 1.6% of all new cancer diagnoses annually and are responsible for about 2% of cancer-related deaths worldwide. This highlights the disproportionate severity of these cancers compared to their incidence, underscoring the need for continued research and improved treatment strategies.

According to the most recent update by the World Health Organization (WHO) in 2021, brain tumours are classified based on molecular and histological features [335]. This classification is crucial for guiding treatment strategies and predicting outcomes. Brain tumours are primarily categorised into two major groups: primary and secondary tumours.

- **Primary brain tumours** refer to malignant tumours that originate either in the brain or in the nerves extending from the brain. These tumours do not frequently metastasise outside of the central nervous system (CNS).
- **Secondary brain tumours** (or metastatic brain tumours) originate from malignant tumours that have spread to the brain from other parts of the body. Secondary brain tumours are more common than primary brain tumours.

There are over 100 types of cancer that can affect the CNS. It is important to note that cancers originating in other locations (such as the breast or lung) and spreading to the brain are treated according to the primary cancer site. Therefore, it is essential to discuss the classification of primary brain cancers:

- **Gliomas**: These are the most common and aggressive brain tumours, originating in the glial cells of the CNS. Gliomas are divided into three main categories:
  - *Astrocytomas*: These develop in astrocytes and are found in the cerebrum and cerebellum. Astrocytomas account for approximately 50% of all primary brain tumours. Notably, Glioblastoma Multiforme (GBM) is a subtype of astrocytoma.
  - *Oligodendrogliomas*: These tumours arise from oligodendrocytes, glial cells responsible for producing myelin, which increases nerve impulse speed.
  - *Ependymomas*: These tumours develop from ependymal cells, which line the ventricles of the brain and spinal cord and are involved in the production and circulation of cerebrospinal fluid (CSF). Ependymomas are typically found in the lining of the ventricles, the spinal cord, or near the cerebellum.
- **Nongliomas**: These tumours do not originate from glial cells. Notable examples include:
  - *Meningiomas*: These develop in the meninges, the protective membranes covering the brain and spinal cord. Meningiomas often arise from arachnoid cells, which are involved in CSF absorption. Most meningiomas are benign, with malignant forms being extremely rare.

- *Medulloblastomas*: These tumours occur in the posterior fossa, a specific region within the intracranial cavity that contains the brainstem and cerebellum. They are more common in children.
- *Pituitary adenomas*: Tumours that arise from the pituitary gland, which is located at the base of the brain. They can affect hormone levels and are usually benign.

Furthermore, the WHO classifies gliomas based on their behaviour and malignancy [335]:

- **Grade I**: Well-circumscribed tumours with low proliferative potential, generally benign and often curable through surgical resection alone.
- **Grade II**: Low-grade malignancies that may progress over time. Their diffuse infiltration makes them challenging to cure with surgery alone.
- **Grade III**: Malignant tumours with abnormal cells, likely to invade surrounding tissues and prone to recurrence.
- **Grade IV**: The most malignant tumours, characterised by rapid growth, pathological angiogenesis, and necrosis. They are invasive and resistant to standard therapies. A prominent example is Glioblastoma Multiforme (GBM).

The following sections elucidate various aspects of brain tumours that are examined in greater detail throughout this thesis. Section 1.1.1 starts with a brief discussion of brain tissue characteristics, where these tumours typically arise, highlighting the unique properties of brain tissue and its influence on tumour growth. The role of brain tissue in tumour invasion along white matter tracts is a central focus of the model presented in Chapters 2, 4 and 5 and is fundamental to the analysis of brain tissue mechanical properties in Chapter 3. Brain tumour progression and metabolism are addressed in Section 1.1.2, with particular attention to the Go-or-Grow mechanism and hypoxia-mediated migration, including the hypoxia-driven metabolic switch between aerobic and anaerobic pathways, which forms the core of the model in Chapter 5. Furthermore, this Section explores also the role of the vasculature in tumour progression. The supply of nutrients from blood vessels to tumours is fundamental to model cancer growth and will be addressed from a homogenized perspective in Chapter 6. Standard and experimental therapeutic approaches for brain tumours are outlined in Section 1.1.3. Finally, Section 1.1.4 provides an overview of the standard imaging modalities used in the evaluation of brain tumours, highlighting how various types of clinical data from medical imaging are incorporated into the models discussed in this thesis.

1.1.1 Characterisation of brain tissue

Characterising brain tissue is essential for a deeper understanding of brain tumours. Brain tissue consists of grey and white matter, covered by thin layers of pia and arachnoid membranes, which together form part of the meninges, the protective layers surrounding the brain and spinal cord. Grey matter primarily contains neuronal cell bodies, distributed on the surface of the cerebral cortex without clear directional preference, while white matter predominantly consists of myelinated axons that facilitate communication between different brain regions and are often highly oriented. This structural organisation is crucial for normal brain function and plays a significant role in tumour progression, as brain tumours frequently invade these tissues, exploiting their distinct properties to spread and grow.

The mechanical behaviour of brain tissue is a critical factor in understanding its response to external forces and processes such as tumour growth. Over the past few decades, the modelling of the mechanical behaviour of the brain has gained significant importance in the scientific community. Despite considerable advancements and extensive research into the brain's functions and operations, our understanding of its mechanical properties remains relatively limited. As noted by Goriely et al. [222], two primary challenges contribute to this knowledge gap. Firstly, the brain is a fully enclosed organ, making it particularly challenging to physically examine and manipulate. Secondly, when considered as a solid, the brain is extremely soft, and its mechanical response is significantly influenced by its fluid content.

Among all human tissues, brain tissue is not only the softest, with a shear modulus on the order of one kilopascal [83], but also one of the most intricate, essential, and least understood. Like most biological soft tissues, brain tissue exhibits highly complex mechanical behaviour: it accommodates finite deformations, displays a markedly nonlinear response to applied forces [45, 149], and exhibits pronounced time-dependent properties [423–425]. The latter is one of the most pronounced features of brain tissue, manifesting itself primarily through so-called viscoelastic effects. For instance, during rapid deformation followed by holding the tissue in place, the stress diminishes over time, a phenomenon known as stress relaxation [84]. Conversely, when a constant load is quickly applied and maintained, the resulting strain increases over time, an effect termed creep [276]. Additional time-dependent behaviours include hysteresis and softening under cyclic loading and unloading [84]. Furthermore, Miller [364] and Miller and Chinzei [365, 366] not only reported the stress-strain rate dependency of brain tissue but also highlighted the asymmetric behaviour under tension and compression. Further experiments conducted by Rashid et al. [423, 425] under intermediate and dynamic strain rates in both compression and tension have reinforced these findings, highlighting a pronounced difference between the two loading conditions and a stiffer response with increasing strain rates. These observations align with studies by Budday et al. [85], who tested human brain specimens under shear in two orthogonal directions as well as in compression and tension. They reported a nonlinear mechanical response, which was significantly stiffer in compression than in tension. Additionally, shear stresses increased with compressive strain but remained unaffected by tensile strain.

Interestingly, Budday et al. [85] demonstrated that the microstructural anisotropy caused by the alignment of nerve fibres does not result in an anisotropic elastic response. This observation is particularly important because it challenges the assumption that the alignment of nerve fibres would lead to directional mechanical behaviour. Therefore, from a mechanical perspective, brain tissue is assumed to behave isotropically in terms of elastic deformation. However, the anisotropic orientation of fibres significantly influences anelastic processes such as growth, remodelling, and the diffusion of oxygen and other molecules.

Another key consideration is whether brain tissue should be modelled as a solid or a fluid. Donnelly et al. [156] show that brain tissue samples immersed in saline return to a defined shape after deformation, supporting the need for a solid model. However, brain tissue, while solid, is extremely soft and its mechanical behaviour is heavily influenced by its fluid phase. Choosing the appropriate model, whether solid or fluid, can significantly influence simulations of tumour growth or surgical interventions, where understanding the behaviour of brain tissue under different forces is crucial. Furthermore, the compressibility of brain tissue requires careful consideration. In this work, we adopt the assumption of brain tissue incompressibility, as commonly done in the mechanical models summarised in Section 1.2. However, some experiments, such as

those conducted by Kyriacou et al. [304], suggest that while brain tissue may behave incompressibly under impact or short-duration processes, it can exhibit compressibility in long-term or quasi-static scenarios. The decision to model brain tissue as compressible or incompressible should, therefore, depend on the specific situation under study.

These are only some of the key characteristics of brain tissue, which will be utilised to construct the mechanical model presented in Chapter 2. Additional properties will be further explored and discussed in Chapter 3. Understanding and characterising brain tissue is essential for a deeper insight into brain tumours and their behaviour within the brain's complex structure.

1.1.2 Brain tumour progression, metabolism, and nutrient supply

Among the numerous issues caused by the growth of malignant brain tumours, the expansion of neoplastic tissue inevitably results in unnatural displacement of the normal cerebrum. As a consequence of this anomalous tissue motion within the skull fixed volume, the tumour can exert considerable pressure and solid stress onto the surrounding healthy tissue, leading to changes in neurological functionalities and in the flow of extracellular fluid. These side effects caused by a tumour growing within the brain are known as *mass effect* and can cause severe neurological dysfunctions, such as fatigue or drowsiness, alterations of consciousness, problems with vision, nausea and vomiting, headaches, epilepsy and seizures, changes in personality and other psychiatric disorders [8, 12, 343, 453, 475]. In general, the growth of a solid mass is associated with an increase in intracranial pressure, which in turn may provoke alterations in brain functions and cerebrospinal fluid flow obstruction. In particular, recent experiments and clinical evaluations underscored the relevant role played by solid stresses in addition to fluid pressure [443] and it was hypothesized that stresses in the tumour microenvironment may promote immune escape [385]. Moreover, pre-surgery tissue displacement due to mass effect may also be an indicator of the overall patient survival expectations [459]. Indeed, the development of unnatural strains and stresses due to tumour growth has been recognized as a relevant prognostic factor, with a negative impact on the patient, especially in the skull-confined brain [199, 275, 374, 459]. For all these reasons, it is important to evaluate brain alterations, displacements, and stresses caused by tumour growth also in distant parts of the tissue with respect to the tumour location [459]. Clinically, the degree of mass effect can be assessed through Magnetic Resonance Imaging (MRI) by quantifying the displacement of some relevant biological structures (e.g. the midline shift, the lateral ventricle displacement [323, 459] or the maximum displacement magnitude of the ventricles [519]), the compression of fluid-filled structures that may result in the obstruction of brain ventricles, and the formation of oedema in the region close to the tumour lesion [459]. In particular, an accurate estimation of ventricular compression caused by the neoplastic mass may also improve the computational reconstruction and segmentation of medical images, which is important to capture the correct tumour volume [274].

Oxygen availability is another key factor influencing tumour cell behaviour, dictating whether cells adopt a migratory or proliferative phenotype and thereby affecting their invasiveness and aggressiveness. Oxygen deprivation, or hypoxia, acts as a powerful environmental stressor, triggering mutations that profoundly impact tumour progression and dynamics [352]. Clinically, solid tumours exhibit heterogeneous oxygen distribution, with regions ranging from well-oxygenated to severely hypoxic. This variability in oxygen levels plays a pivotal role in tumour cell movement, guiding cells toward more favourable regions. Brain tumour cells often migrate along pre-existing pathways, such as perivascular spaces and white-matter tracts, enabling their

spread to distant areas within the brain parenchyma or leptomeningeal space [445]. Beyond influencing migration, oxygen availability also shapes tumour cell phenotypes and their interaction strategies. In hypoxic conditions, tumour cells undergo molecular and morphological adaptations, enabling them to survive in low-oxygen environments and evade apoptosis. The proliferation and migration dichotomy, commonly referred to as the *Go-or-Grow* mechanism, is essential for understanding brain tumour behaviour [198, 208, 211, 239]. In this model, tumour cells alternate between two phenotypes: proliferative cells that focus on rapid division and tumour expansion, and migratory cells that prioritise movement and invade new areas of the brain. The ability of tumour cells to alternate between these phenotypes complicates treatment, as therapies aimed at eliminating rapidly proliferating cells may leave migratory cells untouched, facilitating further invasion.

Additionally, tumour cells activate other mechanisms in response to a hypoxic environment. These adaptive responses include the secretion of factors that promote angiogenesis, the formation of new blood vessels. Another key response is the activation of glycolysis, which allows tumour cells to generate energy even in the absence of sufficient oxygen. In hypoxic regions of tumours cells shift to a glycolytic metabolic phenotype, relying on glucose as their primary energy source [497]. In 1956, Otto Warburg discovered that cancer cells tend to shift their glucose metabolism and energy production towards anaerobic glycolysis, even when oxygen is available [509]. This metabolic pathway converts glucose into pyruvate, which is then transformed into lactate and released into the extracellular environment. While anaerobic glycolysis generates only two molecules of ATP (adenosine triphosphate) per glucose molecule, far less than the 36-38 ATP molecules produced by complete cellular respiration, it is a faster process. This rapid ATP production enables cancer cells to survive in intermittently hypoxic conditions, commonly found in poorly vascularised tumours or areas with unstable blood vessel growth [141]. For this reason, it is common to observe a symbiotic relationship between tumour cell subpopulations, where hypoxic, glucose-dependent cells secrete lactate, and normoxic cells sustain their proliferation via oxidative phosphorylation, i.e. they rely on oxygen as their primary source of energy.

When it comes to accessing vasculature in brain tumours, the newly formed blood vessels are often structurally abnormal and functionally compromised. These vessels frequently exhibit irregular branching patterns, inconsistent diameters, and incomplete basement membranes. As a result, they are prone to leakage and inefficient blood flow, leading to uneven oxygen and nutrient delivery to tumour cells. This disorganised vascular network contributes to regions of hypoxia within the tumour, which in turn drive tumour aggressiveness and resistance to conventional therapies. The inefficient blood supply also poses challenges for the effective delivery of therapeutic agents, further complicating treatment outcomes. Additionally, the heightened permeability of these abnormal vessels can cause elevated intracranial pressure, exacerbating symptoms and worsening the patient's condition. Gaining a deeper understanding of these vascular abnormalities is essential for overcoming the challenges they pose and for designing more effective treatment strategies tailored to brain tumours.

A mechanical model that incorporates mass effect is detailed in Chapter 2. Additionally, Chapter 5 presents a mathematical model of brain tumour progression, capturing both hypoxic and normoxic conditions. Furthermore, Chapter 6 analyse the role of vasculature in tumours and explores various approaches for integrating it into mathematical models.

1.1.3 Clinical therapies for brain tumours

The treatment of brain tumours is complex and varies significantly based on the type, size, location, and aggressiveness of the tumour, as well as the patient's overall health. Currently, the most prevalent approach is multimodal, where various therapies are combined to enhance the treatment's effectiveness. This personalised protocol is crucial, as it tailors treatment plans to each patient's specific condition, weighing the benefits and risks of each modality [346].

Surgical resection remains a cornerstone in the treatment of brain tumours, with the primary objective of removing as much of the tumour mass as possible, ideally 70% or more, while preserving the patient's neurological function. Generally, a better prognosis is linked to a greater extent of tumour removal. However, the success of surgery is highly dependent on the tumour's location. In some cases, complete resection is not feasible without risking significant damage to critical brain areas, potentially leading to neurological deficits. While surgery is essential, it is often insufficient on its own to prevent tumour recurrence, a persistent challenge in managing brain tumours. Recent advancements in surgical techniques have enhanced treatment options. Fluorescence-guided surgery (FGS), for example, uses fluorescent markers to improve tumour visualization, aiding in more precise and complete tumour removal [390]. Another innovation is robot-assisted neurosurgery, which is increasingly employed to improve precision and potentially enhance patient outcomes [350]. Additionally, laser interstitial thermal therapy (LITT) is an emerging minimally invasive technique used to treat brain and spinal cord tumours. LITT employs laser energy to heat and ablate tumour tissue, offering a promising option for certain cases [166].

Radiotherapy (RT), the use of targeted radiation, has been a standard treatment for brain tumours since 2005, particularly in the post-operative phase. Radiotherapy has been effective in improving survival rates and is used both as a palliative measure and as a primary treatment when surgical resection is not an option. Radiation therapy works by using ionizing radiation, typically delivered through a linear accelerator, to control or eliminate malignant cells. In the treatment of high-grade gliomas, the standard dose is 60 Gy, administered in 30-33 fractions, with Gy (gray) representing the absorbed radiation energy per kilogram of tissue. Hypofractionated radiotherapy, which delivers fewer but higher-intensity treatments over a shorter period, is instead beneficial for elderly patients as it reduces treatment duration while maintaining effectiveness. Advances in imaging technology have greatly enhanced the precision of radiotherapy for glioma patients, enabling more accurate determination of the tumour's gross volume (GTV) and improving the planning treatment volume (PTV) to ensure more targeted radiation while minimising damage to surrounding healthy tissue. Modern techniques like intensity-modulated radiotherapy (IMRT) [161] and stereotactic radiosurgery (SRS) [395] offer even greater precision, particularly for tumours located in sensitive or difficult-to-reach areas of the brain. However, despite these advancements, the challenge of preventing tumour recurrence remains significant.

The last standard treatment is *chemotherapy* (CH). Chemotherapy involves the use of drugs that act within cells to inhibit or slow down mitosis and cell division, targeting both healthy and tumour cells. Since most normal adult cells are not actively dividing, they are generally unaffected by chemotherapy. However, certain cell types, such as those in the bone marrow, hair follicles, and the lining of the gastrointestinal tract, are more susceptible, which explains the common side effects associated with the treatment. In the treatment of brain tumours, chemotherapy commonly centres on the drug Temozolomide (TMZ). Approved for recurrent glioblastoma (GB) in 1999 and for primary GB in 2005, its use became formalised in the widely adopted Stupp protocol [466,

467]. Numerous studies have demonstrated that TMZ reduces the relative risk of death, and it is favoured over other chemotherapy drugs due to its relatively less severe side effect profile [119].

There are cases in which gross resection of the mass is not feasible, mainly due to tumour location. This especially happens for patients with multifocal or eloquently located[1] glioblastomas [323] and for deeply infiltrating tumours in locations not amenable to surgery [334], which exhibit an unacceptable risk of post-operative neurological deficits. In these situations, appropriate chemoradiation therapies are even more relevant to reduce tumour burden and extend the survival time of patients while minimizing the side effects [54, 63, 323, 334]. However, the treatment and prognosis for brain tumours have only seen marginal improvement over the last decade due to the complexity of the tumour microenvironment and the limited ability of drugs to penetrate the blood-brain barrier [518]. Indeed, even with currently accepted care protocols, the median survival time does not exceed 15 months [467], and is even less in the absence of surgery [323, 466]. As a result, there is a pressing need for the development of novel and more effective therapeutic approaches to enhance outcomes for patients with brain cancer. Several different drugs, e.g. bevacizumab or irinotecan, as a substitute for or in combination with TMZ have recently been tested [287, 334], sometimes with limited success [107, 287].

New and evolving treatment modalities such as *targeted therapies* and *gene therapy* are showing encouraging results in the treatment of brain tumours. Targeted therapies aim to inhibit specific molecular pathways involved in tumour growth and progression. Among these targeted therapies, angiogenesis inhibitors, which block the formation of new blood vessels that supply the tumour, have been tested as anti-migratory agents for gliomas. A notable example is bevacizumab, a monoclonal antibody that neutralizes VEGF. This drug has shown promising responses in patients with recurrent malignant gliomas when used in combination with other treatments [426]. However, its overall efficacy remains a subject of debate, and ongoing research continues to explore its potential. In fact, antiangiogenic treatment can exacerbate hypoxic effects [460] and cause brain tumour mass fragmentation, cancer cell migration, and tissue invasion [67, 301, 305, 436]. Additionally, intravenous integrin inhibitors, such as cilengitide, have demonstrated effectiveness in inducing apoptosis in U87 glioma cells, while broad-spectrum MMP inhibitors, like marimastat, have shown potential when combined with TMZ [229, 515]. Although these combinations appear promising, further research is needed to fully assess their side effects. Moreover, the treatment modality known as tumour treatment fields (TTFs), which applies low-intensity alternating electrical fields to disrupt cell division, has demonstrated a significant effect on patient survival [89, 407]. However, the daily application of TTFs for up to 18 hours and its high cost have limited its widespread adoption in clinical practice. Gene therapy, another promising avenue, involves the introduction of genetic material into cells to correct genetic abnormalities or enhance the body's natural defences against tumour growth. These emerging therapies represent a promising future in brain tumour treatment, with the potential to significantly improve patient outcomes. However, many of these approaches are still under investigation, and further clinical trials are necessary to determine their long-term efficacy and safety [510].

Finally, another promising treatment is represented by *immunotherapy*. Immunotherapy aims to generate a specific immune response that targets tumour cells, inhibiting tumour growth whilst leaving healthy tissue unharmed [405]. Although not as widespread as conventional treatments, this technique has been approved for various

[1] In the jargon of neurosurgery, eloquent brain areas are defined as zones whose neurological function is clearly identified and hence, if injured, may lead to disabilities [244, 285].

types of cancer, including melanoma and prostate cancer. Consequently, there has been growing interest in its potential application for treating brain tumours. However, this approach faces several challenges, such as the presence of the blood-brain barrier (BBB), which confers immune privilege to the brain [7], the immunosuppressive nature of brain tumours, their intra-tumoural heterogeneity, and the presence of therapy-resistant tumour stem cells. Numerous clinical trials have been conducted and are currently underway, focusing primarily on four techniques: vaccines, immune checkpoint inhibitors, CAR-T cell therapy, and oncolytic viruses.

1. *Vaccines*. Cancer vaccines harness tumour-produced antigens to activate immune surveillance by enhancing the immune response. This process is complicated by the scarcity of specific antigens produced by GBM, which often vary in their expression. Encouraging results have been obtained using the EGFRvIII antigen, expressed in approximately 30% of cases, as a target. Technological advancements in sequencing and bioinformatics have also enabled the discovery of neoantigens—antigens produced by somatic tumour mutations. These can be utilised as triggers for T cells, potentially enabling highly specific targeted treatment [433]. Despite ongoing research for several years, the use of cancer vaccines remains in the study phase, with only three potential candidates reaching phase III trials as of 2023 [7].

2. *Immune checkpoint inhibitors*. During its growth, brain tumours create a highly immunosuppressive microenvironment that impedes immunocyte intervention. This effect is mediated by substances called cytokines, which activate immune checkpoints—receptors present on various immunocytes such as lymphocytes, natural killer cells, and dendritic cells—rendering them inactive. Immune checkpoint inhibitors are monoclonal antibodies that, when introduced into the organism, bind to these receptors, preventing their activation and restoring the normal immune response. As of 2023, several studies have been conducted, and phase III trials are ongoing, particularly targeting the programmed cell death protein 1 (PD-1), which has shown significant results in other types of tumours, and the T-lymphocyte-associated protein 4 (CTLA-4).

3. *Oncolytic viruses*. Another emerging therapy for tumour treatment in recent decades is the use of oncolytic viruses (OVs), administered intravenously or intratumorally. These are weakly pathogenic viruses capable of selectively attacking cancer cells without affecting healthy cells. They act both through direct elimination of target cells and by releasing damage-associated molecular patterns and pathogen-associated molecular patterns during infection, which effectively stimulate the immune system and alter the nature of the microenvironment. This type of treatment, already used in other cases such as prostate cancer, has considerable potential in counteracting the immunosuppressive nature of brain tumours. Currently, several studies are underway, predominantly in phase I and II trials, utilising various viral strains.

4. *CAR-T cell therapy*. The use of Chimeric Antigen Receptor T-Cells is a treatment based on the genetic engineering of T lymphocytes. T cells are collected and separated from the patient's blood and engineered by introducing the CAR receptor, capable of recognising specific antigens produced by tumour cells. This receptor is connected via transmembrane regions to intracellular activation domains. The engineered cells are then reintroduced into the patient, where stimulation of the specific receptor triggers proliferation, cytokine release, and cytotoxicity, enabling

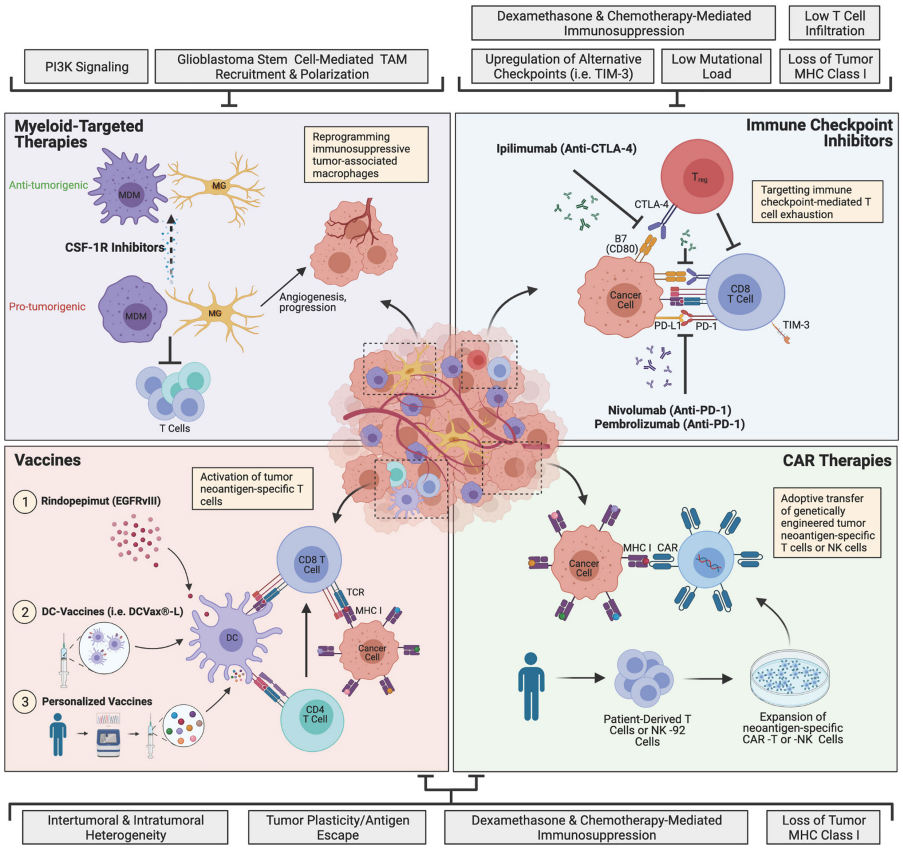

FIGURE 1.2: The current landscape of major glioblastoma immunotherapies and mechanisms of resistance. (Reprinted from [524]).

more effective combat against tumour cells. Various receptors are targeted by the engineered receptor, particularly EGFRvIII, which has already been the subject of study for vaccine therapies. The possibility of making them polyvalent has also been proposed. This therapy, already effective in treating lymphomas, is under study to overcome the difficulties posed by the presence of the BBB, which hinders immunocyte access to the brain, and the immunosuppressive nature of the brain tumour microenvironment.

In Chapter 2, we consider some possible modelling approaches of the standard therapies and protocols used in the clinical context to treat brain tumours patients. Furthermore, in Chapter 4, we introduce a mathematical model aimed at describing the growth of brain tumour cells during the course of the disease, their interaction with the immune system, and the potential effects of an immunotherapeutic treatment consisting of cytotoxic T lymphocyte infusion.

1.1.4 Medical imaging

Any mathematical model describing disease progression must be firmly rooted in the clinical context. Consequently, when relevant biological and clinical data pertaining to the mechanisms of interest are available, such information is extracted and applied to calibrate the model. The following section presents an overview of the key imaging techniques that offer valuable insights into brain tumours.

Magnetic resonance imaging (MRI) is currently the standard imaging modality for evaluating brain tumours. This non-invasive medical technique utilises strong magnetic

fields and radio waves to generate detailed images of the brain by exploiting the magnetic properties of water molecules within the body. By varying the intensity, timing, and duration of radio-frequency pulses and directional gradients, MRI can produce images with different contrasts, allowing for a nuanced view of brain structures. Among the most commonly used sequences are T1- and T2-weighted images, each highlighting distinct aspects of tumour progression [306, 496].

T1-weighted images, for example, are particularly useful in visualising vasculature-related characteristics of brain tumours, especially when a contrast agent like gadolinium is administered, which appears bright on these images. This sequence is often employed to delineate tumour boundaries and assess blood-brain barrier disruptions. On the other hand, T2-weighted images provide enhanced contrast between normal and abnormal brain tissue, as they are sensitive to changes in water content, making them valuable for detecting tumour oedema, cystic regions, and necrosis within the tumour. These two sequences are essential for a comprehensive evaluation of brain tumours, as they offer complementary insights into tumour morphology and surrounding tissue changes.

In addition to these standard sequences, several advanced MRI techniques have been developed to further characterise brain tumours. Diffusion-weighted imaging (DWI) and diffusion tensor imaging (DTI) are employed to quantify the apparent diffusion coefficient (ADC), with DTI offering the added capability of mapping the brain's microstructural architecture by determining the preferential directions of water diffusion. DTI's ability to capture anisotropic water diffusion allows for the visualisation of white matter neural tracts, providing insights into the directional flow of nutrients, cell migration, and tumour growth patterns. Magnetic resonance spectroscopy (MRS) is another advanced MRI technique that measures the concentrations of water-soluble metabolites, helping to detect tumour-specific mutations and assess intratumoural heterogeneity. This technique is often used to study metabolic changes within tumours, which can offer clues about tumour grade and aggressiveness. Finally, vascular perfusion imaging, also known as Perfusion-Weighted Imaging (PWI), plays a crucial role in identifying regions of elevated vascularity. This makes it an invaluable tool for predicting and assessing tumour responses to anti-angiogenic therapies.

In addition to MRI, positron emission tomography (PET) scans have become a valuable functional imaging tool [306]. PET provides insights into the metabolic and physiological processes of brain tumours by using radioactive tracers to visualise the distribution of specific molecules at high sensitivity. This can help in assessing tumour metabolism, identifying areas of high cellular activity, and monitoring treatment response.

None of these imaging techniques alone provides a complete picture of brain tumour progression. Each modality offers unique insights into specific aspects of the tumour and its surrounding environment, but also has limitations. Therefore, using a combination of these imaging techniques is essential to obtain a comprehensive understanding of the tumour's characteristics and behaviour.

An illustrative example of some of the described techniques is provided in Figure 1.3. In this thesis, MRI and DTI are specifically employed to address these challenges by accurately capturing the brain's geometry and its anisotropic features. These techniques are crucial for the mathematical models explored in Chapter 2 and 5.

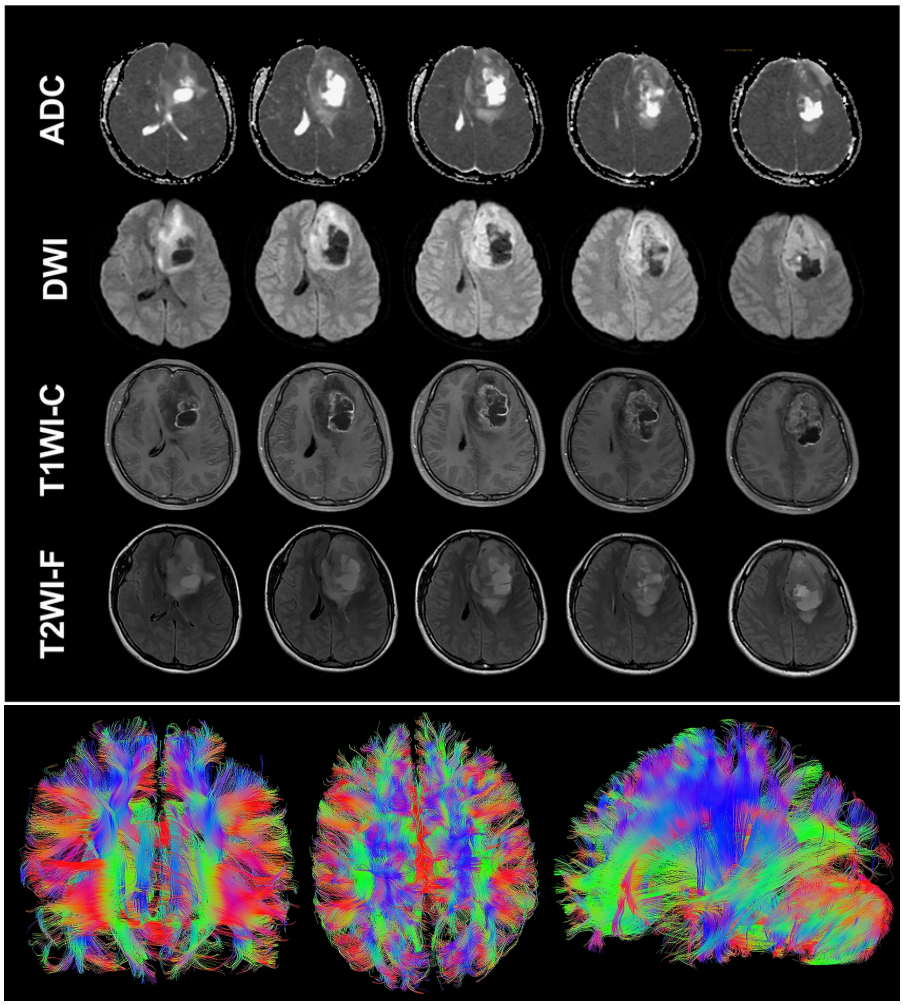

FIGURE 1.3: First figure: MRI images of the brain in patients with grade IV glioma, including apparent diffusion coefficient (ADC), diffusion-weighted imaging (DWI), T1-weighted contrast-enhanced, and T2-weighted FLAIR images, revealed tumour presence and significant surrounding brain edema.
(Source [506]; used under the terms and permission of License CC BY 4.0, see https://creativecommons.org/licenses/by/4.0/)
Second figure: Diffusion Tensor Imaging (DTI) used to track white matter fibres along their whole length.
(Image credits: Diffusion Tensor Imaging Traumatic Brain Injury, written by Brandon A. Woodard, see https://www.porterrennie.com/blog/diffusion-tensor-imaging-traumatic-brain-injury)

1.2 Mathematical models of brain tumours

Despite significant advancements in clinical practice, supported by novel therapies and sophisticated imaging techniques, the treatment of brain tumours remains insufficiently effective in many cases due to the aggressive nature of cancer and the delicate structure of brain tissue. Brain tumours are known for their high invasiveness, and even with the best available treatments, complete eradication is often difficult to achieve without damaging healthy brain tissue. This challenge highlights the need for alternative approaches that go beyond traditional clinical methods.

In response to these challenges, over the past three decades, mathematical modelling of brain tumour growth has gained increasing attention from the research community. The primary goal of these models is twofold. First, they serve as powerful tools to enhance the understanding of tumour progression, providing a deeper, quantitative insight that complements clinical observations. By simulating tumour behaviour under different conditions, mathematical models can help clarify the underlying mechanisms of cancer growth, invasion, and response to treatment. Second, the insights gained from these models through *in silico* simulations can be utilised to develop personalised therapeutic strategies. Personalisation is particularly critical in the treatment of brain tumours, where the location of the tumour and its interactions with surrounding tissues can significantly impact the success of treatments. Simulations can be used to predict how a specific tumour will grow and respond to therapies, enabling the design of treatment plans tailored to the individual patient's tumour characteristics. This is essential for maximising the effectiveness of treatments while minimising harmful side effects, which is especially important given the sensitive nature of brain tissue.

The success of mathematical models in accurately predicting tumour behaviour depends heavily on their ability to integrate clinical data. Models must be carefully calibrated and validated using real-world data to ensure that they reflect the complex biological processes involved in tumour growth. Furthermore, the brain's unique environment, characterised by its highly structured tissue, blood-brain barrier, and heterogeneous microenvironment, must be accurately described within these models, as these factors have a significant impact on tumour progression. The close interaction between the tumour and its surrounding microenvironment, including oxygen availability, nutrient supply, and interactions with the extracellular matrix, all play crucial roles in tumour dynamics and must be incorporated into the model framework [110, 240, 443, 459].

Thus, mathematical models, when developed and applied effectively, offer the potential to bridge the gap between theoretical understanding and practical application in the treatment of brain tumours. By doing so, they hold the promise of improving patient outcomes and advancing the field of oncology through more precise and targeted interventions. To achieve these goals, models of brain tumour growth have become increasingly refined during the years: to give an overview, in Table 1.1 we summarise some of the main contributions that appear in the literature. For detailed and extensive reviews on brain cancer modelling, we refer to [15, 177, 240, 412].

In particular, a first distinction between models can be made according to the mathematical framework they use, which is strictly related to the scale that is considered. The progression of brain tumours is a highly complex process governed by phenomena occurring across multiple spatial and temporal scales. These range from subcellular processes to cellular interactions and, ultimately, tissue-level dynamics. Understanding the mechanisms driving glioma evolution requires a multiscale approach. This intrinsic multiscale nature of the biological system necessitates focusing on three key levels. More specifically:

Type of Model	References	Mechanics	Imaging
CA	[38, 39, 76, 239, 277, 282, 491]	No	No
ODE	[49, 265]	No	No
ABM	[347–349]	No	No
ABM – PDE – RD	[206, 207]	No	No
PDE – RD	[430, 480–485, 494, 517]	No	Yes (CT+MRI)
PDE – RD	[269]	No	Yes (MRI+DTI)
PDE – RD	[238]	No	Yes (DTI)
PDE – ARD	[289]	No	No
PDE – ARD	[477]	No	Yes (DTI)
PDE – ARD – KM	[388, 479]	No	Yes (DTI)
ODE – PDE – ARD – KM	[129, 130, 169–172, 263]	No	Yes (DTI)
PDE – ARD – CM	[75, 123, 167, 249]	Yes (LE)	Yes (MRI+DTI)
PDE – CM	[164, 165, 303]	Yes (NLE)	Yes (MRI+DTI)
PDE – CM	[357]	Yes (FL)	No
PDE – CM	[27, 28]	Yes (NLE)	Yes (MRI+DTI)
PDE – CM	[338]	Yes (NLE)	Yes (MRI+DTI)
PDE – CH	[4–6, 125, 177]	Yes (FL)	Yes (MRI+DTI)
PDE – CH – CM	[319]	Yes (FL)	Yes (MRI+DTI)
HYB	[191, 290, 291, 440]	No	No
HYB	[489, 527]	No	No

TABLE 1.1: Summary of previous contributions concerning brain tumour modelling. The models are classified according to three criteria: (i) the mathematical framework employed to describe the growth of the tumour mass (first column); (ii) the inclusion of tumour and tissue mechanics with quantification of deformations and stresses (third column); (iii) the use of patient-specific imaging data to perform simulations (fourth column). Abbreviations: CA = Cellular Automaton; ABM = Agent-Based Model; ODE = Ordinary Differential Equations model; PDE-RD = Reaction-Diffusion equations; PDE-ARD = Advection-Reaction-Diffusion equations; PDE-KM = Kinetic model; PDE-CH = Cahn-Hilliard model; PDE-CM = Continuum-Mechanics-based model; HYB = Hybrid model; FL = Fluid; LE = Linear elasticity; NLE = Nonlinear elasticity.

- *Microscopic* and *mesoscopic models* provide a description of phenomena taking place at the subcellular or cellular scale. These types of models mainly fulfill the objective of reproducing the early growth of brain tumours, accounting explicitly for interactions at the cellular level: most of them are Cellular Automata (CA), Agent-Based Models (ABM) or Ordinary Differential Equations (ODE) models. These models tend to be computationally faster than those operating at higher scales. They focus mainly on subcellular or cellular level. The subcellular scale represents interactions between molecules and receptors on the cell membrane, which drive cell migration in response to external stimuli and involve alterations in signalling cascades. The cellular scale, on the other hand, models various intercellular interactions, such as those between tumour cells and the extracellular matrix (cell-ECM interactions) or between tumour cells themselves (cell-cell interactions).

- On the other hand, *macroscopic models* based on Partial Differential Equations (PDE) do not consider the intrinsically discrete nature of tumours, in exchange for a more flexible description performed through continuous variables. These models can be obtained from lower-level descriptions through appropriate scaling techniques, as individual cell behaviour is fundamental in driving macroscopic processes, highlighting the importance of linking multiple scales. However, it is also possible to formulate these models directly at the macroscopic level, relying on mechanical or phenomenological assumptions. This approach is commonly used when the complexity and nonlinearity of certain mechanisms make it difficult to rigorously derive a macroscopic system from lower-level descriptions. The first works [480–484, 494, 517] using reaction-diffusion equations for the migration and proliferation of gliomas paved the way for a number of subsequent studies, with an increasing level of detail. Macroscopic models represent the dynamics of cell populations at the tissue level, capturing tumour growth through mechanisms of proliferation and migration. Another approach recently proposed to tackle the problem of brain tumour proliferation employs a Cahn-Hilliard-type (CH) equation to deal with the infiltrative nature of some brain tumours, showing a good agreement with real data [4–6, 125, 177].

- *Multi-scale formulations* bridging the microscopic and macroscopic levels, grounded in Kinetic Models (KM) and their scaling [129, 130, 169–172, 263, 388, 479], offer a compelling extension to purely diffusive, phenomenological models. This approach seeks to connect macroscopic cell behaviour with the underlying dynamics at both the subcellular and individual cell levels. As noted earlier, incorporating all relevant temporal and spatial scales is crucial for a more comprehensive understanding of brain tumour progression.

As discussed above, a fundamental improvement to build reliable models for clinical applications is the inclusion of realistic imaging data, which may be used both for the estimation of parameters and for performing simulations on real geometries. In particular, the very first works [480–484, 494, 517] employed Computed Tomography (CT) and Magnetic Resonance Imaging (MRI) to extrapolate numerical values for the model parameters and to introduce a spatial distinction between white and grey matter. Then, the progress in Diffusion Tensor Imaging (DTI) allowed to account for the intrinsic anisotropy of brain tissue and became of great interest in the modelling process [269].

In the following subsections, we provide a comprehensive review of the literature related to the modelling approaches that will be employed in the subsequent chapters.

Mechanical models

The majority of the models mentioned so far does not take into account the mechanical impact of the growing tumour mass on the healthy brain tissue. Instead, the deformation induced by the proliferating cancer onto the surrounding areas may be harmful for the patient, since it may lead to damage in brain functionalities. In this respect, recent experimental works [108, 380, 381, 443] pointed out the preeminent role of solid stresses due to brain tumour expansion, in addition to the effects of fluid pressure. Moreover, the distribution of such stresses appears to be different even in tumours that exhibit similar imaging volumes [380, 459]. Therefore, it is important to have models that are able to capture the mechanical effects of a tumour inside the skull, to precisely evaluate the brain area affected by the cancer and the consequent possible risks for the patient.

Motivated by these facts, some recent models exploited the framework of Continuum Mechanics to provide a description of the so-called *mass effect* caused by the tumour. Early biomechanical models simplified the brain tissue by treating it as a linear elastic (LE) medium [75, 123, 249]. Clatz et al. [123] specifically combine a reaction-diffusion model, which simulates tumour invasion in the brain parenchyma, with a linear elastic constitutive equation for brain tissue to account for the mechanical interactions between the tumour and the surrounding invaded tissue. Later, more advanced models incorporated non-linear elastic (NLE) constitutive equations, such as Neo-Hookean or Mooney-Rivlin models, to better represent brain tissue mechanics [27, 28, 164, 165, 338]. For instance, Ehlers and Wagner [165] developed a three-phase model for brain tissue and drug delivery, which includes a hyperelastic, mechanically anisotropic solid skeleton, blood, and interstitial fluid. However, since their model does not account for the growth of the solid phase, it is not suitable for describing tumour progression. Modelling the mechanics of a growing mass introduces several challenges. Cells constantly proliferate and die, and tumour growth continuously remodels the surrounding environment. In solid tumours, determining an appropriate reference configuration for measuring deformations is particularly difficult, as the material itself is continuously changing [19, 152, 164, 219, 227, 338, 354, 414]. In the context of tumour growth modelling and biological applications, this challenge was addressed by [20, 21] through the introduction of the concept of *evolving natural configurations* [153, 337, 417]. In essence, this approach separates the evolution into pure elastic deformations and anelastic deformations resulting from growth. Recent studies on macroscopic models of brain tumour growth have adopted this framework [27, 28, 164, 354, 357].

However, most mechanical models do not account for anisotropic growth distortions. The latter are related to tumours growing preferentially along the white matter tracts and displacing the host tissue accordingly. Even though the mechanical framework proposed in [338] is able to evaluate the stress and strain fields associated with brain cancer expansion, it does not include the modelling of anisotropic distortions specifically related to growth. An attempt in this respect has been made in a recent work by Harkos et al. [236], where three different evolution equations for the growth stretches in the principal directions were introduced. However, such equations were based on a purely phenomenological exponential law, to preferentially drive growth along the direction of reduced compression [236, 340].

Another important issue that is generally overlooked in mechanical models of brain tumour growth is the description of therapeutic protocols. Previous mathematical studies about therapies for brain cancer can be found in [4, 51, 74, 128, 250, 263, 265, 321, 410, 430–432], which however are grounded on ordinary differential equations and kinetic equations, not discussing the interplay with mechanics. Recent investigations by Hormuth et al. [255, 257] considered the effect of Von Mises stress in a model for brain

tumour growth and response to chemoradiation. Notably, the stress was used to exponentially dampen the motility coefficient of tumour cells, while the mechanical constitutive equations remained relatively simplified, and fluid stresses were not considered.

A relevant feature that a quantitative mechanical model allows to introduce is the modification of DTI imaging data as a consequence of tumour growth [338]. Indeed, the growing mass displaces and dislodges the surrounding white matter fibres, causing a change in the preferential directions for water diffusion and cell movement. Since for patients affected by aggressive brain cancers it is often difficult to obtain multiple imaging scans at different times, the possibility of providing a computational modification of DTI data by means of mechanics may have valuable clinical implications.

Motivated by these observations, in Chapter 2 we propose a mechanical and computational framework which may be used to describe brain tumour growth, accounting both for a detailed mechanical representation and for the inclusion of patient-specific data. Furthermore, in Chapter 3, we present a detailed viscoelastic characterization of brain tissue, based on mechanical tests, which enhances the accuracy of describing the mechanical behaviour of brain tissues.

Mathematical models of heterogeneous cell populations

In the field of cellular modelling, the initial approach often treats cells as homogeneous entities, governed by a single set of rules. However, this simplification fails to capture the complexities observed in many biological systems, where heterogeneity at genetic, epigenetic, and phenotypic levels plays a crucial role. To address this limitation, researchers have developed models that accommodate diverse cellular behaviors and even allow for transitions between different cellular states. A fundamental strategy in modelling such heterogeneous populations involves categorizing cells into discrete compartments, each following distinct evolutionary rules. This approach is exemplified in individual-based and cellular automata models, where each cell is assigned a label representing its current phenotype, as demonstrated by Scianna et al. [442].

A significant advancement in this field came from Bürger [88], who introduced a non-local PDE model to describe mutation-selection dynamics in populations. In this model, the phenotypic state of each individual is represented by a continuous structuring variable, operating under fixed environmental conditions. The complexity of these models can be further analyzed using the Hamilton-Jacobi formalism, as shown by Diekmann et al. [154], enabling the derivation of an evolution equation for the most advantageous phenotypic state. This seminal work led to the development of a new direction in adaptive dynamics, focusing on non-local partial integro-differential equation (PIDE) models that describe the evolutionary dynamics of phenotype-structured populations. These models consider well-mixed populations, denoted as $n(t, \boldsymbol{y})$, where $t \geq 0$ represents time and $\boldsymbol{y} \in \mathbb{R}^d (d \in \mathbb{N})$ represents a continuous trait. The evolutionary dynamics of such a population can be described by a diffusive non-local variant of the classic Lotka-Volterra equation, as explored by various researchers [53, 333, 403]:

$$\begin{cases} \partial_t n - \beta \Delta_{\boldsymbol{y}} n = R(\boldsymbol{y}, \rho(t)) n \,, & \boldsymbol{y} \in \mathbb{R}^d \,,\ t \geq 0 \,, \\ \rho(t) = \displaystyle\int_{\mathbb{R}^d} n(t, \boldsymbol{y}) \mathrm{d}\boldsymbol{y} \,, & \\ n(0, \boldsymbol{y}) = n^0(\boldsymbol{y}) \in L^1\left(\mathbb{R}^d\right) \,, & n^0 \geq 0 \,. \end{cases}$$

In this equation, the diffusion term models spontaneous phenotypic variations at a rate $\beta > 0$. More sophisticated models have incorporated alternative mechanisms of phenotypic change, such as non-local terms for mutations occurring at birth [98, 154, 266, 370,

402] and advection terms representing stress-induced epimutations [113–115]. These initial-value problems are often tackled by employing an ε parametrisation and time scaling.

These mathematical frameworks have provided valuable insights into the emergence of intratumour phenotypic heterogeneity. For instance, Lavi et al. [308] demonstrated that elevated rates of phenotypic variation, particularly epimutations, contribute to increased intratumour phenotypic diversity. This finding suggests that strategies aimed at reducing such variation could potentially enhance the efficacy of targeted therapies. Subsequent investigations [116, 224, 325–327] have further elucidated the relationship between phenotypic variation rates and heterogeneity, revealing that stronger environmental selective pressures tend to diminish heterogeneity. In particularly harsh environments, tumour populations may face extinction. However, if they manage to persist, the equilibrium population size in constant environments is influenced by factors such as maximum fitness and death rates resulting from competition. Interestingly, in fluctuating environments, such as those characterized by cycling hypoxia, population sizes exhibit oscillatory behavior over time [32, 327]. Research has shown that in periodically changing environments, competing populations with higher rates of phenotypic variation gain an advantage, while lower rates prove beneficial in stable conditions [32, 33, 409]. This dynamic is particularly relevant in the context of vascularized tumours, where oxygen levels fluctuate between normoxia and various states of hypoxia depending on the proximity to blood vessels [32].

These models have also shed light on the development of therapeutic resistance in cancer. Early models examining cancer cell dynamics under therapy employed a continuous variable to represent the degree of therapeutic resistance. These studies revealed that while treatment acts as a selective force, phenotypic variation functions analogously to diffusion [224, 308, 332]. It was demonstrated that the administration of constant, high doses of cytotoxic drugs can trigger a selective sweep, favoring slow-proliferating cells with enhanced resistance, thereby reducing intratumoural phenotypic heterogeneity [115, 326]. However, in more challenging environments, the combination of high phenotypic variability and drug treatment can lead to population extinction, potentially resulting in more effective chemotherapy [326, 458]. Stace et al. [458] further explored this phenomenon by investigating combined chemotherapy and epigenetic therapy strategies. Additional research has evaluated the efficacy of various multidrug treatments and drug delivery schedules, including cytotoxic and cytostatic combination therapies, and comparing continuous versus intermittent drug administration [17, 116, 326, 332, 409]. Some models have also incorporated healthy cells to account for the collateral damage associated with chemotherapy [332, 409].

An extension of these models is represented by non-local PIDE frameworks that consider both space- and phenotype-structured populations. In this approach, populations are denoted as $n(t, \boldsymbol{x}, \boldsymbol{y})$, where $\boldsymbol{x} \in \mathcal{X} \subset \mathbb{R}^d$ indicates the position within a d-dimensional spatial domain. The evolutionary dynamics of populations undergoing explicit spatial movement can be modelled using non-local variants of the Fisher-KPP model. This framework assumes that individuals undergo undirected random movement, mathematically represented by a Fickian diffusion term, similar to the classic Fisher-KPP model [182]. Additionally, individuals experience mortality due to competition for resources and space with other individuals at their location, resulting in a non-local reaction term. A subset of these studies has focused on models where the structuring variable represents individual mobility, aiming to elucidate the mechanisms underlying spatial spread and phenotypic evolution in populations with varying motility, such as cane toads. These models are variations of non-local Fisher-KPP equations,

where the diffusion coefficient is dependent on the structuring variable, and phenotypic changes are incorporated through differential or integral operators [34, 69, 77, 78]. Analytical investigations of these models, often employing small parameterisation and asymptotic analysis, have revealed the existence of travelling front solutions. In scenarios with bounded motility, the most motile individuals are selected at the invasion front, while unbounded motility leads to front acceleration. Similar phenomena have been observed in a non-local advection-reaction-diffusion equation, where movement is driven not by Fickian diffusion but by random migration towards less crowded areas, resulting in a non-local advection term with velocity dependent on local population density [329].

A significant milestone in this field was achieved by Lorz et al. [331], who developed the first spatially explicit non-local PDE model for cancer phenotypic evolution with a continuous phenotypic structure. This model combined a non-local Lotka-Volterra equation with elliptic equations describing abiotic factor dynamics. This approach inspired further analytical research linking the balance equation for phenotypic distribution with abiotic factor equations, accounting for diffusion and consumption based on cell phenotypes [266, 369]. Subsequent work by Cho and Levy [117] enhanced this model by incorporating cell density-dependent drug permeability and pressure-driven cell movement, later expanding their investigations to examine asymmetric tumour growth and competition with healthy cells [118]. Lorenzi et al. [330] further advanced the field by introducing an influx term to model nutrient and drug inflow, employing 3D simulations of a human hepatic tumour. These studies collectively demonstrate that spatial gradients in abiotic factors can significantly influence phenotypic diversity and the emergence of resistant cells within tumours. Numerical simulations suggest that combination therapies may offer improved efficacy [117, 118, 331]. Building on these findings, Villa et al. [503] expanded on the work of Lorenzi et al. [330] by incorporating spatial diffusion and phenotypic variation, assessing the impact of tissue vascularization on phenotypic heterogeneity. In a related study, Fiandaca et al. [181] investigated resistance to hypoxia and acidity at various distances from blood vessels, revealing that resistance to hypoxia typically develops before resistance to acidity.

To the best of our knowledge, no studies have employed these types of models specifically to investigate the progression of brain tumours within a 3D environment representing the brain. Building upon these advancements and addressing this gap in the literature, Chapter 5 of this thesis employs spatial reaction-diffusion models incorporating non-local reaction terms to investigate brain tumour growth in environments characterized by fluctuating oxygen levels. This approach enables the explicit integration of a specific phenotypic trait—namely, resistance to hypoxia—which arises from these environmental variations, into the modelling framework. By doing so, we aim to elucidate the complex interplay between environmental heterogeneity and the emergence of phenotypic diversity within brain tumours.

Mathematical models of cancer immunotherapy

The rise of immunotherapy as a cancer treatment has driven the development of mathematical models aimed at describing the complex interactions between tumours and the immune system. To be effective, these models must first capture tumour growth and its natural interaction with the immune system before incorporating the effects of therapy. Given the complexity of biological mechanisms, selecting key parameters is essential to avoid overcomplicating the model and reducing the risk of overfitting [91]. Cellular populations, particularly tumour cells and immunocytes, are typically the focus. Immunocytes are often represented either collectively as effector cells or differentiated into

specific types, such as cytotoxic T lymphocytes (CTLs) and macrophages. The interactions between these cells and tumour cells are mediated by substances like cytokines and antigens, which are commonly included in models [296, 490].

Early models, such as predator-prey type ODE systems, simplified the dynamics to two equations for tumour and immune cells [302]. Kirschner and Panetta [293] introduced one of the first interaction models, successfully capturing tumour recurrence and immune cell overgrowth due to excessive therapy doses. Similar systems have been used to model immunotherapy with oncolytic viruses (OVs), either acting directly on tumour cells [516] or boosting immune defences [87]. Bunimovich's model was later expanded into a reaction-diffusion PDE system to account for spatio-temporal tumour dynamics [309]. Other research has introduced more complex systems of equations. For instance, [145, 146] proposed a six-equation system that includes different lymphocyte types (CD8+ and NK cells) alongside chemotherapeutic and immunotherapeutic agents. A five-equation model developed by Kirschner, Jackson, and Arciero [292] predicted responses to immune checkpoint inhibitors by tuning parameters for tumour cells, immune cells, and cytokines (TGF-β, IL-2, and siRNA). Models from [344, 488] focus on mechanisms that enable tumour cells to resist immune attack. Spatially explicit models incorporate diffusion and chemotaxis, as seen in [358, 471], where immune cells migrate towards tumour cells' chemical signals. Complex reaction-diffusion systems, such as the 13-equation model in [520], simulate immune checkpoint blockade therapy, taking into account cytokines, lymphocytes, and tumour dendritic cells. Moreover, an integro-differential system for three populations—lymphocytes, tumour cells, and chemoattractants—was proposed in [16], derived from the continuous limit of a hybrid discrete model for avascular tumours undergoing chemotherapy and immune checkpoint therapy. Hybrid discrete-continuous models represent cells on a lattice while chemical signals diffuse continuously, predicting the formation of immunosuppressive zones [511]. Similar approaches are used to simulate vaccine efficacy [389, 392].

Focusing specifically on brain tumours, models like the ODE system in [298] simulate the dynamics of grade III gliomas and glioblastomas in interaction with cytotoxic lymphocytes, including cytokines and MHC complexes. Variants of this model explore tumour stem cells [2] or simplify by maintaining only cellular populations, while the action of cytokines and antigens is modelled through the introduction of delays in the equations [406]. Another nine-equation ODE model [378] incorporates multiple lymphocyte and dendritic cell types, while hybrid ABM and delay models are used to simulate vaccine efficacy [288]. A simpler glioma-immune system interaction model, consisting of coupled ODEs, was proposed by Banerjee et al. [49], with coefficients fitted to in vitro and animal data. Further adaptations, including spatio-temporal extensions using partial differential equations (PDEs), have been developed in subsequent studies [283, 284].

In Chapter 4, we present a mathematical model that captures the dynamics of brain tumour cell growth throughout disease progression, their interaction with the immune system, and the potential impact of immunotherapy through cytotoxic T lymphocyte infusion.

Modelling of vasculature in tumours

To conclude the discussion of brain tumour modelling approaches, recent advances in mathematical modelling of vasculature in tumours have introduced novel frameworks that focus specifically on the interaction between tumour growth and the vascular network. While earlier models concentrated on tumour cell dynamics and their microenvironment, more recent efforts have incorporated the complex role of chemical and

fluid exchange between the vasculature and the tumour and possibly angiogenesis, the process by which tumours stimulate the formation of new blood vessels to sustain their growth. Traditional models, often based on reaction-diffusion equations, have provided insights into the spatial distribution of critical factors like oxygen and growth signals, but they face limitations in capturing the detailed structure of the vascular network. In response to these challenges, different mathematical models have been proposed, employing a range of approaches. These include continuous models [46, 93, 102, 103, 216, 318, 386, 500], as well as discrete and hybrid frameworks [10, 204, 363, 465, 501], with cell branching governed by either deterministic or stochastic rules. In some cases, the boundary between the capillary network and the surrounding tissue is tracked through a diffuse interface approach [500, 502], even if the proposed models are not suitable to evaluate the inner blood flow.

Recent advances in mathematical modelling have increasingly focused on understanding blood flow through newly formed vascular networks and the mechanisms of fluid transport in surrounding tissues. These studies build on the seminal work of Baxter and Jain, who developed both a macroscopic model for fluid and macromolecule transport in tumours with distributed vascular sources [60, 61] and a microscopic model to describe flow around individual vessels [62]. Subsequent research has introduced various mathematical models to describe blood flow in static vascular networks [99, 100]. More recently, efforts have been made to couple discrete angiogenesis models with continuous blood flow models. For example, some studies have expressed flow at each node of an evolving vascular network in terms of nodal pressures and flow resistances, ensuring mass conservation [444]. Similar techniques have been applied in other studies, which utilised discrete models to simulate the spatial and temporal evolution of vascular networks [10, 359, 462, 463]. In many of these studies, flow simulations are performed after generating the vessel network, either by using artificial hexagonal lattice structures [10] or cell migration models [359, 462, 463]. Rieger and colleagues introduced 2D and 3D cellular automata models to account for angiogenesis, vessel co-option, and vessel collapse in time-dependent blood flow and tumour growth simulations [55, 512, 513]. However, these approaches often constrain new vessels to a predefined grid, resulting in unnatural network geometries that can skew blood flow accuracy. Moreover, cellular automata-based methods are limited by computational constraints, restricting the size of the vascular network that can be simulated. To overcome these challenges, Berrone et al. [71] introduced a hybrid model that couples a continuous tissue and chemical diffusion model with a discrete tip-tracking angiogenesis model. This hybrid approach more accurately captures the motion of tip cells and subsequent vessel formation, providing a more realistic simulation of angiogenesis and blood flow within developing vascular networks. This refined understanding of vascular network formation and blood flow simulation opens the door to more realistic representations of tumour vasculature, enhancing the accuracy of tumour growth models.

To further enhance the accuracy of tumour growth models, multiscale approaches have gained prominence, with the homogenization technique emerging as an especially effective method for linking capillary and macroscopic scales [397, 451]. Homogenization allows for the modelling of tumour vasculature at the tissue level while incorporating the intricate details of the vascular network at finer scales, such as individual capillaries. By averaging the effects of small-scale vascular architecture across larger regions of tissue, this method provides a computationally efficient yet accurate representation of angiogenesis. Consequently, models that employ homogenization offer deeper insights into the dynamics of tumour blood supply and have become crucial for exploring therapeutic strategies that target the vascular system in brain tumours.

In Chapter 6, we apply asymptotic homogenisation to model transport phenomena in a growing anisotropic tissue, while also accounting for the complex architecture of the tumour vasculature. This represents an initial, simplified step toward gaining deeper insights into the role of vasculature in tumour growth and its potential responses to therapeutic interventions.

2 A mechanical model for simulating anisotropic brain tumour growth, white matter tract deformation, ventricular compression, and therapeutic protocols

2.1 Preliminaries

In this Chapter, a multiphase mechanical model for brain tumour growth is proposed, capable of quantifying anisotropic deformations, as well as solid and fluid stresses induced by the growing mass, while incorporating therapeutic protocols. A distinctive feature of this work is the investigation of cerebral ventricles compression, caused by tumour expansion, and the resulting alterations in their shape due to cancer-induced deformation.

The model builds upon the framework introduced in [338], with a key modification: the tumour and host tissue are clearly separated by a sharp interface that moves with the solid phase, leading to variables that are not necessarily continuous across this interface. Additionally, the model includes an anisotropic growth tensor designed to capture the directional preferences of brain fibres reconstructed from medical imaging data. Medical imaging has well established that brain tumours exhibit anisotropic growth patterns, influenced by cell migration along white matter tracts and blood vessels [75, 173, 209, 269, 279]. This approach generalizes biomechanical models based on isotropic growth [27, 28, 47, 164, 338] and contrasts with the model proposed by Harkos et al. [236], where the anisotropic growth tensor indirectly reflected patient-specific parameters. In [236], growth stretch rates evolved based on stresses influenced by Magnetic Resonance Elastography data, without direct reconstruction from imaging. Furthermore, the proposed model includes image-based diffusion and permeability tensors, the latter absent in [236]. These features enable the model to capture the irregular and heterogeneous growth patterns of brain tumours, which are shaped by surrounding anatomical structures [173, 495].

To establish a realistic three-dimensional brain geometry and ventricles' shape, patient-specific Magnetic Resonance Imaging (MRI) data were utilised. Diffusion Tensor Imaging (DTI), an MRI technique that measures anisotropic water diffusion to estimate axonal white matter organisation, was processed with a multi-compartment model to isolate free water contributions and emphasise water motion constrained by brain fibres. Additionally, the mechanical variables from the model were employed to adjust the DTI data as the tumour grew, capturing the deformation of the host tissue. By integrating tumour expansion and the resulting deformation of the brain environment, this model advances understanding of the complex interplay between tumour growth and its pathological effects.

The framework also incorporates a simplified therapeutic model, aimed at supporting the development of improved treatment strategies. Unlike recent studies that integrate mechanical effects into chemoradiation models for brain tumours [255–257], this approach accounts for nonlinear elasticity in both tumour and host tissue, guided by experimental data [45], and includes both solid and fluid stresses. The coupling between mechanics and growth is derived through physically motivated Continuum Mechanics principles. Although the feedback of stress on tumour growth is not explicitly considered here, it can be seamlessly integrated, as demonstrated in [338].

In detail, the remainder of this Chapter is organised as follows. In Section 2.2, we outline the mathematical model and the procedures to reconstruct its patient-specific anisotropic components. In Section 2.3 details on the derivation of the Lagrangian formulation of the model are provided. Then, in Section 2.4 the description of the numerical implementation and an estimate of the parameters involved are provided. Section 2.5 is devoted to the presentation and discussion of the main results concerning numerical simulations of the model. Finally, we conclude with Section 2.6, in which we summarise the main aspects of the work and we discuss some possible perspectives for future research.

A significant portion of the research detailed in this Chapter has been published earlier in [47, 48].

2.2 Eulerian modelling setting

In this Section, we introduce the Eulerian formulation of the model for tumour growth and expansion, based on mixture theory [23, 94, 418], which comprises a set of mass and momentum balance equations. Although this general framework could theoretically be applied to describe any solid tumour, we tailor it specifically to model brain tumour progression in a patient-specific context. The goal of this mathematical model is to assess the advancement of the disease, predict the evolution of tumour shape, and quantify the extent and location of damaged areas. We assume that the region occupied by the tumour, denoted by $\Omega_t(t)$, is completely separated from the surrounding healthy tissue, denoted by $\Omega_h(t)$, so that the boundary between the tumour and the surrounding environment can be described by a moving interface. Additionally, the cerebral ventricles are modelled as a hole within the domain, so the boundary of the brain domain is $\partial\Omega(t) = \partial\Omega_{out}(t) \cup \partial\Omega_v(t)$, where $\partial\Omega_{out}(t)$ represents the outer boundary, which can be interpreted as the skull, and $\partial\Omega_v(t)$ represents the boundary of the ventricular region (see Fig. 2.1 for a schematic representation). To properly study the impact of cancer growth on the ventricles without describing the complex mechanisms that may occur within them, appropriate boundary conditions must be imposed on $\partial\Omega_v(t)$.

Both the healthy region and the tumour region are treated as saturated domains consisting of two distinct phases: the cell population (labelled with subscript "s") and the interstitial fluid (labelled with subscript "ℓ"), which fill all the available space. Thus, the volumetric fraction of the cell population, ϕ_s, and the volumetric fraction of the liquid, ϕ_ℓ, satisfy the saturation constraint:

$$\phi_s + \phi_\ell = 1 \tag{2.1}$$

at any time and at any point in the brain domain $\Omega(t) = \Omega_h(t) \cup \Omega_t(t)$. In this description, the cellular phase represents healthy cells in $\Omega_h(t)$ and diseased cells in $\Omega_t(t)$, while the fluid phase includes interstitial brain fluid, blood, and nutrients in both regions. Furthermore, we assume that the materials composing the phases are incompressible, meaning that both phases of the mixture have constant true densities $\hat{\rho}_\alpha$, with

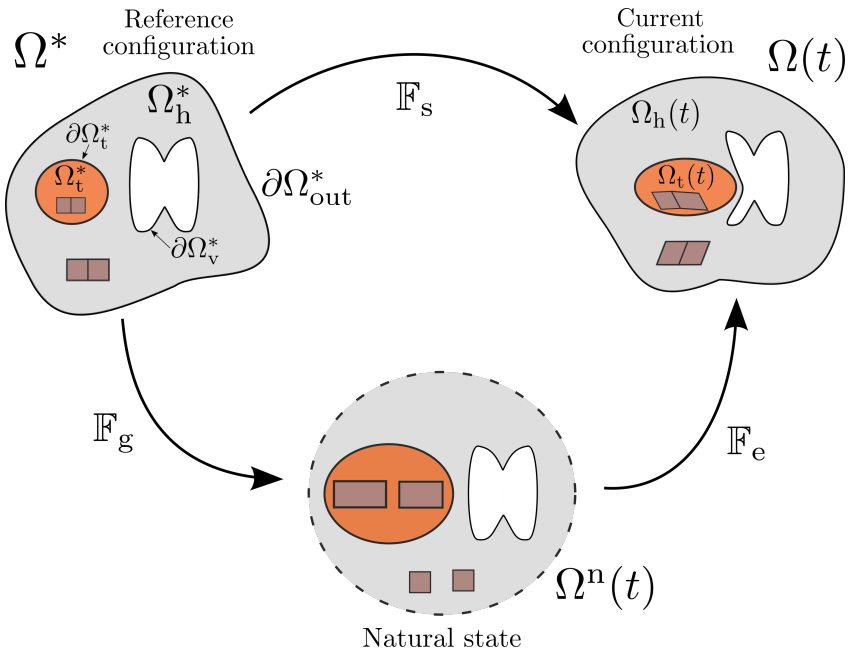

FIGURE 2.1: Multiplicative decomposition of the deformation gradient.

$\alpha \in \{\mathrm{s}, \ell\}$. Once the true density $\hat{\rho}_\alpha$ is specified, the partial phase density $\rho_\alpha := \hat{\rho}_\alpha \phi_\alpha$ of the material composing the α-phase is fully defined by knowing ϕ_α. Since cells are mainly composed of water, we assume that the true densities of both phases are equal, i.e., $\hat{\rho}_{\mathrm{s}} = \hat{\rho}_\ell$.

Throughout this chapter, we denote by Ω^*, Ω^*_{t}, and Ω^*_{h} the reference configurations of the whole brain, the tumour, and the host tissue, respectively, so that $\Omega^* = \Omega^*_{\mathrm{h}} \cup \Omega^*_{\mathrm{t}}$. It is important to note that the tumour region Ω^*_{t} in the reference configuration does not evolve over time. Similarly, $\partial\Omega^*_{\mathrm{v}}$ and $\partial\Omega^*_{\mathrm{out}}$ represent the outer skull and the ventricles boundary in the reference configuration. Regarding the differential operators, "Grad" and "Div" will denote the material gradient and material divergence with derivatives taken with respect to the material point in the reference configuration. In contrast, the notations ∇ and $\nabla\cdot$ will denote the gradient and divergence with respect to the spatial variable in the current configuration $\Omega(t)$. The deformation of the body from the reference configuration to the deformed one can be described using the map $\chi(\mathbf{X}, t)$, which assigns to each material point $\mathbf{X} \in \Omega^*$ its position $\mathbf{x}$ in $\Omega(t)$. By introducing the displacement field of the solid phase, defined by $\mathbf{u}_{\mathrm{s}}(\mathbf{X}, t) = \chi(\mathbf{X}, t) - \mathbf{X}$, we can define the *deformation gradient tensor* of the solid phase as $\mathbb{F}_{\mathrm{s}} = \mathbb{I} + \mathrm{Grad}\, \mathbf{u}_{\mathrm{s}}$, where $\mathbb{I}$ is the second-order identity tensor.

Moreover, the concept of evolving natural configurations is employed to properly describe the mechanics of the growing body. Using the modelling framework proposed in [20, 21] for growing tumours, this approach involves splitting the evolution into pure elastic deformations and deformations resulting from anelastic distortions, such as growth and remodelling. If we assume that a generic particle is cut out of the body and its stress state is relieved while keeping its mass constant, we find the *natural state* of such a particle at time t. The *natural configuration* of the body at time t is then the collection of all the particles in their natural states at time t, denoted by $\Omega^{\mathrm{n}}(t)$.

This allows us to measure the deformation from the natural configuration $\Omega^{\mathrm{n}}(t)$ to $\Omega(t)$ through the tensor $\mathbb{F}_{\mathrm{e}}$, which is connected to the material's stress response, while the transition from the reference configuration Ω^* to the natural configuration is described by the tensor $\mathbb{F}_{\mathrm{g}}$, directly related to growth, hence called the *growth tensor*. This

decomposition is illustrated in Fig. 2.1.

In summary, the deformation gradient $\mathbb{F}_s$ indicates how the body deforms locally when transitioning from the reference configuration Ω^* to $\Omega(t)$, while $\mathbb{F}_e$ shows the local deformation from the natural configuration $\Omega^n(t)$ to $\Omega(t)$, and $\mathbb{F}_g$ shows local growth. The following multiplicative decomposition of the deformation gradient is therefore valid:

$$\mathbb{F}_s = \mathbb{F}_e \mathbb{F}_g \,. \tag{2.2}$$

Furthermore, since the deformation gradient $\mathbb{F}_s$ is invertible, it follows that $\mathbb{F}_e$ and $\mathbb{F}_g$ are also invertible. Indeed, the determinant of the deformation gradient can be expressed as

$$J_s = J_e J_g \,,$$

where $J_e = \det \mathbb{F}_e$ and $J_g = \det \mathbb{F}_g$. In particular, since we are dealing with growth processes, we have $J_g \geq 1$. Generally, if $J_g > 1$, the body is undergoing growth, while if $J_g < 1$, the body is undergoing resorption.

2.2.1 Mass and momentum balance laws

Balance laws in the tumour region $\Omega_t(t)$

To derive the balance equations of our model, we firstly focus on the region occupied by the tumour. We assume that, in this region, cells proliferate since the tumour is growing. Hence, the mass and momentum balances for each phase $\alpha \in \{s, \ell\}$ read

$$\frac{\partial \phi_\alpha}{\partial t} + \nabla \cdot (\phi_\alpha \mathbf{v}_\alpha) = \Gamma_\alpha(\phi_s, c_n, t) \,, \tag{2.3}$$

$$\hat{\rho}_\alpha \phi_\alpha \left(\frac{\partial \mathbf{v}_\alpha}{\partial t} + \mathbf{v}_\alpha \cdot \nabla \mathbf{v}_\alpha \right) = \nabla \cdot \widetilde{\mathbb{T}}_\alpha + \hat{\rho}_\alpha \phi_\alpha \mathbf{b}_\alpha + \widetilde{\mathbf{m}}_\alpha \,, \tag{2.4}$$

where $\mathbf{v}_\alpha$ is the velocity of the α-phase, $\widetilde{\mathbb{T}}_\alpha$ is the partial Cauchy stress tensor of that phase, Γ_α is the mass growth rate and $\widetilde{\mathbf{m}}_\alpha$ represents the rate at which the α-phase exchanges momentum with the other phase. Then, the mixture is assumed to be closed with respect to mass, i.e., $\Gamma_\ell = -\Gamma_s$, so that mass exchanges occur only among the constituents taken into account. A precise definition of $\Gamma_s(\phi_s, c_n, t)$ is reported in Section 2.2.3. Moreover, external body forces (such as the gravitational force) included in $\mathbf{b}_\alpha$ as well as inertial effects are negligible, since the motion of cells and interstitial fluid is very slow, when dealing with biological growth phenomena. Thus, Eq. (2.4) becomes

$$\nabla \cdot \widetilde{\mathbb{T}}_\alpha + \widetilde{\mathbf{m}}_\alpha = \mathbf{0} \,. \tag{2.5}$$

The term $\widetilde{\mathbf{m}}_\alpha$, with $\alpha \in \{s, \ell\}$, can be decomposed, using thermodynamics arguments [219], into a dissipative and a non-dissipative part as $\widetilde{\mathbf{m}}_\alpha = \overline{\mathbf{m}}_{\alpha\beta} + p \nabla \phi_\alpha$, where p is the pressure of the interstitial fluid and the term $\overline{\mathbf{m}}_{\alpha\beta}$ represents the dissipative force acting on the α phase due to the other phase, denoted by subscript β. By invoking the action-reaction principle and the saturation condition (2.1), it holds that

$$\overline{\mathbf{m}}_{s\ell} = -\overline{\mathbf{m}}_{\ell s} \,. \tag{2.6}$$

We remark that, in defining the momentum exchange between phases, we neglected the exchange rates associated with the mass sources and sinks Γ_α, $\alpha \in \{s, \ell\}$. Such an assumption is reasonable in the context of avascular tumour growth, in which the velocities of both the solid and the fluid phase are small [219].

Following standard arguments in mixture theory, the Cauchy stress associated with the α-phase of the mixture can be written as the sum of a purely hydrostatic contribution, which indicates the amount of pressure sustained by the α-phase, and an effective stress

$$\widetilde{\mathbb{T}}_\alpha = -\phi_\alpha p \mathbb{I} + \mathbb{T}_\alpha \,.$$

Moreover, we require that the effective stress of the fluid phase $\mathbb{T}_\ell$ is negligible with respect to the pressure gradient and to the interaction forces between fluid and solid phase. As a consequence, Eq. (2.5), specialised for the two phases, becomes

$$-\phi_{\mathrm{s}} \nabla p + \nabla \cdot \mathbb{T}_{\mathrm{s}} + \overline{\mathbf{m}}_{\mathrm{s}\ell} = \mathbf{0} \,, \tag{2.7}$$

$$-\phi_\ell \nabla p + \overline{\mathbf{m}}_{\ell \mathrm{s}} = \mathbf{0} \,. \tag{2.8}$$

The momentum balance for the mixture can then be obtained by summing (2.7) and (2.8), recalling the saturation condition (2.1) and the action-reaction principle (2.6):

$$-\nabla p + \nabla \cdot \mathbb{T}_{\mathrm{s}} = \mathbf{0} \,. \tag{2.9}$$

Furthermore, calling μ the dynamic viscosity of the fluid component, $\mathbb{K}$ the permeability tensor and taking $\overline{\mathbf{m}}_{\ell \mathrm{s}} = -\mu \phi_\ell^2 \mathbb{K}^{-1} (\mathbf{v}_\ell - \mathbf{v}_{\mathrm{s}})$ [219], it is possible to derive from (2.8) the well-known Darcy's law as a momentum balance for the fluid phase

$$\mathbf{v}_\ell = \mathbf{v}_{\mathrm{s}} - \frac{\mathbb{K}}{\mu \phi_\ell} \nabla p \,. \tag{2.10}$$

Balance laws in the healthy region $\Omega_{\mathrm{h}}(t)$

In the domain occupied by the healthy tissue we assume that the proliferation of cells is compensated by natural cell death, so that the net rate of growth is equal to zero (i.e. $\Gamma_{\mathrm{s}} = 0$). The closed mixture assumption implies that also the source term Γ_ℓ must be null. Hence, the mass balances in the healthy region can be written as

$$\frac{\partial \phi_\alpha}{\partial t} + \nabla \cdot (\phi_\alpha \mathbf{v}_\alpha) = 0 \,, \quad \text{with } \alpha \in \{\mathrm{s}, \ell\} \,.$$

As regards the momentum balance equations, they are the same as in the region occupied by the tumour, namely Eqs. (2.9) and (2.10). The differences in the mechanical properties between the healthy and the diseased tissues, affecting the stress tensor $\mathbb{T}_{\mathrm{s}}$, will be provided through the constitutive equations.

2.2.2 Stress tensor and constitutive equations

In order to close the system of mass and momentum balance equations and to understand how brain tumour growth influences mechanically the surrounding tissues, we have to determine an appropriate evolution law for the effective part of the Cauchy stress tensor $\mathbb{T}_{\mathrm{s}}$, associated with the cellular population, both in the diseased and in the healthy region. In analogy with [20], we assume that the mechanical response is hyperelastic from the natural configuration, that is, both the healthy brain tissue and the tumour are modelled as non-linear elastic materials.

Effective stress tensor in $\Omega_{\mathrm{t}}(t)$

In order to fully describe the elastic response, the generalized Ogden model [384] is often considered appropriate to represent the mechanical behaviour of soft brain tissue

[362]. In particular, we take into account the Mooney-Rivlin model, which represents a particular case of the generalized Ogden energy [45, 149, 362]. Let $\overline{\mathbb{C}}_e := J_e^{-\frac{2}{3}}\mathbb{C}_e$ be the isochoric part of the elastic right Cauchy-Green deformation tensor $\mathbb{C}_e := \mathbb{F}_e^T\mathbb{F}_e$. The strain energy density per unit volume of the natural configuration $\widehat{\mathcal{W}}_{sn}$ can be written as a function of the first two invariants of $\overline{\mathbb{C}}_e$ and J_e:

$$\begin{aligned}\widehat{\mathcal{W}}_{sn}\left(\overline{\mathbb{C}}_e, J_e\right) = \frac{1}{2}\mu_{1t}\left(\mathrm{I}_{\overline{\mathbb{C}}_e} - 3\right) + \frac{1}{2}\mu_{2t}\left(\mathrm{II}_{\overline{\mathbb{C}}_e} - 3\right) + \\ + \kappa_t\left(1-\phi_{sn}\right)^2\left(\frac{J_e - 1}{1-\phi_{sn}} - \ln\frac{J_e-\phi_{sn}}{1-\phi_{sn}}\right),\end{aligned} \tag{2.11}$$

where

$$\mathrm{I}_{\overline{\mathbb{C}}_e} := \mathrm{tr}\left(\overline{\mathbb{C}}_e\right), \qquad \mathrm{II}_{\overline{\mathbb{C}}_e} := \frac{1}{2}\left[\left(\mathrm{tr}\,\overline{\mathbb{C}}_e\right)^2 - \mathrm{tr}\left(\overline{\mathbb{C}}_e^2\right)\right].$$

The last term on the right-hand side of Eq. (2.11) describes volumetric changes in the solid skeleton, occurring below the compaction point, i.e., when all pores in the structure are closed and further volume deformations are impeded due to the incompressibility of the solid phase (see [163] for further details). Furthermore, ϕ_{sn} represents the volumetric fraction of the cell phase in the natural state and it has a constant value. Finally, μ_{1t} and μ_{2t} are the material parameters of the tumour tissue whereas κ_t is the elastic parameter associated with the response of the tumour to volumetric deformations. Given $\widehat{\mathcal{W}}_{sn}$, we can express the Cauchy stress tensor of the cellular phase as

$$\mathbb{T}_s = 2J_e^{-1}\mathbb{F}_e\frac{\partial\widehat{\mathcal{W}}_{sn}}{\partial\mathbb{C}_e}\mathbb{F}_e^T \quad \text{in } \Omega_t(t). \tag{2.12}$$

By working out the derivative in (2.12) we have

$$\begin{aligned}\frac{\partial\widehat{\mathcal{W}}_{sn}\left(\overline{\mathbb{C}}_e, J_e\right)}{\partial\mathbb{C}_e} &= \frac{\partial\overline{\mathbb{C}}_e}{\partial\mathbb{C}_e} : \frac{\partial\widehat{\mathcal{W}}_{sn}}{\partial\overline{\mathbb{C}}_e} + \frac{\partial J_e}{\partial\mathbb{C}_e}\frac{\partial\widehat{\mathcal{W}}_{sn}}{\partial J_e} \\ &= J_e^{-2/3}\left(\underline{\underline{\mathbb{I}}} - \frac{1}{3}\overline{\mathbb{C}}_e^{-1}\otimes\overline{\mathbb{C}}_e\right) : \frac{\partial\widehat{\mathcal{W}}_{sn}}{\partial\overline{\mathbb{C}}_e} + \frac{1}{2}J_e\mathbb{C}_e^{-1}\frac{\partial\widehat{\mathcal{W}}_{sn}}{\partial J_e},\end{aligned}$$

where $\underline{\underline{\mathbb{I}}}$ is the fourth-order identity tensor. For the particular choice of material constitutive relation (2.11), we have

$$\begin{aligned}\frac{\partial\widehat{\mathcal{W}}_{sn}}{\partial\overline{\mathbb{C}}_e} &= \frac{\partial\widehat{\mathcal{W}}_{sn}}{\partial\mathrm{I}_{\overline{\mathbb{C}}_e}}\mathbb{I} + \frac{\partial\widehat{\mathcal{W}}_{sn}}{\partial\mathrm{II}_{\overline{\mathbb{C}}_e}}\left(\mathrm{I}_{\overline{\mathbb{C}}_e}\mathbb{I} - \overline{\mathbb{C}}_e\right) = \frac{1}{2}\mu_{1t}\mathbb{I} + \frac{1}{2}\mu_{2t}\left(\mathrm{I}_{\overline{\mathbb{C}}_e}\mathbb{I} - \overline{\mathbb{C}}_e\right), \\ \frac{\partial\widehat{\mathcal{W}}_{sn}}{\partial J_e} &= \kappa_t\left(1-\phi_{sn}\right)\left(1 - \frac{1-\phi_{sn}}{J_e-\phi_{sn}}\right).\end{aligned}$$

Thus, the constitutive expression of the Cauchy stress tensor $\mathbb{T}_s$ becomes

$$\begin{aligned}\mathbb{T}_s = 2J_e^{-1}\mathbb{F}_e\left[J_e^{-2/3}\left(\underline{\underline{\mathbb{I}}} - \frac{1}{3}\overline{\mathbb{C}}_e^{-1}\otimes\overline{\mathbb{C}}_e\right) : \left(\gamma_1\mathbb{I} + \gamma_2\overline{\mathbb{C}}_e\right)\right]\mathbb{F}_e^T + \\ + \kappa_t\left(1-\phi_{sn}\right)\left(1 - \frac{1-\phi_{sn}}{J_e-\phi_{sn}}\right)\mathbb{I},\end{aligned} \tag{2.13}$$

where we have defined the quantities $\gamma_1 := \frac{1}{2}\mu_{1t} + \frac{1}{2}\mathrm{I}_{\overline{\mathbb{C}}_e}\mu_{2t}$ and $\gamma_2 := -\frac{1}{2}\mu_{2t}$. The constitutive expression of the Cauchy stress tensor should be accompanied by equations determining $\mathbb{F}_s$ and $\mathbb{F}_g$. The tensor $\mathbb{F}_s$ is entirely determined by the motion of the cell

phase and for this reason it is not an additional unknown for the model. In fact, it satisfies

$$\dot{\mathbb{F}}_s \mathbb{F}_s^{-1} = \nabla \mathbf{v}_s \,.$$

Finally, since we are considering a growth phenomenon, we also need to provide a constitutive equation which describes the evolution of the growth tensor $\mathbb{F}_g$ in the tumour region. We enforce the natural condition that the variation of body mass is given by the strain rate tensor associated with growth [22, 23, 219, 354], so that the following relation has to hold:

$$\mathrm{tr}\left(\mathbb{L}_g\right) = \frac{\Gamma_s(\phi_s, c_n, t)}{\phi_s}\,, \tag{2.14}$$

where $\mathbb{L}_g := \dot{\mathbb{F}}_g \mathbb{F}_g^{-1}$ is the strain rate tensor (or velocity gradient) associated to $\mathbb{F}_g$. This assumption also entails that the solid volumetric fraction in the natural state ϕ_{sn} is constant in time [23, 354]. For what concerns the inelastic distortions related to growth, several models in the literature consider $\mathbb{F}_g$ as isotropic (see for instance [21–23, 27, 219, 338, 354]). In this chapter, differently from previous mechanical models for brain tumour growth [27, 338], we present instead an anisotropic growth tensor. Indeed, clinical evidence showed that brain cancers often grow following the white matter tracts [75, 173, 210, 269, 279], which preferentially drive tumour expansion along certain directions. To include such an effect in our model, we will consider a general anisotropic growth tensor in the form

$$\mathbb{F}_g = g_1 \mathbf{w}_1 \otimes \mathbf{w}_1 + g_2 \mathbf{w}_2 \otimes \mathbf{w}_2 + g_3 \mathbf{w}_3 \otimes \mathbf{w}_3\,, \tag{2.15}$$

where $\mathbf{w}_i$, $i = 1,2,3$ are the unit orthogonal eigenvectors representing the principal directions of growth and g_i, $i = 1,2,3$ are the corresponding eigenvalues. Since the eigenvectors $\mathbf{w}_i$, with $i = 1,2,3$, are assumed to be time-independent, from Eq. (2.14) it follows that the three distinct eigenvalues of $\mathbb{F}_g$ must satisfy

$$\frac{\dot{g}_1}{g_1} + \frac{\dot{g}_2}{g_2} + \frac{\dot{g}_3}{g_3} = \frac{\Gamma_s(\phi_s, c_n, t)}{\phi_s}\,. \tag{2.16}$$

This condition is for instance fulfilled if the evolution laws of the eigenvalues g_i are written as:

$$\frac{\dot{g}_1}{g_1} = \beta_1 \frac{\Gamma_s(\phi_s, c_n, t)}{\phi_s}\,, \quad \frac{\dot{g}_2}{g_2} = \beta_2 \frac{\Gamma_s(\phi_s, c_n, t)}{\phi_s}\,, \quad \frac{\dot{g}_3}{g_3} = \beta_3 \frac{\Gamma_s(\phi_s, c_n, t)}{\phi_s}\,, \tag{2.17}$$

where β_i, $i = 1,2,3$ are proper coefficients that weigh growth along the principal directions and such that $\beta_1 + \beta_2 + \beta_3 = 1$. The choice of the coefficients β_i and the eigenvectors $\mathbf{w}_i$ will be discussed properly in Section 2.2.5, referring to medical patient-specific data.

Effective stress tensor in $\Omega_h(t)$

In the host healthy tissue, as stated before, the net source term $\Gamma_s(\phi_s, c_n, t)$ is null, since the death of healthy cells is compensated by proliferation. This implies that, in principle, the multiplicative decomposition (2.2) is not needed in $\Omega_h(t)$. However, for simplicity, in order to have all quantities defined on both the tumour and the healthy tissue, it is possible to apply a fictitious multiplicative decomposition of the deformation gradient $\mathbb{F}_s$, by taking $\mathbb{F}_g = \mathbb{I}$ in $\Omega_h(t)$. Then, even though the constitutive mechanical model for the healthy tissue might be taken as totally different from the one describing the tumour, we assume that the solid phase is described by a Mooney-Rivlin strain energy density

function $\widehat{\mathcal{W}}_{\mathrm{sn}}$ as in (2.11) also in the healthy domain. Nevertheless, even assuming the same functional form, the material parameters could be different, i.e., we could use $\mu_{1\mathrm{h}}$, $\mu_{2\mathrm{h}}$ and κ_{h} different from $\mu_{1\mathrm{t}}$, $\mu_{2\mathrm{t}}$ and κ_{t}, respectively.

2.2.3 Mass growth rate and and definition of the therapeutic protocol

In writing mass balance laws in tumour domain (see Eqs. (2.3)), we have assumed that growth of the solid phase happens at the expense of the liquid phase. This assumption stands from the biological observation that cells need to absorb fluid from the extracellular environment in order to increase their volume and proliferate. At the same time, when cells die, in the absence of calcification, they release the intracellular fluid into the environment. However, a tissue is generally not a closed system in terms of mass since fluid can come from the vasculature within the tissue or from the boundary between the tissue and fluid regions, such as the brain ventricles. In the present description, as largely done in the literature [5, 94, 125, 357], we neglect the description of the extra fluid coming from the vasculature, but fluid can eventually flow across the boundary between the tissue and the liquid region of the brain ventricles, therefore, the total mass of the mixture is not conserved. More in detail, we assume the following form for the net rate of growth:

$$\Gamma_{\mathrm{s}}(\phi_{\mathrm{s}}, c_n, t) = \begin{cases} \nu\phi_{\mathrm{s}}\left(\phi_{\max} - \phi_{\mathrm{s}}\right)\left(c_n - c_0\right)_+ - R(\phi_{\mathrm{s}}, t) - G(\phi_{\mathrm{s}}, t) & \text{in } \Omega_{\mathrm{t}}(t) \\ 0 & \text{in } \Omega_{\mathrm{h}}(t) \end{cases}, \tag{2.18}$$

where $(\cdot)_+$ denotes the positive part of its argument and $\nu > 0$. Specifically, in the domain occupied by the host tissue $\Omega_{\mathrm{h}}(t)$, we assume that proliferation of healthy cells is compensated by their natural death, so that the net rate of growth Γ_{s} can be taken as equal to zero therein. Conversely, the first term on the right-hand side of Eq. (2.18) in $\Omega_{\mathrm{t}}(t)$ models contact inhibition of proliferation above a maximum cell volume fraction $\phi_{\max}$ as well as the dependence of proliferation on the concentration of nutrients c_n, with an hypoxia threshold c_0 [47, 48, 125, 338]. For what concerns the loss terms $R(\phi_{\mathrm{s}}, t)$ and $G(\phi_{\mathrm{s}}, t)$, they represent cell death due to radiotherapy and chemotherapy, respectively. We define them by referring to the current standard of care for newly diagnosed brain tumours, which consists of adjuvant radiotherapy (RT) and chemotherapy (CHT), very often after surgical resection. In some cases, however, resection of the tumour mass is unfeasible, and only RT and CHT are administered. A protocol about the administration of the drug temozolomide (TMZ) combined with radiotherapy treatment for brain tumours was proposed by Roger Stupp in 2005 [467]. In particular, he found that the addition of TMZ to radiotherapy for newly diagnosed glioblastoma resulted in a clinically meaningful and statistically significant survival benefit with minimal additional toxicity for the patient. The radiotherapy administration of the Stupp protocol consists of fractionated focal irradiation at a dose of 2 Gy per fraction ($1\,\mathrm{Gy} = 1\,\mathrm{J/kg}$), given once a day five days per week (Monday through Friday) over a period of six weeks, for a total dose of 60 Gy. Concomitant chemotherapy consists of TMZ at a dose of $75\ \mathrm{mg/m^2}$, to be administered 7 days per week starting from the first day of radiotherapy until the last day of radiotherapy. After a 4-week break, patients receive up to six additional cycles of chemotherapy according to the standard 5-day schedule every 28 days. The standard dose of TMZ in the second adjuvant CHT cycle is $150\ \mathrm{mg/m^2}$ and it is increased to $200\ \mathrm{mg/m^2}$ beginning with the third cycle. The effects of radiotherapy and chemotherapy according to a therapeutic protocol similar to the standard Stupp protocol, with just three cycles of chemotherapy, as illustrated in Fig. 2.2, are introduced in our model by taking $R(\phi_{\mathrm{s}}, t)$ and $G(\phi_{\mathrm{s}}, t)$ as directly proportional to the fraction of tumour cells [4,

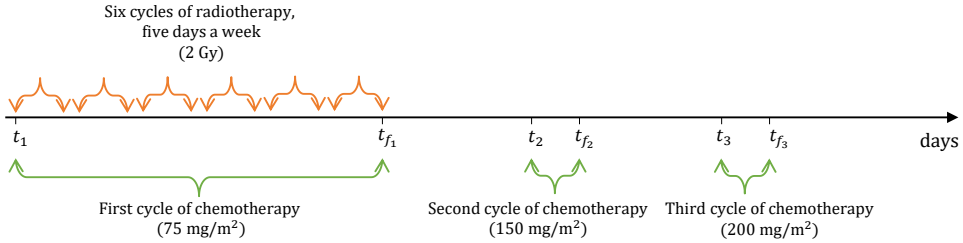

FIGURE 2.2: The therapeutic protocol considered in this work: radiotherapy (in orange) and three cycles of chemotherapy (in green).

128, 410, 430]:

$$R(\phi_s, t) = k_R(t)\phi_s\,, \qquad G(\phi_s, t) = k_C(t)\phi_s\,. \tag{2.19}$$

Following other works in the literature [4, 128, 410], we firstly investigate the case in which the two time-dependent coefficients $k_R(t)$ and $k_C(t)$ are equal to zero when the therapy is not administered, while they are constant and equal to the specific cell death rate during the days of treatment, i.e.,

$$k_R(t) = \begin{cases} R_{\text{eff}} & t_1 + 7j \text{ days} \leq t \leq t_1 + (4 + 7j) \text{ days} \\ 0 & \text{otherwise} \end{cases}, \tag{2.20a}$$

$$k_C(t) = \begin{cases} k_{C1} & t_1 \leq t \leq t_{f1} \\ k_{C2} & t_2 \leq t \leq t_{f2} \\ k_{C3} & t_3 \leq t \leq t_{f3} \\ 0 & \text{otherwise} \end{cases}, \tag{2.20b}$$

where $j = 0, ..., 5$, t_1 is the time when the patient starts therapies, t_2 and t_3 are the days when the patient starts the second and the third cycle of chemotherapy (i.e., in our case, $t_2 = t_1 + 70$ days and $t_3 = t_1 + 105$ days) and t_{f_i} are the days in which each chemotherapeutic cycle ends (i.e. $t_{f_1} = t_1 + 39$ days, $t_{f_2} = t_1 + 74$ days and $t_{f_3} = t_1 + 109$ days). For what concerns radiotherapy, the term R_{eff} represents the effect of n fractions per day and it is estimated through the linear-quadratic model, commonly used for studying the survival response and clinical results in radiotherapy [4, 410, 507]:

$$R_{\text{eff}} = \alpha n d + \beta n d^2\,, \tag{2.21}$$

where d [Gy] is the dose radiation for every fraction, while α [Gy^{-1}] and β [Gy^{-2}] are the linear and quadratic coefficients for RT-induced cell death, respectively. For what concerns chemotherapy, the parameters k_{C1}, k_{C2} and k_{C3} appearing in Eq. (2.20b) reflect the cell death response for increasing drug dosage, as described above. Then, we investigate another modelling assumption to take into account the fact that the effects of drug administration persist even after the drug has been cleared out from the body, since complex biological processes are triggered [189]. Indeed, late apoptosis/necrosis induced by TMZ may occur even after some days from the last treatment [68, 241, 434]. To account for this prolonged effect of chemotherapy on tumour cells without resorting to a complex pharmacodynamics model, we consider an exponential decay of the tumour cell response (in terms of the cell death rate k_C) when each chemotherapy cycle is stopped. As a consequence, the coefficient $k_C(t)$ in Eq. (2.19) in this case is not null

when the chemotherapy is not administered, but instead it decays in time as follows:

$$k_C(t) = \sum_{i=1}^{3} k_{Ci} \mathbb{1}_{[t_i, t_{fi}]}(t) + k_{Ci} e^{-\lambda_c (t - t_{fi})} \mathbb{1}_{[t_{fi}, +\infty)}(t)\,, \tag{2.22}$$

where $\mathbb{1}_{[a,b]}(t)$ is the indicator function whose value is one for $a \leq t \leq b$ and is equal to zero otherwise. More details on the values of the parameters k_{Ci} are given in Section 2.4.3 together with the plot of the time evolution of $k_R(t)$ and $k_C(t)$ for all the considered scenarios (see Fig. 2.10).

2.2.4 Nutrients

The rate of tumour growth $\Gamma_s(\phi_s, c_n, t)$ is influenced by many different factors, but of course the amount of nutrients plays a fundamental role, because it strongly affects the cells capability to duplicate. Consequently, it is necessary to introduce in the model an equation describing nutrients evolution in the domain. We assume that they are transported by the fluid phase and they can diffuse into it. On the other side, they are taken by the growing tumour and uniformly supplied by blood vessels. We introduce the hypothesis that the nutrients absorbed by the healthy tissue are immediately replaced by the vasculature, whereas the nutrients uptake by the tumour tissue is not negligible. Following these assumptions, we can write the mass balance equation governing the concentration of available nutrients c_n in $\Omega(t)$, normalising it with respect to the physiological concentration taken at the border of the brain:

$$\frac{\partial}{\partial t}\left(\phi_\ell c_n\right) + \nabla \cdot \left(\phi_\ell c_n \mathbf{v}_\ell\right) = \nabla \cdot \left(\phi_\ell \mathbb{D} \nabla c_n\right) + \Gamma_\ell c_n + G_n\,, \tag{2.23}$$

where $\mathbb{D}$ is the Eulerian diffusion tensor (discussed later in Section 2.2.5), the term $\Gamma_\ell c_n$ is related to the variation of the nutrients amount due to absorption/production of the liquid in which the chemical is dissolved, and G_n is the chemical source term occurring without net variation of the liquid amount. In particular, we will consider the form

$$G_n = \begin{cases} -\zeta \phi_s \phi_\ell c_n + S_n \left(1 - c_n\right) \phi_\ell & \text{in } \Omega_t(t) \\ 0 & \text{in } \Omega_h(t) \end{cases}. \tag{2.24}$$

The expression of G_n in the tumour domain describes the fact that nutrients are consumed by the tumour with a constant rate ζ. Furthermore, nutrients are supplied at a rate S_n as far as their concentration is below the physiological value, whereas above the physiological value they are absorbed. The consumption and the delivery of nutrients is also weighted with a factor ϕ_ℓ to describe the fact that if there is a higher availability of fluid phase, then a greater uptake or supply of nutrients can be provided. On the other hand, in the healthy region we assume that production and absorption of nutrients are reciprocally balanced. Using standard calculus techniques and recalling the mass balance equation of the fluid phase, with $\Gamma_\ell = 0$ in $\Omega_h(t)$, we can rewrite Eq. (2.23) in the tumour and in the healthy domain as

$$\frac{\partial c_n}{\partial t} + \mathbf{v}_\ell \cdot \nabla c_n = \frac{1}{\phi_\ell} \nabla \cdot \left(\phi_\ell \mathbb{D} \nabla c_n\right) + \left[-\zeta \phi_s c_n + S_n \left(1 - c_n\right)\right] \qquad \text{in } \Omega_t(t)\,, \tag{2.25a}$$

$$\frac{\partial c_n}{\partial t} + \mathbf{v}_\ell \cdot \nabla c_n = \frac{1}{\phi_\ell} \nabla \cdot \left(\phi_\ell \mathbb{D} \nabla c_n\right) \qquad \text{in } \Omega_h(t)\,. \tag{2.25b}$$

2.2.5 Anisotropic diffusion, permeability, and growth

The presence of white matter tracts within the brain introduces directional anisotropy that clearly affects all the relevant phenomena, including diffusion, fluid motion, and tumour growth. To properly account for the role of preferential directions, it is therefore necessary to provide definitions for the diffusion tensor $\mathbb{D}$, the permeability tensor $\mathbb{K}$, and the growth tensor $\mathbb{F}_g$ which reflect the *in vivo* anisotropy. In addition, the expansion of the tumour mass displaces the fibres in the surrounding environment, leading to a modification of the directions of anisotropy in the current configuration $\Omega(t)$. Thus, we use the mechanical description included in our model to progressively modify the tensors as time evolves.

To model anisotropic phenomena, we start from a set of patient-specific data collected through Magnetic Resonance Imaging (MRI), and, in particular, Diffusion Tensor Imaging (DTI), provided by Istituto Neurologico Carlo Besta in Milan (Italy). This procedure allows to reconstruct a realistic brain geometry and environment, with the aim of providing a framework potentially capable of embedding patient-specific information. A more detailed explanation of these imaging techniques is provided in Section 1.1.4. The reconstruction of the boundaries of the brain and the ventricles, as well as the processing of DTI data, are summarized in Section 2.2.5. We then take advantage of the DTI images to extrapolate the relevant information on the diffusion, permeability and growth tensors.

Image acquisition

In this Section, we provide details on the process by which information regarding the shape and tissues of the patient's brain, as well as the most probable direction of the white matter fibres, was derived from MRI and DTI. Imaging data were acquired at the Fondazione IRCCS Istituto Neurologico Besta (Milan, Italy). The patient signed a written consent to the MRI and DTI tests in the context of normal clinical practice, including clinical research. The patient was not submitted to any specific procedure different from normal clinical practice and the collected patient data was anonymized and de-identified prior to analysis. Anonymization was performed by the neuroradiology unit of the Besta Neurological Institute, independently from the researchers involved in the paper.

To visualize the MRI data of the patient's brain, we use the open-source software *3D Slicer* [1, 179]. Since we are interested in identifying fluid regions, we focus on T1-weighted images, where fluid appears dark and tissue white. The initial step involves image segmentation, dividing it into distinct and homogeneous regions, emphasizing the areas of interest to facilitate analysis. We then choose a task, leveraging provided atlases (images from various patients that are already labelled) to identify the ventricular region within the new image and assign an appropriate label. In our case, we select the MRI Human Brain task and perform segmentation through *3D Slicer*'s automatic segmentation. Additionally, smoothing can be applied to the generated maps. The next step involves extracting the brain external surface and ventricle surface from the segmented map using *Vmtk* (Vascular Modelling ToolKit) [493]. Finally, using *Tetgen* [235, 492], a program capable of generating tetrahedral meshes for any 3D polyhedral domain, the mesh is constructed. The external surface represents the brain's outer surface, while the inner surface corresponds to the brain-ventricle boundary. We observe that we construct a tumour-conformal mesh to distinctly separate the healthy from the tumour domain. The latter is considered as a sphere with a radius of 2.5 mm. *Tetgen* is again

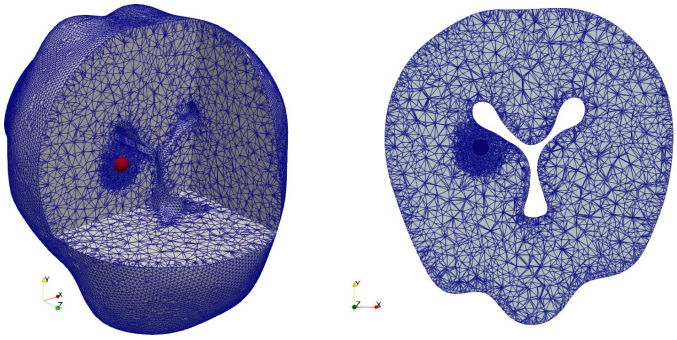

FIGURE 2.3: Computational brain mesh and refinement, with tumour region highlighted in red.

employed to refine the tetrahedral mesh within a spherical area centred on the tumour. In Fig. 2.3, the constructed mesh is shown.

Now it is necessary to incorporate information from Diffusion Tensor Imaging (DTI) into the mesh. Each cell of the 3D mesh requires assignment of a symmetric 3×3 tensor, specifically the symmetric tensor denoted as $\mathbb{D}^0_{\text{NFW}}$, containing water diffusion values along the principal spatial directions. In this specific case, the initial data consists of medical images that only contain the non-free water information, already available from the files provided by the medical professionals. Our task involves processing the medical images and subsequently transferring the values to the three-dimensional mesh. In detail, we generate six meshes, each dedicated to one independent component of the tensor. Since perfect alignment is required for transferring data from images to meshes, *image registration* becomes necessary. This involves realigning the images as accurately as possible with our reference map. For this purpose, we use *FSL* (FMRIB Software Library) [185, 270] and select FLIRT, the FMRIB's linear registration tool specifically designed for images from the same patient, as in our scenario. With all diffusion tensor components aligned with the maps segmented from magnetic resonances and, consequently, with the tetrahedral mesh, we can proceed to assign diffusion values to the cells of the mesh. This task can be accomplished using specific commands in *Vmtk* [493].

Diffusion tensor $\mathbb{D}$

The diffusion tensor at the initial time instant $\mathbb{D}^0$ is reconstructed by using data from DTI medical images. In detail, the patient-specific images are processed with a particular approach based on a multi-compartment model, which separates the diffusion signal into a free-water (FW) and a tract-related, non-free-water (NFW) compartments [394]. This approach allows to overcome the limit of inaccurate estimation of white matter tract directions in regions with a high content of free water, such as cerebrospinal fluid or oedema. This is particularly important in our model to correctly estimate diffusion data in the region close to the brain ventricles. For this reason, initial data consist of 6 diffusion images, concerning only the non-free water component, which are assembled in a symmetric tensor called $\mathbb{D}^0_{\text{NFW}}$. Then, the initial diffusion tensor $\mathbb{D}^0$ is obtained from a weighted sum of two different contributions: an isotropic tensor, related to the unconstrained diffusion of substances in the free water, and the tensor constructed with DTI data, taking into account the diffusion limited by the tissue structures. Therefore, we set

$$\mathbb{D}^0 = \phi_\ell^0 \mathbb{D}^0_{\text{FW}} + (1 - \phi_\ell^0)\mathbb{D}^0_{\text{NFW}}\,, \tag{2.26}$$

where $\mathbb{D}^0_{\text{FW}} := D_w \mathbb{I}$, with D_w a scalar value which represents the diffusivity of free water at 37°C. The value $\phi_\ell^0(\mathbf{X})$ represents the liquid volumetric fraction at the initial time

and it considers the fluid content in different regions of the brain. As a consequence, in regions where a high amount of liquid is present, diffusion is dominated by the purely isotropic free water component $\mathbb{D}^0_{\text{FW}}$, whereas more weight is given to diffusion along the white matter fibres in regions with reduced presence of fluid. Starting from the definition of Eq. (2.26), the diffusion tensor $\mathbb{D}$ at the current instant of time is derived from $\mathbb{D}^0$ by accounting for the fact that the growing tumour displaces the surrounding white matter fibres and thereby modifies the preferential directions of diffusion. We remark that such a change is only supposed to affect the non-free water component $\mathbb{D}^0_{\text{NFW}}$, while the free water one remains unaltered, i.e., $\mathbb{D}_{\text{FW}} \equiv \mathbb{D}^0_{\text{FW}}$. We also underline that the free water content evolves in time and space and it is here assumed to be equivalent to the fluid phase volume fraction $\phi_\ell(\mathbf{x}, t)$. With these observations in mind, if we call $\lambda^0_1 \geq \lambda^0_2 \geq \lambda^0_3$ the eigenvalues of $\mathbb{D}^0_{\text{NFW}}$ and $\mathbf{e}^0_1$, $\mathbf{e}^0_2$, $\mathbf{e}^0_3$ the corresponding orthonormal eigenvectors, we can define the current diffusion tensor as

$$\mathbb{D} = \phi_\ell \mathbb{D}_{\text{FW}} + (1 - \phi_\ell)\mathbb{D}_{\text{NFW}}\,, \tag{2.27}$$

where $\mathbb{D}_{\text{FW}} = D_w \mathbb{I}$, while $\mathbb{D}_{\text{NFW}}$ is constructed as follows:

$$\mathbb{D}_{\text{NFW}} = \sum_{i=1}^{3} \lambda^0_i \frac{\mathbb{F}_{\text{s}}\mathbf{e}^0_i \otimes \mathbb{F}_{\text{s}}\mathbf{e}^0_i}{\mathbf{e}^0_i \cdot \mathbb{C}_{\text{s}}\mathbf{e}^0_i}\,. \tag{2.28}$$

The representation given by Eq. (2.28) stems from the discussions above and prescribes that each eigenvector of the initial diffusion tensor $\mathbb{D}^0_{\text{NFW}}$ is deformed through the solid deformation gradient $\mathbb{F}_{\text{s}}$, to account for possible alterations of the anisotropy directions following cancer expansion. Then, the deformed eigenvectors $\mathbb{F}_{\text{s}}\mathbf{e}^0_i$, $i = 1, 2, 3$ are normalised dividing by $|\mathbb{F}_{\text{s}}\mathbf{e}^0_i| = \sqrt{\mathbf{e}^0_i \cdot \mathbb{C}_{\text{s}}\mathbf{e}^0_i}$, with $\mathbb{C}_{\text{s}} = \mathbb{F}^{\text{T}}_{\text{s}}\mathbb{F}_{\text{s}}$. Such a choice is motivated by the will of changing only the directions of diffusion while keeping the average diffusivity along the fibres, i.e. the trace of $\mathbb{D}_{\text{NFW}}$, unmodified in time. Indeed, a simple push-forward operation on $\mathbb{D}^0_{\text{NFW}}$ would result not only in a change of the preferential directions, but also in a change of diffusivity due to fibre extension or shortening. Therefore, in choosing an appropriate normalisation, we decided to preserve the average diffusivity. It is here important to emphasize that, given the definition of Eq. (2.28), a pull-back of $\mathbb{D}_{\text{NFW}}$ to the reference configuration results in a tensor with the same eigenvectors as $\mathbb{D}^0_{\text{NFW}}$, but with different eigenvalues, due to the aforementioned modelling choices. Indeed, introducing $\mathbb{D}^*_{\text{NFW}}$, which is the tensor $\mathbb{D}_{\text{NFW}}$ mapped to the reference configuration

$$\begin{aligned}\mathbb{D}^*_{\text{NFW}} :&= J_{\text{s}}\mathbb{F}_{\text{s}}^{-1}\mathbb{D}_{\text{NFW}}\mathbb{F}_{\text{s}}^{-\text{T}} \\ &= \sum_{i=1}^{3} \frac{\lambda^0_i J_{\text{s}}}{\mathbf{e}^0_i \cdot \mathbb{C}_{\text{s}}\mathbf{e}^0_i}\mathbb{F}_{\text{s}}^{-1}(\mathbb{F}_{\text{s}}\mathbf{e}^0_i \otimes \mathbb{F}_{\text{s}}\mathbf{e}^0_i)\mathbb{F}_{\text{s}}^{-\text{T}} = \sum_{i=1}^{3} \frac{\lambda^0_i J_{\text{s}}}{\mathbf{e}^0_i \cdot \mathbb{C}_{\text{s}}\mathbf{e}^0_i}\mathbf{e}^0_i \otimes \mathbf{e}^0_i\,,\end{aligned} \tag{2.29}$$

the eigenvalues $\tilde{\lambda}_i$ of this tensor [47, 48, 338] are

$$\tilde{\lambda}_i := \frac{\lambda^0_i J_{\text{s}}}{\mathbf{e}^0_i \cdot \mathbb{C}_{\text{s}}\mathbf{e}^0_i}\,, \qquad i = 1, 2, 3\,. \tag{2.30}$$

Finally, we note that, by defining the diffusion tensor weighted by ϕ_ℓ, we can effectively account for variations in intratumoural cellularity, which in turn influence the Apparent Diffusion Coefficient (ADC), a metric that reflects the magnitude of diffusion [13, 255, 295].

Permeability tensor $\mathbb{K}$

As much as diffusion, also the fluid motion due to pressure gradients follows some preferential directions, due to the anisotropic nature of brain tissue [498]. This information is encapsulated in the permeability tensor $\mathbb{K}$ appearing in (2.10), which is also built from imaging data appropriately modified to account for tissue deformation. In particular, we can derive the permeability tensor $\mathbb{K}$ by using the information about the fibre directions contained in the tensor $\mathbb{D}^0_{\text{NFW}}$, namely the eigenvalues λ^0_1, λ^0_2, λ^0_3, and the eigenvectors $\mathbf{e}^0_1$, $\mathbf{e}^0_2$, and $\mathbf{e}^0_3$, suitably modified to account for tissue deformations, as is done for the diffusion tensor. Specifically, we define $\mathbb{K}$ as

$$\mathbb{K} = K(\phi_s)\,\mathbb{A}\,, \tag{2.31}$$

where $K(\phi_s)$ is a proper function of the solid volume fraction and $\mathbb{A}$ is the *tensor of preferential directions*, reconstructed from the patient-specific DTI data.

In more detail, with the same procedure used for the definition of $\mathbb{D}_{\text{NFW}}$, we assume that $\mathbb{A}$ can be reconstructed from the eigenvectors of $\mathbb{D}^0_{\text{NFW}}$ deformed through the solid deformation gradient $\mathbb{F}_s$. However, in the case of the permeability tensor, the eigenvalues are rescaled to enhance the anisotropy along the fibres by appropriate anisotropy tuning functions as described in [4, 6, 269], and a normalisation is performed to preserve the mean permeability as done in [4, 6, 338]. Therefore, the tensor $\mathbb{A}$ is defined as

$$\mathbb{A} = \frac{1}{\mathrm{A}_{av}}\widehat{\mathbb{A}}\,, \quad \mathrm{A}_{av} = \frac{1}{3}\,\mathrm{tr}(\widehat{\mathbb{A}})\,, \tag{2.32}$$

$$\widehat{\mathbb{A}} = \tilde{a}_1(r)\lambda^0_1\frac{\mathbb{F}_s\mathbf{e}^0_1\otimes\mathbb{F}_s\mathbf{e}^0_1}{\mathbf{e}^0_1\cdot\mathbb{C}_s\mathbf{e}^0_1} + \tilde{a}_2(r)\lambda^0_2\frac{\mathbb{F}_s\mathbf{e}^0_2\otimes\mathbb{F}_s\mathbf{e}^0_2}{\mathbf{e}^0_2\cdot\mathbb{C}_s\mathbf{e}^0_2} + \tilde{a}_3(r)\lambda^0_3\frac{\mathbb{F}_s\mathbf{e}^0_3\otimes\mathbb{F}_s\mathbf{e}^0_3}{\mathbf{e}^0_3\cdot\mathbb{C}_s\mathbf{e}^0_3}\,, \tag{2.33}$$

where the normalisation by A_{av} keeps the trace of $\mathbb{A}$ equal to 3 (as for the identity tensor), r is the anisotropy tuning parameter, and $\tilde{a}_i(r)$ are functions of r such that, if $r > 1$, anisotropy is enhanced (see [4, 6, 269] for further details). In order to understand the extent of anisotropy and to correctly define the functional forms of $\tilde{a}_i(r)$ allowing to represent scenarios of monodirectional, planar, and spherical growth as a consequence of the fibre orientation in the brain, we need to look at the eigenvalues $\tilde{\lambda}_i$, given by Eq. (2.30), of the deformed diffusion tensor $\mathbb{D}_{\text{NFW}}$ pulled back to the reference configuration, as defined in Eq. (2.29). We sort the eigenvalues $\tilde{\lambda}_i$ in descending order and introduce $\lambda_{\max} = \max\{\tilde{\lambda}_1, \tilde{\lambda}_2, \tilde{\lambda}_3\}$, $\lambda_{\min} = \min\{\tilde{\lambda}_1, \tilde{\lambda}_2, \tilde{\lambda}_3\}$ and λ_{mid} the remaining one. Then we calculate the linear, planar, and spherical anisotropy coefficients [269] respectively defined by

$$c_l := \frac{\lambda_{\max} - \lambda_{\text{mid}}}{\lambda_{\max} + \lambda_{\text{mid}} + \lambda_{\min}}\,, c_p := \frac{2(\lambda_{\text{mid}} - \lambda_{\min})}{\lambda_{\max} + \lambda_{\text{mid}} + \lambda_{\min}}\,, c_s := \frac{3\lambda_{\min}}{\lambda_{\max} + \lambda_{\text{mid}} + \lambda_{\min}}\,, \tag{2.34}$$

and we introduce

$$a_{\max}(r) := rc_l + rc_p + c_s\,,\ a_{\text{mid}}(r) := c_l + rc_p + c_s\,,\ a_{\min}(r) := c_l + c_p + c_s\,. \tag{2.35}$$

From the definition of c_l, c_p and c_s, we can observe that $a_{\min}(r) \equiv 1$. Finally, depending on the descending order of the eigenvalues $\tilde{\lambda}_i$, we associate $\tilde{a}_1(r)$, $\tilde{a}_2(r)$, and $\tilde{a}_3(r)$ with the corresponding coefficients between $a_{\max}(r)$, $a_{\text{mid}}(r)$ and $a_{\min}(r)$. We observe that, similarly to the diffusion tensor, such a construction allows us to take advantage of the mechanical variables of the model to make the permeability evolve in time, enforcing the correct anisotropy, derived from the mechanical deformation. In this case as well, the

eigenvectors of the tensor remapped to the reference configuration remain unchanged and are still represented by $\mathbf{e}_1^0$, $\mathbf{e}_2^0$ and $\mathbf{e}_3^0$.

As a functional form for the term $K(\phi_s)$, we will consider the exponential Holmes-Mow expression [37, 252], which is frequently used in the modelling of soft, hydrated biological structures [150, 151, 508]:

$$K(\phi_s) = k_0 \left[\frac{\phi_{sn}(1-\phi_s)}{\phi_s(1-\phi_{sn})}\right]^{\alpha_0} \exp\left(\frac{m}{2}\frac{\phi_{sn}^2 - \phi_s^2}{\phi_s^2}\right), \tag{2.36}$$

being α_0 and m model parameters, and k_0 the reference permeability value. The choice of the coefficient $K(\phi_s)$ is motivated by the will of introducing a deformation-dependent permeability, which is not constant as the tumour grows and the tissue experiences stresses and strains. In particular, it is required that the permeability decreases as the solid volume fraction increases. The linearised version of Eq. (2.36) for small strains has often been adopted to describe the permeability of brain tissue [200, 454, 456, 526]. However, since we deal with finite deformations and non-linear mechanics of the brain, we choose to use the non-linear permeability of Eq. (2.36) as in a previous work [338], looking forward to further experimental confirmation for brain tissue.

Anisotropic growth tensor $\mathbb{F}_g$

Finally, we have to provide an expression for the tensor $\mathbb{F}_g$ that describes inelastic mechanical distortions related to growth. Recalling Eq. (2.15), we define it as follows:

$$\mathbb{F}_g = g_1 \mathbf{e}_1^0 \otimes \mathbf{e}_1^0 + g_2 \mathbf{e}_2^0 \otimes \mathbf{e}_2^0 + g_3 \mathbf{e}_3^0 \otimes \mathbf{e}_3^0, \tag{2.37}$$

where $\mathbf{e}_1^0$, $\mathbf{e}_2^0$ and $\mathbf{e}_3^0$ are the eigenvectors of $\mathbb{D}_{NFW}^0$. Such a choice for the principal directions of growth deformation reflects the anisotropic structure of the tissue, with growth preferentially happening along the white matter tracts. This is a relevant difference from previous works on brain tumour growth since, as discussed before, $\mathbb{F}_g$ is often considered to be isotropic.

Given that the growth tensor has to match the condition of Eq. (2.14), and recalling Eq. (2.17), we need to prescribe the evolution in time of the stretch ratios g_1, g_2 and g_3 by means of a proper choice of the coefficients β_i, $i = 1, 2, 3$. This choice should take into account that white matter tracts and other physical structures in the brain (such as vessels) are used by tumour cells to expand along preferential directions. The tumour expansion is dictated not only by cell migration, but also by cell division/growth. Therefore, we define the coefficients β_i, $i = 1, 2, 3$ in order to enhance cell growth along the principal directions of the brain physical structures, which can be determined through the eigenvectors of the $\mathbb{D}_{NFW}^0$ tensor inferred from DTI data. Then, as done for the permeability tensor, we assume that the extent of growth in each direction is related to the eigenvalue of the deformed diffusion ellipsoid associated with that growth direction, possibly rescaled by a factor to enhance anisotropic growth. Specifically, we will

consider the following evolution equations and initial conditions:

$$\frac{\dot{g_1}}{g_1} = \frac{\tilde{\lambda}_1\tilde{a}_1(r)}{\tilde{\lambda}_1\tilde{a}_1(r)+\tilde{\lambda}_2\tilde{a}_2(r)+\tilde{\lambda}_3\tilde{a}_3(r)}\frac{\Gamma_s(\phi_s,c_n,t)}{\phi_s}, \qquad \text{with } g_1(0)=1\,, \tag{2.38a}$$

$$\frac{\dot{g_2}}{g_2} = \frac{\tilde{\lambda}_2\tilde{a}_2(r)}{\tilde{\lambda}_1\tilde{a}_1(r)+\tilde{\lambda}_2\tilde{a}_2(r)+\tilde{\lambda}_3\tilde{a}_3(r)}\frac{\Gamma_s(\phi_s,c_n,t)}{\phi_s}, \qquad \text{with } g_2(0)=1\,, \tag{2.38b}$$

$$\frac{\dot{g_3}}{g_3} = \frac{\tilde{\lambda}_3\tilde{a}_3(r)}{\tilde{\lambda}_1\tilde{a}_1(r)+\tilde{\lambda}_2\tilde{a}_2(r)+\tilde{\lambda}_3\tilde{a}_3(r)}\frac{\Gamma_s(\phi_s,c_n,t)}{\phi_s}, \qquad \text{with } g_3(0)=1\,, \tag{2.38c}$$

where $\tilde{\lambda}_1$, $\tilde{\lambda}_2$ and $\tilde{\lambda}_3$ are defined in Eq. (2.30) and $\tilde{a}_1(r)$, $\tilde{a}_2(r)$, and $\tilde{a}_3(r)$ are obtained by association with $a_{\max}(r)$, $a_{\text{mid}}(r)$ and $a_{\min}(r)$ defined by Eq. (2.35), through the same permutation required to sort the eigenvalues $\tilde{\lambda}_i$ in descending order. Consequently, the choice of the β_i coefficients is closely related to the eigenvalues $\tilde{\lambda}_i$, which are tied to the biomechanical properties of the tumour and its interaction with the surrounding tissue, reflecting the impact of tumour-induced deformations on the eigenvalues. We remark that the mathematical assumption for the choice of the β_i is grounded on the idea that the alignment of the cell mitotic spindle during cell division is guided by the physical structures in the surrounding environment. This hypothesis has been tested (mathematically and biologically) in other anisotropic environments (see for example the work of Hoehme et al. for the liver [248]) and needs to be validated by experimental tests for brain tissue. For the sake of completeness, we note that other assumptions that take into account, for instance, the stress experienced by cells in a particular direction can be considered [236].

2.2.6 Interface conditions at the boundary between the tumour and the healthy tissue

Since the material interface $\partial\Omega_t(t)$ between the tumour and the healthy tissue moves with the tumour cells with velocity $\mathbf{v}_s|_{\partial\Omega_t(t)}$, we have to satisfy the following interface conditions on the two sides of the boundary, in order to guarantee the continuity of the normal displacement, the normal stress, chemical concentration and fluxes at the interface:

$$[\![\mathbf{v}_s\cdot\mathbf{n}]\!]|_{\partial\Omega_t(t)} = 0\,, \tag{2.39a}$$

$$[\![\phi_\ell\,(\mathbf{v}_\ell-\mathbf{v}_s)\cdot\mathbf{n}d\Sigma]\!]|_{\partial\Omega_t(t)} = 0\,, \tag{2.39b}$$

$$[\![p]\!]|_{\partial\Omega_t(t)} = 0\,, \tag{2.39c}$$

$$[\![c_n]\!]|_{\partial\Omega_t(t)} = 0\,, \tag{2.39d}$$

$$[\![\mathbb{T}\mathbf{n}d\Sigma]\!]|_{\partial\Omega_t(t)} = \mathbf{0}\,, \tag{2.39e}$$

$$[\![(\phi_\ell c_n\,(\mathbf{v}_\ell-\mathbf{v}_s)-\phi_\ell\mathbb{D}\nabla c_n)\cdot\mathbf{n}d\Sigma]\!]|_{\partial\Omega_t(t)} = 0\,, \tag{2.39f}$$

where $[\![\cdot]\!]|_{\partial\Omega_t(t)}$ denotes the jump across the interface, $\mathbf{n}$ is the unit normal vector to $\partial\Omega_t(t)$ pointing outwards and $d\Sigma$ is the area element at the interface. In particular we underline that, by combining the continuity across the interface of the total stress $\mathbb{T} = -p\mathbb{I}+\mathbb{T}_s$, prescribed by Eq. (2.39e), and the continuity of the pressure p, prescribed by Eq. (2.39c), it follows that also the effective stress $\mathbb{T}_s$ is continuous. Furthermore, due to the presence in biological tissues of cell-cell and cell-extracellular matrix adhesion molecules (mainly cadherins and integrins), it is physically reasonable to assume not only the continuity of the velocity $\mathbf{v}_s$ along the normal direction, but also that there are

not breakages and rotations between the tumour and the healthy tissue. This hypothesis requires that tangential displacements (and thus velocities) at the tumour-healthy tissue boundary are also continuous:

$$[\![\mathbf{v}_s \cdot \boldsymbol{\tau}]\!]|_{\partial\Omega_t(t)} = 0\,.$$

This assumption leads us to say that the displacement field $\mathbf{u}_s$ is continuous along $\partial\Omega_t(t)$ and that the areas $d\Sigma$ deform in the same way at the interface, but it does not imply that also $\mathbb{F}_s$ and J_s are continuous. Finally, we observe that, without this requirement, appropriate conditions describing the slipping at the tumour-host interface, possibly taking into account the attachment/detachment of bonds, should be defined. Furthermore, in the case of discontinuous tangential displacements, the healthy tissue boundary should be defined and meshed separately from the tumour boundary to allow the two surfaces to deform in different ways.

In the end, removing $d\Sigma$ in (2.39b), (2.39e) and (2.39f) for the assumption made above, the interface conditions that we impose are

$$[\![\mathbf{u}_s]\!]|_{\partial\Omega_t(t)} = \mathbf{0}\,, \tag{2.40a}$$
$$[\![\phi_\ell\,(\mathbf{v}_\ell - \mathbf{v}_s)\cdot\mathbf{n}]\!]|_{\partial\Omega_t(t)} = 0\,, \tag{2.40b}$$
$$[\![p]\!]|_{\partial\Omega_t(t)} = 0\,, \tag{2.40c}$$
$$[\![c_n]\!]|_{\partial\Omega_t(t)} = 0\,, \tag{2.40d}$$
$$[\![\mathbb{T}_s\mathbf{n}]\!]|_{\partial\Omega_t(t)} = \mathbf{0}\,, \tag{2.40e}$$
$$[\![(\phi_\ell c_n\,(\mathbf{v}_\ell - \mathbf{v}_s) - \phi_\ell \mathbb{D}\nabla c_n)\cdot\mathbf{n}]\!]|_{\partial\Omega_t(t)} = 0\,. \tag{2.40f}$$

2.3 Lagrangian formulation of the model

To approach the numerical implementation of the model, our aim is to rewrite the equations derived in Section 2.2 using a Lagrangian description of motion. In this way, all the quantities of interest are considered in terms of material coordinates. Henceforth, we will then use a superscript * to denote any material element. Furthermore, we will use the same symbols to denote the variables in the spatial and material description, omitting the explicit spatial dependence. We recall the following equalities, which will be useful in the successive computations:

$$d\boldsymbol{\Sigma} = J_s\mathbb{F}_s^{-T}d\boldsymbol{\Sigma}^*\,, \qquad dV = J_s dV^*\,, \tag{2.41}$$

where $d\boldsymbol{\Sigma} = \mathbf{n}d\Sigma$ and dV represent the infinitesimal element of area and volume in spatial coordinates, respectively, $d\boldsymbol{\Sigma}^* = \mathbf{N}d\Sigma^*$ and dV^* denote the infinitesimal element of area and volume in material coordinates, while $\mathbf{N}$ denotes the unit normal vector to $\partial\Omega_t^*$ pointing outwards [231].

Firstly, we rewrite the equations defined in the tumour domain $\Omega_t(t)$ using a Lagrangian formulation. We integrate Eq. (2.3) for $\alpha = s$ over $\Omega_t(t)$ to obtain

$$\int_{\Omega_t(t)}\left[\frac{\partial\phi_s}{\partial t} + \nabla\cdot(\phi_s\mathbf{v}_s)\right]dV = \int_{\Omega_t(t)}\Gamma_s(\phi_s, c_n, t)\,dV\,.$$

Using Reynolds' transport theorem, see for example [231], and moving the volume elements to the reference configuration by means of (2.41), we obtain

$$\frac{d}{dt}\int_{\Omega_t^*} J_s\phi_s\, dV^* = \int_{\Omega_t^*} J_s\Gamma_s(\phi_s, c_n, t)\, dV^*\,,$$

which locally becomes

$$\dot{\overline{J_s\phi_s}} = J_s\Gamma_s(\phi_s, c_n, t)\,. \tag{2.42}$$

For what concerns Eq. (2.3) for $\alpha = \ell$, integrating over the tumour domain gives

$$\int_{\Omega_t(t)} \left[\frac{\partial \phi_\ell}{\partial t} + \nabla\cdot(\phi_\ell \mathbf{v}_\ell)\right] dV = -\int_{\Omega_t(t)} \Gamma_s(\phi_s, c_n, t)\, dV\,.$$

Since the interface does not move with the fluid, we have to make use of the generalized Reynolds' transport theorem [231] which, together with the divergence theorem and Eq. (2.41), yields

$$\frac{d}{dt}\int_{\Omega_t^*} J_s\phi_\ell\, dV^* - \int_{\Omega_t^*} \mathrm{Div}\left[J_s\phi_\ell \mathbb{F}_s^{-1}(\mathbf{v}_s - \mathbf{v}_\ell)\right] dV^* = -\int_{\Omega_t^*} J_s\Gamma_s(\phi_s, c_n, t)\, dV^*\,,$$

which localized gives

$$\dot{\overline{J_s\phi_\ell}} + \mathrm{Div}\left[J_s\phi_\ell \mathbb{F}_s^{-1}(\mathbf{v}_\ell - \mathbf{v}_s)\right] = -J_s\Gamma_s(\phi_s, c_n, t)\,. \tag{2.43}$$

Regarding the growth evolution in the tumour region, by substituting the product $J_s = J_g J_e$ into Eq. (2.42), the mass balance law of the solid phase takes the form:

$$J_g\dot{\overline{J_e\phi_s}} + \dot{J}_g J_e\phi_s = J_s\Gamma_s(\phi_s, c_n, t)\,. \tag{2.44}$$

Recalling that volumetric fraction in the natural state is constant in time and it is given by the relation $\phi_{sn} = J_e\phi_s$, we take advantage of the identity $\dot{J}_g = J_g\,\mathrm{tr}\left(\mathbb{L}_g\right)$ to rewrite Eq. (2.44) as

$$J_g\,\mathrm{tr}\left(\mathbb{L}_g\right)\phi_{sn} = J_s\Gamma_s(\phi_s, c_n, t)\,. \tag{2.45}$$

Finally, using relation (2.14), we can rewrite Eq. (2.42) as

$$J_s\phi_s = J_g\phi_{sn}\,, \tag{2.46}$$

stating that ϕ_s is fully determined once J_s and J_g are known.

As regards the momentum balance of the solid phase, if we integrate (2.9) over the tumour domain and we remember that $\mathbb{T} = -p\mathbb{I} + \mathbb{T}_s$ is the Cauchy stress tensor of the mixture, we obtain

$$\int_{\Omega_t(t)} \nabla\cdot\mathbb{T}\, dV = \mathbf{0}\,.$$

Introducing the first Piola-Kirchhoff stress tensor $\mathbb{P} := J_s\mathbb{T}\mathbb{F}_s^{-\mathrm{T}}$, the latter becomes

$$\int_{\Omega_t^*} \mathrm{Div}\,\mathbb{P}\, dV^* = \mathbf{0} \quad\Longrightarrow\quad \mathrm{Div}\,\mathbb{P} = \mathbf{0}\,.$$

Recalling that $\mathbb{P} = J_s\mathbb{T}\mathbb{F}_s^{-\mathrm{T}} = -J_s p\mathbb{F}_s^{-\mathrm{T}} + \mathbb{P}_s$, where $\mathbb{P}_s$ is the constitutive elastic part of the first Piola-Kirchhoff stress tensor, it follows that (2.9) becomes:

$$\mathrm{Div}\left[-J_s p\mathbb{F}_s^{-\mathrm{T}} + \mathbb{P}_s\right] = \mathbf{0}\,.$$

In order to rewrite (2.10) using the Lagrangian formulation, we integrate over a surface

$$\int_S \phi_\ell \left(\mathbf{v}_\ell - \mathbf{v}_\mathrm{s}\right) \cdot d\boldsymbol{\Sigma} = -\int_S \frac{\mathbb{K}(\phi_\ell)}{\mu} \nabla p \cdot d\boldsymbol{\Sigma}\,.$$

Moving the integrals to the reference configuration, we get

$$\int_{S^*} \left[\frac{\mathbb{K}}{\mu} \mathbb{F}_\mathrm{s}^{-\mathrm{T}} \operatorname{Grad} p + \phi_\ell \left(\mathbf{v}_\ell - \mathbf{v}_\mathrm{s}\right)\right] \cdot J_\mathrm{s} \mathbb{F}_\mathrm{s}^{-\mathrm{T}} d\boldsymbol{\Sigma}^* = 0\,.$$

Let us assume that all the involved quantities are regular, we have then the local form

$$\mathbf{v}_\ell - \mathbf{v}_\mathbf{s} = -\mathbb{F}_\mathrm{s} \frac{\mathbb{K}^*}{J_\mathrm{s} \mu \phi_\ell} \operatorname{Grad} p\,, \tag{2.47}$$

defining the tensor pull-back $\mathbb{K}^* := J_\mathrm{s} \mathbb{F}_\mathrm{s}^{-1} \mathbb{K} \mathbb{F}_\mathrm{s}^{-\mathrm{T}}$.

In the light of Eq. (2.47), it is then convenient to further reformulate the mass balances by summing up Eqs. (2.42) and (2.43). Using the saturation condition and the closed mixture assumption, the mass balance for the mixture therefore reads

$$\dot{J}_\mathrm{s} = \operatorname{Div}\left[\frac{\mathbb{K}^*}{\mu} \operatorname{Grad} p\right]\,.$$

Referring to the nutrients balance equation (2.25a), integrating it over the tumour domain and recalling the closed mixture assumption, we obtain

$$\int_{\Omega_\mathrm{t}(t)} \left[\frac{\partial \left(\phi_\ell c_n\right)}{\partial t} + \nabla \cdot \left(\phi_\ell c_n \mathbf{v}_\ell\right)\right] dV = \int_{\Omega_\mathrm{t}(t)} \nabla \cdot \left(\phi_\ell \mathbb{D} \nabla c_n\right) dV - \int_{\Omega_\mathrm{t}(t)} \left(\Gamma_\mathrm{s} c_n - G_n\right) dV\,,$$

that localized by means of the generalized Reynolds' transport theorem and the Gauss theorem leads to

$$\frac{d}{dt} \int_{\Omega_\mathrm{t}^*} \phi_\ell c_n J_\mathrm{s} dV^* - \int_{\partial\Omega_\mathrm{t}^*} \phi_\ell \left[c_n \left(\mathbf{v}_\mathrm{s} - \mathbf{v}_\ell\right) + \mathbb{D} \mathbb{F}_\mathrm{s}^{-T} \operatorname{Grad} c_n\right] \cdot J_\mathrm{s} \mathbb{F}_\mathrm{s}^{-T} d\boldsymbol{\Sigma}^* = - \int_{\Omega_\mathrm{t}^*} \left(\Gamma_\mathrm{s} c_n J_\mathrm{s} - G_n J_\mathrm{s}\right) dV^*\,,$$

and in this way the local form becomes:

$$\overline{J_\mathrm{s} \phi_\ell c_n}^{\cdot} - \operatorname{Div}\left[J_\mathrm{s} \phi_\ell c_n \mathbb{F}_\mathrm{s}^{-1} \left(\mathbf{v}_\mathrm{s} - \mathbf{v}_\ell\right)\right] - \operatorname{Div}\left[J_\mathrm{s} \phi_\ell \mathbb{F}_\mathrm{s}^{-1} \mathbb{D} \mathbb{F}_\mathrm{s}^{-\mathrm{T}} \operatorname{Grad} c_n\right] = - \Gamma_\mathrm{s} c_n J_\mathrm{s} + G_n J_\mathrm{s}\,.$$

If we define $\mathbb{D}^* := J_\mathrm{s} \mathbb{F}_\mathrm{s}^{-1} \mathbb{D} \mathbb{F}_\mathrm{s}^{-\mathrm{T}}$ and we recall the mass balance of the fluid phase (2.43), substituting Darcy's law in the reference configuration (2.47) we can rewrite it as

$$J_\mathrm{s} \phi_\ell \dot{c}_n - \frac{\mathbb{K}^*}{\mu} \operatorname{Grad} p \cdot \operatorname{Grad} c_n - \operatorname{Div}\left[\phi_\ell \mathbb{D}^* \operatorname{Grad} c_n\right] = J_\mathrm{s} G_n\,. \tag{2.48}$$

In conclusion, the set of equations in Lagrangian form in the tumour reference domain Ω_t^* is:

$$\dot{J}_s = \text{Div}\left[\frac{\mathbb{K}^*}{\mu}\,\text{Grad}\,p\right], \tag{2.49a}$$

$$J_s\phi_s = J_g\phi_{sn}, \tag{2.49b}$$

$$\phi_s + \phi_\ell = 1, \tag{2.49c}$$

$$\text{Div}\left[-J_s p\mathbb{F}_s^{-T} + \mathbb{P}_s\right] = \mathbf{0}, \tag{2.49d}$$

$$\frac{\dot{g}_i}{g_i} = \frac{\tilde{\lambda}_i\tilde{a}_1(r)}{\tilde{\lambda}_1\tilde{a}_1(r) + \tilde{\lambda}_2\tilde{a}_2(r) + \tilde{\lambda}_3\tilde{a}_3(r)}\frac{\Gamma_s(\phi_s, c_n, t)}{\phi_s} \quad \text{with } g_i(0) = 1,\ i = 1,2,3, \tag{2.49e}$$

$$J_s\phi_\ell\dot{c}_n - \frac{\mathbb{K}^*}{\mu}\,\text{Grad}\,p\cdot\text{Grad}\,c_n - \text{Div}\left[\phi_\ell\mathbb{D}^*\,\text{Grad}\,c_n\right] = J_s G_n. \tag{2.49f}$$

A similar reasoning and analogous computations can be used to derive the Lagrangian equations in the healthy tissue reference domain, so that we end up with the following set of equations in Ω_h^*:

$$\dot{J}_s = \text{Div}\left[\frac{\mathbb{K}^*}{\mu}\,\text{Grad}\,p\right], \tag{2.50a}$$

$$J_s\phi_s = J_g\phi_{sn}, \tag{2.50b}$$

$$\phi_s + \phi_\ell = 1, \tag{2.50c}$$

$$\text{Div}\left[-J_s p\mathbb{F}_s^{-T} + \mathbb{P}_s\right] = \mathbf{0}, \tag{2.50d}$$

$$\dot{g}_i = 0,\ i = 1,2,3, \tag{2.50e}$$

$$J_s\phi_\ell\dot{c}_n - \frac{\mathbb{K}^*}{\mu}\,\text{Grad}\,p\cdot\text{Grad}\,c_n - \text{Div}\left[\phi_\ell\mathbb{D}^*\,\text{Grad}\,c_n\right] = 0. \tag{2.50f}$$

The systems (2.49) and (2.50) allow to determine all the unknown fields, namely, the displacement field $\mathbf{u}_s(\mathbf{X},t)$ and the scalar fields $p(\mathbf{X},t)$, $\phi_s(\mathbf{X},t)$, $\phi_\ell(\mathbf{X},t)$, $g_1(\mathbf{X},t)$, $g_2(\mathbf{X},t)$, $g_3(\mathbf{X},t)$ and $c_n(\mathbf{X},t)$, $\forall\mathbf{X}\in\Omega^* = \Omega_t^*\cup\Omega_h^*$ and $\forall t\in(0,T)$, if we provide proper interface, initial and boundary conditions.

2.3.1 Interface, boundary, and initial conditions

Before solving the model to describe brain tumour growth, we need to provide appropriate conditions at the interface between the tumour and the host tissue, as well as boundary and initial conditions.

Interface conditions at the boundary $\partial\Omega_t^*$ between the tumour and the healthy tissue

The interface conditions derived in Section 2.2.6, i.e. Eqs. (2.40a)-(2.40f), need to be reformulated in Lagrangian coordinates, by making use of the relations (2.41). Then,

the set of interface conditions we obtain are the following:

$$[\![\mathbf{u}_s]\!]|_{\partial\Omega_t^*} = \mathbf{0}\,, \tag{2.51a}$$

$$\left[\!\!\left[\frac{\mathbb{K}^*}{\mu}\,\mathrm{Grad}\,p\cdot\mathbf{N}\right]\!\!\right]|_{\partial\Omega_t^*} = 0\,, \tag{2.51b}$$

$$[\![\mathbb{P}_s\mathbf{N}]\!]|_{\partial\Omega_t^*} = \mathbf{0}\,, \tag{2.51c}$$

$$[\![p]\!]|_{\partial\Omega_t^*} = 0\,, \tag{2.51d}$$

$$[\![c_n]\!]|_{\partial\Omega_t^*} = 0\,, \tag{2.51e}$$

$$[\![\phi_\ell\mathbb{D}^*\,\mathrm{Grad}\,c_n\cdot\mathbf{N}]\!]|_{\partial\Omega_t^*} = 0\,, \tag{2.51f}$$

where $[\![\cdot]\!]|_{\partial\Omega_t^*}$ denotes the jump across the interface and $\mathbf{N}$ is the unit normal vector to $\partial\Omega_t^*$ pointing outwards.

Boundary conditions

Before imposing the boundary conditions, it is important to remark (see Fig. 2.1) that the boundary of our domain $\partial\Omega^* = \partial\Omega_{\text{out}}^* \cup \partial\Omega_v^*$ is composed by the external boundary $\partial\Omega_{\text{out}}^*$, corresponding to the cranial skull, and by the edges of brain ventricles $\partial\Omega_v^*$. Specifically, in our simulations for tumour growth in the brain, we consider the following boundary conditions on $\partial\Omega_{\text{out}}^*$:

$$\mathbf{u}_s = \mathbf{0} \qquad \text{on } \partial\Omega_{\text{out}}^*\,, \quad \forall t\in(0,T)\,, \tag{2.52a}$$

$$\mathbb{K}^*\,\mathrm{Grad}\,p\cdot\mathbf{N} = 0 \qquad \text{on } \partial\Omega_{\text{out}}^*\,, \quad \forall t\in(0,T)\,, \tag{2.52b}$$

$$c_n = 1 \qquad \text{on } \partial\Omega_{\text{out}}^*\,, \quad \forall t\in(0,T)\,. \tag{2.52c}$$

In detail, we impose a null Dirichlet boundary condition for the displacement $\mathbf{u}_s$, given that the skull is fixed. For what concerns the pressure p, we take into account a Neumann boundary condition since we assume that fluid cannot flow outside the skull. Finally, for the nutrients' concentration, we suppose that the brain boundary is sufficiently far from the tumour, so we can assume that the oxygen concentration is maintained constant at the physiological value, leading to the condition (2.52c) for the normalized concentration.

Instead, on the boundary of the ventricles $\partial\Omega_v^*$ we impose the continuity of the stresses and an outflow boundary condition for the chemical mass to model an outlet where the species can leave the domain with the fluid flow, i.e.,

$$\mathbb{P}_s\mathbf{N} = \mathbf{0} \qquad \text{on } \partial\Omega_v^*\,, \quad \forall t\in(0,T)\,, \tag{2.53a}$$

$$p = p_v \qquad \text{on } \partial\Omega_v^*\,, \quad \forall t\in(0,T)\,, \tag{2.53b}$$

$$\phi_\ell\mathbb{D}^*\,\mathrm{Grad}\,c_n\cdot\mathbf{N} = 0 \qquad \text{on } \partial\Omega_v^*\,, \quad \forall t\in(0,T)\,. \tag{2.53c}$$

The first and second conditions are a consequence of the continuity of stresses imposed at the ventricles' interface, which leads to a boundary condition that involves only the constitutively determined part of the first Piola-Kirchhoff stress tensor $\mathbb{P}_s$, and to the condition (2.53b) that enforces a fixed value for the pressure equal to the physiological intracranial pressure p_v on $\partial\Omega_v^*$. This condition takes into account the capability of the interconnected brain ventricular system to maintain a physiological pressure. Furthermore, for c_n we consider an outflow boundary condition [307], considering that mass transfer at the outlet boundary only happens by convection, while the net diffusive flux

is negligible. This condition implies that the fluid is flowing across the boundary (at an unchanged velocity along the normal direction) and that the local concentration of chemicals on either side of the brain-ventricle interface is equal, so that the normal component of the chemical species gradient is zero at $\partial\Omega_{\mathrm{v}}^*$. This condition may be reasonable in the absence of physical barriers that could impede fluid and mass transport across the ventricles and maintain different chemical concentrations on either side. More complex conditions may require a detailed description of the hydrodynamics of the ventricles, taking into account washout and uptake of chemicals.

Initial conditions

At the beginning of the tumour growth process, we assume that the displacement and the pressure are equal to zero. In addition, we take the scalar fields g_1, g_2 and g_3 as equal to 1 everywhere in the tumour domain at $t = 0$. The volumetric fraction of the cell phase is instead initialized to a value $\phi_{\mathrm{s}}^0(\mathbf{X})$, whose estimate will be discussed in Section 2.4.3. Finally, in order to obtain the initial nutrients concentration $c_n^0(\mathbf{X})$, we solve the steady version of the nutrients governing equation, neglecting advection:

$$-\operatorname{Div}\left[\phi_\ell \mathbb{D}^0 \operatorname{Grad} c_n^0\right] = J_{\mathrm{s}} G_n \,. \tag{2.54}$$

In conclusion, we have the following set of initial conditions:

$$\mathbf{u}_{\mathrm{s}}(\mathbf{X},0) = \mathbf{0}\,, \qquad \forall \mathbf{X} \in \Omega^*\,, \tag{2.55a}$$
$$p(\mathbf{X},0) = 0\,, \qquad \forall \mathbf{X} \in \Omega^*\,, \tag{2.55b}$$
$$g_i(\mathbf{X},0) = 1\,,\ i = 1,2,3\,, \qquad \forall \mathbf{X} \in \Omega^*\,, \tag{2.55c}$$
$$\phi_{\mathrm{s}}(\mathbf{X},0) = \phi_{\mathrm{s}}^0(\mathbf{X})\,, \qquad \forall \mathbf{X} \in \Omega^*\,, \tag{2.55d}$$
$$c_n(\mathbf{X},0) = c_n^0(\mathbf{X})\,, \qquad \forall \mathbf{X} \in \Omega^*\,. \tag{2.55e}$$

2.4 Numerical implementation

The set of equations governing the evolution of the system in the domain Ω_{t}^* are summarised in Eqs. (2.49), while the governing equations in the healthy domain Ω_{h}^* are resumed in Eqs. (2.50). The system allows to determine all the unknown fields, namely, the displacement field $\mathbf{u}_{\mathrm{s}}(\mathbf{X},t)$ and the scalar fields $p(\mathbf{X},t)$, $\phi_{\mathrm{s}}(\mathbf{X},t)$, $\phi_\ell(\mathbf{X},t)$, $g_1(\mathbf{X},t)$, $g_2(\mathbf{X},t)$, $g_3(\mathbf{X},t)$ and $c_n(\mathbf{X},t)$, $\forall \mathbf{X} \in \Omega^* = \Omega_{\mathrm{t}}^* \cup \Omega_{\mathrm{h}}^*$ and $\forall t \in (0,T)$, equipped with the interface, boundary and initial conditions discussed in Section 2.3.1.

In this Section, we discuss how the Lagrangian model for brain tumour growth is solved through numerical simulations. The weak formulation of the model is derived in Section 2.4.1. The discretization in time and space of the weak formulation is instead reported and summarised in Section 2.4.2. Finally, in Section 2.4.3, we assess the values of the parameters that appear in the system.

2.4.1 Weak formulation of the Lagrangian model

The weak formulation of the Lagrangian model is derived in the following. The weak form is first written in each domain Ω_{t}^* and Ω_{h}^* separately and then it is extended to the whole domain $\Omega^* = \Omega_{\mathrm{t}}^* \cup \Omega_{\mathrm{h}}^*$. First of all, it is necessary to define the test functions spaces that meet the Dirichlet conditions imposed on the external boundary for c_n (2.52c) and on ventricles boundary for p (2.53b), recalling that p and c_n are continuous functions

over Ω^*:

$$H^1_{0,\partial\Omega^*_{\text{out}}}(\Omega^*) := \left\{ q \in H^1(\Omega^*) \colon q = 0 \text{ on } \partial\Omega^*_{\text{out}} \right\},$$

$$H^1_{0,\partial\Omega^*_{\text{v}}}(\Omega^*) := \left\{ q \in H^1(\Omega^*) \colon q = 0 \text{ on } \partial\Omega^*_{\text{v}} \right\}.$$

Furthermore we establish the vector test functions space that meets the Dirichlet conditions we impose on the external boundary for the continuous vector function $\mathbf{u}_{\text{s}}$ (2.52a):

$$\boldsymbol{H}^1_{0,\partial\Omega^*_{\text{out}}}(\Omega^*) := \left\{ \boldsymbol{q} \in \boldsymbol{H}^1(\Omega^*) \colon \boldsymbol{q} = \mathbf{0} \text{ on } \partial\Omega^*_{\text{out}} \right\}.$$

Then, starting from Eq. (2.49a), we multiply each side by a test function $q_{\text{t}} \in H^1_{0,\partial\Omega^*_{\text{v}}}(\Omega^*)$ and we integrate the whole equation over the Lagrangian tumour domain Ω^*_{t}:

$$\int_{\Omega^*_{\text{t}}} \dot{J}_{\text{s}} q_{\text{t}} \, dV^* = \int_{\Omega^*_{\text{t}}} \text{Div} \left[\frac{\mathbb{K}^*}{\mu} \text{Grad}\, p \right] q_{\text{t}} \, dV^* . \tag{2.56}$$

Integrating by parts the second order derivatives, we obtain

$$\int_{\Omega^*_{\text{t}}} \dot{J}_{\text{s}} q_{\text{t}} \, dV^* = - \int_{\Omega^*_{\text{t}}} \text{Grad}\, q_{\text{t}} \cdot \frac{\mathbb{K}^*}{\mu} \text{Grad}\, p \, dV^* + \int_{\partial\Omega^*_{\text{t}}} q_{\text{t}} \frac{\mathbb{K}^*}{\mu} \text{Grad}\, p \cdot \mathbf{N} d\Sigma^* . \tag{2.57}$$

In the healthy domain, considering Eq. (2.50a), we take as test function $q_{\text{h}} \in H^1_{0,\partial\Omega^*_{\text{v}}}(\Omega^*)$ and we find

$$\begin{aligned} \int_{\Omega^*_{\text{h}}} \dot{J}_{\text{s}} q_{\text{h}} \, dV^* = &- \int_{\Omega^*_{\text{h}}} \text{Grad}\, q_{\text{h}} \cdot \frac{\mathbb{K}^*}{\mu} \text{Grad}\, p \, dV^* + \int_{\partial\Omega^*_{\text{t}}} q_{\text{h}} \frac{\mathbb{K}^*}{\mu} \text{Grad}\, p \cdot \mathbf{N} d\Sigma^* + \\ &+ \int_{\partial\Omega^*_{\text{out}}} q_{\text{h}} \frac{\mathbb{K}^*}{\mu} \text{Grad}\, p \cdot \mathbf{N} d\Sigma^* + \int_{\partial\Omega^*_{\text{v}}} q_{\text{h}} \frac{\mathbb{K}^*}{\mu} \text{Grad}\, p \cdot \mathbf{N} d\Sigma^* . \end{aligned} \tag{2.58}$$

The test function q_{h} is required to vanish on the boundary $\partial\Omega^*_{\text{v}}$ because it belongs to $H^1_{0,\partial\Omega^*_{\text{v}}}(\Omega^*)$. Furthermore, the second-last integral vanishes due to the boundary condition (2.52b). Summing up the equations in the healthy and tumour domain and taking $q \in H^1_{0,\partial\Omega^*_{\text{v}}}(\Omega^*)$ we have

$$\int_{\Omega^*} \dot{J}_{\text{s}} q \, dV^* = - \int_{\Omega^*} \text{Grad}\, q \cdot \frac{\mathbb{K}^*}{\mu} \text{Grad}\, p \, dV^* - \int_{\partial\Omega^*_{\text{t}}} \left[\!\left[q \frac{\mathbb{K}^*}{\mu} \text{Grad}\, p \right]\!\right] \cdot \mathbf{N} d\Sigma^* , \tag{2.59}$$

where $[\![\cdot]\!]$ denotes the jump across the interface. Since the test function q belongs to $H^1_{0,\partial\Omega^*_{\text{v}}}(\Omega^*)$ and for this reason it is continuous inside the domain, remembering interface condition (2.51b) we finally have

$$\int_{\Omega^*} \dot{J}_{\text{s}} q \, dV^* = - \int_{\Omega^*} \text{Grad}\, q \cdot \frac{\mathbb{K}^*}{\mu} \text{Grad}\, p \, dV^* , \tag{2.60}$$

for all test functions $q \in H^1_{0,\partial\Omega^*_{\text{v}}}(\Omega^*)$.
For what concerns the momentum balance, we multiply Eq. (2.49d) by a vector test function $\boldsymbol{q}_{\text{t}} \in \boldsymbol{H}^1_{0,\partial\Omega^*_{\text{out}}}(\Omega^*)$ and then we integrate over the tumour reference domain, obtaining

$$\int_{\Omega^*_{\text{t}}} \text{Div} \left[-J_{\text{s}} p \mathbb{F}_{\text{s}}^{-\text{T}} + \mathbb{P}_{\text{s}} \right] \cdot \boldsymbol{q}_{\text{t}} \, dV^* = 0 . \tag{2.61}$$

Using tensor integration by parts, we get

$$-\int_{\Omega_t^*}\left(-J_s p\mathbb{F}_s^{-T}+\mathbb{P}_s\right):\operatorname{Grad}\boldsymbol{q}_t\,dV^*+\int_{\partial\Omega_t^*}\left(-J_s p\mathbb{F}_s^{-T}+\mathbb{P}_s\right)\mathbf{N}\cdot\boldsymbol{q}_t\,d\Sigma^*=0\,,\quad(2.62)$$

where ":" denotes the double contraction between tensors. If we do the same in the healthy domain for Eq. (2.50d) using as test function $\boldsymbol{q}_h\in\boldsymbol{H}^1_{0,\partial\Omega^*_{out}}(\Omega^*)$, we obtain

$$\begin{aligned}-\int_{\Omega_h^*}\left(-J_s p\mathbb{F}_s^{-T}+\mathbb{P}_s\right):\operatorname{Grad}\boldsymbol{q}_h\,dV^*+\int_{\partial\Omega_t^*}\left(-J_s p\mathbb{F}_s^{-T}+\mathbb{P}_s\right)\mathbf{N}\cdot\boldsymbol{q}_h\,d\Sigma^*+\\+\int_{\partial\Omega^*_{out}}\left(-J_s p\mathbb{F}_s^{-T}+\mathbb{P}_s\right)\mathbf{N}\cdot\boldsymbol{q}_h\,d\Sigma^*+\int_{\partial\Omega_v^*}\left(-J_s p\mathbb{F}_s^{-T}+\mathbb{P}_s\right)\mathbf{N}\cdot\boldsymbol{q}_h\,d\Sigma^*=0\,.\quad(2.63)\end{aligned}$$

If we remember that $\boldsymbol{q}_h\in\boldsymbol{H}^1_{0,\partial\Omega^*_{out}}(\Omega^*)$, the second last integral vanishes. Using condition (2.53a), the last summand of the last integral is equal to zero, and therefore we have

$$\begin{aligned}-\int_{\Omega_h^*}\left(-J_s p\mathbb{F}_s^{-T}+\mathbb{P}_s\right):\operatorname{Grad}\boldsymbol{q}_h\,dV^*+\int_{\partial\Omega_t^*}\left(-J_s p\mathbb{F}_s^{-T}+\mathbb{P}_s\right)\mathbf{N}\cdot\boldsymbol{q}_h\,d\Sigma^*+\\-\int_{\partial\Omega_v^*}J_s p\mathbb{F}_s^{-T}\mathbf{N}\cdot\boldsymbol{q}_h\,d\Sigma^*=0\,.\quad(2.64)\end{aligned}$$

Summing up Eqs. (2.62) and (2.64) and taking $\boldsymbol{q}\in\boldsymbol{H}^1_{0,\partial\Omega^*_{out}}(\Omega^*)$, the weak formulation on the whole domain is

$$\begin{aligned}-\int_{\Omega^*}\left(-J_s p\mathbb{F}_s^{-T}+\mathbb{P}_s\right):\operatorname{Grad}\boldsymbol{q}\,dV^*-\int_{\partial\Omega_t^*}\left[\!\left[\left(-J_s p\mathbb{F}_s^{-T}+\mathbb{P}_s\right)\mathbf{N}\cdot\boldsymbol{q}\right]\!\right]d\Sigma^*+\\-\int_{\partial\Omega_v^*}J_s p\mathbb{F}_s^{-T}\mathbf{N}\cdot\boldsymbol{q}\,d\Sigma^*=0\,.\quad(2.65)\end{aligned}$$

Recalling that the displacement is taken continuous in all directions (2.51a), the areas deform in the same way at the interface. The relation $d\boldsymbol{\Sigma}=J_s\mathbb{F}_s^{-T}d\boldsymbol{\Sigma}^*$, where $d\boldsymbol{\Sigma}=\mathbf{n}d\Sigma$ represents the infinitesimal element of area in spatial coordinates and $d\boldsymbol{\Sigma}^*=\mathbf{N}d\Sigma^*$ denotes the infinitesimal element of area in material coordinates, implies $[\![J_s\mathbb{F}_s^{-T}\mathbf{N}]\!]|_{\partial\Omega_t^*}=\mathbf{0}$. Looking at this condition and at the interface conditions (2.51c) and (2.51d) and recalling that $\boldsymbol{q}\in\boldsymbol{H}^1_{0,\partial\Omega^*_{out}}(\Omega^*)$, the jump in Eq. (2.65) vanishes. Furthermore, the pressure p on $\partial\Omega_v^*$ is fixed by (2.53b) and it assumes the constant value p_v. At the end we are left with

$$-\int_{\Omega^*}\left(-J_s p\mathbb{F}_s^{-T}+\mathbb{P}_s\right):\operatorname{Grad}\boldsymbol{q}\,dV^*-\int_{\partial\Omega_v^*}J_s p_v\mathbb{F}_s^{-T}\mathbf{N}\cdot\boldsymbol{q}_t\,d\Sigma^*=0\,.\quad(2.66)$$

The variational problems in Eqs. (2.60) and (2.66) are non-linear and coupled: in view of the numerical implementation, it is convenient to rewrite them into a single non-linear variational problem by summing them. If we do that, we obtain a variational problem for the displacement and the pressure:

$$\begin{aligned}\int_{\Omega^*}\dot{J}_s q\,dV^*+\int_{\Omega^*}\operatorname{Grad}q\cdot\frac{\mathbb{K}^*}{\mu}\operatorname{Grad}p\,dV^*+\\-\int_{\Omega^*}\left(-J_s p\mathbb{F}_s^{-T}+\mathbb{P}_s\right):\operatorname{Grad}\boldsymbol{q}\,dV^*-\int_{\partial\Omega_v^*}J_s p_v\mathbb{F}_s^{-T}\mathbf{N}\cdot\boldsymbol{q}_t\,d\Sigma^*=0\,.\quad(2.67)\end{aligned}$$

We need then a weak formulation for the equation of the nutrients. In order to derive

it, we multiply Eq. (2.49f) by a test function $q_\mathrm{t} \in H^1_{0,\partial\Omega^*_\mathrm{out}}(\Omega^*)$ and we integrate by parts, obtaining

$$\int_{\Omega^*_\mathrm{t}} \left(J_\mathrm{s}\phi_\ell \dot{c}_n - \frac{\mathbb{K}^*}{\mu} \operatorname{Grad} p \cdot \operatorname{Grad} c_n \right) q_\mathrm{t}\, dV^* + \int_{\Omega^*_\mathrm{t}} \phi_\ell \operatorname{Grad} q_\mathrm{t} \cdot \mathbb{D}^* \operatorname{Grad} c_n\, dV^* + \\ - \int_{\partial\Omega^*_\mathrm{t}} q_\mathrm{t}\phi_\ell \mathbb{D}^* \operatorname{Grad} c_n \cdot \mathbf{N} d\Sigma^* = \int_{\Omega^*_\mathrm{t}} J_\mathrm{s} G_n q_\mathrm{t}\, dV^* . \quad (2.68)$$

We follow the same approach in the healthy domain for Eq. (2.50f):

$$\int_{\Omega^*_\mathrm{h}} \left(J_\mathrm{s}\phi_\ell \dot{c}_n - \frac{\mathbb{K}^*}{\mu} \operatorname{Grad} p \cdot \operatorname{Grad} c_n \right) q_\mathrm{h}\, dV^* + \int_{\Omega^*_\mathrm{h}} \phi_\ell \operatorname{Grad} q_\mathrm{h} \cdot \mathbb{D}^* \operatorname{Grad} c_n\, dV^* + \\ - \int_{\partial\Omega^*_\mathrm{t}} q_\mathrm{h}\phi_\ell \mathbb{D}^* \operatorname{Grad} c_n \cdot \mathbf{N} d\Sigma^* - \int_{\partial\Omega^*_\mathrm{out}} q_\mathrm{h}\phi_\ell \mathbb{D}^* \operatorname{Grad} c_n \cdot \mathbf{N} d\Sigma^* + \\ - \int_{\partial\Omega^*_\mathrm{v}} q_\mathrm{h}\phi_\ell \mathbb{D}^* \operatorname{Grad} c_n \cdot \mathbf{N} d\Sigma^* = \int_{\Omega^*_\mathrm{h}} J_\mathrm{s} G_n q_\mathrm{h}\, dV^* . \quad (2.69)$$

For what concerns the last two surface integrals on the l.h.s., they vanish using the fact that $q_\mathrm{h} \in H^1_{0,\partial\Omega^*_\mathrm{out}}(\Omega^*)$ and the boundary condition (2.53c) on $\partial\Omega^*_\mathrm{v}$. Then we sum Eqs. (2.68) and (2.69) and, recalling the interface condition (2.51f) and the fact that the test function $q \in H^1_{0,\partial\Omega^*_\mathrm{out}}(\Omega^*)$ is continuous along $\partial\Omega^*_\mathrm{t}$, we finally have

$$\int_{\Omega^*} \left(J_\mathrm{s}\phi_\ell \dot{c}_n - \frac{\mathbb{K}^*}{\mu} \operatorname{Grad} p \cdot \operatorname{Grad} c_n \right) q\, dV^* + \int_{\Omega^*} \phi_\ell \operatorname{Grad} q \cdot \mathbb{D}^* \operatorname{Grad} c_n\, dV^* = \\ = \int_{\Omega^*} J_\mathrm{s} G_n q\, dV^* . \quad (2.70)$$

We remark that, given the pressure p and the displacement $\mathbf{u}_\mathrm{s}$ obtained by solving Eq. (2.67), Eq. (2.70) represents a linear variational problem to be solved for the unknown c_n.

2.4.2 Discrete formulation of the continuous variational problems

In order to implement our model and solve the equations by means of the Finite Element Method, it is customary to introduce a discrete formulation in time and space of the continuous variational problems derived in Section 2.4.1, namely, Eqs. (2.67) and (2.70). We make use of linear tetrahedron $\mathbb{P}_1$ elements, so we introduce the following finite element spaces:

$$\boldsymbol{V}_{h,\mathrm{out}} := \left\{ \boldsymbol{q}_h \in \left[C^0\left(\overline{\Omega^*}\right) \right]^3 : \boldsymbol{q}_h|_K \in [\mathbb{P}_1(K)]^3 \ \forall K \in \mathcal{T}_h,\ \boldsymbol{q}_h = \mathbf{0} \text{ on } \partial\Omega^*_\mathrm{out} \right\} \subset \boldsymbol{H}^1_{0,\partial\Omega^*_\mathrm{out}}(\Omega^*) ,$$

$$W_{h0,\mathrm{out}} := \left\{ q_h \in C^0\left(\overline{\Omega^*}\right) : q_h|_K \in \mathbb{P}_1(K)\ \forall K \in \mathcal{T}_h,\ q_h = 0 \text{ on } \partial\Omega^*_\mathrm{out} \right\} \subset H^1_{0,\partial\Omega^*_\mathrm{out}}(\Omega^*) ,$$

$$W_{h0,\mathrm{v}} := \left\{ q_h \in C^0\left(\overline{\Omega^*}\right) : q_h|_K \in \mathbb{P}_1(K)\ \forall K \in \mathcal{T}_h,\ q_h = 0 \text{ on } \partial\Omega^*_\mathrm{v} \right\} \subset H^1_{0,\partial\Omega^*_\mathrm{v}}(\Omega^*) ,$$

$$W_{h1,\mathrm{out}} := \left\{ q_h \in C^0\left(\overline{\Omega^*}\right) : q_h|_K \in \mathbb{P}_1(K)\ \forall K \in \mathcal{T}_h,\ q_h = 1 \text{ on } \partial\Omega^*_\mathrm{out} \right\} \subset H^1(\Omega^*) ,$$

$$W_{hp_\mathrm{v},\mathrm{v}} := \left\{ q_h \in C^0\left(\overline{\Omega^*}\right) : q_h|_K \in \mathbb{P}_1(K)\ \forall K \in \mathcal{T}_h,\ q_h = p_\mathrm{v} \text{ on } \partial\Omega^*_\mathrm{v} \right\} \subset H^1(\Omega^*) ,$$

where $\mathcal{T}_h$ is a decomposition of the domain Ω^* into tetrahedra K conforming to the tumour boundary.

For what concerns the time discretization, given N time instants on the interval $(0,T)$, $\Delta t := T/N$ is the time step and we use a superscript k to denote the value of a quantity at time $t_k = k\Delta t$. Moreover, we use the superscript $k+1$ to denote the value of a quantity of interest at the next time step.

First, we have to introduce a proper discretization of the ordinary differential equations for g_1, g_2 and g_3 in (2.49e). Let $g_{1,h}^{k+1}$, $g_{2,h}^{k+1}$, $g_{3,h}^{k+1}$ be piecewise-constant functions defined on Ω^* approximating g_1, g_2, g_3, respectively. The equations of the system (2.49e) are discretized in time using an explicit Euler method, only in the nodes which belong to the tumour domain Ω_{t}^*:

$$g_{i,h}^{k+1} = g_{i,h}^{k}\left(1 + \Delta t \frac{\tilde{\lambda}_i^k \tilde{a}_i^k(r)}{\tilde{\lambda}_1^k \tilde{a}_1^k(r) + \tilde{\lambda}_2^k \tilde{a}_2^k(r) + \tilde{\lambda}_3^k \tilde{a}_3^k(r)} \frac{\Gamma_{\mathrm{s}}(c_h^k, \phi_{\mathrm{s},h}^k)}{\phi_{\mathrm{s},h}^k}\right), \quad i = 1,2,3\,, \tag{2.71}$$

where $\tilde{\lambda}_i$ and $\tilde{a}_i(r)$ are respectively the eigenvalues and the coefficients of Eqs. (2.30) and (2.35) computed with the information acquired at time step k.

We can then formulate the discrete variational problem for $\mathbf{u}_h^{k+1}$ and p_h^{k+1} as follows: for $k = 1, ..., N$, given $\left(\mathbf{u}_h^k, p_h^k\right) \in \boldsymbol{V}_{h,\mathrm{out}} \times W_{hp_{\mathrm{v}},\mathrm{v}}$ find $\left(\mathbf{u}_h^{k+1}, p_h^{k+1}\right) \in \boldsymbol{V}_{h,\mathrm{out}} \times W_{hp_{\mathrm{v}},\mathrm{v}}$ such that $\forall (\mathbf{v}_h, w_h) \in \boldsymbol{V}_{h,\mathrm{out}} \times W_{h0,\mathrm{v}}$ it holds

$$\begin{aligned}\left(J_{\mathrm{s}}\left(\mathbf{u}_h^{k+1}\right), w_h\right) + \Delta t \left(\operatorname{Grad} w_h, \frac{\mathbb{K}^*\left(\mathbf{u}_h^{k+1}\right)}{\mu} \operatorname{Grad} p_h^{k+1}\right) + \\ - \left(\mathbb{P}\left(\mathbf{u}_h^{k+1}, p_h^{k+1}\right), \operatorname{Grad} \mathbf{v}_h\right) - \left(J_{\mathrm{s}}\left(\mathbf{u}_h^{k+1}\right) p_{\mathrm{v}} \mathbb{F}_{\mathrm{s}}^{-\mathrm{T}}\left(\mathbf{u}_h^{k+1}\right) \mathbf{N}, \mathbf{v}_h\right)_S = \\ = \left(J_{\mathrm{s}}\left(\mathbf{u}_h^{k}\right), w_h\right),\end{aligned} \tag{2.72}$$

where we have used an implicit method for time integration. For simplicity, we have denoted by $(\cdot,\cdot)$ the standard scalar product on the spaces $L^2(\Omega^*)$, $L^2(\Omega^*;\mathbb{R}^3)$ and $L^2(\Omega^*;\mathbb{R}^{3\times 3})$ when appropriate, and by $(\cdot,\cdot)_S$ the integral on the surface $\partial\Omega_{\mathrm{v}}^*$.

Afterwards, we need to introduce adequate discretization of the mass balance (2.49b)-(2.50b) and the saturation condition (2.49c)-(2.50c), where $\phi_{\mathrm{s},h}^{k+1}$ and $\phi_{\ell,h}^{k+1}$ represent piecewise-constant functions approximating ϕ_{s} and ϕ_{ℓ}. The first equation is discretized as

$$\phi_{\mathrm{s},h}^{k+1} = J_{\mathrm{s}}^{-1}(\mathbf{u}_h^{k+1}) g_{1,h}^{k+1} g_{2,h}^{k+1} g_{3,h}^{k+1} \phi_{\mathrm{sn}}\,. \tag{2.73}$$

Once we have computed $\phi_{\mathrm{s},h}^{k+1}$, we can derive $\phi_{\ell,h}^{k+1}$ using the saturation condition

$$\phi_{\ell,h}^{k+1} = 1 - \phi_{\mathrm{s},h}^{k+1}\,. \tag{2.74}$$

Finally, we can solve the variational problem for the nutrients. Given $c_h^k \in W_{h1,\text{out}}$, we have to find $c_h^{k+1} \in W_{h1,\text{out}}$ such that $\forall q_h \in W_{h0,\text{out}}$ it holds

$$\left(J_\text{s}\left(\mathbf{u}_h^{k+1}\right)c_h^{k+1}, q_h\right) - \Delta t\left(\frac{\mathbb{K}^*\left(\mathbf{u}_h^{k+1}\right)}{\mu\phi_\ell^{k+1}}\,\text{Grad}\,p_h^{k+1}\cdot\text{Grad}\,c_h^{k+1}, q_h\right) +$$

$$+\,\Delta t\left(\text{Grad}\,q_h, \mathbb{D}^*\left(\mathbf{u}_h^{k+1}\right)\text{Grad}\,c_h^{k+1}\right) - \Delta t\left(J_\text{s}\left(\mathbf{u}_h^{k+1}\right)\frac{G_n\left(c_h^{k+1}\right)}{\phi_\ell^{k+1}}, q_h\right) =$$

$$= \left(J_\text{s}\left(\mathbf{u}_h^{k+1}\right)c_h^k, q_h\right). \quad (2.75)$$

Also in this case, we have used an implicit Euler method for time integration. Furthermore, an adaptive time-step was used in order to ensure the convergence of the numerical simulations. Specifically, our equations are solved with a constant time-step, but if, at any given temporal instance, our method does not converge, Δt is halved until convergence is achieved. Once the next time-step is reached, the time-step is reset to the initial value.

2.4.3 Parameters estimation

Before running numerical simulations, it is essential to identify suitable values for the parameters involved in the model. While obtaining precise estimates for these parameters can be challenging, selecting reasonable values is crucial to generate a realistic outcome, which is one of the goals of our work. The selected parameter values, together with the biological ranges found in the literature and the relative references, are summarised in Table 2.1.

For what concerns the mechanical parameters $\mu_{1\text{h}}$ and $\mu_{2\text{h}}$ of the healthy tissue, we refer to the estimates of mean values provided by Balbi et al. for human brain matter [45], that is, we take $\mu_{1\text{h}} = 3.06 \cdot 10^{-4}$ MPa and $\mu_{2\text{h}} = 5.94 \cdot 10^{-4}$ MPa. These parameters are also in the range found by other authors [83, 85], even though also smaller values of the order of 10^{-5} MPa are sometimes found. Regarding the tumour, the choice of material parameters for brain cancer is debated in the literature. Several studies point out that the tumour is stiffer than the healthy tissue, even more than ten times in some cases [5, 109, 123, 368, 464, 469]. However, some works suggest that brain tumours may be as stiff as the normal tissue, or even softer [381, 478]. A study of different values for the mechanical parameters of healthy and tumour tissue was carried out computationally in [338]. In the present work, we choose $\mu_{1\text{t}}$ and $\mu_{2\text{t}}$ as ten times greater than their healthy counterparts. Ideally, these parameters could be estimated by means of patient-specific Magnetic Resonance Elastography (MRE), as done in [236]. However, accurate tools for the reconstruction of complex non-linear constitutive responses by means of MRE are still lacking. The volumetric moduli κ_t and κ_h are also difficult to be estimated, given that very few experiments are carried out by accounting for poroelastic effects. Following [413], we take $\kappa_\text{h} = 1.389 \cdot 10^{-4}$ MPa, and $\kappa_\text{t} = 10\kappa_\text{h}$. We remark that we choose not to differentiate the mechanical parameters between grey and white matter. Although some experiments showed rheological differences between them [86, 223], some subsequent investigations such as [85] do not seem to underline a substantial distinction. Furthermore, since in the present work we are focusing on a tumour which is ten times stiffer than the healthy tissue, the possible mechanical difference between grey and white matter appears to be less relevant. Therefore, we decided to prioritize simplicity and computational efficiency in the present version of the model, so we did

not adopt this differentiation, which could have a greater impact if the cancer and the healthy tissue have comparable stiffness.

The parameter ν appearing in Eq. (2.18) is estimated as in [125] by using typical proliferation times for glioma cells in vitro, which range between 24 and 48 hours. Hence, we choose an intermediate value of $\nu = 0.65$ day^{-1}. The hypoxia threshold c_0 is set to 0.30, given that values in the literature range from 0.15 to 0.5 [4, 191, 205, 489]. The nutrients consumption rate ζ in Eq. (2.18) is estimated as done in [125], resorting to measurements of oxygen diffusion in the brain. In particular, we set $\zeta = 8640$ day^{-1}. Instead, for the nutrients supply rate S_n, we refer to the value of 10^4 days^{-1} proposed in [104], as in [4, 47, 48, 125, 338]. The maximum cell volume fraction $\phi_{\max}$, representing contact inhibition of cell growth, is set to be $\phi_{\max} = 0.95$. Even if, to the best of our knowledge, such a parameter is not estimated experimentally, we assume that a minimum amount of extracellular fluid remains present in the tissue, since we are not considering the formation of calcification and necrotic regions.

Then, we need to estimate the values of the parameters that appear in the radiotherapy and chemotherapy terms defined in Eq. (2.19). Inspired by the standard Stupp protocol [467] and recalling Eq. (2.21), we take the dose of radiation for every fraction d equal to 2 Gy, given once daily, i.e. $n = 1$ day^{-1}. Furthermore, the dose at which the contributions from the first and the second term in Eq. (2.21) are equal is given by α/β [Gy], which is an inverse measure of a tissue's sensitivity to the dosage administered during each treatment. In the following, the value prescribed in [410, 432] is used, where this ratio is taken as equal to 10 Gy. For what concerns the linear coefficient for RT-induced cell killing, we assume a value of $\alpha = 0.027$ Gy^{-1}, in agreement with [4, 410, 430]. As a consequence, we have that $\beta = 0.0027$ Gy^{-2}. Introducing all these parameters in Eq. (2.21), we obtain the value of the radiotherapy death rate $R_{\text{eff}} = 0.0648$ day^{-1}. On the other hand, the values of CHT-induced cell killing rate are chosen with reference to [4, 410], i.e. $k_{C1} = 0.00735$ day^{-1}, $k_{C2} = 0.0147$ day^{-1} and $k_{C3} = 0.0196$ day^{-1}. Finally, in the simulations where therapy decay is accounted for as in Eq. (2.22), we consider a value of $\lambda_c = 0.05$ day^{-1}. We remark that such a choice is not motivated by the will of reproducing the chemotherapeutic drug half life, which is indeed much shorter [192]. Instead, it is rather made with the intention of capturing the prolonged effects of chemotherapy over time. This allows to incorporate in our model the processes initiated by the drug and their effects on the tumour, in terms of cell late apoptosis, which gradually decline over time. Indeed, late apoptosis/necrosis induced by TMZ has been experimentally recorded even after many days from the last treatment [68, 241, 434]. However, we acknowledge that the correct estimation of such a parameter deserves further experimental studies and medical data.

Regarding the free water diffusivity coefficient D_w at 37°C, which appears in Eqs. (2.26) and (2.27), the mean value reported in the literature is $D_w = 259.2$ mm^2 day^{-1} [310], and we decide to adopt such a value. Furthermore, it is necessary to estimate the cell volumetric fraction $\phi_{\text{s}}^0(\mathbf{X})$ at the initial time. We assume it to be equal to the cell volumetric fraction in the natural state, denoted as ϕ_{sn}, which is a predefined constant. In this study, we consider a value of $\phi_{\text{sn}} = 0.45$, based on the approximate estimation that the extracellular space, which is complementary to the solid volume fraction, constitutes around $50 - 60\%$ [82]. By prescribing $\phi_{\text{s}}^0(\mathbf{X})$, we also define the initial fluid volumetric fraction $\phi_\ell^0(\mathbf{X}) = 1 - \phi_{\text{s}}^0(\mathbf{X}) = 1 - \phi_{\text{sn}}$, which is utilized in the construction of the initial diffusion tensor of Eq. (2.26). We remark that, although an ideal approach would involve the use of a voxel-wise estimation of the free-water content to determine a spatially dependent initial value for ϕ_ℓ^0 [13, 255], in this work we have chosen not to consider it for specific reasons. Firstly, the impact of this simplification on the results is not remarkable, as it is greatly mitigated by the exclusion of the ventricular region from our domain. In fact,

the ventricles are mainly filled with water and therefore the inclusion of this area in the computational domain would have been most affected by this choice. Furthermore, in the specific region where the brain tumour was initially localised, we identified a homogeneous distribution of the free water estimated from the DTI data. Moreover, to account for a spatially inhomogeneous distribution of ϕ_ℓ, it would be necessary to address an initial mechanical problem to establish the condition of mechanical equilibrium, in order to avoid tissue evolution unrelated to growth. Finally, simulations with highly inhomogeneous conditions face numerical convergence problems that require further analysis. Regarding the permeability parameters of Eq. (2.36), we remark that the reference permeability k_0 has units of mm^2, while in the literature it is frequent to estimate the hydraulic conductivity $k_c := k_0/\mu$, with μ the dynamic viscosity. Values for k_c, which has units $\text{mm}^2\ \text{MPa}^{-1}\ \text{day}^{-1}$, range in the literature between $10^4 - 10^5\ \text{mm}^2\ \text{MPa}^{-1}\ \text{day}^{-1}$ for the brain [35, 58, 272, 357, 498, 499]. We adopt the value of $k_c = 7.8 \cdot 10^4\ \text{mm}^2\ \text{MPa}^{-1}\ \text{day}^{-1}$, as in [272]. Instead, we take $\alpha_0 = 0.0848$ and $m = 4.638$ as for other soft tissues [150, 252], though specific experimental estimates for them in the brain are still lacking.

Finally, it is necessary to estimate the pressure p_v of cerebrospinal fluid (CSF) in the brain ventricles, which appears in the boundary condition (2.53b). Intracranial pressure measurements suggest that normal mean pressure exerted by CSF is in the range of 0 to 10 mmHg [11, 26]. We consider therefore an intermediate value within this range, i.e. 5 mmHg, which is equivalent to a value of $p_\text{v} = 6.67 \times 10^{-4}$ MPa. To be precise, this value could have also been set to zero as it merely causes a shift in pressure.

2.5 Results and discussion

The mechanical model used in our study simulates the progression of brain tumours to determine their preferential directions of growth and the resulting stresses and strains on the healthy surrounding brain tissue. The tumour is considered as a sphere of initial radius 2.5 mm, located near the right lateral ventricle of the brain. The evolution is then simulated for a time period of 140 days, both with and without therapies. In this way, we are able to evaluate how the growth and the mechanical alterations provoked by the tumour may adversely impact on the cerebral ventricles. Moreover, we can test different therapeutic protocols in the simulations and observe the consequences on cancer growth. Simulations have been performed using the discrete formulation described in Section 2.4.2, implemented in the software *FEniCS* [18, 324], which provides a high-level Python and C++ interface for solving PDEs through the Finite Element Method.

2.5.1 Simulation without any therapeutic intervention

A first simulation is performed without including neither radiotherapy nor chemotherapy, so the tumour is free to grow. Fig. 2.4 illustrates the temporal progression of the solid cell fraction on the brain geometry. As cancer cells proliferate within the tumour region, there is a noticeable increase in the volumetric fraction occupied by the solid phase. After an uninterrupted growth period of approximately five months, ϕ_s approaches a value of 0.85 within the tumour domain, indicating a higher density of cancer cells as the tumour evolves. From Fig. 2.4, it is evident that the volumetric fraction of the cell phase, ϕ_s, exhibits an anisotropic expansion, extending beyond the tumour region and into the surrounding healthy tissue. This expansion is primarily driven by the compressive effects exerted by the expanding tumour mass on the neighbouring

Parameter	Description	Value	Biological range	Ref.
μ_{1h}	Mooney-Rivlin material parameter (healthy)	$3.06 \cdot 10^{-4}$ MPa	$3.0 \cdot 10^{-7} - 6.436 \cdot 10^{-4}$ MPa	[45]
μ_{2h}	Mooney-Rivlin material parameter (healthy)	$5.94 \cdot 10^{-4}$ MPa	$1.1936 \cdot 10^{-4} - 1.42058 \cdot 10^{-3}$ MPa	[45]
κ_h	Volumetric modulus (healthy)	$1.389 \cdot 10^{-4}$ MPa	$2 \cdot 10^{-4} - 2 \cdot 10^{-2}$ Pa	[413]
μ_{1t}	Mooney-Rivlin material parameter (tumour)	$3.06 \cdot 10^{-3}$ MPa	$10^{-5} - 10^{-2}$ MPa	[109, 368, 464]
μ_{2t}	Mooney-Rivlin material parameter (tumour)	$5.94 \cdot 10^{-3}$ MPa	-	[109, 368, 464]
κ_t	Volumetric modulus (tumour)	$1.389 \cdot 10^{-3}$ MPa	-	[413]
ν	Cell proliferation constant	0.65 day^{-1}	$0.5 - 1$ day^{-1}	[191]
c_0	Hypoxia threshold	0.30	$0.15 - 0.5$	[4]
ζ	Nutrients consumption rate	8640 day^{-1}	$8640 - 15650$ day^{-1}	[125, 338]
S_n	Nutrients supply rate	10^4 day^{-1}	-	[4, 104, 125]
ϕ_{sn}	Cell volume fraction in the natural state	0.45	$0.3 - 0.5$	[82]
ϕ_{max}	Maximum cell volume fraction	0.95	$0.8 - 1$	[47, 48, 338]
R_{eff}	Radiotherapy death rate	0.0648 day^{-1}	$0.06 - 0.0792$ day^{-1}	[4, 410, 430, 432]
k_{C1}	Concomitant CHT death rate	0.00735 day^{-1}	-	[4, 410, 430, 432]
k_{C2}	First cycle of adjuvant CHT death rate	0.0147 day^{-1}	-	[4, 410, 430, 432]
k_{C3}	Other cycles of adjuvant CHT death rate	0.0196 day^{-1}	-	[4, 410, 430, 432]
λ_c	Chemotherapy decay rate	0.05 day^{-1}	-	Estimated
D_w	Diffusivity of free water at 37°	259.2 mm$^2 \cdot$ day^{-1}	$43.2 - 259.2$ mm$^2 \cdot$ day^{-1}	[310]
k_0/μ	Hydraulic conductivity	$7.8 \cdot 10^4$ mm$^2 \cdot$ MPa$^{-1} \cdot$ day^{-1}	$10^4 - 10^5$ mm$^2 \cdot$ MPa$^{-1} \cdot$ day^{-1}	[272]
α_0	Holmes-Mow permeability parameter	0.0848	-	[150]
m	Holmes-Mow permeability parameter	4.638	-	[150]
p_v	Pressure exerted by cerebrospinal fluid	$6.67 \cdot 10^{-4}$ MPa	$0 - 1.3332 \cdot 10^{-3}$MPa	[11, 26]

TABLE 2.1: List of the values of the model parameters employed in the numerical simulations.

healthy region and ventricle. Conversely, a decrease in ϕ_s is observed near the ventricles, indicating an increased presence of the liquid phase in that specific zone and fluid flow near the compressed ventricles. These observations highlight the spatial heterogeneity of tumour-induced changes in the cell phase and the influence of neighbouring structures on these alterations. For what concerns the magnitude of the displacement $\|\mathbf{u}_s\|$ shown in Fig. 2.4b, it is immediately evident a substantial anisotropic growth behaviour, which follows the orientation of the surrounding white matter tracts. We can observe that values of the displacement are not negligible, since they reach a maximum value of 9.3 mm, which is almost four times bigger than the initial radius. Furthermore, a contour line is plotted to indicate the magnitude of displacement values equal to 1 mm. It is worth to observe that the area affected by unnatural displacements around the tumour is quite extended, indicating that not only the region near the tumour boundary experiences deformations, but there are relevant strains also far from the cancer mass. Moreover, the final volume of the tumour is significantly increased, as it reaches the value of 1737.92 mm^3, while the initial one was 63.24 mm^3, that is more than 27 times smaller, indicating a significant boost in the dimensions of the tumour. To make a comparison with clinical references, we computed some measures of tumour growth that are often used in the biomedical literature. Specifically, we find a volume doubling time (VDT) of about 29.3 days, which is aligned with data from Stensjoen et al. [461] (median VDT: 29.8 days) and from Ellingson et al. [168] (median VDT: 21.1 days). The specific growth rate (SGR), defined as $(\ln 2)/\text{VDT}$, is therefore 2.4%/day, which is also consistent with the mentioned references. However, we remark that such measures are often computed in the clinical literature by assuming an exponential growth law, which might be oversimplified. Another parameter that is sometimes used to quantify brain tumour growth is the average velocity of radial expansion (VRE). In our case, given that we have a strongly anisotropic tumour which consistently differs from a sphere, we computed the velocity of expansion along the three axes of the tumour ellipsoid. We find that the VRE along the major axis is approximately $v_{\text{RE}}^{\text{max}} \approx 19.1$ mm/year, whereas the VRE along the intermediate axis is $v_{\text{RE}}^{\text{int}} \approx 12.1$ mm/year and the one along the minor axis is $v_{\text{RE}}^{\text{min}} \approx 10.2$ mm/year. These values are comparable with clinical data [461, 505], even though there is a high variability from patient to patient. In all these simulations, it is visibly evident that the shape of the tumour is no longer a sphere as it was initially, but the mass has grown along the preferential directions. In order to assess how much anisotropic growth impacts the final shape of the tumour and the size it reaches, we perform the same simulations as before using an isotropic form of the growth tensor $\mathbb{F}_g = g\mathbb{I}$, while keeping an anisotropic diffusion of the nutrients and permeability tensor (*isotropic growth model*), as done in [47]. In Fig. 2.5, the magnitude of the displacement at time $t = 140$ days obtained in the latter case is compared to the one obtained with the *anisotropic growth model* proposed in the present work. It is evident that the hypothesis of an anisotropic growth tensor has a strong impact on the shape that the tumour develops and for this reason it is important to model the presence of preferential growth directions in $\mathbb{F}_g$ to predict the correct tumour expansion. Thus, this work overcomes the limitations of previous mechanical models [47, 338], in which isotropic growth strains were used and the predicted final tumour shapes did not deviate too much from the spherical one. To provide also a quantitative measure of these differences, it is possible to compute a sphericity index, by measuring the lengths of the three representative axes of the tumour at $t = 140$ days in both cases. If we call a the length of the longest axis, b the intermediate one, and c the shortest, we can define the *intercept sphericity* as the cubic root of the ratio between the volume of an ellipsoid having the three diameters a,

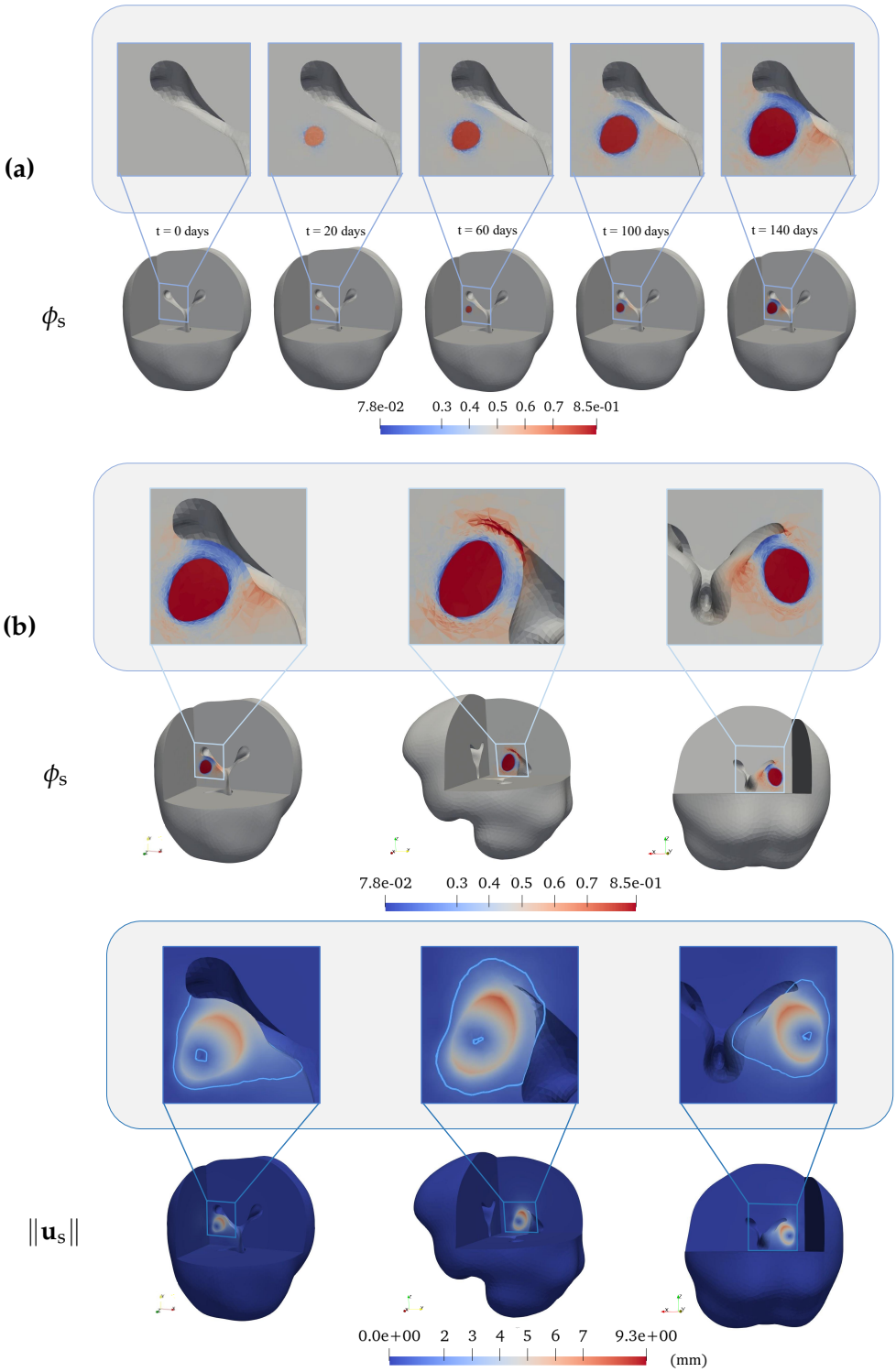

FIGURE 2.4: **(a)** Temporal evolution of the volumetric fraction of cell population ϕ_s in the brain domain. **(b)** Comparison between the volumetric fraction of cell population ϕ_s and the displacement magnitude $\|\mathbf{u}_s\|$ after $t = 140$ days of tumour growth in the brain, clipped along three different planes. The insets show a magnification near the ventricles, where the growth phenomenon is primarily happening.

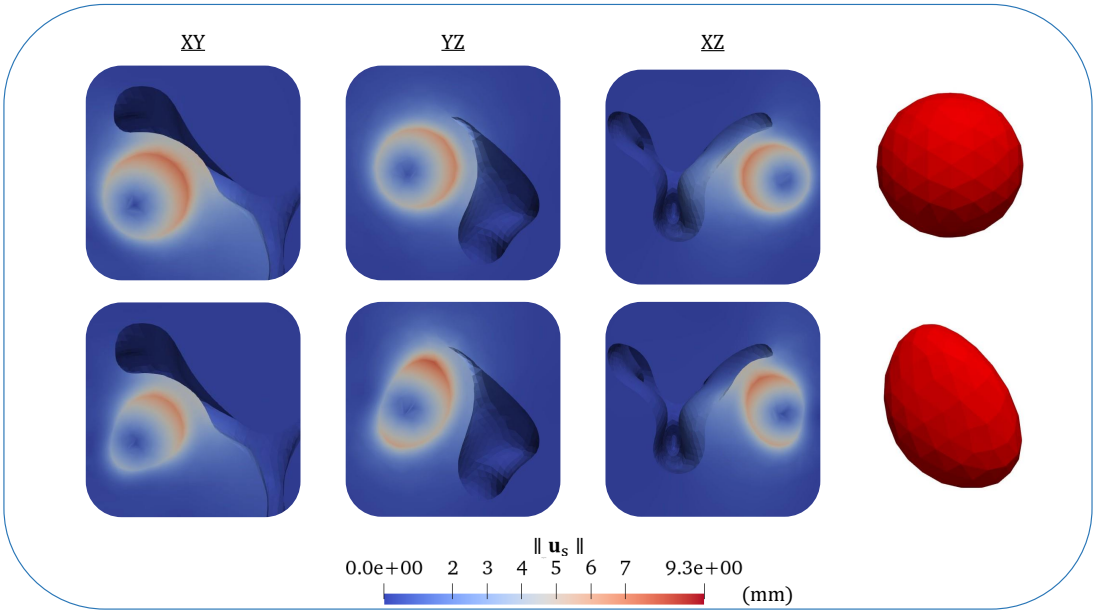

FIGURE 2.5: Comparison between the final magnitude of displacement using *isotropic growth model* (first row) and *anisotropic growth model* (second row), clipped in three different planes at time $t = 140$ days. The last column shows the 3D final shape reached by the tumour at time $t = 140$ days.

b, and c and the volume of the circumscribing sphere of diameter a [133, 299, 455]:

$$\psi := \sqrt[3]{bc/a^2}\,. \tag{2.76}$$

In our cases, for the isotropic growth simulation we obtain $\psi = 0.9834$, whereas we get $\psi = 0.7792$ for the anisotropic case, which means that the latter is definitely more elongated, while the first is more spherical. Furthermore, in order to characterize the anisotropic behaviour of the growth tensor $\mathbb{F}_g$, we introduce two parameters called *linear anisotropy coefficient* (g_ℓ) and *spherical anisotropy coefficient* (g_s), motivated by the definition of c_ℓ and c_s used in evaluating the anisotropy of diffusion in Eq. (2.34):

$$g_\ell := \frac{g_{\max} - g_{\text{mid}}}{g_{\max} + g_{\text{mid}} + g_{\min}}\,, \quad g_s := \frac{3g_{\min}}{g_{\max} + g_{\text{mid}} + g_{\min}}\,, \tag{2.77}$$

where $g_{\max} = \max\{g_1, g_2, g_3\}$, $g_{\min} = \min\{g_1, g_2, g_3\}$ and g_{mid} is the remaining one, recalling that g_1, g_2 and g_3 are the eigenvalues of $\mathbb{F}_g$. These coefficients provide insights into the directional preference and overall isotropy of the growth tensor, respectively: a value of $g_\ell \approx 1$ denotes that growth is happening almost entirely along a preferential direction, whereas $g_s \approx 1$ is indicative of isotropic growth. In Fig. 2.6, the coefficients g_ℓ and g_s across different brain sections are presented at the specific time point of $t = 140$ days. Regarding the results of the linear anisotropy coefficient, g_ℓ, certain regions within the tumour display values closer to 1, indicating a preference for growth along a specific axis. In contrast, values closer to 0 suggest a more planar or isotropic behaviour. As for the results of g_s, in some regions they generally tend to be closer to zero than to one. This indicates that, in those areas, the deformation within the tumour zone is not isotropic but rather exhibits preferential deformation along specific directions.

As mentioned above, it can be noted that tumour-induced displacement compresses the near brain ventricles: such a clinical issue was pointed out for instance in [8, 459].

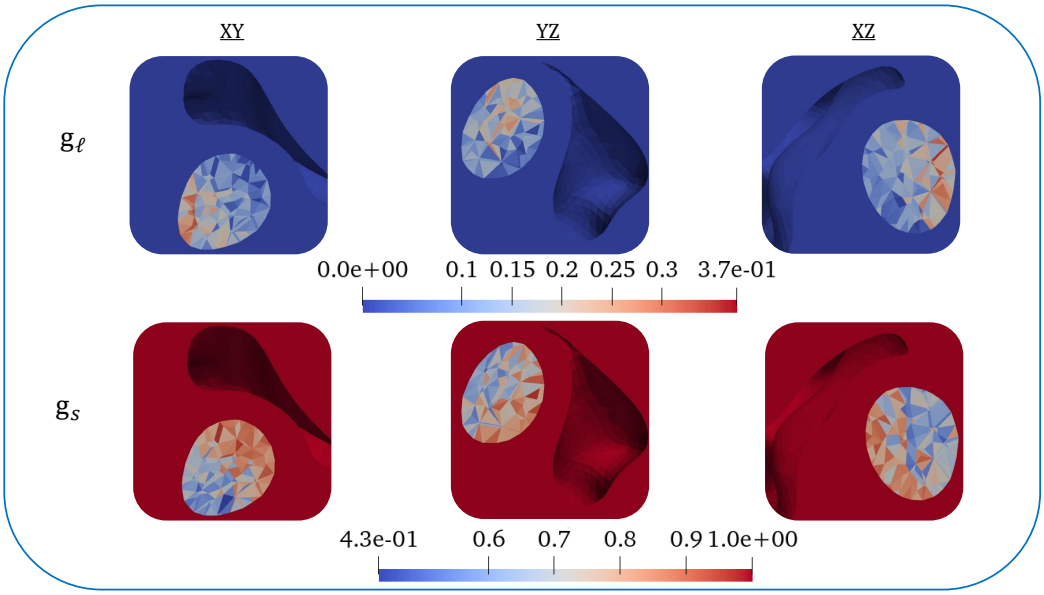

FIGURE 2.6: Visualization of linear (g_ℓ) and spherical (g_s) anisotropy coefficients in three different planes at time $t = 140$ days.

The amount of compression can be quantified in terms of volume reduction of the ventricles with respect to the initial configuration. More specifically, we concentrate our analysis on the posterior section of the right lateral ventricle, which is adjacent to the tumour area. This particular region represents approximately half of the total volume of the right lateral ventricle. By tracking its temporal evolution, we observe changes in volume over time. The initial volume, measured computationally, is recorded as 7693.25 mm^3. The evolution in time of the ventricular volume in the region under consideration is then reported in Fig. 2.7, together with a representation of the portion of compressed ventricles. We find that the volume of the portion of the ventricle considered is reduced to a value of 6738.23 mm^3 (corresponding to a decrease of 12.4% of the initial volume) after 140 days of tumour growth, highlighting that a significant compression has occurred in that region. Moreover, we find that the maximum displacement magnitude of the ventricular portion considered amounts at 6.7 mm, which is a notable value, in line with clinical evaluations of ventricular displacement [459, 519]. We remark that in our simulation the edges of the cerebral ventricles never collapse and get into contact. When comparing the compression of the cerebral ventricles between the anisotropic and isotropic simulations, we observe that, with the same tumour volume equal to 1737.92 mm^3, the final volume of the ventricular portion in the isotropic simulation is 6915.51 mm^3. Consequently, in that case the ventricles experience reduced compression. This underscores the significance of incorporating anisotropy into our model, providing a more precise representation of the intricate behaviour of brain tumours within a realistic anatomical environment.

Fig. 2.8 presents the outcomes related to the pressure p, the nutrient concentration c_n and the volumetric solid Cauchy stress $\sigma := -\frac{1}{3}\mathrm{tr}(\mathbb{T}_s)$, where $\mathbb{T}_s = J_s^{-1}\mathbb{P}_s\mathbb{F}_s^T$, at the final time step, depicted in three distinct brain sections. Looking at the pressure, negative values emerge in the tumour zone, since the fluid is consumed by the cancer mass during uncontrolled cellular growth. Coherently, the concentration of nutrients decreases inside the tumour, where nutrients are consumed by proliferative cells, and near its boundary due to diffusion and transport towards the cancer, while it is maintained at

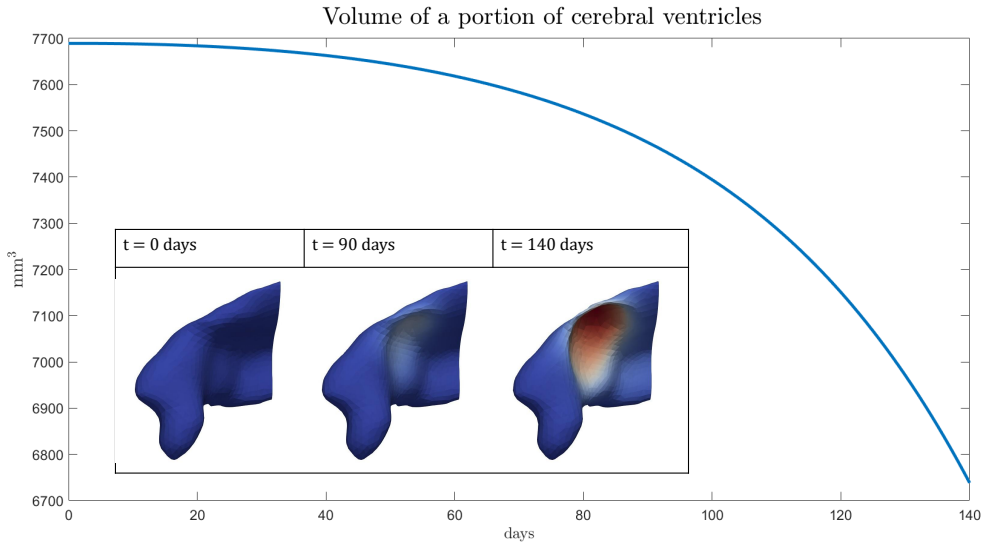

FIGURE 2.7: Volume of a portion of cerebral ventricles over time. In the bottom left, a graphical representation of the cerebral ventricles at three different time instants ($t = 0,\ 90,\ 140$ days) is shown.

the physiological value of 1 far from the cancer region. We observe that, for the chosen set of parameters, the concentration of nutrients is never above the physiological threshold, i.e. $c_n \leq 1$. Finally, concerning the volumetric solid Cauchy stress σ, positive values within the tumour region indicate tissue compression therein and suggest the presence of compressive forces acting on the cells. In contrast, negative values surrounding the tumour mass indicate tissue traction, implying the existence of stretching forces in this area. This distribution of stresses highlights the mechanical interactions within the tumour micro-environment and provides insights into the biomechanical behaviour of the surrounding tissue under the influence of the growing tumour. Indeed, the presence of gradients of solid stresses, with tractions near the tumour boundary and compression inside the proliferating mass, is frequently found in experimental analyses [381, 443]. To compare our outcomes with experimental and clinical evidence, first of all we remark that, in our results, $\sigma > 0$ denotes compression, differently from other references in the literature. Given this sign convention, we find that the amount of compressive stress within the tumour area is quantitatively comparable with experimental results on glioma tumour spheroids by Stylianopoulos et al. [469], where compressive stresses range between 5–8 kPa. These values are coherent both with the hydrostatic stress plotted in Fig. 2.8 and with the hoop stress values of our model, which inside the tumour area vary between 1–9 kPa of compressive stress. A range of 1.3–13.3 kPa is pointed out by Stylianopoulos et al. in another work about tumour spheroids [468], though in that case the results are not brain-specific. Moreover, by using a poroelastic model with experimentally informed parameters for tumour spheroids, Fraldi and Carotenuto [188] found compressive stress values that are comparable with ours. Instead, measurements of stresses in murine brain tumours by Seano and co-workers [443] display compressive stress values of the order of 10^{-1} kPa. This discrepancy might be due to the material model chosen and to the difference in stiffness between the tumour and the host tissue, as pointed out in [338]. Furthermore, we observe that relatively high compression values of the volumetric solid Cauchy stress σ can also be found at the interface between the healthy tissue and the ventricles, in the presence of high deformations. Indeed, at this boundary, while the normal component of the stress is null, the tangential/hoop

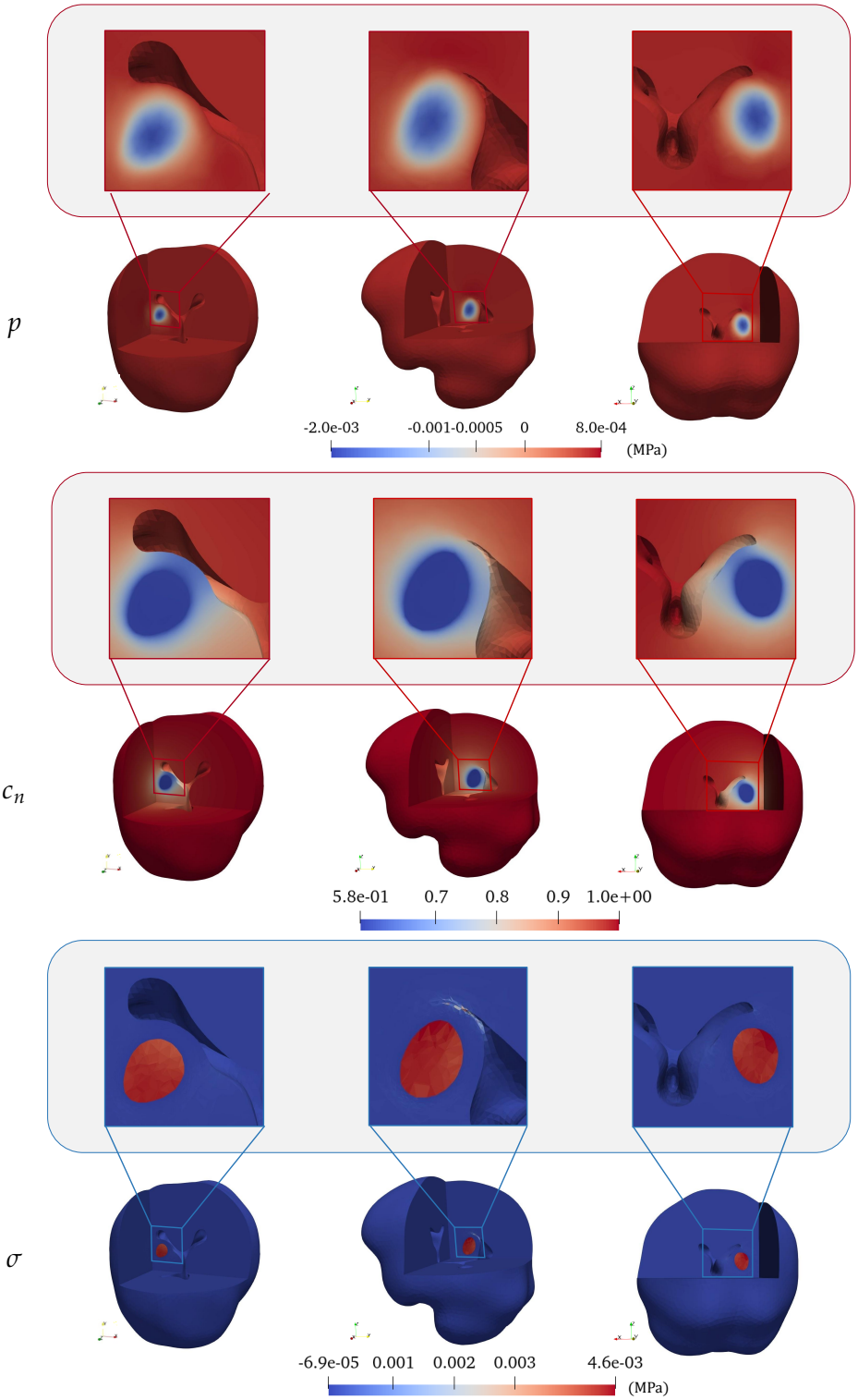

FIGURE 2.8: Comparison between the pressure p, the concentration of nutrients c_n and $\sigma := -\frac{1}{3}\mathrm{tr}(\mathbb{T}_s)$ after $t = 140$ days of tumour growth in the brain, clipped along three different planes. The insets show a magnification near the ventricles, where the growth phenomenon is primarily happening.

component of the stress may be significantly elevated. In this case, given the forthcoming contact scenario, it will be important to model contact boundary conditions for a thorough analysis of the stress distribution in this region, a consideration that will be addressed in future research. Concerning the fluid pressure, our results display a decrease inside the tumour region due to the cells consuming fluid therein, in accordance with other works using mixture models [218, 219]. However, other references [188, 468] report an increase in the interstitial fluid pressure within the tumour. The discrepancy is due to the fact that these models also account for possible fluid inflow due to vessel leakage and osmotic pressure differences, as well as for outflow due to lymphatic drainage. We did not consider such effects in our model, although a Starling-like law could be easily incorporated and would be interesting to investigate.

Finally, we present the findings concerning the impact of tumour growth on DTI data. As the tumour expands and displaces the surrounding tissue, it alters the natural arrangement of fibre tracts, resulting in noticeable modifications in the preferred directions of diffusion and fluid motion. To quantify this effect, we employ a scalar parameter known as *fractional anisotropy* (FA), which is calculated based on the descending order eigenvalues of the diffusion tensor (λ_1, λ_2, and λ_3) as

$$\mathrm{FA} := \sqrt{\frac{1}{2}\frac{(\lambda_1-\lambda_2)^2+(\lambda_2-\lambda_3)^2+(\lambda_1-\lambda_3)^2}{\lambda_1^2+\lambda_2^2+\lambda_3^2}}\,. \tag{2.78}$$

A fractional anisotropy value of 0 indicates an isotropic environment where the eigenvalues are all equal to each other, resulting in a diffusion ellipsoid resembling a sphere with no preferred direction. Conversely, a fractional anisotropy value of 1 identifies the presence of a single preferential direction, limiting diffusion to happen exclusively along one of the eigenvectors. To assess the alteration of the diffusion tensor over time due to tumour-induced deformation, we compute the fractional anisotropy of the diffusion tensor $\mathbb{D}$ at the final time point ($t = 140$ days) of the simulation where no therapies were included and subtract it from the fractional anisotropy of the initial time diffusion tensor $\mathbb{D}^0$, i.e. we evaluate $\Delta\mathrm{FA}_{\mathbb{D}} := \mathrm{FA}_{\mathbb{D}} - \mathrm{FA}_{\mathbb{D}^0}$. Similarly, we compute the variation of fractional anisotropy for the tensor $\mathbb{D}_{\mathrm{NFW}}$ at $t = 140$ days, which takes into account the motion influenced by the fibres. This variation is denoted as $\Delta\mathrm{FA}_{\mathbb{D}_{\mathrm{NFW}}} := \mathrm{FA}_{\mathbb{D}_{\mathrm{NFW}}} - \mathrm{FA}_{\mathbb{D}^0_{\mathrm{NFW}}}$. Such an index is comparable to the so-called Free Water Eliminated Fractional Anisotropy (FWE–FA) reported in certain medical studies [59]. The findings derived from computing differences between initial and final data on each cell of the mesh are presented in Fig. 2.9. For what concerns the non-free water diffusion tensor $\mathbb{D}_{\mathrm{NFW}}$, there is a notable increase in diffusive anisotropy in the region surrounding the expanding tumour. The variations in fractional anisotropy are not uniform around the tumour area, revealing distinct zones that experience significant changes in anisotropy while others maintain their initial preferred directions. In particular, we notice that the FA associated to $\mathbb{D}_{\mathrm{NFW}}$ within the tumour bulk mostly remains constant. This is due to the fact that we modify the tensor $\mathbb{D}_{\mathrm{NFW}}$ by means of the solid deformation, which is greater around the tumour domain. As a consequence, the most relevant alterations in anisotropy are observed in the surroundings, where displacements attain higher values and the cancer mass dislocates the white matter fibres. The reconstruction of DTI data inside the tumour is a non-trivial problem, given that such data often appear to be altered by the cancerous mass in patients, even at the first scan. Therefore, the modelling of anisotropy changes inside the tumour may require further research efforts [479], also accounting for damage of fibres and reconstruction algorithms. On the other hand, as far as the diffusion tensor $\mathbb{D}$ is concerned, it can be observed that, in

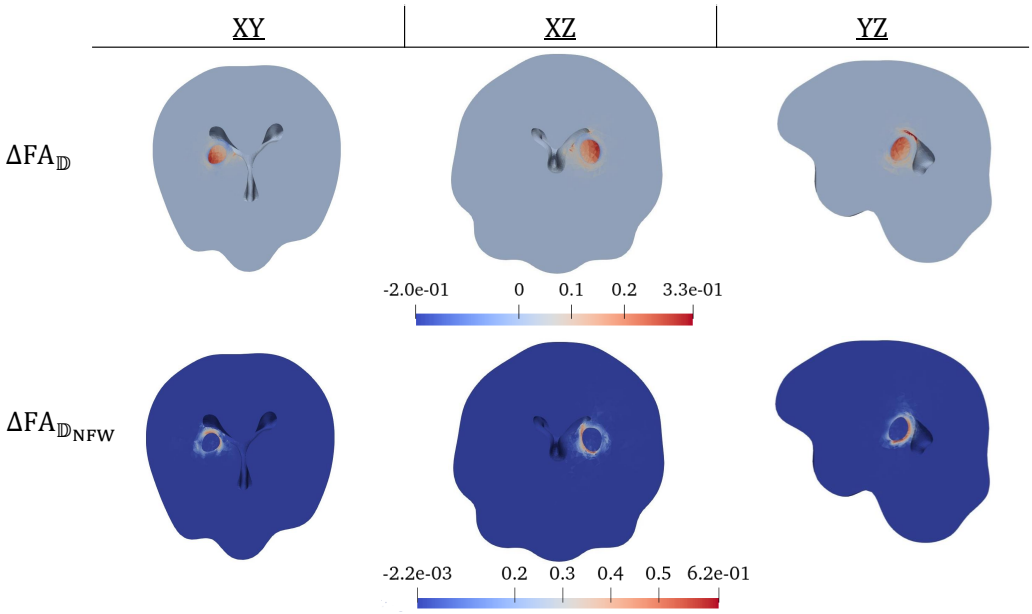

FIGURE 2.9: Variation in fractional anisotropy (FA) over 140 days of tumour growth, comparing the diffusion tensor ($\mathbb{D}$) and its non-free water component ($\mathbb{D}_{NFW}$).

the regions near the ventricles, there is a decrease in fractional anisotropy, which is reflected in negative values of $\Delta FA_{\mathbb{D}}$. This is because the presence of more fluid results in a higher weighting of the isotropic component of the tensor, recalling Eq. (2.27). On the contrary, in the area within the tumour, the increase in ϕ_s results in a greater importance attributed to the non-free water component of $\mathbb{D}$, leading to observed increases in FA with respect to initial DTI data, where more fluid was present.

2.5.2 Simulations including radiotherapy and chemotherapy

After having studied the effect of anisotropic growth and its impact on cerebral ventricles, we incorporate radiotherapy and chemotherapy into our mathematical model. Such a capability represents a relevant feature of our framework, as it may allow to evaluate treatment efficacy by simulating the effects of therapies on tumour progression. This might be of help in understanding how the tumour responds to treatments and provide insights into potential therapeutic strategies, which are often very challenging for brain tumours. Secondly, the model may assist in optimising treatment protocols by simulating different schedules, dosages, and drug combinations, aiding in personalised treatment planning.

First of all, we conducted a simulation by incorporating the first protocol presented in Section 2.2.3 and defined by Eqs. (2.20a)–(2.20b), using the parameters discussed in Section 2.4.3, and we refer to this case as *standard therapy*. Secondly, we performed a simulation adding to the model the prolonged effects of the chemotherapeutic drug in treating the tumour, as modelled in Eq. (2.22), applying the parameters discussed in Section 2.4.3. We denote this second scenario as *standard therapy with decay*. Finally, in a third simulation, we increased the parameters of the therapies, by using $R_{\text{eff}} = 0.07128$ day^{-1} and $k_{C1} = 0.043$ day^{-1}, always preserving the decay. For what concerns the radiotherapy coefficient, this is equivalent to an approximate increase of 11% from the initial value, which remains within the clinically acceptable range [430],

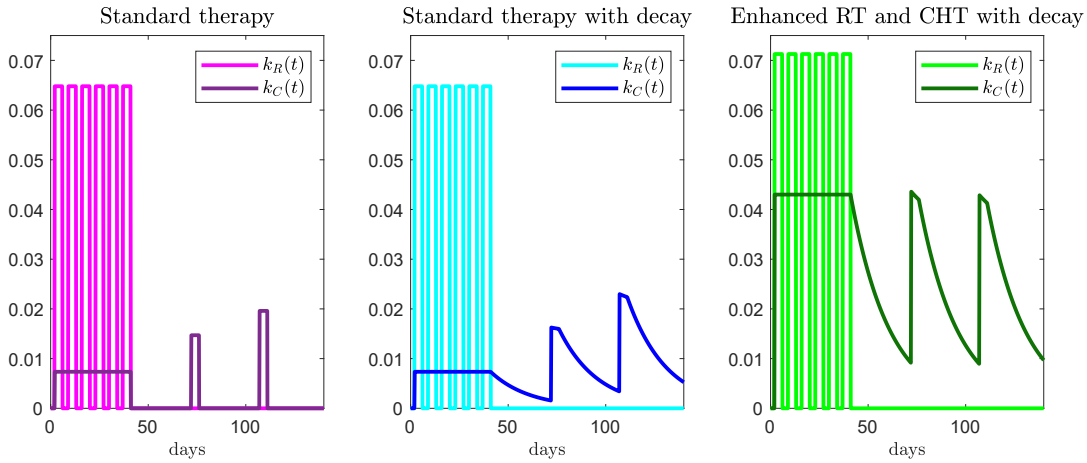

FIGURE 2.10: In the graphs, a comparison between the variations of $k_R(t)$ and $k_C(t)$ over time in the three therapeutic protocols analysed.

whereas the chemotherapy coefficient exhibits a significantly higher increase, specifically 485%. This could be interpreted as the use of a more powerful drug or a combination of different drugs to control tumour growth, as done in some medical trials. In this third scenario, the parameters k_{C2} and k_{C3} are instead chosen to achieve the same response in terms of chemotherapy-induced cell death rate at the beginning of each cycle, taking into account the prolonged effect of the drug. The aim of the second and third cycles is therefore to restore the already high lethal effect on cancer cells achieved in the first cycle. Specifically, the required values are $k_{C2} = 0.035$ day^{-1} and $k_{C3} = 0.034$ day^{-1}. We refer to the latter case as *enhanced RT and CHT with decay*. Graphs illustrating the temporal evolution of $k_R(t)$ and $k_C(t)$ for the three different scenarios are reported in Fig. 2.10. The results obtained in all these three cases with therapies are compared in Fig. 2.11 with the case where the tumour is not treated. In particular, Fig. 2.11a displays the variation of the average value of Γ_s, which represents a measure of the growth rate of the tumour mass. In Fig. 2.11b we show the evolution of the average value of the fraction of solid phase ϕ_s, whereas Fig. 2.11c reports the changes in tumour volume over time. From these results, it is possible to observe how the tumour responds differently by changing the therapeutic approach. As expected, the case without therapy leads to the fastest and greatest growth, while the introduction of therapies is reflected by the reduction in volume and growth rate. In particular, an enhancement in therapies may allow to significantly contain the progression of the cancer. This could be highly beneficial from a medical perspective, as it suggests that an intensified treatment strategy has the potential to significantly impact tumour growth and potentially improve patient outcomes. Hence, these results demonstrate that, by integrating diverse parameters and variables, including drug concentration, tumour growth rate, and drug sensitivity, the model can effectively simulate and predict the outcomes of different drug treatments. Simulations like these could therefore be useful to tune the dosage of drugs or the intervals of administration of therapies, for instance, in order to minimise the growth of the cancer.

Finally, in Fig. 2.12, the volume fraction of the solid phase is plotted at the initial time instant and at $t = 140$ days, in order to compare the initial size of the tumour with the shape reached at the end of the simulations performed both without introducing any therapy and including a treatment. It can be observed that the case without therapy

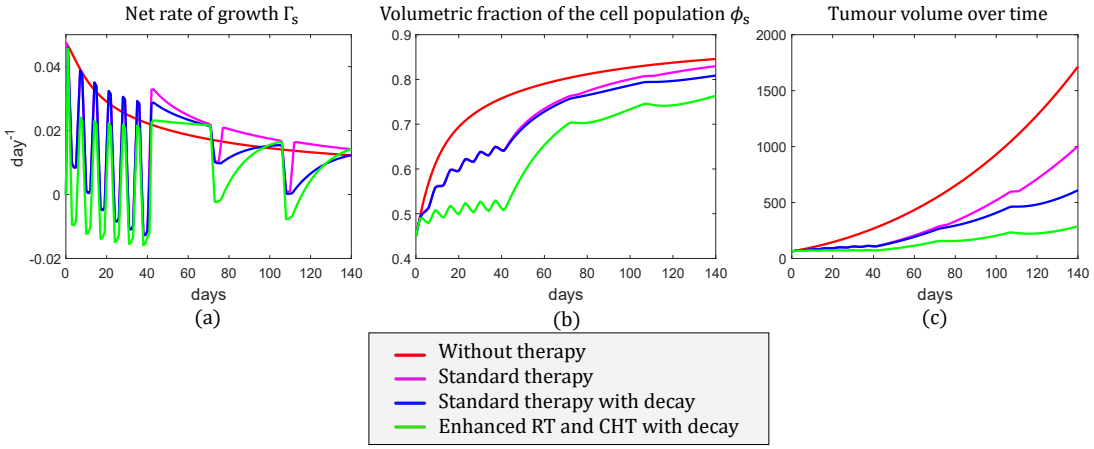

FIGURE 2.11: In the graphs, a comparison between the variations of Γ_s (a), ϕ_s (b) and the volume of the tumour (c) over time is shown. The red line represents the scenario without any therapy, while the magenta line corresponds to the scenario including the standard therapy. Additionally, we included the blue line to illustrate the standard therapy with the consideration of a time decay of the drugs. Lastly, the green line represents the scenario with enhanced radiotherapy and chemotherapy.

obviously leads to the biggest tumour mass after about five months of growth, whereas the introduction of therapeutic protocols is able to contain the expansion of the cancer. Such an outcome is especially important when growth near delicate cerebral structures like the ventricles is studied, given that a proper therapeutic treatment may be helpful to avoid unnatural ventricular compression. To quantify the response of the tumour to therapies in the first 39 days, where RT and CHT are simultaneously performed, we computed the percent variation in the tumour principal diameters with respect to the initial size, following the RECIST criteria for solid tumours [387]. First of all, we notice that, in the case without therapy, the major axis of the tumour increases by 92%, while the increase along the minor one amounts at 32%, with an average along the three directions of about 56% increase in diameter. Instead we find that, for the case of standard therapy, the major axis of the tumour increases by 54% and the minor axis by 3%, with an average of about 24% increase. The case of standard therapy with decay improves the outcomes, but only slightly. In these cases, even if growth is slowed down, the tumour is still classified as progressive according to medical standards [387]. Instead, when we consider enhanced RT and CHT with decay, the percent increase of the tumour major axis amounts at 16%, whereas a -1% reduction is observed along the minor axis, with an average in the three directions of about only 6% increase. In the latter case, resorting to the RECIST criteria, the tumour can be classified as stable and not progressive any more [387], falling within the typical response window also highlighted in other models of brain tumour treatment [430, 432].

2.6 Summary

Brain tumours are among the most difficult to treat with current therapeutic protocols, due to their aggressiveness and to a significant resistance to therapies. In addition, the impact of a growing cancer mass inside the brain may be particularly harmful for the patient, since it may deform and compress delicate structures like the ventricles. As a consequence of damage affecting healthy areas of the brain, neurological issues can emerge and negatively affect the prognosis of patients affected by such cancers. Based

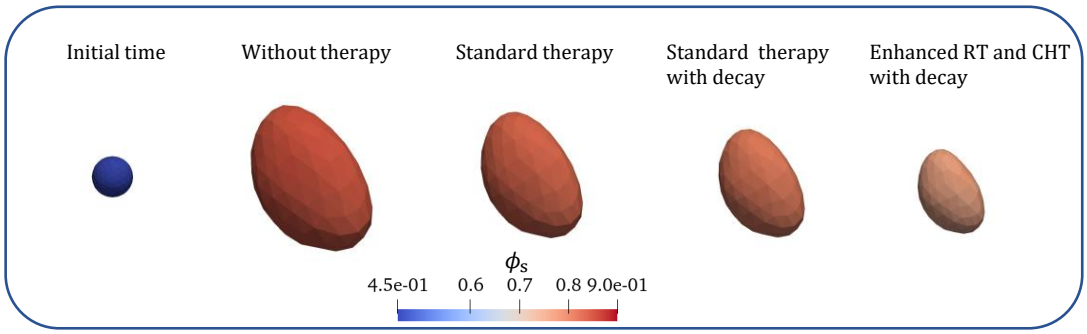

FIGURE 2.12: Volumetric fraction of the cell population, plotted at the initial time and after different simulations both with and without therapeutic protocols, at time $t = 140$ days.

on these observations, in this paper we have proposed a mathematical model and computational framework that feature three main novelties compared with previous works. First of all, we explicitly accounted for the presence of ventricles in the cerebral geometry, so that a precise quantification of unnatural ventricular compression following tumour growth can be performed. In particular, the deformation and volume variation of the ventricles can be studied thanks to the mechanical nature of the model, which is able to evaluate tumour-induced strains as well as fluid motion. Indeed, we consider the brain as a mixture of a nonlinear elastic solid phase and an ideal fluid phase, within the framework of mixture theory. Moreover, we employ a sharp interface model to simulate solid localized brain tumours, which are responsible for the higher mechanical deformations of the surrounding tissue. This choice, however, does not allow to capture the behavior of infiltrating cancers, which are characterized by small clusters of tumour cells and show extensive growth and dissemination far from the primary cancer mass, as considered for instance in [255, 320, 379]. Secondly, we consider growth distortions as anisotropic, to overcome the simplified assumption of isotropic growth which is frequently made in the literature. Such a choice is justified by the presence of oriented fibre structures in the brain, i.e. the white matter tracts, along which tumour cells may preferentially move and grow. This anisotropy creates irregular and heterogeneous growth patterns, with tumours becoming highly non-spherical during their proliferation. In addition, we consider also diffusion and fluid motion as anisotropic phenomena affecting the tumour and its environment, so that the proposed framework embeds three anisotropic components: the diffusion tensor $\mathbb{D}$, the permeability tensor $\mathbb{K}$, and the growth-related distortion tensor $\mathbb{F}_g$. As an additional capability of the model, all these tensors are computationally reconstructed from medical imaging data, with a specific focus on free-water diffusion, related to the free liquid in the brain, and non-free-water diffusion, characterised by preferential motion along the fibres. Thirdly, the model includes cancer treatment via chemotherapy and radiotherapy, and it can be fruitfully employed to simulate different therapeutic strategies aimed at slowing down tumour growth.

Our numerical results confirm the validity of the proposed model as a proof-of-concept for simulating fully anisotropic brain tumour progression, as well as therapeutic protocols and ventricular compression. In particular, we find that an initially spherical tumour can become highly elongated during growth and may exert a significant compression on the nearby ventricles, increasing the risk of neurological damage due to excessive intracranial pressure and fluid flow obstruction. Clear differences are highlighted between the case of isotropic and anisotropic growth, suggesting that the role of brain fibre structures is fundamental in driving the evolution of the tumour shape

and size. A large region around the tumour zone is also found to be affected by unnatural displacements, which might be harmful for patients. Finally, we have shown that the model is capable of reproducing therapeutic strategies, pointing out methods to slow down cancer progression. Furthermore, the model can be readily adapted to simulate different therapies and schedules, such as concomitant treatment with different chemoterapies [54] or ultra-fractionated radiotherapy [63, 64], allowing the exploration of potentially effective, tailored protocols.

In conclusion, we have proposed a framework that can represent a first step towards a realistic simulation of anisotropic, patient-specific, mechanically motivated brain tumour growth, together with therapeutic treatment. Regarding possible future developments, it would be important to model the contact of ventricle edges when they touch due to deformations caused by cancer. Such a situation, which is never reached in our simulations, would require an appropriate treatment by means of contact mechanics. Furthermore, we aim to integrate a voxel-wise estimation of free water in the brain to establish a more appropriate and spatially-dependent initial value for ϕ_ℓ^0 and, consequently, for ϕ_s^0. Possible heterogeneity between grey and white matter from a mechanical viewpoint could also be incorporated in the proposed framework, especially if tumours of comparable stiffness to the healthy tissue are considered. Moreover, the model's ability to accurately capture cellular-scale interactions remains an open question and warrants further investigation to ensure its applicability at finer biological scales. We also note that in our model we have neglected fluid exchange between the tissue and the vasculature, assuming that the only source of fluid is cell death within the domain and fluid flow at the tissue-ventricle boundary. This assumption is more appropriate for representing avascular or poorly vascularised tumours. Therefore, future models should focus on the description of the vasculature and lymphatic system (either from a homogenised point of view [188, 355] or by implementing a 3D-1D coupling between the tissue and the vasculature [71]) in order to properly describe the vascular growth phase of the tumour. An initial attempt is made in Chapter 6, where we propose a mathematical model for tumour growth that incorporates the vasculature. Moreover, we are aware that our model for therapies is a simplification of the much more complex biological phenomenon, but this approach allows us to simulate the ongoing effects of therapies without taking into account the intricate biological processes initiated by the drug, or eventually radiation, in the context of a computationally sophisticated model. In this respect, clinical data could be used to test, validate and possibly modify the model about therapies, establishing the values of RT and CHT parameters, and explicitly including TMZ pharmacodynamics to better represent the late cell death after treatment. In addition, the integration of optimal control theories presents an intriguing avenue to enhance our research. Future perspectives could be focused on exploring this promising approach for developing optimal timing and dosing strategies for chemotherapeutic drugs, addressing a prominent issue of medical significance, as exemplified in [124]. Finally, the model should be adapted to simulate surgical resection before chemoradiation therapies, which represents a challenging modelling task and has not been targeted in the present work.

3 Quasi-linear viscoelasticity and application to brain tissue mechanics

3.1 Preliminaries

Significant progress has been made in recent years in the field of brain mechanics. It is now widely recognised that mechanical properties play a crucial role in various conditions and pathologies, including traumatic brain injury, brain development, and brain tumours. The remarkable growth in computational power and technology since the turn of the millennium has led to increased demand from the clinical and biomedical communities for robust, accurate and efficient *in silico* mechanical models that can capture the behaviour of brain tissue in complex real-world scenarios, such as predicting disease progression [83], surgical planning and training [144] and estimating injury risk for contact [271] and equestrian sports [127]. The wide range of applications above highlights one of the significant challenges facing the computational mechanics community: realistic predictions of brain tissue's mechanical response require sophisticated constitutive models that capture as much of the underlying physics as possible, yet these models must be simple and tractable enough to enable rapid and reliable estimation of their material parameters through calibration with experimental data.

Brain tissue exhibits the ability to undergo non-linear deformations and demonstrates time-dependent mechanical behaviour. The latter is one of the most pronounced features of brain tissue, manifesting itself primarily through viscoelastic effects such as stress relaxation, as detailed in Section 1.1.1. In addition to this behaviour of the solid skeleton, brain tissue exhibits poroelastic effects due to interstitial fluid flow through the solid skeleton, especially at sufficiently large time scales [470]. While sophisticated models that account for coupling between porous and viscous effects in brain tissue behaviour are available in the literature [126, 259], current testing protocols are not advanced enough to reliably estimate their material parameters through calibration with experimental data [83, 225]. In this work, we, therefore, treat brain tissue as a monophasic viscoelastic solid and ignore poroelastic effects.

Along with its high water content, the development of testing protocols to characterise brain tissue's viscoelastic properties presents numerous challenges [83, 105]. For instance, brain tissue's fragile, brittle and tacky nature makes it susceptible to damage during sample preparation and testing [83]. Furthermore, brain tissue is highly compliant and ultra-soft, which can lead to significant deformation under the action of its own weight, making it difficult to control sample geometry during extraction and testing [83]. Additionally, the forces measured during testing often approach the resolution limits of commercially available testing equipment. All these factors and others—for example, age [342], species [342], anatomical region [361], post-mortem storage time [201] and temperature [420, 422]—may contribute to the variations in the mechanical properties of brain tissue reported in the literature.

Budday et al. [83] and Chatelin et al. [105] provide extensive reviews of the viscoelastic properties of brain tissue as measured in various studies, drawing on over 50 years of research in brain mechanics. These studies demonstrate that stress relaxation in brain tissue has been tested under various deformation modes, including uniaxial tension [425], uniaxial compression [422], simple shear [424] and torsion [30]. Typically, uniaxial tension and compression tests on brain tissue are performed by glueing the ends of a cylindrical sample to the platens [423, 425], restricting lateral expansion or contraction at the sample's ends. This restriction leads to inhomogeneous deformations [421, 425], which cannot be accurately modelled using the analytical solutions available for such tests [140]; instead, the equations of motion must be solved numerically, complicating model fitting. By contrast, compression tests with lubricated platens can achieve homogeneous deformation conditions but only up to a strain of approximately 10% [45, 425]. Another standard testing protocol for brain tissue that can achieve a stretch of more than 60% is simple shear, which is performed by glueing the opposite faces of a cuboidal sample to the platens and recording the shear and normal forces required to move one platen parallel to the other [149]. Additionally, surface tractions must be applied to the slanted faces of the deformed sample to prevent bending [147]. In reality, these tractions are never applied; more practically, the effect of deviation from ideal simple shear conditions on the measured shear and normal forces is minimised by using a thin sample whose width is less than four times its height [79, 147, 149, 424]. Furthermore, accurately quantifying the normal force is currently neither feasible nor practical, as it requires recently developed, custom-designed testing equipment [147, 521]. Thus, in practice, simple shear generates a single dataset for the shear force, similar to uniaxial tension or compression tests that produce a single dataset for the tensile or compressive force. Alternatively, torsion is a more robust and reliable testing protocol that can be readily implemented for brain tissue using commercial devices known as rheometers. These devices measure the torque and normal force required to twist a cylindrical sample, generating two independent datasets (the appearance of a normal force as a result of twisting is an example of the so-called Poynting effect [411, 429]). The first study to apply this protocol to brain tissue was carried out by Balbi et al. [45], who showed that the instantaneous elastic response of brain tissue in torsion is well-captured by a hyperelastic Mooney–Rivlin model and estimated the corresponding elastic material parameters (the instantaneous shear modulus and Mooney–Rivlin parameters). Although stress relaxation in torsion has been investigated in animal (porcine and bovine) and human brain tissues [83, 105], anterior studies have focused on measuring only the torque, neglecting the normal force. In addition, torsion was modelled as simple shear but only locally is the torsion deformation that of simple shear [45]. Consequently, the potential of torsion as a robust and reliable testing protocol for determining the viscoelastic properties of brain tissue has yet to be fully realised. We note that Narayan et al. [376] devised a similar protocol for asphalt binders in torsion, measuring both torque and normal force during relaxation. However, to the best of the authors' knowledge, an analogous protocol for soft tissues has yet to be developed.

This Chapter seeks to enhance the hyperelastic brain constitutive model presented in Chapter 2 by incorporating viscoelastic effects. We exploit the latent potentials of the torsion protocol and the quasi-linear viscoelasticity (QLV) model to determine the viscoelastic properties of brain tissue. In Section 3.2, we begin with a review of the standard linear viscoelastic theory and its rheological interpretation, followed by a comprehensive exposition of the MQLV theory as formulated in [140, 427]. In Section 3.3, we describe the procedure for preparing the cylindrical brain samples and testing them with the rotational rheometer, with the results of the torsion tests presented in Section 3.4. In Section 3.5, we propose a novel fitting procedure for determining brain tissue's

viscoelastic material parameters based on the MQLV model. Following this, in Section 3.6 we present a finite element implementation of the MQLV model in the open-source software FEniCS, which we use to validate our estimates of the viscoelastic material parameters through numerical simulations of the experiments. We discuss the results and summarise the important features of the Chapter in Section 3.7.

The majority of the content in this chapter originates from an international collaboration with Valentina Balbi and Griffen Small from the School of Mathematical and Statistical Sciences at the University of Galway. The material has been written in the paper by Small, Ballatore, Giverso and Balbi *"Modelling the non-linear viscoelastic behaviour of brain tissue in torsion"*.

3.2 Viscoelastic models

Viscoelasticity is a major and active area of interest within the field of soft tissue mechanics. The most straightforward constitutive theory that can be used to predict the viscoelastic behaviour of brain tissue is linear viscoelasticity, where the instantaneous stress is determined by convolving the strain history with a time-dependent function that depends on brain tissue's material properties [25, 120]. In reality, brain tissue's viscoelastic response is markedly non-linear: it can accommodate finite deformations and its stress relaxation curves depend on the strain level. A non-linear viscoelastic constitutive theory is, therefore, essential for accurate predictions. Although the literature is replete with non-linear models [157, 514], they are generally difficult to employ in real-world biomechanical scenarios and numerically costly vis-à-vis model fitting and material parameter estimation. To this end, Fung, in his seminal work [196], proposed a compromise approach now known as quasi-linear viscoelasticity (QLV). The QLV model, which falls under the umbrella of the more general Pipkin–Rogers model [514], is the simplest extension of the linear viscoelastic theory to finite deformations. In contrast to the Pipkin–Rogers model, QLV is limited to materials whose viscous relaxation rates are independent of the instantaneous local strain [140] and thereby cannot account for the non-linear phenomenon of strain-dependent relaxation commonly observed in biological soft tissues [105, 158, 377, 448]. Nevertheless, its relative simplicity compared to more general non-linear viscoelastic models has led to its widespread use: the model has been employed to model a myriad of biological soft tissues including the skin [184, 278], liver [341], brain [106, 260, 423–425, 439, 473, 474], lung [136], eye [529], spinal cord [268, 437, 523], prostate gland [242], eardrum [373], oesophagal tissue [522], heart muscle tissue [264], ligaments [3, 132, 197], tendons [41, 158], cartilage [446, 457], arteries [215] and membranes [134]. As noted by De Pascalis et al. [140], QLV has been criticised for not always exhibiting "physically reasonable behaviour". In that article, the authors thoroughly reappraised the theory and elucidated that its supposed unphysical behaviour stemmed from different interpretations of Fung's original one-dimensional relationship. The main deficiencies in these anterior studies, as summarised by De Pascalis et al. [138], were using an incorrect QLV relation (especially for incompressible materials) and employing a stress measure other than the second Piola–Kirchhoff stress, which guarantees objectivity. Using the reappraised QLV model (subsequently referred to as modified quasi-linear viscoelasticity or MQLV), De Pascalis et al. studied uniaxial tension [140] and simple shear [138], while Righi and Balbi [427] considered torsion. Balbi et al. [43, 44] extended the model to transversely isotropic materials. In contrast to Fung's QLV model, there is a paucity of experimental studies on the MQLV model. To the authors' knowledge, the only relevant example is the paper by De Pascalis et al. [139], which demonstrated that the MQLV model provided a better

fit to the relaxation data from inflation tests on murine bladders compared to Fung's model or linear viscoelasticity. Consequently, MQLV's potential vis-à-vis model fitting and material parameter estimation has yet to be fully exploited.

3.2.1 Linear viscoelastic theory

Linear viscoelastic constitutive models are developed by incorporating time-dependent material parameters, which reflect a fading memory effect. This effect enables the material to retain information about its strain history up to the present state. Hence, the stress tensor $\mathbb{T}(t)$ can be written as

$$\mathbb{T}(t) = \int_{-\infty}^{t} \mathbb{K}(t-\tau) : \frac{\mathrm{d}\varepsilon(\tau)}{\mathrm{d}\tau}\mathrm{d}\tau\,, \tag{3.1}$$

where ε is the second-order strain tensor and $\mathbb{K}(t)$ is called *tensorial relaxation function* and it is a fourth-order tensor whose entries are the time-dependent material parameters. Since the brain behaves isotropically from a mechanical viewpoint [85], the mechanical behaviour can be fully characterized by two independent parameters: the bulk modulus, $\kappa(t)$, and the shear modulus, $\mu(t)$. The tensorial relaxation function $\mathbb{K}(t)$ for an isotropic material has two independent components $K_1(t)$ and $K_2(t)$ with respect to two bases $\mathbb{J}_1$ and $\mathbb{J}_2$, respectively, such that:

$$\mathbb{K}(t) = \sum_{n=1,2} K_n(t)\mathbb{J}_n\,. \tag{3.2}$$

A widely recognised form of the constitutive equation for a homogeneous and isotropic material is derived by decomposing the strain tensor ε into its hydrostatic and deviatoric components. The hydrostatic component corresponds to changes in volume, while the deviatoric component represents the deformation that preserves volume. The following basis set separates the strain tensor into its hydrostatic and deviatoric parts:

$$\mathbb{J}_{1abcd} = \frac{1}{3}\delta_{ab}\delta_{cd} \quad \text{and} \quad \mathbb{J}_{2abcd} = \frac{1}{2}\left(\delta_{ac}\delta_{bd} + \delta_{ad}\delta_{bc}\right) - \frac{1}{3}\delta_{ab}\delta_{cd}\,. \tag{3.3}$$

Here, δ_{ab} represents the Kronecker delta, which is equal to 1 if $a = b$ and 0 if $a \neq b$. Accordingly, Eq. (3.1) takes the following form:

$$\begin{aligned}
\mathbb{T}(t) &= \int_{-\infty}^{t} \sum_{n=1,2} K_n(t-\tau)\mathbb{J}_n : \frac{\mathrm{d}\varepsilon(\tau)}{\mathrm{d}\tau}\mathrm{d}\tau \\
&= \int_{-\infty}^{t} K_1(t-\tau)\frac{\mathrm{d}\mathbb{J}_1 : \varepsilon(\tau)}{\mathrm{d}\tau}\mathrm{d}\tau + \int_{-\infty}^{t} K_2(t-\tau)\frac{\mathrm{d}\mathbb{J}_2 : \varepsilon(\tau)}{\mathrm{d}\tau}\mathrm{d}\tau \\
&= \int_{-\infty}^{t} K_1(t-\tau)\frac{\mathrm{d}}{\mathrm{d}\tau}\left(\frac{1}{3}\operatorname{tr}(\varepsilon(\tau))\mathbb{I}\right)\mathrm{d}\tau + \int_{-\infty}^{t} K_2(t-\tau)\frac{\mathrm{d}}{\mathrm{d}\tau}\left(\varepsilon(\tau) - \frac{1}{3}\operatorname{tr}(\varepsilon(\tau))\mathbb{I}\right)\mathrm{d}\tau \\
&= \int_{-\infty}^{t} \kappa(t-\tau)\frac{\mathrm{d}}{\mathrm{d}\tau}(\operatorname{tr}(\varepsilon(\tau))\mathbb{I})\mathrm{d}\tau + 2\int_{-\infty}^{t} \mu(t-\tau)\frac{\mathrm{d}}{\mathrm{d}\tau}(\operatorname{dev}(\varepsilon(\tau)))\mathrm{d}\tau\,.
\end{aligned} \tag{3.4}$$

The symbol $\mathbb{I}$ denotes the second-order identity tensor, while $\operatorname{dev}\varepsilon = \varepsilon - \frac{1}{3}\operatorname{tr}(\varepsilon)\mathbb{I}$ represents the deviatoric component of the second-order tensor ε. The corresponding material parameters, $\kappa(t)$ and $\mu(t)$, are the time-dependent bulk and shear moduli.

For incompressible materials, that deform without any change in volume, the bulk modulus $\kappa(t)$ is significantly larger than the shear modulus $\mu(t)$ ($\kappa(t) \gg \mu(t)$ for all t). Additionally, under these conditions, the following assumptions hold: $\operatorname{tr}(\varepsilon(t)) \to 0$ and

$\kappa(t) \to \infty$ for all t. In this incompressible limit, Eq. (3.4) simplifies to:

$$\mathbb{T}(t) = -p(t)\mathbb{I} + 2\int_{-\infty}^{t} \mu(t-\tau)\frac{\mathrm{d}}{\mathrm{d}\tau}(\mathrm{dev}(\varepsilon(\tau)))\mathrm{d}\tau\,, \tag{3.5}$$

where we have introduced the Lagrange multiplier $p(t)$:

$$-p(t) = \lim_{\mathrm{tr}\,\varepsilon(t)\to 0\kappa}\lim_{(t)\to\infty}\int_{-\infty}^{t}\kappa(t-\tau)\frac{\mathrm{d}}{\mathrm{d}\tau}(\mathrm{tr}(\varepsilon(\tau))\mathbb{I})\mathrm{d}\tau\,. \tag{3.6}$$

The scalar $p(t)$ can be interpreted as the hydrostatic pressure and is determined by solving the governing equations of motion for a continuum body, subject to the imposed boundary conditions. It is important to note that the stress component $-p(t)\mathbb{I}$ represents a workless reaction force, in response to the kinematic constraint of the deformation field. There is no energy dissipation during the isochoric deformation of the body. Therefore, for materials that can be considered incompressible, only the deviatoric component of the stress displays viscoelastic behaviour.

3.2.2 QLV theory

The linear viscoelastic model described in Sec. 3.2.1 provides accurate results only within the small deformation regime. However, it fails to accurately predict the stress response when a tissue undergoes large deformations. To address this limitation, Fung introduced the theory of Quasi-Linear Viscoelasticity (QLV) [196], an extension of the linear theory discussed in the previous section to accommodate large deformations. In this Section, we review the QLV theory, following [140, 427] to derive the constitutive equations for isotropic and incompressible soft tissues.

The QLV theory builds on the same foundational assumptions as the linear theory, namely the Boltzmann superposition principle and the concept of fading memory. Additionally, Fung proposed that the total stress can be separated into a product of two functions: one dependent on time, the relaxation function, and the other on deformation, representing the elastic stress. The relaxation function captures the time-dependent decay of stress, while the elastic stress function accounts for the tissue's elastic response. Unlike in the linear theory, the relationship between elastic stress and strain in the QLV formulation is inherently non-linear.

Fung proposed to write the the second Piola-Kirchhoff stress tensor $\mathbb{\Pi}(t)$ as follows:

$$\mathbb{\Pi}(t) = \int_{-\infty}^{t}\mathbb{G}(t-\tau) : \frac{\mathrm{d}\mathbb{\Pi}^{\mathrm{e}}(\tau)}{\mathrm{d}\tau}\mathrm{d}\tau\,, \tag{3.7}$$

where $\mathbb{G}$ is called *reduced relaxation function tensor* and $\mathbb{\Pi}^{\mathrm{e}}(t)$ is the elastic second Piola-Kirchhoff stress tensor, defined as:

$$\mathbb{\Pi}^{\mathrm{e}} = J\mathbb{F}^{-1}\mathbb{T}^{\mathrm{e}}\mathbb{F}^{-\mathrm{T}}\,. \tag{3.8}$$

In definition (3.8), $\mathbb{T}^{\mathrm{e}}$ is the elastic Cauchy stress, $\mathbb{F} = \mathbb{I} - \nabla\boldsymbol{u}$ is the deformation gradient associated to the large deformation $\mathbf{x} = \chi(\mathbf{X})$, and $J = \det\mathbb{F}$. $\mathbf{X}$ and $\mathbf{x}$ are the position vectors in the undeformed and deformed configurations, respectively.

The fundamental simplification of Fung's theory is that $\mathbb{G}$ is independent of the strain and, if the material is isotropic, then this tensor of rank four has just two independent components. For this reason, for isotropic materials, it is convenient to split the elastic Cauchy stress into two parts, one which accounts for microscopic isochoric deformations of the material and the other that measures purely compressive deformations.

This could be achieved by taking its hydrostatic and deviatoric components:

$$\mathbb{T}^{\mathrm{e}} = \mathbb{T}^{\mathrm{e}}_H + \mathbb{T}^{\mathrm{e}}_D \,, \tag{3.9}$$

which can be expressed as:

$$\mathbb{T}^{\mathrm{e}}_H = \frac{1}{3}\,\mathrm{tr}\,(\mathbb{T}^{\mathrm{e}})\,\mathbb{I} \quad \text{and} \quad \mathbb{T}^{\mathrm{e}}_D = \mathbb{T}^{\mathrm{e}} - \frac{1}{3}\,\mathrm{tr}\,(\mathbb{T}^{\mathrm{e}})\,. \tag{3.10}$$

Assuming a superposition principle as for the linear case, it is now possible to introduce an objective viscoelastic law, relating the second Piola–Kirchhoff stress to the past history of the non-linear rate of strain measure. In this way, we rewrite Eq. (3.7) in the following form:

$$\mathbb{\Pi}(t) = \int_{-\infty}^{t} \mathcal{H}(t-\tau)\frac{\mathrm{d}\mathbb{\Pi}^{\mathrm{e}}_H(\tau)}{\mathrm{d}\tau}\mathrm{d}\tau + \int_{-\infty}^{t} \mathcal{D}(t-\tau)\frac{\mathrm{d}\mathbb{\Pi}^{\mathrm{e}}_D(\tau)}{\mathrm{d}\tau}\mathrm{d}\tau \,, \tag{3.11}$$

where the terms are defined by

$$\mathbb{\Pi}^{\mathrm{e}} = \mathbb{\Pi}^{\mathrm{e}}_H + \mathbb{\Pi}^{\mathrm{e}}_D \,, \tag{3.12}$$

$$\mathbb{\Pi}^{\mathrm{e}}_H = J\mathbb{F}^{-1}\left(\frac{1}{3}\,\mathrm{tr}\,(\mathbb{T}^{\mathrm{e}})\,\mathbb{I}\right)\mathbb{F}^{-\mathrm{T}} \quad \text{and} \quad \mathbb{\Pi}^{\mathrm{e}}_D = J\mathbb{F}^{-1}\,\mathrm{dev}\,(\mathbb{T}^{\mathrm{e}})\,\mathbb{F}^{-\mathrm{T}} \,, \tag{3.13}$$

and $\mathcal{D}(t)$ and $\mathcal{H}(t)$ are two scalar independent-reduced relaxation functions (with $\mathcal{D}(0) = \mathcal{H}(0) = 1$ without loss of generality). It must be emphasized that the subscripts D and H in this case do not refer to the deviatoric and hydrostatic parts of the second Piola–Kirchhoff stress, but correspond to the second Piola–Kirchhoff stress of the deviatoric and hydrostatic Cauchy stress components, respectively. Furthermore, it is important to underline that $\mathcal{H}(t) = \kappa(t)/\kappa_0$ and $\mathcal{D}(t) = \mu(t)/\mu_0$ are the non-dimensional version of the relaxation functions $\kappa(t)$ and $\mu(t)$, where $\kappa(0) = \kappa_0$ and $\mu(0) = \mu_0$ are the instantaneous elastic bulk and shear modulus which appear in the linear viscoelastic theory resumed in Section 3.2.1. Finally, the Cauchy stress tensor follows from applying the transformation $\mathbb{T}(t) = J^{-1}\mathbb{F}\mathbb{\Pi}(t)\mathbb{F}^{T}$ to Eq. (3.11) and it is given by:

$$\mathbb{T}(t) = J^{-1}\mathbb{F}\left(\int_{-\infty}^{t} \frac{\kappa(t-\tau)}{\kappa_0} : \frac{\mathrm{d}\mathbb{\Pi}^{\mathrm{e}}_H(\tau)}{\mathrm{d}\tau}\mathrm{d}\tau + \int_{-\infty}^{t} \frac{\mu(t-\tau)}{\mu_0} : \frac{\mathrm{d}\mathbb{\Pi}^{\mathrm{e}}_D(\tau)}{\mathrm{d}\tau}\mathrm{d}\tau\right)\mathbb{F}^{T} \,. \tag{3.14}$$

Integrating by parts, and assuming that the deformation commences at $t = 0$, yields

$$\begin{aligned}\mathbb{T}(t) = J^{-1}\mathbb{F}\left(\mathbb{\Pi}^{\mathrm{e}}_H(t) + \int_0^t \frac{\kappa'(t-\tau)}{\kappa_0} : \mathbb{\Pi}^{\mathrm{e}}_H(\tau)\,\mathrm{d}\tau\right)\mathbb{F}^{T} + \\ J^{-1}\mathbb{F}\left(\mathbb{\Pi}^{\mathrm{e}}_D(t) + \int_0^t \frac{\mu'(t-\tau)}{\mu_0} : \mathbb{\Pi}^{\mathrm{e}}_D(\tau)\,\mathrm{d}\tau\right)\mathbb{F}^{T} \,.\end{aligned} \tag{3.15}$$

In the incompressible limit $J \to 1$ and $\kappa(t) \to \kappa(0) \to \infty$, $\forall t$, Eq. (3.15) reduces to the following form:

$$\mathbb{T}(t) = -p(t)\mathbb{I} + \mathbb{F}\left(\mathbb{\Pi}^{\mathrm{e}}_D(t) + \int_0^t \frac{\mu'(t-\tau)}{\mu_0} : \mathbb{\Pi}^{\mathrm{e}}_D(\tau)\,\mathrm{d}\tau\right)\mathbb{F}^{T} \,, \tag{3.16}$$

where the Lagrange multiplier $p(t)$ is given by:

$$-\,p(t) = \lim_{J\to 1\,,\ \kappa(t)\to\infty} J^{-1}\mathbb{F}\left(\mathbb{\Pi}^{\mathrm{e}}_H(t) + \int_0^t \frac{\kappa'(t-\tau)}{\kappa_0} : \mathbb{\Pi}^{\mathrm{e}}_H(\tau)\,\mathrm{d}\tau\right)\mathbb{F}^{T} \,. \tag{3.17}$$

3.3 Materials and methods

In this Section, we provide a brief overview of the procedure developed by Griffen Small and Valentina Balbi at the University of Galway for preparing cylindrical brain samples and testing them using a rotational rheometer.

Tissue preparation

All experiments were performed using brains from 6 to 9-month-old, mixed-sex sheep obtained from a local European Union-approved slaughterhouse (Athenry Quality Meats Ltd, Galway, Ireland, Approval Number EC2875). As the animals were not sacrificed specifically for this study, ethical approval was not required from the University of Galway's Research Ethics Committee.

The brains, which were received as separated cerebral hemispheres, were placed in a phosphate buffered saline (PBS) solution within 1 hour post-mortem to avoid tissue dehydration and maintained at 11–15 °C during transportation. All samples were prepared and tested at room temperature (19–23 °C). The tests were conducted at CÚRAM, a national research centre based at the University of Galway. As shown in Fig. 3.1(a), mixed grey and white matter cylindrical samples were excised from the cerebral halves using a sharp 25 mm diameter stainless steel punch. To prepare flat cylindrical samples of radius $R_0 = 12.5$ mm and height $H_0 = 10$ mm for testing, each long sample was first inserted into a cutting guide of height 13 mm. The excess brain matter was then removed from the top of the sample using an 8 inch MacroKnife (CellPath, Wales, United Kingdom), as shown in Fig. 3.1(b). Finally, the opposite end of the sample was cut flat with the aid of a cutting guide of height 10 mm, as shown in Fig. 3.1(c); the exact heights of the samples were measured before testing. After this, the prepared sample and cerebral hemisphere were placed in a PBS solution. Instead of preparing all the samples at once, each sample was tested immediately after preparation, and then, if possible, another was extracted from the cerebral hemisphere [424]. All samples were tested within 8 hours post-mortem.

Mechanical testing

An Anton Paar MCR 302e rotational rheometer with parallel plate geometry (Anton Paar, Graz, Austria) was used for the mechanical testing (see Fig. 3.2). During the tests, the bottom Peltier plate remained fixed, while the motion of the upper plate (which contains the motors and sensors that measure the torque and normal force) was controlled through the software RheoCompass (Version 1.31). To match the dimension of the samples tested, a 25 mm diameter upper plate was used. Masking tape of negligible thickness (≤ 1 mm) was applied to both plates to prevent damage to the rheometer and enable easy removal of the tested samples [45, 424, 425]. The sample was secured to the tape using a thin layer of cyanoacrylate (RS Radionics, Dublin, Ireland) [423–425]. A small pre-compression of approximately 0.03 N was applied by manually lowering the upper plate to ensure proper sample adhesion to the upper and lower plates. A minute and a half was sufficient time for the glue to set, after which the position of the upper plate was slowly adjusted until the normal force read 0 N.

Our torsion testing protocol is summarised in Table 3.1. We performed three sets of ramp-and-hold relaxation tests in torsion on the cylindrical samples at varying twist rates of $\dot{\phi}_0 \in \{40, 240, 400\}$ rad m^{-1} s^{-1} (angular velocity of the upper plate per unit deformed height), while keeping the twist fixed at $\phi_0 = 88$ rad m^{-1} (angle of rotation per unit deformed height). Each torsion test consisted of two phases: a ramp

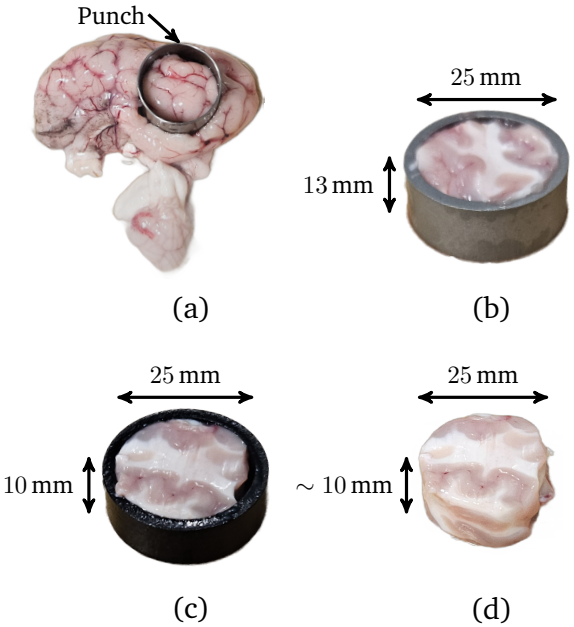

FIGURE 3.1: Procedure for preparing cylindrical brain samples of radius 12.5 mm and height 10 mm for testing: (a) long cylindrical sample excised from the cerebral hemisphere using a steel punch; (b) top face cut flat using a cutting guide of height 13 mm; (c) opposite face cut flat using a cutting guide of height 10 mm and (d) flat cylindrical sample ready for testing.

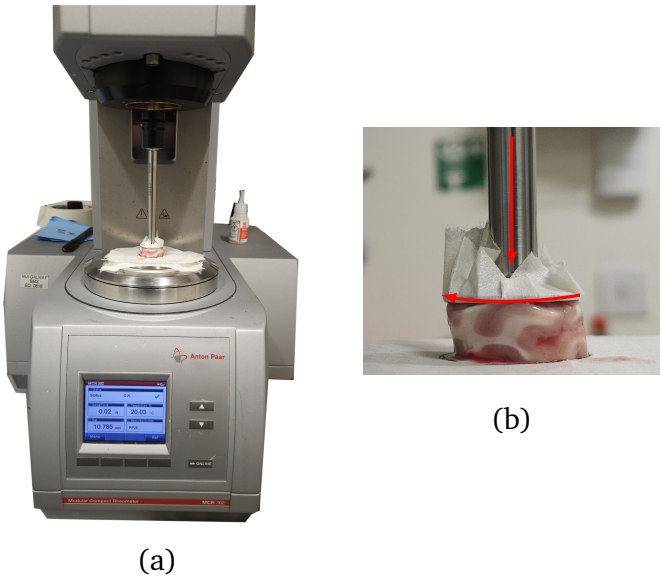

FIGURE 3.2: (a) Anton Paar MCR 302e rotational rheometer with parallel plate geometry used to perform the torsion tests and (b) side view of a twisted sample during testing.

phase, in which the twist was increased linearly to $\phi_0 = 88$ rad m^{-1} over a time $t^\star \in \{2.2, 0.367, 0.22\}$ s, followed by a hold phase lasting 200 s, during which the final value of the twist reached at the end of the ramp phase was maintained. Both the torque τ and normal force N_z required to twist the sample during the ramp phase and maintain the sample in its deformed state during the hold phase were recorded versus time t. No pre-conditioning was performed on the samples, and each was tested only once before being discarded. A total of 30 samples were tested over several campaigns: 10 at 40 rad m^{-1} s^{-1} (samples S_1 to S_{10}); 10 at 240 rad m^{-1} s^{-1} (samples S_{11} to S_{20}) and 10 at

400 rad m^{-1} s^{-1} (samples S_{21} to S_{30}).

TABLE 3.1: Torsion testing protocol

- **Ramp phase:** twist increased linearly to $\phi_0 = 88$ rad m^{-1} over a time $t^\star \in \{2.2, 0.367, 0.22\}$ s at a twist rate of $\dot{\phi}_0 \in \{40, 240, 400\}$ rad m^{-1} s^{-1}
- **Hold phase:** twist maintained at $\phi_0 = 88$ rad m^{-1} for 200 s

3.4 Experimental results

In this section, we present representative torque and normal force data from the rheometer for each of the twist rates $\dot{\phi}_0 \in \{40, 240, 400\}$ rad m^{-1} s^{-1} and describe the filtering procedure applied to the data to prepare it for model fitting and material parameter estimation.

As an example, the raw output data for sample S_{16}, recorded during a torsion test performed at a twist rate of $\dot{\phi}_0 = 240$ rad m^{-1} s^{-1}, are presented in Fig. 3.3. Fig. 3.3(a,b) show the twist ϕ and twist rate $\dot{\phi}$ profiles for the test, while Fig. 3.3(c,d) display the measured torque τ and Fig. 3.3(e,f) the measured normal force N_z. Since the rheometer outputs the normal force exerted by the sample on the upper plate, we changed the sign of the data so that it represents the normal force that must be applied to the sample to maintain the deformation, consistent with the modelling conventions adopted in Section 3.5 and anterior studies [45, 427].

From the data presented in Fig. 3.3(a,b), we can identify four regions: (i) a region (black data) at the start of the ramp phase, where the upper plate accelerates from rest to the target twist rate of $\dot{\phi}_0 = 240$ rad m^{-1} s^{-1}; (ii) a region (purple data), where this twist rate is maintained until the twist reaches $\phi_0 = 85$ rad m^{-1} at the end of the ramp phase at time $t^\star = 0.367$ s (indicated by a dashed line); (iii) a region (red data) at the start of the hold phase, where the upper plate decelerates to rest and (iv) the remainder (orange data) of the hold phase, where the final value of the twist reached at the end of the ramp phase is maintained. We also note the apparition of experimental artefacts in the torque data in Fig. 3.3(c) in regions where there is a rapid change in the twist rate, notably at the start of the ramp phase when the upper plate is accelerating (black data) and the start of the hold phase when it is decelerating (red data); see Fig. 3.3(b). Accordingly, these artefacts—potentially due to the inertia of the motors in the upper plate [376]—were excluded from the proper torque data in Fig. 3.3(d). Likewise, the proper normal force data in Fig. 3.3(c) excludes the less pronounced artefacts in the normal force data at the start of the ramp phase, the mechanical origin of which is unclear. However, unlike the torque, the normal force data generated at the start of the hold phase does not appear to be adversely affected by the rapid change in twist rate and was therefore included in the proper normal force data in Fig. 3.3(c).

During the gamut of tests, the achieved twist rates $\dot{\phi}_0$ were measured as 40.26 ± 0.42, 239.95 ± 0.25 and 400.06 ± 0.27 rad m^{-1} s^{-1} (mean $\pm$ SD). The corresponding ramp times $t^\star$ were set to 2.2, 0.367 and 0.22 s to achieve the target twist of $\phi_0 = 88$ rad m^{-1} at the end of the ramp phase. However, in practice, the actual twist values reached were slightly lower and decreased with increasing twist rate: 87.48 ± 0.51, 85.25 ± 0.1 and 83.23 ± 0.1 rad m^{-1}. This discrepancy was due to the inertia of the upper plate, which caused the twist to continue increasing slightly at the start of the hold phase while the upper plate decelerated to rest (see Fig. 3.3(a)). As a result, the target twist was reached during the hold phase rather than at the end of the ramp phase. This deviation between the target and actual twist values at the end of the ramp phase is a practical limitation of our protocol.

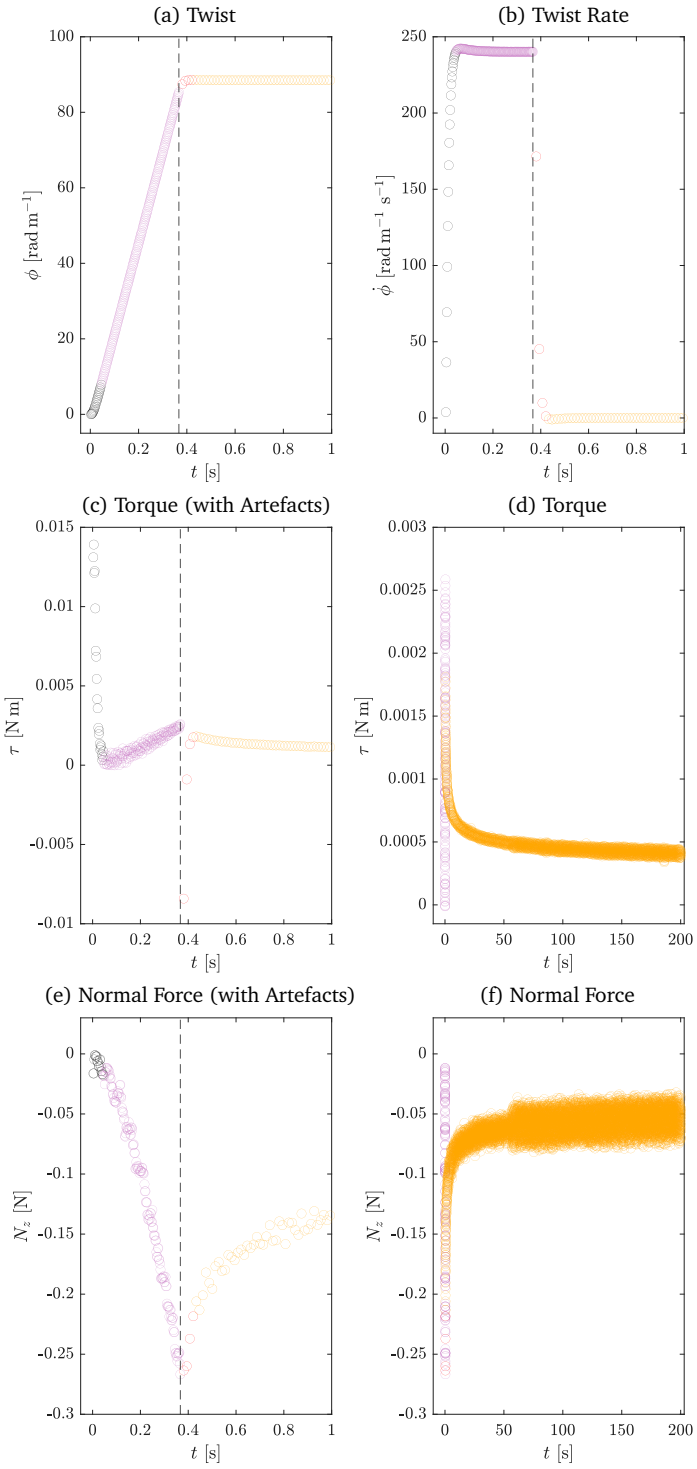

FIGURE 3.3: Raw output data for sample S_{16} from a torsion test performed at a twist rate of 240 rad m^{-1} s^{-1}: (a,b) twist and twist rate profiles; (c,e) measured torque and normal force for the first second of the test (including experimental artefacts) and (d,f) measured torque and normal force for the entire duration of the test (excluding experimental artefacts). Both the torque data generated when the upper plate was accelerating (black) and decelerating (red) were excluded from the proper torque data in (c), whereas only the normal force data generated when the upper plate was accelerating were excluded from the proper normal force data in (f). A dashed line indicates the end of the ramp phase.

Following the protocol of Narayan et al. [376], we estimated the rheometer's torque and normal force resolutions to be approximately 0.15 mN m and 0.03 N by performing

torsion tests at each of the twist rates $\{40, 240, 400\}$ rad m^{-1} s^{-1} without any samples between the plates. Another source of noise in the experiments was the attached compressor, which was required for the proper operation of the rheometer. During each test, the compressor would activate to supply fresh compressed air to the air bearings of the rheometer's motors, generating vibrations that increased the noise in the torque and normal force measurements (see Fig. 3.3(d,f) at $t \approx 50$ s). In preparation for model fitting, we smoothed the data by applying a Savitzky–Golay filter using the MATLAB function sgolayfilt. For the 40 rad m^{-1} s^{-1} data, we used a polynomial order of 5 and a window length of 31, whereas for the 240 and 400 rad m^{-1} s^{-1} data, we used a polynomial order of 5 and a window length of 61. Fig. 3.4 shows representative torque, normal force and filtered data for samples S_2, S_{16} and S_{24} at each twist rate.

3.5 Modelling

In this section, we use the MQLV theory to derive analytical expressions for the torque and normal force for a ramp-and-hold test. We then propose a fitting procedure for determining brain tissue's viscoelastic material parameters and apply it to the experimental data.

3.5.1 Theory

Here, we calculate the torque and normal force required to maintain an isotropic, incompressible, viscoelastic cylinder in a state of torsion, according to the MQLV theory. Although brain tissue is neither strictly isotropic nor incompressible, experiments indicate these are reasonable assumptions [83].

We consider a cylinder of radius R_0 and height H_0 subjected to a torsional deformation that takes the point with cylindrical polar coordinates (R, Θ, Z) in the undeformed configuration (at time $t = 0$) to the point with cylindrical polar coordinates (r, θ, z) in the deformed configuration (at time $t > 0$), both relative to a fixed origin O. Since the rheometer's normal force sensor has a resolution of approximately 0.03 N, the device cannot detect variations of the normal force within this range. We, therefore, expect the samples to undergo a slight axial contraction before being twisted, even though the upper plate is adjusted until the normal force reads 0 N before each test.[45] This combined contraction–torsion can be modelled by the deformation [45, 121]

$$r(t) = \frac{R}{\sqrt{\lambda}}, \qquad \theta(t) = \Theta + \phi(t)\lambda Z, \qquad z(t) = \lambda Z, \tag{3.18}$$

where $0 < \lambda \leq 1$ is the (axial) pre-stretch and the twist $\phi(t) = \alpha(t)/\lambda H_0$ is the angle of rotation α per unit deformed height (see Fig. 3.5). The pure torsion case ($\lambda = 1$) was considered by Righi and Balbi [427]. By introducing the cylindrical bases $\{\boldsymbol{E}_R, \boldsymbol{E}_\Theta, \boldsymbol{E}_Z\}$ and $\{\boldsymbol{e}_r, \boldsymbol{e}_\theta, \boldsymbol{e}_z\}$ for the undeformed and deformed configurations, we can write the deformation gradient $\mathbb{F} = F_{aA}\, \boldsymbol{e}_a \otimes \boldsymbol{E}_A$ associated with the deformation (3.18) as

$$\mathbb{F}(r,t) = \begin{pmatrix} \frac{1}{\sqrt{\lambda}} & 0 & 0 \\ 0 & \frac{1}{\sqrt{\lambda}} & r\lambda\phi(t) \\ 0 & 0 & \lambda \end{pmatrix}. \tag{3.19}$$

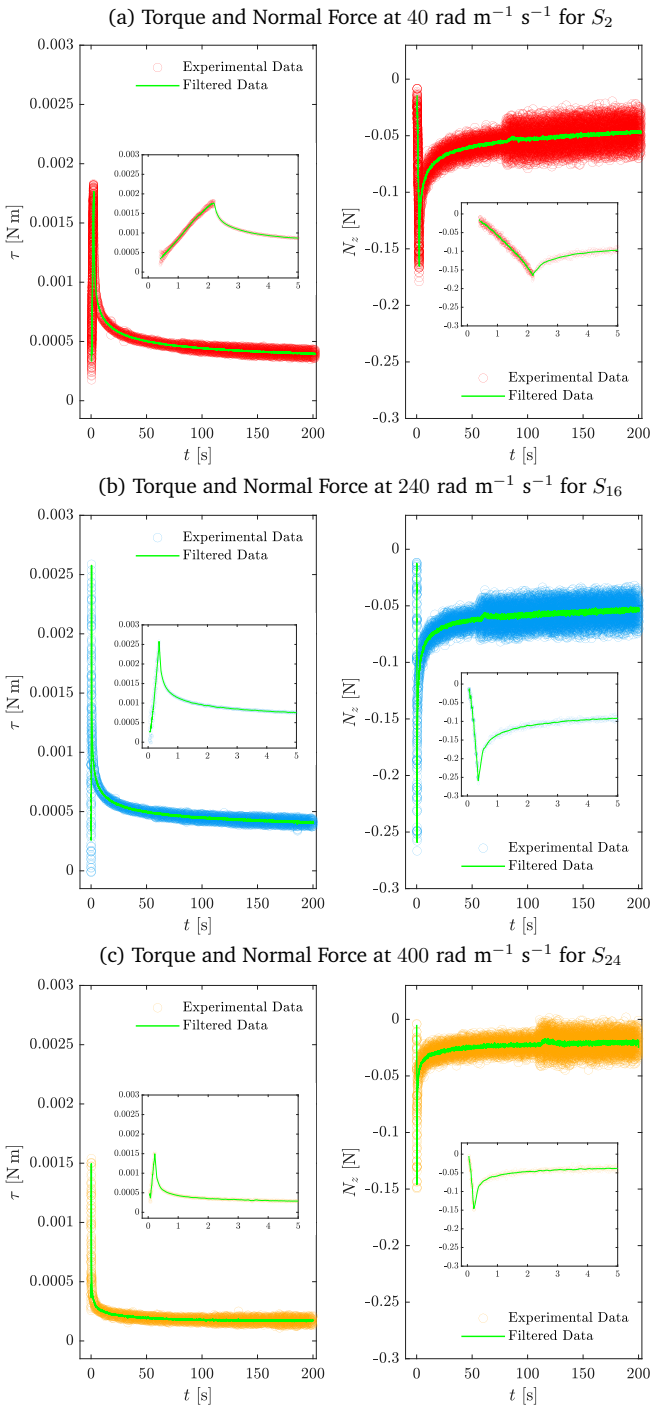

FIGURE 3.4: Representative torque, normal force and filtered data for samples S_2 (a), S_{16} (b) and S_{24} (c) from torsion tests performed at twist rates of 40, 240, 400 rad m^{-1} s^{-1}. The insets show the ramp phase and the initial part of the hold phase in more detail.

Various tensors can be computed from the deformation gradient, such as the left Cauchy–Green deformation tensor $\mathbb{B} = \mathbb{F}\mathbb{F}^{\mathrm{T}}$ and right Cauchy–Green deformation tensor $\mathbb{C} = \mathbb{F}^{\mathrm{T}}\mathbb{F}$.

In their experimental study, Balbi et al. [45] showed that the instantaneous elastic response of brain tissue in torsion is well-captured by a Mooney–Rivlin strain energy

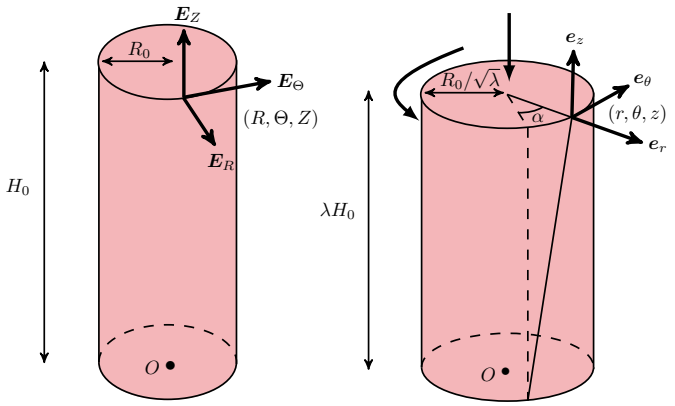

(a) Undeformed Cylinder (b) Deformed Cylinder

FIGURE 3.5: (a) Undeformed and (b) deformed cylinder. Torque and normal force must be applied at the end of the cylinder to maintain the torsion deformation.

function [140, 371, 428]:

$$\mathcal{W}^{\mathrm{e}} = \frac{\mu_0}{2}\left(\frac{1}{2}+\gamma\right)(I_1-3) + \frac{\mu_0}{2}\left(\frac{1}{2}-\gamma\right)(I_2-3)\,, \tag{3.20}$$

where μ_0 is the instantaneous shear modulus, γ is a constant, $I_1 = \operatorname{tr}\mathbb{B}$ and $I_2 = \operatorname{tr}\mathbb{B}^{-1}$. For this model, the Mooney–Rivlin parameters c_1 and c_2 are connected to μ_0 and γ through $\mu_0 = 2(c_1+c_2)$ and $\gamma = 1/2 - 2c_2/\mu_0$. The same Mooney–Rivlin behaviour was observed in simple shear [149] and at dynamic strain rates in simple shear,[424] uniaxial tension [425] and uniaxial compression [423]. Under our assumptions, the elastic Cauchy stress corresponding to (3.20) reads [253, 383]

$$\mathbb{T}^{\mathrm{e}} = \frac{\mu_0}{2}(1+2\gamma)\,\mathbb{B} - \frac{\mu_0}{2}(1-2\gamma)\,\mathbb{B}^{-1} - p^{\mathrm{e}}\mathbb{I}, \tag{3.21}$$

where p^{e} is the elastic Lagrange multiplier introduced to enforce the incompressibility constraint and $\mathbb{I}$ is the second-order identity tensor.

According to the MQLV theory, the viscoelastic Cauchy stress can be expressed as [139, 140, 427]

$$\mathbb{T}(r,t) = \mathbb{F}(r,t)\left(\mathbb{\Pi}^{\mathrm{e}}_{\mathrm{D}}(r,t) + \frac{1}{\mu_0}\int_0^t \mu'(t-s)\mathbb{\Pi}^{\mathrm{e}}_{\mathrm{D}}(r,s)\mathrm{d}s\right)\mathbb{F}(r,t)^{\mathrm{T}} - p(r,t)\mathbb{I}, \tag{3.22}$$

where p^{e} has been incorporated into the viscoelastic Lagrange multiplier p, taken to be a function of r and t only without loss of generality [427]. The elastic response in the above is captured by the second Piola–Kirchhoff stress tensor

$$\begin{aligned}\mathbb{\Pi}^{\mathrm{e}}_{\mathrm{D}} &= \mathbb{F}^{-1}\mathbb{T}^{\mathrm{e}}_{\mathrm{D}}\mathbb{F}^{-\mathrm{T}} \\ &= \frac{\mu_0}{3}(1-2\gamma)\,\mathbb{C}^{-1} - \frac{\mu_0}{2}(1-2\gamma)\,\mathbb{C}^{-2} + \frac{\mu_0}{2}(1+2\gamma)\,\mathbb{I},\end{aligned} \tag{3.23}$$

corresponding to the deviatoric Cauchy stress $\mathbb{T}^{\mathrm{e}}_{\mathrm{D}} = \mathbb{T}^{\mathrm{e}} - (\operatorname{tr}\mathbb{T}^{\mathrm{e}}/3)\,\mathbb{I}$, while the time-dependent behaviour is associated with the scalar relaxation function $\mu(t)$, taken to be an n-term Prony series of the form [372, 424, 427]

$$\mu(t) = \mu_\infty + \sum_{i=1}^{n}\mu_i \mathrm{e}^{-t/\tau_i}, \tag{3.24}$$

where $\mu(0) = \mu_0$ and μ_∞ are the instantaneous and long-time shear moduli, μ_i are the relaxation coefficients and τ_i are the relaxation times. From (3.19), (3.22), (3.23) and (3.24), we can determine the components of $\mathbb{T}$:

$$\begin{aligned}
T_{rr}(r,t) =& -\mu_0\left[\lambda+1+2\gamma\left(\lambda-1\right)\right]\left(\frac{\lambda^3-1}{6\lambda^2}\right)+\\
&-\frac{\mu_0 r^2}{6}\left[\lambda-1+2\gamma\left(\lambda+1\right)\right]\lambda\phi(t)^2\\
&+\frac{1}{6\lambda^2}\sum_{i=1}^{n}\int_0^t\frac{1}{\tau_i}\mu_i \mathrm{e}^{-(t-s)/\tau_i}[\left\{\lambda-1+2\gamma\left(\lambda+1\right)\right\}r^2R_0^2\lambda^2\phi(s)^2+\\
&+\left\{\lambda+1+2\gamma\left(\lambda-1\right)\right\}\left(\lambda^3-1\right)]\mathrm{d}s-p(r,t)\,,
\end{aligned} \tag{3.25}$$

$$\begin{aligned}
T_{\theta\theta}(r,t) =& -\mu_0\left[\lambda+1+2\gamma\left(\lambda-1\right)\right]\left(\frac{\lambda^3-1}{6\lambda^2}\right)+\frac{\mu_0 r^2}{3}\left[1+2\gamma\left(2\lambda-1\right)\right]\lambda\phi(t)^2+\\
&-\frac{1}{6\lambda^2}\sum_{i=1}^{n}\int_0^t\frac{1}{\tau_i}\mu_i \mathrm{e}^{-(t-s)/\tau_i}[\left\{\lambda+2+2\gamma\left(\lambda-2\right)\right\}r^4\lambda^3\phi(s)^4+\\
&-2\left\{\lambda+2+2\gamma\left(\lambda-2\right)\right\}r^4\lambda^3\phi(s)^3\phi(t)+\\
&+\left\{\lambda+2+2\gamma\left(\lambda-2\right)\right\}r^4\lambda^3\phi(s)^2\phi(t)^2+\\
&+\left\{2\lambda^4+3\lambda^3-6\lambda+2+2\gamma\left(2\lambda^4-3\lambda^3+2\lambda-2\right)\right\}r^2\phi(s)^2+\\
&-2\left\{\lambda+1+2\gamma\left(\lambda-1\right)\right\}r^2\left(\lambda^3+2\right)\phi(s)\phi(t)+\\
&-2\left\{\lambda+1+2\gamma\left(\lambda-1\right)\right\}r^2\lambda\left(\lambda^3-1\right)\phi(t)^2\\
&+\left\{\lambda+1+2\gamma\left(\lambda-1\right)\right\}\left(\lambda^3-1\right)]\mathrm{d}s-p(r,t)\,,
\end{aligned} \tag{3.26}$$

$$\begin{aligned}
T_{zz}(r,t) =& \mu_0\left[\lambda+1+2\gamma\left(\lambda-1\right)\right]\left(\frac{\lambda^3-1}{3\lambda^2}\right)+\\
&-\frac{\mu_0 r^2}{6}\left[\lambda+2+2\gamma\left(\lambda-2\right)\right]\lambda\phi(t)^2+\\
&+\frac{1}{6\lambda^2}\sum_{i=1}^{n}\int_0^t\frac{1}{\tau_i}\mu_i \mathrm{e}^{-(t-s)/\tau_i}[\left\{\lambda+2+2\gamma\left(\lambda-2\right)\right\}r^2\lambda^3\phi(s)^2+\\
&-2\left\{\lambda+1+2\gamma\left(\lambda-1\right)\right\}\left(\lambda^3-1\right)]\mathrm{d}s-p(r,t)\,,
\end{aligned} \tag{3.27}$$

$$\begin{aligned}
T_{\theta z}(r,t) =& \frac{\mu_0 r}{2}\left[\lambda+1+2\gamma\left(\lambda-1\right)\right]\lambda\phi_0(t)+\\
&+\frac{r}{6\lambda^2}\sum_{i=1}^{n}\int_0^t\frac{1}{\tau_i}\mu_i \mathrm{e}^{-(t-s)/\tau_i}[\left\{3\lambda-2-2\gamma\left(\lambda-2\right)\right\}r^2\lambda^3\phi(s)^3+\\
&+\left\{\lambda+2+2\gamma\left(\lambda-2\right)\right\}r^2\lambda^3\phi(s)^2\phi(t)\\
&-\left\{\lambda+1+2\gamma\left(\lambda-1\right)\right\}\left(\lambda^3-1\right)\phi(s)+\\
&-2\left\{\lambda+1+2\gamma\left(\lambda-1\right)\right\}\left(\lambda^3-1\right)\phi(t)]\mathrm{d}s\,,
\end{aligned} \tag{3.28}$$

$$T_{r\theta}(r,t)=0\,,\qquad T_{rz}(r,t)=0 \tag{3.29}$$

In this work, we assume that the deformation is slow enough that inertial effects can be ignored, and we neglect external body forces [43, 212]. The motion of the cylinder is therefore governed by the momentum balance equation $\operatorname{div}\mathbb{T}=\mathbf{0}$, where div is the divergence operator in the deformed configuration [253, 383]. Upon inspection of the components of the equation of motion, and assuming that the lateral surface of the

cylinder is traction-free, we arrive at the following equilibrium problem [427] :

$$\begin{cases} T_{rr}(r,t)r + \dfrac{T_{rr}(r,t) - T_{\theta\theta}(r,t)}{r} = 0\,, \\ T_{rr}(R_0,t) = 0\,. \end{cases} \tag{3.30}$$

By integrating $(3.30)_1$ subject to $(3.30)_2$, we can determine the Lagrange multiplier p:

$$\begin{aligned} p(r,t) = &-\mu_0\left[\lambda+1+2\gamma\left(\lambda-1\right)\right]\left(\frac{\lambda^3-1}{6\lambda^2}\right)+\\ &-\frac{\mu_0}{12}\left[\left\{5\lambda-2+2\gamma\left(5\lambda+2\right)\right\}r^2-3\left(1+2\gamma\right)R_0^2\right]\lambda\phi(t)^2+\\ &+\frac{1}{24\lambda^3}\sum_{i=1}^{n}\int_0^t\frac{1}{\tau_i}\mu_i\mathrm{e}^{-(t-s)/\tau_i}\big[\left\{\lambda+2+2\gamma\left(\lambda-2\right)\right\}\left(r^4\lambda^2-R_0^4\right)\lambda^2\phi(s)^4+\\ &-2\left\{\lambda+2+2\gamma\left(\lambda-2\right)\right\}\left(r^4\lambda^2-R_0^4\right)\lambda^2\phi(s)^3\phi(t)+\\ &+\left\{\lambda+2+2\gamma\left(\lambda-2\right)\right\}\left(r^4\lambda^2-R_0^4\right)\lambda^2\phi(s)^2\phi(t)^2+\\ &-\left\{\left[2\lambda^4-12\lambda^3-4\lambda-4+4\gamma\left(\lambda^4+6\lambda^3-2\lambda+2\right)\right]r^2\lambda+\right.\\ &\left.+2\left[\lambda^4+4\lambda^3+2\lambda+2+2\gamma\left(\lambda^4-4\lambda^3+2\lambda-2\right)\right]R_0^2\right\}\lambda\phi(s)^2+\\ &-4\left\{\lambda+1+2\gamma\left(\lambda-1\right)\right\}\left(r^2\lambda-R_0^2\right)\lambda\left(\lambda^3+2\right)\phi(s)\phi(t)+\\ &-4\left\{\lambda+1+2\gamma\left(\lambda-1\right)\right\}\left(r^2\lambda-R_0^2\right)\left(\lambda^3-1\right)\phi(t)^2+\\ &-4\left\{\lambda+1+2\gamma\left(\lambda-1\right)\right\}\lambda\left(\lambda^3-1\right)\big]\mathrm{d}s\,. \end{aligned} \tag{3.31}$$

Given the expressions for the stress components $T_{\theta z}$ and T_{zz} (3.28)-(3.27), the torque $\tau(t) = 2\pi\int_0^{R_0/\sqrt{\lambda}} r^2 T_{\theta z}(r,t)\mathrm{d}r$ and normal force $N_z(t) = 2\pi\int_0^{R_0/\sqrt{\lambda}} r T_{zz}(r,t)\mathrm{d}r$ required to maintain the deformation (3.18) can be determined by direct integration:

$$\begin{aligned} \tau(t) = &\frac{\pi\mu_0 R_0^4}{4}A(\lambda,\gamma)\phi(t)+\\ &-\frac{\pi R_0^4}{36\lambda^4}\sum_{i=1}^{n}\int_0^t\frac{1}{\tau_i}\mu_i\mathrm{e}^{-(t-s)/\tau_i}\big[2R_0^3\lambda^3B(\lambda,\gamma)\phi(s)^3-2R_0^3\lambda^3B(\lambda,\gamma)\phi(s)^2\phi(t)+\\ &+3\lambda\left(\lambda^3+2\right)A(\lambda,\gamma)\phi(s)+6\lambda\left(\lambda^3-1\right)A(\lambda,\gamma)\phi(t)\big]\mathrm{d}s\,, \end{aligned} \tag{3.32}$$

$$\begin{aligned} N_z(t) = &\pi\mu_0 R_0^2\left(\frac{\lambda^3-1}{2\lambda^2}\right)B(\lambda,\gamma)-\frac{\pi\mu_0 R_0^4}{8}B(\lambda,\gamma)\phi(t)^2+\\ &-\frac{\pi R_0^2}{72\lambda^4}\sum_{i=1}^{n}\int_0^t\frac{1}{\tau_i}\mu_i\mathrm{e}^{-(t-s)/\tau_i}\big[2R_0^4\lambda^3B(\lambda,\gamma)\phi(s)^4+\\ &-4R_0^4\lambda^3B(\lambda,\gamma)\phi(s)^3\phi(t)+2R_0^4\lambda^3B(\lambda,\gamma)\phi(s)^2\phi(t)^2+\\ &+3R_0^2\left(\lambda^4-2\lambda^3+2\lambda+2+2\gamma C(\lambda)\right)\phi(s)^2+\\ &-6R_0^2\lambda\left(\lambda^3+2\right)A(\lambda,\gamma)\phi(s)\phi(t)-6R_0\lambda^{3/2}\left(\lambda^3-1\right)A(\lambda,\gamma)\phi(t)+\\ &+36\lambda^2\left(\lambda^3-1\right)A(\lambda,\gamma)\big]\mathrm{d}s\,. \end{aligned} \tag{3.33}$$

Specialising these equations to a ramp-and-hold test, which corresponds to a twist history of the form (see Fig. 3.3(a))

$$\phi(t) = \begin{cases} \dfrac{\phi_0 t}{t^\star}, & 0 \le t \le t^\star \\ \phi_0, & t > t^\star, \end{cases} \tag{3.34}$$

we find that the torque and normal force during the hold phase ($t > t^\star$) read

$$\begin{aligned}\tau^{\text{hold}}(t) =& \frac{\pi\mu_\infty R_0^4}{4} A(\lambda,\gamma)\phi_0 + \\ &+ \frac{\pi R_0^4}{12\lambda^3 t^\star} A(\lambda,\gamma) \sum_{i=1}^{n} \mu_i \mathrm{e}^{-t/\tau_i} \left[2(\lambda^3-1)t^\star + (\lambda^3+2)\,\tau_i\,(\mathrm{e}^{t^\star/\tau_i}-1)\right]\phi_0 + \\ &+ \frac{\pi R_0^6}{18\lambda t^{\star 3}} B(\lambda,\gamma) \sum_{i=1}^{n} \mu_i \tau_i \mathrm{e}^{-t/\tau_i} \left[-2\tau_i\,(t^\star+3\tau_i) + \mathrm{e}^{t^\star/\tau_i}\left(t^{\star 2} - 4\tau_i t^\star + 6\tau_i^2\right)\right]\phi_0^3 ,\end{aligned}$$

and

$$\begin{aligned}N_z^{\text{hold}}(t) =& \pi\mu(t) R_0^2 \left(\frac{\lambda^3-1}{2\lambda^2}\right) A(\lambda,\gamma) - \frac{\pi\mu_\infty R_0^4}{8} B(\lambda,\gamma)\phi_0^2 + \\ &- \frac{\pi R_0^4}{12\lambda^4 t^{\star 2}} \sum_{i=1}^{n} \mu_i \mathrm{e}^{-t/\tau_i} \Big[\,(1-2\gamma)\left\{\mathrm{e}^{t^\star/\tau_i}\left(3\lambda^3\tau_i t^\star - C(\lambda)\tau_i^2\right) - D(\lambda)t^{\star 2} + \right. \\ &+ E(\lambda)\tau_i t^\star + C(\lambda)\tau_i^2\Big\} + 2\lambda(\lambda^3+2)\tau_i^2 \mathrm{e}^{t^\star/\tau_i} + 2\lambda(\lambda^3-1)t^{\star 2} + \\ &- 2\lambda(\lambda^3+2)\tau_i t^\star - 2\lambda(\lambda^3+2)\tau_i^2\Big]\phi_0^2 + \\ &- \frac{\pi R_0^6}{18\lambda t^{\star 4}} B(\lambda,\gamma) \sum_{i=1}^{n} \mu_i \tau_i^2 \mathrm{e}^{-t/\tau_i} \left[\mathrm{e}^{t^\star/\tau_i}(t^{\star 2} - 6\tau_i t^\star + 12\tau_i^2) + \right. \\ &- t^{\star 2} - 6\tau_i t^\star - 12\tau_i^2\Big]\phi_0^4 ,\end{aligned}$$

where the expressions for the functions A, B, C, D and E are given by

$$A(\lambda,\gamma) = \frac{1}{\lambda}[\lambda + 1 + 2\gamma\,(\lambda-1)]\,, \tag{3.35}$$

$$B(\lambda,\gamma) = \frac{1}{\lambda}[\lambda + 2 + 2\gamma\,(\lambda-2)]\,, \tag{3.36}$$

$$C(\lambda) = \lambda^4 + 2\lambda^3 + 2\lambda - 2\,, \tag{3.37}$$

$$D(\lambda) = \lambda^4 - \lambda^3 - \lambda + 1\,, \tag{3.38}$$

$$E(\lambda) = \lambda^4 - \lambda^3 + 2\lambda - 2\,. \tag{3.39}$$

Analogous expressions for the ramp phase ($0 \le t \le t^\star$) are derived

$$\begin{aligned}\tau^{\text{ramp}}(t) =& \frac{\pi\mu_\infty R_0^4 t}{4t^\star} A(\lambda,\gamma)\phi_0 + \\ &+ \frac{\pi R_0^4}{12\lambda^3 t^\star} A(\lambda,\gamma) \sum_{i=1}^{n} \mu_i \left[2\left(\lambda^3-1\right) t\mathrm{e}^{-t/\tau_i} + \left(\lambda^3+2\right)\tau_i\left(1-\mathrm{e}^{-t/\tau_i}\right)\right]\phi_0 + \\ &+ \frac{\pi R_0^6}{18\lambda t^{\star 3}} B(\lambda,\gamma) \sum_{i=1}^{n} \mu_i \tau_i \mathrm{e}^{-t/\tau_i} \left[-2\tau_i\,(t+3\tau_i) + \mathrm{e}^{t/\tau_i}\left(t^2 - 4t\tau_i + 6\tau_i^2\right)\right]\phi_0^3 ,\end{aligned}$$

$$
\begin{aligned}
N_z^{\text{ramp}}(t) =& \pi\mu(t)R_0^2\left(\frac{\lambda^3-1}{2\lambda^2}\right)A(\lambda,\gamma) - \frac{\pi\mu_\infty R_0^4 t^2}{8t^{\star 2}}B(\lambda,\gamma)\phi_0^2 + \\
&- \frac{\pi R_0^4}{12\lambda^4 t^{\star 2}}\sum_{i=1}^{n}\mu_i \mathrm{e}^{-t/\tau_i}\big[(1-2\gamma)\left\{\mathrm{e}^{t/\tau_i}\left(3\lambda^3\tau_i t - C(\lambda)\tau_i^2\right) - D(\lambda)t^2 + \right. \\
&\left. + E(\lambda)\tau_i t + C(\lambda)\tau_i^2\right\} + 2\lambda\left(\lambda^3+2\right)\tau_i^2\mathrm{e}^{t/\tau_i} + 2\lambda\left(\lambda^3-1\right)t^2 + \\
&- 2\lambda\left(\lambda^3+2\right)\tau_i t - 2\lambda\left(\lambda^3+2\right)\tau_i^2\big]\phi_0^2 + \\
&- \frac{\pi R_0^6}{18\lambda t^{\star 4}}B(\lambda,\gamma)\sum_{i=1}^{n}\mu_i\tau_i^2\mathrm{e}^{-t/\tau_i}\left[\mathrm{e}^{t/\tau_i}\left(t^2-6\tau_i t+12\tau_i^2\right) - t^2 - 6\tau_i t - 12\tau_i^2\right]\phi_0^4 .
\end{aligned}
$$

The results of Righi and Balbi [427] are recovered by setting $\lambda = 1$.

3.5.2 Material parameter estimation

Righi and Balbi [427] proposed a fitting procedure for estimating brain tissue's viscoelastic properties in torsion based on the MQLV model for the case when there is no pre-stretch ($\lambda = 1$). In their method, the material parameters μ_∞ and c_2 are determined from the long-time (asymptotic) values of the torque and normal force, while μ_i and τ_i are obtained by fitting the measured torque for the hold phase to the MQLV analytical prediction. However, this procedure (which does not incorporate a pre-stretch) leads to non-physical large negative values for c_1 when applied to the experimental data from Section 3.4. Therefore, an alternative fitting procedure that accounts for the effect of pre-stretch on the torque and normal force is required to fit the experimental data accurately.

To this end, we estimated the complete set of viscoelastic material parameters by simultaneously fitting the torque and normal force datasets for each of the twist rates $\dot{\phi}_0 \in \{40, 240, 400\}$ rad m^{-1} s^{-1} to the MQLV analytical predictions (3.5.1) and (3.5.1), using the MATLAB function fmincon. Due to the increased noise during the ramp phase, we confined the fitting to the final ramp phase point and the entire hold phase, i.e. $t \geq t^\star$. For the twists ϕ_0, we used the measured values at the end of the ramp phase rather than the target value. We minimised the objective function

$$
\chi^2 = \sum_{i=1}^{n_1}\left(\frac{\tau_i^{\text{MQLV}} - \tau_i^{\text{Exp}}}{\tau_i^{\text{Exp}}}\right)^2 + \sum_{i=1}^{n_2}\left(\frac{N_{z,i}^{\text{MQLV}} - N_{z,i}^{\text{Exp}}}{N_{z,i}^{\text{Exp}}}\right)^2 , \tag{3.40}
$$

where n_1 and n_2 are the numbers of considered torque and normal force datapoints τ_i^{Exp} and $N_{z,i}^{\text{Exp}}$, while τ_i^{MQLV} and $N_{z,i}^{\text{MQLV}}$ are the corresponding MQLV analytical predictions. This method is similar to that used by Anssari–Benam et al. [29] The advantage of this approach, which minimises the relative error, over the more common approach of minimising the absolute error was discussed by Destrade et al. [148] We estimated the Prony parameters (μ_∞, μ_i and τ_i) from a 4-term Prony series. To ensure that the fitting results were physically plausible, we constrained the Prony and Mooney–Rivlin parameters to be positive and limited the pre-stretch to no more than 1%.

The fitting results for each of the twist rates are reported in Tables 3.2, 3.3 and 3.4. The goodness of fit was assessed based on the relative errors (%) in the torque and normal force, defined by

$$
\text{err}_\tau = \left|\left(\tau^{\text{MQLV}} - \tau^{\text{Exp}}\right)/\tau^{\text{Exp}}\right| \times 100
$$

and

$$\mathrm{err}_{N_z} = \left| \left(N_z^{\mathrm{MQLV}} - N_z^{\mathrm{Exp}} \right) / N_z^{\mathrm{Exp}} \right| \times 100\,.$$

The MQLV model provides good fits to both the torque and normal force datasets simultaneously, exhibiting small to moderate maximal relative errors over the fitting range for all samples, with the exception of S_{24} (see Tables 3.2, 3.3 and 3.4). We note that the relative errors observed here for the MQLV model are similar to those reported by Anssari–Benam et al.[29], who simultaneously fit uniaxial tension/compression and simple shear datasets for brain tissue to different hyperelastic models.

As an example, Fig. 3.6 shows the MQLV analytical predictions for the torque and normal force for samples S_2, S_{16} and S_{24}, while Fig. 3.7 displays the corresponding relative errors. As the insets in Fig. 3.7 indicate, the relative errors in the torque are initially moderate to large but rapidly decrease towards the end of the ramp phase. By contrast, the relative errors in the force during the ramp phase are small to moderate. Over the fitting range, comprised of the final ramp phase point and the entire hold phase, the relative errors in both the torque and normal force are similarly small to moderate. The exception is sample S_{24}, where the relative error in the torque at the start of the hold phase increases sharply before decreasing at a similar rate. This is likely due to the high twist rate of 400 rad m^{-1} s^{-1} and deviations from the ideal cylindrical geometry assumed by the rheometer and MQLV model. Nevertheless, the relative errors for the remainder of the hold phase are in line with those of samples S_2 and S_{16}.

TABLE 3.2: Heights, estimated MQLV parameters and maximal relative errors in the torque and normal force over the fitting range for samples tested at 40 rad m^{-1} s^{-1}.

Sample	H_0 [mm]	λ	μ_0 [Pa]	μ_∞ [Pa]	μ_1 [Pa]	μ_2 [Pa]	μ_3 [Pa]	μ_4 [Pa]	τ_1 [s]	τ_2 [s]	τ_3 [s]	τ_4 [s]	c_1 [μPa]	c_2 [Pa]	max err_τ $t\geq t^\star$ [%]	max err_{N_z} $t\geq t^\star$ [%]
S_1	9.3125	0.99	651.16	105.67	213.34	192.34	85.831	53.892	0.8397	0.244	6.4136	55.312	0.10225	325.58	11.609	16.054
S_2	8.7436	0.99	917.69	125.55	606.76	111.28	73.07	1.0213	0.6811	9.5764	82.406	48.45	2.0793	458.84	13.725	18.992
S_3	8.6727	0.99	973.9	128.37	583.34	95.025	91.207	75.954	0.443	9.4962	2.3379	75.888	0.4711	486.95	13.415	18.628
S_4	9.1733	0.99	1048	142.97	628.57	110.42	91.321	74.705	0.4005	2.398	10.442	72.484	0.13183	523.99	14.281	19.4
S_5	8.8116	0.99	1308.8	161.91	455.32	455.31	137.22	99.052	0.6455	0.1715	5.9739	58.745	0.021216	654.41	18.485	25.642
S_6	9.2796	0.99	581.02	64.313	368.49	66.885	44.183	37.148	0.3159	1.782	8.4904	65.141	1.5548	290.51	10.915	17.506
S_7	9.1747	0.99	1195.4	116.2	816.85	137.58	70.991	53.785	0.3639	2.5286	10.9	63.17	0.028749	597.7	14.239	19.997
S_8	8.3262	0.99	739.23	107.05	258.68	242.45	76.34	54.709	0.194	0.7838	6.3087	43.982	0.003838	369.61	15.575	28.523
S_9	7.9015	0.99	1216	149.53	704.25	187.15	103.02	72.031	0.3057	1.9388	10.93	78.995	0.0094199	607.99	15.803	21.589
S_{10}	8.2687	0.99	754.36	71.934	437.68	151.71	55.116	37.911	0.2027	1.1376	8.1273	58.425	4.2268	377.18	12.582	21.687
Mean ± SD	—	—	943 ± 258	117 ± 32	496 ± 177	188 ± 114	85 ± 26	57 ± 27	0.43 ± 0.22	2.88 ± 3.58	14.96 ± 23.82	61.32 ± 11.61	0.93 ± 1.36	471 ± 129	14.06 ± 2.2	20.8 ± 3.78

TABLE 3.3: Heights, estimated MQLV parameters and maximal relative errors in the torque and normal force over the fitting range for samples tested at 240 rad m^{-1} s^{-1}.

Sample	H_0 [mm]	λ	μ_0 [Pa]	μ_∞ [Pa]	μ_1 [Pa]	μ_2 [Pa]	μ_3 [Pa]	μ_4 [Pa]	τ_1 [s]	τ_2 [s]	τ_3 [s]	τ_4 [s]	c_1 [μPa]	c_2 [Pa]	max err_τ $t\geq t^\star$ [%]	max err_{N_z} $t\geq t^\star$ [%]
S_{11}	8.1034	0.99	1020	88.511	359.74	359.41	132.2	80.179	0.1117	0.0941	1.2096	20.497	91.948	510.02	19.497	18.886
S_{12}	8.6848	0.99	861.35	105.47	334.31	315.94	61.799	43.828	0.12	0.5626	17.937	19.834	1.39	430.68	30.806	31.609
S_{13}	8.7703	0.99	1253.8	177.06	740.79	194.66	141.29	3.9931×10^{-4}	0.209	2.9542	38.93	18.451	10.197	626.9	18.992	22.226
S_{14}	9.8294	0.99	714.17	107.18	181.16	154.9	153.56	117.37	0.4112	0.4929	0.259	15.306	28.933	357.08	35.938	31.804
S_{15}	9.6486	0.99	809.24	110.98	267.8	240.32	108.64	81.494	0.2705	0.1037	2.187	28.974	6.2476	335.51	23.35	30.089
S_{16}	9.3726	0.99	1264.4	148.86	431.27	399.57	170.89	113.81	0.1179	0.2148	1.7763	25.905	11.289	632.2	22.962	26.81
S_{17}	9.3543	0.99	941.46	142.06	605.37	130.48	63.541	0.0062	0.2915	7.3912	89.376	105.57	1.3055	470.73	28.384	34.375
S_{18}	11.228	0.99	1159.5	134.3	384.24	381.77	161.17	197.97	0.1539	0.1917	2.0081	33.052	8.7216	579.73	25.468	31.333
S_{19}	8.0385	0.99	1216	149.53	704.25	187.15	103.02	72.031	0.3057	1.9388	10.93	78.995	0.0094199	607.99	22.622	26.891
S_{20}	8.9375	0.99	1238.3	168.98	389.22	377.06	171.6	131.48	0.3024	0.1172	2.806	36.611	2.1066	619.17	21.601	25.781
Mean ± SD	—	—	1041 ± 201	130 ± 29	447 ± 198	270 ± 108	126 ± 41	77 ± 66	0.22 ± 0.1	1.45 ± 2.32	19.04 ± 28.62	33.03 ± 26.35	17.23 ± 27.45	513 ± 111	24.96 ± 5.33	27.98 ± 4.8

TABLE 3.4: Heights, estimated MQLV parameters and maximal relative errors in the torque and normal force over the fitting range for samples tested at 400 rad m^{-1} s^{-1}.

Sample	H_0 [mm]	λ	μ_0 [Pa]	μ_∞ [Pa]	μ_1 [Pa]	μ_2 [Pa]	μ_3 [Pa]	μ_4 [Pa]	τ_1 [s]	τ_2 [s]	τ_3 [s]	τ_4 [s]	c_1 [μPa]	c_2 [Pa]	$\max_{t\geq t^\star} \mathrm{err}_T$ [%]	$\max_{t\geq t^\star} \mathrm{err}_{N_z}$ [%]
S_{21}	11.288	0.99	989.56	116.08	359.18	344.12	170.18	2.3359×10^{-4}	0.114	0.2938	13.187	12.323	10.829	494.78	29.252	29.349
S_{22}	11.812	0.99	774.72	89.185	497.42	113.66	74.464	2.1×10^{-4}	0.185	2.7482	33.279	8.6742	0.92322	387.36	31.812	40.139
S_{23}	8.4216	0.99	388.24	58.62	133.86	123.86	71.964	4.4007×10^{-5}	0.6331	6.4661	40.349	60.757	0.0059017	223.98	27.018	34.238
S_{24}	10.111	0.99	920.46	62.668	535.86	244.75	77.299	0.0013	0.2815	0.0011	12.829	0.9428	42.44	460.23	69.909	32.426
S_{25}	10.474	0.99	1379.5	127.36	370.45	352.02	351.55	178.14	0.0674	0.3406	0.0671	12.155	0.10553	689.77	30.786	36.412
S_{26}	11.132	0.99	497.15	65.435	114.21	114.15	112.31	91.044	0.1048	0.4212	0.397	11.621	4.0076	248.57	34.013	37.783
S_{27}	8.0194	0.99	1005.8	83.491	264.95	260.9	256.02	140.45	0.1004	0.0621	0.317	11.814	6.3762	502.91	35.692	44.153
S_{28}	8.6042	0.99	1178.7	157.1	304.35	274.33	267.27	175.67	0.4461	0.0826	0.0828	14.472	9.6969	589.36	28.884	30.932
S_{29}	8.7223	0.99	1495.9	137.88	512.7	507.84	216.32	121.2	0.0826	0.1105	1.2196	24.011	3.8003	747.97	19.828	19.538
S_{30}	8.7558	0.99	1161.9	125	375.42	374.91	170.68	115.85	0.114	0.1037	0.9253	19.031	7.6129	580.93	30.257	37.282
Mean $\pm$ SD	—	—	979 $\pm$ 354	102 $\pm$ 35	347 $\pm$ 147	271 $\pm$ 129	166 $\pm$ 98	82 $\pm$ 75	0.21 $\pm$ 0.19	1.06 $\pm$ 2.07	10.27 $\pm$ 14.99	17.58 $\pm$ 16.33	8.58 $\pm$ 12.5	493 $\pm$ 172	33.75 $\pm$ 13.41	34.23 $\pm$ 6.78

3.6 Computational validation

To validate our fitting results from Section 3.5.2, we conducted brain torsion simulations using the open-source software FEniCS [18, 324], which offers a high-level Python and C++ interface for solving partial differential equations through the Finite Element Method.

The governing equations for the simple torsion of a solid cylinder for any time $t > 0$, expressed in Cartesian coordinates to facilitate their resolution, are as follows:

$$\begin{cases} \mathrm{div}\mathbb{T}(\mathbf{x}, t) = \mathbf{0} \quad \text{on } \Omega(t)\,, \\ J = 1\,, \end{cases} \tag{3.41}$$

where the last equation represents the incompressibility constraint.

To approach the numerical implementation of the model, it is better to rewrite the system using a Lagrangian description of motion. This approach allows all quantities of interest to be expressed in terms of material coordinates within the undeformed domain, denoted as Ω^*. In this case, the set of equations in Lagrangian form is:

$$\begin{cases} \mathrm{Div}\mathbb{P}(\mathbf{X}, t) = \mathbf{0} \quad \text{on } \Omega^*\,, \\ J = 1\,, \end{cases} \tag{3.42}$$

where $\mathbb{P}(\mathbf{X}, t)$ is the first Piola-Kirchhoff stress tensor $\mathbb{P} := J\mathbb{T}\mathbb{F}^{-\mathrm{T}}$.

We then impose the appropriate boundary conditions. First, we ensure that the lateral surface of the cylinder is free of traction at all times t, which is expressed as $\mathbb{P}\mathbf{n} = \mathbf{0}$ at $r = R_0$. Additionally, before introducing torsion, an initial step simulates pre-compression by applying an axial pre-stretch of $\lambda = 0.99$. To implement the twist, we defined a reference point at the centre of the cylinder's top surface, which was coupled to all other points on the surface to ensure a uniform rotational displacement around the longitudinal axis. The twist was then ramped up linearly to the measured values at the end of the ramp phase in the experiments in time $\{2.2, 0.367, 0.22\}$ s. The bottom surface of the cylinder was fixed to prevent any movement. Mathematically, we superpose an axial contraction to the actual rotation so that the total deformation is written in

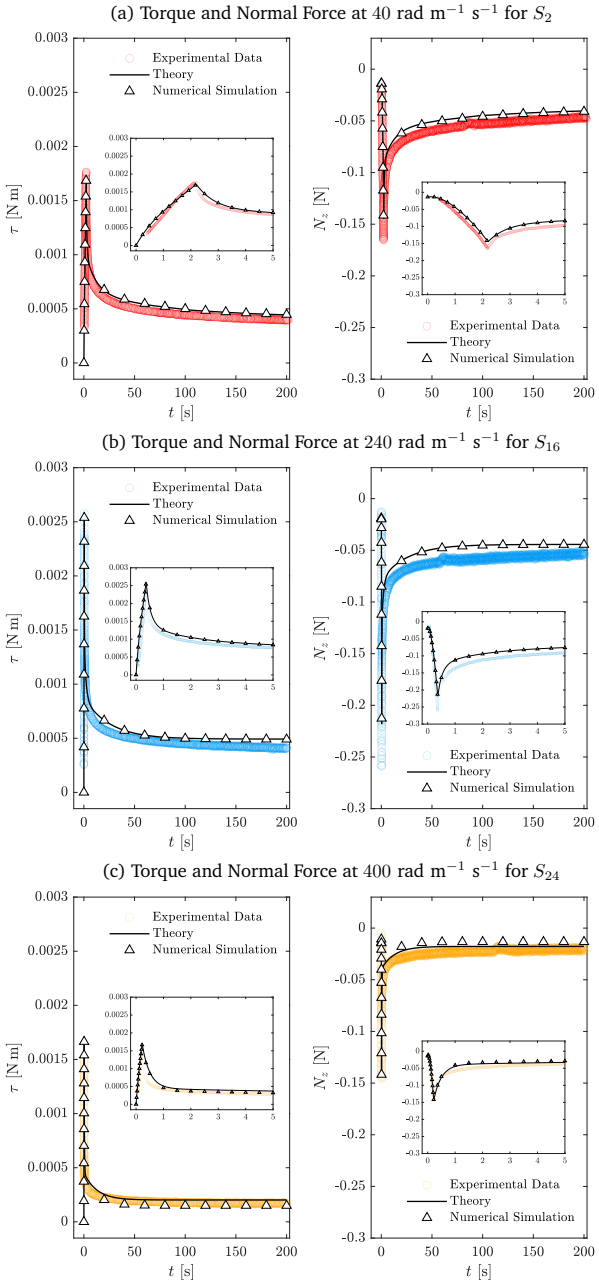

FIGURE 3.6: Comparison of the resultant torque τ and normal force N_z for samples (a) S_2, (b) S_{16} and (c) S_{24} at twist rates of $\{40, 240, 400\}$ rad m^{-1} s^{-1}. Experimental data are denoted by circles, analytical predictions using the MQLV model by solid black lines and the results of the numerical simulations in FEniCS by triangles. The insets show the ramp phase and the initial part of the hold phase in more detail.

Cartesian coordinates as follows:

$$\boldsymbol{u}_{\text{top}} = \begin{bmatrix} \dfrac{\sqrt{X^2+Y^2}}{\sqrt{\lambda}} \cos\left(\arctan\left(Y/X\right) + \lambda\phi(t)Z\right) - X \\ \dfrac{\sqrt{X^2+Y^2}}{\sqrt{\lambda}} \sin\left(\arctan\left(Y/X\right) + \lambda\phi(t)Z\right) - Y \\ (1-\lambda)Z \end{bmatrix} \text{ on } \partial\Omega^*_{D_{\text{top}}}. \tag{3.43}$$

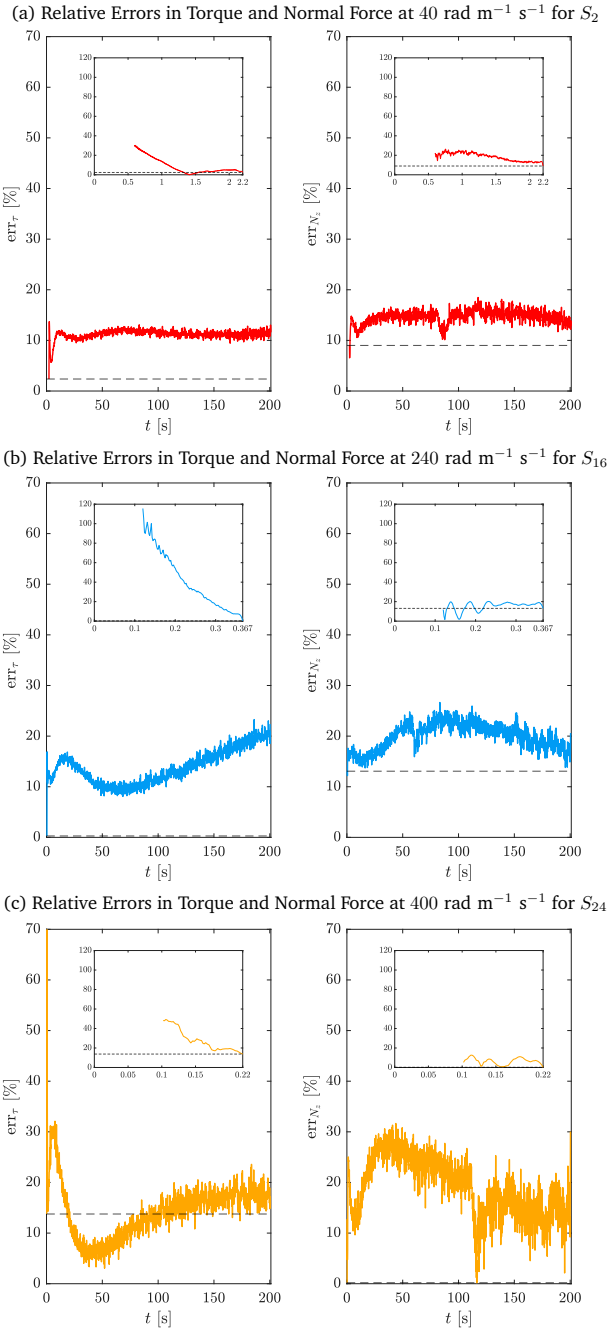

FIGURE 3.7: Relative errors in the torque err_τ and force err_{N_z} for samples (a) S_2, (b) S_{16} and (c) S_{24} at twist rates of $\{40, 240, 400\}$ rad m^{-1} s^{-1}. The insets show the ramp phase in more detail. The dashed lines indicate the relative errors at the end of the ramp phase.

For what concerns the bottom boundary, the Dirichlet condition we impose is:

$$\boldsymbol{u} = \boldsymbol{u}_0 \text{ on } \partial\Omega^*_{D_{\text{bottom}}}\,, \tag{3.44}$$

where $\boldsymbol{u}_0$ is the solution of the problem at time $t = 0$, when only the pre-stretch has occurred and the twist has not yet been applied.

The resultant torque and normal force were obtained from the output of the simulations. The torque $\tau(t)$ required to twist the cylinder can be computed as

$$\tau(t) = \int_0^{2\pi} \int_0^{R_0/\sqrt{\lambda}} \tilde{T}_{\theta z} r^2 \, \mathrm{d}r\mathrm{d}\theta \,, \tag{3.45}$$

and the normal force $N(t)$ necessary to keep the cylinder length constant reads

$$N_z(t) = \int_0^{2\pi} \int_0^{R_0/\sqrt{\lambda}} \tilde{T}_{zz} r \, \mathrm{d}r\mathrm{d}\theta \,. \tag{3.46}$$

Here, $\tilde{T}_{\theta z}$ and $\tilde{T}_{zz}$ are the components of the tensor $\tilde{\mathbb{T}}(t)$, which represents the Cauchy tensor $\mathbb{T}(t)$ expressed in cylindrical coordinates, i.e.

$$\tilde{\mathbb{T}}(t) = \mathbb{R}\mathbb{T}(t)\mathbb{R}^T \tag{3.47}$$

with

$$\mathbb{R} = \begin{bmatrix} \cos\theta & \sin\theta & 0 \\ -\sin\theta & \cos\theta & 0 \\ 0 & 0 & 1 \end{bmatrix}, \quad r = \sqrt{x^2 + y^2}\,, \quad \theta = \arctan(y/x)\,. \tag{3.48}$$

Weak formulation of the Lagrangian model

We derive the weak formulation of the Lagrangian model to enable solving the system (3.42), equipped with the boundary conditions (3.43)-(3.44), using the Finite Element Method (FEM). We define the following functional spaces to facilitate the formulation of our problem:

$$\boldsymbol{H}_0^1(\Omega^*) = \left\{ \boldsymbol{v} \in \boldsymbol{H}^1(\Omega^*) : \ \boldsymbol{v} = \boldsymbol{0} \text{ on } \partial\Omega^*_{\text{bottom}} \text{ and } \partial\Omega^*_{\text{top}} \right\},$$
$$\boldsymbol{H}_\star^1(\Omega^*) = \left\{ \boldsymbol{v} \in \boldsymbol{H}^1(\Omega^*) : \ \boldsymbol{v} = \boldsymbol{u}_0 \text{ on } \partial\Omega^*_{\text{bottom}} \text{ and } \boldsymbol{v} = \boldsymbol{u}_{\text{top}} \text{ on } \partial\Omega^*_{\text{top}} \right\}.$$

Then, we multiply by a test function $\boldsymbol{v} \in \boldsymbol{H}_0^1(\Omega^*)$ the first equation of (3.42) and integrate by parts to obtain:

$$-\int_{\Omega^*} \mathbb{P} : \mathrm{Grad}\, \boldsymbol{v} \, dV^* + \int_{\partial\Omega^*} \mathbb{P}\mathbf{N} \cdot \boldsymbol{v} \, d\Sigma^* = 0 \,.$$

Since the test function $\boldsymbol{v}$ vanishes on the Dirichlet boundary where the solution $\boldsymbol{u}$ is known and remembering that $\mathbb{P}\mathbf{N}$ is null at the lateral surface of the cylinder, we arrive at the following variational problem:

$$-\int_{\Omega^*} \mathbb{P} : \mathrm{Grad}\, \boldsymbol{v} \, dV^* = 0 \,.$$

For what concern the incompressibility constraint, we multiply that equation for the test function $q \in H^1(\Omega^*)$:

$$\int_{\Omega^*} (J-1) q \, dV^* = 0 \,. \tag{3.49}$$

Finally, we can define the variational problem: find $\boldsymbol{u} \in \boldsymbol{H}_\star^1(\Omega^*)$ and $p \in H^1(\Omega^*)$ such that, for all $\boldsymbol{v} \in \boldsymbol{H}_0^1(\Omega^*)$ and $q \in H^1(\Omega^*)$, it holds

$$-\int_{\Omega^*} \mathbb{P}\,(\boldsymbol{u}, p) : \mathrm{Grad}\, \boldsymbol{v} \, dV^* + \int_{\Omega^*} (J(\boldsymbol{u}) - 1) q \, dV^* = 0 \,. \tag{3.50}$$

Discrete formulation of the continuous variational problems

To proceed, we must introduce a spatial discretization of the continuous variational problem given in Eq. (3.50). For this purpose, we employ quadratic tetrahedral elements, $\mathbb{P}_2$, for the displacement field, and linear tetrahedral elements, $\mathbb{P}_1$, for the pressure field. This combination, commonly referred to as the *Taylor-Hood (or Hood-Taylor) elements*, offers several advantages, including numerical stability due to the satisfaction of the inf-sup condition, improved accuracy in capturing displacement gradients with quadratic elements, and computational efficiency by using linear elements for the pressure field. These properties make Taylor-Hood elements a robust and widely adopted choice for problems involving incompressibility constraints or mixed finite element formulations. Accordingly, we define the following finite element spaces:

$$\begin{aligned}
\boldsymbol{V}_{h0} &:= \left\{ \boldsymbol{v}_h \in \left[C^0\left(\overline{\Omega^*}\right)\right]^3 : \boldsymbol{v}_h|_K \in \left[\mathbb{P}_2(K)\right]^3 \ \forall K \in \mathcal{T}_h,\ \boldsymbol{v}_h = \boldsymbol{0} \text{ on } \partial\Omega^*_{\text{top}} \text{ and } \Omega^*_{\text{bottom}} \right\} , \\
\boldsymbol{V}_h &:= \left\{ \boldsymbol{v}_h \in \left[C^0\left(\overline{\Omega^*}\right)\right]^3 : \boldsymbol{v}_h|_K \in \left[\mathbb{P}_2(K)\right]^3 \ \forall K \in \mathcal{T}_h,\ \boldsymbol{v}_h \text{ meets (3.43)-(3.44)} \right\} , \\
W_h &:= \left\{ q_h \in C^0\left(\overline{\Omega^*}\right) : q_h|_K \in \mathbb{P}_1(K)\ \forall K \in \mathcal{T}_h \right\} ,
\end{aligned}$$

where $\mathcal{T}_h$ is a decomposition of the domain Ω^* into tetrahedra K. For what concerns the time discretization, given N time instants on the interval $(0, T)$, $\Delta t := T/N$ is the time step and we use a superscript k to denote the value of a quantity at time $t_k = k\Delta t$. Thus, we can formulate the problem as follows: for $k = 1, ..., N$, find $\left(\boldsymbol{u}_h^k, p_h^k\right) \in \boldsymbol{V}_h \times W_h$ such that $\forall (\boldsymbol{v}_h, q_h) \in \boldsymbol{V}_{h0} \times W_h$ it holds

$$- \int_{\boldsymbol{\Omega}^*} \mathbb{P}\left(\boldsymbol{u}_h^k, p_h^k\right) : \text{Grad}\, \boldsymbol{v}_h \, dV^* + \int_{\boldsymbol{\Omega}^*} \left(J\left(\boldsymbol{u}_h^k\right) - 1\right) q_h \, dV^* = 0 \,. \tag{3.51}$$

Numerical implementation

Numerical simulations were performed for samples S_2, S_{16} and S_{24} at twist rates of $\{40, 240, 400\}$ rad m^{-1} s^{-1}. The initial cylindrical geometry of each sample was built by setting the radius $R_0 = 12.5$ mm and the heights H_0 according to Tables 3.2, 3.3 and 3.4. The computational mesh was generated using the software *Tetgen* [235, 492], where the appropriate radius and height were specified. Additionally, we assigned the estimated material parameters listed in the aforementioned tables according to the MQLV theory. The implemented system (3.51) allows to determine all the unknown fields, namely, the displacement field $\boldsymbol{u}_h^k(\mathbf{X}, t)$ and the scalar fields $p_h^k(\mathbf{X}, t)$. From these values, we reconstruct the Cauchy stress tensor $\mathbb{T}(t)$ and save it to an output file, expressed in cylindrical coordinates as defined in (3.47). The magnitude of the displacement field and the Cauchy stress tensor components $\tilde{T}_{\theta z}$ and $\tilde{T}_{zz}$ for sample S_{24} at time $t = 5$ *s* are shown in Figure 3.8 as an example. Subsequently, the torque and normal force are computed using Eqs. (3.45)-(3.46) with *ParaView* [393], an open-source application for interactive scientific visualisation.

Fig. 3.6 demonstrates that the torque and normal force calculated in *FEniCS* agree well with the MQLV analytical predictions and the experimental data. However, a slight discrepancy is observed between the analytical predictions and the simulations for sample S_{24}, likely due to the high twist rate of 400 rad m^{-1} s^{-1}. In particular, achieving convergence at high twist rates requires a very small time step, which substantially increases the complexity of the simulations and poses challenges in obtaining accurate results.

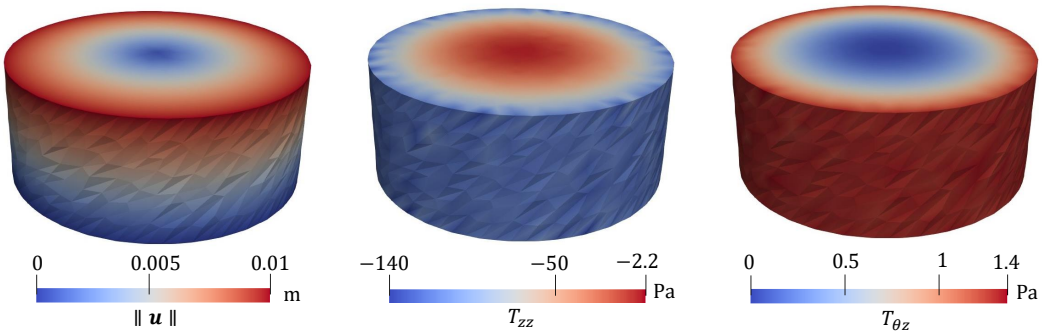

FIGURE 3.8: Magnitude of the displacement field and the Cauchy stress tensor components $\tilde{T}_{\theta z}$ and $\tilde{T}_{zz}$ for sample S_{24} at time $t = 5$ s.

3.7 Discussion and summary

In this Chapter, we devised the first experimental protocol to determine the non-linear viscoelastic properties of brain tissue in torsion. This protocol allows us to obtain two independent datasets (torque and normal force) with a single test, providing us with a much more efficient protocol compared to protocols involving multiple loading modes. The latter require a sample to be sequentially tested under different deformation modes to obtain independent datasets. Moreover, they often rely on expensive, custom-made experimental rings or multiple testing devices. Our novel protocol can be easily implemented in any commercially available rheometer and has huge potential to accurately model the non-linear viscoelastic properties of brain tissue.

Here, we applied the protocol to study the viscoelastic behaviour of the brain in torsion at varying twist rates. This protocol has huge potential not only to study the strain-dependent relaxation of the brain but also its non-linear creep behaviour. From the theoretical viewpoint, we showed that the MQLV model provides an accurate fit to the experimental data and allows us to estimate the time-dependent shear modulus of an incompressible, viscoelastic, soft material such as the brain. The fitting procedure that we proposed can also be applied to compressible, viscoelastic, soft materials, whose mechanical behaviour is determined by at least two material functions.

Finally, when coupled with bespoke finite element models such as the University College Dublin Brain Trauma Model [254], the viscoelastic material parameters estimated in this study could enhance our understanding of the forces and deformations involved in traumatic brain injury and contribute to the design of improved headgear for sports such as boxing and motorsports. Our novel testing protocol also offers new insights into the mechanical behaviour of soft tissues other than the brain.

To investigate the differences between the estimated MQLV parameters at the twist rates $\{40, 240, 400\}$ rad m^{-1} s^{-1}, we performed Tukey multiple comparisons tests using the R (Version 4.4.2) function TukeyHSD [416]. The column plots in Fig. 3.9 show that there are no statistically significant differences between the shear moduli and second Mooney–Rivlin parameters at the three twist rates, except for the μ_3 values at 40 rad m^{-1} s^{-1} and 400 rad m^{-1} s^{-1}. By contrast, there are statistically significant differences between several of the relaxation times at the three twist rates (see Fig. 3.10). However, the statistically significant differences for these Prony parameters may be attributed to their large standard deviations, particularly for the relaxation times. In pracice, the representation of relaxation data by a Prony series is non-unique, with the Prony parameters being highly sensitive to small changes in the data [196]. Finally, we

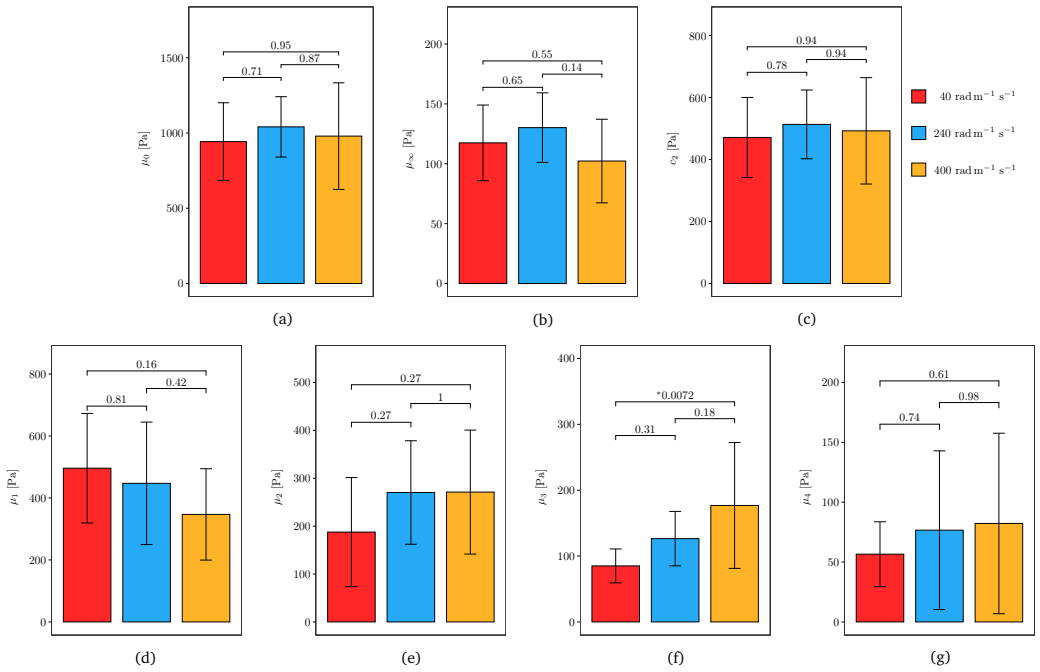

FIGURE 3.9: Column plots (mean $\pm$ SD) of the estimated MQLV parameters (a) μ_0, (b) μ_∞, (c) c_2, (d) μ_1, (e) μ_2, (f) μ_3 and (g) μ_4 for samples tested at 40 rad m^{-1} s^{-1} (red), 240 rad m^{-1} s^{-1} (blue) and 400 rad m^{-1} s^{-1} (orange). Also shown are the p-values obtained from Tukey multiple comparisons tests, with asterisks denoting a statistically significant difference ($p < 0.05$).

note that the values of μ_0 and c_2 obtained here for ovine brain tissue are in line with those reported by Balbi *et al.* [45] for porcine brain tissue at 300 rad m^{-1} s^{-1}.

Our proposed testing protocol presents some challenges and limitations. Due to natural variations in brain size between sheep and brain tissue's highly compliant and ultra-soft nature, it was difficult to consistently and reliably prepare cylindrical samples of similar dimensions, as in Fig. 3.1. As a result, difficult-to-obtain and otherwise useful brain samples were wasted, leading to a smaller sample size. Furthermore, if the samples are not satisfactorily cylindrical (as the rotational rheometer requires), artefacts could potentially be introduced into the measured torque and normal force.

Currently, there is no consensus on the effects of temperature and post-mortem storage time on the mechanical properties of brain tissue [83]. Therefore, it is important to

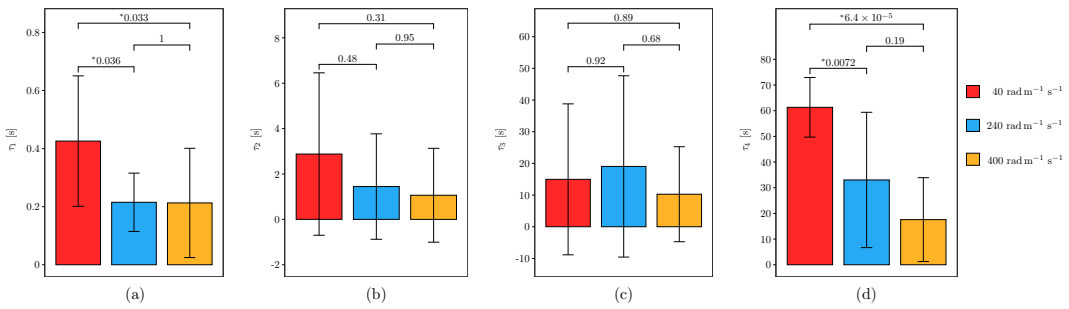

FIGURE 3.10: Column plots (mean $\pm$ SD) of the estimated MQLV parameters (a) τ_1, (b) τ_2, (c) τ_3 and (d) τ_4 for samples tested at 40 rad m^{-1} s^{-1} (red), 240 rad m^{-1} s^{-1} (blue) and 400 rad m^{-1} s^{-1} (orange). Also shown are the p-values obtained from Tukey multiple comparisons tests, with asterisks denoting a statistically significant difference ($p < 0.05$).

note that the brains in this study were prepared and tested at room temperature (19–23 °C) within 8 hours post-mortem.

Given the limited availability and ethical challenges associated with obtaining fresh human brains in Ireland, ovine brains were used in this work. Despite the widespread use of porcine [30, 45, 425, 474] and bovine [73, 86, 487] brain tissues as surrogates for characterising the mechanical properties of human brain tissue, there are relatively few studies that focus on ovine brain tissue [180, 317]. By contrast, due to the neuroanatomical similarities between the sheep and human brains [50], there is a growing body of literature that utilises the ovine model to investigate brain injuries, including strokes and epilepsy, among others [312]. It stands to reason that ovine brain tissue, like porcine and bovine brain tissues, is an appropriate alternative to human brain tissue for our purposes.

4 A PDE-based approach to model immunotherapy for Glioblastoma Multiforme

4.1 Preliminaries

As stated in Chapter 1, immunotherapy aims to generate a specific immune response that targets cancer cells, countering tumour growth while sparing the surrounding healthy tissue [405]. Despite its limited use compared to conventional treatments, immunotherapy has been approved for various types of cancer, including melanoma and prostate cancer, and has sparked interest as a potential approach for Glioblastoma Multiforme (GBM). However, its application in GBM faces numerous challenges, such as the immunosuppressive tumour microenvironment, the presence of the blood-brain barrier (BBB) that grants the brain immune privilege, the intratumoural heterogeneity of GBM, and the existence of therapy-resistant cancer stem cells [7]. These obstacles have led to the development and testing of various immunotherapy strategies, primarily focusing on vaccines, immune checkpoint inhibitors, chimeric antigen receptor T cells (CAR-T), and oncolytic viruses.

Cancer vaccines aim to enhance immune surveillance by leveraging tumour-derived antigens [433], but their effectiveness for GBM is constrained by the rarity and variability of specific antigens. For instance, targeting the EGFRvIII antigen, present in approximately 30% of GBM cases, has shown promise. Recent advances in sequencing technologies have further identified neoantigens arising from somatic mutations, providing a highly specific basis for therapy. Similarly, immune checkpoint inhibitors have demonstrated the ability to counteract the suppressive tumour microenvironment by blocking receptors, such as PD-1 and CTLA-4, thereby restoring immune function. Meanwhile, oncolytic viruses have emerged as a novel approach, selectively targeting cancer cells while activating the immune response through molecular patterns released during infection. CAR-T cell therapy, which involves engineering T cells to recognise tumour-specific antigens, also holds significant potential, though its efficacy against GBM is hindered by the BBB and the tumour's immunosuppressive environment.

The emergence of immunotherapy has spurred the development of mathematical models to describe the complex interactions between tumours and the immune system. These models typically focus on tumour cells and immunocytes, such as cytotoxic T lymphocytes (CTLs) and macrophages, and often include mediators like cytokines and antigens [296, 490]. Early approaches employed predator-prey ODE systems, such as those by Kuznetsov [302] and Kirschner and Panetta [293], to capture tumour recurrence and immune cell overgrowth. More recent models incorporate spatial effects using reaction-diffusion PDEs [309] or hybrid frameworks, integrating cellular dynamics with chemical diffusion [511]. Brain tumour-specific models include ODE frameworks

that simulate glioblastoma interactions with CTLs [298], and extensions with delays or spatio-temporal dynamics for capturing therapeutic responses [283, 284].

In this Chapter, an advection-diffusion-reaction model is proposed to characterise the immunotherapy response in tumours growing within highly anisotropic environments, such as glioblastoma. The model is designed to capture tumour cell proliferation throughout disease progression and its interactions with the immune system, including the potential effects of immunotherapy through cytotoxic T lymphocyte infusions. Section 4.2 provides an overview of the mathematical model considered in this study. Section 4.3 introduces an ODE-based version of the model to describe tumour proliferation and the impact of the infusion on the malignant cell population. The system's equilibria and the influence of therapy on the trajectories are analysed both analytically and numerically, with conditions for the effectiveness of the therapy derived, alongside bifurcation studies for the model parameters. Finally, Section 4.4 presents the results of numerical simulations. The system is initially solved in a simple 2D geometry to test the stability of the code and the model's behaviour, followed by a sensitivity analysis to quantify the relative importance of each parameter in tumour treatment progression. The model is then applied to real 3D brain geometry obtained from MRI scans, using diffusion tensors derived from the DTI technique, which characterises the orientation of fibres in the brain to describe the anisotropic motion of cells.

This work was partially developed by Lorenzo Scolaris as part of his master's thesis, under the supervision of the present author and Chiara Giverso.

4.2 Mathematical model

This section introduces a model that qualitatively captures the growth patterns of malignant gliomas and the administration of an immunotherapeutic treatment, specifically T-cell infusions. In an earlier mathematical model [49], glioma cell proliferation and their interactions with the immune system were described by a set of coupled nonlinear ordinary differential equations, incorporating the effects of the immunotherapeutic drug T11 target structure. While this model provided valuable insights, it was somewhat restricted in scope, as it did not account for the migration of malignant gliomas or the immune system's dynamic responses.

Numerous factors influence the migration of glioma cells within the brain. Their motility is further enhanced by the secretion of various signalling molecules that induce chemotactic migration. In patients, glioma cells often follow preferential paths of dispersion, such as white matter tracts and the basal lamina of brain blood vessels. This behaviour indicates that glioma cell migration relies on specific substrates and structural features within the brain. Ultimately, the extent and pattern of invasion are shaped by a complex interplay between the intrinsic properties of glioma cells and the characteristics of their surrounding microenvironment.

We model the pointwise concentration of tumour cells and lymphocytes, denoted by $G(\boldsymbol{x}, t)$ and $C(\boldsymbol{x}, t)$, respectively, as functions of space and time. The model incorporates diffusion for both cell populations, which is anisotropic in general. Additionally, we introduce chemotactic movement, whereby the lymphocytes are directed towards areas with higher concentrations of TGF-β, $T(\boldsymbol{x}, t)$, produced by tumour cells. The behaviour of the diffusing chemoattractant is described by an additional equation, and the

complete model is expressed as follows:

$$\begin{cases} \dfrac{\partial G}{\partial t} = \nabla \cdot (\mathbb{D}_G \nabla G) + rG(1 - \dfrac{G}{G_{\max}}) - \alpha_G C \dfrac{G}{k_G + G}\,, \\ \dfrac{\partial C}{\partial t} = \nabla \cdot (\mathbb{D}_C \nabla C) - \nabla \cdot [\chi(G, C, T) C \nabla T] + b_C - \mu_C C - \alpha_C C \dfrac{G}{k_C + G} + S_T(\boldsymbol{x}, t)\,, \\ \dfrac{\partial T}{\partial t} = \nabla \cdot (\mathbb{D}_T \nabla T) + p_T G - \mu_T T\,. \end{cases} \tag{4.1}$$

The first term on the right-hand side of the first equation of system (4.1) represents the random motility of malignant glioma cells, where $\mathbb{D}_G$ is the diffusion tensor. The second term models the growth of malignant gliomas using a logistic growth function, with r denoting the proliferation rate. The final term accounts for the eradication of glioma cells by cytotoxic T-lymphocytes, occurring at a rate of α_G.

Next, we examine the second equation of system (4.1), accounting for the kinetics of activated cytotoxic T-lymphocytes, along with their mechanisms of migration and diffusion. First, we include a diffusion term where $\mathbb{D}_C$ is the diffusion tensor. The second term represents chemotaxis, modelling the movement of cytotoxic T-lymphocytes towards regions of higher concentrations of TGF-β. The chemotactic coefficient, denoted by χ, is, in principle, a function that may depend on the tumour cell concentration, the T-cell concentration, and the TGF-β concentration. The proliferation of cytotoxic T-lymphocytes is assumed to occur at a constant rate b_C, while their decay happens at a rate of μ_C. The clearance of cytotoxic T-lymphocytes by malignant gliomas follows Michaelis-Menten saturation dynamics, with a rate of α_C and a half-saturation constant k_C. This Michaelis-Menten form captures the saturating effects of the immune response due to the presence of glioma cells. Finally, we account for the infusion of T-cells as part of the immunotherapeutic treatment, represented by the term $S_T(\boldsymbol{x}, t)$.

Finally, we consider the last equation of system (4.1), which describes the dynamics of the chemoattractant TGF-β. Glioma cells release TGF-β as part of their interaction with the tumour microenvironment, with the amount secreted increasing proportionally to the tumour cell population. For simplicity, a linear relationship between TGF-β secretion and tumour cell density is assumed in this model, acknowledging that the underlying biological mechanisms are far more complex and may involve non-linear interactions and context-dependent regulatory effects. We assume that TGF-β diffuse throughout the tissue with rate dictated by diffusion tensor $\mathbb{D}_T$. Production of TGF-β is proportional to the size of glioma cell population, at the rate p_T. TGF-β is also supposed to decay linearly at the rate μ_T.

Concerning the boundary conditions, Neumann boundary conditions are applied to all variables. This approach is equivalent to requiring that the inflow or outflow across the domain's boundary is zero for each variable:

$$\nabla G \cdot \boldsymbol{n} = \nabla C \cdot \boldsymbol{n} = \nabla T \cdot \boldsymbol{n} = 0\,, \quad \text{on } \partial\Omega\,,\ t > 0\,. \tag{4.2}$$

For the initial conditions, we suppose:

$$G(\boldsymbol{x}, 0) = G_0(\boldsymbol{x}) > 0\,,\ C(\boldsymbol{x}, 0) = C_0(\boldsymbol{x}) > 0\,,\ T(\boldsymbol{x}, 0) = T_0(\boldsymbol{x}) > 0\,,\ \boldsymbol{x} \in \Omega\,, \tag{4.3}$$

where Ω represents a bounded, simply connected domain with boundary $\partial\Omega$.

4.2.1 Parameter selection

Identifying and accurately understanding the appropriate numerical parameters is essential to building robust and reliable predictive models. However, such parameters are challenging to obtain through direct measurements and must be derived from in vitro experiments or estimations. Given the inability to conduct experiments, parameters have been obtained from findings across various sources in the literature, which will be discussed in this Section. A summary of all the parameters used in system (4.1) is provided in Table 4.1, distinguishing the values for the 1D, 2D, and 3D settings.

Parameter	Value (1D setting)	Value (2D and 3D settings)
r	$0.01\,\mathrm{h}^{-1}$	$0.003125\,\mathrm{h}^{-1}$
$G_{\max}$	882650 cells	$2.39 \cdot 10^8$ cells/mL
α_G	$0.12\,\mathrm{h}^{-1}$	$0.12\,\mathrm{h}^{-1}$
k_G	27362.15 cells	$7.409 \cdot 10^6$ cells/mL
α_C	$0.168\,\mathrm{h}^{-1}$	$0.168\,\mathrm{h}^{-1}$
k_C	334524.35 cells	$9.0581 \cdot 10^7$ cells/mL
μ_C	$0.0074\,\mathrm{h}^{-1}$	$0.0074\,\mathrm{h}^{-1}$
b_C	740 cells h^{-1}	1.85 cells/(mL $\cdot$ h)
μ_T	$0.1022\,\mathrm{h}^{-1}$	$0.1022\,\mathrm{h}^{-1}$
p_T	$5.7 \cdot 10^{-6}$ pg/(cells $\cdot$ h)	$5.7 \cdot 10^{-6}$ pg/(cells $\cdot$ h)
D_G	-	$5.417 \cdot 10^{-5}\,\mathrm{cm}^2/\mathrm{h}$
D_C	-	$4.167 \cdot 10^{-4}\,\mathrm{cm}^2/\mathrm{h}$
D_T	-	$6.6336 \cdot 10^{-3}\,\mathrm{cm}^2/\mathrm{h}$

TABLE 4.1: List of dimentionalised parameters used in stability analysis.

Regarding the equation governing tumour cell dynamics in the brain, the proliferation rate is set at $r = 0.01\,\mathrm{h}^{-1}$, and the carrying capacity is defined as $G_{\max} = 882650$ cells, calibrated using growth curves from in vitro experiments [49]. These parameters do not take into account the spatial distribution of cells and are thus suitable for the ODE system to describe tumour progression in time. For 2D and 3D simulations within brain geometry, where the focus is the local concentration of cells, we set $r = 0.003125\,\mathrm{h}^{-1}$ [482], while considering $G_{\max} = 2.39 \cdot 10^8$ cells/mL, assuming a cellular radius of $10\,\mu$m [230].

The tumour cell elimination coefficient is obtained from [49], with $\alpha_G = 0.12\ \mathrm{h}^{-1}$, thus disregarding immunosuppressive effects from TGF-beta. The Michaelis-Menten saturation coefficient for tumour cell elimination is set at $k_G = 0.031\ G_{\max}$, as determined from in vitro experiments [49].

The lymphocyte elimination coefficient is considered to be $\alpha_C = 0.168\,\mathrm{h}^{-1}$, while the Michaelis-Menten coefficient is set at $k_C = 0.379\ G_{\max}$, derived from in vitro experiments [49].

The half-life of lymphocytes is 3.9 days [49], giving a natural lymphocyte death coefficient of $\mu_C = 0.0074\,\mathrm{h}^{-1}$. The central nervous system (CNS) of a healthy individual contains approximately $1.5 \cdot 10^5$ lymphocytes [175]. Considering an inflammatory process, this number is hypothesised to double as a result of the innate immune response. To maintain a stable lymphocyte count of $3.0 \cdot 10^5$ cells in the absence of elimination by tumour cells and therapy, the following calculation is made. For the 1D setting, we set $b_C = 3.0 \cdot 10^5\,\mu_C$ cells $= 740\,\mathrm{cells}\,\mathrm{h}^{-1}$. Dividing this value by an estimated brain volume of 1200 mL yields a cell density of 250 cells/mL. Consequently, for the 2D and 3D simulations, the parameter is set as $b_C = 250\,\mathrm{cells/mL} \cdot \mu_C \approx 1.85\,\mathrm{cells}/(\mathrm{mL} \cdot \mathrm{h})$.

The TGF-β decay coefficient is derived from [49]. However, due to the rapid decay rate of TGF-β, which prevents the formation of a significant concentration gradient beyond the tumour region, we adopt the IL-2 cytokine decay rate, $\mu_T = 0.102\,\mathrm{h}^{-1}$. Additionally, the release rate per glioma cell, p_T, is also taken from [49], with an assumed value of $p_T = 5.7 \cdot 10^{-6}\,\mathrm{pg}/(\mathrm{cell}\cdot\mathrm{h})$.

The mean diffusivity of tumour cells, lymphocytes, and cytokines is defined as one-third of the trace of their respective diffusion tensors, $\mathbb{D}_G$, $\mathbb{D}_C$, and $\mathbb{D}_T$. A mean diffusivity of $D_G = 5.417 \cdot 10^{-5}\,\mathrm{cm}^2/\mathrm{h}$ is assigned to tumour cells, derived from data in [482]. For lymphocytes, *in vitro* experiments have shown a diffusivity of up to $10^{-2}\,\mathrm{cm}^2/\mathrm{day}$ in the presence of a tumour [358], resulting in a selected value of $D_C = 4.167 \cdot 10^{-4}\,\mathrm{cm}^2/\mathrm{h}$. In contrast, cytokines exhibit mean diffusivities several orders of magnitude higher than those of cells [358]. Based on estimates from [284], the cytokine mean diffusivity is approximated to be 16 times greater than that of lymphocytes.

The values for the chemotactic coefficient in the simplified 2D geometry are not readily available in the literature and will therefore be estimated through numerical simulations, as detailed in Section 4.4.1. Similarly, for the three-dimensional brain geometry, the value for the chemotactic coefficient used in simulations will be estimated in Section 4.4.2.

4.3 Qualitative analysis of the model

In this Section, we investigate the spatially homogeneous steady states of the glioma-cytotoxic T-lymphocytes interaction system (i.e. the two first equations of system (4.1)) and its local stability analysis. In order to do that, we do not consider diffusion and chemotaxis. The model reduces to the following ODE system:

$$\begin{cases} \dfrac{dG}{dt} = rG\left(1 - \dfrac{G}{G_{\max}}\right) - \alpha_G C \dfrac{G}{k_G + G}\,, \\ \dfrac{dC}{dt} = b_C - \mu_C C - \alpha_C C \dfrac{G}{k_C + G} + S_T(t)\,. \end{cases} \tag{4.4}$$

The system is firstly adimensionalized, and the following relationships are introduced:

$$G = \tilde{G} G_{\max}\,,\ C = \tilde{C} C_{\max}\,,\ t = \tilde{t}\tau\,, \tag{4.5}$$

where the tumour cell population is adimensionalized by its carrying capacity, and other quantities are adimensionalized by defining:

$$C_{\max} := \frac{r G_{\max}}{\alpha_G}\,,\ \tau := \frac{1}{r}\,. \tag{4.6}$$

The total production rate is defined as $S(t) := S_T(t) + b_C$, with $S(t) \geq b_C$. The system then becomes:

$$\begin{cases} \dfrac{d\tilde{G}}{d\tilde{t}} = \tilde{G}(1 - \tilde{G}) - \tilde{C}\dfrac{\tilde{G}}{\tilde{G} + \tilde{k}_G}\,, \\ \dfrac{d\tilde{C}}{d\tilde{t}} = \tilde{S} - \tilde{\mu_C}\tilde{C} - \tilde{\alpha_C}\tilde{C}\dfrac{\tilde{G}}{\tilde{k}_C + \tilde{G}}\,, \end{cases} \tag{4.7}$$

where $\tilde{\alpha}_C = \alpha_C/r$, $\tilde{k}_G = k_G/G_{\max}$, $\tilde{k}_C = k_C/G_{\max}$, $\tilde{\mu}_C = \mu_C/r$ e $\tilde{S}(t) = S(t)\alpha_G/r^2 G_{\max}$. For simplicity, the tildes are omitted from G, C and t in the subsequent equations.

To analyse the equilibria of the system and their stability, we consider the set of dimensional parameters listed in Table 4.1. The values are realistic and sourced from

the literature, as previously discussed in Section 4.2.1. The system is first studied in the case of a constant therapy rate $\tilde{S}(t) \equiv \tilde{S}$. The system's equilibria are examined: if (G^*, C^*) is an equilibrium, the value C^* can be explicitly calculated as a function of G^* and $\tilde{S}$:

$$C^* = \frac{\tilde{S}}{\tilde{\mu}_C + \tilde{\alpha}_C \dfrac{G^*}{G^* + \tilde{k}_C}}. \tag{4.8}$$

By substituting into the equation for G, we derive a fourth-degree polynomial in the unknown G^*:

$$\begin{aligned} G^* \Big\{ \tilde{\mu}_C(\tilde{\alpha}_C + 1) G^{*3} + \left[1 - \tilde{\mu}_C(1 - \tilde{k}_G)(\tilde{\alpha}_C + 1)\right] G^{*2} + \\ + \left(\tilde{k}_C \tilde{k}_G + \tilde{S} - \tilde{k}_C - \tilde{k}_G \tilde{\mu}_C - \tilde{\mu}_C \tilde{\alpha}_C \tilde{k}_G\right) G^* + \tilde{S} - \tilde{k}_G \tilde{k}_C \Big\} = 0 . \end{aligned} \tag{4.9}$$

The solutions consist of $G^* = 0$, followed by three additional solutions, at least one of which is real. These solutions are not presented in their general form, which can be derived using Cardano's formula, as the analytical expressions are too lengthy to be explicitly stated. Therefore, we present the equilibrium points corresponding to the parameter set in Table 4.1 computed numerically. Under biologically plausible conditions (i.e., $G^* \geq 0$), the analysis shows that for low values of $\tilde{S}$, specifically $\tilde{S} < \tilde{S}^*$, three biological physical equilibria exist: a healthy equilibrium $(G^*, C^*) = (0, \tilde{S}/\tilde{\mu}_C)$, a tumour-developed equilibrium, and a intermediate branch of equilibria where G^* lies between 0 and the value corresponding to the tumour-developed equilibrium. As $\tilde{S}$ increases (representing higher therapy levels), the tumour-developed equilibrium and the intermediate branch merge and eventually vanish, leaving only the healthy equilibrium for $\tilde{S} > \tilde{S}^*$. Figure 4.1 illustrates all the equilibria G^* for different therapy intensities setting the model parameters as in Table 4.1.

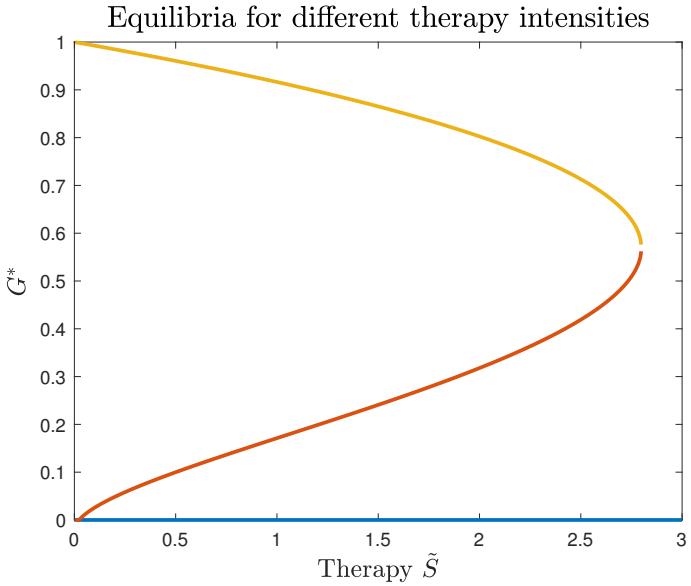

FIGURE 4.1: All equilibria G^* corresponding to varying therapy intensities.

The Jacobian of the system evaluated in (G^*, C^*) is:

$$J|_{(G^*,C^*)} = \begin{bmatrix} 1 - 2G^* - C^* \dfrac{\tilde{k}_G}{\left(G^* + \tilde{k}_G\right)^2} & -\dfrac{G^*}{G^* + \tilde{k}_G} \\ -\tilde{\alpha}_C C^* \dfrac{\tilde{k}_C}{\left(G^* + \tilde{k}_C\right)^2} & -\tilde{\mu}_C - \tilde{\alpha}_C \dfrac{G^*}{G^* + \tilde{k}_C} \end{bmatrix}. \tag{4.10}$$

Proposition 4.1 *The healthy equilibrium $(G^*, C^*) = (0, \tilde{S}/\tilde{\mu}_C)$ is locally stable for a certain value of total therapy $\tilde{S} > \tilde{S}_{\text{cr}}$.*
Proof *At the healthy equilibrium $(G^*, C^*) = (0, \tilde{S}/\tilde{\mu}_C)$, the Jacobian* (4.10) *reduces to:*

$$J|_{(0,\tilde{S}/\tilde{\mu}_C)} = \begin{bmatrix} 1 - \dfrac{\tilde{S}}{\tilde{\mu}_C \tilde{k}_G} & 0 \\ -\dfrac{\tilde{\alpha}_C \tilde{S}}{\tilde{\mu}_C \tilde{k}_C} & -\tilde{\mu}_C \end{bmatrix}. \tag{4.11}$$

Given that one eigenvalue is always negative (equal to $-\tilde{\mu}_C$), the healthy equilibrium is stable if also the other eigenvalue is negative. This is valid if the total therapy $\tilde{S}$ exceeds a critical value:

$$\tilde{S} > \tilde{S}_{\text{cr}} := \tilde{k}_G \tilde{\mu}_C \,. \tag{4.12}$$

Looking at the parameter set in Table 4.1, it should be noted that those are dimensional values, while we are currently working in a dimensionless framework. The dimensional value of $\tilde{S}_{\text{cr}}$ derived in Proposition 4.1 corresponds to $S_{\text{cr}} = G_{\max} k_G r \mu_C \alpha_G^{-1}$, and it is found to be less than b_C. This indicates that the healthy equilibrium remains stable even without administrated therapy, as the production term b_C is sufficient to sustain it. However, if the immune system is severely compromised ($b_C < S_{\text{cr}}$), the model predicts that even a small perturbation from $G^* = 0$ can trigger tumour onset, underscoring the pivotal role of immune system robustness in preventing tumour development.

The analysis of the other equilibrium branches is more challenging to address explicitly, so a numerical approach was adopted. The system of equations was solved numerically, and the resulting equilibrium values were substituted into the Jacobian matrix. This allowed for the assessment of stability by analysing the eigenvalues of the Jacobian. Within the explored range of $\tilde{S}$ values, the Jacobian matrix typically exhibited eigenvalues with non-zero real parts, enabling the application of the Hartman-Grobman theorem to deduce stability from the signs of the eigenvalues. Figure 4.2 shows the bifurcation diagram, generated using MATLAB, which highlights the stability characteristics of the identified equilibria. The analysis revealed that both the healthy and diseased equilibria are stable, whereas the intermediate equilibrium remains unstable.

The next step involves analysing the global behaviour of the solutions.

Proposition 4.2 *There exists a therapy intensity $\bar{S} \geq \tilde{S}^*$ above which the system* (4.7) *admits the unique equilibrium point $(G^*, C^*) = (0, \tilde{S}/\tilde{\mu}_C)$, which is globally asymptotically stable on $\mathcal{D} := [0,1] \times [0, \tilde{S}/\tilde{\mu}_C]$.*
Proof *To establish that the healthy equilibrium $(G^*, C^*) = (0, \tilde{S}/\tilde{\mu}_C)$ is globally asymptotically stable, it is necessary to verify both its local stability and global attractivity. Specifically, we consider the case where $\tilde{S} > \tilde{S}^*$, ensuring that $(G^*, C^*) = (0, \tilde{S}/\tilde{\mu}_C)$ is the system's only equilibrium point. Local stability has already been confirmed by examining the signs of the eigenvalues of the Jacobian matrix in Proposition 4.1. The remaining task is to demonstrate*

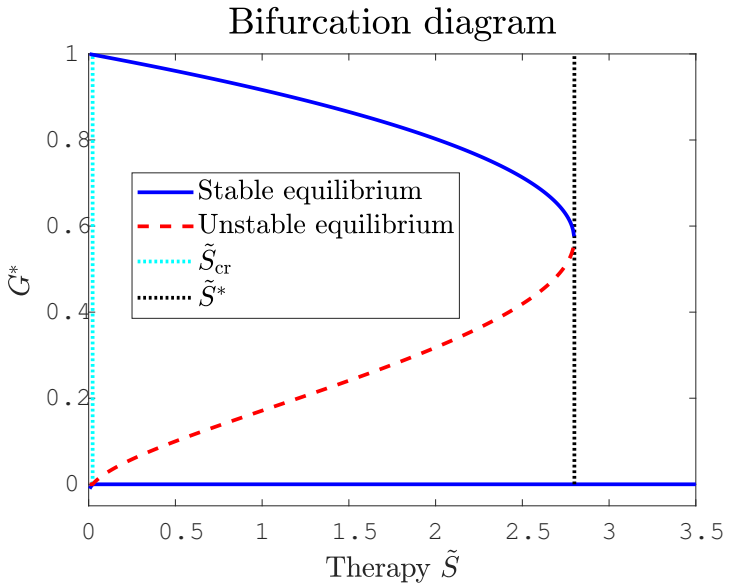

FIGURE 4.2: Bifurcation diagram highlighting the stability of the identified equilibria.

the global attractivity of this equilibrium, thereby completing the proof of its global asymptotic stability.

First of all, we observe that the set $\mathcal{D}$ is invariant under the dynamics of the system:

$$\begin{aligned}
\left.\frac{dG}{dt}\right|_{G=0} &= 0\,,\\
\left.\frac{dG}{dt}\right|_{G=1} &= -C\frac{1}{1+\tilde{k}_G} \leq 0\,,\\
\left.\frac{dC}{dt}\right|_{C=0} &= \tilde{S} > 0\,,\\
\left.\frac{dC}{dt}\right|_{C=\tilde{S}/\tilde{\mu}_C} &= -\tilde{\alpha}_C\frac{\tilde{S}}{\tilde{\mu}_C}\frac{G}{\tilde{k}_C+G} \leq 0\,.
\end{aligned}$$

Thus, since trajectories starting from the set $\mathcal{D}$ remain within it, $\mathcal{D}$ is indeed an invariant set for the dynamical system.

Next, we demonstrate that for a specific range of therapy intensities $\tilde{S}$, the time derivative of the tumour cell concentration G is negative, ensuring a consistent decrease in G over time. This monotonic behaviour confirms that G asymptotically approaches zero, the system's unique stable equilibrium point, as the presence of stable limit cycles is excluded due to the lack of oscillatory dynamics. Specifically, we observe:

$$\frac{dG}{dt} = G(1-G) - C\frac{G}{G+\tilde{k}_G} \leq G - C\frac{G}{G+\tilde{k}_G} \leq G - C\frac{G}{1+\tilde{k}_G} = G\left(1-\frac{C}{1+\tilde{k}_G}\right). \tag{4.13}$$

Moreover

$$\frac{dC}{dt} = \tilde{S} - \tilde{\mu}_C C - \tilde{\alpha}_C C\frac{G}{G+\tilde{k}_C} \geq \tilde{S} - \tilde{\mu}_C C - \tilde{\alpha}_C C\frac{1}{1+\tilde{k}_C} = \tilde{S} - C\left(\tilde{\mu}_C + \frac{\tilde{\alpha}_C}{1+\tilde{k}_C}\right), \tag{4.14}$$

from which we can derive

$$C(t) > \frac{\tilde{S}}{\tilde{\mu}_C + \frac{\tilde{\alpha}_C}{1+\tilde{k}_C}} - \frac{\tilde{S}}{\tilde{\mu}_C + \frac{\tilde{\alpha}_C}{1+\tilde{k}_C}} e^{-(\tilde{\mu}_C+\tilde{\alpha}_C)t} = \frac{\tilde{S}}{\tilde{\mu}_C + \frac{\tilde{\alpha}_C}{1+\tilde{k}_C}} \left(1 - e^{-(\tilde{\mu}_C+\tilde{\alpha}_C)t}\right) > \frac{\tilde{S}}{\tilde{\mu}_C + \frac{\tilde{\alpha}_C}{1+\tilde{k}_C}}, \tag{4.15}$$

for all time $t \in (0, +\infty)$. *Inserting this inequality into* (4.13), *it follows that*

$$\frac{\mathrm{d}G}{\mathrm{d}t} < G\left(1 - \frac{\tilde{S}}{\tilde{\mu}_C + \frac{\tilde{\alpha}_C}{1+\tilde{k}_C}} \frac{1}{1+\tilde{k}_G}\right) \tag{4.16}$$

and it is certainly smaller than zero if

$$1 - \frac{\tilde{S}}{\tilde{\mu}_C + \frac{\tilde{\alpha}_C}{1+\tilde{k}_C}} \frac{1}{1+\tilde{k}_G} \leq 0 \Rightarrow \tilde{S} \geq \tilde{\mu}_C(1+\tilde{k}_G) + \frac{1+\tilde{k}_G}{1+\tilde{k}_C}\tilde{\alpha}_C = (1+\tilde{k}_G)\left(\tilde{\mu}_C + \frac{\tilde{\alpha}_C}{1+\tilde{k}_C}\right) =: \hat{S}\,. \tag{4.17}$$

Thus, if $\tilde{S} \geq \bar{S} := \max\left(\tilde{S}^*,\ \hat{S}\right)$, *all trajectories converge to the globally stable equilibrium point* $(G^*, C^*) = \left(0, \tilde{S}/\tilde{\mu}_C\right)$.

Next, we investigate the asymptotic behaviour of the system's solutions across the region $\mathcal{D}$ of the phase space. Given the complexity introduced by the system's nonlinearities, an analytical approach proves challenging, prompting the adoption of a numerical strategy. MATLAB is employed to generate phase portraits for various values of the parameter $\tilde{S}$. The system described by Eq. (4.7) is solved numerically over the time interval $[0, 10000]$. Figures 4.3 and 4.4 illustrate the resulting trajectories for each selected value of $\tilde{S}$, with multiple initial conditions considered. These phase portraits provide insight into the long-term dynamics of the system and the influence of $\tilde{S}$ on the stability and behaviour of the trajectories. To provide a more expressive portrait, the

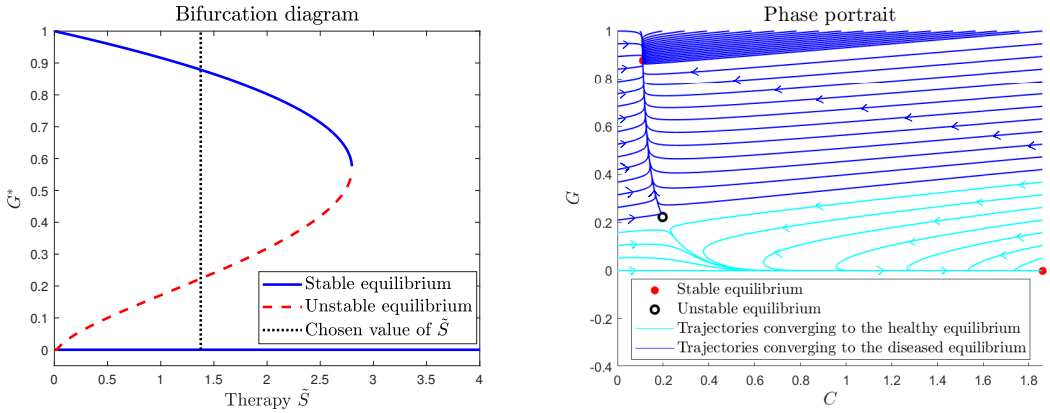

FIGURE 4.3: Phase portrait for a value of $\tilde{S}$ where three equilibria exist.

initial conditions are chosen to be evenly spaced along the perimeter of a rectangle in the $G - C$ phase plane, corresponding to the set $[0, 1] \times [0, \tilde{S}/\tilde{\mu}_C]$. As observed in Figure 4.2, a bifurcation exists within the system, necessitating the distinction between two cases. First, the case where the therapy intensity is relatively low is examined. As shown in Figure 4.3, there are three equilibria: two stable equilibrium points, each of which is attractive, meaning that nearly every point in the phase space generates a trajectory that asymptotically tends toward one of these points. Additionally, an unstable equilibrium point exists along the critical line, acting as a saddle node that delineates the two basins

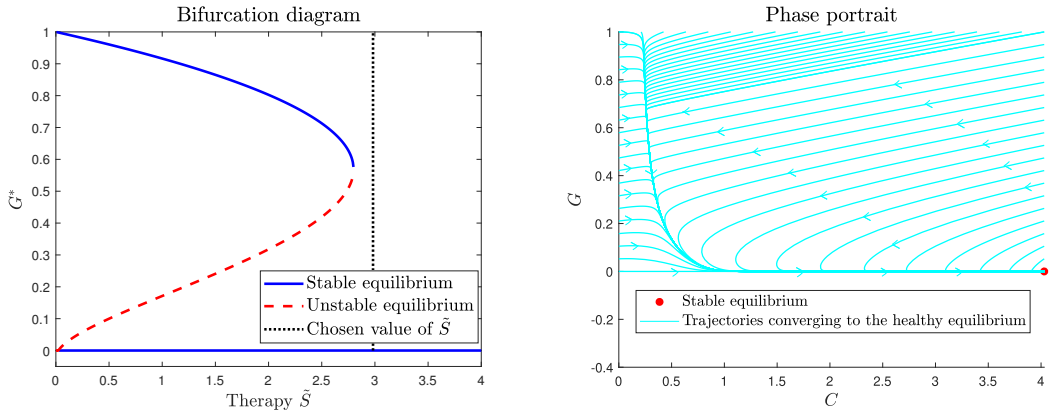

FIGURE 4.4: Phase portrait for a value of $\tilde{S}$ where only one equilibrium exists.

of attraction. In the second case, illustrated in Figure 4.4 for therapy values exceeding the collision of the developed tumour and intermediate equilibria, resulting in their disappearance, there is a single equilibrium point at $(G^*, C^*) = (0, \tilde{S}/\tilde{\mu}_C)$. We can observe from the numerical simulation that this point is globally asymptotically stable and attractive throughout the considered region of space.

Numerical analysis of the system's equilibria as other parameters vary. The behaviour of the system is studied for variations in the parameters $\tilde{\alpha}_C$, $\tilde{k}_G$, $\tilde{k}_C$, and $\tilde{\mu}_C$. For each of these values, the system obtained by setting the time derivatives to zero is solved numerically. The stability of the resulting equilibria is analysed by examining the sign of the eigenvalues of the system's Jacobian, which are also determined through numerical methods. As in previous cases, the result is supported by the Hartman-Grobman theorem, as the eigenvalues almost always have non-zero real parts. For each parameter, two studies are conducted corresponding to two different therapy values: specifically for $\tilde{S} = 60\tilde{S}_{\text{cr}}$ and $\tilde{S} = 130\tilde{S}_{\text{cr}}$. In each graph, the baseline values from Table 4.1 are indicated.

For the lymphocyte elimination parameter $\tilde{\alpha}_C$, it follows from (4.11) that the stability of the healthy equilibrium is independent of this parameter. Consequently, no bifurcations can occur at $G^* = 0$ for any value of $\tilde{\alpha}_C$. Figure 4.5 illustrates the bifurcation diagrams with respect to $\tilde{\alpha}_C$. For intermediate therapy levels, as $\tilde{\alpha}_C$ increases, the diseased equilibrium asymptotically approaches 1, while the intermediate equilibrium tends to 0. Conversely, as $\tilde{\alpha}_C$ decreases, the diseased and intermediate equilibria merge in a saddle-node bifurcation, leaving the healthy equilibrium as the sole stable state. For $\tilde{S} = 130\tilde{S}_{\text{cr}}$, the bifurcation diagram resembles the previous case, with the key difference being that the saddle-node bifurcation occurs at values of $\tilde{\alpha}_C$ exceeding the baseline parameter value chosen in the analysis for varying $\tilde{S}$. Thus, if the rate at which tumour cells eliminate lymphocytes falls below a critical threshold, the system retains $G^* = 0$ as the only stable equilibrium.

In Figure 4.6, the bifurcation diagrams for the Michaelis-Menten coefficient for glioma, $\tilde{k}_G$, are shown. For low values of $\tilde{S}$, as $\tilde{k}_G$ increases, a transcritical bifurcation arises in the branch of healthy equilibria, introducing an unstable non-physical equilibrium. This causes the disappearance of the intermediate equilibrium and renders $G^* = 0$ unstable, while the diseased equilibrium asymptotically approaches 1. For $\tilde{S} = 130\tilde{S}_{\text{cr}}$, at the baseline, only the healthy equilibrium exists. However, as $\tilde{k}_G$ increases, saddle-node bifurcations emerge, introducing both the diseased equilibrium (which will approach 1 as $\tilde{k}_G \to +\infty$) and the intermediate equilibrium, which will collide with the healthy

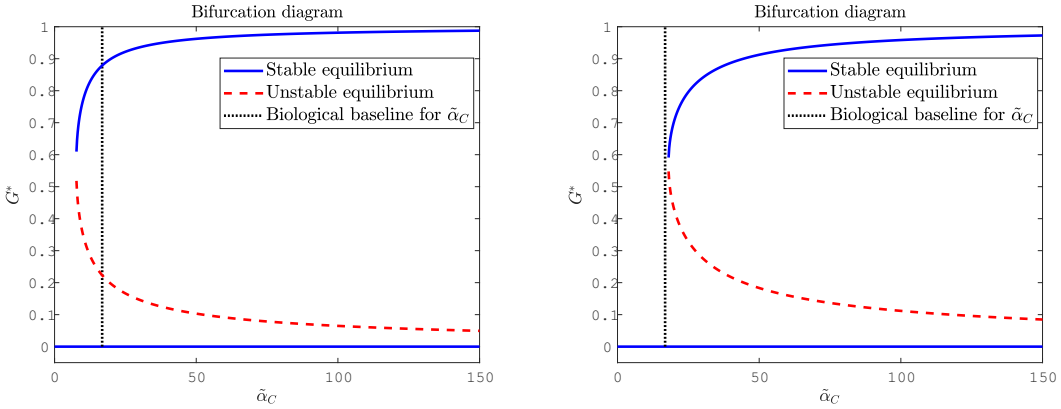

FIGURE 4.5: Bifurcations diagram of $\tilde{\alpha}_C$ for $\tilde{S} = 60\tilde{S}_{\text{cr}}$ and $\tilde{S} = 130\tilde{S}_{\text{cr}}$.

equilibrium in a transcritical bifurcation, making $G^* = 0$ unstable. Therefore, as $\tilde{k}_G$ increases, the only physically meaningful (i.e., non-negative) stable equilibrium appears to be the diseased state. This outcome arises because the system operates far from saturation, resulting in a tumour cell elimination term by lymphocytes that is too low.

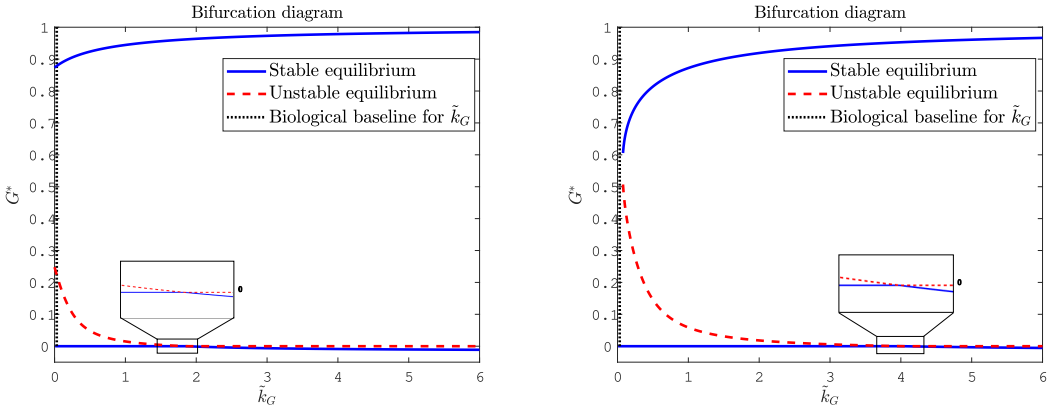

FIGURE 4.6: Bifurcations diagram of $\tilde{k}_G$ for $\tilde{S} = 60\tilde{S}_{\text{cr}}$ and $\tilde{S} = 130\tilde{S}_{\text{cr}}$.

From the Jacobian (4.11), it can be observed that the Michaelis-Menten coefficient for lymphocytes, $\tilde{k}_C$, does not affect the sign of the Jacobian's eigenvalues at the healthy equilibrium, ensuring the absence of bifurcations at $G^* = 0$. For $\tilde{S} = 60\tilde{S}_{\text{cr}}$, the origin remains a stable equilibrium for all $\tilde{k}_C > 0$, with no bifurcations present for values of $\tilde{k}_C$ less than or equal to the baseline. However, for higher values, the intermediate and diseased equilibria collide and disappear. The case for $\tilde{S} = 130\tilde{S}_{\text{cr}}$ is similar, but the saddle-node bifurcation occurs as $\tilde{k}_C$ decreases. The bifurcation diagrams are shown in Figure 3.9.

For the parameter $\tilde{\mu}_C$, the bifurcation diagrams are shown in Figure 4.8. For $\tilde{S} = 60\tilde{S}_{\text{cr}}$, the system shows healthy equilibrium (stable), diseased equilibrium (unstable), and intermediate equilibrium (stable) for values equal to or less than the baseline. For higher values, a transcritical bifurcation of the healthy equilibrium occurs, rendering it unstable and causing the resulting stable critical equilibrium to lose physical relevance, becoming negative. For $\tilde{S} = 130\tilde{S}_{\text{cr}}$, the origin is the only equilibrium for values of $\tilde{\mu}_C$ equal to or less than the baseline. As $\tilde{\mu}_C$ increases, a saddle-node bifurcation gives rise to the unstable intermediate equilibrium and the stable diseased equilibrium. Additionally, for high values of $\tilde{\mu}_C$, a transcritical bifurcation at $G^* = 0$ makes the healthy equilibrium unstable, while the intermediate equilibrium becomes unphysical.

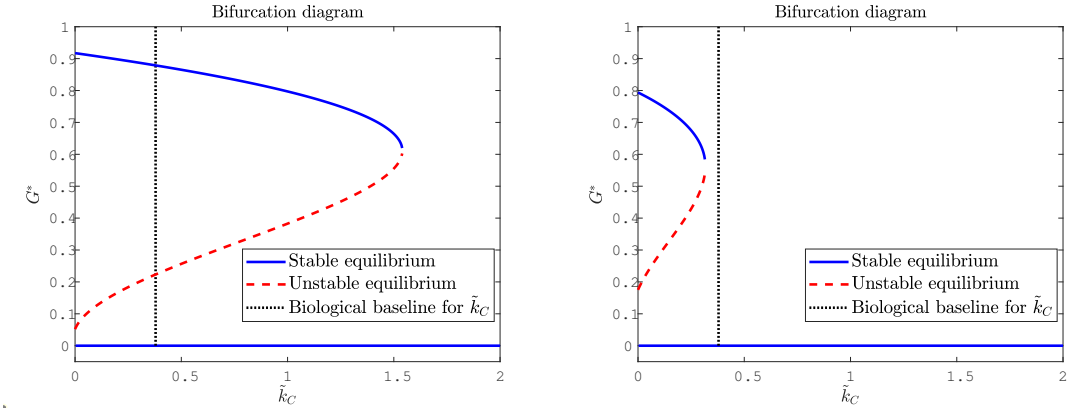

FIGURE 4.7: Bifurcations diagram of $\tilde{k}_C$ for $\tilde{S} = 60\tilde{S}_{\text{cr}}$ and $\tilde{S} = 130\tilde{S}_{\text{cr}}$.

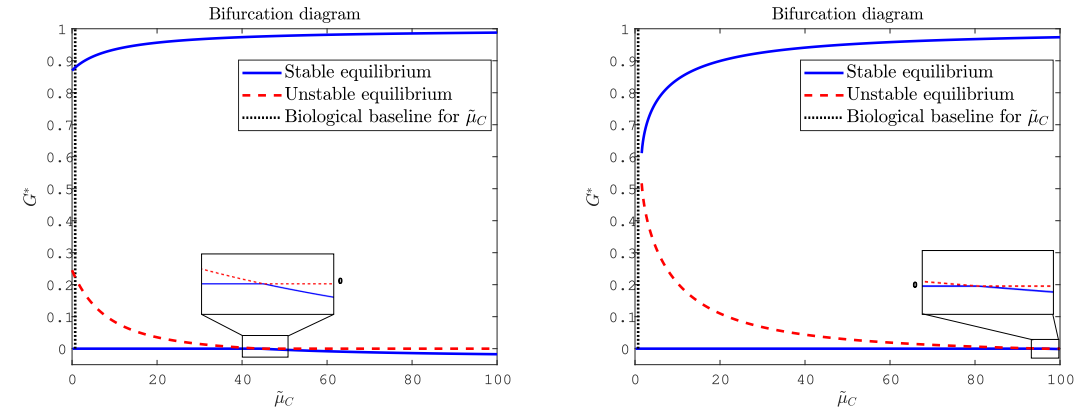

FIGURE 4.8: Bifurcations diagram of $\tilde{\mu}_C$ for $\tilde{S} = 60\tilde{S}_{\text{cr}}$ and $\tilde{S} = 130\tilde{S}_{\text{cr}}$.

Solution of the system of ODEs. The results of the model simulation, obtained by numerically solving the system (4.7) using Matlab, are now presented for some test cases. In each simulation, the initial condition for the lymphocyte population has been set to $C(0) = \tilde{b}_C$. Figure 4.9 shows the results of tumour and lymphocyte growth in the absence of therapy ($\tilde{S} = \tilde{b}_C$), with an initial tumour condition of $G(0) = 0.3$. As can be seen, the immune system is insufficient in counteracting the progression of the glioma, which grows nearly to its carrying capacity. Moreover, Figure 4.10 shows the results of tumour growth for a therapy intensity of $\tilde{S} = 60\tilde{S}_{\text{cr}}$, a therapy value at which both tumour eradication and tumour development can occur. Two different initial conditions for G are considered, with $G(0) = 0.3$ and $G(0) = 0.4$. As observed, in the first case, the therapy is sufficient to stop tumour growth and lead to its eradication, while in the second case it proves inadequate. Finally, Figure 4.11 illustrates the evolution of G and C for a therapy intensity of $\tilde{S} = 130\tilde{S}_{\text{cr}}$, recalling that this scenario leads to tumour eradication, with an initial condition of $G(0) = 0.5$. As shown, the therapy successfully halts tumour growth and eradicates it.

4.4 Numerical simulations

In this Section, the model represented by system (4.1), as introduced in Section 4.2, is solved numerically. Initially, the results of model simulations in a simplified 2D geometry will be presented. The relative importance of different parameters will be assessed

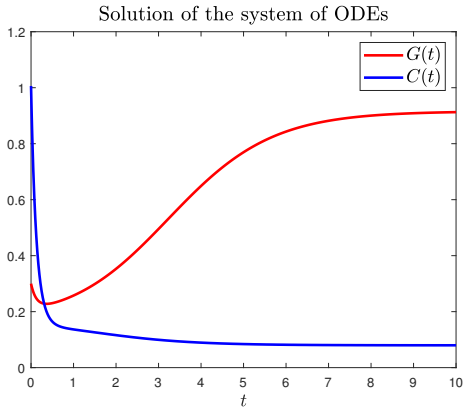

FIGURE 4.9: The evolution of the system for $\tilde{S} = \tilde{b}_C$ and an initial tumour condition of $G(0) = 0.3$.

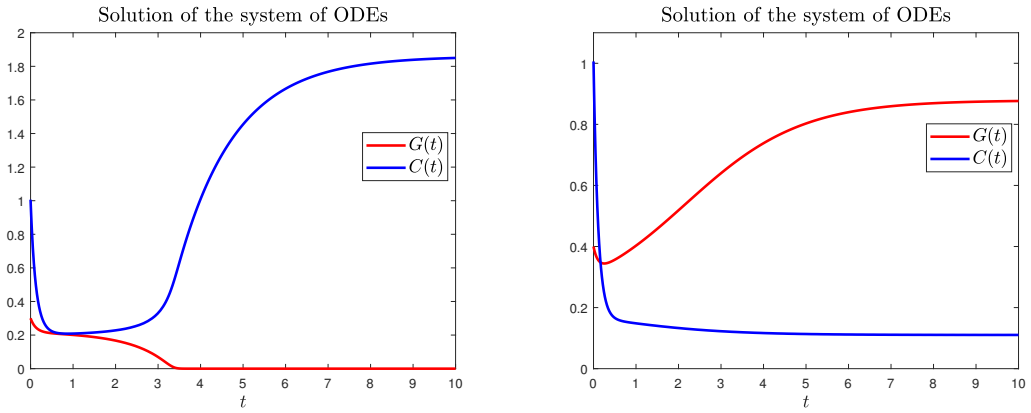

FIGURE 4.10: The evolution of the system for $\tilde{S} = 60\tilde{S}_{\text{cr}}$ and an initial tumour condition of $G(0) = 0.3$ and $G(0) = 0.4$.

through a sensitivity analysis on the simulation outcomes conducted with various parameter sets. Subsequently, the system will be simulated in 3D within the brain geometry, considering both the assumption of isotropy and using DTI data to identify preferential directions.

4.4.1 2D simulations on a simplified domain

This section aims to describe tumour growth in a simplified 2D domain, examining the effects of therapy application. The concentration of tumour cells is normalised by its carrying capacity, the lymphocyte concentration by a constant $C_{\max} := 10^6$ cells/mL and the TGF-β concentration by a constant $T_{\max} := 10$ pg/mL, applying a similar procedure as in Section 4.3. The system of equations simulated is:

$$\begin{cases} \dfrac{\partial G}{\partial t} &= \nabla \cdot (\mathbb{D}_G \nabla G) + rG(1-G) - \hat{\alpha}_G C \dfrac{G}{\hat{k}_G + G}\,, \\ \dfrac{\partial C}{\partial t} &= \nabla \cdot (\mathbb{D}_C \nabla C) - \nabla \cdot [\hat{\chi}(G,C,T)\, C \nabla T] + \hat{b}_C - \mu_C C - \alpha_C C \dfrac{G}{\hat{k}_C + G} + \hat{S}_T(\boldsymbol{x},t)\,, \\ \dfrac{\partial T}{\partial t} &= \nabla \cdot (\mathbb{D}_T \nabla T) + \hat{p}_T G - \mu_T T\,, \end{cases} \tag{4.18}$$

where the model parameters are adequately rescaled: $\hat{\alpha}_G = \alpha_G C_{\max}/G_{\max}$, $\hat{k}_G = k_G/G_{\max}$, $\hat{\chi} = T_{\max}\chi$, $\hat{b}_C = b_C/C_{\max}$, $\hat{k}_C = k_C/G_{\max}$, $\hat{S}_T(\boldsymbol{x},t) = S_T(\boldsymbol{x},t)/C_{\max}$ and $\hat{p}_T = p_T G_{\max}/T_{\max}$.

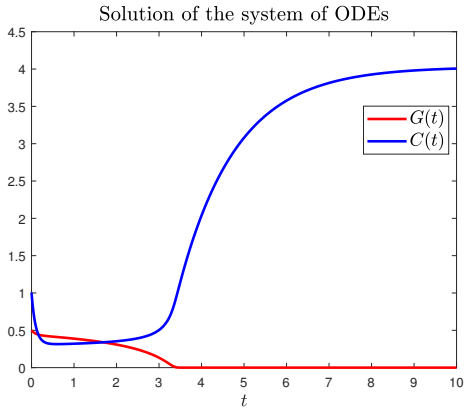

FIGURE 4.11: The evolution of the system for $\tilde{S} = 130\tilde{S}_{\text{cr}}$ and an initial tumour condition of $G(0) = 0.5$.

From now on we interpret G, C and T as the rescaled concentrations. To interpret the output from a diffusive model for concentration, a threshold value is set to define the actual location of the tumour, as there is no distinct interface between it and healthy tissue. The region where concentration G exceeds this threshold will represent the tumour's extent [480]. A threshold value of 8000 cells/mL is chosen, following previous studies [482]. With a carrying capacity set at $G_{\max} = 2.39 \cdot 10^8$ cells/mL [56], this corresponds to a value of 0.0335 for the normalised concentration. In the following, isotropic diffusion is assumed, i.e. $\mathbb{D}_G = D_G\mathbb{I}$, $\mathbb{D}_C = D_C\mathbb{I}$ and $\mathbb{D}_T = D_T\mathbb{I}$.

Numerical simulation setup

For what concerns the computational domain, it is assumed that, under free growth, the tumour exhibits radial symmetry. To make the simulation less computationally demanding, the domain is reduced to a circular sector of 90°. The simulations run for a maximum of 2400 hours (equivalent to 100 days, the median survival for untreated GBM). Since a typical GBM has a diameter of around 3 cm at patient death, the radius of the circular sector is set to this size. The mesh is generated automatically in FEniCS, and it is refined in two successive steps where necessary. The computational mesh and the subsequent refinement are shown in Figure 4.12. Firstly, since a test simulation without treatment (i.e. $\hat{S}_T(x, y) \equiv 0$) shows that the maximum concentration of tumour cells at $t = 2400$ h remains within a circle of radius $R = 2.5$ cm, cells in this region are refined accordingly. Moreover, the transport term is known to introduce numerical instabilities, which are typically handled using stabilisation techniques. In this study, however, we limit the effect of these instabilities by refining the mesh. Given the radial symmetry of the domain, it is reasonable to expect a significant lymphocyte flow near the segment between the origin and the point located in $(1.1\text{ cm}, 1.1\text{ cm})$. The second refinement step focuses on cells in this region, with a sufficiently large margin to prevent numerical instabilities when interaction and chemotaxis parameters vary.

Treatment of GBM via lymphocyte infusion is currently being investigated in clinical studies, particularly in conjunction with CAR-T genetic engineering techniques [405]. Various delivery methods have been proposed: T-cells may be injected peripherally through intravenous infusion [9], encouraged to cross the blood–brain barrier (BBB) through chemical signals [49], or infused directly into the brain using a catheter [80]. This work models the latter approach by introducing a spatially limited lymphocyte

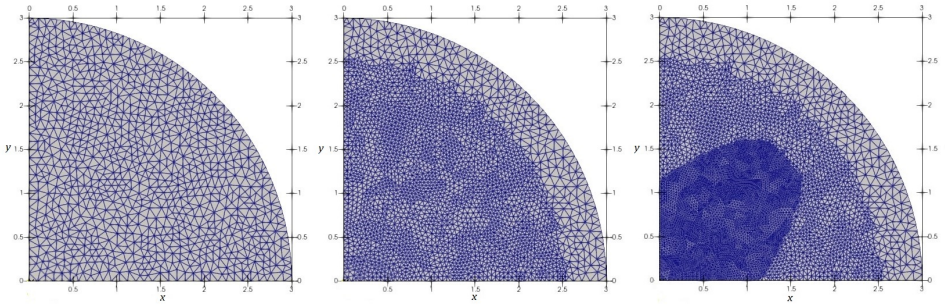

FIGURE 4.12: Mesh created in FEniCS and two subsequent refinement steps

source. During these simulations, the infusion term $\hat{S}_T(x,y)$ is modelled as a time-constant Gaussian source

$$\hat{S}_T(x,y) = S_0 \exp\left(-\frac{(x-x_T)^2+(y-y_T)^2}{2\sigma_S^2}\right), \tag{4.19}$$

with $\sigma_S = 0.044$ cm. Therapy intensities are modulated by adjusting S_0. The centre of the Gaussian represents the catheter tip position for therapy infusion, set at $(x_T, y_T) = (1.1\text{ cm}, 1.1\text{ cm})$.

Moreover, the initial tumour cell concentration is a Gaussian centred at the origin of the XY plane:

$$G(x,y,t=0) = G_0 \exp\left(-\frac{x^2+y^2}{2\sigma_G^2}\right), \tag{4.20}$$

with $\sigma_G = 0.124$ cm. This gives the maximum concentration equal to $G_0 = 0.5$, meaning that the concentration at the origin is half of the carrying capacity. For both lymphocyte and chemoattractant infusions, the initial concentrations are set to zero:

$$C(x,y,t=0) \equiv 0\,, \quad T(x,y,t=0) \equiv 0\,. \tag{4.21}$$

The initial conditions for tumour concentration and for the therapy source term are shown in Figure 4.13.

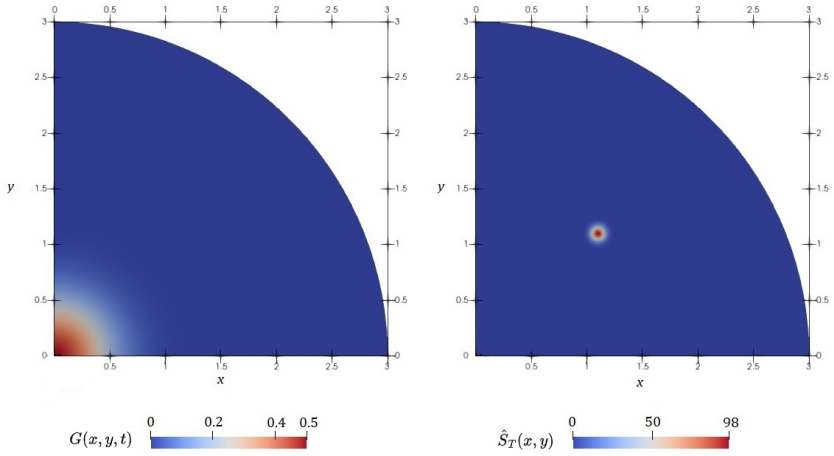

FIGURE 4.13: Initial conditions for tumour concentration $G(x,y,t=0)$ and therapy source term $\hat{S}_T(x,y)$ for $S_0 = 10^2\ \text{h}^{-1}$.

Finally, Neumann boundary conditions are applied for all variables:

$$\nabla G \cdot \mathbf{n} = \nabla C \cdot \mathbf{n} = \nabla T \cdot \mathbf{n} = 0\,. \tag{4.22}$$

This enforces zero flux across the domain boundary, preventing any chemical or cellular factors from leaving the domain [95].

Tumour expansion without therapy

Firstly, tumours growth without any treatment is solved:

$$\frac{\partial G}{\partial t} = D_G \nabla^2 G + rG(1-G)\,. \tag{4.23}$$

Rewriting the equation in a polar coordinate system, where ρ represents the radial distance, allows us to analyse the system more effectively:

$$\frac{\partial G}{\partial t} = D_G \frac{\partial^2 G}{\partial \rho^2} + \frac{D_G}{\rho}\frac{\partial G}{\partial \rho} + rG(1-G)\,. \tag{4.24}$$

Assuming that the wavefront is fully developed and considering very large radii, the equation simplifies to the KPP–Fisher equation. In this case, the predicted dimensional radial velocity c of the wavefront expansion is expressed as:

$$c = 2\sqrt{rD_G}\,. \tag{4.25}$$

We compare the wavefront expansion velocity predicted by this equation with the results obtained from our numerical simulations. Figures 4.14 show the expansion of the wavefront, visualising points in the domain where cell concentration exceeds concentrations greater than 0.1, 0.2, and 0.5 times the carrying capacity at time points $t_1 = 1200$ h and $t_2 = 2400$ h. The wavefront expansion measures 0.889 ± 0.01 cm, with the fronts propagating at an average speed $c_{\text{num}} = 7.41 \cdot 10^{-4}$ cm /h. Moreover, by substituting the numerical values provided in Table 4.1 into (4.25), we obtain $c \approx 8.23 \cdot 10^{-4}$ cm/h. The relative error between theoretical and numerical results is approximately 10%, likely due to the finite domain, the assumption of a constant and very large radius during propagation, and numerical approximation errors.

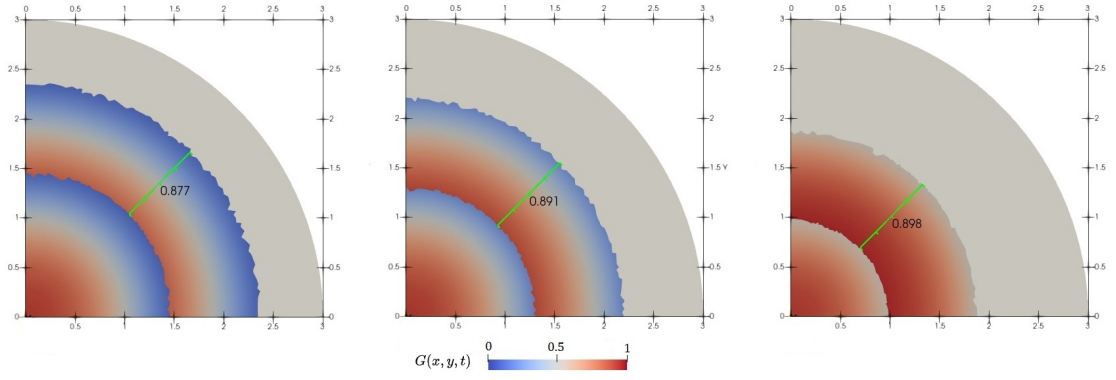

FIGURE 4.14: Wavefront advancement for concentrations greater than 0.1, 0.2, and 0.5 times the carrying capacity at time points $t_1 = 1200$ h and $t_2 = 2400$ h.

Estimation of the chemotactic coefficient

To incorporate chemotaxis into the model and solve the complete system (4.18), an estimate of the chemotactic coefficient $\hat{\chi}(G, C, T)$ is required. Initially, a constant chemotactic coefficient $\hat{\chi}$ is assumed. The system is first solved considering only the G and T populations to approximate $\hat{\chi}$. The concentration of C is set to zero by imposing $\hat{b}_C = 0$ and $\hat{S}_T(x, y) \equiv 0$.

At $t = 2400\,\text{h}$, the gradient magnitude of T reaches a maximum value of approximately $\overline{\nabla T} \sim 4.9\,\text{cm}^{-1}$. According to [314], lymphocyte velocities during migration can reach up to $v = 120\,\mu\text{m/min}$, although typical speeds are often below $20\,\mu\text{m/min}$. Here, a conservative reference value of $v = 4\,\mu\text{m/min} = 0.024\,\text{cm/h}$ is adopted. Using this value, the constant chemotactic coefficient is estimated as $\hat{\chi}(G, C, T) = v/\overline{\nabla T} \sim 4.9 \cdot 10^{-3}\,\text{cm}^2/\text{h}$.

The complete system (4.18) is then solved with the estimated chemotaxis parameters, assuming $\alpha_G = \alpha_C = 0$, to examine lymphocyte movement. Figure 4.15 presents the resulting lymphocyte concentrations at $t = 600\,\text{h}$, $t = 1200\,\text{h}$, and $t = 2400\,\text{h}$ under these conditions. In this simulation, lymphocytes exhibit free movement, traversing the tumour and accumulating near its centre, demonstrating their chemotactic response.

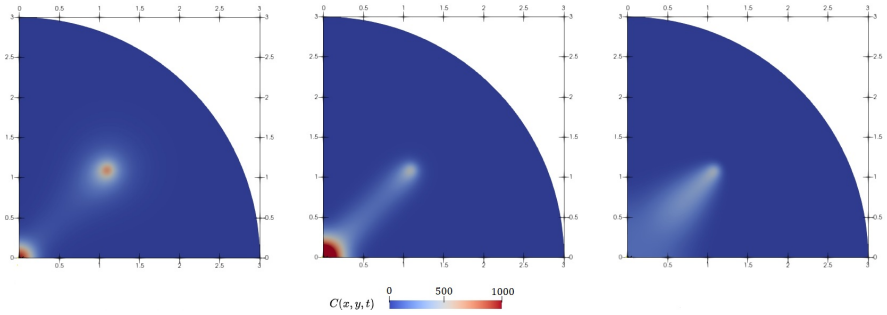

FIGURE 4.15: Concentration of $C(x, y, t)$ at $t = 600\,\text{h}$, $t = 1200\,\text{h}$, and $t = 2400\,\text{h}$ with constant $\hat{\chi}$.

Since we aim for lymphocytes to remain at the tumour boundary, whereas in this simulation with a constant chemotactic coefficient they instead concentrate at the tumour centre, we propose a saturation-dependent chemotactic coefficient based on T, inspired by the receptor saturation model introduced in [245].

$$\hat{\chi}(G, C, T) = \frac{\tilde{\chi}}{(1 + \epsilon T)^2}, \tag{4.26}$$

where ϵ represents the receptor saturation coefficient. The parameter $\tilde{\chi}$ is taken as the same value used for the constant case: $\tilde{\chi} = 4.9 \cdot 10^{-3}\,\text{cm}^2/\text{h}$. At the tumour surface, the chemoattractant concentration reaches a value of 0.35. In the absence of specific parameters from the literature, it is hypothesised that lymphocytes at the tumour boundary experience a reduction in speed to 30% of their maximum velocity. Consequently, the value $\epsilon = 0.56$ is chosen for the adimensionalised system.

Figure 4.16 shows the results of the simulation with the saturation-dependent chemotactic coefficient. As observed, despite significant lymphocyte movement, their excessive concentration at the tumour centre is mitigated, with lymphocytes primarily remaining in the tumour's outer regions.

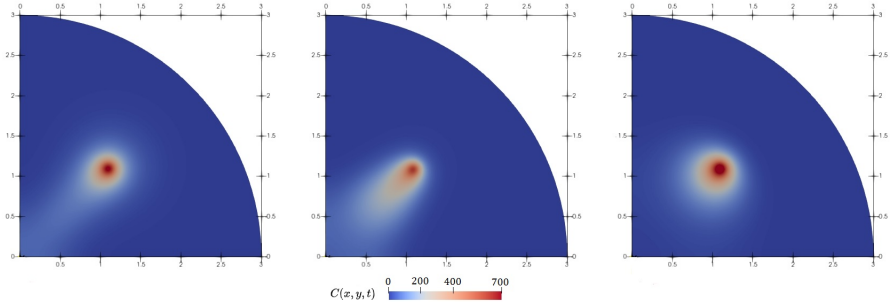

FIGURE 4.16: Concentration of $C(x, y, t)$ at $t = 600\,\text{h}$, $t = 1200\,\text{h}$, and $t = 2400\,\text{h}$ with a saturation-dependent $\hat{\chi}$.

Verification of the CFL condition

The Courant-Friedrichs-Lewy (CFL) condition is a necessary requirement for the convergence of numerical methods for solving transport problems. Intuitively, it ensures that a signal does not propagate across non-adjacent cells within a single time step. The Courant number is defined as:

$$C_T := \Delta t \sum_i \frac{u_{x_i}}{\Delta x_i}, \tag{4.27}$$

where Δx_i is the spatial discretisation size in the i-th dimension of the domain, u_{x_i} represents the velocity component, and Δt is the temporal discretisation step. The CFL condition is expressed as $C_T < C_{T\max}$, where $C_{T\max}$ is a constant dependent on the problem's nature and the numerical scheme employed. For explicit schemes, $C_{T\max} = 1$ is typical, while implicit schemes allow for higher values. In this case, by construction, the expected flow intensity in every direction is $u \leq 0.024\,\text{cm/h}$. For the mesh employed in this section, the minimum value of h (the longest side of a triangular cell) is $h_{\min} = 0.019\,\text{cm}$. This value is used to approximate the spatial discretisation sizes as $\Delta x \sim \Delta y \sim h_{\min}$. In the simulations, a time step of $\Delta t = 0.2\,\text{h}$ is used. Using these estimates, the Courant number is estimated as $C_T \sim 0.258 < 1 \leq C_{T\max}$, thereby satisfying the CFL condition. The Courant number is intentionally kept particularly small, as this approach ensures stability even during sensitivity analyses, where significantly larger values of $\hat{\chi}$ will be tested.

Sensitivity analysis of model parameters

The model described incorporates various parameters obtained from multiple sources. A sensitivity analysis is conducted to determine which parameters significantly influence the model's outcomes. Following the procedure outlined in [351], the *partial rank correlation coefficient* (PRCC) is computed. The process involves selecting M parameters of interest, with corresponding vectors $\boldsymbol{z_j} = \{z_{j1}, z_{j2}, \ldots, z_{jN}\}$, $j = 1, ..., M$, each containing equispaced values from a specified interval, which are then randomly permuted. A matrix, referred to as the *Latin hypercube sample* (LHS) matrix, is generated. This matrix consists of N rows, representing the number of simulations (sample size), and M columns, corresponding to the different parameters.

The model is solved numerically for each parameter combination defined by a row of the LHS matrix, and an appropriate measure of the numerical output is selected to obtain a real-valued objective function. The results of these simulations form the vector $\boldsymbol{y} = \{y_1, y_2, \ldots, y_N\}$. For each parameter vector $\boldsymbol{z_j}$, the Pearson correlation coefficient

with the objective vector $\boldsymbol{y}$ is calculated as:

$$r_{z_j y} = \frac{\mathrm{Cov}\left(\boldsymbol{z_j}, \boldsymbol{y}\right)}{\sqrt{\mathrm{Var}\left(\boldsymbol{z_j}\right)\mathrm{Var}(\boldsymbol{y})}} = \frac{\sum_{i=1}^{N}\left(z_{ij}-\bar{z}_j\right)\left(y_i-\bar{y}\right)}{\sqrt{\sum_{i=1}^{N}\left(z_{ij}-\bar{z}_j\right)^2\sum_{i=1}^{N}\left(y_i-\bar{y}\right)^2}}\,, \tag{4.28}$$

where $\bar{z}_j$ and $\bar{y}$ denote the mean values of $\boldsymbol{z_j}$ and $\boldsymbol{y}$, respectively. This method is particularly effective for analysing model parameters that exhibit a monotonic influence on the outcomes.

Two objective functions, representing the mass and the volume of the tumour, are employed to evaluate the system:

$$M(G(x,y)) = \int_{\mathcal{D}} G(x,y)\,dx\,dy\,, \tag{4.29}$$

$$V_\tau(G(x,y)) = \int_{\mathcal{D}} \mathbf{1}_\tau(G(x,y))\,dx\,dy\,, \tag{4.30}$$

where $\mathbf{1}_\tau(G(x,y))$ is a thresholding function defined as:

$$\mathbf{1}_\tau(G(x,y)) = \begin{cases} 1, & G(x,y) \geq \tau\,, \\ 0, & G(x,y) < \tau\,, \end{cases} \tag{4.31}$$

where the parameter τ denotes the volume threshold, set to 0.2 in this study.

The sensitivity analysis examines the effects of parameters $\hat{\alpha}_G$, α_C, $\hat{k}_G$, $\hat{k}_C$, and the chemotactic parameter $\hat{\chi}$, which are assumed to mitigate tumour growth. Additionally, the influence of the diffusion coefficients D_G and D_C is assessed. All the values are varied within the range of 0.1 to 1.5 times their reference values outlined in Section 4.2.1. The objective functions are evaluated based on the tumour density $G(x,y)$ at specific time points: $t = 200, 400, 600$ h. A total of $N = 1200$ simulations are conducted for the sensitivity analysis.

Figures 4.17 illustrate the test results. As expected, $\hat{\alpha}_G$ exhibits a strong negative correlation with both objectives, while α_C is positively correlated, particularly with tumour mass, though it also moderately influences tumour volume. Parameter $\hat{k}_G$ shows a positive correlation of similar magnitude with both measures of tumour extension, whereas parameter $\hat{k}_C$ exhibits a negative correlation with both. The chemotactic parameter $\hat{\chi}$ demonstrates a negative correlation, indicating that lymphocyte motility aids tumour cell eradication. For D_C, increased lymphocyte diffusion positively impacts tumour elimination in both metrics, particularly at early times, before chemotactic flux becomes dominant. Conversely, tumour cell diffusion D_G consistently correlates positively.

Numerical solution of the complete system

The system in (4.18) is solved using the parameter values outlined in Section 4.2.1. Figure 4.18 illustrates the tumour cell concentration at $t = 600$ h, $t = 1200$ h, and $t = 2400$ h, under varying therapy intensities: $S_0 = 0\ \mathrm{h}^{-1}$, $S_0 = 20\ \mathrm{h}^{-1}$, and $S_0 = 40\ \mathrm{h}^{-1}$. These scenarios highlight the differential effects of therapy on tumour growth. Specifically, the first simulation demonstrates uncontrolled tumour proliferation in the absence of therapy. In the second case, therapy slows tumour expansion but does not achieve adequate containment. Conversely, the highest therapy intensity effectively suppresses tumour growth, resulting in a final tumour size comparable to the initial one.

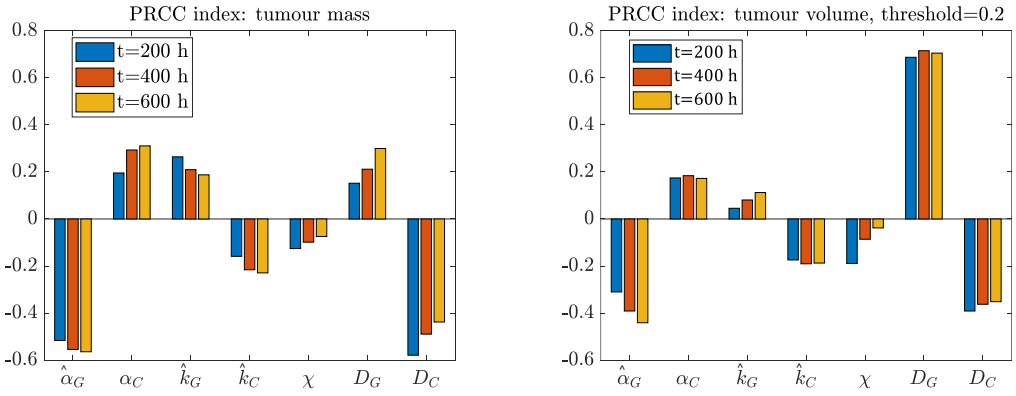

FIGURE 4.17: Partial rank correlation coefficient (PRCC) analysis of tumour mass (left) and tumour volume (right) as objective functions.

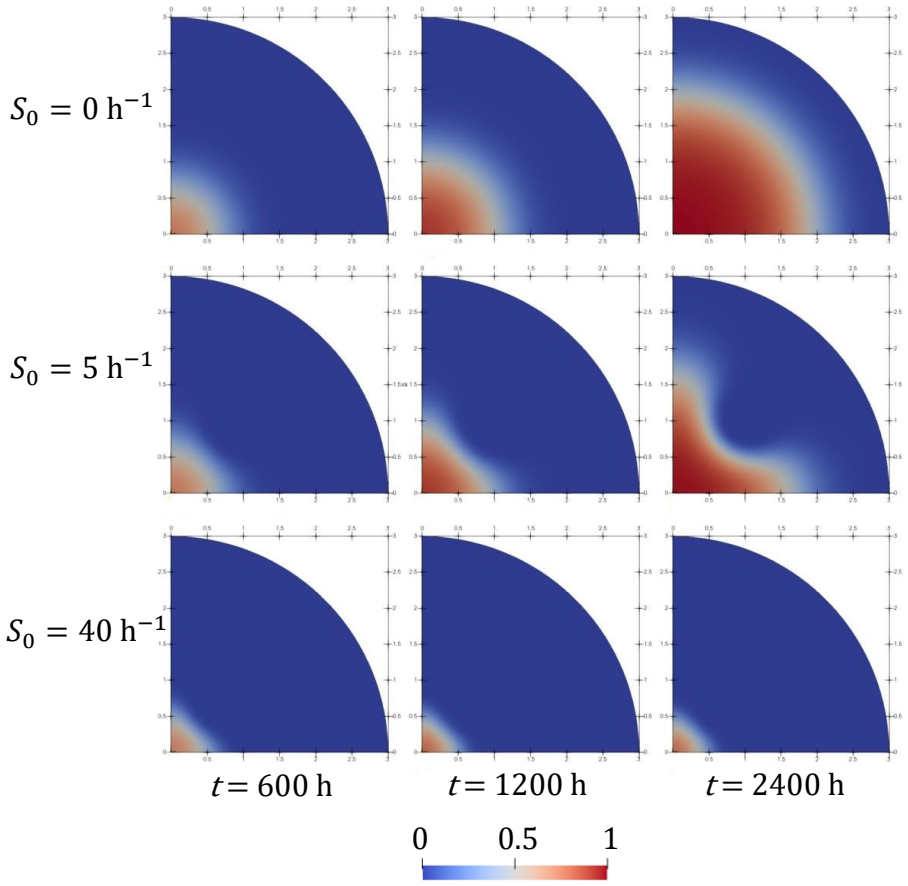

FIGURE 4.18: Tumour cell concentration $G(x, y, t)$ at different time instants for therapy intensities $S_0 = 0, 5, 40\,\mathrm{h}^{-1}$.

4.4.2 Simulations in a 3D brain geometry

Numerical simulations setup

Finally, the system (4.18) is solved numerically within a brain domain reconstructed from MRI data provided by patients at the Carlo Besta Neurological Institute in Milan.

The data were anonymised, and patients gave informed consent for their images to be used for research purposes. Regarding the computational mesh, a heterogeneous mesh size is employed, similar to the approach used for the simplified 2D geometry. The software *Tetgen* [492] is used to generate a tetrahedral mesh of the brain, refined in regions of interest. *Tetgen* generates a conforming mesh from a supplied list of points (nodes). To achieve mesh refinement, a value h is assigned to each node, specifying the maximum edge length of the cells adjacent to that node. The mesh is refined with $h = 0.6$ mm in the spherical region where tumour expansion occurs, and $h = 0.3$ mm in the region where lymphocyte motion takes place. Four distinct meshes are constructed, each corresponding to a different tumour location. Figure 4.19 presents the same cross-section of all the meshes, taken along a plane passing through the tumour's centre. Clockwise from the top left, they are referred to as the central-right, central-left, left, and right hemispheres.

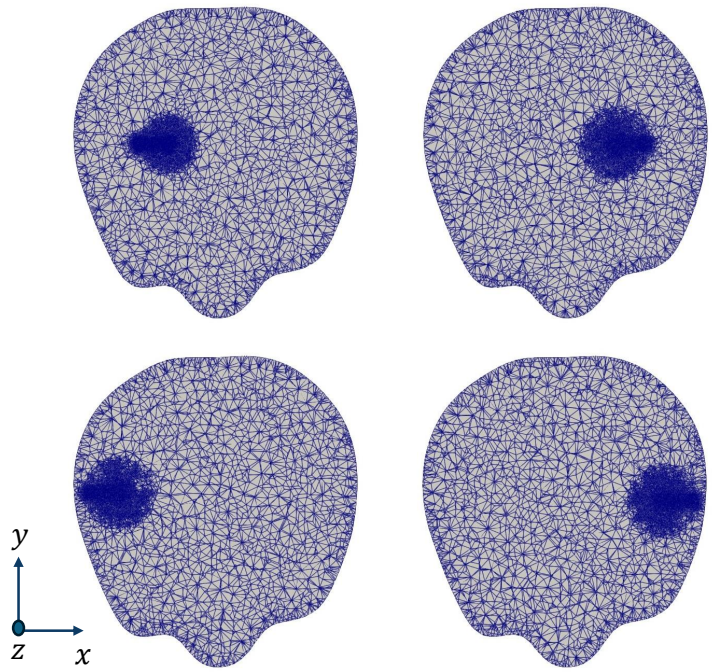

FIGURE 4.19: Cross-sections of the meshes. Clockwise from top left: tumour centre at (217 mm, 277 mm, 17 mm), (265 mm, 277 mm, 17 mm), (289 mm, 273 mm, 17 mm) and (193 mm, 277 mm, 17 mm).

As in the 2D simulation, the forcing term which models lymphocyte infusion is represented by a time-independent Gaussian function:

$$\hat{S}_T(x,y,z) = S_0 \exp\left(\frac{(x-x_T)^2 + (y-y_T)^2 + (z-z_T)^2}{2\sigma_S^2}\right), \tag{4.32}$$

with $\sigma_S = 0.44$ mm. Several infusion points (x_T, y_T, z_T) are considered, maintaining a distance of 14 mm from the tumour centre.

The initial tumour cell concentration is modelled as a Gaussian distribution centred at (x_G, y_G, z_G):

$$G(x,y,z,t=0) = G_0 \exp\left[\frac{(x-x_G)^2 + (y-y_G)^2 + (z-z_G)^2}{2\sigma_G^2}\right], \tag{4.33}$$

with $\sigma_G = 0.44\,\text{mm}$. The maximum concentration is set to $G_0 = 0.5$, as in the 2D case. As the model's behaviour is studied under conditions of spatially non-uniform anisotropy, tumours in different regions of the domain expand differently. To compare these differences, the system has been solved for various initial conditions, i.e. for various set of (x_G, y_G, z_G).

The initial conditions for the chemoattractant and lymphocyte concentrations are set to zero:

$$C(x, y, z, t = 0) \equiv 0\,, \quad T(x, y, z, t = 0) \equiv 0\,. \tag{4.34}$$

Finally, Neumann boundary conditions are applied to all variables:

$$\nabla G \cdot \mathbf{n} = \nabla C \cdot \mathbf{n} = \nabla T \cdot \mathbf{n} = 0\,. \tag{4.35}$$

To estimate the chemotaxis coefficients, a simplified simulation was performed by solving the model for C and T alone, with $\hat{b}_C = 0$ and $\hat{S}_T(x, y, z) \equiv 0$, similar to the 2D case. The results indicate that the chemoattractant gradient at $t = 1200\,\text{h}$ reaches a maximum value of $\overline{\nabla T} = 0.0144\,\text{mm}^{-1}$. Based on the same assumptions as in the 2D scenario, the chemotaxis parameter is set to $\hat{\chi} = 16.6\,\text{mm}^2\,\text{h}^{-1}$. The simulation further reveals the chemoattractant concentration outside the tumour at $t = 1200\,\text{h}$. Assuming, as in the 2D case, that lymphocytes lose 30% of their velocity inside the tumour, the parameter $\epsilon = 1.6$ is derived.

Finally, it is necessary to verify whether the CFL condition is satisfied. In the isotropic case, the flow intensity is expected to satisfy $u \leq 0.24\,\text{mm/h}$ in every direction. As in the 2D scenario, the smallest edge length of the mesh cells is used to estimate the spatial discretisation. The minimum value specified for *Tetgen* is $h_{\min} = 0.3\,\text{mm}$, which is used to approximate $\Delta x \sim \Delta y \sim h_{\min}$. Using these values, the Courant number is estimated as $C_T \leq 0.8\,\Delta t$. For the simulations, a time step of $\Delta t = 0.167\,\text{h}$ is employed, yielding $C_T \sim 0.133 < 1 \leq C_{T\max}$, thereby satisfying the CFL condition. This value provides a comfortable margin, ensuring that the simulation setup remains valid even in anisotropic cases where numerical stability may be more challenging to maintain.

Numerical solution for the isotropic case

The system (4.18) is solved numerically within the geometry of the brain for isotropic diffusion, using the parameters discussed in Section 4.2.1 and under the setup conditions described in the previous section.

Initially, a preliminary simulation is performed to model tumour growth in the absence of therapeutic intervention. The tumour's initial position is set at coordinates (193 mm, 277 mm, 17 mm). Figure 4.20 presents the results at the final time point, $t = 2000\,\text{h}$, shown on the right hemisphere in an axial brain section intersecting the tumour's centre.

To interpret these results physically, it is essential to define a criterion for identifying the tumour's actual location. This is necessary because diffusion propagates information instantaneously, leading to G assuming non-zero values across the entire domain. The criterion involves the application of a threshold value, whereby regions with a concentration G exceeding this value are classified as tumour-occupied, as outlined in Section 4.4.1. In the following study, a threshold of 8000 cells/mL is adopted [482], corresponding to a normalised concentration value of 0.0335, based on the selected carrying capacity [56].

Under this criterion, the tumour adopts a spheroidal shape, with its diameter increasing from approximately 1.6 cm at $t = 0\,\text{h}$ to roughly 4.4 cm at $t = 2000\,\text{h}$, resulting in an average radial expansion rate of $v_{RE} = 7 \cdot 10^{-4}\,\text{cm/h}$. Glioblastomas are known

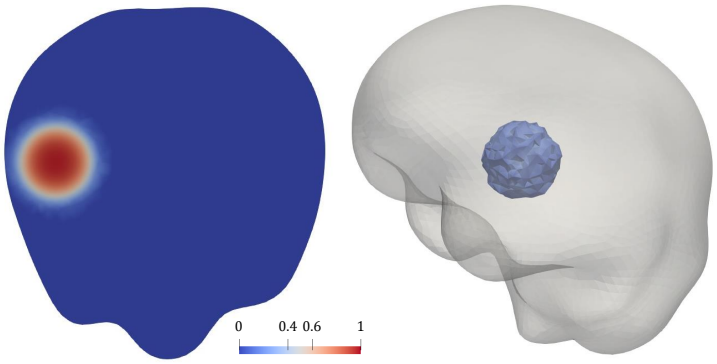

FIGURE 4.20: Tumour expansion in absence of therapeutic intervention at $t = 2000\,\text{h}$.

to grow to diameters of up to 6 cm before causing patient death [482], with reported expansion rates reaching $v_{RE} = 7.5 \cdot 10^{-4}\,\text{cm/h}$ [480]. These findings demonstrate that the simulation results closely align with the natural progression of the disease.

Subsequently, therapy is administered to target tumour progression. Figure 4.21 illustrates the therapeutic effects on an externally located tumour for varying values of S_0, which represent the intensity of the treatment. The cases analysed correspond to total lymphocyte infusion rates of 0 cells/h, $1.34 \cdot 10^5$ cells/h, and $1.34 \cdot 10^7$ cells/h. Figure 4.22 shows the evolution of the cell population and the tumour-invaded volume for the different orders of magnitude of S_0. In clinical research, infusions involving up to 10^7 lymphocytes (e.g., CAR-T cells) within a single day have been tested [80], often administered at weekly intervals. The results reveal that as therapy intensity increases, the treatment's effectiveness improves, culminating in near-complete tumour eradication at the highest intensity. While these therapies do not entirely halt tumour growth, they substantially decelerate its progression, underscoring their potential in managing tumour dynamics when optimally dosed and timed.

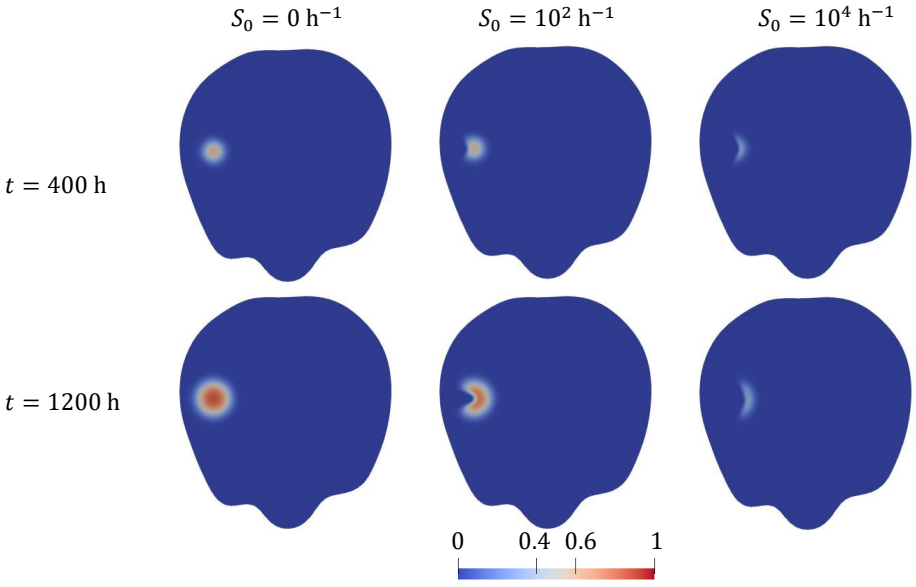

FIGURE 4.21: Tumour expansion in the isotropic case within the right hemisphere is depicted at $t = 400\,\text{h}$ and $t = 1200\,\text{h}$, showcasing the effects of varying therapy intensities: $S_0 = 0$, $S_0 = 10^2\,\text{h}^{-1}$, and $S_0 = 10^4\,\text{h}^{-1}$.

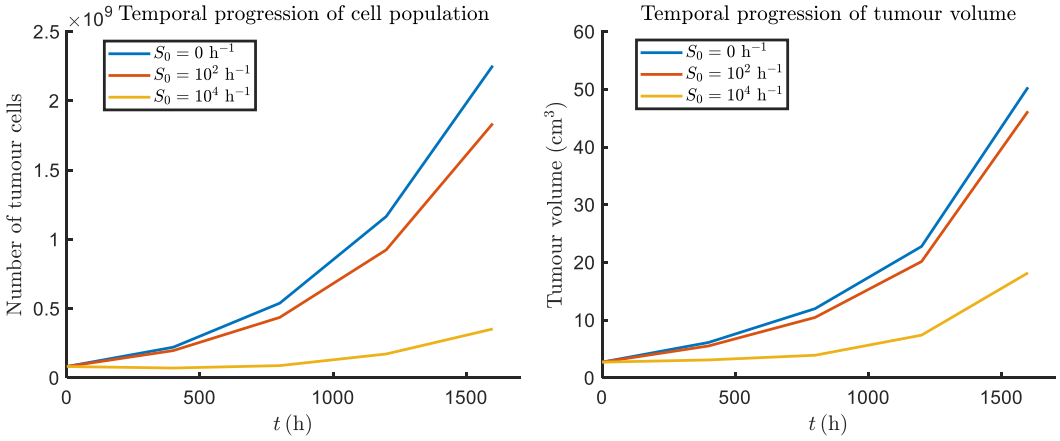

FIGURE 4.22: Therapeutic impact on tumour cell population and volume for varying therapy intensities: $S_0 = 0$, 10^2, 10^4 h^{-1}.

Introduction of anisotropy

In the previous section, isotropic diffusion was considered, assuming that cells and lymphocytes move uniformly in all directions. However, from a biological perspective, brain tissue is composed of oriented fibres that give rise to anisotropic behaviour.

As explained in Chapter 2, we use diffusion tensor imaging (DTI) to obtain the symmetric diffusion tensor $\mathbb{D}_0$, which characterises the anisotropy of water molecule diffusion across different directions within a subject's brain. To compute the effective diffusion value at each point, a weighted average is performed between $\mathbb{D}_0$ and the diffusion coefficient of water under isotropic conditions. This averaging process incorporates the free water fraction ρ_{fw} at each point, a parameter also derived through magnetic resonance imaging, to reflect the contributions of both free and tissue-bound water:

$$\mathbb{D}_w = (1 - \rho_{fw})\mathbb{D}_0 + \rho_{fw} d_{fw} \mathbb{I}\,, \tag{4.36}$$

where d_{fw} is the diffusion coefficient of free water. It is widely accepted that glioma cells also follow the preferential directions obtained from DTI for water diffusion. Furthermore, it has been shown that a more accurate description can be achieved when the anisotropy of the tensor used for cellular diffusion is increased compared to the water tensor obtained from DTI [269]. One possible method to enhance anisotropy involves multiplying the largest eigenvalue of $\mathbb{D}_w$ by a factor greater than one. However, this approach does not account for the presence of more than one principal direction, such as cases where multiple fibre bundles intersect. Following the methodology outlined in [269], it is possible to define the linear c_l, planar c_p, and spherical c_s indices:

$$\begin{aligned} c_l &= \frac{\lambda_1 - \lambda_2}{\lambda_1 + \lambda_2 + \lambda_3}\,, \\ c_\mathrm{p} &= \frac{2\,(\lambda_2 - \lambda_3)}{\lambda_1 + \lambda_2 + \lambda_3}\,, \\ c_\mathrm{s} &= \frac{3\lambda_3}{\lambda_1 + \lambda_2 + \lambda_3}\,, \end{aligned} \tag{4.37}$$

where λ_1, λ_2, and λ_3 are the eigenvalues of the tensor $\mathbb{D}_w$ obtained from DTI, ordered by magnitude. The tensor of preferential directions is then constructed as

$$\mathbb{D}_{pd} = a_1(r)\lambda_1 \hat{e}_1 \otimes \hat{e}_1 + a_2(r)\lambda_2 \hat{e}_2 \otimes \hat{e}_2 + a_3(r)\lambda_3 \hat{e}_3 \otimes \hat{e}_3\,, \tag{4.38}$$

where $\hat{e}_i$ is the eigenvector of $\mathbb{D}_w$ associated with λ_i, and $a_i(r)$ are coefficients dependent on a tuning parameter r, defined as

$$\begin{aligned} a_1(r) &= r\left(c_l + c_\mathrm{p}\right) + c_\mathrm{s}\,, \\ a_2(r) &= c_l + r c_\mathrm{p} + c_\mathrm{s}\,, \\ a_3(r) &= c_l + c_\mathrm{p} + c_\mathrm{s} = 1\,. \end{aligned} \tag{4.39}$$

This approach allows for the following adjustments: when one eigenvalue dominates (i.e. $c_l \sim 1$), the diffusion is increased along the principal direction; in the case of fibre intersections along two different directions ($c_p \sim 1$), diffusion is restricted in the direction orthogonal to the plane spanned by the two principal eigenvectors; and when no preferential direction is present ($c_s \sim 1$), the tensor remains unchanged.

To obtain the diffusion tensors for the various populations, the tensor of preferential directions is normalised by dividing it by one-third of its trace and then multiplied by the mean diffusivity coefficient discussed in Section 4.2.1:

$$\begin{aligned} \mathbb{D}_G &= D_G \frac{3\mathbb{D}_{pd}}{\mathrm{tr}(\mathbb{D}_{pd})}\,, \\ \mathbb{D}_C &= D_C \frac{3\mathbb{D}_{pd}}{\mathrm{tr}(\mathbb{D}_{pd})}\,, \\ \mathbb{D}_T &= D_T \frac{3\mathbb{D}_{pd}}{\mathrm{tr}(\mathbb{D}_{pd})}\,. \end{aligned} \tag{4.40}$$

DTI data were utilised to introduce preferential directions in the motion of different populations. However, the diffusive movement of cells and nutrients within the brain varies not only in direction but also in velocity. The brain is not a homogeneous medium; it comprises grey matter and white matter, while the ventricles and other cavities surrounding the cerebellum are filled with cerebrospinal fluid. These different media affect cell motility differently [482]. Using the *Slicer* software, it was possible to associate each cell in the computational domain with the type of tissue it represents. The segmentation was classified into three types: grey matter, white matter, and cerebrospinal fluid. Figure 4.23 displays the segmented brain across three orthogonal planes. Dark grey regions correspond to grey matter, light grey regions to white matter, and light blue regions represent ventricles filled with cerebrospinal fluid. Additionally, darker cells resulting from domain smoothing are visible; these areas are excluded from simulations by assigning null values to the tensors. In the third panel of Figure 4.23, it can be observed that the automated segmentation failed to differentiate structures deep within the right hemisphere. This discrepancy arises due to the tumour present in the patient from whom the resonance imaging data were obtained. To ensure the accuracy of numerical simulations, the non-segmented region will not be selected as the initial tumour site.

Notably, tumour cells diffuse approximately five times faster in white matter than in grey matter [480]. In cerebrospinal fluid regions, cells are assumed to be non-motile as they typically adhere to a substrate during movement. Furthermore, it is hypothesised that chemoattractants do not penetrate the barrier formed by ependymal cells lining the ventricular walls and, thus, cannot diffuse in these regions. The tensor of preferential directions is modified as follows:

- for voxels corresponding to white matter, the tensor remains unchanged;
- for voxels corresponding to grey matter, all tensor components are scaled by a factor of 0.2, consistent with estimates in the literature [480, 482];

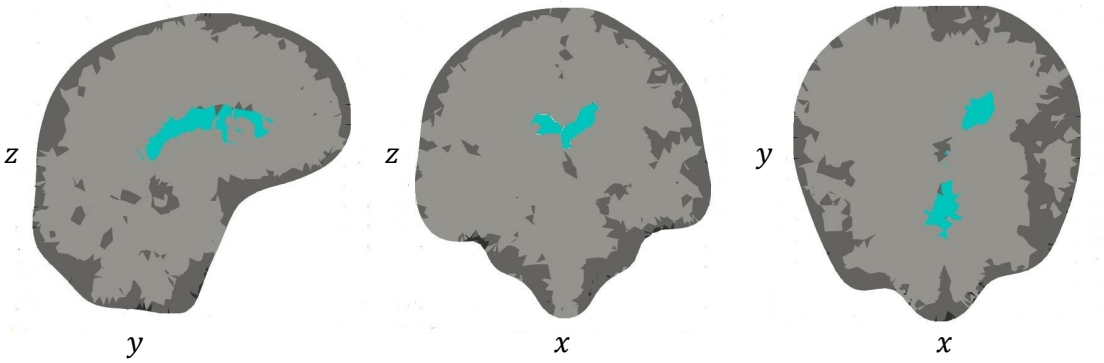

FIGURE 4.23: Segmentation: sagittal, coronal, and transverse sections.

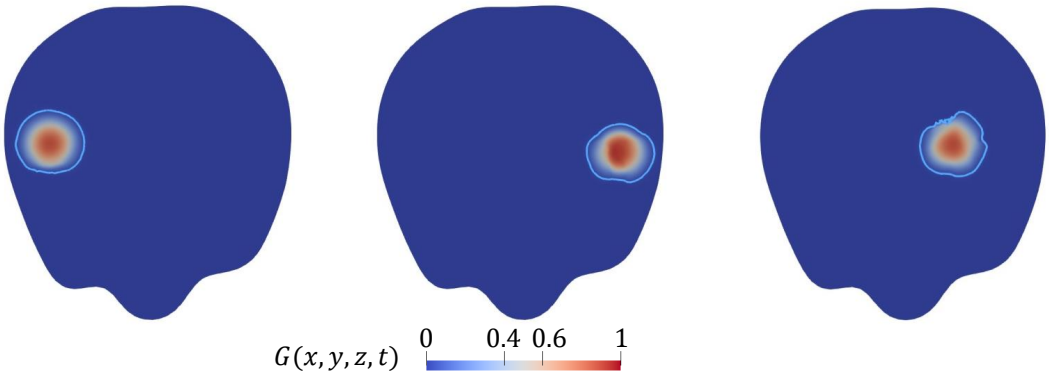

FIGURE 4.24: Tumour growth profiles in the right, left, and central-left hemispheres at $t = 1200\,\text{h}$ are illustrated. The contour line represents the region where the tumour concentration exceeds 0.0335, delineating the tumour-occupied zone.

- for voxels containing cerebrospinal fluid, all tensor components are set to zero.

It is important to note that both the segmentation and DTI results are specific to an individual patient as they depend on the internal structure of their brain. This structure varies significantly between individuals and changes over time with age. Therefore, to make patient-specific predictions, MRI data from the patient in question must be used.

The system described by Eqs. (4.18) is first numerically solved without the application of therapy, considering various spatially displaced initial conditions. The diffusion tensor incorporates segmentation data and an anisotropy amplification parameter of $r = 5$ in Eqs. (4.39). Figure 4.24 illustrates the tumour growth profiles at $t = 1200\,\text{h}$ for tumours located in the right, left, and central-left hemispheres. The results reveal significant deviations from the isotropic spherical growth pattern, with the tumour's spatial expansion notably impeded in regions of grey matter, highlighting the influence of brain tissue heterogeneity on tumour progression.

Therapy is then introduced to the model. Figure 4.25 illustrates tumour concentrations at $t = 400\,\text{h}$ and $t = 1200\,\text{h}$ for a tumour located in the right hemisphere, comparing cases with and without therapy. Similarly, Figure 4.26 presents the corresponding tumour concentrations for a tumour in the left hemisphere under the same conditions. The two graphs in Figure 4.27 illustrate the temporal evolution of the tumour cell population and tumour volume for different therapy intensities and tumour locations. Despite the application of therapy with an intensity of $S_0 = 10^3\,\text{h}^{-1}$, the treatment is unable to completely halt tumour growth but effectively slows its progression. The results also reveal significant differences in tumour growth based on the surrounding tissue type.

Specifically, the tumour in the left hemisphere, which is surrounded by regions with a higher proportion of white matter, exhibits a volume approximately 20.77% larger and a 12.5% higher cell population at $t = 1200\,\mathrm{h}$. These findings underscore the influence of tissue heterogeneity on tumour dynamics.

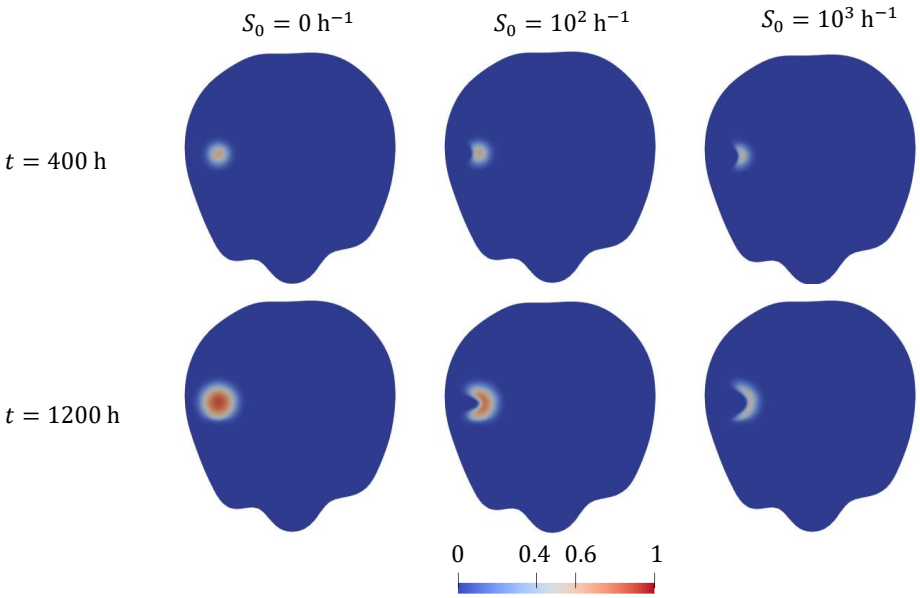

FIGURE 4.25: Tumour progression in the right hemisphere at various time points and under different therapy intensities.

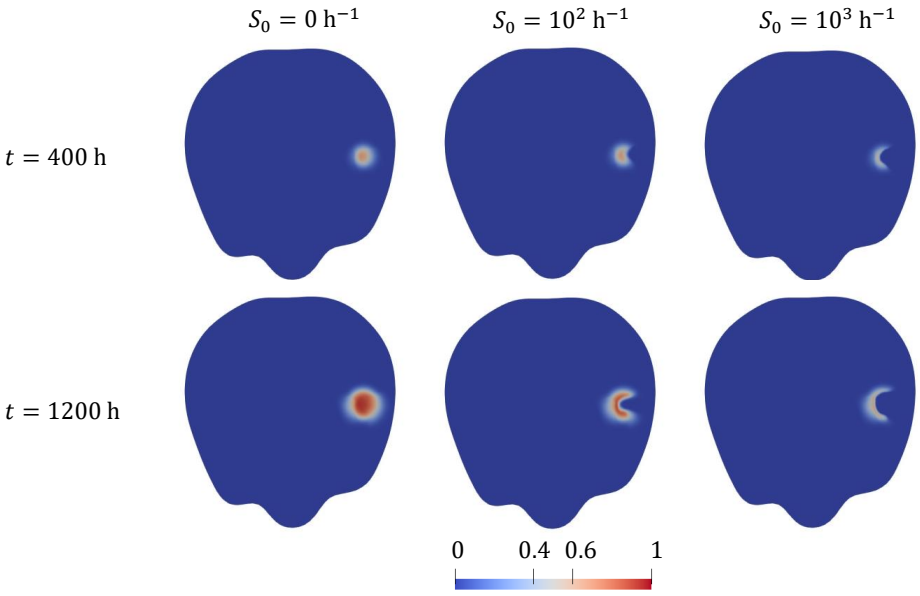

FIGURE 4.26: Tumour progression in the left hemisphere at various time points and under different therapy intensities.

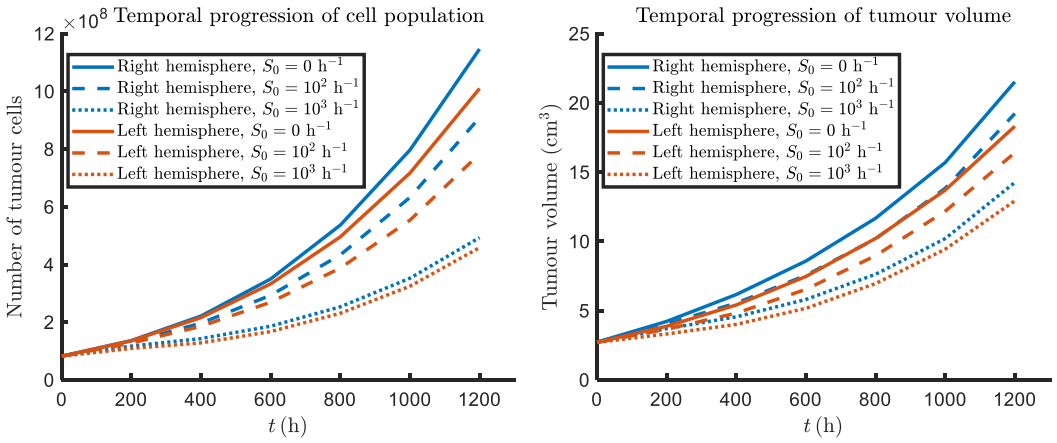

FIGURE 4.27: Therapeutic impact on tumour cell population and volume for different tumour location and varying therapy intensities: $S_0 = 0$, 10^2, 10^3 h^{-1}.

4.5 Summary

Glioblastoma Multiforme (GBM) represents one of the most lethal and aggressive forms of cancer that develop in the brain. Despite advancements in medicine, its prognosis remains predominantly poor, motivating the exploration of novel therapeutic approaches. In this context, immunotherapy emerges as a promising strategy.

This work aims to develop mathematical models that can describe the complex tumour-immune interactions. The proposed model, formulated using partial differential equations (PDEs), focuses on the interactions between tumour cells and lymphocytes to represent a specific type of immunotherapy: the infusion of cytotoxic T lymphocytes, a therapeutic approach that is the subject of extensive research globally.

As a first approximation, disregarding the spatial distribution of cells, the PDE model is simplified into an ODE system consisting of two equations: one representing the population of tumour cells and the other the number of lymphocytes in the central nervous system (CNS), with therapeutic infusion modelled as a time-constant source term in the second equation. The system's behaviour is studied under varying therapy intensities. Analytically, a threshold is derived that guarantees the system evolves towards a healthy equilibrium, where the tumour cell population is eradicated. The corresponding lymphocyte infusion levels are comparable to those observed in clinical studies. Numerical methods are employed to generate bifurcation diagrams of the system, exploring variations in each parameter.

The PDE model expands the analysis by incorporating the spatial dynamics of tumour progression. The diffusive terms account for the spatial expansion of the cells. Additionally, a chemotaxis term is included in the lymphocyte equation to model their directed movement towards tumour-secreted chemical signals. Various modelling approaches for the chemoattractant are also explored and discussed. This model is solved using a finite element code implemented in Python, leveraging the FEniCS libraries. For this purpose, the weak variational formulation of the PDE model is derived. Initial simulations are performed on a simplified two-dimensional geometry, specifically a circular sector, to test code stability and model behaviour. These simulations illustrate glioma proliferation and spatial expansion while lymphocytes migrate via chemotaxis to attack tumour cells. Based on these two-dimensional simulations, a sensitivity analysis is conducted. The parameters found to have the greatest impact on tumour volume, a critical prognostic indicator, are the cancer cell elimination rate by lymphocytes and glioma diffusivity. These findings suggest these aspects should be prioritised in synergistic

therapeutic strategies. The system is subsequently simulated in a three-dimensional brain geometry reconstructed from MRI data of a GBM patient. Therapeutic infusion is assumed to be delivered directly into the brain, as described in medical literature, and is modelled as a time-constant and spatially Gaussian source term in the lymphocyte equation. Simulations initially assume isotropic diffusion, and the results are compared with the natural progression of GBM to assess model plausibility. Under these conditions, the therapy's effects are evaluated for varying intensities. To enhance predictions of tumour-invaded regions, diffusion tensor imaging (DTI) data are utilised to account for anisotropy. This approach is based on the hypothesis that both cells and fluids in the brain preferentially migrate along the spatial arrangement of tissue fibres. The brain is further segmented into different tissue types—white matter, grey matter, and cerebrospinal fluid—and the diffusion and chemotaxis tensors are appropriately modified for each voxel's composition. Results are presented for simulations under this setup, including both free tumour growth in the absence of therapy and the response to varying infusion intensities. Significant differences are observed based on the tumour's growth location and compared to the isotropic case. In all cases, therapy successfully slows tumour growth to varying degrees depending on the lymphocyte infusion rate. However, it does not achieve complete tumour eradication. The method employed is patient-specific, requiring information about brain structure and fibre arrangement obtained via MRI techniques. These techniques could also provide data on the initial tumour cell concentration, leading to more accurate simulations.

Multiple directions for further research remain open. In this work, only time-constant infusions are considered. However, in clinical practice, therapy administration often occurs in intervals spanning several days. The study of time-varying therapy regimes could be undertaken using the ODE model to identify treatment schedules that minimise intervention while reducing adverse effects, drawing on control theory principles. The PDE model could also be refined by considering alternative infusion techniques. For improved numerical stability, stabilisation techniques such as the streamline upwind Petrov–Galerkin (SUPG) formulation might be employed. This analysis focuses exclusively on interactions between lymphocytes and tumour cells, neglecting contributions from other cell populations, such as macrophages and stem cells, as well as cytokines mediating intercellular interactions. In particular, the impact of TGF-β, a cytokine secreted by the tumour that significantly contributes to the immunosuppressive GBM microenvironment, could be modelled alongside the inclusion of feedback mechanisms and inter-patient variability. Finally, exploring the interaction between immunotherapy and other treatment modalities, such as radiotherapy and chemotherapy, may pave the way for developing multimodal strategies.

5 Incorporating phenotypic heterogeneity into mathematical models for the growth of brain tumours

5.1 Preliminaries

In this Chapter, we present a reaction-diffusion model incorporating non-local reaction terms, as the ones outlined in Section 1.2. This model is designed to investigate the growth of brain tumours within a highly anisotropic environment, characterised by heterogeneous oxygen distributions and phenotypic diversity.

Numerous experimental and clinical studies [14, 213, 353, 472] underscore the critical influence of spatial oxygen gradients in driving phenotypic heterogeneity within tumours, as described in Section 1.1.2. Different regions of a tumour experience varying oxygen concentrations, leading to distinct phenotypic adaptations. Hypoxic regions, characterized by below-normal oxygen levels, are often populated by cells with elevated expression of hypoxia-inducible factors such as HIF-1. Conversely, well-oxygenated regions, such as the periphery of avascular tumours or areas near blood vessels in vascularized tumours, are occupied by cells with lower levels of hypoxia-inducible factor expression. On the other hand, the availability of glucose is generally a less limiting factor for tumour growth compared to oxygen [202, 203, 509]. For this reason, in this study, we focus solely on oxygen availability to model the metabolic constraints on tumour dynamics.

The mathematical model combines a balance equation for the population distribution function of brain tumour cells with a differential equation describing the dynamics of oxygen concentration. This coupling incorporates oxygen consumption by cells, which depends on both the local oxygen availability in the brain and the phenotypic state of the tumour cells. In line with previous works [181, 328–330, 503], intra-population heterogeneity is captured using a continuous structuring variable that represents the phenotypic state of cells. However, to the best of our knowledge, these types of models have not yet been specifically applied to investigate tumour progression within an anisotropic environment. In particular, we focus on the brain environment, which is characterised by the presence of white matter tracts, making it highly anisotropic. We analyse the qualitative behaviour of the solutions in simplified one-dimensional settings, following the methodology outlined in [328, 329, 503]. In contrast to [503], our analysis includes the investigation of travelling wave solutions. We then extend the framework to achieve more realistic outcomes, with a key step being the integration of clinical data to ensure an accurate mathematical representation of the brain's environment. Given the significant anisotropy of brain tissue, this characteristic is incorporated through an anisotropic diffusion tensor for both oxygen and cells, derived from

Diffusion Tensor Imaging (DTI) data. Simulations are conducted on a realistic three-dimensional brain geometry reconstructed using Magnetic Resonance Imaging (MRI). This approach is pivotal for developing a personalised tool capable of capturing tumour evolution in individual patients. In order to properly solve the model on the 3D patient-specific geometry, we use a time-splitting, separating the finite element solution in space from the finite difference approximation in phenotype and time. This approach represents a significant novelty compared to previous PIDE models.

The structure of the Chapter is as follows: Section 5.2 introduces the model equations and the underlying assumptions of the modelling approach. In Section 5.3, we conduct a formal asymptotic analysis of the evolutionary dynamics. Section 5.4 elaborates on the primary outcomes derived from numerical simulations. Furthermore, 3D simulations on a brain geometry are shown, in order to provide a possible application. Finally, Section 5.5 summarizes the findings and we provide a brief overview of possible research perspectives.

The findings presented in this chapter are part of the manuscript by F. Ballatore, X. Ruan, C. Giverso, and T. Lorenzi, titled *Non-local anisotropic reaction-diffusion modelling of phenotypic heterogeneity in growing brain tumours under spatially inhomogeneous oxygen gradients*, which is currently in preparation.

5.2 Mathematical model

We consider a mathematical model describing the dynamics of a growing tumour cell population characterized by phenotypic diversity. In this framework, the phenotypic state of each cell is represented by a variable $y \in \mathbb{R}_+$, which lies in the range $[0, Y]$, with $Y > 0$. This variable quantifies the normalized level of expression of a hypoxia-resistant factor: values of y near 0 correspond to lower resistance to environmental hypoxic conditions, while values approaching Y indicate higher resistance. The (total) cell population density at a specific location $\boldsymbol{x} \in \Omega \subset \mathbb{R}^n$ (with $n = 2, 3$) and time $t \in [0, +\infty)$, denoted by $\rho(t, \boldsymbol{x})$, is defined as the integral over all phenotypic states of the cell distribution function $n(t, \boldsymbol{x}, y)$. Furthermore, the oxygen concentration is modelled by the function $S(t, \boldsymbol{x})$. The evolution of $n(t, \boldsymbol{x}, y)$ and $S(t, \boldsymbol{x})$ is governed by the following non-local reaction-diffusion equations:

$$\begin{cases} \partial_t n - \operatorname{div}\left(\mathbf{D}_n(\boldsymbol{x})\,\nabla n\right) = R(y, \rho, S)n + \beta \partial^2_{yy} n\,, \ (\boldsymbol{x}, y) \in \Omega \times (0, Y)\,, \\ \rho(t, \boldsymbol{x}) := \displaystyle\int_0^Y n(t, \boldsymbol{x}, y)\,\mathrm{d}y\,, \\ \partial_t S - \operatorname{div}\left(\mathbf{D}_S(\boldsymbol{x})\,\nabla S\right) = -\nu S \displaystyle\int_0^Y r(y)\, n(t, \boldsymbol{x}, y)\,\mathrm{d}y\,. \end{cases} \tag{5.1}$$

where $\mathbf{D}_n(\boldsymbol{x})$ and $\mathbf{D}_S(\boldsymbol{x})$ are non-negative tensors representing the diffusion of the cell population and the diffusion of the oxygen, respectively.

The first term on the right-hand side of the first non-local PDE of (5.1) represents the change in cell distribution due to proliferation and death, being $R(y, \rho, S)$ the net proliferation rate of cells in the phenotypic state y at time t and position $\boldsymbol{x}$ under the local environmental conditions given by the cell density $\rho(t, \boldsymbol{x})$ and the oxygen availability $S(t, \boldsymbol{x})$. Specifically, we take

$$R(y, \rho, S) := \alpha \left(r(y) \frac{S}{S_0} + f(y) - \frac{\rho}{\rho_0} \right), \tag{5.2}$$

where S_0 and ρ_0 are the reference values for oxygen and cell density, respectively. For what concern the function $r(y)$, it is a smooth and bounded function representing the proliferation rate in the presence of oxygen. It is maximal for cells with an aerobic metabolism and vanishes for cells relying solely on anaerobic metabolism. Therefore $r(y)$ satisfies the following conditions

$$r(0) = 1\,,\ r(Y) = 0\,,\ \frac{\mathrm{d}r(y)}{\mathrm{d}y} < 0 \text{ for } y \in (0, Y)\,. \tag{5.3}$$

Under these assumptions, we infer that $r(y) > 0\,, \forall y \in (0, Y)$. The function $f(y)$, on the other hand, represents the proliferation rate under hypoxic conditions. It is an increasing function of the phenotypic state y, satisfying

$$f(0) = 0\,,\ f(Y) = \zeta\,,\ \frac{\mathrm{d}f(y)}{\mathrm{d}y} > 0 \text{ for } y \in (0, Y)\,, \tag{5.4}$$

where ζ is the maximum rate of cell division via anaerobic pathways. The last term in (5.2) represents instead cells death due to competition for space.
The second term on the right-hand side of the first equation in (5.1) represents the effects of spontaneous, heritable phenotypic changes, which occur at a rate $\beta > 0$ [261].
The integral term on the right-hand side of the oxygen balance equation in (5.1) accounts for oxygen consumption for the proliferation of cells in the phenotypic state y, at a rate given by the function $r(y)$. This choice reflects the idea that cells with a higher proliferation rate consume oxygen more rapidly.

To adimensionalize the dependent variables of the system (5.1), we divide the first two equations by ρ_0 and the third equation by S_0, where ρ_0 and S_0 are the reference values for cell density and oxygen concentration, respectively. We define the rescaled variables

$$\hat{n} = \frac{n}{\rho_0}\,,\quad \hat{\rho} = \frac{\rho}{\rho_0}\,,\quad \hat{S} = \frac{S}{S_0}\,,\quad \hat{v} = \rho_0 v\,, \tag{5.5}$$

and obtain the nondimensionalized system

$$\begin{cases} \partial_t \hat{n} - \operatorname{div}\left(\mathbf{D}_n(\boldsymbol{x})\,\nabla \hat{n}\right) = \alpha\Big(r(y)\hat{S} + f(y) - \hat{\rho}\Big)\hat{n} + \beta\partial^2_{yy}\hat{n}\,,\ (\boldsymbol{x}, y) \in \Omega \times (0, Y)\,, \\ \hat{\rho}(t, x) := \displaystyle\int_0^Y \hat{n}(t, \boldsymbol{x}, y)\,\mathrm{d}y\,, \\ \partial_t \hat{S} - \operatorname{div}\left(\mathbf{D}_S(\boldsymbol{x})\,\nabla \hat{S}\right) = -\hat{v}\hat{S}\displaystyle\int_0^Y r(y)\,\hat{n}(t, \boldsymbol{x}, y)\,\mathrm{d}y\,, \end{cases} \tag{5.6}$$

subject to suitable initial conditions such that

$$0 \le \hat{\rho}(0, \boldsymbol{x}) \le 1 \quad \text{and} \quad 0 \le \hat{S}(0, \boldsymbol{x}) \le 1 \quad \text{for } \boldsymbol{x} \in \overline{\Omega}\,. \tag{5.7}$$

Furthermore, zero-flux boundary conditions are imposed on the cell population distribution at $\partial\Omega$, as well as at $y = 0$ and $y = Y$:

$$\nabla \hat{n}(t, \boldsymbol{x}, y) \cdot \boldsymbol{n} = 0 \text{ on } \partial\Omega\,,\quad \partial_y \hat{n}(t, \boldsymbol{x}, y)\big|_{y=0} \cdot \boldsymbol{n} = 0\,,\quad \partial_y \hat{n}(t, \boldsymbol{x}, y)\big|_{y=0} \cdot \boldsymbol{n} = 0\,. \tag{5.8}$$

For the oxygen concentration, the Dirichlet boundary condition $\hat{S}(t, \boldsymbol{x}) = 1$ is applied on $\partial\Omega$, based on the assumption that the boundary is sufficiently distant from the tumour. This allows us to reasonably approximate the oxygen concentration as constant and

equal to its physiological value at these locations.

Finally, for the way the PDEs are formulated and for the initial and boundary conditions imposed, we have:

$$0 \leq \hat{\rho}(t, \boldsymbol{x}) \leq 1\,, \quad 0 \leq \hat{S}(t, \boldsymbol{x}) \leq 1\,, \quad \forall \boldsymbol{x} \in \Omega \text{ and } \forall t \in [0, +\infty)\,. \tag{5.9}$$

5.3 Formal asymptotic analysis

5.3.1 Object of study

To investigate the long-term behaviour of the cell population, considering its dynamics across numerous cell generations, we introduce the time scaling $t \to t/\varepsilon$, where $\varepsilon > 0$ is a small parameter. Furthermore, we make the hypothesis that heritable phenotypic changes occur on a slower timescale compared to cell proliferation and death, i.e. $\beta = \varepsilon^2$. Focusing on a three-dimensional scenario, we assume that cells diffuse on the same timescale as phenotypic changes, implying that $\mathbf{D}_n(\boldsymbol{x}) = \varepsilon^2 \mathbf{D}(\boldsymbol{x})$. Furthermore, in the following analysis we take the tensor $\mathbf{D}(\boldsymbol{x})$ as a constant diagonal anisotropic tensor of components D_i, with $i = 1, 2, 3$. Moreover, when analysing the oxygen diffusion tensor, we consider a scenario in which oxygen diffuses faster than cells. This difference is reflected in their diffusion coefficients, even though both share the same preferential directions. Specifically, we set $\mathbf{D}_S(\boldsymbol{x}) = \varepsilon \mathbf{D}(\boldsymbol{x})$. Similarly, we assume that the oxygen consumption rate operates on the same timescale as oxygen diffusion, i.e. $\nu = \varepsilon$. Similarly, we assume the oxygen consumption rate operates on the same timescale as oxygen diffusion, i.e. $\nu = \varepsilon$. Under these assumptions, the rescaled population density $\hat{n}(\frac{t}{\varepsilon}, \boldsymbol{x}, y) \equiv n_\varepsilon(t, \boldsymbol{x}, y)$ and the oxygen concentration $\hat{S}(\frac{t}{\varepsilon}, \boldsymbol{x}) \equiv S_\varepsilon(t, \boldsymbol{x})$ satisfy the following system of partial differential equations for $(\boldsymbol{x}, y) \in \Omega \times (0, Y)$:

$$\begin{cases} \varepsilon \partial_t n_\varepsilon - \varepsilon^2 \displaystyle\sum_{i=1}^{3} D_i \partial^2_{x_i x_i} n_\varepsilon = \alpha \Big(r(y) S_\varepsilon + f(y) - \rho_\varepsilon \Big) n_\varepsilon + \varepsilon^2 \partial^2_{yy} n_\varepsilon\,, \\ \rho_\varepsilon(t, x) := \displaystyle\int_0^Y n_\varepsilon(t, \boldsymbol{x}, y)\, \mathrm{d}y\,, \\ \varepsilon \partial_t S_\varepsilon - \varepsilon \displaystyle\sum_{i=1}^{3} D_i \partial^2_{x_i x_i} S_\varepsilon = -\varepsilon S_\varepsilon \displaystyle\int_0^Y r(y)\, n_\varepsilon(t, \boldsymbol{x}, y)\, \mathrm{d}y\,. \end{cases} \tag{5.10}$$

5.3.2 Asymptotic analysis for $\varepsilon \to 0$

Building on prior research into the mathematical analysis of evolutionary dynamics in continuously-structured populations [403], we focus on the scenario where, at time $t = 0$, tumour cells at a given position are primarily concentrated in the same phenotypic state. Specifically, for each position $\boldsymbol{x}$, the initial phenotypic distribution of tumour cells, denoted $n_\varepsilon(0, \boldsymbol{x}, y)$, is modelled as a sharp Gaussian-like function with a mean value $\bar{y}_\varepsilon(0, \boldsymbol{x})$ and an integral $\rho_\varepsilon(0, \boldsymbol{x})$. We define this distribution as follows:

$$n_\varepsilon(0, \boldsymbol{x}, y) = e^{\frac{u_\varepsilon^0(\boldsymbol{x}, y)}{\varepsilon}}\,, \tag{5.11}$$

where $u_\varepsilon^0(\boldsymbol{x}, y)$ is a smooth function of y, uniformly concave for all $\boldsymbol{x} \in \Omega$ and with an unique maximum at $\bar{y}_\varepsilon(0, \boldsymbol{x})$ for any $\boldsymbol{x} \in \Omega$, which is such that, in the sense of measures,

$$e^{\frac{u_\varepsilon^0(\boldsymbol{x}, y)}{\varepsilon}} \xrightarrow{\varepsilon \to 0} \rho(0, \boldsymbol{x}) \delta_{\bar{y}(0, \boldsymbol{x})}(y)\,, \tag{5.12}$$

being $\rho(0, \boldsymbol{x})$ the leading-order term in the asymptotic expansion of $\rho_\varepsilon(0, \boldsymbol{x})$, and $\delta_{\bar{y}(0, \boldsymbol{x})}(y)$ the Dirac delta function centred at $\bar{y}(0, \boldsymbol{x})$.
Building on the Hamilton-Jacobi approach, we make the real phase WKB ansatz [52, 176, 183]

$$n_\varepsilon(t, \boldsymbol{x}, y) = e^{\frac{u_\varepsilon(t, \boldsymbol{x}, y)}{\varepsilon}}\,. \tag{5.13}$$

which gives

$$\begin{aligned}
\partial_t n_\varepsilon &= \frac{\partial_t u_\varepsilon}{\varepsilon} n_\varepsilon\,, \\
\partial^2_{x_i x_i} n_\varepsilon &= \left(\frac{1}{\varepsilon^2} \left(\partial_{x_i} u_\varepsilon\right)^2 + \frac{1}{\varepsilon} \partial^2_{x_i x_i} u_\varepsilon \right) n_\varepsilon\,, \quad i = 1, 2, 3\,, \\
\partial^2_{yy} n_\varepsilon &= \left(\frac{1}{\varepsilon^2} \left(\partial_y u_\varepsilon\right)^2 + \frac{1}{\varepsilon} \partial^2_{yy} u_\varepsilon \right) n_\varepsilon\,.
\end{aligned}$$

Substituting the above expressions into the first non-local PDE (5.10), we obtain the following Hamilton-Jacobi equation for $u_\varepsilon(t, \boldsymbol{x}, y)$

$$\begin{aligned}
\partial_t u_\varepsilon - \left[\varepsilon \sum_{i=1}^{3} D_i \partial^2_{x_i x_i} u_\varepsilon + \sum_{i=1}^{3} D_i \left(\partial_{x_i} u_\varepsilon\right)^2 \right] &= \alpha \Big(r(y) S_\varepsilon + f(y) - \rho_\varepsilon \Big) + \\
&+ \left[\left(\partial_y u_\varepsilon\right)^2 + \varepsilon \partial^2_{yy} u_\varepsilon \right]\,, \quad (\boldsymbol{x}, y) \in \Omega \times (0, Y)\,.
\end{aligned} \tag{5.14}$$

Letting $\varepsilon \to 0$ in (5.14), and denoting by $u(t, \boldsymbol{x}, y)$ the leading-order term of the asymptotic expansion for $u_\varepsilon(t, \boldsymbol{x}, y)$, we formally obtain

$$\partial_t u - \sum_{i=1}^{3} D_i \left(\partial_{x_i} u_\varepsilon\right)^2 = \alpha \Big(r(y) S + f(y) - \rho \Big) + \left(\partial_y u\right)^2\,, \quad (\boldsymbol{x}, y) \in \mathbb{R} \times (0, Y)\,, \tag{5.15}$$

where $\rho(t, \boldsymbol{x})$ and $S(t, \boldsymbol{x})$ are the leading-order terms of the asymptotic expansions for $\rho_\varepsilon(t, \boldsymbol{x})$ and $S_\varepsilon(t, \boldsymbol{x})$.

Constraint on $u(t, \boldsymbol{x}, y)$ Consider $\boldsymbol{x} \in \Omega$ such that $\rho(t, \boldsymbol{x}) > 0$, i.e. $\boldsymbol{x} \in \operatorname{supp}(\rho)$, and let $\bar{y}(t, \boldsymbol{x})$ be a nondegenerate maximum point of $u(t, \boldsymbol{x}, y)$, meaning $\bar{y}(t, \boldsymbol{x}) \in \arg\max_{y \in [0, Y]} u(t, \boldsymbol{x}, y)$, with

$$\partial_y u(t, \boldsymbol{x}, \bar{y}(t, \boldsymbol{x})) = 0 \quad \text{and} \quad \partial^2_{yy} u(t, \boldsymbol{x}, \bar{y}(t, \boldsymbol{x})) < 0\,. \tag{5.16}$$

If $u_\varepsilon(t, \boldsymbol{x}, y)$ is a strictly concave function of y and $u(t, \boldsymbol{x}, y)$ is also a strictly concave function of y whose unique maximum point is $\bar{y}(t, \boldsymbol{x})$, letting $\varepsilon \to 0$ in (5.13) formally gives the following constraint

$$u(t, \boldsymbol{x}, \bar{y}(t, \boldsymbol{x})) = \max_{y \in [0, Y]} u(t, \boldsymbol{x}, y) = 0, \quad \forall t > 0\,,\ \boldsymbol{x} \in \operatorname{supp}(\rho)\,. \tag{5.17}$$

By differentiating once with respect to space and once with respect to time, we additionally obtain

$$\partial_{x_i} u(t, \boldsymbol{x}, \bar{y}(t, \boldsymbol{x})) = 0\,,\ i = 1, 2, 3\,,\ \text{and}\ \partial_t u(t, \boldsymbol{x}, \bar{y}(t, \boldsymbol{x})) = 0\,. \tag{5.18}$$

Relation between $\bar{y}(t, \boldsymbol{x})$ and $\rho(t, \boldsymbol{x})$ Consider $\boldsymbol{x} \in \text{supp}(\rho)$. Evaluating (5.15) at $\bar{y}(t, \boldsymbol{x})$ and using (5.16) and (5.18), we obtain

$$\begin{aligned} r(\bar{y}(t, \boldsymbol{x}))S(t, \boldsymbol{x}) + f(\bar{y}(t, \boldsymbol{x})) - \rho(t, \boldsymbol{x}) = 0 \implies \\ \rho(t, \boldsymbol{x}) = r\left(\bar{y}(t, \boldsymbol{x})\right) S(t, \boldsymbol{x}) + f\left(\bar{y}(t, \boldsymbol{x})\right)\,,\ \boldsymbol{x} \in \text{supp}(\rho)\,. \end{aligned} \tag{5.19}$$

Differential equation for $S(t, \boldsymbol{x})$ When $n_\varepsilon(t, \boldsymbol{x}, y)$ takes the form (5.13), and both $u_\varepsilon(t, \boldsymbol{x}, y)$ and $u(t, \boldsymbol{x}, y)$ satisfy the concavity conditions with respect to the variable y, as well as the constraint (5.17), the following asymptotic result formally holds:

$$\int_0^Y r(y) n_\varepsilon(t, \boldsymbol{x}, y) \overset{\varepsilon \to 0}{\longrightarrow} r(\bar{y}) \rho(t, \boldsymbol{x})\,. \tag{5.20}$$

Using this asymptotic result in the differential equation for the oxygen in (5.10), one obtains the following PDE for $S(t, \boldsymbol{x})$:

$$\partial_t S(t, \boldsymbol{x}) - \sum_{i=1}^{3} D_i \partial^2_{x_i x_i} S(t, \boldsymbol{x}) = -S(t, \boldsymbol{x}) r(\bar{y}(t, \boldsymbol{x})) \rho(t, \boldsymbol{x})\,. \tag{5.21}$$

Transport equation for $\bar{y}(t, \boldsymbol{x})$ Consider again $\boldsymbol{x} \in \text{supp}(\rho)$. If we differentiate (5.15) with respect to y, we obtain:

$$\partial^2_{ty} u - 2 \sum_{i=1}^{3} D_i \left(\partial_{x_i} u\right) \left(\partial^2_{x_i y} u\right) = \alpha \left(\frac{\mathrm{d} r(y)}{\mathrm{d} y} S + \frac{\mathrm{d} f(y)}{\mathrm{d} y} \right) + 2 \left(\partial_y u\right) \left(\partial^2_{yy} u\right)\,,\ \boldsymbol{x} \in \text{supp}(\rho)\,.$$

Evaluating the resulting equation at $\bar{y}(t, \boldsymbol{x})$ and recalling the first conditions of (5.16) and (5.18), we obtain

$$\partial^2_{ty} u(t, \boldsymbol{x}, \bar{y}(t, \boldsymbol{x})) = \alpha \left(\frac{\mathrm{d} r}{\mathrm{d} y}(\bar{y}(t, \boldsymbol{x})) S(t, \boldsymbol{x}) + \frac{\mathrm{d} f}{\mathrm{d} y}(\bar{y}(t, \boldsymbol{x})) \right)\,. \tag{5.22}$$

Moreover, differentiating the first condition of (5.16) with respect to t, we have

$$\begin{aligned} \partial^2_{ty} u(t, \boldsymbol{x}, \bar{y}(t, \boldsymbol{x})) + \partial^2_{yy} u(t, \boldsymbol{x}, \bar{y}(t, \boldsymbol{x})) \partial_t \bar{y}(t, \boldsymbol{x}) = 0 \\ \Rightarrow \partial^2_{ty} u(t, \boldsymbol{x}, \bar{y}(t, \boldsymbol{x})) = -\partial^2_{yy} u(t, \boldsymbol{x}, \bar{y}(t, \boldsymbol{x})) \partial_t \bar{y}(t, \boldsymbol{x})\,. \end{aligned}$$

Substituting the above expression into (5.22), and using the first condition of (5.16), we finally obtain

$$\partial_t \bar{y}(t, \boldsymbol{x}) = \frac{\alpha}{-\partial^2_{\bar{y}y} u(t, \boldsymbol{x}, \bar{y}(t, \boldsymbol{x}))} \left(\frac{\mathrm{d} r}{\mathrm{d} y}(\bar{y}(t, \boldsymbol{x})) S(t, \boldsymbol{x}) + \frac{\mathrm{d} f}{\mathrm{d} y}(\bar{y}(t, \boldsymbol{x})) \right)\,,\ \boldsymbol{x} \in \text{supp}(\rho)\,. \tag{5.23}$$

Travelling wave analysis To investigate the travelling wave problem, we focus on the case where $\boldsymbol{x} \equiv x \in \mathbb{R}$. The problem we are addressing can therefore be described as

follows:

$$\partial_t u(t,x,y) - D(\partial_x u(t,x,y))^2 = \alpha\left(r(y)S(t,x) + f(y) - \rho(t,x)\right) + \left(\partial_y u(t,x,y)\right)^2 , \quad (x,y) \in \mathbb{R} \times (0,Y) ; \tag{5.24}$$

$$u(t,x,\bar{y}(t,x)) = \max_{y\in[0,Y]} u(t,x,y) = 0, \quad \forall t > 0 , \ x \in \operatorname{supp}(\rho) ; \tag{5.25}$$

$$\partial_y u(t,x,\bar{y}(t,x)) = 0 , \ \partial_x u(t,x,\bar{y}(t,x)) = 0 , \ \partial_t u(t,x,\bar{y}(t,x)) = 0 , \ x \in \operatorname{supp}(\rho) ; \tag{5.26}$$

$$\rho(t,x) = r(\bar{y}(t,x))S(t,x) + f(\bar{y}(t,x)) , \ x \in \operatorname{supp}(\rho) ; \tag{5.27}$$

$$\partial_t \bar{y}(t,x) = \frac{-\alpha}{\partial^2_{yy} u(t,x,\bar{y}(t,x))} \left(\frac{\mathrm{d}r}{\mathrm{d}y}(\bar{y}(t,x))S(t,x) + \frac{\mathrm{d}f}{\mathrm{d}y}(\bar{y}(t,x)) \right) , \ x \in \operatorname{supp}(\rho) ; \tag{5.28}$$

$$\partial_t S(t,x) - D\partial^2_{xx} S(t,x) = -S(t,x)r(\bar{y}(t,x))\rho(t,x) . \tag{5.29}$$

Substituting the travelling-wave ansatz

$$\rho(t,x) = \rho(z) , \ u(t,x,y) = u(z,y) , \ \bar{y}(t,x) = \bar{y}(z) \text{ and } S(t,x) = S(z) ,$$

with $z = x - ct$, $c > 0$, in the equations (5.24), (5.25), (5.26), (5.27), (5.28) and (5.29) we obtain:

$$-c\partial_z u(z,y) - D\left(\partial_z u(z,y)\right)^2 = \alpha\Big(r(y)S(z) + f(y) - \rho(z)\Big) + \left(\partial_y u(z,y)\right)^2 , \quad (z,y) \in \mathbb{R} \times (0,Y) ; \tag{5.30}$$

$$u(z,\bar{y}(z)) = \max_{y\in[0,Y]} u(z,y) = 0, \quad \forall t > 0 , \ z \in \operatorname{supp}(\rho) ; \tag{5.31}$$

$$\partial_y u(z,\bar{y}(z)) = 0 , \ \partial_z u(z,\bar{y}(z)) = 0 , \ z \in \operatorname{supp}(\rho) ; \tag{5.32}$$

$$\rho(z) = r(\bar{y}(z))S(z) + f(\bar{y}(z)) , \ z \in \operatorname{supp}(\rho) ; \tag{5.33}$$

$$\bar{y}'(z) = \frac{\alpha}{c\partial^2_{yy} u(z,\bar{y}(z))} \left(\frac{\mathrm{d}r}{\mathrm{d}y}(\bar{y}(z))S(z) + \frac{\mathrm{d}f}{\mathrm{d}y}(\bar{y}(z)) \right) , \ z \in \operatorname{supp}(\rho) ; \tag{5.34}$$

$$DS''(z) + cS'(z) = r(\bar{y}(z))\rho(z)S(z) . \tag{5.35}$$

Considering a biological scenario where the oxygen concentration is at equilibrium prior to tumour cell invasion, and recalling that $S(z)$ represents the rescaled oxygen concentration (see Eq. (5.5)), we complement the differential equation (5.35) with the following asymptotic condition:

$$\lim_{z\to+\infty} S(z) = 1 . \tag{5.36}$$

Moreover, since we expect the tumour's core to be hypoxic and, in the travelling-wave framework, this is positioned at $z = -\infty$, a reasonable choice for the other boundary condition that is needed to close (5.35) is:

$$\lim_{z\to-\infty} S(z) = 0 . \tag{5.37}$$

Since $r(\bar{y}(z))\rho(z) \geq 0$ for all z in the domain and $S(z)$ satisfies the boundary conditions given by (5.36) and (5.37), we can invoke the Maximum Principle, which leads us to conclude that:

$$S'(z) \geq 0 , \tag{5.38}$$

which indicates that $S(z)$ is a monotonically non-decreasing function.

Regarding Eq. (5.34), it becomes:

$$\bar{y}'(z) = \frac{\alpha}{c\,\partial^2_{yy}u(z,\bar{y}(z))}\left(\frac{\mathrm{d}r}{\mathrm{d}y}(\bar{y}(z))S(z) + \frac{\mathrm{d}f}{\mathrm{d}y}(\bar{y}(z))\right). \tag{5.39}$$

Given the hypoxia of the tumour core, we consider a travelling-front solution $\bar{y}(z)$ that satisfies the following condition

$$\lim_{z\to-\infty}\bar{y}(z) = Y\,, \tag{5.40}$$

indicating that the cells at the centre of the tumour are in a phenotypic state equivalent to Y, allowing them to proliferate in a hypoxic environment. Since $\partial^2_{yy}u(z,\bar{y}(z)) < 0$, the monotonicity of $\bar{y}(z)$ depends on the analytical forms of $r(y)$ and $f(y)$. Specifically, the first term inside brackets is negative, due to (5.3), whereas the second term is positive, due to (5.4). We aim to ensure that $\bar{y}(z)$ is a monotonically decreasing function. This condition ensures that cells with a high level of hypoxia resistance are concentrated in the hypoxic region, while cells with an aerobic mechanism and lower hypoxia resistance are positioned at the tumour border. Consequently, the following condition must be satisfied:

$$\frac{\mathrm{d}r}{\mathrm{d}y}(\bar{y}(z))S(z) + \frac{\mathrm{d}f}{\mathrm{d}y}(\bar{y}(z)) \geq 0\,. \tag{5.41}$$

Integrating Eq. (5.35) between $-\infty$ and z, we obtain:

$$\begin{aligned} S'(z) + cS(z) &= \int_{-\infty}^{z} S(z')r(\bar{y}(z'))\rho(z')\,dz' \Rightarrow \\ S(z) &= \frac{\displaystyle\int_{-\infty}^{z} S(z')r(\bar{y}(z'))\rho(z')\,dz' - S'(z)}{c}\,. \end{aligned} \tag{5.42}$$

Then, we can assert that

$$S(z) \leq \frac{\displaystyle\int_{-\infty}^{z} S(z')r(\bar{y}(z'))\rho(z')\,\mathrm{d}z'}{c}\,, \tag{5.43}$$

since (5.38) holds.

By substituting this expression into (5.41), we derive a more stringent requirement:

$$\frac{\mathrm{d}r}{\mathrm{d}y}(\bar{y}(z))\frac{\displaystyle\int_{-\infty}^{z} S(z')r(\bar{y}(z'))\rho(z')\,\mathrm{d}z'}{c} + \frac{\mathrm{d}f}{\mathrm{d}y}(\bar{y}(z)) \geq 0\,. \tag{5.44}$$

If this stronger condition is met, then (5.41) is inherently satisfied as well. The required monotonicity is certainly ensured if the travelling wave propagates at a minimum wave speed. This speed, derived from Eq. (5.44), must satisfy the following condition:

$$c \geq c^* = \max_{z\in\mathrm{supp}(z)}\left\{-\frac{\dfrac{\mathrm{d}r}{\mathrm{d}y}(\bar{y}(z))}{\dfrac{\mathrm{d}f}{\mathrm{d}y}(\bar{y}(z))}\left[\int_{-\infty}^{z} S(z')r(\bar{y}(z'))\rho(z')\,\mathrm{d}z'\right]\right\}. \tag{5.45}$$

Provided that the travelling wave propagates at or above this minimum wave speed, $\bar{y}(z)$ is a monotonically decreasing function.

Furthermore, starting from (5.33) and applying the asymptotic condition (5.40), we obtain the following limit for the cell density at the tumour's core:

$$\lim_{z\to-\infty}\rho(z)=\zeta\,, \tag{5.46}$$

being ζ the cell division factor via anaerobic pathways, as previously defined. This is valid since $f(\bar{y}(z))\to\zeta$ and $r(\bar{y}(z))\to 0$ as $\bar{y}(z)\to Y$ and $S(z)\to 0$ as $z\to-\infty$.

Furthermore, if we consider the boundary condition (5.36), we have that $S'(z)=S''(z)=0$ at the limit as $z\to+\infty$. Thus, Eq. (5.35) as $z\to+\infty$ becomes:

$$r(\bar{y}(z))\rho(z)S(z)=0\,. \tag{5.47}$$

Since $r(\bar{y}(z))$ cannot vanish because $\bar{y}(z)$ is a decreasing function and $S(z)$ cannot vanish due to the boundary condition, it follows that $\rho(z)$ must go to zero. As $\rho(z)$ is forced to approach zero, the function $\bar{y}(z)$ halts at the value it has reached.

5.4 Numerical simulations

5.4.1 Numerical method

To numerically solve the problem, we choose a sufficiently large domain $(\boldsymbol{x},y)\in\Omega\times(0,Y)$ with Neumann boundary condition both in the $\boldsymbol{x}$-direction and in the y-direction. For time t and phenotype y, we use finite difference discretization while for the space variable $\boldsymbol{x}$, we use finite element discretization. We choose the time step to be $\Delta t:=T_{\mathbf{end}}/K$ and mesh size in the y-direction to be $\Delta y:=Y/M$ with time steps and grid points

$$t_k=k\Delta t\,,\quad y_j=j\Delta y\,,\quad k=0,1,2,...,K\,,\quad j=0,1,...M\,.$$

Let $\mathcal{T}$ be a triangular mesh of the spatial domain Ω and $T\in\mathcal{T}$ be a general element. We define the finite element space

$$V_h=\{f\in C(\Omega)\,:\,f|_T\in P_1\}\subset H^1(\Omega),$$

where P_1 stands for polynomials with degree at most 1. The numerical approximations of $S(t_k,\boldsymbol{x})$, $n(t_k,\boldsymbol{x},y_j)\in V_h$ are denoted by S^k and n_j^k, respectively.

The time-splitting method is employed to solve the model, allowing the spatial and phenotypic dimensions to be treated separately using distinct numerical techniques. Specifically, we present the main steps for the rescaled system (5.10), but everything can be easily adapted to solve the non-rescaled system (5.6).

From time $t=t_k$ to time $t=t_{k+1}$, the equation for S_ε is solved in two steps. One solves

$$\partial_t S_\varepsilon-\sum_{i=1}^{3}D_i\partial^2_{x_ix_i}S_\varepsilon=0\,.$$

for one time step Δt, followed by solving

$$\partial_t S_\varepsilon=-S_\varepsilon\int_0^Y r(y)\,n_\varepsilon(t,\boldsymbol{x},y)\,\mathrm{d}y\,.$$

for exactly the same time step.

The equation for n_ε is solved in a similar way. We solve sequentially the diffusion part

$$\partial_t n_\varepsilon - \varepsilon \sum_{i=1}^{3} D_i \partial^2_{x_i x_i} n_\varepsilon = 0\,,$$

the mutation part

$$\partial_t n_\varepsilon = \varepsilon \partial^2_{yy} n_\varepsilon\,,$$

and finally the growth part

$$\varepsilon \partial_t n_\varepsilon = \alpha \Big(r(y) S_\varepsilon + f(y) - \rho_\varepsilon \Big) n_\varepsilon\,,$$

with the same time step Δt, where $\rho_\varepsilon(t, \boldsymbol{x}) := \int_0^Y n_\varepsilon(t, \boldsymbol{x}, y)\, dy$. The last equation is relatively difficult to be solved in a fully implicit way. An alternative way is to transform the equation as

$$\partial_t u_\varepsilon = \alpha \Big(r(y) S_\varepsilon + f(y) - \rho_\varepsilon \Big),$$

via $u_\varepsilon = \varepsilon \ln(n_\varepsilon)$, which can be solved more easily.

To balance stability and efficiency, a semi-implicit discretization in time is applied. The detailed schemes read as follows. We solve S^{k+1} from S^k and n_j^k by solving sequentially the two different parts. The diffusion part is solved via standard finite element method to get S^*

$$< S^*, v > + \Delta t \sum_{i=1}^{3} < D_i \partial_{x_i} S^*, \partial_{x_i} v > = < S^k, v >\,, \quad \forall v \in V_h\,, \tag{5.48}$$

where $< \cdot, \cdot >$ denote the standard L^2-inner product over Ω. Then we solve

$$S^{k+1} = S^* - S^{k+1} \Delta t \Delta y \sum_{j=1}^{M} \frac{r_{j-1} n_{j-1}^k + r_j n_j^k}{2}\,, \tag{5.49}$$

where $r_j = r(y_j)$, to get S^{k+1}.

Next, we compute n_j^{k+1} from S^{k+1} and n_j^k by first solving the diffusion component using the standard finite element method to obtain an intermediate value n_j^*

$$< n_j^*, v > + \varepsilon \Delta t \sum_{i=1}^{3} D_i < \partial_{x_i} n_j^*, \partial_{x_i} v > = < n_j^k, v >, \quad \forall v \in V_h, \quad j = 0, 1, \cdots, M\,. \tag{5.50}$$

Then we solve the mutation part to get n_j^{**}

$$\frac{n_j^{**} - n_j^*}{\Delta t} = \varepsilon \frac{n_{j-1}^{**} - 2 n_j^{**} + n_{j+1}^{**}}{(\Delta y)^2}, \quad j = 0, ..., M\,, \tag{5.51}$$

with the Neumann boundary condition $n_{-1}^{**} = n_1^{**}$, $n_{M-1}^{**} = n_{M+1}^{**}$, which can be solved by looping over all elements in the mesh $\mathcal{T}$. Finally we solve the growth part

$$\frac{u_j^{k+1} - u_j^{**}}{\Delta t} = \alpha \left(r_j S^{k+1} + f_j - \rho^{k+1} \right), \quad j = 0, ..., M\,, \tag{5.52}$$

where $r_j = r(y_j)$, $f_j = f(y_j)$ and ρ^{k+1} satisfies the equation,

$$\rho^{k+1} = \Delta y \exp\left(\frac{-\alpha \Delta t}{\varepsilon}\rho^{k+1}\right) \sum_{j=1}^{M} \frac{N_{j-1}^{k+1} + N_j^{k+1}}{2}, \tag{5.53}$$

where

$$N_j^{k+1} = n_j^{**} \exp\left[\frac{\alpha \Delta t}{\varepsilon}\left(r_j S^{k+1} + f_j\right)\right].$$

Equation (5.53) is derived from the relation

$$\rho^{k+1} = \Delta y \sum_{j=1}^{M} \frac{n_{j-1}^{k+1} + n_j^{k+1}}{2},$$

by combining $u_j^k = \varepsilon \ln(n_j^k)$ and (5.52). This equation can be solved using root-finding algorithms, such as the bisection method. Once ρ^{k+1} is determined, equation (5.52) can be easily solved.

5.4.2 Rescaled model for small ε in one dimensional domain

Initially, we conduct a numerical exploration of the dynamics associated with the ε-rescaled model, described in Subsection 5.3.1. To compare the numerical results with the analytical conclusions obtained from the traveling wave analysis, we perform the numerical simulations in a one-dimensional domain. Accordingly, the system of equations is represented by (5.10), rewritten in a one-dimensional setting and implemented with the following set of initial conditions:

$$\begin{aligned} n_\varepsilon(0,x,y) &= C e^{-x^2} e^{-\frac{(y-0.5)^2}{\varepsilon}}, \text{ with } C \text{ s.t. } C\int_0^Y e^{-\frac{(y-0.5)^2}{\varepsilon}}\,\mathrm{d}y = 1, \\ \rho_\varepsilon(0,x) &= \int_0^Y n_\varepsilon(0,x,y)\,\mathrm{d}y, \quad S_\varepsilon(0,x) = 1 - \rho_\varepsilon(0,x). \end{aligned} \tag{5.54}$$

The numerical results are obtained under the following conditions

$$Y := 1, \quad r(y) = 1 - y^2, \quad f(y) = \zeta\left[1 - (1-y)^2\right].$$

We use a uniform discretization with steps Δt, Δx and Δy for the intervals $(0, T]$, $(0, L)$ and $(0, 1)$, respectively, as computational domains of the independent variables t, x and y. Moreover, the parameter α is set to 1 day^{-1}, and the parameter ζ is taken equal to 0.1. Typical dynamics are depicted in Fig. 5.1, where we present the cell density $\rho_\varepsilon(t,x)$, the dominant trait $\bar{y}_\varepsilon(t,x) = \max_{y\in[0,1]} n_\varepsilon(t,x,y)$, and the oxygen concentration $S_\varepsilon(t,x)$ at two different time step.

Moreover, oxygen is consumed in the tumour's centre, creating a hypoxic region, while it remains at 1 in areas where cell invasion has not yet occurred. We observe that $\bar{y}_\varepsilon(t,x)$ is a decreasing function, starting at 1 in the centre of the tumour and decreasing to zero towards the edge. We verify condition (5.45), and it is found to be satisfied. Specifically, the propagation speed of the travelling wave solution, that can be evaluated from the slopes of the curves reported in the inset of Fig. 5.1, aligns with the value c^* on the right-hand side evaluated numerically. Conversely, the cell density increases until it reaches its maximum value at the tumour's edge. In the centre of the tumour, this density is not zero but equal to ζ, indicating that cells can still proliferate in hypoxic regions, due to their adaptation to oxygen deprivation. Finally, if we plot the rescaled

cell population distribution $n_\varepsilon(t,x,y)/\rho_\varepsilon(t,x)$, the outcomes are illustrated in the second column of Figure 5.1. We can observe that in the central region of the tumour, the tumour cells exhibit, on average, a phenotype closer to 1, allowing them to proliferate in the hypoxic environment. Conversely, at the tumour edge, the majority of the cells have a phenotype closer to 0, which is more efficient for their proliferation in the presence of oxygen. It is important to note that the graphs are plotted for $x \in \mathrm{supp}(\rho_\varepsilon)$. The numerical results presented in this work align well with biological evidence observed in tumour spheroids, particularly in avascular conditions. Indeed both experimental tests [97, 187, 233, 476, 509] and previous mathematical studies [190, 202, 404] provide insights into the metabolic and proliferative dynamics within tumour spheroids that corroborate the numerical findings. Specifically, avascular tumour spheroids are characterized by a proliferative rim composed of a small number of cells that primarily utilize aerobic metabolism, although not exclusively. Moving inward, the quiescent rim and necrotic core of the spheroid contain only a few viable cells. These cells are unable to rely on aerobic metabolism due to hypoxia and instead rely on glycolysis, consuming glucose to sustain minimal survival.

5.4.3 Non-rescaled model in a square domain

We consider the dynamics associated with the non-rescaled model, described by the system of equations (5.6), in a simplified setting. The simulations are performed in a two-dimensional square domain. The system is solved with the following set of initial conditions

$$\begin{aligned} \hat{n}(0,\boldsymbol{x},y) = Ce^{-\boldsymbol{x}^2}e^{-\frac{(y-0.2)^2}{0.1}}\,, \text{ with } C \text{ s.t. } C\int_0^Y e^{-\frac{(y-0.2)^2}{0.1}}\,\mathrm{d}y = 1\,, \\ \hat{\rho}(0,\boldsymbol{x}) = \int_0^Y \hat{n}(0,\boldsymbol{x},y)\,\mathrm{d}y\,, \quad \hat{S}(0,x) = 1-\hat{\rho}(0,\boldsymbol{x})\,. \end{aligned} \tag{5.55}$$

The numerical results are obtained in the case where

$$Y := 1\,, \quad r(y) = 1-y^2\,, \quad f(y) = \zeta\left[1-(1-y)^2\right]\,. \tag{5.56}$$

The diffusion tensors $\mathbf{D}_n(\boldsymbol{x})$ and $\mathbf{D}_S(\boldsymbol{x})$ are chosen of the following form

$$\mathbf{D}_n(\boldsymbol{x}) := D_n\mathbf{D}(\boldsymbol{x}) \text{ and } \mathbf{D}_S(\boldsymbol{x}) := D_S\mathbf{D}(\boldsymbol{x})\,, \tag{5.57}$$

where $\mathbf{D}(\boldsymbol{x}) = \mathrm{diag}(D_1, D_2)$ is a diagonal tensor, which may be anisotropic for $D_1 \neq D_2$. Specifically, to highlight the effect of anisotropy on cell dynamics, we set $D_1 = 1.6$ and $D_2 = 0.4$. Numerical solutions are constructed using a uniform discretization of the square $[-L,L]\times[-L,L]$, with $L = 75$ mm, as the computational domain of the independent variable $\boldsymbol{x}$ and a uniform discretization of the set $[0,1]$ as the computational domain of the independent variable y. We also use a uniform step for the time interval $[0,T]$. Unless otherwise explicitly stated, we use the values of the model parameters listed in Table 5.1, which are chosen to be consistent with the existing literature. Typical dynamics are depicted in Figure 5.2, where we present the cell density $\hat{\rho}(t,\boldsymbol{x})$, the dominant trait $\bar{y}(t,\boldsymbol{x})$, and the oxygen concentration $\hat{S}(t,\boldsymbol{x})$ at $t = 60$ days and $t = 100$ days.

The numerical results align with the behaviours observed during the analysis of the equations, except for anisotropy, which is not captured by the formal asymptotic analysis. The cell density is lower at the centre of the tumour and increases towards

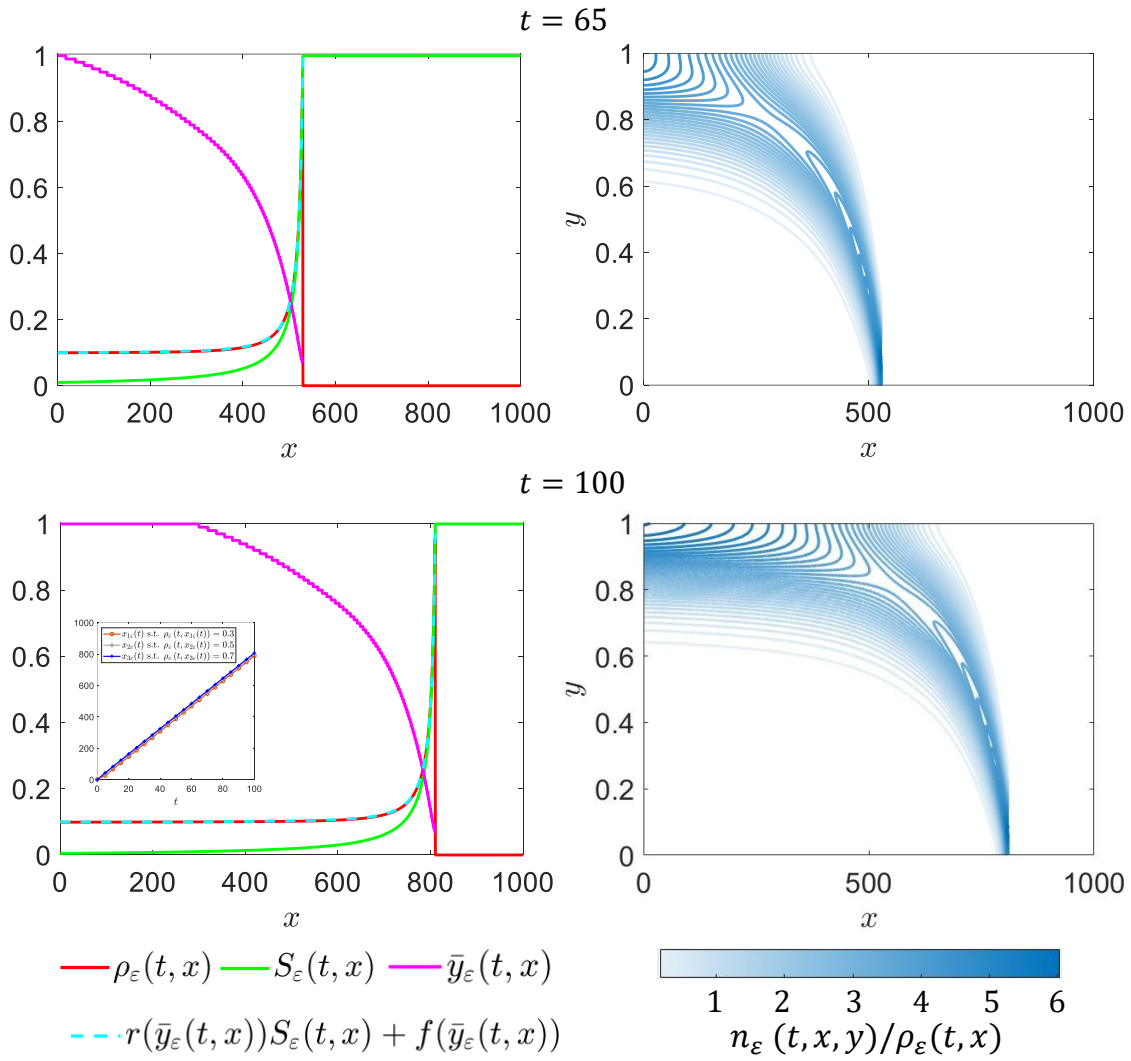

FIGURE 5.1: First column: The dominant trait $\bar{y}_\varepsilon(t,x)$, the cell density $\rho_\varepsilon(t,x)$ and the oxygen concentration $S_\varepsilon(t,x)$ at $t = 65$ and $t = 100$. Second column: Normalised cell population distribution $n_\varepsilon(t,x,y)/\rho_\varepsilon(t,x)$ at $t = 65$ and $t = 100$, where the contour lines transition from light to dark, indicating increasing density, as shown in the bottom-right colour bar. The inset of the bottom left panel displays the plots of $x_{1\varepsilon}(t)$ (red), $x_{2\varepsilon}(t)$ (green) and $x_{3\varepsilon}(t)$ (blue) such that $\rho_\varepsilon(t, x_{1\varepsilon}(t)) = 0.3$, $\rho_\varepsilon(t, x_{1\varepsilon}(t)) = 0.5$ and $\rho_\varepsilon(t, x_{1\varepsilon}(t)) = 0.7$. The slope of the curves, which is consistent across the three values of ρ_ε considered, allows us to compute the velocity of the travelling wave.

Par.	Biological meaning	Value	Ref.
ρ_0	Carrying capacity for cell density	$3.183 \cdot 10^5$ cells/cm^2	[230]
S_0	Reference value for oxygen concentration	$6.3996 \cdot 10^{-7}$ g/cm^2	[300, 503]
$\hat{v}$	Scaling factor for cell consumption of oxygen	9.95	[330, 503]
α	Basal proliferation rate	0.864 1/day	[330]
ζ	Cell division factor via anaerobic pathways	0.1	[221, 330]
β	Rate of phenotypic changes	$8.64 \cdot 10^{-8}$ 1/day	[181, 503]
D_n	Diffusion coefficient of glioma cells	0.13 mm^2/day	[480]
D_S	Diffusion coefficient of oxygen	86.4 mm^2/day	[246, 503]

TABLE 5.1: List of the values of the model parameters employed in the numerical simulations.

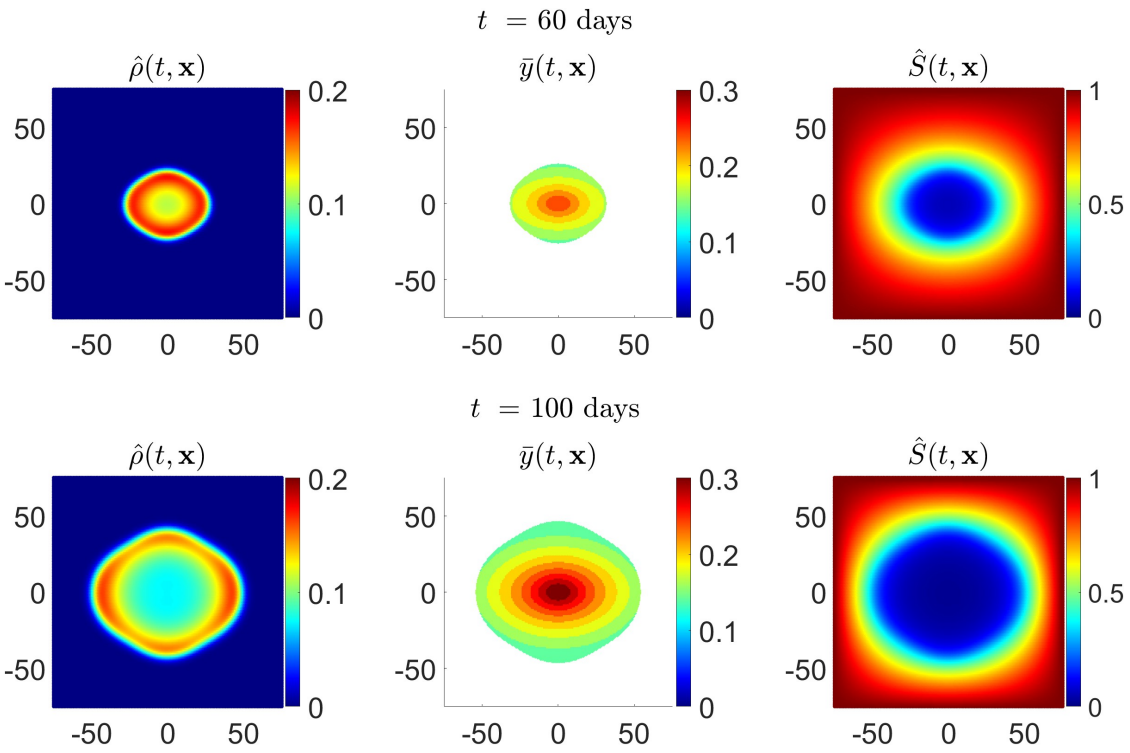

FIGURE 5.2: Cell density $\hat{\rho}(t, \boldsymbol{x})$, dominant trait $\bar{y}(t, \boldsymbol{x})$, and the oxygen concentration $\hat{S}(t, \boldsymbol{x})$ at $t = 90$ days and $t = 100$ days.

the tumour's edge, where the oxygen concentration is higher. Additionally, the phenotypic trait is higher at the centre and decreases toward the tumour's periphery. Oxygen consumption is observed in tumour-affected areas, while the oxygen level remains at value 1 far from the tumour. Furthermore, in this 2D setup, we also observe the influence of anisotropy on the phenotypic trait. At the tumour's edge, the phenotype tends to be higher in the preferential growth directions and lower in others. A higher dominant phenotype corresponds to cells with a greater predisposition to anaerobic metabolism, and the finding that these cells are concentrated along the main direction of tumour growth aligns with the well-established Warburg effect [286, 316, 509]. This phenomenon describes how cancer cells, even in the presence of oxygen, preferentially rely on glycolytic pathways, as this metabolic strategy enhances their invasive potential within the surrounding tissue. The qualitative agreement between the numerical results and the biological evidence supports the validity of the computational approach and its relevance in understanding tumour dynamics in anisotropic and resource-limited environments. We note that in this model, the dominant phenotype is primarily influenced by oxygen availability and its anisotropic diffusion, whereas the Warburg effect depends on a variety of cellular mechanisms. Nevertheless, the observed connection to the Warburg effect underscores its broader biological significance. Further investigation into this relationship could be pursued with slight modifications to the current model (see e.g. [181]), providing deeper insights into the interplay between metabolic strategies and tumour invasion dynamics.

5.4.4 Non-rescaled model in brain domain

Finally, we aim to perform a simulation using real brain geometry. The first step involves constructing the computational mesh, created using Magnetic Resonance Imaging (MRI) data from a single patient, acquired during routine clinical practice at the Istituto Neurologico Carlo Besta in Milan, Italy. The diffusion tensors, defined as in (5.57), are derived from Diffusion Tensor Imaging (DTI) data [36, 57]. These data are used to construct $\mathbf{D}(\boldsymbol{x})$, which represents the spatially varying directions of diffusion. DTI provides a symmetric, positive-definite tensor that describes water diffusivity within each voxel. The diagonal elements of this tensor correspond to the apparent diffusivities along the principal measurement axes, while the off-diagonal elements quantify the correlations between molecular displacements in orthogonal directions. Finally, all the components of the tensor are normalised by the mean diffusivity, ensuring that the resulting tensor reflects only the principal directions of diffusion. By capturing the anisotropic diffusion of water molecules, DTI facilitates the identification and visualisation of white matter tract orientations and the preferential directions of cell migration. This functionality is essential for modelling processes such as tumour infiltration in brain tissues.

First, we segmented the MRI grey-scale images to partition them into segments and label each pixel to reconstruct the brain's boundary. This process can be carried out using software packages such as *Slicer3D* [1]. After segmentation, the computational mesh was constructed using *Tetgen* [492], a tool for generating tetrahedral meshes of any 3D polyhedral domain. Then, to incorporate DTI data into our model, the six images from DTI, corresponding to the six independent components of the diffusion tensor, needed to be aligned with the MRI images. This alignment was achieved using *FSL* (FMRIB Software Library) [185]. Once the images were aligned, the six components of the tensor $\mathbf{D}(\boldsymbol{x})$ were integrated into the computational mesh built from the MRI data using custom scripts implemented in the *VMTK* software library [493].

The mathematical model we solve is given by the system (5.6), with initial conditions (5.55) and assumptions (5.56)-(5.57). The parameters used are summarised in Table 5.1. The results are shown in Figure 5.3.

Similar to the anisotropic case studied in Section 5.4.3, it can be observed that the cell density is higher at the periphery of the tumour, where oxygen availability is greater. Furthermore, in the brain environment, the influence of anisotropy is more pronounced, aligning with the direction of the surrounding white matter tracts, obtained from the patient data. Additionally, the dominant phenotype is more prevalent at the tumour centre and decreases toward the tumour edge. This simulation highlights how anisotropy also affects the phenotypic traits of the cells. Indeed, as observed in the simulations for the simplified 2D setting, at the tumour's edge, the phenotype tends to be higher in the preferential growth directions and lower in others. This finding indicates that in regions of higher expansion, cells exhibit a greater predisposition to anaerobic metabolism. Furthermore, at the tumour boundary, regions where the phenotypic trait is higher also show an increased cell density. Also in this case, the anisotropic distribution of nutrients is evident from the simulations.

We observe that the simulated tumour corresponds to a highly invasive mass. To facilitate comparisons with clinical references, we computed several tumour growth metrics commonly employed in the biomedical literature. At $t = 35$ days, the final tumour volume reaches $29870.8\,\mathrm{mm}^3$, reflecting a substantial increase in size. This result was obtained by applying a threshold to differentiate tumour tissue from non-tumour tissue, with the threshold set at $\hat{\rho}(t, \boldsymbol{x}) \geq 0.05$, corresponding to a cell density of 5% of the tumour's carrying capacity. More specifically, we find a volume doubling time (VDT)

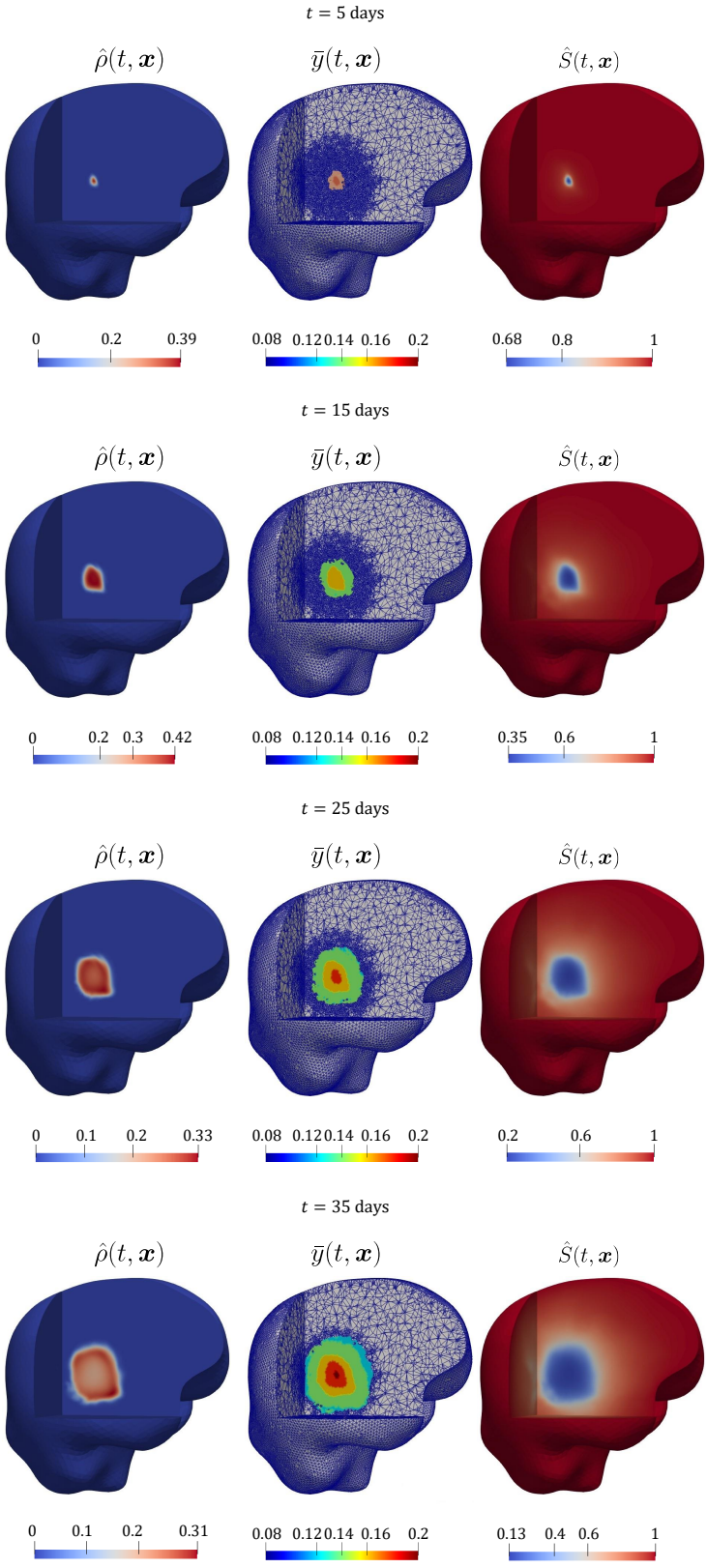

FIGURE 5.3: Cell density $\hat{\rho}(t, \boldsymbol{x})$, dominant trait $\bar{y}(t, \boldsymbol{x})$, and the oxygen concentration $\hat{S}(t, \boldsymbol{x})$ at $t = 5$ days, $t = 15$ days, $t = 25$ days and $t = 35$ days.

of approximately 7.14 days, indicating that the tumour is growing substantially faster than the average data reported in clinical studies. For comparison, Stensjøen et al. [461] reported a median VDT of 29.8 days, while Ellingson et al. [168] found a median VDT of 21.1 days. Furthermore, it is worth noting that, in our simulation, the cell density remains relatively low, denoting a diffusely distributed invasion. This pattern suggests that the tumour grows predominantly by spreading its cells outward over a larger area, rather than by increasing the concentration of cells in its immediate vicinity through rapid cell division. This behaviour is characteristic of highly invasive tumour types, where diffusion dominates over local cell proliferation.

Moreover, the specific growth rate (SGR), or percentage increase per unit time, defined as $(\ln 2)/\mathrm{VDT}$, is 9.71% per day, which is higher compared to the values reported in the aforementioned references. However, we emphasize that such measures are often computed in the clinical literature by assuming simplified growth law, which might alter the metrics obtained.

Another parameter frequently used to quantify brain tumour growth is the average radial expansion velocity (VRE). In our simulation, the VRE is approximately $v_{\mathrm{RE}} \approx 0.53\,\mathrm{mm/day}$. As expected, this value exceeds those reported in the model presented by [48] and in clinical studies [461, 505], although it is important to note the significant variability observed between individual patients. Furthermore, this parameter is typically calculated under the assumption of isotropic growth, which does not align with the anisotropic nature of our model.

To obtain more realistic results, additional simulations were performed by reducing the parameters in the tumour cell distribution equation, specifically the diffusion coefficient D_n and the basal proliferation rate α, to two-thirds of their original values. The results of these simulations are shown in Fig. 5.4, highlighting the impact of reduced diffusion and proliferation rates on tumour growth dynamics. In this simulation, we observe that at $t = 35$ days, the final tumour volume is reduced to $9166.42\,\mathrm{mm}^3$, markedly lower than in the previous simulation. These results emphasise the crucial importance of precise parameter calibration to improve the model's predictive accuracy.

5.5 Summary

In this Chapter, we presented a mathematical model to describe the growth of brain tumours by incorporating phenotypic heterogeneity among tumour cells. The model employs reaction-diffusion equations with non-local reaction terms to capture the complex spatial dynamics and evolutionary trajectories of tumour cell populations under varying oxygen concentrations. According to our model, regions of the tumour with high oxygen levels will be densely populated by cancer cells with an aerobic metabolism. In contrast, hypoxic regions with lower oxygen concentrations will be colonised by cells with reduced proliferation rates.

Our modelling framework provides a theoretical basis for experimental observations that suggest the periphery and centre of avascular tumours function as distinct ecological niches [81, 247, 322, 528]. Additionally, histological studies show that solid tumours contain cancer cells with a wide range of gene expression profiles. Our theoretical findings align with the ideas proposed by Alfarouk et al. [14], who argued that cancer cell phenotypes are shaped, to some extent, by predictable spatial gradients of abiotic factors (such as oxygen), which can be visualised using non-invasive imaging techniques [66]. From this perspective, understanding how abiotic factors influence the

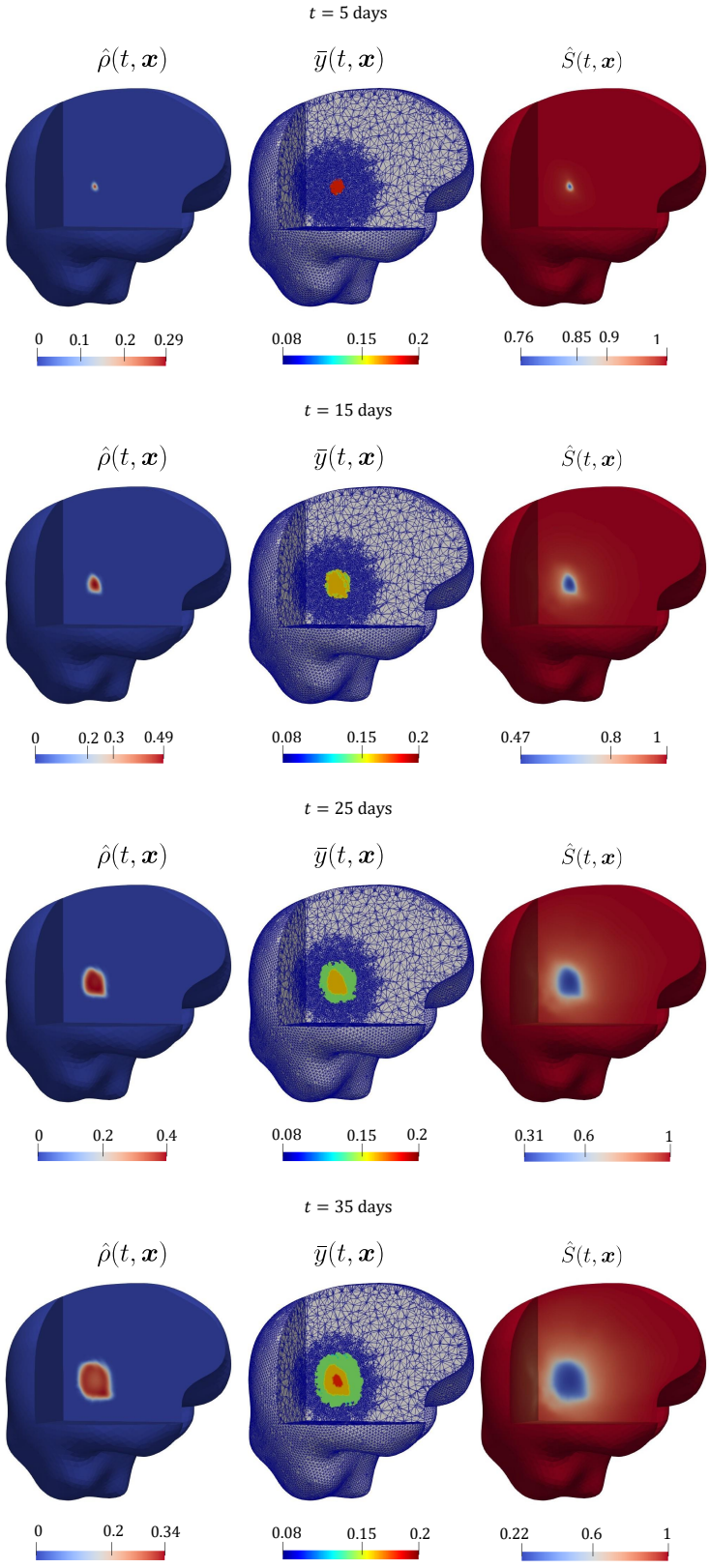

FIGURE 5.4: Cell density $\hat{\rho}(t, \boldsymbol{x})$, dominant trait $\bar{y}(t, \boldsymbol{x})$, and the oxygen concentration $\hat{S}(t, \boldsymbol{x})$ at $t = 5$ days, $t = 15$ days, $t = 25$ days and $t = 35$ days using reduced diffusion coefficients D_n and D_S.

phenotypic characteristics of cancer cells could allow spatial patterns of tumour perfusion, reconstructed from clinical images, to guide the selection of molecularly targeted therapies.

The main findings of our study include a comprehensive formal asymptotic analysis, which provides valuable insights into the long-term behaviour of tumour cell populations and the influence of phenotypic diversity. We carried out this analysis on the non-local PDEs (5.10) in the asymptotic limit as $\varepsilon \to 0$, using a Hamilton-Jacobi framework. In particular, we showed that $\bar{y}(t, \boldsymbol{x})$, which represents the dominant phenotypic trait at position $\boldsymbol{x}$ and time t, satisfies the transport equation (5.23). This transport equation can be interpreted as a generalised canonical equation of adaptive dynamics [154], describing the spatio-temporal evolution of the dominant phenotypic trait. Furthermore, we found that $\rho(t, \boldsymbol{x})$, the total cell density, is governed by the relation (5.19). We also explored travelling wave solutions, which allowed us to characterise the expected behaviour of $\bar{y}(z)$, $\rho(z)$, and $S(z)$, providing a deeper understanding of the tumour's growth dynamics under different conditions.

Numerical simulations were initially conducted on a simplified 1D domain to validate the analytical results. Subsequently, simulations were extended to a 2D domain and a realistic 3D brain geometry, reconstructed from MRI and DTI data. The parameter values for these simulations were sourced from existing literature. The simulations effectively demonstrate the model's capability to replicate key characteristics of tumour growth, including the spatial distribution of cell density, the phenotypic diversity of cells, and oxygen concentration gradients. The results underscore the critical role of anisotropic diffusion in the brain and its influence on tumour invasion patterns.

Future developments of this work could involve extending the model to incorporate additional biological factors, such as the influence of acidity on the evolutionary dynamics of cancer cells, and developing more sophisticated representations of tumour micro-environments. It would also be beneficial to include the effects of various therapies, as resistance to hypoxia is known to correlate with resistance to chemotherapy and radiotherapy [131, 142, 315, 415]. Furthermore, ongoing validation against experimental data and clinical observations is essential for refining model parameters and enhancing its relevance to real-world applications. For instance, Magnetic Resonance Spectroscopy (MRS), an advanced MRI technique, provides insights into the concentrations of water-soluble metabolites, enabling the detection of tumour-specific mutations and the assessment of intratumoural heterogeneity. MRS is frequently employed to study metabolic alterations within tumours, offering valuable information about tumour grade and aggressiveness. Integrating such data could significantly improve the precision and predictive capabilities of our model. Finally, it would be valuable to incorporate the effects of stress-induced phenotypic changes caused by hypoxia, thereby integrating phenotypic heterogeneity into a mechanical framework, such as the ones presented in [48, 338]. Therefore, we believe that this work paves the way for a better understanding, through mathematical modelling, of the phenotypic cellular distribution within tumour masses in highly anisotropic environments, also considering patient-specific data, with the potential to target therapies more effectively.

6 Multiscale homogenization for blood and nutrient transport in vascularized tumours

6.1 Preliminaries

Asymptotic homogenisation is a widely-used upscaling technique designed to analyse and model multiscale systems, where phenomena manifest across different scales, see, e.g., [42, 360, 391] on classic, formal, homogenisation for composites, as well as [122] on more rigorous aspects concerning the two-scale convergence.

By exploiting the separation of scales, asymptotic homogenisation enables a systematic transition from detailed microscopic descriptions to simplified macroscopic models, while preserving essential microscale information encapsulated in effective parameters at a reduced computational cost [398]. The method involves expanding the system's variables in terms of a small parameter that represents the ratio between microscopic and macroscopic scales. Through this expansion, a hierarchy of equations emerges, describing the system's behaviour at different scales. Homogenising these equations allows for the derivation of effective properties and governing equations at the macroscopic level. These effective equations typically include parameters that reflect the influence of the underlying microscale structures, thus bridging the gap between intricate microscale behaviour and observable macroscale phenomena.

The multiple scales method has proven to be highly effective in a wide range of physical systems, particularly in the analysis of porous media flow [258]. These systems normally exhibit different hierarchical levels of organization related to different, typically increasingly larger length scales associated for example with the size of the pores, distance between individual branches of interconnected networks, and size of the overall domain. Relevant application of the asymptotic homogenisation technique to hierarchical porous materials include, for example, geomaterials [31, 339], which can for instance play a role in the drainage of disposed liquid, oil and gas extraction, consolidation, as well as glaciers and aquifers dynamics, industrial applications, such as filters' optimisation [135] as well as biological and bio-inspired tissues. The latter include, but are not limited to, bone and tendons [396], implants [159], and organs, such as the brain [143], the heart [367]), the lymphatic system [214, 435], as well as healthy [382] and malignant cell aggregates, e.g. avascular [152, 419] and vascular tumours [397, 399, 451].

The framework developed in the latter works is particularly valuable for studying the intricate interactions between tumour growth and drug [486] and nutrients transport in the surrounding capillary network. Tumours depend on blood vessels to supply essential nutrients and oxygen, a process driven by angiogenesis [97]. However, the vasculature formed through angiogenesis is often irregular and heterogeneous, resulting in

spatial variations in fluid flow and nutrient distribution. Understanding the dynamics of flow and chemical exchange between this complex vasculature and the tissue and its impact on tumour growth is critical for deepening our knowledge of cancer progression and enhancing the development of more effective treatments.

Therefore, in this study, we apply asymptotic homogenisation to model transport processes within a tissue, that might represent a tumour mass, with an embedded vascular capillary network, incorporating microscale effects such as vessel geometry and flow patterns into a macroscopic framework. By assuming a distinct separation of scales between the typical vessel spacing and the characteristic length of the tissue, we derive differential equations governing the macroscale behaviour of the tissue and fluid and nutrient transport. Our methodology involves formulating a system of differential equations through non-dimensionalisation and scaling, with the asymptotic expansion parameter representing the ratio of vessel distance to the characteristic tissue length scale. The resulting macroscale model for fluid dynamics in the vascular domain is governed by Darcy's law, determining the velocity and pressure fields. In the tumour domain, the dynamics of the ensemble of fluids and cells is described by a modified Darcy's law, where nutrient concentration significantly influences flow. Nutrient transport is modelled across both domains using a coupled advection-diffusion-reaction system, and the interaction between tissue and vascular network is captured through effective mass source terms, reflecting the exchange of nutrients and other essential substances. Effective parameters in the model, which account for the role of microvascular geometry, are computed by solving cell-level differential equations that are coupled with the macroscale governing equations. Although this multiscale coupling poses significant computational challenges, it is possible to obtain computationally manageable systems by assuming additional constraints on the model parameters.

We remark that, despite the specific application presented, the developed mathematical method is general and can be applied to the description of other problems in different contexts governed by stationary balance equations and chemical exchange processes, typically modeled by diffusion-advection-reaction problems. Notable examples include the transport of nutrients from tree roots into the soil [294], or a system of aquifers exchanging liquids and chemicals with the surrounding rock domain [72, 441], as well as peatlands [345].

The Chapter is organised as follows: Section 6.2 introduces the asymptotic homogenisation technique and explains its fundamental principles and key concepts. Section 6.3 presents the balance equations and their corresponding boundary and interface conditions within the physical domain, distinguishing between the tumour tissue and vessel compartment. Section 6.4 introduces the governing equations in a non-dimensional form. Section 6.5 applies a two-scale asymptotic expansion to derive the effective governing equations that describe the physical behaviour at the tissue scale. In Subsection 6.5.2, we explore a particular case that simplifies the computational complexity of the model, making it more tractable for numerical investigation in future work. Finally, Section 6.6 offers concluding remarks and future research perspectives.

The majority of the content in this chapter stems from an international collaboration with Raimondo Penta from the School of Mathematics and Statistics at the University of Glasgow. The material has been documented in the paper by Ballatore, Giverso, and Penta *"Effective macroscopic equations for biological fluid and nutrients' transport in vascularized tumours growing via proliferation and chemotaxis"* submitted for publication.

6.2 Fundamentals of asymptotic homogenization theory

Physical systems in the real world are intrinsically multiscale, exhibiting complex geometries, pronounced heterogeneities, and interactions across various levels of organisation. From a modelling perspective, the primary aim is to represent these phenomena in a manner that enables both qualitative insights and quantitative predictions, validated against experimental observations. Achieving this, however, poses significant challenges due to two key factors:

1. resolving the full microscale complexity of materials and geometries is computationally impractical for three-dimensional problems;
2. experimental data often represent averages at the macroscale, obscuring finer structural details.

To address these challenges, mathematical methodologies have been developed to construct macroscopic descriptions that retain the critical effects of microstructural features. Among these approaches, asymptotic homogenization has emerged as a robust and versatile tool, leveraging the distinct separation of scales characteristic of multiscale systems. By employing a power series expansion of the fields, this technique derives macroscopic partial differential equations (PDEs) with coefficients (such as hydraulic conductivity, diffusivity, or stiffness) that encode the impact of the underlying microstructure.

In what follows, we outline the fundamental assumptions underlying the asymptotic homogenization method [40, 251, 360, 391, 398], which serve as the foundation for the analyses conducted throughout this Chapter.

Assumption I: Length scale separation It is assumed the existence of two distinct spatial scales, the microscale d and the macroscale L, such that their ratio satisfies:

$$\varepsilon = \frac{d}{L} \ll 1.$$

This parameter quantifies the spatial disparity between the two scales.

Assumption II: Spatial variations decoupling It is further assumed that the unknown fields and the coefficients of the model taken into account depend on two formally independent spatial variables:

$$\begin{aligned} \boldsymbol{x}\,, &\quad \text{the macroscale variable,} \\ \boldsymbol{y} = \frac{\boldsymbol{x}}{\varepsilon}\,, &\quad \text{the microscale variable.} \end{aligned}$$

This decoupling assumption enables the description of the fields and the coefficients involved as functions of both $\boldsymbol{x}$ and $\boldsymbol{y}$, where $\boldsymbol{x}$ captures the slow spatial variations on the macroscale and $\boldsymbol{y}$ represents the rapid oscillations on the microscale. As a direct consequence of Assumption II, derivatives with respect to the physical spatial scale are now interpreted as total (material) derivatives, meaning:

$$\nabla \to \nabla_{\boldsymbol{x}} + \frac{1}{\varepsilon}\nabla_{\boldsymbol{y}}\,. \tag{6.1}$$

Assumption III: Power series expansion The multiscale unknown fields are assumed to be representable as a regular expansion in a power series of ε. Specifically, for a generic unknown field ψ, this can be expressed as:

$$\psi(\boldsymbol{x}, \boldsymbol{y}, t) \equiv \psi^{\varepsilon}(\boldsymbol{x}, \boldsymbol{y}, t) = \sum_{l=0}^{\infty} \psi^{(l)}(\boldsymbol{x}, \boldsymbol{y}, t)\varepsilon^{l} .$$

Assumption IV: Regularity and local periodicity It is assumed that every field and coefficient preserves, with respect to the macroscale variable $\boldsymbol{x}$, the same level of smoothness that characterizes the original fields.

Furthermore, a family of vectors is assumed to exist:

$$\mathbf{R}(\eta, \kappa, v) := \eta \mathbf{I}_1 + \kappa \mathbf{I}_2 + v \mathbf{I}_3 , \quad \eta , \kappa , v \in \mathbb{Z} ,$$

with fixed vectors $\mathbf{I}_1$, $\mathbf{I}_2$ and $\mathbf{I}_3 \in \mathbb{R}^3$ that constitute a basis of $\mathbb{R}^3$, such that, for every generic field ψ we have:

$$\psi(\mathbf{x}, \mathbf{y}) = \psi(\mathbf{x}, \mathbf{y} + \mathbf{R}(\eta, \kappa, v)) , \quad \forall \eta , \kappa , v \in \mathbb{Z} .$$

It is possible to notice that this assumption is stated for arbitrarily shaped periodic cells and that rectangular (cuboid in three dimensions) periodic cells are simply obtained assuming $\mathbf{I}_1 \propto \boldsymbol{e}_n$ for every n.

The assumption of periodicity at the microscale is primarily driven by practical considerations, as it allows the reconstruction of microscopic information by focusing on a limited portion of the microstructure, specifically the periodic cell. However, this assumption is not strictly required to derive the homogenized problem. In fact, the analytical formulation of the microstructural problem could have been developed under the assumption of local boundedness instead.

Assumption V: Macroscopic uniformity In the following, it is also assumed macroscopic uniformity, meaning that the periodic cell itself does not depend on the macroscale variable $\boldsymbol{x}$. This is a common assumption in asymptotic homogenisation, as illustrated for instance in [400], and it is equivalent to assuming that we can identify the microscale domain with a single periodic cell, which is the same for every point of the macroscale domain [251]. Generalization to non-macroscopic uniformity can be carried out via different approaches (see, e.g., [397] versus [135]). Thus it holds [399]:

$$\nabla_{\boldsymbol{x}} \cdot \int_{\Omega} (\bullet) d\boldsymbol{y} = \int_{\Omega} \nabla_{\boldsymbol{x}} \cdot (\bullet) d\boldsymbol{y} . \tag{6.2}$$

6.3 Balance equations

In this Section, we present the mathematical model taken into account. We consider a domain $\Omega \subset \mathbb{R}^3$, where $\Omega = \Omega_t \cup \Omega_v$, with Ω_t and Ω_v representing the tumour tissue and the vessel network, respectively. The flow of fluid in both domains, as well as the motion of the ensemble of cells, treated as a fluid, in the tissue region must satisfy mass and momentum balances, which vary in form depending on the specific portion of the domain under consideration. The movement and proliferation of cells are guided by the availability of nutrients. The chemical transport in both regions obeys an advection-diffusion-reaction equation, with different coefficients in each domain. The final problem thus involves determining the unknown fields of interest, namely the pressure p,

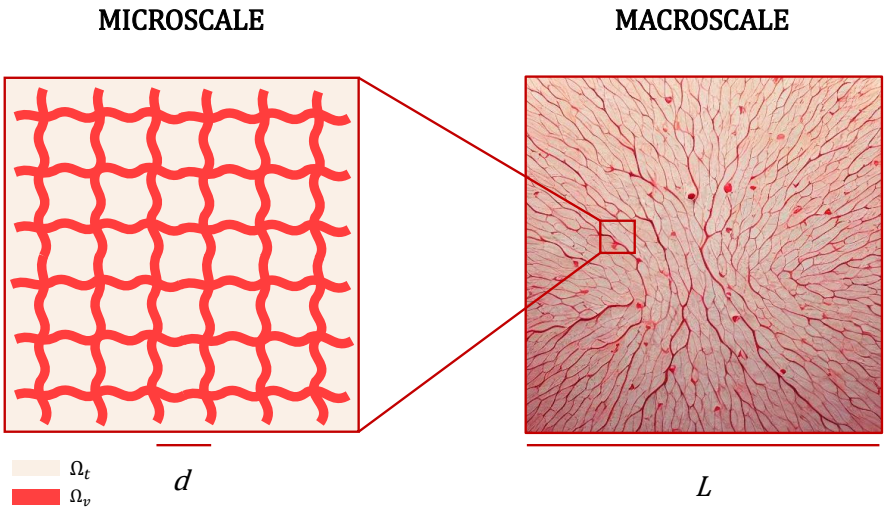

FIGURE 6.1: A 2D schematic representation of the microscale and macroscale domains. This illustration highlights the distinction between the microscale dimension d and the typical macroscale dimension L, which defines the homogenized domain where the detailed vessel geometry is averaged and smoothed out.

the velocity $\boldsymbol{u}$, and the concentration of the nutrients c, which are functions of both space $\boldsymbol{x}$ and time t. The restrictions of these fields to the tissue and vessel compartments are denoted by the subscripts t and v, respectively. We will first analyze the fluid and nutrients transport in each portion of Ω, followed by establishing appropriate interface conditions on $\Gamma = \partial\Omega_t \cap \partial\Omega_v$ to finalize the coupled differential problem. To apply asymptotic homogenization techniques, we further assume that the typical mean distance between fluid vessels, d, is small compared to the characteristic length L of the tissue domain (see Figure 6.1). This assumption aligns with the biological scenario considered, as the characteristic intercapillary distance is on the order of $50\,\mu$m [313], whereas the characteristic size of a vascular tumour can range from a few millimetres to centimetres [101, 186]. Therefore, we define the appropriate spatial scale ratio as

$$\varepsilon = \frac{d}{L} \ll 1\,. \tag{6.3}$$

6.3.1 Tumour tissue domain

The tumour region Ω_t is considered as a porous medium composed of a mixture of cells and biological fluid, flowing through a rigid scaffold of extracellular matrix. The extracellular porous scaffold is assumed to be homogeneously distributed in Ω_t and to be neither produced nor degraded by cells. Furthermore, the interstitial fluid and the cells can be collectively treated as a single Newtonian fluid, to which Darcy's law is applicable [24, 92, 217]. Thus, inside Ω_t, the biological fluid velocity $\boldsymbol{u}_t$ is related to the gradient of the pressure field p_t through the symmetric and positive-definite second-order tensor K, which is related to permeability of the medium and the viscosity of the fluid phase. Therefore the following relation holds

$$\boldsymbol{u}_t = -\mathsf{K}(\boldsymbol{x})\nabla p_t \quad \text{in } \Omega_t\,. \tag{6.4}$$

Additionally, the ensemble of cells and biological fluid inside Ω_t should satisfy the mass balance law. Assuming the intrinsic incompressibility of the biological material, which is mostly composed by water, it is possible to take the density of ensemble of cells and liquid constant in time, so that the following equations describe the behaviour inside Ω_t

$$\nabla \cdot \boldsymbol{u}_t = \Gamma_t(c_t) + \nabla \cdot \boldsymbol{m}_i(c_t) \quad \text{in } \Omega_t \,. \tag{6.5}$$

The first term on the r.h.s. of (6.5) represents volumetric growth, while the second term corresponds to a non-convective mass flux. Both terms may be influenced by nutrient availability (along with other potential factors), represented, in this work, by a single general nutrient species (e.g., oxygen) with volume concentration $c_t(\boldsymbol{x}, t)$. Nutrients, that are provided by the vessel network, are transported by $\boldsymbol{u}_t$ and diffuse with diffusion coefficient represented by the symmetric, positive-definite, second-order tensors $\mathsf{D}_t(\boldsymbol{x})$ inside Ω_t. The diffusion coefficient is a tensor that can vary in space and can be anisotropic in general, being affected by the local extracellular matrix alignment. Furthermore nutrients are consumed, with an uptake rate h. Thus, the concentration per unit volume of the generic chemical species obeys the following advection-diffusion-reaction equation

$$\frac{\partial c_t}{\partial t} + \nabla \cdot (c_t \boldsymbol{u}_t - \mathsf{D}_t(\boldsymbol{x}) \nabla c_t) = -h c_t \quad \text{in } \Omega_t \,. \tag{6.6}$$

We remark that, in principle, the uptake rate h and the diffusion coefficient $\mathsf{D}_t(\boldsymbol{x})$ should depend on the tumour cell density. However, consistent with the hypothesis of an inert, rigid, and homogeneously distributed extracellular matrix, this dependency can be disregarded.

In the following, the system of equations (6.4)-(6.6) is specialized to describe the motion of fluids and nutrients inside a tumour domain. Thus, for the volumetric growth in Eq. (6.5), we will set $\Gamma_t = \gamma c_t$, considering a net proliferation inside the tissue domain proportional to the amount of chemical. However, if the parameter γ is set to zero, the closed mass assumption is retrieved and the growth of the cellular phase occurs at the expense of the biological fluid phase [24]. In the following, for the sake of generality, we allow $\gamma \neq 0$. With slight modification, the present work can be also easily adapt to include a the volumetric source, for example representing the role of fluid exchanged between the interstitium and an additional network of vessels (see, e.g., [194] where the vascularisation is considered as a source term rather than geometrically resolved). For instance, the effect of the lymphatic system could be capture by considering a source term of the form $\Gamma_t = \beta_{LS}(p_t - p_{LS})$, being p_{LS} the pressure of the lymphatic system, assumed to be given, and β_{LS} a coefficient related to the permeability of the lymphatic wall and the surface area of lymphatic vessels per unit of tissue volume [71, 99].

Regarding the non-convective mass flux $\boldsymbol{m}_i$ in eq.(6.5), it may be related to the chemotactic expansion of cells driven by a nutrient gradient [245, 281]. Following the model proposed in [217, 220], where the flux $\boldsymbol{m}_i$ represents an accretion of mass that enables the chemotactic expansion of the tumour mass, we set

$$\boldsymbol{m}_i = \mathsf{X}(\boldsymbol{x}) \nabla c_t \,, \tag{6.7}$$

being $\mathsf{X}(\boldsymbol{x})$ the chemotactic tensor. We note that the chemotactic tensor may, in principle, depend on c_t [245, 281]. However, as a first approximation, this dependency can be neglected [112, 245, 402].

Finally, since the motion and diffusion of cells and liquid inside the tissue all follows

the orientation of the extracellular matrix fibers, we assume that the tensors representing the diffusion and motion of fluids and cells share the same preferential directions. Thus, defining $\mathsf{A}(\boldsymbol{x})$ the positive-definite preferential direction tensor, encoding information about the microstructural geometry and guiding the movement of cells and fluids [47, 48, 338], we can set $\mathsf{K}(\boldsymbol{x}) = \kappa\mathsf{A}(\boldsymbol{x})$, $\mathsf{X}(\boldsymbol{x}) = \chi(\boldsymbol{x})\mathsf{A}(\boldsymbol{x})$, and $\mathsf{D}_t(\boldsymbol{x}) = D_t\mathsf{A}(\boldsymbol{x})$. In the context of biological tissues, the preferential direction tensor could be derived from diffusion tensor imaging (DTI), which maps the tissue microstructural architecture by determining water diffusion directions [36, 57]. This procedure allows to reconstruct a realistic geometry and environment, with the aim of providing a framework based on patient-specific information. The parameter κ is the hydraulic conductivity, which is related to the tissue permeability k and the dynamic viscosity μ by the relation:

$$\kappa = \frac{k}{\mu}\,. \tag{6.8}$$

Moreover, D_t represents the diffusion coefficient in the tissue, while $\chi(\boldsymbol{x})$ is the chemotactic coefficient. It is worth noting that, unlike the other parameters, $\chi(\boldsymbol{x})$ varies spatially, depending on $\boldsymbol{x}$ within the domain. This is due to retain in the model the fact that cells in different locations may respond differently to chemotaxis. On the other hand, for what concerns the permeability and diffusion, the dependency on space can be kept only inside the preferential direction tensor. Furthermore, we note that while κ and D_t are positive coefficients, the chemotactic coefficient $\chi(\boldsymbol{x})$ may be either positive or negative [281].

6.3.2 Vessel network domain

Inside the vessel network Ω_v, the motion of the fluid, modelled as an incompressible Newtonian fluid, neglecting inertial effects and body forces, can be appropriately described by Stokes flow:

$$\mu\Delta\boldsymbol{u}_v = \nabla p_v \quad \text{in } \Omega_v\,, \tag{6.9}$$

$$\nabla\cdot\boldsymbol{u}_v = 0 \quad \text{in } \Omega_v\,, \tag{6.10}$$

where μ is a positive parameter representing the dynamic viscosity of the fluid. In the context of this work, the fluid inside the vessel network represents blood, which, generally speaking, is a non-Newtonian fluid composed of plasma and red blood cells [70, 111, 375]. However, in vessels much larger than red blood cells, at constant temperature and haematocrit, blood can be assumed,as a first approximation, to behave like a Newtonian fluid, with a viscosity greater than that of plasma [70, 397].

Finally, the nutrients concentration c_v in the capillary network can be described by an advection-diffusion equation:

$$\frac{\partial c_v}{\partial t} + \nabla\cdot(c_v\boldsymbol{u}_v - \mathsf{D}_v(\boldsymbol{x})\nabla c_v) = 0 \quad \text{in } \Omega_v\,, \tag{6.11}$$

being $\mathsf{D}_v(\boldsymbol{x})$ the symmetric, positive-definite, second-order tensors representing nutrients diffusion inside the blood. In the following, we will assume $\mathsf{D}_v(\boldsymbol{x}) = D_v\mathsf{A}(\boldsymbol{x})$, considering that diffusion follows the preferential directions dictated by the environment's microstructure, even within the vessel domain. Finally, we observe that nutrients consumption/decay inside the vessel domain is disregarded.

6.3.3 Interface conditions

To close the problem, appropriate conditions should be prescribed at the boundary between the tissue and vessel network domains. In the context of the present Chapter, we consider a tissue comprising a fluid phase that continuously exchanges with the surrounding vasculature, along with nutrients. By assuming that the Kedem-Katchalsky formulation [280] applies to both the fluid flux J_b and the nutrients flux J_d, we derive:

$$J_b = L_p \left[(p_v - p_t) - \sigma RT \left(c_v - c_t \right) \right] , \tag{6.12}$$

$$J_d = J_b (1 - \sigma) c_v + K_d \left(c_v - c_t \right) . \tag{6.13}$$

The parameter L_p stands for the hydraulic permeability of the vessel wall, which governs the fluid leakage from the capillaries. In tumour-induced vessels, this conductivity can be significantly elevated, potentially up to two orders of magnitude higher than in healthy tissue vessels, due to the presence of openings and defects characteristic of tumour vascular networks [267]. Additionally, R denotes the universal gas constant, T represents the absolute temperature, and K_d stands for the diffusive permeability of the vessel wall. The osmotic reflection coefficient $0 \leq \sigma \leq 1$ measures the membrane's selectivity for the solute and depends on the relative geometry and size of the specific molecule and the membrane pores. For an ideally fully impermeable membrane (which allows no solute flux due to convection), $\sigma = 1$, maximizing osmotic flow. Conversely, for an unselective membrane, $\sigma = 0$, indicating no osmosis and the transport of solutes entirely carried by the fluid flow. Therefore, Eq. (6.13) outlines that the nutrients flux across the vessel membrane comprises a convective component, proportional to the fluid flux, and a diffusive component, proportional to the concentration differential, whereas Eq. (6.12) represents that the flux of fluid across the vessel interface results from both the hydrostatic pressure gradient and the osmotic pressure disparity, with the latter being directly related to the difference in concentration for dilute solutions. We observe that, in general, the concentration of all chemicals dissolved in blood should be considered in the osmotic pressure disparity [193, 401]. Specifically, in healthy vessels, only the large molecules, such as proteins and in particular albumin, can induce a significant osmotic pressure gradient. Since the concentration of this large molecules can reasonably be taken constant, the oncotic pressure (i.e. the osmotic pressure exerted by plasma proteins, particularly albumin) transmural gradient is generally taken as a constant (equal to 25 mmHg) [193, 401]. On the contrary, in tumour induced vessels, it is possible to assume that solutes such as oxygen can significantly contribute to the oncotic pressure [267, 397].

It is important to note that Equation (6.13) represents a linearized form of the relationship established in [397]. This linearization is particularly valid for extreme values of Pe_v, the transvascular Péclet number, which quantifies the relative importance of convection versus diffusion across capillary walls.

In order to impose the correct interface conditions, we assume continuity of the nutrients and fluid fluxes through the interface boundary $\Gamma = \partial\Omega_t \cap \partial\Omega_v$:

$$\boldsymbol{u}_t \cdot \boldsymbol{n} = \boldsymbol{u}_v \cdot \boldsymbol{n} = \tilde{J}_b \, , \tag{6.14}$$

$$(c_t \boldsymbol{u}_t - D_t \mathsf{A}(\boldsymbol{x}) \nabla c_t) \cdot \boldsymbol{n} = (c_v \boldsymbol{u}_v - D_v \mathsf{A}(\boldsymbol{x}) \nabla c_n) \cdot \boldsymbol{n} = \tilde{J}_d \, . \tag{6.15}$$

Here, $\boldsymbol{n}$ represents the outward unit vector normal to the capillary surface, while we denote by

$$\tilde{J}_b = J_b \left(\hat{p}_v, p_t, c_v, c_t \right) \tag{6.16}$$

$$\tilde{J}_d = J_d\left(\hat{p}_v, p_t, c_v, c_t\right) \tag{6.17}$$

the flux prescriptions, given in their general form by (6.12) and (6.13), which are functions of the normal component of the viscous stress rather than solely the pressure [397]. Specifically, we adopt the following formulation [399]:

$$\hat{p}_v = p_v - 2\mu\left[\mathsf{E}\left(\boldsymbol{u}_v\right)\boldsymbol{n}\right]\cdot\boldsymbol{n}\,, \tag{6.18}$$

where $\hat{p}_v$ is the normal component of the stress tensor in the vessels' compartment and $\mathsf{E}(\boldsymbol{u}_v)$ is the symmetric part of the velocity gradient defined as

$$\mathsf{E}(\boldsymbol{u}_v) = \frac{1}{2}\left(\nabla\boldsymbol{u}_v + (\nabla\boldsymbol{u}_v)^T\right)\,. \tag{6.19}$$

We remark that in many work on physiological blood flux transport and exchange with the tissue [71, 99, 450], the viscous term in (6.18) is usually neglected. However, boundary conditions involving the Stokes' pressure should include the viscous contribution as well in order to get a coherent variational form of the problem and well-posedness [155], along with convenient a priori estimates for the convergence of the homogenization process [31]. In order to close the problem, an additional boundary condition is required for the tangential components of the fluid velocity in the capillaries. Given that the solid compartment acts as a porous medium, as per, e.g., Refs. [31, 399, 451], we assume that the following Beavers-Joseph-Saffman slip conditions [65, 273, 438] apply:

$$\boldsymbol{u}_v\cdot\boldsymbol{\tau} = -\frac{\sqrt{k}}{\alpha}\left[2\mathsf{E}(\boldsymbol{u}_v)\boldsymbol{n}\right]\cdot\boldsymbol{\tau}\,. \tag{6.20}$$

Equation (6.20) relates the tangent component of the stress to the tangent component of the velocity. In particular, α is a non-dimensional parameter that depends on the properties of the porous interface, $\boldsymbol{\tau}$ is any unit vector tangent to the capillary surface, $\mathsf{E}(\boldsymbol{u}_v)$ is the symmetric strain tensor defined in (6.19) and k is the tissue permeability, which is related to the hydraulic conductivity by relation (6.8). We further note that since the flow is assumed to be anisotropic, alternative formulations could be considered in place of (6.20), which would replace the role of the tissue permeability parameter k, for example involving the trace of the full permeability tensor [214], or the tangential projection of its tangent component [96]. While our model could readily accommodate such alternatives, since there is neither agreement on the specific modification that should be carried out, nor consensus on the appropriateness of the interface conditions (6.20) as such [162], we have chosen to embrace the most standard formulation of such conditions. The latter are however encoding the role of the properties of the interface, and reduce to the two crucial limit cases that are most usually explored in practice: the no-slip conditions (for small permeabilities k), and the free-slip conditions (formally for large permeabilities k).

6.4 The system of PDEs in non-dimensional form

Equations (6.4), (6.5), (6.6), (6.9), (6.10), and (6.11), along with the interface conditions (6.14), (6.15), and (6.20), as well as the appropriate flux prescriptions such as (6.12) and (6.13), form a coupled system of partial differential equations (PDEs). These equations govern the variables $\boldsymbol{u}_t$, $\boldsymbol{u}_v$, p_t, p_v, c_t, and c_v over the entire domain Ω, which includes both the tumour microenvironment Ω_t and the capillary network Ω_v. For the system to be well-defined, appropriate initial conditions and external boundary conditions on

$\partial\Omega$ must be prescribed, tailored to the specific physical system being modeled. We now express the system using non-dimensional variables:

$$x = Lx', \quad \boldsymbol{u} = \frac{Cd^2}{\mu}\boldsymbol{u}', \quad p = CLp', \quad c = C_r c', \quad t = \frac{L\mu}{Cd^2}t', \tag{6.21}$$

where C_r and C are the reference nutrients concentration and pressure gradient, respectively. Additionally, we recall (6.3), where we have defined the ratio between d and L as ε.

Furthermore, as previously discussed in [397, 399], it is essential to ensure that the total fluid flux (which is proportional to J_b by the total vessel surface area) remains finite as more vessels or channels are added within a fixed portion of the domain, or equivalently, as $\varepsilon \to 0$ (see Eq. (6.3)). This can be managed by noting that the parameters L_p and K_d are typically measured with respect to the total fluid flux. Since the latter is also proportional to the total vessel surface, which scales with the number of vessels (i.e., $\sim 1/\varepsilon$), it is assumed that the specific flux (per unit surface) scales as $O(\varepsilon)$. We account for this asymptotic behaviour of the fluid flux by redefining the parameters accordingly:

$$L_p = \varepsilon L_p^*, \quad K_d = \varepsilon K_d^*. \tag{6.22}$$

The corresponding system of partial differential equations in non-dimensional form is then given by (with primes omitted for simplicity):

$$\boldsymbol{u}_t = -\bar{\kappa}\bar{\mathsf{A}}(\boldsymbol{x})\nabla p_t \quad \text{in } \Omega_t, \tag{6.23}$$

$$\nabla \cdot \boldsymbol{u}_t = \bar{\gamma} c_t + \nabla \cdot (\bar{\chi}(\boldsymbol{x})\bar{\mathsf{A}}(\boldsymbol{x})\nabla c_t) \quad \text{in } \Omega_t, \tag{6.24}$$

$$\varepsilon^2 \Delta \boldsymbol{u}_v = \nabla p_v \quad \text{in } \Omega_v, \tag{6.25}$$

$$\nabla \cdot \boldsymbol{u}_v = 0 \quad \text{in } \Omega_v, \tag{6.26}$$

$$\frac{\partial c_t}{\partial t} + \nabla \cdot (c_t \boldsymbol{u}_t - \bar{D}_t \bar{\mathsf{A}}(\boldsymbol{x})\nabla c_t) = -\bar{h} c_t \quad \text{in } \Omega_t, \tag{6.27}$$

$$\frac{\partial c_v}{\partial t} + \nabla \cdot (c_v \boldsymbol{u}_v - \bar{D}_v \bar{\mathsf{A}}(\boldsymbol{x})\nabla c_v) = 0 \quad \text{in } \Omega_v, \tag{6.28}$$

supplemented by the interface conditions:

$$\boldsymbol{u}_v \cdot \boldsymbol{n} = \boldsymbol{u}_t \cdot \boldsymbol{n} = \varepsilon \bar{\mathcal{J}}_b \quad \text{on } \Gamma, \tag{6.29}$$

$$\boldsymbol{u}_v \cdot \boldsymbol{\tau} = -\varepsilon \bar{\theta} \left[(\nabla \boldsymbol{u}_v)\, \boldsymbol{n} \right] \cdot \boldsymbol{\tau} \quad \text{on } \Gamma, \tag{6.30}$$

$$(c_v \boldsymbol{u}_v - \bar{D}_v \bar{\mathsf{A}}(\boldsymbol{x})\nabla c_n) \cdot \boldsymbol{n} = (c_t \boldsymbol{u}_t - \bar{D}_t \bar{\mathsf{A}}(\boldsymbol{x})\nabla c_t) \cdot \boldsymbol{n} = \varepsilon \bar{\mathcal{J}}_d \quad \text{on } \Gamma. \tag{6.31}$$

Here, $\bar{\mathcal{J}}_b$ and $\bar{\mathcal{J}}_d$ represent the non-dimensional fluid and nutrients fluxes, defined as:

$$\bar{\mathcal{J}}_b = \bar{L}_p \left(\hat{p}_v - p_t \right) - \bar{\Pi} \left(c_v - c_t \right), \tag{6.32}$$

$$\bar{\mathcal{J}}_d = \bar{\mathcal{J}}_b (1 - \sigma) c_v + \bar{\Upsilon} \left(c_v - c_t \right), \tag{6.33}$$

where $\hat{p}_v$ is the non-dimensional normal stress given by

$$\hat{p}_v = p_v - 2\varepsilon^2 \left[\mathsf{E}\left(\boldsymbol{u}_v \right) \boldsymbol{n} \right] \cdot \boldsymbol{n}. \tag{6.34}$$

The non-dimensional numbers, tensors and functions introduced above are defined as follows:

$$\bar{\mathsf{A}}(\boldsymbol{x}) = \mathsf{A}(L\boldsymbol{x})\,, \quad \bar{\kappa} = \kappa\frac{\mu}{d^2}\,, \quad \bar{\gamma} = \gamma\frac{C_r L\mu}{Cd^2}\,, \quad \bar{\chi}(\boldsymbol{x}) = \chi(L\boldsymbol{x})\frac{C_r\mu}{Cd^2L}\,,$$
$$\bar{D}_v = D_v\frac{\mu}{Cd^2L}\,, \quad \bar{D}_t = D_t\frac{\mu}{Cd^2L}\,, \quad \bar{h} = h\frac{L\mu}{Cd^2}\,, \quad \bar{L}_p = L_p^*\frac{\mu L^2}{d^3}\,,$$
$$\bar{\Pi} = \frac{\mu L L_p\sigma RTC_r}{Cd^3}\,, \quad \bar{\theta} = \frac{\sqrt{\bar{\kappa}}}{\alpha}\,, \quad \bar{\Upsilon} = K_d^*\frac{\mu L}{Cd^3}\,. \tag{6.35}$$

6.5 Multiscale formulation

In this Section, we use the two-scales technique to derive a continuum macroscale model for the system of Eqs. (6.23)-(6.31). Given that $\varepsilon \ll 1$, we enforce a sharp separation between the intercapillary distance d (the microscale) and the tissue characteristic dimension L (the macroscale) and define:

$$\boldsymbol{y} := \frac{\boldsymbol{x}}{\varepsilon}\,. \tag{6.36}$$

In accordance with standard multiscale analysis [397, 399], $\boldsymbol{x}$ and $\boldsymbol{y}$ are treated as independent variables, representing the macro- and micro-spatial scales, respectively. We assume that any unknown field, such as $\boldsymbol{u}_t$, $\boldsymbol{u}_v$, p_t, p_v, c_t and c_v depends on these independent spatial variables, which transforms the differential operator as depicted in (6.1). For each field, we perform a multiple scales expansion in a power series of ε:

$$\boldsymbol{u}(\boldsymbol{x}) = \boldsymbol{u}^\varepsilon(\boldsymbol{x},\boldsymbol{y},t) = \sum_{l=0}^{\infty}\boldsymbol{u}^{(l)}(\boldsymbol{x},\boldsymbol{y},t)\varepsilon^l\,, \tag{6.37}$$

$$p(\boldsymbol{x}) = p^\varepsilon(\boldsymbol{x},\boldsymbol{y},t) = \sum_{l=0}^{\infty}p^{(l)}(\boldsymbol{x},\boldsymbol{y},t)\varepsilon^l\,, \tag{6.38}$$

$$c(\boldsymbol{x}) = c^\varepsilon(\boldsymbol{x},\boldsymbol{y},t) = \sum_{l=0}^{\infty}c^{(l)}(\boldsymbol{x},\boldsymbol{y},t)\varepsilon^l\,. \tag{6.39}$$

We assume periodicity in the microscale variable, so each component is $\boldsymbol{y}$-periodic. As such, all the fields $\boldsymbol{u}^\varepsilon(\boldsymbol{x},\boldsymbol{y},t)$, $p^\varepsilon(\boldsymbol{x},\boldsymbol{y},t)$, and $c^\varepsilon(\boldsymbol{x},\boldsymbol{y},t)$, as well as $\bar{\chi}(\boldsymbol{x},\boldsymbol{y})$ and $\bar{\mathsf{A}}(\boldsymbol{x},\boldsymbol{y})$ are assumed $\boldsymbol{y}$-periodic. We also assume macroscopic uniformity, meaning that, although we consider a scenario where the geometry can be locally arbitrarily complex and anisotropic, the periodic cell itself does not depend on the macroscale variable $\boldsymbol{x}$. All these hypotheses are further elaborated and summarised in Section 6.2.

The aim of this Section is to derive a closed system of PDEs for the leading-order variables $\boldsymbol{u}_t^{(0)}$, $\boldsymbol{u}_v^{(0)}$, $p_t^{(0)}$, $p_v^{(0)}$, $c_t^{(0)}$ and $c_v^{(0)}$ over the macroscale domain represented by the variable $\boldsymbol{x}$. This is achieved by exploiting the conditions that arise from equating terms of the same order of ε in equations (6.23)-(6.31). To focus on obtaining a system of PDEs that applies solely to the macroscale, we introduce the following cell average operator:

$$\langle\bullet\rangle_s = \frac{1}{|\Omega_s|}\int_{\Omega_s}(\bullet)d\boldsymbol{y}\,, \quad s = t,\, v\,. \tag{6.40}$$

Exploiting the spatial scale decoupling (6.1), Eqs. (6.23)-(6.31) read (after multiplying each of them by an appropriate power of ε):

$$\varepsilon\boldsymbol{u}_t = -\varepsilon\bar{\kappa}\bar{\mathsf{A}}(\boldsymbol{x},\boldsymbol{y})\nabla_{\boldsymbol{x}}p_t - \bar{\kappa}\bar{\mathsf{A}}(\boldsymbol{x},\boldsymbol{y})\nabla_{\boldsymbol{y}}p_t \quad \text{in } \Omega_t\,, \tag{6.41}$$

$$\begin{aligned}\varepsilon^2\nabla_{\boldsymbol{x}}\cdot\boldsymbol{u}_t+\varepsilon\nabla_{\boldsymbol{y}}\cdot\boldsymbol{u}_t=\varepsilon^2\bar{\gamma}c_t+\varepsilon^2\nabla_{\boldsymbol{x}}\cdot(\bar{\chi}(\boldsymbol{x},\boldsymbol{y})\bar{\mathbb{A}}(\boldsymbol{x},\boldsymbol{y})\nabla_{\boldsymbol{x}}c_t)+\\ +\varepsilon\nabla_{\boldsymbol{x}}\cdot(\bar{\chi}(\boldsymbol{x},\boldsymbol{y})\bar{\mathbb{A}}(\boldsymbol{x},\boldsymbol{y})\nabla_{\boldsymbol{y}}c_t)+\varepsilon\nabla_{\boldsymbol{y}}\cdot(\bar{\chi}(\boldsymbol{x},\boldsymbol{y})\bar{\mathbb{A}}(\boldsymbol{x},\boldsymbol{y})\nabla_{\boldsymbol{x}}c_t)+\\ +\nabla_{\boldsymbol{y}}\cdot(\bar{\chi}(\boldsymbol{x},\boldsymbol{y})\bar{\mathbb{A}}(\boldsymbol{x},\boldsymbol{y})\nabla_{\boldsymbol{y}}c_t)\quad\text{in }\Omega_t\,,\end{aligned}\tag{6.42}$$

$$\varepsilon^3\Delta_{\boldsymbol{x}}\boldsymbol{u}_v+\varepsilon^2\nabla_{\boldsymbol{x}}\cdot(\nabla_{\boldsymbol{y}}\boldsymbol{u}_v)+\varepsilon^2\nabla_{\boldsymbol{y}}\cdot(\nabla_{\boldsymbol{x}}\boldsymbol{u}_v)+\varepsilon\Delta_{\boldsymbol{y}}\boldsymbol{u}_v=\varepsilon\nabla_{\boldsymbol{x}}p_v+\nabla_{\boldsymbol{y}}p_v\quad\text{in }\Omega_v\,,\tag{6.43}$$

$$\nabla_{\boldsymbol{y}}\cdot\boldsymbol{u}_v+\varepsilon\nabla_{\boldsymbol{x}}\cdot\boldsymbol{u}_v=0\quad\text{in }\Omega_v\,,\tag{6.44}$$

$$\begin{aligned}\varepsilon^2\frac{\partial c_t}{\partial t}+\nabla_{\boldsymbol{x}}\cdot\left(\varepsilon^2c_t\boldsymbol{u}_t-\varepsilon^2\bar{D}_t\bar{\mathbb{A}}(\boldsymbol{x},\boldsymbol{y})\nabla_{\boldsymbol{x}}c_t-\varepsilon\bar{D}_t\bar{\mathbb{A}}(\boldsymbol{x},\boldsymbol{y})\nabla_{\boldsymbol{y}}c_t\right)+\\ +\nabla_{\boldsymbol{y}}\cdot(\varepsilon c_t\boldsymbol{u}_t-\varepsilon\bar{D}_t\bar{\mathbb{A}}(\boldsymbol{x},\boldsymbol{y})\nabla_{\boldsymbol{x}}c_t-\bar{D}_t\bar{\mathbb{A}}(\boldsymbol{x},\boldsymbol{y})\nabla_{\boldsymbol{y}}c_t)=-\varepsilon^2\bar{h}c_t\quad\text{in }\Omega_t\,,\end{aligned}\tag{6.45}$$

$$\begin{aligned}\varepsilon^2\frac{\partial c_v}{\partial t}+\nabla_{\boldsymbol{x}}\cdot\left(\varepsilon^2c_v\boldsymbol{u}_v-\varepsilon^2\bar{D}_v\bar{\mathbb{A}}(\boldsymbol{x},\boldsymbol{y})\nabla_{\boldsymbol{x}}c_v-\varepsilon\bar{D}_v\bar{\mathbb{A}}(\boldsymbol{x},\boldsymbol{y})\nabla_{\boldsymbol{y}}c_v\right)+\\ +\nabla_{\boldsymbol{y}}\cdot(\varepsilon c_v\boldsymbol{u}_v-\varepsilon\bar{D}_v\bar{\mathbb{A}}(\boldsymbol{x},\boldsymbol{y})\nabla_{\boldsymbol{x}}c_v-\bar{D}_v\bar{\mathbb{A}}(\boldsymbol{x},\boldsymbol{y})\nabla_{\boldsymbol{y}}c_v)=0\quad\text{in }\Omega_v\,,\end{aligned}\tag{6.46}$$

equipped with the following interface conditions:

$$\boldsymbol{u}_v\cdot\boldsymbol{n}=\boldsymbol{u}_t\cdot\boldsymbol{n}=\varepsilon\bar{\mathcal{J}}_b\quad\text{on }\Gamma\,,\tag{6.47}$$

$$\boldsymbol{u}_v\cdot\boldsymbol{\tau}=-\varepsilon\bar{\theta}\left[(\nabla_{\boldsymbol{x}}\boldsymbol{u}_v)\,\boldsymbol{n}\right]\cdot\boldsymbol{\tau}-\bar{\theta}\left[(\nabla_{\boldsymbol{y}}\boldsymbol{u}_v)\,\boldsymbol{n}\right]\cdot\boldsymbol{\tau}\quad\text{on }\Gamma\,,\tag{6.48}$$

$$\begin{aligned}(\varepsilon c_v\boldsymbol{u}_v-\varepsilon\bar{D}_v\bar{\mathbb{A}}(\boldsymbol{x},\boldsymbol{y})\nabla_{\boldsymbol{x}}c_v-\bar{D}_v\bar{\mathbb{A}}(\boldsymbol{x},\boldsymbol{y})\nabla_{\boldsymbol{y}}c_v)\cdot\boldsymbol{n}=\\ =(\varepsilon c_t\boldsymbol{u}_t-\varepsilon\bar{D}_t\bar{\mathbb{A}}(\boldsymbol{x},\boldsymbol{y})\nabla_{\boldsymbol{x}}c_t-\bar{D}_t\bar{\mathbb{A}}(\boldsymbol{x},\boldsymbol{y})\nabla_{\boldsymbol{y}}c_t)\cdot\boldsymbol{n}=\varepsilon^2\bar{\mathcal{J}}_d\quad\text{on }\Gamma\,,\end{aligned}\tag{6.49}$$

where the general formulation for the fluid non-dimensional flux (6.32) reads:

$$\begin{aligned}\bar{\mathcal{J}}_b=\bar{L}_p(p_v-p_t)-\bar{\Pi}(c_v-c_t)-\varepsilon^2\left[\frac{1}{2}\left(\nabla_{\boldsymbol{x}}\boldsymbol{u}_v+(\nabla_{\boldsymbol{x}}\boldsymbol{u}_v)^T\right)\boldsymbol{n}\right]\cdot\boldsymbol{n}+\\ -\varepsilon\left[\frac{1}{2}\left(\nabla_{\boldsymbol{y}}\boldsymbol{u}_v+(\nabla_{\boldsymbol{y}}\boldsymbol{u}_v)^T\right)\boldsymbol{n}\right]\cdot\boldsymbol{n}\,,\end{aligned}\tag{6.50}$$

while nutrients non-dimensional flux remains defined by (6.33).

6.5.1 Capillary fluid dynamics

We start by considering the capillary problem for fluid and nutrients transport in Ω_v, which is composed by equations (6.43), (6.44) and (6.46), equipped by interface conditions (6.47), (6.48) and (6.49). Our goal is to establish a closed system for the zero-th order fields $\boldsymbol{u}_v^{(0)}$, $p_v^{(0)}$ and $c_v^{(0)}$. We begin by examining the fluid flow in the capillaries. By collecting terms of order ε^0 in (6.43), we obtain:

$$\nabla_{\boldsymbol{y}}p_v^{(0)}=0\Rightarrow p_v^{(0)}=p_v^{(0)}(\boldsymbol{x},t)\quad\text{in }\Omega_v\,,\tag{6.51}$$

that means that $p_v^{(0)}$ is $\boldsymbol{y}$-constant. By equating the coefficients of ε^1 in (6.43) and ε^0 in (6.44), (6.47) and (6.48), we derive the following Stokes-type boundary value problem for $\left(\boldsymbol{u}_v^{(0)},p_v^{(1)}\right)$:

$$\Delta_{\boldsymbol{y}}\boldsymbol{u}_v^{(0)}=\nabla_{\boldsymbol{x}}p_v^{(0)}+\nabla_{\boldsymbol{y}}p_v^{(1)}\quad\text{in }\Omega_v\,,\tag{6.52}$$

$$\nabla_{\boldsymbol{y}}\cdot\boldsymbol{u}_v^{(0)}=0\quad\text{in }\Omega_v\,,\tag{6.53}$$

$$\boldsymbol{u}_v^{(0)}\cdot\boldsymbol{n}=0\quad\text{on }\Gamma\,,\tag{6.54}$$

$$\boldsymbol{u}_v^{(0)}\cdot\boldsymbol{\tau}=-\bar{\theta}\left[\left(\nabla_{\boldsymbol{y}}\boldsymbol{u}_v^{(0)}\right)\boldsymbol{n}\right]\cdot\boldsymbol{\tau}\quad\text{on }\Gamma\,.\tag{6.55}$$

Next, we utilize the linearity of Eqs. (6.52)-(6.55), along with (6.51), to propose the following ansatz for the solution:

$$\boldsymbol{u}_v^{(0)}(\boldsymbol{x},\boldsymbol{y},t) = -\mathsf{W}(\boldsymbol{x},\boldsymbol{y})\nabla_{\boldsymbol{x}} p_v^{(0)}(\boldsymbol{x},t)\,, \tag{6.56}$$

$$p_v^{(1)}(\boldsymbol{x},\boldsymbol{y},t) = -\boldsymbol{P}_v(\boldsymbol{x},\boldsymbol{y})\cdot\nabla_{\boldsymbol{x}} p_v^{(0)}(\boldsymbol{x},t) + \tilde{p}(\boldsymbol{x},t)\,. \tag{6.57}$$

where $\tilde{p}(\boldsymbol{x},t)$ represents the part which does not depend on $\boldsymbol{y}$.

Rewriting the problem in components and omitting the subscript v for simplicity, it becomes:

$$\begin{cases} \dfrac{\partial^2 u_i^{(0)}}{\partial y_k \partial y_k} = \dfrac{\partial p^{(0)}}{\partial x_i} + \dfrac{\partial p^{(1)}}{\partial y_i} & \text{in } \Omega_v\,, \\ \dfrac{\partial u_k^{(0)}}{\partial y_k} = 0 & \text{in } \Omega_v\,, \\ u_k^{(0)} n_k = 0 & \text{on } \Gamma\,, \\ u_k^{(0)}\tau_k = -\bar{\theta}\dfrac{\partial u_i}{\partial y_\ell} n_\ell \tau_i & \text{on } \Gamma\,. \end{cases} \tag{6.58}$$

Inserting the ansatz we obtain:

$$\begin{cases} -\dfrac{\partial^2\left(W_{ij}\dfrac{\partial p^{(0)}}{\partial x_j}\right)}{\partial y_k \partial y_k} - \delta_{ij}\dfrac{\partial p^{(0)}}{\partial x_j} + \dfrac{\partial\left(P_j\dfrac{\partial p^{(0)}}{\partial x_j}\right)}{\partial y_i} = 0_i & \text{in } \Omega_v\,, \\ \dfrac{\partial\left(W_{kj}\dfrac{\partial p^{(0)}}{\partial x_j}\right)}{\partial y_k} = 0 & \text{in } \Omega_v\,, \\ W_{kj}\dfrac{\partial p^{(0)}}{\partial x_j} n_k = 0 & \text{on } \Gamma\,, \\ W_{kj}\dfrac{\partial p^{(0)}}{\partial x_j}\tau_k = -\bar{\theta}\dfrac{\partial\left(W_{ij}\dfrac{\partial p^{(0)}}{\partial x_j}\right)}{\partial y_\ell} n_\ell \tau_i & \text{on } \Gamma\,. \end{cases} \tag{6.59}$$

Since $p^{(0)}$ is $\boldsymbol{y}$-independent, the system can be rewritten:

$$\begin{cases} \left(-\dfrac{\partial^2 W_{ij}}{\partial y_k \partial y_k} - \delta_{ij} + \dfrac{\partial P_j}{\partial y_i}\right)\dfrac{\partial p^{(0)}}{\partial x_j} = 0_i & \text{in } \Omega_v\,, \\ \dfrac{\partial W_{kj}}{\partial y_k}\dfrac{\partial p^{(0)}}{\partial x_j} = 0 & \text{in } \Omega_v\,, \\ W_{kj} n_k \dfrac{\partial p^{(0)}}{\partial x_j} = 0 & \text{on } \Gamma\,, \\ \left(W_{kj}\tau_k + \bar{\theta}\dfrac{\partial W_{ij}}{\partial y_\ell} n_\ell \tau_i\right)\dfrac{\partial p^{(0)}}{\partial x_j} = 0 & \text{on } \Gamma\,. \end{cases} \tag{6.60}$$

This means that the cell fields $(\mathsf{W}, \boldsymbol{P}_v)$ satisfy the following Stokes' type problem:

$$\begin{cases} -\dfrac{\partial^2 W_{ij}}{\partial y_k \partial y_k} - \delta_{ij} + \dfrac{\partial P_j}{\partial y_i} = 0_{ij} & \text{in } \Omega_v\,, \\ \dfrac{\partial W_{kj}}{\partial y_k} = 0_j & \text{in } \Omega_v\,, \\ W_{kj} n_k = 0_j & \text{on } \Gamma\,, \\ W_{kj}\tau_k + \bar{\theta}\dfrac{\partial W_{ij}}{\partial y_\ell} n_\ell \tau_i = 0_j & \text{on } \Gamma\,, \end{cases} \tag{6.61}$$

which in tensor notation reads:

$$\begin{cases} \nabla_{\boldsymbol{y}} \boldsymbol{P}_v = \Delta_{\boldsymbol{y}} \mathsf{W}^{\mathrm{T}} + \mathsf{I} & \text{in } \Omega_v\,, \\ \nabla_{\boldsymbol{y}} \cdot \mathsf{W}^{\mathrm{T}} = \boldsymbol{0} & \text{in } \Omega_v\,, \\ \mathsf{W}^{\mathrm{T}} \boldsymbol{n} = \boldsymbol{0} & \text{on } \Gamma\,, \\ -\bar{\theta}\left[\left(\nabla_{\boldsymbol{y}} \mathsf{W}^{\mathrm{T}}\right)\boldsymbol{n}\right]\boldsymbol{\tau} = \mathsf{W}^{\mathrm{T}}\boldsymbol{\tau} & \text{on } \Gamma\,. \end{cases} \tag{6.62}$$

The above system of partial differential equations is supplemented by periodicity conditions in $\boldsymbol{y}$ together with suitable conditions that guarantee uniqueness for the auxiliary vector $\boldsymbol{P}_v$, for example

$$\left\langle \boldsymbol{P}_v\left(\boldsymbol{x}, \boldsymbol{y}\right)\right\rangle_v = \boldsymbol{0}\,. \tag{6.63}$$

We can now provide a macroscale equation for the average capillary velocity by integrating (6.56) over Ω_v:

$$\left\langle \boldsymbol{u}_v^{(0)}\right\rangle_v = -\mathsf{M}\nabla_{\boldsymbol{x}} p_v^{(0)}\,, \tag{6.64}$$

where $\mathsf{M} = \langle \mathsf{W}\rangle_v$, or, componentwise, $M_{ij} = \dfrac{1}{|\Omega_v|}\int_{\Omega_v} W_{ij} d\boldsymbol{y}$. Equation (6.64) entails that, at the macroscale, the average velocity profile in the capillaries follows an anisotropic form of Darcy's law. The flow is primarily driven by the leading-order pressure $p_v^{(0)}$ within the capillaries, while the microstructural characteristics are represented by the permeability tensor M.

To derive a macroscale equation for $p_v^{(0)}$, we gather the coefficients of order ε^1 in equations (6.44) and (6.47):

$$\nabla_{\boldsymbol{y}} \cdot \boldsymbol{u}_v^{(1)} + \nabla_{\boldsymbol{x}} \cdot \boldsymbol{u}_v^{(0)} = 0 \Longrightarrow \nabla_{\boldsymbol{x}} \cdot \boldsymbol{u}_v^{(0)} = -\nabla_{\boldsymbol{y}} \cdot \boldsymbol{u}_v^{(1)}\,, \tag{6.65}$$

$$\boldsymbol{u}_v^{(1)} \cdot \boldsymbol{n} = \bar{\mathcal{J}}_b^{(0)}\,. \tag{6.66}$$

Integrating (6.65) over Ω_v:

$$\left\langle \nabla_{\boldsymbol{x}} \cdot \boldsymbol{u}_v^{(0)}\right\rangle_v = -\left\langle \nabla_{\boldsymbol{y}} \cdot \boldsymbol{u}_v^{(1)}\right\rangle_v\,. \tag{6.67}$$

Exploiting the macroscopic uniformity, the divergence theorem with respect to $\boldsymbol{y}$ and the $\boldsymbol{y}$-periodicity, we obtain:

$$\nabla_{\boldsymbol{x}} \cdot \left\langle \boldsymbol{u}_v^{(0)}\right\rangle_v = -\frac{1}{|\Omega_v|}\int_\Gamma \boldsymbol{u}_v^{(1)} \cdot \boldsymbol{n}\, dS_{\boldsymbol{y}}\,. \tag{6.68}$$

Using (6.66), we can write:

$$\nabla_{\boldsymbol{x}} \cdot \left\langle \boldsymbol{u}_v^{(0)} \right\rangle_v = -\frac{1}{|\Omega_v|} \int_\Gamma \bar{\mathcal{J}}_b^{(0)} \, dS_{\boldsymbol{y}} \,. \tag{6.69}$$

Finally, we can incorporate Eq. (6.64) to derive the equation for the leading-order pressure $p_v^{(0)}$:

$$\nabla_{\boldsymbol{x}} \cdot \left(\mathsf{M} \nabla_{\boldsymbol{x}} p_v^{(0)} \right) = \frac{1}{|\Omega_v|} \int_\Gamma \bar{\mathcal{J}}_b^{(0)} \, dS_{\boldsymbol{y}} \,. \tag{6.70}$$

The fluid flow within the capillaries compartment is not incompressible at the macroscale. The source term on the right-hand side of above equation arises from the leading-order fluid flux $\bar{\mathcal{J}}_b^{(0)}$, defined as:

$$\bar{\mathcal{J}}_b^{(0)} = \bar{L}_p (p_v^{(0)} - p_t^{(0)}) - \bar{\Pi} (c_v^{(0)} - c_t^{(0)}) \,. \tag{6.71}$$

Consequently, the microscale exchange between the tumour and capillary compartments across the interface Γ translates into a volumetric contribution on the global scale.

Finally, a macroscale equation for the leading-order nutrient concentration in the capillaries is derived by collecting the coefficients of ε^0 in (6.46) and (6.49):

$$\nabla_{\boldsymbol{y}} \cdot \left(\bar{D}_v \bar{\mathsf{A}} \left(\boldsymbol{x}, \boldsymbol{y} \right) \nabla_{\boldsymbol{y}} c^{(0)} \right) = 0 \quad \text{in } \Omega_v \,, \tag{6.72}$$

$$\left(\bar{D}_v \bar{\mathsf{A}} \left(\boldsymbol{x}, \boldsymbol{y} \right) \nabla_{\boldsymbol{y}} c^{(0)} \right) \cdot \boldsymbol{n} = 0 \quad \text{on } \Gamma \,. \tag{6.73}$$

Eq. (6.72), together with (6.73) and $\boldsymbol{y}$-periodicity, has a constant solution with respect to $\boldsymbol{y}$, i.e.,

$$c_v^{(0)} = c_v^{(0)} \left(\boldsymbol{x}, t \right) \,. \tag{6.74}$$

Then, we collect the coefficients of ε^1-terms, obtaining:

$$\begin{aligned} &- \nabla_{\boldsymbol{x}} \cdot \left(\bar{D}_v \bar{\mathsf{A}} (\boldsymbol{x}, \boldsymbol{y}) \nabla_{\boldsymbol{y}} c_v^{(0)} \right) + \\ &+ \nabla_{\boldsymbol{y}} \cdot \left(c_v^{(0)} \boldsymbol{u}_v^{(0)} - \bar{D}_v \bar{\mathsf{A}} (\boldsymbol{x}, \boldsymbol{y}) \nabla_{\boldsymbol{x}} c_v^{(0)} - \bar{D}_v \bar{\mathsf{A}} (\boldsymbol{x}, \boldsymbol{y}) \nabla_{\boldsymbol{y}} c_v^{(1)} \right) = 0 \quad \text{in } \Omega_v \,, \end{aligned} \tag{6.75}$$

$$\left(c_v^{(0)} \boldsymbol{u}_v^{(0)} - \bar{D}_v \bar{\mathsf{A}} (\boldsymbol{x}, \boldsymbol{y}) \nabla_{\boldsymbol{x}} c_v^{(0)} - \bar{D}_v \bar{\mathsf{A}} (\boldsymbol{x}, \boldsymbol{y}) \nabla_{\boldsymbol{y}} c_v^{(1)} \right) \cdot \boldsymbol{n} = 0 \quad \text{on } \Gamma \,. \tag{6.76}$$

Then, in Eq. (6.75) we utilize the fact that $c_v^{(0)}$ is $\boldsymbol{y}$-independent and apply (6.53) while in Eq. (6.76) we apply (6.54) to derive:

$$\nabla_{\boldsymbol{y}} \cdot \left(\bar{\mathsf{A}} (\boldsymbol{x}, \boldsymbol{y}) \nabla_{\boldsymbol{x}} c_v^{(0)} + \bar{\mathsf{A}} (\boldsymbol{x}, \boldsymbol{y}) \nabla_{\boldsymbol{y}} c_v^{(1)} \right) = 0 \quad \text{in } \Omega_v \,, \tag{6.77}$$

$$\left(\bar{\mathsf{A}} (\boldsymbol{x}, \boldsymbol{y}) \nabla_{\boldsymbol{x}} c_v^{(0)} + \bar{\mathsf{A}} (\boldsymbol{x}, \boldsymbol{y}) \nabla_{\boldsymbol{y}} c_v^{(1)} \right) \cdot \boldsymbol{n} = 0 \quad \text{on } \Gamma \,. \tag{6.78}$$

At this point we can state the following ansatz:

$$c_v^{(1)} (\boldsymbol{x}, \boldsymbol{y}, t) = -\boldsymbol{a} \left(\boldsymbol{x}, \boldsymbol{y} \right) \cdot \nabla_{\boldsymbol{x}} c_v^{(0)} (\boldsymbol{x}, t) + \tilde{c}_v (\boldsymbol{x}, t) \,, \tag{6.79}$$

where $\tilde{c}_v(\boldsymbol{x}, t)$ represents the part which does not depend on $\boldsymbol{y}$. The ansatz can be expressed in components as (removing the subscript v for convenience):

$$c^{(1)} = -a_i \frac{\partial c^{(0)}}{\partial x_i} + \tilde{c}\,. \tag{6.80}$$

Rewriting Eq. (6.77) in terms of its components and incorporating the ansatz, we obtain:

$$\begin{aligned} &\frac{\partial\left(A_{ik}\dfrac{\partial c^0}{\partial x_k}\right)}{\partial y_i} - \frac{\partial\left(A_{ij}\dfrac{\partial}{\partial y_j}\left(a_k\dfrac{\partial c^{(0)}}{\partial x_k}\right)\right)}{\partial y_i} = 0\,, \\ &\Rightarrow \left(\frac{\partial A_{ik}}{\partial y_i} - \frac{\partial\left(A_{ij}\dfrac{\partial a_k}{\partial y_j}\right)}{\partial y_i}\right)\frac{\partial c^{(0)}}{\partial x_k} = 0\,, \\ &\Rightarrow \frac{\partial\left(\dfrac{\partial a_k}{\partial y_j}A_{ij}\right)}{\partial y_i} = \frac{\partial A_{ik}}{\partial y_i} \quad \text{in } \Omega_v\,. \end{aligned} \tag{6.81}$$

In tensor notation, it reads:

$$\nabla_{\boldsymbol{y}} \cdot \left[(\nabla_{\boldsymbol{y}}\boldsymbol{a})\,\mathsf{A}^{\mathrm{T}}\right] = \nabla_{\boldsymbol{y}} \cdot \mathsf{A}^{\mathrm{T}} \quad \text{in } \Omega_v\,. \tag{6.82}$$

Expressing Eq. (6.78) in component form and incorporating the ansatz, we obtain:

$$\begin{aligned} &-A_{ij}\frac{\partial}{\partial y_i}\left(a_k\frac{\partial c^{(0)}}{\partial x_k}\right)n_i = -A_{ik}\frac{\partial c^{(0)}}{\partial x_k}n_i\,, \\ &\Rightarrow \left(A_{ij}\frac{\partial a_k}{\partial y_j} - A_{ik}\right)n_i\frac{\partial c^{(0)}}{\partial x_k} = 0\,, \\ &\Rightarrow \frac{\partial a_k}{\partial y_j}A_{ij}n_i = A_{ik}n_i \quad \text{on } \Gamma\,; \end{aligned} \tag{6.83}$$

which in tensor components reads:

$$(\nabla_{\boldsymbol{y}}\boldsymbol{a})\,\mathsf{A}^{\mathrm{T}}\boldsymbol{n} = \mathsf{A}^{\mathrm{T}}\boldsymbol{n} \quad \text{on } \Gamma\,. \tag{6.84}$$

Finally, the auxiliary vector $\boldsymbol{a}\,(\boldsymbol{x}, \boldsymbol{y})$ solve the cell problem:

$$\begin{cases} \nabla_{\boldsymbol{y}} \cdot \left[(\nabla_{\boldsymbol{y}}\boldsymbol{a})\,\mathsf{A}^{\mathrm{T}}\right] = \nabla_{\boldsymbol{y}} \cdot \mathsf{A}^{\mathrm{T}} & \text{in } \Omega_v\,, \\ (\nabla_{\boldsymbol{y}}\boldsymbol{a})\,\mathsf{A}^{\mathrm{T}}\boldsymbol{n} = \mathsf{A}^{\mathrm{T}}\boldsymbol{n} & \text{on } \Gamma\,. \end{cases} \tag{6.85}$$

A further condition for $\boldsymbol{a}$ is required to ensure uniqueness, for example:

$$\langle \boldsymbol{a}\,(\boldsymbol{x}, \boldsymbol{y})\rangle_v = \boldsymbol{0}\,. \tag{6.86}$$

Next, we aim to derive a macroscale equation for the leading-order concentration in the capillaries $c_v^{(0)}$. We begin by equating the ε^2 coefficients in equations (6.46) and (6.49),

resulting in:

$$\begin{aligned}&\frac{\partial c_v^{(0)}}{\partial t}+\nabla_{\boldsymbol{x}}\cdot\left(c_v^{(0)}\boldsymbol{u}_v^{(0)}-\bar{D}_v\bar{\mathsf{A}}\nabla_{\boldsymbol{x}}c_v^{(0)}-\bar{D}_v\bar{\mathsf{A}}\nabla_{\boldsymbol{y}}c_v^{(1)}\right)+\\&\quad+\nabla_{\boldsymbol{y}}\cdot\left(c_v^{(0)}\boldsymbol{u}_v^{(1)}+c_v^{(1)}\boldsymbol{u}_v^{(0)}-\bar{D}_v\bar{\mathsf{A}}\nabla_{\boldsymbol{x}}c_v^{(1)}-\bar{D}_v\bar{\mathsf{A}}\nabla_{\boldsymbol{y}}c_v^{(2)}\right)=0\quad\text{in }\Omega_v\,,\end{aligned}\tag{6.87}$$

$$\left(c_v^{(0)}\boldsymbol{u}_v^{(1)}+c_v^{(1)}\boldsymbol{u}_v^{(0)}-\bar{D}_v\bar{\mathsf{A}}\nabla_{\boldsymbol{x}}c_v^{(1)}-\bar{D}_v\bar{\mathsf{A}}\nabla_{\boldsymbol{y}}c_v^{(2)}\right)\cdot\boldsymbol{n}=\bar{\mathcal{J}}_d^{(0)}\quad\text{on }\Gamma\,,\tag{6.88}$$

where the zero-th order nutrients flux is given by

$$\bar{\mathcal{J}}_d^{(0)}=\bar{\mathcal{J}}_b^{(0)}\left(1-\sigma\right)c_v^{(0)}+\bar{\Upsilon}\left(c_v^{(0)}-c_t^{(0)}\right).\tag{6.89}$$

Taking the integral average over Ω_v of the first equation, exploiting the divergence theorem, the $\boldsymbol{y}$-periodicity and the interface condition given from the second equation, we obtain:

$$\begin{aligned}&\frac{\partial c_v^{(0)}}{\partial t}+\nabla_{\boldsymbol{x}}\cdot\left(c_v^{(0)}\left\langle\boldsymbol{u}_v^{(0)}\right\rangle_v\right)-\nabla_{\boldsymbol{x}}\cdot\left(\bar{D}_v\left\langle\bar{\mathsf{A}}\right\rangle_v\nabla_{\boldsymbol{x}}c_v^{(0)}\right)+\\&\quad-\nabla_{\boldsymbol{x}}\cdot\left(\bar{D}_v\left\langle\bar{\mathsf{A}}\nabla_{\boldsymbol{y}}c_v^{(1)}\right\rangle_v\right)+\frac{1}{|\Omega_v|}\int_\Gamma\bar{\mathcal{J}}_d^{(0)}\,dS_{\boldsymbol{y}}=0\quad\text{in }\Omega_v\,.\end{aligned}\tag{6.90}$$

Using the ansatz we can write:

$$\begin{aligned}&\frac{\partial c_v^{(0)}}{\partial t}+\nabla_{\boldsymbol{x}}\cdot\left(c_v^{(0)}\left\langle\boldsymbol{u}_v^{(0)}\right\rangle_v\right)-\nabla_{\boldsymbol{x}}\cdot\left(\bar{D}_v\left\langle\bar{\mathsf{A}}\right\rangle_v\nabla_{\boldsymbol{x}}c_v^{(0)}\right)+\\&\quad+\nabla_{\boldsymbol{x}}\cdot\left(\bar{D}_v\left\langle\bar{\mathsf{A}}\left(\nabla_{\boldsymbol{y}}\boldsymbol{a}\right)^{\mathrm{T}}\right\rangle_v\nabla_{\boldsymbol{x}}c_v^{(0)}\right)=-\frac{1}{|\Omega_v|}\int_\Gamma\bar{\mathcal{J}}_d^{(0)}\,dS_{\boldsymbol{y}}\quad\text{in }\Omega_v\,.\end{aligned}\tag{6.91}$$

By defining the second order tensor $\mathsf{D}_v=D_v\left\langle\bar{\mathsf{A}}-\bar{\mathsf{A}}\left(\nabla_{\boldsymbol{y}}\boldsymbol{a}\right)^{\mathrm{T}}\right\rangle_v$, which represents the effective diffusivity tensor for the capillary compartment, we can reformulate Eq. (6.91) to finally obtain the following reaction-diffusion-advection equation for nutrients concentration $c_v^{(0)}$:

$$\frac{\partial c_v^{(0)}}{\partial t}+\nabla_{\boldsymbol{x}}\cdot\left(c_v^{(0)}\left\langle\boldsymbol{u}_v^{(0)}\right\rangle_v-\mathsf{D}_v\nabla_{\boldsymbol{x}}c_v^{(0)}\right)=-\frac{1}{|\Omega_v|}\int_\Gamma\bar{\mathcal{J}}_d^{(0)}\,dS_{\boldsymbol{y}}\quad\text{in }\Omega_v\,.\tag{6.92}$$

To conclude, the differential problem in the capillary domain is given by (6.64), (6.70) and (6.92) for variables $\left\langle\boldsymbol{u}_v^{(0)}\right\rangle_v$, $p_v^{(0)}$ and $c_v^{(0)}$. The system is not closed, because the fluid and nutrients fluxes $\bar{\mathcal{J}}_b^{(0)}$ and $\bar{\mathcal{J}}_d^{(0)}$ depend on the tumour micro-environment variables too. Hence, we proceed to derive the macroscale differential system for the tumour micro-environment compartment, allowing us to formulate a closed coupled problem involving both capillary and tumour micro-environment variables.

6.5.2 Tumour microenvironment problem

We consider now the tumour micro-environment problem, which consists of Eqs. (6.41), (6.42) and (6.45) and the first part of the interface boundary conditions (6.47) and (6.49). We start equating coefficients of ε^0 in (6.41) to obtain:

$$-\bar{\kappa}\bar{\mathsf{A}}\left(\boldsymbol{x},\boldsymbol{y}\right)\nabla_{\boldsymbol{y}}p_t^{(0)}=0\Rightarrow p_t^{(0)}=p_t^{(0)}(\boldsymbol{x},t)\quad\text{in }\Omega_t\,,\tag{6.93}$$

that means that $p_t^{(0)}$ is $\boldsymbol{y}$-constant.

By equating the coefficients of ε^1 in (6.41) and (6.42) and of ε^0 in (6.47), we obtain:

$$\boldsymbol{u}_t^{(0)} = -\bar{\kappa}\bar{\mathsf{A}}(\boldsymbol{x},\boldsymbol{y})\nabla_{\boldsymbol{x}} p_t^{(0)} - \bar{\kappa}\bar{\mathsf{A}}(\boldsymbol{x},\boldsymbol{y})\nabla_{\boldsymbol{y}} p_t^{(1)} \quad \text{in } \Omega_t\,, \tag{6.94}$$

$$\begin{aligned}\nabla_{\boldsymbol{y}}\cdot\boldsymbol{u}_t^{(0)} = {}& \nabla_{\boldsymbol{x}}\cdot(\bar{\chi}(\boldsymbol{x},\boldsymbol{y})\bar{\mathsf{A}}(\boldsymbol{x},\boldsymbol{y})\nabla_{\boldsymbol{y}} c_t^{(0)}) + \\ & + \nabla_{\boldsymbol{y}}\cdot(\bar{\chi}(\boldsymbol{x},\boldsymbol{y})\bar{\mathsf{A}}(\boldsymbol{x},\boldsymbol{y})\nabla_{\boldsymbol{x}} c_t^{(0)}) + \nabla_{\boldsymbol{y}}\cdot(\bar{\chi}(\boldsymbol{x},\boldsymbol{y})\bar{\mathsf{A}}(\boldsymbol{x},\boldsymbol{y})\nabla_{\boldsymbol{y}} c_t^{(1)}) \quad \text{in } \Omega_t\,,\end{aligned} \tag{6.95}$$

$$\boldsymbol{u}_t^{(0)}\cdot\boldsymbol{n}_t = 0 \quad \text{on } \Gamma\,, \tag{6.96}$$

where $\boldsymbol{n}_t = -\boldsymbol{n}$ is the outward unit vector normal to the tumour micro-environment surface. Now, we can substitute Eq. (6.94) into Eqs. (6.95) and (6.96) to obtain:

$$\begin{aligned}-\nabla_{\boldsymbol{y}}\cdot\left(\bar{\kappa}\bar{\mathsf{A}}(\boldsymbol{x},\boldsymbol{y})\nabla_{\boldsymbol{x}} p_t^{(0)} + \bar{\kappa}\bar{\mathsf{A}}(\boldsymbol{x},\boldsymbol{y})\nabla_{\boldsymbol{y}} p_t^{(1)}\right) = {}& \nabla_{\boldsymbol{x}}\cdot(\bar{\chi}(\boldsymbol{x},\boldsymbol{y})\bar{\mathsf{A}}(\boldsymbol{x},\boldsymbol{y})\nabla_{\boldsymbol{y}} c_t^{(0)}) + \\ & + \nabla_{\boldsymbol{y}}\cdot(\bar{\chi}(\boldsymbol{x},\boldsymbol{y})\bar{\mathsf{A}}(\boldsymbol{x},\boldsymbol{y})\nabla_{\boldsymbol{x}} c_t^{(0)}) + \nabla_{\boldsymbol{y}}\cdot(\bar{\chi}(\boldsymbol{x},\boldsymbol{y})\bar{\mathsf{A}}(\boldsymbol{x},\boldsymbol{y})\nabla_{\boldsymbol{y}} c_t^{(1)}) \quad \text{in } \Omega_t\,,\end{aligned} \tag{6.97}$$

$$\bar{\mathsf{A}}(\boldsymbol{x},\boldsymbol{y})\nabla_{\boldsymbol{y}} p_t^{(1)}\cdot\boldsymbol{n}_t = -\bar{\mathsf{A}}(\boldsymbol{x},\boldsymbol{y})\nabla_{\boldsymbol{x}} p_t^{(0)}\cdot\boldsymbol{n}_t \quad \text{on } \Gamma\,. \tag{6.98}$$

At this stage, we need to derive an equation for the leading-order pressure, $p_t^{(0)}$. Before proceeding with this, we will first derive an equation for the leading-order nutrient concentration, $c_t^{(0)}$, and propose an ansatz for $c_t^{(1)}$, as these quantities are present in Eq. (6.97). To achieve this, we collect the coefficients of ε^0 from Eqs. (6.45) and (6.49):

$$-\nabla_{\boldsymbol{y}}\left(\bar{D}_t\bar{\mathsf{A}}(\boldsymbol{x},\boldsymbol{y})\nabla_{\boldsymbol{y}} c_t^{(0)}\right) = 0 \quad \text{in } \Omega_t\,, \tag{6.99}$$

$$\left(\bar{D}_t\bar{\mathsf{A}}(\boldsymbol{x},\boldsymbol{y})\nabla_{\boldsymbol{y}} c_t^{(0)}\right)\cdot\boldsymbol{n}_t = 0 \quad \text{on } \Gamma\,. \tag{6.100}$$

The first equation, together with periodicity conditions in $\boldsymbol{y}$ and homogeneous Neumann conditions on Γ, has a constant solution with respect to $\boldsymbol{y}$, i.e.

$$c_t^{(0)} = c_t^{(0)}(\boldsymbol{x},t)\,. \tag{6.101}$$

Collecting terms of order ε^1 in Eqs. (6.45) and (6.49) we obtain the following differential problem:

$$\begin{aligned}&-\nabla_{\boldsymbol{x}}\cdot\left(\bar{D}_t\bar{\mathsf{A}}(\boldsymbol{x},\boldsymbol{y})\nabla_{\boldsymbol{y}} c_t^{(0)}\right) + \\ &+\nabla_{\boldsymbol{y}}\cdot\left(c_t^{(0)}\boldsymbol{u}_t^{(0)} - \bar{D}_t\bar{\mathsf{A}}(\boldsymbol{x},\boldsymbol{y})\nabla_{\boldsymbol{x}} c_t^{(0)} - \bar{D}_t\bar{\mathsf{A}}(\boldsymbol{x},\boldsymbol{y})\nabla_{\boldsymbol{y}} c_t^{(1)}\right) = 0 \quad \text{in } \Omega_t\,,\end{aligned} \tag{6.102}$$

$$\left(c_t^{(0)}\boldsymbol{u}_t^{(0)} - \bar{D}_t\bar{\mathsf{A}}(\boldsymbol{x},\boldsymbol{y})\nabla_{\boldsymbol{x}} c_t^{(0)} - \bar{D}_t\bar{\mathsf{A}}(\boldsymbol{x},\boldsymbol{y})\nabla_{\boldsymbol{y}} c_t^{(1)}\right)\cdot\boldsymbol{n}_t = 0 \quad \text{on } \Gamma\,. \tag{6.103}$$

Then, in Eq. (6.102) we utilize the fact that $c_t^{(0)}$ is $\boldsymbol{y}$-independent and substitute $\nabla_{\boldsymbol{y}}\cdot\boldsymbol{u}_t^{(0)}$ recalling Eq. (6.95), while in Eq. (6.103) we apply (6.96) to derive:

$$\begin{aligned}\nabla_{\boldsymbol{y}}\cdot\left[\left(\bar{\chi}(\boldsymbol{x},\boldsymbol{y})c_t^{(0)} - \bar{D}_t\right)\bar{\mathsf{A}}(\boldsymbol{x},\boldsymbol{y})\nabla_{\boldsymbol{y}} c_t^{(1)}\right] = {}& \\ -\nabla_{\boldsymbol{y}}\cdot\left[\left(\bar{\chi}(\boldsymbol{x},\boldsymbol{y})c_t^{(0)} - \bar{D}_t\right)\bar{\mathsf{A}}(\boldsymbol{x},\boldsymbol{y})\nabla_{\boldsymbol{x}} c_t^{(0)}\right] \quad & \text{in } \Omega_t\,,\end{aligned} \tag{6.104}$$

$$\bar{\mathsf{A}}(\boldsymbol{x},\boldsymbol{y})\nabla_{\boldsymbol{y}} c_t^{(1)}\cdot\boldsymbol{n}_t = -\bar{\mathsf{A}}(\boldsymbol{x},\boldsymbol{y})\nabla_{\boldsymbol{x}} c_t^{(0)}\cdot\boldsymbol{n}_t \quad \text{on } \Gamma\,. \tag{6.105}$$

We can then state the following ansatz for $c_t^{(1)}$:

$$c_t^{(1)}(\boldsymbol{x},\boldsymbol{y},t) = -\boldsymbol{b}(\boldsymbol{x},\boldsymbol{y})\cdot\nabla_{\boldsymbol{x}} c_t^{(0)}(\boldsymbol{x},t) + \tilde{c}_t(\boldsymbol{x},t)\,, \tag{6.106}$$

where $\tilde{c}_t(\boldsymbol{x},t)$ denotes the component that is independent of $\boldsymbol{y}$. In components it can be written as (removing the subscript t for convenience):

$$c^{(1)} = -b_i\frac{\partial c^{(0)}}{\partial x_i} + \tilde{c}\,. \tag{6.107}$$

Then, we insert the ansatz in (6.104), which in components reads:

$$\begin{aligned}
&\frac{\partial\left[\left(\bar{\chi}c_t^{(0)} - \bar{D}_t\right)\bar{A}_{ij}\dfrac{\partial}{\partial y_j}\left(b_k\dfrac{\partial c^{(0)}}{\partial x_k}\right)\right]}{\partial y_i} - \frac{\partial\left[\left(\bar{\chi}c_t^{(0)} - \bar{D}_t\right)\bar{A}_{ik}\dfrac{\partial c^0}{\partial x_k}\right]}{\partial y_i} = 0\,,\\
&\Rightarrow\left\{\frac{\partial\left[\left(\bar{\chi}c_t^{(0)} - \bar{D}_t\right)\bar{A}_{ij}\dfrac{\partial b_k}{\partial y_j}\right]}{\partial y_i} - \frac{\partial\left[\left(\bar{\chi}c_t^{(0)} - \bar{D}_t\right)\bar{A}_{ik}\right]}{\partial y_i}\right\}\frac{\partial c^{(0)}}{\partial x_k} = 0\,,\\
&\Rightarrow\frac{\partial\left[\left(\bar{\chi}c_t^{(0)} - \bar{D}_t\right)\dfrac{\partial b_k}{\partial y_j}\bar{A}_{ij}\right]}{\partial y_i} = \frac{\partial\left[\left(\bar{\chi}c_t^{(0)} - \bar{D}_t\right)\bar{A}_{ik}\right]}{\partial y_i}\quad\text{in }\Omega_t\,.
\end{aligned} \tag{6.108}$$

In tensor notation, we obtain:

$$\nabla_{\boldsymbol{y}}\cdot\left[\left(\bar{\chi}c_t^{(0)} - \bar{D}_t\right)(\nabla_{\boldsymbol{y}}\boldsymbol{b})\,\bar{\mathsf{A}}^{\mathrm{T}}\right] = \nabla_{\boldsymbol{y}}\cdot\left[\left(\bar{\chi}c_t^{(0)} - \bar{D}_t\right)\bar{\mathsf{A}}^{\mathrm{T}}\right]\quad\text{in }\Omega_t\,. \tag{6.109}$$

Expressing Eq. (6.105) in component form and incorporating the ansatz, we obtain:

$$\begin{aligned}
-\bar{A}_{ij}\frac{\partial}{\partial y_i}\left(b_k\frac{\partial c^{(0)}}{\partial x_k}\right)n_i &= -\bar{A}_{ik}\frac{\partial c^{(0)}}{\partial x_k}n_i\,,\\
\Rightarrow\left(\bar{A}_{ij}\frac{\partial b_k}{\partial y_j} - \bar{A}_{ik}\right)n_i\frac{\partial c^{(0)}}{\partial x_k} &= 0\,,\\
\Rightarrow\frac{\partial b_k}{\partial y_j}\bar{A}_{ij}n_i &= \bar{A}_{ik}n_i\quad\text{on }\Gamma\,,
\end{aligned} \tag{6.110}$$

which in tensor components reads:

$$(\nabla_{\boldsymbol{y}}\boldsymbol{b})\,\bar{\mathsf{A}}^{\mathrm{T}}\boldsymbol{n} = \bar{\mathsf{A}}^{\mathrm{T}}\boldsymbol{n}\quad\text{on }\Gamma\,. \tag{6.111}$$

Finally, the auxiliary vector $\boldsymbol{b}(\boldsymbol{x},\boldsymbol{y})$ solve the cell problem:

$$\begin{cases}
\nabla_{\boldsymbol{y}}\cdot\left[\left(\bar{\chi}c_t^{(0)} - \bar{D}_t\right)(\nabla_{\boldsymbol{y}}\boldsymbol{b})\,\bar{\mathsf{A}}^{\mathrm{T}}\right] = \nabla_{\boldsymbol{y}}\cdot\left[\left(\bar{\chi}c_t^{(0)} - \bar{D}_t\right)\bar{\mathsf{A}}^{\mathrm{T}}\right] & \text{in }\Omega_t\,,\\
(\nabla_{\boldsymbol{y}}\boldsymbol{b})\,\bar{\mathsf{A}}^{\mathrm{T}}\boldsymbol{n} = \bar{\mathsf{A}}^{\mathrm{T}}\boldsymbol{n} & \text{on }\Gamma\,.
\end{cases} \tag{6.112}$$

A further condition for $\boldsymbol{b}$ is required to ensure uniqueness, for example:

$$\langle\boldsymbol{b}(\boldsymbol{x},\boldsymbol{y})\rangle_t = \boldsymbol{0}\,. \tag{6.113}$$

Next, our goal is to derive a macroscale equation for the leading-order concentration

$c_t^{(0)}$ in Ω_t. To do this, we start by matching the ε^2 terms in equations (6.45) and (6.49), leading to:

$$\begin{aligned}\frac{\partial c_t^{(0)}}{\partial t} &+ \nabla_{\boldsymbol{x}} \cdot \left(c_t^{(0)} \boldsymbol{u}_t^{(0)} - \bar{D}_t \bar{\mathsf{A}} \nabla_{\boldsymbol{x}} c_t^{(0)} - \bar{D}_t \bar{\mathsf{A}} \nabla_{\boldsymbol{y}} c_t^{(1)} \right) + \\ &+ \nabla_{\boldsymbol{y}} \cdot \left(c_t^{(0)} \boldsymbol{u}_t^{(1)} + c_t^{(1)} \boldsymbol{u}_t^{(0)} - \bar{D}_t \bar{\mathsf{A}} \nabla_{\boldsymbol{x}} c_t^{(1)} - \bar{D}_t \bar{\mathsf{A}} \nabla_{\boldsymbol{y}} c_t^{(2)} \right) = -\bar{h} c_t^{(0)} \quad \text{in } \Omega_t \,,\end{aligned} \tag{6.114}$$

$$\left(c_t^{(0)} \boldsymbol{u}_t^{(1)} + c_t^{(1)} \boldsymbol{u}_t^{(0)} - \bar{D}_t \bar{\mathsf{A}} \nabla_{\boldsymbol{x}} c_t^{(1)} - \bar{D}_t \bar{\mathsf{A}} \nabla_{\boldsymbol{y}} c_t^{(2)} \right) \cdot \boldsymbol{n}_t = -\bar{\mathcal{J}}_d^{(0)} \quad \text{on } \Gamma \,, \tag{6.115}$$

where the zero-th order fluxes $\bar{\mathcal{J}}_b^{(0)}$ and $\bar{\mathcal{J}}_d^{(0)}$ are defined by (6.71) and (6.89). Taking the integral average over Ω_t of the first equation, exploiting the divergence theorem, the $\boldsymbol{y}$-periodicity and the interface condition given from Eq. (6.115), we can rewrite Eq. (6.114) as:

$$\begin{aligned}\frac{\partial c_t^{(0)}}{\partial t} &+ \nabla_{\boldsymbol{x}} \cdot \left(c_t^{(0)} \left\langle \boldsymbol{u}_t^{(0)} \right\rangle_t \right) - \nabla_{\boldsymbol{x}} \cdot \left(\bar{D}_t \left\langle \bar{\mathsf{A}} \right\rangle_t \nabla_{\boldsymbol{x}} c_t^{(0)} \right) + \\ &- \nabla_{\boldsymbol{x}} \cdot \left(\bar{D}_t \left\langle \bar{\mathsf{A}} \nabla_{\boldsymbol{y}} c_t^{(1)} \right\rangle_t \right) - \frac{1}{|\Omega_t|} \int_\Gamma \bar{\mathcal{J}}_d^{(0)} \, dS_{\boldsymbol{y}} = -\bar{h} c_t^{(0)} \quad \text{in } \Omega_t \,.\end{aligned} \tag{6.116}$$

Using ansatz (6.106) we can write:

$$\begin{aligned}\frac{\partial c_t^{(0)}}{\partial t} &+ \nabla_{\boldsymbol{x}} \cdot \left(c_t^{(0)} \left\langle \boldsymbol{u}_t^{(0)} \right\rangle_t \right) - \nabla_{\boldsymbol{x}} \cdot \left(\bar{D}_t \left\langle \bar{\mathsf{A}} \right\rangle_t \nabla_{\boldsymbol{x}} c_t^{(0)} \right) + \\ &+ \nabla_{\boldsymbol{x}} \cdot \left(\bar{D}_t \left\langle \bar{\mathsf{A}} \left(\nabla_{\boldsymbol{y}} \boldsymbol{b} \right)^{\mathrm{T}} \right\rangle_t \nabla_{\boldsymbol{x}} c_v^{(0)} \right) = \frac{1}{|\Omega_t|} \int_\Gamma \bar{\mathcal{J}}_d^{(0)} \, dS_{\boldsymbol{y}} - \bar{h} c_t^{(0)} \quad \text{in } \Omega_t \,.\end{aligned} \tag{6.117}$$

Firstly, we observe that the zero-th order nutrient flux, $\bar{\mathcal{J}}_d^{(0)}$, which appears in the surface integral term on the right-hand side and defined by (6.89), is independent of $\boldsymbol{y}$ due to the conditions given in (6.51), (6.74), (6.93), and (6.101). Next, we define the second-order tensor $\mathsf{D}_t = D_t \left\langle \bar{\mathsf{A}} - \bar{\mathsf{A}} \left(\nabla_{\boldsymbol{y}} \boldsymbol{b} \right)^{\mathrm{T}} \right\rangle_t$, which represents the effective diffusivity tensor for the tumour compartment. Incorporating these two observations into Eq. (6.117), we obtain the following reaction-diffusion-advection equation for the nutrient concentration $c_t^{(0)}$:

$$\frac{\partial c_t^{(0)}}{\partial t} + \nabla_{\boldsymbol{x}} \cdot \left(c_t^{(0)} \left\langle \boldsymbol{u}_t^{(0)} \right\rangle_t - \mathsf{D}_t \nabla_{\boldsymbol{x}} c_t^{(0)} \right) = \frac{|\Gamma|}{|\Omega_t|} \bar{\mathcal{J}}_d^{(0)} - \bar{h} c_t^{(0)} \quad \text{in } \Omega_t \,, \tag{6.118}$$

where $|\Gamma|$ is the total surface of the interface Γ.

We have now to write an equation for the leading order velocity $\boldsymbol{u}_t^{(0)}$ and pressure $p_t^{(0)}$. Examining equations (6.97) and (6.98), we can now rewrite them by considering that $c_t^{(0)}$ is $\boldsymbol{y}$-independent. Furthermore, we can consider the ansatz (6.106) made for $c_t^{(1)}$:

$$\begin{aligned}\nabla_{\boldsymbol{y}} \cdot \left(\bar{\kappa} \bar{\mathsf{A}}(\boldsymbol{x}, \boldsymbol{y}) \nabla_{\boldsymbol{y}} p_t^{(1)} \right) &= -\nabla_{\boldsymbol{y}} \cdot \left(\bar{\kappa} \bar{\mathsf{A}}(\boldsymbol{x}, \boldsymbol{y}) \nabla_{\boldsymbol{x}} p_t^{(0)} \right) - \nabla_{\boldsymbol{y}} \cdot \left(\bar{\chi}(\boldsymbol{x}, \boldsymbol{y}) \bar{\mathsf{A}}(\boldsymbol{x}, \boldsymbol{y}) \nabla_{\boldsymbol{x}} c_t^{(0)} \right) + \\ &+ \nabla_{\boldsymbol{y}} \cdot \left(\bar{\chi}(\boldsymbol{x}, \boldsymbol{y}) \bar{\mathsf{A}}(\boldsymbol{x}, \boldsymbol{y}) \left(\nabla_{\boldsymbol{y}} \boldsymbol{b} \right)^{\mathrm{T}} \nabla_{\boldsymbol{x}} c_t^{(0)} \right) \text{ in } \Omega_t \,,\end{aligned} \tag{6.119}$$

$$\bar{\mathsf{A}}(\boldsymbol{x}, \boldsymbol{y}) \nabla_{\boldsymbol{y}} p_t^{(1)} \cdot \boldsymbol{n}_t = -\bar{\mathsf{A}}(\boldsymbol{x}, \boldsymbol{y}) \nabla_{\boldsymbol{x}} p_t^{(0)} \cdot \boldsymbol{n}_t \quad \text{on } \Gamma \,. \tag{6.120}$$

At this point we can state the following ansatz:

$$p_t^{(1)}(\boldsymbol{x},\boldsymbol{y},t) = -\boldsymbol{P}_t(\boldsymbol{x},\boldsymbol{y})\cdot\nabla_{\boldsymbol{x}} p_t^{(0)}(\boldsymbol{x},t) - \boldsymbol{C}_t(\boldsymbol{x},\boldsymbol{y})\cdot\nabla_{\boldsymbol{x}} c_t^{(0)}(\boldsymbol{x},t) + \tilde{p}_t(\boldsymbol{x},t)\,, \tag{6.121}$$

where $\tilde{p}_t(\boldsymbol{x},t)$ represents the term independent of $\boldsymbol{y}$. The ansatz can be written in components as (removing the subscript t for convenience):

$$p^{(1)} = -P_i\frac{\partial p^{(0)}}{\partial x_i} - C_i\frac{\partial c^{(0)}}{\partial x_i} + \tilde{p}\,. \tag{6.122}$$

Rewriting Eq. (6.119) in terms of its components and incorporating the ansatz (6.121), we obtain:

$$\begin{aligned}
&\frac{\partial}{\partial y_i}\left(\bar{\kappa}\bar{A}_{ij}\frac{\partial P_k}{\partial y_j}\frac{\partial p^0}{\partial x_k}\right) + \frac{\partial}{\partial y_i}\left(\bar{\kappa}\bar{A}_{ij}\frac{\partial C_k}{\partial y_j}\frac{\partial c^0}{\partial x_k}\right) = \frac{\partial}{\partial y_i}\left(\bar{\kappa}\bar{A}_{ik}\frac{\partial p^{(0)}}{\partial x_k}\right) + \\
&\qquad + \frac{\partial}{\partial y_i}\left(\bar{\chi}\bar{A}_{ik}\frac{\partial c^{(0)}}{\partial x_k}\right) - \frac{\partial}{\partial y_i}\left(\bar{\chi}\bar{A}_{ij}\frac{\partial b_k}{\partial y_j}\frac{\partial c^{(0)}}{\partial x_k}\right) \\
&\Rightarrow \left[\frac{\partial}{\partial y_i}\left(\bar{\kappa}\bar{A}_{ij}\frac{\partial P_k}{\partial y_j}\right) - \frac{\partial}{\partial y_i}\left(\bar{\kappa}\bar{A}_{ik}\right)\right]\frac{\partial p^0}{\partial x_k} + \\
&\qquad \left[\frac{\partial}{\partial y_i}\left(\bar{\kappa}\bar{A}_{ij}\frac{\partial C_k}{\partial y_j}\right) - \frac{\partial}{\partial y_i}\left(\bar{\chi}\bar{A}_{ik} - \bar{\chi}\bar{A}_{ij}\frac{\partial b_k}{\partial y_j}\right)\right]\frac{\partial c^0}{\partial x_k} = 0 \quad \text{in } \Omega_t\,.
\end{aligned} \tag{6.123}$$

By equating the terms in the first parenthesis, we obtain:

$$\frac{\partial}{\partial y_i}\left(\bar{\kappa}\bar{A}_{ij}\frac{\partial P_k}{\partial y_j}\right) = \frac{\partial}{\partial y_i}\left(\bar{\kappa}\bar{A}_{ik}\right) \Rightarrow \frac{\partial}{\partial y_i}\left(\bar{A}_{ij}\frac{\partial P_k}{\partial y_j}\right) = \frac{\partial}{\partial y_i}\left(\bar{A}_{ik}\right)\,, \tag{6.124}$$

which in tensor notation reads:

$$\nabla_{\boldsymbol{y}}\cdot\left[\left(\nabla_{\boldsymbol{y}}\boldsymbol{P}_t\right)\bar{\mathrm{A}}^{\mathrm{T}}\right] = \nabla_{\boldsymbol{y}}\cdot\bar{\mathrm{A}}^{\mathrm{T}} \quad \text{in } \Omega_t\,. \tag{6.125}$$

Furthermore, by matching the terms in the second parenthesis, we get:

$$\frac{\partial}{\partial y_i}\left(\bar{\kappa}\bar{A}_{ij}\frac{\partial C_k}{\partial y_j}\right) = \frac{\partial}{\partial y_i}\left(\bar{\chi}\bar{A}_{ik} - \bar{\chi}\bar{A}_{ij}\frac{\partial b_k}{\partial y_j}\right)\,, \tag{6.126}$$

which in tensor notations reads:

$$\nabla_{\boldsymbol{y}}\cdot\left[\bar{\kappa}\left(\nabla_{\boldsymbol{y}}\boldsymbol{C}_t\right)\bar{\mathrm{A}}^{\mathrm{T}}\right] = \nabla_{\boldsymbol{y}}\cdot\left[\bar{\chi}\bar{\mathrm{A}}^{\mathrm{T}} - \bar{\chi}\left(\nabla_{\boldsymbol{y}}\boldsymbol{b}\right)\bar{\mathrm{A}}^{\mathrm{T}}\right] \quad \text{in } \Omega_t\,. \tag{6.127}$$

Expressing Eq. (6.120) in component form and incorporating the ansatz, we obtain:

$$\begin{aligned}
&-\bar{A}_{ij}\frac{\partial}{\partial y_i}\left(P_k\frac{\partial p^{(0)}}{\partial x_k}\right)n_i - \bar{A}_{ij}\frac{\partial}{\partial y_i}\left(C_k\frac{\partial c^{(0)}}{\partial x_k}\right)n_i = -\bar{A}_{ik}\frac{\partial p^{(0)}}{\partial x_k}n_i \\
&\Rightarrow \left(\bar{A}_{ij}\frac{\partial P_k}{\partial y_j} - \bar{A}_{ik}\right)n_i\frac{\partial p^{(0)}}{\partial x_k} + \left(\bar{A}_{ij}\frac{\partial C_k}{\partial y_i}\right)n_i\frac{\partial c^{(0)}}{\partial x_k} = 0 \quad \text{on } \Gamma\,.
\end{aligned} \tag{6.128}$$

By equating the terms in the first parenthesis we obtain:

$$\bar{A}_{ij}\frac{\partial P_k}{\partial y_j}n_i = \bar{A}_{ik}n_i \quad \text{on } \Gamma\,, \tag{6.129}$$

which in tensor components reads:

$$(\nabla_{\boldsymbol{y}} \boldsymbol{P}_t)\, \bar{\mathsf{A}}^{\mathrm{T}} \boldsymbol{n} = \bar{\mathsf{A}}^{\mathrm{T}} \boldsymbol{n} \quad \text{on } \Gamma\,. \tag{6.130}$$

By equating the terms in the second set of parentheses, we obtain:

$$\bar{A}_{ij} \frac{\partial C_k}{\partial y_j} n_i = 0_k \quad \text{on } \Gamma\,, \tag{6.131}$$

which in tensor components reads:

$$(\nabla_{\boldsymbol{y}} \boldsymbol{C}_t)\, \bar{\mathsf{A}}^{\mathrm{T}} \boldsymbol{n} = \boldsymbol{0} \quad \text{on } \Gamma\,. \tag{6.132}$$

Finally, the auxiliary vector $\boldsymbol{P}_t\,(\boldsymbol{x}, \boldsymbol{y})$ solve the cell problem:

$$\begin{cases} \nabla_{\boldsymbol{y}} \cdot \left[(\nabla_{\boldsymbol{y}} \boldsymbol{P}_t)\, \bar{\mathsf{A}}^{\mathrm{T}} \right] = \nabla_{\boldsymbol{y}} \cdot \bar{\mathsf{A}}^{\mathrm{T}} & \text{in } \Omega_t\,, \\ (\nabla_{\boldsymbol{y}} \boldsymbol{P}_t)\, \bar{\mathsf{A}}^{\mathrm{T}} \boldsymbol{n} = \bar{\mathsf{A}}^{\mathrm{T}} \boldsymbol{n} & \text{on } \Gamma\,, \end{cases} \tag{6.133}$$

while the auxiliary vector $\boldsymbol{C}_t\,(\boldsymbol{x}, \boldsymbol{y})$ solve the cell problem:

$$\begin{cases} \nabla_{\boldsymbol{y}} \cdot \left[\bar{\kappa}\, (\nabla_{\boldsymbol{y}} \boldsymbol{C}_t)\, \bar{\mathsf{A}}^{\mathrm{T}} \right] = \nabla_{\boldsymbol{y}} \cdot \left[\bar{\chi} \bar{\mathsf{A}}^{\mathrm{T}} - \bar{\chi}\, (\nabla_{\boldsymbol{y}} \boldsymbol{b})\, \bar{\mathsf{A}}^{\mathrm{T}} \right] & \text{in } \Omega_t\,, \\ (\nabla_{\boldsymbol{y}} \boldsymbol{C}_t)\, \bar{\mathsf{A}}^{\mathrm{T}} \boldsymbol{n} = \boldsymbol{0} & \text{on } \Gamma\,. \end{cases} \tag{6.134}$$

An additional condition for $\boldsymbol{P}_t\,(\boldsymbol{x}, \boldsymbol{y})$ and $\boldsymbol{C}_t\,(\boldsymbol{x}, \boldsymbol{y})$ is needed to ensure uniqueness, such as:

$$\left\langle \boldsymbol{P}_t\,(\boldsymbol{x}, \boldsymbol{y}) \right\rangle_t = \boldsymbol{0} \quad \text{and} \quad \left\langle \boldsymbol{C}_t\,(\boldsymbol{x}, \boldsymbol{y}) \right\rangle_t = \boldsymbol{0}\,. \tag{6.135}$$

Then, a cell averaging of Eq. (6.94) over Ω_t provides:

$$\left\langle \boldsymbol{u}_t^{(0)} \right\rangle_t = -\bar{\kappa}\, \langle \bar{\mathsf{A}} \rangle_t\, \nabla_{\boldsymbol{x}} p_t^{(0)} + \bar{\kappa} \left\langle \bar{\mathsf{A}}\, (\nabla_{\boldsymbol{y}} \boldsymbol{P}_t)^{\mathrm{T}} \right\rangle_t \nabla_{\boldsymbol{x}} p_t^{(0)} + \bar{\kappa} \left\langle \bar{\mathsf{A}}\, (\nabla_{\boldsymbol{y}} \boldsymbol{C}_t)^{\mathrm{T}} \right\rangle_t \nabla_{\boldsymbol{x}} c_t^{(0)} \quad \text{in } \Omega_t\,. \tag{6.136}$$

Finally, defining the tensors

$$\mathsf{F} = \bar{\kappa} \left\langle \bar{\mathsf{A}} - \bar{\mathsf{A}}\, (\nabla_{\boldsymbol{y}} \boldsymbol{P}_t)^{\mathrm{T}} \right\rangle_t \tag{6.137}$$

and

$$\mathsf{G} = \bar{\kappa} \left\langle \bar{\mathsf{A}}\, (\nabla_{\boldsymbol{y}} \boldsymbol{C}_t)^{\mathrm{T}} \right\rangle_t\,, \tag{6.138}$$

we obtain a macroscale equation for the average velocity in tumour micro-environment:

$$\left\langle \boldsymbol{u}_t^{(0)} \right\rangle_t = -\mathsf{F} \nabla_{\boldsymbol{x}} p_t^{(0)} + \mathsf{G} \nabla_{\boldsymbol{x}} c_t^{(0)} \quad \text{in } \Omega_t\,. \tag{6.139}$$

The average velocity profile in the tumour micro-environment from the combination of two factors. The first term on the r.h.s. of (6.139) states that the flux is proportional to the gradient of the leading-order pressure, $p_t^{(0)}$, and it can thus be seen as an anisotropic Darcy's law at the macroscale. The second term on the r.h.s. of (6.139) accounts for cell motion driven by the gradient of the leading-order chemical concentration $c_t^{(0)}$, resembling a generalization of the Keller-Segel chemotactic velocity at the macroscale.

The influence of the microstructure is incorporated through the tensors F and G, respectively.

To close the entire macroscale model, we need a macroscale equation for the leading order pressure $p_t^{(0)}$. To obtain it, we collect the ε^2 coefficients in (6.42) and the ε^1 coefficients in (6.47):

$$\begin{aligned}
&\nabla_{\boldsymbol{x}} \cdot \boldsymbol{u}_t^{(0)} + \nabla_{\boldsymbol{y}} \cdot \boldsymbol{u}_t^{(1)} = \bar{\gamma} c_t^{(0)} + \\
&+ \nabla_{\boldsymbol{x}} \cdot \left(\bar{\chi}\left(\boldsymbol{x},\boldsymbol{y}\right) \bar{\mathsf{A}}\left(\boldsymbol{x},\boldsymbol{y}\right) \nabla_{\boldsymbol{x}} c_t^{(0)} \right) + \nabla_{\boldsymbol{x}} \cdot \left(\bar{\chi}\left(\boldsymbol{x},\boldsymbol{y}\right) \bar{\mathsf{A}}\left(\boldsymbol{x},\boldsymbol{y}\right) \nabla_{\boldsymbol{y}} c_t^{(1)} \right) + \\
&+ \nabla_{\boldsymbol{y}} \cdot \left(\bar{\chi}\left(\boldsymbol{x},\boldsymbol{y}\right) \bar{\mathsf{A}}\left(\boldsymbol{x},\boldsymbol{y}\right) \nabla_{\boldsymbol{x}} c_t^{(1)} \right) + \nabla_{\boldsymbol{y}} \cdot \left(\bar{\chi}\left(\boldsymbol{x},\boldsymbol{y}\right) \bar{\mathsf{A}}\left(\boldsymbol{x},\boldsymbol{y}\right) \nabla_{\boldsymbol{y}} c_t^{(2)} \right) \text{ in } \Omega_t \,,
\end{aligned} \tag{6.140}$$

$$\boldsymbol{u}_t^{(1)} \cdot \boldsymbol{n}_t = -\bar{\mathcal{J}}_b^{(0)} \quad \text{on } \Gamma \,, \tag{6.141}$$

where we recall that $\boldsymbol{n}_t = -\boldsymbol{n}$.
An integral averaging of the first equation over Ω_t, using the divergence theorem in the $\boldsymbol{y}$ variable, provides:

$$\begin{aligned}
\nabla_{\boldsymbol{x}} \cdot \left\langle \boldsymbol{u}_t^{(0)} \right\rangle_t + \frac{1}{|\Omega_t|} \int_\Gamma \boldsymbol{u}_t^{(1)} \cdot \boldsymbol{n}_t \, dS_{\boldsymbol{y}} = \bar{\gamma} c_t^{(0)} + \\
+ \nabla_{\boldsymbol{x}} \cdot \left(\langle \bar{\chi} \bar{\mathsf{A}} \rangle_t \nabla_{\boldsymbol{x}} c_t^{(0)} \right) - \nabla_{\boldsymbol{x}} \cdot \left(\left\langle \bar{\chi} \bar{\mathsf{A}} \left(\nabla_{\boldsymbol{y}} \boldsymbol{b} \right)^{\mathrm{T}} \right\rangle_t \nabla_{\boldsymbol{x}} c_t^{(0)} \right) + \\
+ \frac{1}{|\Omega_t|} \int_\Gamma \bar{\chi} \left(\bar{\mathsf{A}} \nabla_{\boldsymbol{x}} c_t^{(1)} + \bar{\mathsf{A}} \nabla_{\boldsymbol{y}} c_t^{(2)} \right) \cdot \boldsymbol{n}_t \, dS_{\boldsymbol{y}} \quad \text{in } \Omega_t \,.
\end{aligned} \tag{6.142}$$

Taking into account the interface condition (6.96) and (6.141), we can rewrite the interface condition (6.115) as:

$$\left(\bar{\mathsf{A}} \nabla_{\boldsymbol{x}} c_t^{(1)} + \bar{\mathsf{A}} \nabla_{\boldsymbol{y}} c_t^{(2)} \right) \cdot \boldsymbol{n}_t = -\frac{\bar{\mathcal{J}}_b^{(0)}}{\bar{D}_t} c_t^{(0)} + \frac{\bar{\mathcal{J}}_d^{(0)}}{\bar{D}_t} \quad \text{on } \Gamma \,. \tag{6.143}$$

Using the interface conditions (6.141) and (6.143) and defining $\mathsf{C} = \left\langle \bar{\chi} \bar{\mathsf{A}} - \bar{\chi} \bar{\mathsf{A}} \left(\nabla_{\boldsymbol{y}} \boldsymbol{b} \right)^{\mathrm{T}} \right\rangle_t$, we can rewrite equation (6.142) as:

$$\begin{aligned}
\nabla_{\boldsymbol{x}} \cdot \left\langle \boldsymbol{u}_t^{(0)} \right\rangle_t = \bar{\gamma} c_t^{(0)} + \frac{1}{|\Omega_t|} \int_\Gamma \bar{\mathcal{J}}_b^{(0)} \, dS_{\boldsymbol{y}} + \frac{1}{|\Omega_t|} \int_\Gamma \bar{\chi}(\boldsymbol{x},\boldsymbol{y}) \frac{\bar{\mathcal{J}}_d^{(0)}}{\bar{D}_t} \, dS_{\boldsymbol{y}} + \\
- \frac{1}{|\Omega_t|} \int_\Gamma \bar{\chi}(\boldsymbol{x},\boldsymbol{y}) \frac{\bar{\mathcal{J}}_b^{(0)}}{\bar{D}_t} c_t^{(0)} \, dS_{\boldsymbol{y}} + \nabla_{\boldsymbol{x}} \cdot \left(\mathsf{C} \nabla_{\boldsymbol{x}} c_t^{(0)} \right) \quad \text{in } \Omega_t \,.
\end{aligned} \tag{6.144}$$

Next, we observe that the fluxes $\bar{\mathcal{J}}_b^{(0)}$ and $\bar{\mathcal{J}}_d^{(0)}$, as defined in Eqs. (6.71)-(6.89), are independent of $\boldsymbol{y}$ due to the conditions specified in (6.51), (6.74), (6.93), and (6.101). Consequently, we obtain:

$$\begin{aligned}
\nabla_{\boldsymbol{x}} \cdot \left\langle \boldsymbol{u}_t^{(0)} \right\rangle_t = \bar{\gamma} c_t^{(0)} + \frac{|\Gamma|}{|\Omega_t|} \bar{\mathcal{J}}_b^{(0)} + \frac{1}{|\Omega_t|} \frac{\bar{\mathcal{J}}_d^{(0)}}{\bar{D}_t} \int_\Gamma \bar{\chi}(\boldsymbol{x},\boldsymbol{y}) \, dS_{\boldsymbol{y}} + \\
- \frac{1}{|\Omega_t|} \frac{\bar{\mathcal{J}}_b^{(0)}}{\bar{D}_t} c_t^{(0)} \int_\Gamma \bar{\chi}(\boldsymbol{x},\boldsymbol{y}) \, dS_{\boldsymbol{y}} + \nabla_{\boldsymbol{x}} \cdot \left(\mathsf{C} \nabla_{\boldsymbol{x}} c_t^{(0)} \right) \quad \text{in } \Omega_t \,.
\end{aligned} \tag{6.145}$$

Finally, we define $X(\boldsymbol{x}) = \int_\Gamma \bar{\chi}(\boldsymbol{x},\boldsymbol{y})\, dS_{\boldsymbol{y}}$ and we use Eq. (6.139) to obtain:

$$\begin{aligned}\nabla_{\boldsymbol{x}} \cdot \left(\mathsf{F}\nabla_{\boldsymbol{x}} p_t^{(0)}\right) = &- \bar{\gamma} c_t^{(0)} + \frac{|\Gamma|}{|\Omega_t|}\bar{\mathcal{J}}_b^{(0)} - \frac{1}{|\Omega_t|}\frac{\bar{\mathcal{J}}_d^{(0)}}{\bar{D}_t} X(\boldsymbol{x}) + \\ &+ \frac{1}{|\Omega_t|}\frac{\bar{\mathcal{J}}_b^{(0)}}{\bar{D}_t} c_t^{(0)} X(\boldsymbol{x}) + \nabla_{\boldsymbol{x}} \cdot \left[(\mathsf{G}-\mathsf{C})\,\nabla_{\boldsymbol{x}} c_t^{(0)}\right] \quad \text{in } \Omega_t\,.\end{aligned} \tag{6.146}$$

In this case, the effective source term on the right-hand side of Eq. (6.146) primarily arises from the leading-order fluid and nutrient fluxes, $\bar{\mathcal{J}}_b^{(0)}$ and $\bar{\mathcal{J}}_d^{(0)}$. Additionally, there is a further contribution from the gradient of the nutrient concentration.

The differential problem for tumour micro-environment is finally given by Eqs. (6.139), (6.146) and (6.118) for the tumour micro-environment variables $\left\langle \boldsymbol{u}_t^{(0)} \right\rangle_t$, $p_t^{(0)}$ and $c_t^{(0)}$.

Particular case

A particular case arises when the parameter $\bar{\chi}$ is independent both of $\boldsymbol{x}$ and of $\boldsymbol{y}$, i.e., $\bar{\chi}(\boldsymbol{x},\boldsymbol{y}) \equiv \bar{\chi}$. In this specific scenario, we observe a simplification of the tumour micro-environment problem. In fact, Eq. (6.104) can be rewritten as:

$$\left(\bar{\chi} c_t^{(0)} - \bar{D}_t\right) \nabla_{\boldsymbol{y}} \cdot \left(\bar{\mathsf{A}}(\boldsymbol{x},\boldsymbol{y})\nabla_{\boldsymbol{y}} c_t^{(1)} + \bar{\mathsf{A}}(\boldsymbol{x},\boldsymbol{y})\nabla_{\boldsymbol{x}} c_t^{(0)}\right) = 0 \quad \text{in } \Omega_t\,. \tag{6.147}$$

One solution of Eq. (6.147) could be

$$c_t^{(0)}(\boldsymbol{x},t) \equiv \frac{\bar{D}_t}{\bar{\chi}}\,, \quad \forall t\,,\ \forall \boldsymbol{x} \in \Omega_t\,. \tag{6.148}$$

Assuming that solution, Eq. (6.147) is trivially satisfied and is valid for any $c_t^{(1)}$. Therefore, without loss of generality, we can state the following ansatz:

$$c_t^{(1)}(\boldsymbol{x},\boldsymbol{y},t) = -\boldsymbol{b}(\boldsymbol{x},\boldsymbol{y}) \cdot \nabla_{\boldsymbol{x}} c_t^{(0)}(\boldsymbol{x},t) + \tilde{c}_t(\boldsymbol{x},t)\,, \tag{6.149}$$

which in components can be written as (removing the subscript t for convenience):

$$c^{(1)} = -b_i \frac{\partial c^{(0)}}{\partial x_i} + \tilde{c}\,. \tag{6.150}$$

The above ansatz is valid both when $c_t^{(0)}(\boldsymbol{x},t) = \dfrac{\bar{D}_t}{\bar{\chi}}$, since (6.147) is trivially satisfied for any $c_t^{(1)}$, and in this specific case $c_t^{(1)} \equiv \tilde{c}_t(\boldsymbol{x},t)$ is $\boldsymbol{y}$-independent. It is also valid when $c_t^{(0)}(\boldsymbol{x},t) \neq \dfrac{\bar{D}_t}{\bar{\chi}}$, in which case Eq. (6.147) can be rewritten as:

$$\nabla_{\boldsymbol{y}} \cdot \left(\bar{\mathsf{A}}(\boldsymbol{x},\boldsymbol{y})\nabla_{\boldsymbol{x}} c_t^{(0)} + \bar{\mathsf{A}}(\boldsymbol{x},\boldsymbol{y})\nabla_{\boldsymbol{y}} c_t^{(1)}\right) = 0 \quad \text{in } \Omega_t\,. \tag{6.151}$$

In the second scenario, in order to find the correct vector $\boldsymbol{b}(\boldsymbol{x},\boldsymbol{y})$, we insert the ansatz (6.149) in (6.151), which in components reads:

$$\begin{aligned}
&\frac{\partial\left(A_{ik}\dfrac{\partial c^0}{\partial x_k}\right)}{\partial y_i}-\frac{\partial\left(A_{ij}\dfrac{\partial}{\partial y_j}\left(b_k\dfrac{\partial c^{(0)}}{\partial x_k}\right)\right)}{\partial y_i}=0\,,\\
&\qquad\Rightarrow\left(\frac{\partial A_{ik}}{\partial y_i}-\frac{\partial\left(A_{ij}\dfrac{\partial b_k}{\partial y_j}\right)}{\partial y_i}\right)\frac{\partial c^{(0)}}{\partial x_k}=0\,,\\
&\qquad\qquad\Rightarrow\frac{\partial\left(\dfrac{\partial b_k}{\partial y_j}A_{ij}\right)}{\partial y_i}=\frac{\partial A_{ik}}{\partial y_i}\quad\text{in }\Omega_t\,.
\end{aligned}\tag{6.152}$$

In tensor notation, we obtain:

$$\nabla_{\boldsymbol{y}}\cdot\left[(\nabla_{\boldsymbol{y}}\boldsymbol{b})\,\mathsf{A}^{\mathrm{T}}\right]=\nabla_{\boldsymbol{y}}\cdot\mathsf{A}^{\mathrm{T}}\quad\text{in }\Omega_t\,.\tag{6.153}$$

Expressing Eq. (6.105) in component form and incorporating the ansatz, we obtain:

$$\begin{aligned}
&-A_{ij}\frac{\partial}{\partial y_i}\left(b_k\frac{\partial c^{(0)}}{\partial x_k}\right)n_i=-A_{ik}\frac{\partial c^{(0)}}{\partial x_k}n_i\,,\\
&\qquad\Rightarrow\left(A_{ij}\frac{\partial b_k}{\partial y_j}-A_{ik}\right)n_i\frac{\partial c^{(0)}}{\partial x_k}=0\,,\\
&\qquad\qquad\Rightarrow\frac{\partial b_k}{\partial y_j}A_{ij}n_i=A_{ik}n_i\quad\text{on }\Gamma\,;
\end{aligned}\tag{6.154}$$

which in tensor components reads:

$$(\nabla_{\boldsymbol{y}}\boldsymbol{b})\,\mathsf{A}^{\mathrm{T}}\boldsymbol{n}=\mathsf{A}^{\mathrm{T}}\boldsymbol{n}\quad\text{on }\Gamma\,.\tag{6.155}$$

Finally, the auxiliary vector $\boldsymbol{b}(\boldsymbol{x},\boldsymbol{y})$ solve the cell problem:

$$\begin{cases}\nabla_{\boldsymbol{y}}\cdot\left[(\nabla_{\boldsymbol{y}}\boldsymbol{b})\,\mathsf{A}^{\mathrm{T}}\right]=\nabla_{\boldsymbol{y}}\cdot\mathsf{A}^{\mathrm{T}} & \text{in }\Omega_t\,,\\ (\nabla_{\boldsymbol{y}}\boldsymbol{b})\,\mathsf{A}^{\mathrm{T}}\boldsymbol{n}=\mathsf{A}^{\mathrm{T}}\boldsymbol{n} & \text{on }\Gamma\,.\end{cases}\tag{6.156}$$

A further condition for $\boldsymbol{b}$ is required to ensure uniqueness, for example:

$$\langle\boldsymbol{b}(\boldsymbol{x},\boldsymbol{y})\rangle_t=\boldsymbol{0}\,.\tag{6.157}$$

Next, our goal is to derive a macroscale equation for the leading-order concentration $c_t^{(0)}$ in Ω_t. To do this, with analogous steps as the general case, we obtain Eq. (6.118). The main difference in this equation lies in the distinct and easier cell problem that the auxiliary vector $\boldsymbol{b}(\boldsymbol{x},\boldsymbol{y})$ must satisfy. In fact, the cell problem (6.156) is independent of $c_t^{(0)}(\boldsymbol{x},t)$ and, therefore, can be solved once at the outset.

We have now to write an equation for the leading order velocity $\boldsymbol{u}_t^{(0)}$ and pressure $p_t^{(0)}$. Examining equations (6.97) and (6.98), we can now reformulate these expressions, taking into account that $c_t^{(0)}$ is, in any case, independent of $\boldsymbol{y}$. Furthermore, we can either

consider the alternative solution (6.148), which entails that $c_t^{(0)}$ is a global constant and $c_t^{(1)}$ is a $\boldsymbol{y}$-constant function, or utilise Eq. (6.151) to obtain:

$$\nabla_{\boldsymbol{y}} \cdot \left(\bar{\mathsf{A}}(\boldsymbol{x},\boldsymbol{y}) \nabla_{\boldsymbol{y}} p_t^{(1)} \right) = -\nabla_{\boldsymbol{y}} \cdot \left(\bar{\mathsf{A}}(\boldsymbol{x},\boldsymbol{y}) \nabla_{\boldsymbol{x}} p_t^{(0)} \right) \quad \text{in } \Omega_t \,, \tag{6.158}$$

$$\bar{\mathsf{A}}(\boldsymbol{x},\boldsymbol{y}) \nabla_{\boldsymbol{y}} p_t^{(1)} \cdot \boldsymbol{n}_t = -\bar{\mathsf{A}}(\boldsymbol{x},\boldsymbol{y}) \nabla_{\boldsymbol{x}} p_t^{(0)} \cdot \boldsymbol{n}_t \quad \text{on } \Gamma \,. \tag{6.159}$$

At this point we can state the following ansatz:

$$p_t^{(1)}(\boldsymbol{x},\boldsymbol{y},t) = -\boldsymbol{P}_t(\boldsymbol{x},\boldsymbol{y}) \cdot \nabla_{\boldsymbol{x}} p_t^{(0)}(\boldsymbol{x},t) + \tilde{p}_t(\boldsymbol{x},t) \,, \tag{6.160}$$

where $\tilde{p}_t(\boldsymbol{x},t)$ denotes the component that is independent of $\boldsymbol{y}$. The ansatz can be rewritten in components as (removing the subscript t for convenience):

$$p^{(1)} = -P_i \frac{\partial p^{(0)}}{\partial x_i} + \tilde{p} \,. \tag{6.161}$$

Rewriting Eq. (6.158) in terms of its components and incorporating the ansatz, we obtain:

$$\begin{aligned} &\frac{\partial \left(A_{ik} \dfrac{\partial p^0}{\partial x_k} \right)}{\partial y_i} - \frac{\partial \left(A_{ij} \dfrac{\partial}{\partial y_j} \left(P_k \dfrac{\partial p^{(0)}}{\partial x_k} \right) \right)}{\partial y_i} = 0 \,, \\ &\Rightarrow \left(\frac{\partial A_{ik}}{\partial y_i} - \frac{\partial \left(A_{ij} \dfrac{\partial P_k}{\partial y_j} \right)}{\partial y_i} \right) \frac{\partial p^{(0)}}{\partial x_k} = 0 \,, \\ &\Rightarrow \frac{\partial \left(\dfrac{\partial P_k}{\partial y_j} A_{ij} \right)}{\partial y_i} = \frac{\partial A_{ik}}{\partial y_i} \quad \text{in } \Omega_t \,. \end{aligned} \tag{6.162}$$

In tensor notation, it reads:

$$\nabla_{\boldsymbol{y}} \cdot \left[(\nabla_{\boldsymbol{y}} \boldsymbol{P}_t)\, \mathsf{A}^{\mathrm{T}} \right] = \nabla_{\boldsymbol{y}} \cdot \mathsf{A}^{\mathrm{T}} \quad \text{in } \Omega_t \,. \tag{6.163}$$

Expressing Eq. (6.159) in component form and incorporating the ansatz, we obtain:

$$\begin{aligned} -A_{ij} \frac{\partial}{\partial y_i} \left(P_k \frac{\partial p^{(0)}}{\partial x_k} \right) n_i &= -A_{ik} \frac{\partial p^{(0)}}{\partial x_k} n_i \,, \\ \Rightarrow \left(A_{ij} \frac{\partial P_k}{\partial y_j} - A_{ik} \right) n_i \frac{\partial p^{(0)}}{\partial x_k} &= 0 \,, \\ \Rightarrow \frac{\partial P_k}{\partial y_j} A_{ij} n_i &= A_{ik} n_i \quad \text{on } \Gamma \,, \end{aligned} \tag{6.164}$$

which in tensor components reads:

$$(\nabla_{\boldsymbol{y}} \boldsymbol{P}_t)\, \mathsf{A}^{\mathrm{T}} \boldsymbol{n} = \mathsf{A}^{\mathrm{T}} \boldsymbol{n} \quad \text{on } \Gamma \,. \tag{6.165}$$

Finally, the auxiliary vector $\boldsymbol{P}_t(\boldsymbol{x},\boldsymbol{y})$ solve the cell problem:

$$\begin{cases} \nabla_{\boldsymbol{y}} \cdot \left[(\nabla_{\boldsymbol{y}} \boldsymbol{P}_t)\, \mathsf{A}^{\mathrm{T}} \right] = \nabla_{\boldsymbol{y}} \cdot \mathsf{A}^{\mathrm{T}} & \text{in } \Omega_t\,, \\ (\nabla_{\boldsymbol{y}} \boldsymbol{P}_t)\, \mathsf{A}^{\mathrm{T}} \boldsymbol{n} = \mathsf{A}^{\mathrm{T}} \boldsymbol{n} & \text{on } \Gamma\,. \end{cases} \tag{6.166}$$

A further condition for $\boldsymbol{P}_t$ is required to ensure uniqueness, for example:

$$\langle \boldsymbol{P}_t(\boldsymbol{x},\boldsymbol{y}) \rangle_t = \boldsymbol{0}\,. \tag{6.167}$$

Then, an integral averaging of Eq. (6.94) over Ω_t provides the macroscale equation for the velocity in the tumour microenvironment:

$$\left\langle \boldsymbol{u}_t^{(0)} \right\rangle_t = -\bar{\kappa} \langle \bar{\mathsf{A}} \rangle_t \nabla_{\boldsymbol{x}} p_t^{(0)} - \bar{\kappa} \left\langle \bar{\mathsf{A}} (\nabla_{\boldsymbol{y}} \boldsymbol{P}_t)^{\mathrm{T}} \right\rangle_t \nabla_{\boldsymbol{x}} p_t^{(0)} \quad \text{in } \Omega_t\,. \tag{6.168}$$

Defining $\mathsf{F} = \bar{\kappa} \left\langle \bar{\mathsf{A}} - \bar{\mathsf{A}} (\nabla_{\boldsymbol{y}} \boldsymbol{P}_t)^{\mathrm{T}} \right\rangle_t$, we obtain a macroscale equation for the average velocity in tumour microenvironment:

$$\left\langle \boldsymbol{u}_t^{(0)} \right\rangle_t = -\mathsf{F} \nabla_{\boldsymbol{x}} p_t^{(0)} \quad \text{in } \Omega_t\,. \tag{6.169}$$

In this particular case, in the tumour micro-environment compartment, the average velocity profile is given by an anisotropic Darcy's law. The role of the microstructure is encoded in the permeability tensor, which is given by F. In this formulation, the term representing cell movement driven by the gradient of the leading-order chemical concentration $c_t^{(0)}$, which would otherwise represent the macroscale chemotactic velocity similar to the Keller-Segel model, is absent.

To close the entire macroscale model, we need a macroscale equation for the leading order pressure $p_t^{(0)}$. To derive this result, we gather the ε^2 terms from (6.42) and the ε^1 terms from (6.47) and we obtain:

$$\begin{aligned} \nabla_{\boldsymbol{x}} \cdot \boldsymbol{u}_t^{(0)} + \nabla_{\boldsymbol{y}} \cdot \boldsymbol{u}_t^{(1)} = \bar{\gamma} c_t^{(0)} + \nabla_{\boldsymbol{x}} \cdot (\bar{\chi} \bar{\mathsf{A}}(\boldsymbol{x},\boldsymbol{y}) \nabla_{\boldsymbol{x}} c_t^{(0)}) + \nabla_{\boldsymbol{x}} \cdot (\bar{\chi} \bar{\mathsf{A}}(\boldsymbol{x},\boldsymbol{y}) \nabla_{\boldsymbol{y}} c_t^{(1)}) + \\ + \nabla_{\boldsymbol{y}} \cdot (\bar{\chi} \bar{\mathsf{A}}(\boldsymbol{x},\boldsymbol{y}) \nabla_{\boldsymbol{x}} c_t^{(1)}) + \nabla_{\boldsymbol{y}} \cdot (\bar{\chi} \bar{\mathsf{A}}(\boldsymbol{x},\boldsymbol{y}) \nabla_{\boldsymbol{y}} c_t^{(2)}) \quad \text{in } \Omega_t\,, \end{aligned} \tag{6.170}$$

$$\boldsymbol{u}_t^{(1)} \cdot \boldsymbol{n}_t = -\bar{\mathcal{J}}_b^{(0)} \quad \text{on } \Gamma\,. \tag{6.171}$$

An integral averaging of the first equation over Ω_t, using the divergence theorem in the $\boldsymbol{y}$ variable and $\boldsymbol{y}$-periodicity, provides:

$$\begin{aligned} \nabla_{\boldsymbol{x}} \cdot \left\langle \boldsymbol{u}_t^{(0)} \right\rangle_t + \frac{1}{|\Omega_t|} \int_\Gamma \boldsymbol{u}_t^{(1)} \cdot \boldsymbol{n}_t \, dS_{\boldsymbol{y}} = \bar{\gamma} c_t^{(0)} + \\ + \nabla_{\boldsymbol{x}} \cdot (\bar{\chi} \langle \bar{\mathsf{A}} \rangle_t \nabla_{\boldsymbol{x}} c_t^{(0)}) - \nabla_{\boldsymbol{x}} \cdot (\bar{\chi} \left\langle \bar{\mathsf{A}} (\nabla_{\boldsymbol{y}} \boldsymbol{b})^{\mathrm{T}} \right\rangle_t \nabla_{\boldsymbol{x}} c_t^{(0)}) + \\ + \frac{1}{|\Omega_t|} \int_\Gamma \bar{\chi} \left(\bar{\mathsf{A}} \nabla_{\boldsymbol{x}} c_t^{(1)} + \bar{\mathsf{A}} \nabla_{\boldsymbol{y}} c_t^{(2)} \right) \cdot \boldsymbol{n}_t \, dS_{\boldsymbol{y}} \quad \text{in } \Omega_t\,. \end{aligned} \tag{6.172}$$

Taking into account the interface condition (6.96) and (6.171), we can rewrite the interface condition (6.115) as:

$$\left(\mathsf{A} \nabla_{\boldsymbol{x}} c_t^{(1)} + \mathsf{A} \nabla_{\boldsymbol{y}} c_t^{(2)} \right) \cdot \boldsymbol{n}_t = -\frac{\bar{\mathcal{J}}_b^{(0)}}{\bar{D}_t} c_t^{(0)} + \frac{\bar{\mathcal{J}}_d^{(0)}}{\bar{D}_t} \quad \text{on } \Gamma\,. \tag{6.173}$$

Using the interface conditions (6.171) and (6.173) and defining $\mathsf{C} = \bar{\chi}\left\langle \bar{\mathsf{A}} - \bar{\mathsf{A}}\left(\nabla_{\boldsymbol{y}}\boldsymbol{b}\right)^{\mathrm{T}}\right\rangle_t$, we can rewrite equation (6.172) as:

$$\begin{aligned}\nabla_{\boldsymbol{x}}\cdot\left\langle \boldsymbol{u}_t^{(0)}\right\rangle_t = \bar{\gamma}c_t^{(0)} + \frac{1}{|\Omega_t|}\int_\Gamma \bar{\mathcal{J}}_b^{(0)}\,dS_{\boldsymbol{y}} + \frac{1}{|\Omega_t|}\int_\Gamma \bar{\chi}\frac{\bar{\mathcal{J}}_d^{(0)}}{\bar{D}_t}\,dS_{\boldsymbol{y}} + \\ - \frac{1}{|\Omega_t|}\int_\Gamma \bar{\chi}\frac{\bar{\mathcal{J}}_b^{(0)}}{\bar{D}_t}c_t^{(0)}\,dS_{\boldsymbol{y}} + \nabla_{\boldsymbol{x}}\cdot\left(\mathsf{C}\nabla_{\boldsymbol{x}}c_t^{(0)}\right) \quad \text{in } \Omega_t\,.\end{aligned} \tag{6.174}$$

Next, we observe that the fluxes $\bar{\mathcal{J}}_b^{(0)}$ and $\bar{\mathcal{J}}_d^{(0)}$, as defined in Eqs. (6.71)-(6.89), are independent of $\boldsymbol{y}$ due to the conditions specified in (6.51), (6.74), (6.93), and (6.101). Consequently, we obtain:

$$\begin{aligned}\nabla_{\boldsymbol{x}}\cdot\left\langle \boldsymbol{u}_t^{(0)}\right\rangle_t = \bar{\gamma}c_t^{(0)} + \frac{|\Gamma|}{|\Omega_t|}\bar{\mathcal{J}}_b^{(0)} + \bar{\chi}\frac{|\Gamma|}{|\Omega_t|}\frac{\bar{\mathcal{J}}_d^{(0)}}{\bar{D}_t} + \\ - \bar{\chi}\frac{|\Gamma|}{|\Omega_t|}\frac{\bar{\mathcal{J}}_b^{(0)}}{\bar{D}_t}c_t^{(0)} + \nabla_{\boldsymbol{x}}\cdot\left(\mathsf{C}\nabla_{\boldsymbol{x}}c_t^{(0)}\right) \quad \text{in } \Omega_t\,.\end{aligned} \tag{6.175}$$

Finally, we use Eq. (6.169) to obtain:

$$\begin{aligned}\nabla_{\boldsymbol{x}}\cdot\left(\mathsf{F}\nabla_{\boldsymbol{x}}p_t^{(0)}\right) = -\bar{\gamma}c_t^{(0)} - \frac{|\Gamma|}{|\Omega_t|}\bar{\mathcal{J}}_b^{(0)} - \bar{\chi}\frac{|\Gamma|}{|\Omega_t|}\frac{\bar{\mathcal{J}}_d^{(0)}}{\bar{D}_t} + \\ + \bar{\chi}\frac{|\Gamma|}{|\Omega_t|}\frac{\bar{\mathcal{J}}_b^{(0)}}{\bar{D}_t}c_t^{(0)} - \nabla_{\boldsymbol{x}}\cdot\left[\mathsf{C}\nabla_{\boldsymbol{x}}c_t^{(0)}\right] \quad \text{in } \Omega_t\,.\end{aligned} \tag{6.176}$$

Also in this particular case, the effective source term on the right-hand side primarily arises from the leading-order fluid and nutrient fluxes, $\bar{\mathcal{J}}_b^{(0)}$ and $\bar{\mathcal{J}}_d^{(0)}$ and a further contribution from the gradient of the nutrient concentration.

The differential problem in this particular case is defined by (6.169), (6.176), and (6.118) for the variables $\left\langle \boldsymbol{u}_t^{(0)}\right\rangle_t$, $p_t^{(0)}$ and $c_t^{(0)}$.

Remark 6.1 *We would like to highlight that the particular case can be directly derived from the general case by assuming a constant value for $\bar{\chi}$. Since* G *is defined by* (6.138) *in terms of the auxiliary vector $\boldsymbol{C}_t$, we notice that problem* (6.134)*, when $\bar{\chi}$ is a constant, reduces to:*

$$\begin{cases}\nabla_{\boldsymbol{y}}\cdot\left[\bar{\kappa}\left(\nabla_{\boldsymbol{y}}\boldsymbol{C}_t\right)\bar{\mathsf{A}}^{\mathrm{T}}\right] = \bar{\chi}\nabla_{\boldsymbol{y}}\cdot\left[\bar{\mathsf{A}}^{\mathrm{T}} - \left(\nabla_{\boldsymbol{y}}\boldsymbol{b}\right)\bar{\mathsf{A}}^{\mathrm{T}}\right] & \text{in } \Omega_t\,,\\ \left(\nabla_{\boldsymbol{y}}\boldsymbol{C}_t\right)\bar{\mathsf{A}}^{\mathrm{T}}\boldsymbol{n} = \boldsymbol{0} & \text{on } \Gamma\,.\end{cases} \tag{6.177}$$

In this system, the right-hand side equals zero as it corresponds to the first equation of (6.112) *in the case of a constant $\bar{\chi}$. Consequently, the solution to the system* (6.177) *implies that the vector $\boldsymbol{C}_t$ is constant with respect to $\boldsymbol{y}$. Based on the definition of* G *in* (6.138)*, it follows that* G *is the null tensor, and therefore it does not appear in* (6.169)*. As such, the contribution to the modified Darcy's law which is proportional to the gradient of the concentration is directly related to spatial variations of the chemotactic coefficient. However, even when the chemotactic coefficient is a constant, the final model still features additional contributions mediated by the chemotactic coefficient to both the drug and blood fluxes at the macroscale, as per equation* (6.176)*.*

6.6 Summary

In this Chapter, we have analysed a system of partial differential equations (PDEs) in non-dimensional form, defined over two distinct domains, Ω_t and Ω_v, governed by the balance laws (6.23)-(6.28). The interaction between these domains is described through the interface conditions (6.29)-(6.31). The model is derived with a focus on a specific application: the description of flow exchange and motion in a tumour microenvironment. Therefore Ω_t represents the tumour region, while Ω_v corresponds to the capillary network. In this context, net growth may occur, either as a volumetric term or as a mass flux associated with chemotactic accretion. The interface conditions accounts for the exchange of blood and nutrients across the capillary walls. With slight modifications, the model could also be adapted to describe a healthy tissue microenvironment or even other scenarios, such as the exchange of substances between roots and soil [345]. By leveraging the separation of scales between the macroscale and microscale, we employed homogenisation techniques under the assumptions of local periodicity and macroscopic uniformity to derive a closed system of differential equations for the leading-order quantities: $\left\langle \boldsymbol{u}_t^{(0)} \right\rangle_t$, $\left\langle \boldsymbol{u}_v^{(0)} \right\rangle_v$, $p_t^{(0)}$, $p_v^{(0)}$, $c_t^{(0)}$, and $c_v^{(0)}$.

The resulting system of equations describes fluid flow using a porous medium model. In the tumour microenvironment, the mass balance equation at the macroscopic scale accounts for effective transport between the compartments Ω_t and Ω_v through mass source terms that encapsulate macroscopic changes in the microvasculature. Additionally, the mass balance incorporates a macroscopic form of the non-convective mass flux related to chemotactic growth. The average velocity $\left\langle \boldsymbol{u}_t^{(0)} \right\rangle_t$, describing the flow of the biological material, modelled as a fluid, is driven by both the pressure gradient and the nutrient concentration gradient. In contrast, within the capillary domain Ω_v, the fluid flow adheres to classical Darcy's law. The permeability tensors involved in these relations can be computed by solving differential cell problems.

The effective governing equations for nutrients transport are formulated as a coupled advection-diffusion-reaction model. The reaction terms in this model account for nutrient exchange between the two compartments and also reflect the influence of microvascular geometry. The role of the microstructure is also encoded in the effective diffusivity tensors; in Ω_v, these tensors can be computed by solving classical differential problems on a representative unit cell. In contrast, a more complex cell problem, incorporating macroscopic quantities, is necessary for Ω_t.

The primary contribution of this work is the derivation of a mathematical model that captures the key physical phenomena driving tumour growth and fluid flow at the tissue scale. The influence of the microvasculature is integrated through effective macroscale coefficients, which are obtained by solving associated cell problems. Our model represents an initial effort to incorporate the effects of the microstructural characteristics of capillary network into tumour growth simulations, accounting for both volumetric growth and cell mass flux driven by chemotactic processes. Additionally, the model captures the local anisotropy of the microenvironment, which fundamentally affects fluid flow, nutrients transport and diffusion, cell dynamics and chemotactic accretion in highly anisotropic tissue [237], such as brain [48, 143] and cartilage [178, 226]. However, in its current form, the tumour domain does not evolve over time, a limitation that should be addressed in future studies by employing, for instance, a level set method to account for domain expansion. Additionally, the tumour tissue is represented as an ensemble of cells and liquid, macroscopically modelled as a simple Newtonian fluid, without differentiating between the liquid and cellular components. This assumption limits the ability to fully capture the proliferative nature of tumour growth, suggesting

that this aspect should be refined in future work. Furthermore, while mechanical deformations are neglected in the present formulation, extension of this work should consider the poro-mechanical response that typically characterizes tumours [19, 143, 399].

This study lays the groundwork for understanding the impact of vascular geometry and nutrient delivery on tumour growth and its response to chemicals. The proposed mathematical framework can be adapted for numerical simulations of fluid and nutrient transport in realistic tumour geometries reconstructed from medical imaging data. These numerical results can then be validated against clinical observations, and in the long term, the model's predictions could contribute to improving anti-cancer treatment strategies and support rapidly emerging sophisticated attempts to couple mathematical modelling and machine learning, see, e.g., [356].

7 Conclusions

This thesis investigates brain tumour growth through advanced mathematical models, integrating mechanical deformation, phenotypic heterogeneity, and fluid-nutrient transport. The study employs multiscale and multiphase approaches to capture tumour dynamics and their impact on surrounding brain tissues, paving the way for patient-specific therapeutic strategies.

Chapter 2 presents a multiphase mechanical model that quantifies tumour-induced deformations and stresses. By incorporating anisotropic growth driven by brain fibres, it captures the irregular and heterogeneous behaviour of tumours. Patient-specific MRI and DTI data are used to reconstruct realistic 3D brain geometries, enabling precise simulations of ventricular compression and its impact on adjacent healthy tissues. The model also simulates therapeutic treatments like chemotherapy and radiotherapy. Numerical results, obtained using FEniCS, validate the model's ability to replicate the complex dynamics of tumour growth and its mechanical effects, offering insights into tailored therapeutic strategies.

Chapter 3 focuses on the viscoelastic behaviour of brain tissue, performing ramp-and-hold relaxation tests in torsion on freshly slaughtered cylindrical ovine brain samples. The complete set of viscoelastic material parameters was estimated via a simultaneous fit to the analytical expressions for the torque and normal force predicted by the modified Quasi-Linear Viscoelastic (MQLV) model. The model's predictions were further validated through finite element simulations in FEniCS. Our results show that the modified quasi-linear viscoelastic model accurately fits the experimental data. The derived material parameters have implications beyond tumour modelling, potentially aiding studies on traumatic brain injury and the development of protective sports headgear.

Chapter 4 introduces differential equation models to capture cancer cell dynamics and immune interactions, focusing on immunotherapeutic treatments involving T-lymphocyte infusions. An ordinary differential equation (ODE) model identifies thresholds for therapy effectiveness through analytical and numerical bifurcation analyses. Building on this, a partial differential equation (PDE) model adds spatial dynamics via diffusion and chemotaxis, allowing for simulations of tumour growth and immune response within 3D patient-specific brain geometries. Sensitivity analyses provide insights into tumour-immune interactions, guiding personalised immunotherapeutic strategies.

Chapter 5 explores phenotypic heterogeneity in tumour cells under varying oxygen conditions using a reaction-diffusion partial integro-differential equation (PIDE) framework. The model incorporates anisotropic diffusion tensors to account for the directional properties of the extracellular environment. Numerical simulations reveal complex wavefront dynamics influenced by spatial variations in oxygen and phenotypic traits. Analyses on 3D brain geometries reconstructed from MRI and DTI data highlight the interplay between tumour growth, oxygen diffusion, and cell migration along white matter tracts, advancing personalised therapy design.

Lastly, Chapter 6 develops a PDE-based model to describe fluid and nutrient transport within the tumour microenvironment. By leveraging asymptotic homogenisation, the model integrates microscale vascular details into a double porous medium framework, coupling fluid dynamics with nutrient transport. Permeability and diffusivity tensors, derived through cell-problem analyses, encapsulate microvascular geometry's role in macroscopic behaviour. The Kedem-Katchalsky formulation is employed for nutrient and fluid exchange across capillary walls. While some limitations remain, this framework offers a foundation for numerical simulations of realistic tumour geometries and supports the development of anti-cancer treatments.

Therefore, this thesis opens several promising avenues for future researches in the continuously evolving field of brain tumour modelling, with four main directions outlined below.

For the mechanical model presented in Chapter 2, future efforts could focus on addressing the contact of ventricle edges caused by tumour-induced deformations using contact mechanics. Additionally, refining the initial conditions for fluid phases by incorporating voxel-wise estimations of free water in the brain would enhance model precision. It could be also interesting to retain the brain ventricles within the domain and couple the poromechanics system with the Stokes or Navier-Stokes equations to model the flow within the ventricles [195]. Moreover, accounting for mechanical heterogeneity between grey and white matter, especially for tumours with stiffness comparable to healthy tissue, could further improve the framework. Integrating fluid exchange between tissue and vasculature, currently omitted, would enable a more realistic representation of vascularised tumours. This could be achieved through homogenisation techniques, as discussed in Chapter 6, or by employing 3D-1D coupling methods. Therapy modelling represents another critical area for advancement. Incorporating detailed pharmacodynamic processes and validating them against clinical data could refine predictions of treatment outcomes. Moreover, integrating the immunotherapeutic strategies explored in Chapter 4 could provide a more comprehensive understanding of therapeutic interventions. Lastly, adapting the model to simulate surgical resection prior to chemo-radiation therapy poses a significant challenge but could yield valuable insights

Regarding the model in Chapter 4, which incorporates immunotherapy, several enhancements could be introduced. In this study, only constant infusion therapies were considered. However, in clinical practice, treatment is often administered intermittently, with intervals spanning several days. Exploring the effects of non-constant therapy administration within the ODE model framework could help identify optimal treatment regimens that minimise intervention while mitigating adverse effects, potentially employing control theory techniques. Additionally, the PDE model could be extended to incorporate various infusion strategies, with numerical stability further enhanced through stabilisation methods such as the Streamline Upwind Petrov–Galerkin (SUPG) formulation, to properly handle the chemotactic term. Drawing from the experience gained in Chapter 5, the model could also be expanded into a reaction-diffusion partial integro-differential equation (PIDE) framework to better account for spatial heterogeneity and complex dynamics. The current analysis is limited to interactions between lymphocytes and tumour cells, excluding the roles of other cell populations, such as macrophages and stem cells, and the influence of cytokines mediating cellular interactions. Specifically, the model could be expanded to include the effects of TGF-β, a cytokine secreted by the tumour that plays a critical role in establishing an immunosuppressive microenvironment in brain tumours. Moreover, modelling the interplay between immunotherapy and other treatment modalities, such as radiotherapy and chemotherapy, could provide valuable insights for developing multimodal therapeutic strategies. Finally, it would be valuable to incorporate mechanical effects into this

model. Building on the mechanical framework presented in Chapter 2, an initial approximation could involve modelling T cells and TGF-β as part of the fluid phase to explore the role of mechanics in immunotherapy. Subsequently, the model could be extended to include T cells as a distinct third population, enabling a more comprehensive analysis of their interactions with the tumour and the fluid phase.

Future developments of the work presented in Chapter 5 could focus on extending the model to incorporate additional biological factors, such as the impact of acidity on the evolutionary dynamics of cancer cells, and refining representations of tumour microenvironments to better capture their complexity. Including the effects of various therapies would also be beneficial, as resistance to hypoxia is strongly linked to resistance to both chemotherapy and radiotherapy [131, 142, 315, 415]. Moreover, rigorous validation against experimental data and clinical observations will be critical for fine-tuning the model parameters and enhancing its relevance to practical applications. Incorporating stress-induced phenotypic changes caused by hypoxia would also be valuable, enabling the integration of phenotypic heterogeneity into a mechanical framework. Such an approach could build upon the models described in Chapter 2, providing a more comprehensive understanding of the interplay between mechanical forces and phenotypic dynamics in tumour progression.

Finally, Chapter 6 also presents opportunities for significant improvements. In its current form, the tumour domain is static and does not evolve over time, a limitation that could be addressed in future studies by implementing dynamic domain expansion methods. Furthermore, the tumour tissue is currently modelled macroscopically as a simple Newtonian fluid, representing a mixture of cells and liquid without differentiating between these components. This simplification limits the model's capacity to fully capture the proliferative nature of tumour growth, highlighting the need for refinements that explicitly account for cellular and liquid contributions. Moreover, the present formulation neglects mechanical deformations, which are a critical aspect of tumour progression, as discussed in Chapter 2. Future extensions should incorporate the poro-mechanical behaviour typically observed in tumours, as described in the literature [19, 143, 399], to achieve a more comprehensive and realistic representation of tumour dynamics.

Overall, this thesis introduces novel methodologies and insights into the mathematical modelling of brain tumours, advancing the understanding of tumour growth mechanisms and therapeutic responses. By integrating mechanical, biological, and fluid-dynamic aspects, it lays the foundation for future research that bridges experimental, clinical, and computational approaches. These findings have the potential to inform the development of personalised treatment strategies, ultimately contributing to improved patient outcomes in oncology.

Bibliography

[1] *3D Slicer image computing platform*. URL: https://www.slicer.org/ (cit. on pp. 45, 147).

[2] K. Abernathy and J. Burke. "Modeling the treatment of Glioblastoma Multiforme and cancer stem cells with ordinary differential equations". *Computational and Mathematical Methods in Medicine* 2016 (2016), pp. 1–11. DOI: 10.1155/2016/1239861 (cit. on p. 31).

[3] S. D. Abramowitch and S. L. Woo. "An improved method to analyze the stress relaxation of ligaments following a finite ramp time based on the quasi-linear viscoelastic theory". *Journal of Biomedical Engineering* 126.1 (2004), pp. 92–97. DOI: 10.1115/1.1645528 (cit. on p. 79).

[4] A. Agosti, C. Cattaneo, C. Giverso, D. Ambrosi, and P. Ciarletta. "A computational framework for the personalized clinical treatment of glioblastoma multiforme". *ZAMM - Journal of Applied Mathematics and Mechanics / Zeitschrift für Angewandte Mathematik und Mechanik* 98.12 (2018), pp. 2307–2327. DOI: 10.1002/zamm.201700294 (cit. on pp. 25, 26, 27, 42, 43, 48, 62, 64).

[5] A. Agosti, P. Ciarletta, H. Garcke, and M. Hinze. "Learning patient-specific parameters for a diffuse interface glioblastoma model from neuroimaging data". *Mathematical Methods in the Applied Sciences* 43.15 (2020), pp. 8945–8979. DOI: 10.1002/mma.6588 (cit. on pp. 25, 26, 42, 61).

[6] A. Agosti, C. Giverso, E. Faggiano, A. Stamm, and P. Ciarletta. "A personalized mathematical tool for neuro-oncology: A clinical case study". *International Journal of Non-Linear Mechanics* 107 (2018). DOI: 10.1016/j.ijnonlinmec.2018.06.004 (cit. on pp. 25, 26, 48).

[7] E. Agosti, M. Zeppieri, L. De Maria, C. Tedeschi, M. Fontanella, P. P. Panciani, and T. Ius. "Glioblastoma immunotherapy: A systematic review of the present strategies and prospects for advancements". *International Journal of Molecular Sciences* 24 (2023), p. 15037. DOI: 10.3390/ijms242015037 (cit. on pp. 20, 103).

[8] A. Ahmed, M. U. UlHaq, Z. Mustansar, A. Shaukat, and L. Margetts. "How growing tumour impacts intracranial pressure and deformation mechanics of brain". *Royal Society Open Science* 8.9 (2021). DOI: 10.1098/rsos.210165 (cit. on pp. 16, 67).

[9] N. Ahmed et al. "HER2-specific chimeric antigen receptor-modified virus-specific T cells for progressive Glioblastoma: A phase 1 dose-escalation trial". *JAMA oncology* 3 (2017). DOI: 10.1001/jamaoncol.2017.0184 (cit. on p. 116).

[10] T. Alarcon, H. Byrne, and P. Maini. "A cellular automaton model for tumour growth in inhomogeneous environment". *Journal of Theoretical Biology* 225 (2003), pp. 257–274. DOI: 10.1016/S0022-5193(03)00214-5 (cit. on p. 32).

[11] M. J. Albeck, S. E. Børgesen, F. Gjerris, J. F. Schmidt, and P. S. Sørensen. "Intracranial pressure and cerebrospinal fluid outflow conductance in healthy subjects". *Journal of Neurosurgery* 74.4 (1991), pp. 597–600. DOI: 10.3171/jns.1991.74.4.0597 (cit. on pp. 63, 64).

[12] A. Alentorn, K. Hoang-Xuan, and T. Mikkelsen. "Presenting signs and symptoms in brain tumors". *Handbook of Clinical Neurology* 134 (2006), pp. 19–26. DOI: 10.1016/B978-0-12-802997-8.00002-5 (cit. on p. 16).

[13] A. L. Alexander, J. E. Lee, M. Lazar, and A. S. Field. "Diffusion Tensor Imaging of the brain". *Neurotherapeutics* 4.3 (2007), pp. 316–329. DOI: 10.1016/j.nurt.2007.05.011 (cit. on pp. 47, 62).

[14] K. O. Alfarouk, M. E. Ibrahim, R. A. Gatenby, and J. S. Brown. "Riparian ecosystems in human cancers". *Evolutionary Applications* 6.1 (2013), pp. 46–53. DOI: 10.1111/eva.12015 (cit. on pp. 133, 149).

[15] J. Alfonso, K. Talkenberger, M. Seifert, B. Klink, A. Hawkins-Daarud, K. Swanson, H. Hatzikirou, and A. Deutsch. "The biology and mathematical modelling of glioma invasion: A review". *Journal of The Royal Society Interface* 14 (2017), p. 20170490. DOI: 10.1098/rsif.2017.0490 (cit. on p. 24).

[16] L. Almeida, C. Audebert, E. Leschiera, and T. Lorenzi. "A hybrid discrete–continuum modelling approach to explore the impact of T-cell infiltration on anti-tumour immune response". *Bulletin of Mathematical Biology* 84 (2022). DOI: 10.1007/s11538-022-01095-3 (cit. on p. 31).

[17] L. Almeida, P. Bagnerini, G. Fabrini, B. Hughes, and T. Lorenzi. "Evolution of cancer cell populations under cytotoxic therapy and treatment optimisation: insight from a phenotype-structured model". *ESAIM: Mathematical Modelling and Numerical Analysis* 53 (2019). DOI: 10.1051/m2an/2019010 (cit. on p. 29).

[18] M. Alnaes, J. Blechta, J. Hake, A. Johansson, B. Kehlet, A. Logg, C. Richardson, J. Ring, M. E. Rognes, and G. N. Wells. "The FEniCS Project Version 1.5". *Archive of Numerical Software* 3 (2015). DOI: 10.11588/ans.2015.100.20553 (cit. on pp. 63, 95).

[19] D. Ambrosi, S. Pezzuto, D. Riccobelli, T. Stylianopoulos, and P. Ciarletta. "Solid tumors are poroelastic solids with a chemo-mechanical feedback on growth". *Journal of Elasticity* 129 (2017), p. 107. DOI: 10.1007/s10659-016-9619-9 (cit. on pp. 27, 182, 185).

[20] D. Ambrosi and F. Mollica. "On the mechanics of a growing tumor". *International Journal of Engineering Science* 40.12 (2002), pp. 1297–1316. DOI: 10.1016/S0020-7225(02)00014-9 (cit. on pp. 27, 37, 39).

[21] D. Ambrosi and F. Mollica. "The role of stress in the growth of a multicell spheroid". *Journal of Mathematical Biology* 48 (2004), pp. 477–499. DOI: 10.1007/s00285-003-0238-2 (cit. on pp. 27, 37, 41).

[22] D. Ambrosi and L. Preziosi. "Cell adhesion mechanisms and stress relaxation in the mechanics of tumours". *Biomechanics and Modeling in Mechanobiology* 8 (2009), pp. 397–413. DOI: 10.1007/s10237-008-0145-y (cit. on p. 41).

[23] D. Ambrosi and L. Preziosi. "On the closure of mass balance models for tumor growth". *Mathematical Models and Methods in Applied Sciences* 12.05 (2002), pp. 737–754. DOI: 10.1142/S0218202502001878 (cit. on pp. 36, 41).

[24] D. Ambrosi and L. Preziosi. "On the closure of mass balance models for tumor growth". *Math. Models Methods Appl. Sci.* 12 (2011), pp. 737–754. DOI: 10.1142/S0218202502001878 (cit. on pp. 157, 158).

[25] L. Anand and S. Govindjee. *Continuum Mechanics of Solids*. Oxford University Press, 2020. DOI: 10.1093/oso/9780198864721.001.0001 (cit. on p. 79).

[26] M. Andresen and M. Juhler. "Intracranial pressure following complete removal of a small demarcated brain tumor: A model for normal intracranial pressure in humans". *Journal of Neurosurgery JNS* 121.4 (2014), pp. 797–801. DOI: 10.3171/2014.2.JNS132209 (cit. on pp. 63, 64).

[27] S. Angeli, K. E. Emblem, P. Due-Tonnessen, and T. Stylianopoulos. "Towards patient-specific modeling of brain tumor growth and formation of secondary nodes guided by DTI-MRI". *NeuroImage: Clinical* 20 (2018), pp. 664–673. DOI: 10.1016/j.nicl.2018.08.032 (cit. on pp. 25, 27, 35, 41).

[28] S. Angeli and T. Stylianopoulos. "Biphasic modeling of brain tumor biomechanics and response to radiation treatment". *Journal of Biomechanics* 49.9 (2016), pp. 1524–1531. DOI: 10.1016/j.jbiomech.2016.03.029 (cit. on pp. 25, 27, 35).

[29] A. Anssari–Benam, M. Destrade, and G. Saccomandi. "Modelling brain tissue elasticity with the Ogden model and an alternative family of constitutive models". *Philosophical Transactions of the Royal Society A: Mathematical, Physical and Engineering Sciences* 380.2234 (2022), p. 20210325. DOI: 10.1098/rsta.2021.0325 (cit. on pp. 93, 94).

[30] K. B. Arbogast and S. S. Margulies. "Material characterization of the brainstem from oscillatory shear tests". *Journal of Biomechanics* 31.9 (1998), pp. 801–807. DOI: 10.1016/S0021-9290(98)00068-2 (cit. on pp. 78, 102).

[31] T. Arbogast and H. Lehr. "Homogenization of a Darcy-Stokes system modeling vuggy porous media". *Computational Geosciences* 10 (2006), pp. 291–302. DOI: 10.1007/s10596-006-9024-8 (cit. on pp. 153, 161).

[32] A. Ardaševa, R. Gatenby, A. Anderson, H. Byrne, P. Maini, and T. Lorenzi. "A mathematical dissection of the adaptation of cell populations to fluctuating oxygen levels". *Bulletin of Mathematical Biology* 82 (2020). DOI: 10.1007/s11538-020-00754-7 (cit. on p. 29).

[33] A. Ardaševa, R. Gatenby, A. Anderson, H. Byrne, P. Maini, and T. Lorenzi. "Evolutionary dynamics of competing phenotype-structured populations in periodically fluctuating environments". *Journal of Mathematical Biology* 80 (2020), pp. 1–33. DOI: 10.1007/s00285-019-01441-5 (cit. on p. 29).

[34] A. Arnold, L. Desvillettes, and C. Prévost. "Existence of nontrivial steady states for populations structured with respect to space and a continuous trait". *Communications on Pure and Applied Analysis* 11 (2012). DOI: 10.3934/cpaa.2012.11.83 (cit. on p. 30).

[35] M. Asgari, D. de Zelicourt, and V. Kurtcuoglu. "Glymphatic solute transport does not require bulk flow". *Scientific Reports* 6 (2016), p. 38635. DOI: 10.1038/srep38635 (cit. on p. 63).

[36] Y. Assaf and O. Pasternak. "Diffusion Tensor Imaging (DTI)-based white matter mapping in brain research: A review". *Journal of molecular neuroscience : MN* 34 (2008), pp. 51–61. DOI: 10.1007/s12031-007-0029-0 (cit. on pp. 147, 159).

[37] G. Athesian and J. Weiss. "Anisotropic hydraulic permeability under finite deformation". *Journal of Biomechanical Engineering* 132 (2010), pp. 111004–1. DOI: 10.1115/1.4002588 (cit. on p. 49).

[38] M. Aubert, M. Badoual, C. Christov, and B. Grammaticos. "A model for glioma cell migration on collagen and astrocytes". *Journal of The Royal Society Interface* 5.18 (2008), pp. 75–83. DOI: 10.1098/rsif.2007.1070 (cit. on p. 25).

[39] M. Aubert, M. Badoual, S. Féréol, C. Christov, and B. Grammaticos. "A cellular automaton model for the migration of glioma cells". *Physical biology* 3 (2006), pp. 93–100. DOI: 10.1088/1478-3975/3/2/001 (cit. on p. 25).

[40] J. Auriault, C. Boutin, and C. Geindreau. *Homogenization of coupled phenomena in heterogenous media*. 2010. DOI: 10.1002/9780470612033 (cit. on p. 155).

[41] I. Bah, N. R. J. Fernandes, R. L. Chimenti, J. Ketz, A. S. Flemister, and M. R. Buckley. "Tensile mechanical changes in the Achilles tendon due to insertional Achilles tendinopathy". *Journal of the Mechanical Behavior of Biomedical Materials* 112 (2020), p. 104031. DOI: 10.1016/j.jmbbm.2020.104031 (cit. on p. 79).

[42] N. S. Bakhvalov and G. Panasenko. *Homogenisation: averaging processes in periodic media: mathematical problems in the mechanics of composite materials*. Vol. 36. The Netherlands: Springer Science & Business Media, 1989 (cit. on p. 153).

[43] V. Balbi, T. Shearer, and W. J. Parnell. "A modified formulation of quasi-linear viscoelasticity for transversely isotropic materials under finite deformation". *Proceedings of the Royal Society A: Mathematical, Physical and Engineering Sciences* 474.2217 (2018), p. 20180231. DOI: 10.1098/rspa.2018.0231 (cit. on pp. 79, 90).

[44] V. Balbi, T. Shearer, and W. J. Parnell. "Tensor decomposition for modified quasi-linear viscoelastic models: Towards a fully non-linear theory". *Mathematics and Mechanics of Solid* 0.0 (2023), pp. 1–25. DOI: 10.1177/10812865231165232 (cit. on p. 79).

[45] V. Balbi, A. Trotta, M. Destrade, and A. Ní Annaidh. "Poynting effect of brain matter in torsion". *Soft Matter* 15 (25 2019), pp. 5147–5153. DOI: 10.1039/C9SM00131J (cit. on pp. 15, 36, 40, 61, 64, 78, 83, 85, 87, 88, 101, 102).

[46] D. Balding and D. McElwain. "A mathematical model of tumour-induced capillary growth". *Journal of Theoretical Biology* 114 (1985), pp. 53–73. DOI: 10.1016/S0022-5193(85)80153-0 (cit. on p. 32).

[47] F. Ballatore, G. Lucci, A. Borio, and C. Giverso. "An imaging-informed mechanical framework to provide a quantitative description of brain tumour growth and the subsequent deformation of white matter tracts". In: *Mathematical models and computer simulations for biomedical applications*. Ed. by G. Bretti, R. Natalini, P. Palumbo, and L. Preziosi. Springer Series, 2023. DOI: 10.1007/978-3-031-35715-2_5 (cit. on pp. 35, 36, 42, 47, 62, 64, 65, 159).

[48] F. Ballatore, G. Lucci, and C. Giverso. "Modelling and simulation of anisotropic growth in brain tumours through poroelasticity: A study of ventricular compression and therapeutic protocols". *Computational Mechanics* (2024). DOI: 10.1007/s00466-024-02471-7 (cit. on pp. 36, 42, 47, 62, 64, 149, 151, 159, 181).

[49] S. Banerjee, S. Khajanchi, and S. Chaudhuri. "A mathematical model to elucidate brain tumor abrogation by immunotherapy with T11 target structure". *PLOS ONE* 10.5 (2015), pp. 1–21. DOI: 10.1371/journal.pone.0123611 (cit. on pp. 25, 31, 104, 106, 107, 116).

[50] A. Banstola and J. N. J. Reynolds. "Mapping sheep to human brain: The need for a sheep brain atlas". *Frontiers in Veterinary Science* 9 (2022), p. 961413. DOI: 10.3389/fvets.2022.961413 (cit. on p. 102).

[51] L. Barazzuol, N. Burnet, R. Jena, B. Jones, S. Jefferies, and N. Kirkby. "A mathematical model of brain tumour response to radiotherapy and chemotherapy considering radiobiological aspects". *Journal of Theoretical Biology* 262 (2010), pp. 553–565. DOI: 10.1016/j.jtbi.2009.10.021 (cit. on p. 27).

[52] G. Barles, L. Evans, and P. Souganidis. "Wavefront propagation for reaction-diffusion systems of PDE". *Duke Mathematical Journal* 61 (1990). DOI: 10.1215/S0012-7094-90-06132-0 (cit. on p. 137).

[53] G. Barles, S. Mirrahimi, and B. Perthame. "Concentration in Lotka-Volterra parabolic or integral equations: A general convergence result". *Methods and Applications of Analysis* 16 (2009). DOI: 10.4310/MAA.2009.v16.n3.a4 (cit. on p. 28).

[54] M. Barrié et al. "Temozolomide in combination with BCNU before and after radiotherapy in patients with inoperable newly diagnosed glioblastoma multiforme". *Annals of Oncology* 16.7 (2005), pp. 1177–1184. DOI: https://doi.org/10.1093/annonc/mdi225 (cit. on pp. 19, 76).

[55] K. Bartha and H. Rieger. "Vascular network remodeling via vessel cooption, regression and growth in tumors". *Journal of Theoretical Biology* 241.4 (2006), pp. 903–918. DOI: 10.1016/j.jtbi.2006.01.024 (cit. on p. 32).

[56] D. Basanta, J. Scott, R. Rockne, K. Swanson, and A. Anderson. "The role of IDH1 mutated tumour cells in secondary glioblastomas: an evolutionary game theoretical view". *Physical biology* 8 (2011), p. 015016. DOI: 10.1088/1478-3975/8/1/015016 (cit. on pp. 116, 124).

[57] P. Basser. "Inferring microstructural features and the physiological state of tissues from Diffusion-Weighted Images". *NMR in biomedicine* 8 (1995), pp. 333–44. DOI: 10.1002/nbm.1940080707 (cit. on pp. 147, 159).

[58] P. J. Basser. "Interstitial pressure, volume, and flow during infusion into brain tissue". *Microvascular Research* 44.2 (1992), pp. 143–165. DOI: 10.1016/0026-2862(92)90077-3 (cit. on p. 63).

[59] C. E. Bauer, V. Zachariou, P. Maillard, A. Caprihan, and B. T. Gold. "Multi-compartment diffusion magnetic resonance imaging models link tract-related characteristics with working memory performance in healthy older adults". *Frontiers in Aging Neuroscience* 14 (2022). DOI: 10.3389/fnagi.2022.995425 (cit. on p. 71).

[60] L. T. Baxter and R. K. Jain. "Transport of fluid and macromolecules in tumors. I. Role of interstitial pressure and convection". *Microvascular Research* 37.1 (1989), pp. 77–104. DOI: 10.1016/0026-2862(89)90074-5 (cit. on p. 32).

[61] L. T. Baxter and R. K. Jain. "Transport of fluid and macromolecules in tumors. II. Role of heterogeneous perfusion and lymphatics". *Microvascular Research* 40 (1990), pp. 246–263. DOI: 10.1016/0026-2862(90)90023-K (cit. on p. 32).

[62] L. T. Baxter and R. K. Jain. "Transport of fluid and macromolecules in tumors. IV. A microscopic model of the perivascular distribution". *Microvascular Research* 41 (1991), pp. 252–272. DOI: 10.1016/0026-2862(91)90027-4 (cit. on p. 32).

[63] P. Beauchesne, V. Quillien, G. Faure, V. Bernier, G. Noel, P. Quetin, T. Gorlia, C. Carnin, and R. Pedeux. "A concurrent ultra-fractionated radiation therapy and temozolomide treatment: A promising therapy for newly diagnosed, inoperable glioblastoma". *International Journal of Cancer* 138.6 (2016), pp. 1538–1544. DOI: 10.1002/ijc.29898 (cit. on pp. 19, 76).

[64] P. Beauchesne et al. "Prolonged survival for patients with newly diagnosed, inoperable glioblastoma with 3-times daily ultrafractionated radiation therapy". *Neuro-Oncology* 12 (6 2010), pp. 595–602. DOI: 10.1093/neuonc/noq008 (cit. on p. 76).

[65] G. S. Beavers and D. D. Joseph. "Boundary conditions at a naturally permeable wall". *Journal of Fluid Mechanics* 30.1 (1967), pp. 197–207. DOI: 10.1017/S0022112067001375 (cit. on p. 161).

[66] N. Beerenwinkel, C. D. Greenman, and J. Lagergren. "Computational cancer biology: An evolutionary perspective". *PLOS Computational Biology* 12.2 (2016), pp. 1–12. DOI: 10.1371/journal.pcbi.1004717 (cit. on p. 149).

[67] L. Bello et al. "Combinatorial administration of molecules that simultaneously inhibit angiogenesis and invasion leads to increased therapeutic efficacy in mouse models of malignant glioma". *Clinical cancer research : an official journal of the American Association for Cancer Research* 10 (2004), pp. 4527–37. DOI: 10.1158/1078-0432.CCR-04-0194 (cit. on p. 19).

[68] L. Beltzig, B. Stratenwerth, and B. Kaina. "Accumulation of temozolomide-induced apoptosis, senescence and DNA damage by metronomic dose schedule: A proof-of-principle study with Glioblastoma cells". *Cancers* 13.24 (2021). DOI: 10.3390/cancers13246287 (cit. on pp. 43, 62).

[69] O. Benichou, V. Calvez, N. Meunier, and R. Voituriez. "Front acceleration by dynamic selection in Fisher population waves". *Physical review. E, Statistical, nonlinear, and soft matter physics* 86 (2012), p. 041908. DOI: 10.1103/PhysRevE.86.041908 (cit. on p. 30).

[70] A. Beris, J. Horner, S. Jariwala, M. Armstrong, and N. Wagner. "Recent advances in blood rheology: A review". *Soft Matter* 17 (47 2021), pp. 10591–10613. DOI: 10.1039/D1SM01212F (cit. on p. 159).

[71] S. Berrone, C. Giverso, D. Grappein, L. Preziosi, and S. Scialò. "An optimization based 3D-1D coupling strategy for tissue perfusion and chemical transport during tumor-induced angiogenesis". *Computers and Mathematics with Applications* 151 (2023), pp. 252–270. DOI: 10.1016/j.camwa.2023.09.046 (cit. on pp. 32, 76, 158, 161).

[72] S. Berrone, D. Grappein, S. Scialò, and F. Vicini. "A gradient based resolution strategy for a PDE-constrained optimization approach for 3D-1D coupled problems". *Int J Geomath* 13 (2022), pp. 1–25. DOI: 10.1007/s13137-021-00192-0 (cit. on p. 154).

[73] L. E. Bilston, Z. Liu, and N. Phan–Thien. "Large strain behaviour of brain tissue in shear: some experimental data and differential constitutive model". *Biorheology* 38.4 (2001), pp. 335–345. DOI: 10.1177/0006355X2001038004004 (cit. on p. 102).

[74] M. Bogdanska, M. Bodnar, J. Belmonte-Beitia, M. Murek, P. Schucht, J. Beck, and V. Perez-Garcia. "A mathematical model of low grade gliomas treated with temozolomide and its therapeutical implications". *Mathematical Biosciences* 288 (2017), pp. 1–13. DOI: 10.1016/j.mbs.2017.02.003 (cit. on p. 27).

[75] P.-Y. Bondiau, E. Konukoglu, O. Clatz, H. Delingette, M. Frenay, and P. Paquis. "Biocomputing: numerical simulation of glioblastoma growth and comparison with conventional irradiation margins". *Physica Medica* 27.2 (2011), pp. 103–108. DOI: 10.1016/j.ejmp.2010.05.002 (cit. on pp. 25, 27, 35, 41).

[76] K. Böttger, H. Hatzikirou, A. Chauviere, and A. Deutsch. "Investigation of the migration/proliferation dichotomy and its impact on avascular glioma invasion". *Mathematical Modelling of Natural Phenomena* 7.1 (2012), pp. 105–135. DOI: 10.1051/mmnp/20127106 (cit. on p. 25).

[77] E. Bouin and V. Calvez. "Travelling waves for the cane toads equation with bounded traits". *Nonlinearity* 27 (2014). DOI: 10.1088/0951-7715/27/9/2233 (cit. on p. 30).

[78] E. Bouin, V. Calvez, N. Meunier, S. Mirrahimi, B. Perthame, G. Raoul, and R. Voituriez. "Invasion fronts with variable motility: Phenotype selection, spatial sorting and wave acceleration". *Comptes Rendus Mathematique* 350.15 (2012), pp. 761–766. DOI: 10.1016/j.crma.2012.09.010 (cit. on p. 30).

[79] British Standards. *Physical Testing of Rubber*. Tech. rep. BS 903-0:2012. British Standards Institution, 2012 (cit. on p. 78).

[80] C. Brown et al. "Regression of Glioblastoma after chimeric antigen receptor T-cell therapy". *New England Journal of Medicine* 375 (2016), pp. 2561–2569. DOI: 10.1056/NEJMoa1610497 (cit. on pp. 116, 125).

[81] J. M. Y. Brown and A. J. Giaccia. "The unique physiology of solid tumors: opportunities (and problems) for cancer therapy". *Cancer research* 58 7 (1998), pp. 1408–16 (cit. on p. 149).

[82] M. Bruehlmeier, U. Roelcke, P. Bläuenstein, J. Missimer, P. Schubiger, J. Locher, R. Pellikka, and S. Ametamey. "Measurement of the extracellular space in brain tumors using 76Br-bromide and PET". *Journal of Nuclear Medicine* 44 (2003), pp. 1210–8 (cit. on pp. 62, 64).

[83] S. Budday, T. C. Ovaert, G. A. Holzapfel, P. Steinmann, and E. Kuhl. "Fifty shades of brain: A review on the mechanical testing and modeling of brain tissue". *Archives of Computational Methods in Engineering* 27.4 (2020), pp. 1187–1230. DOI: 10.1007/s11831-019-09352-w (cit. on pp. 15, 61, 77, 78, 87, 101).

[84] S. Budday, G. Sommer, J. Haybaeck, P. Steinmann, G. Holzapfel, and E. Kuhl. "Rheological characterization of human brain tissue". *Acta Biomaterialia* 60 (2017), pp. 315–329. DOI: 10.1016/j.actbio.2017.06.024 (cit. on p. 15).

[85] S. Budday et al. "Mechanical characterization of human brain tissue". *Acta Biomaterialia* 48 (2017), pp. 319–340. DOI: 10.1016/j.actbio.2016.10.036 (cit. on pp. 15, 61, 80).

[86] S. Budday, R. Nay, R. de Rooij, P. Steinmann, T. Wyrobek, T. Ovaert, and E. Kuhl. "Mechanical properties of gray and white matter brain tissue by indentation". *Journal of the Mechanical Behavior of Biomedical Materials* 46 (2015), pp. 318–330. DOI: 10.1016/j.jmbbm.2015.02.024 (cit. on pp. 61, 102).

[87] S. Bunimovich-Mendrazitsky, E. Shochat, and L. Stone. "Mathematical model of BCG immunotherapy in superficial bladder cancer". *Bulletin of mathematical biology* 69 (2007), pp. 1847–70. DOI: 10.1007/s11538-007-9195-z (cit. on p. 31).

[88] R. Bürger. *The mathematical theory of selection, recombination and mutation*. 2000 (cit. on p. 28).

[89] S. Burri, V. Gondi, P. Brown, and M. Mehta. "The evolving role of tumor treating fields in managing Glioblastoma: Guide for oncologists". *American Journal of Clinical Oncology* 41 (2017), p. 1. DOI: 10.1097/COC.0000000000000395 (cit. on p. 19).

[90] F. Bussolino, M. Arese, E. Audero, E. Giraudo, S. Mitola, L. Primo, and G. Serini. "Biological aspects of tumour angiogenesis" (2003). DOI: 10.1201/9780203494899.ch1 (cit. on p. 12).

[91] J. Butner, P. Dogra, C. Chung, R. Pasqualini, W. Arap, J. Lowengrub, V. Cristini, and Z. Wang. "Mathematical modeling of cancer immunotherapy for personalized clinical translation". *Nature Computational Science* 2 (2022), pp. 785–796. DOI: 10.1038/s43588-022-00377-z (cit. on p. 30).

[92] H. M. Byrne and M. A. J. Chaplain. "Free boundary value problems associated with the growth and development of multicellular spheroids". *European Journal of Applied Mathematics* 8.6 (1997), pp. 639–658. DOI: 10.1017/S0956792597003264 (cit. on p. 157).

[93] H. Byrne and M. Chaplain. "Mathematical models for tumour angiogenesis: numerical simulations and nonlinear wave solutions". *Bulletin of Mathematical Biology* 57 (1995), pp. 461–486. DOI: 10.1007/BF02460674 (cit. on p. 32).

[94] H. Byrne and L. Preziosi. "Modelling solid tumour growth using the theory of mixtures". *Mathematical medicine and biology : a journal of the IMA* 20 (2004), pp. 341–66. DOI: 10.1093/imammb20.4.341 (cit. on pp. 36, 42).

[95] R. Cantrell and C. Cosner. "Spatial ecology via reaction-diffusion equations" (2004), pp. 395–408. DOI: 10.1002/0470871296.refs (cit. on p. 118).

[96] Y. Cao, M. Gunzburger, F. Hua, and X. Wang. "Coupled Stokes-Darcy model with Beavers-Joseph interface boundary condition". *Communications in Mathematical Sciences* 8.1 (2010), pp. 1–25. DOI: 10.4310/CMS.2010.v8.n1.a2 (cit. on p. 161).

[97] P. Carmeliet. "Mechanisms of angiogenesis and arteriogenesis". *Nature medicine* 6 (2000), pp. 389–95. DOI: 10.1038/74651 (cit. on pp. 12, 144, 153).

[98] J. Carrillo, S. Cuadrado, and B. Perthame. "Adaptive dynamics via Hamilton–Jacobi approach and entropy methods for a juvenile-adult model". *Mathematical biosciences* 205 (2007), pp. 137–61. DOI: 10.1016/j.mbs.2006.09.012 (cit. on p. 28).

[99] L. Cattaneo and P. Zunino. "Computational models for fluid exchange between microcirculation and tissue interstitium". *Networks and Heterogeneous media* 9.1 (2014), pp. 135–159. DOI: 10.3934/nhm.2014.9.135 (cit. on pp. 32, 158, 161).

[100] L. Cattaneo and P. Zunino. "A computational model of drug delivery through microcirculation to compare different tumor treatments". *International Journal for Numerical Methods in Biomedical Engineering* 30.11 (2014), pp. 1347–1371. DOI: 10.1002/cnm.2661 (cit. on p. 32).

[101] M. Chaplain. "Avascular growth, angiogenesis and vascular growth in solid tumours: The mathematical modelling of the stages of tumour development". *Mathematical and Computer Modelling* 23.6 (1996), pp. 47–87. DOI: 10.1016/0895-7177(96)00019-2 (cit. on p. 157).

[102] M. Chaplain and B. Sleeman. "A mathematical model for the production and secretion of tumour angiogenesis factor in tumours". *IMA Journal of Mathematics Applied in Medicine and Biology* 7 (1990), pp. 93–108. DOI: 10.1093/imammb/7.2.93 (cit. on p. 32).

[103] M. Chaplain and A. Stuart. "A model mechanism for the chemotactic response of endothelial cells to tumour angiogenesis factor". *IMA Journal of Mathematics Applied in Medicine and Biology* 10 (1993), pp. 149–168. DOI: 10.1093/imammb/10.2.149 (cit. on p. 32).

[104] C. Chatelain, T. Balois, P. Ciarletta, and M. Ben Amar. "Emergence of microstructural patterns in skin cancer: a phase separation analysis in a binary mixture". *New Journal of Physics* 13.11 (2011), p. 115013. DOI: 10.1088/1367-2630/13/11/115013 (cit. on pp. 62, 64).

[105] S. Chatelin, A. Constantinesco, and R. Willinger. "Fifty years of brain tissue mechanical testing: from *in vitro* to *in vivo* investigations". *Biorheology* 47.5–6 (2010), pp. 255–276. DOI: 10.3233/BIR-2010-0576 (cit. on pp. 77, 78, 79).

[106] S. Chatelin, C. Deck, and R. Willinger. "An anisotropic viscous hyperelastic constitutive law for brain material finite-element modeling". *Journal of Biorheology* 27 (2013), pp. 26–37. DOI: 10.1007/s12573-012-0055-6 (cit. on p. 79).

[107] B. Chauffert, L. Feuvret, F. Bonnetain, L. Taillandier, et al. "Randomized phase II trial of irinotecan and bevacizumab as neo-adjuvant and adjuvant to temozolomide-based chemoradiation compared with temozolomide-chemoradiation for unresectable glioblastoma: final results of the TEMAVIR study from ANOCEF". *Annals of Oncology* 25 (2014), pp. 1442–1447. DOI: 10.1093/annonc/mdu148. (cit. on p. 19).

[108] V. P. Chauhan et al. "Compression of pancreatic tumor blood vessels by hyaluronan is caused by solid stress and not interstitial fluid pressure". *Cancer cell* 26.1 (2014), pp. 14–15. DOI: 10.1016/j.ccr.2014.06.003 (cit. on p. 27).

[109] D. Chauvet, M. Imbault, L. Capelle, C. Demené, M. Mossad, C. Karachi, A. Boch, J.-L. Gennisson, and M. Tanter. "In vivo measurement of brain tumor elasticity using intraoperative shear wave elastography". *Ultraschall in der Medizin* 37 (2015). DOI: 10.1055/s-0034-1399152 (cit. on pp. 61, 64).

[110] G. Cheng, J. Tse, R. Jain, and L. Munn. "Micro-environmental mechanical stress controls tumor spheroid size and morphology by suppressing proliferation and inducing apoptosis in cancer cells". *PloS one* 4 (2009). DOI: 10.1371/journal.pone.0004632 (cit. on p. 24).

[111] S. Chien, S. Usami, R. J. Dellenback, and M. I. Gregersen. "Shear-dependent deformation of erythrocytes in rheology of human blood". *American Journal of Physiology-Legacy Content* 219.1 (1970), pp. 136–142. DOI: 10.1152/ajplegacy.1970.219.1.136 (cit. on p. 159).

[112] S. Childress and J. Percus. "Nonlinear aspects of chemotaxis". *Mathematical Biosciences* 56.3 (1981), pp. 217–237. DOI: 10.1016/0025-5564(81)90055-9 (cit. on p. 158).

[113] R. Chisholm, T. Lorenzi, L. Desvillettes, and B. Hughes. "Evolutionary dynamics of phenotype-structured populations: from individual-level mechanisms to population-level consequences:" *Zeitschrift für angewandte Mathematik und Physik* 67 (2016). DOI: 10.1007/s00033-016-0690-7 (cit. on p. 29).

[114] R. Chisholm, T. Lorenzi, and A. Lorz. "Effects of an advection term in nonlocal Lotka–Volterra equations". *Communications in Mathematical Sciences* 14 (2016), pp. 1181–1188. DOI: 10.4310/CMS.2016.v14.n4.a16 (cit. on p. 29).

[115] R. Chisholm, T. Lorenzi, A. Lorz, A. Larsen, L. Almeida, A. Escargueil, and J. Clairambault. "Emergence of drug tolerance in cancer cell populations: An evolutionary outcome of selection, nongenetic instability, and stress-induced adaptation". *Cancer research* 75 (2015). DOI: 10.1158/0008-5472.CAN-14-2103 (cit. on p. 29).

[116] H. Cho and D. Levy. "Modeling continuous levels of resistance to multidrug therapy in cancer". *Applied Mathematical Modelling* 64 (2018). DOI: 10.1016/j.apm.2018.07.025 (cit. on p. 29).

[117] H. Cho and D. Levy. "Modeling the dynamics of heterogeneity of solid tumors in response to chemotherapy". *Bulletin of Mathematical Biology* 79 (2017). DOI: 10.1007/s11538-017-0359-1 (cit. on p. 30).

[118] H. Cho and D. Levy. "The impact of competition between cancer cells and healthy cells on optimal drug delivery". *Mathematical Modelling of Natural Phenomena* 15 (2020). DOI: 10.1051/mmnp/2019043 (cit. on p. 30).

[119] M. Chowdhary, C. Ene, and D. Silbergeld. "Treatment of gliomas: How did we get here?" *Surgical neurology international* 6 (2015), S85–8. DOI: 10.4103/2152-7806.151348 (cit. on p. 19).

[120] R. M. Christensen. *Theory of Viscoelasticity: An Introduction*. 2nd. Dover Publications, 2003 (cit. on p. 79).

[121] P. Ciarletta and M. Destrade. "Torsion instability of soft solid cylinders". *The IMA Journal of Applied Mathematics* 79.5 (2014), pp. 804–819. DOI: 10.1093/imamat/hxt052 (cit. on p. 87).

[122] D. Cioranescu and P. Donato. *An introduction to homogenization*. Vol. 17. Oxford: Oxford University Press, 1999. DOI: 10.1093/oso/9780198565543.001.0001 (cit. on p. 153).

[123] O. Clatz, M. Sermesant, P.-Y. Bondiau, H. Delingette, S. K. Warfield, G. Malandain, and N. Ayache. "Realistic simulation of the 3-D growth of brain tumors in MR images coupling diffusion with biomechanical deformation". *IEEE Transactions on Medical Imaging* 24 (2005), pp. 1334–1346. DOI: 10.1109/TMI.2005.857217 (cit. on pp. 25, 27, 61).

[124] P. Colli, H. Gomez, G. Lorenzo, G. Marinoschi, A. Reali, and E. Rocca. "Optimal control of cytotoxic and antiangiogenic therapies on prostate cancer growth". *Mathematical Models and Methods in Applied Sciences* 31.07 (2021), pp. 1419–1468. DOI: 10.1142/S0218202521500299 (cit. on p. 76).

[125] M. C. Colombo, C. Giverso, E. Faggiano, C. Boffano, F. Acerbi, and P. Ciarletta. "Towards the personalized treatment of Glioblastoma: integrating patient-specific clinical data in a Continuous Mechanical model". *PLOS ONE* 10.7 (2015), pp. 1–23. DOI: 10.1371/journal.pone.0132887 (cit. on pp. 25, 26, 42, 62, 64).

[126] E. Comellas, S. Budday, J. Pelteret, G. A. Holzapfel, and P. Steinmann. "Modeling the porous and viscous responses of human brain tissue behavior". *Computer Methods in Applied Mechanics and Engineering* 369 (2020), p. 113128. DOI: 10.1016/j.cma.2020.113128 (cit. on p. 77).

[127] T. A. Connor, J. M. Clark, J. Jayamohan, M. Stewart, A. McGoldrick, C. Williams, B. M. Seemungal, R. Smith, R. Burek, and M. D. Gilchrist. "Do equestrian helmets prevent concussion? A retrospective analysis of head injuries and helmet damage from real-world equestrian accidents". *Sports Medicine* 5 (2019), pp. 1–8. DOI: 10.1186/s40798-019-0193-0 (cit. on p. 77).

[128] M. Conte, Y. Dzierma, S. Knobe, and C. Surulescu. "Mathematical modeling of glioma invasion and therapy approaches via kinetic theory of active particles". *Mathematical Models and Methods in Applied Sciences* 33.05 (2023), pp. 1009–1051. DOI: 10.1142/S0218202523500227 (cit. on pp. 27, 42, 43).

[129] M. Conte, L. Gerardo-Giorda, and M. Groppi. "Glioma invasion and its interplay with nervous tissue and therapy: A multiscale model". *Journal of Theoretical Biology* 486 (2019), p. 110088. DOI: 10.1016/j.jtbi.2019.110088 (cit. on pp. 25, 26).

[130] M. Conte and C. Surulescu. "Mathematical modeling of glioma invasion: Acid- and vasculature mediated go-or-grow dichotomy and the influence of tissue anisotropy". *Applied Mathematics and Computation* 407 (2021), p. 126305. DOI: 10.1016/j.amc.2021.126305 (cit. on pp. 25, 26).

[131] J.-P. Cosse and C. Michiels. "Tumour hypoxia affects the responsiveness of cancer cells to chemotherapy and promotes cancer progression". *Anti-Cancer Agents in Medicinal Chemistry* 8.7 (2008), pp. 790–797. DOI: 10.2174/187152008785914798 (cit. on pp. 151, 185).

[132] G. Criscenti, C. De Maria, E. Sebastiani, M. Tei, G. Placella, A. Speziali, G. Vozzi, and G. Cerulli. "Quasi-linear viscoelastic properties of the human medial patello-femoral ligament". *Journal of Biomechanics* 48.16 (2015), pp. 4297–4302. DOI: 10.1016/j.jbiomech.2015.10.042 (cit. on p. 79).

[133] I. Cruz-Matías, D. Ayala, D. Hiller, S. Gutsch, M. Zacharias, S. Estradé, and F. Peiró. "Sphericity and roundness computation for particles using the extreme vertices model". *Journal of Computational Science* 30 (2019), pp. 28–40. DOI: 10.1016/j.jocs.2018.11.005 (cit. on p. 67).

[134] F. Dadgar–Rad and N. Firouzi. "Time-dependent response of incompressible membranes based on quasi-linear viscoelasticity theory". *International Journal of Applied Mechanics* 13.03 (2021), p. 2150036. DOI: 10.1142/S1758825121500368 (cit. on p. 79).

[135] M. P. Dalwadi, M. Bruna, and I. M. Griffiths. "A multiscale method to calculate filter blockage". *Journal of Fluid Mechanics* 809 (2016), pp. 264–289. DOI: 10.1017/jfm.2016.656 (cit. on pp. 153, 156).

[136] N. Daphalapurkar, J. Riglin, A. Mohan, J. Harris, and J. Bernardin. "Quasi-dynamic breathing model of the lung incorporating viscoelasticity of the lung tissue". *International Journal for Numerical Methods in Biomedical Engineering* 39.8 (2023), e3744. DOI: 10.1002/cnm.3744 (cit. on p. 79).

[137] N. Darwiche. "Epigenetic mechanisms and the hallmarks of cancer: an intimate affair". *American journal of cancer research* 10 (2020), pp. 1954–1978. DOI: 10(7):1954-1978 (cit. on p. 12).

[138] R. De Pascalis, D. I. Abrahams, and W. J. Parnell. "Simple shear of a compressible quasilinear viscoelastic material". *International Journal of Engineering Science* 88 (2015), pp. 64–72. DOI: 10.1016/j.ijengsci.2014.11.011 (cit. on p. 79).

[139] R. De Pascalis, W. J. Parnell, D. I. Abrahams, T. Shearer, D. M. Daly, and D. Grundy. "The inflation of viscoelastic balloons and hollow viscera". *Proceedings of the Royal Society A: Mathematical, Physical and Engineering Sciences* 474.2218 (2018), p. 20180102. DOI: 10.1098/rspa.2018.0102 (cit. on pp. 79, 89).

[140] R. De Pascalis, I. D. Abrahams, and W. J. Parnell. "On nonlinear viscoelastic deformations: a reappraisal of Fung's quasi-linear viscoelastic model". *Proceedings. Mathematical, Physical, and Engineering Sciences / The Royal Society* 470 (2014). DOI: 10.1098/rspa.2014.0058 (cit. on pp. 78, 79, 81, 89).

[141] R. Deberardinis, J. Lum, G. Hatzivassiliou, and C. Thompson. "The biology of cancer: Metabolic reprogramming fuels cell growth and proliferation". *Cell metabolism* 7 (2008), pp. 11–20. DOI: 10.1016/j.cmet.2007.10.002 (cit. on pp. 12, 17).

[142] K. DeClerck and R. Elble. "The role of hypoxia and acidosis in promoting metastasis and resistance to chemotherapy". *Frontiers in bioscience : a journal and virtual library* 15 (2010), pp. 213–25. DOI: 10.2741/3616 (cit. on pp. 151, 185).

[143] H. Dehghani, I. Noll, R. Penta, A. Menzel, and J. Merodio. "The role of microscale solid matrix compressibility on the mechanical behaviour of poroelastic materials". *European Journal of Mechanics-A/Solids* 83 (2020), p. 103996. DOI: 10.1016/j.euromechsol.2020.103996 (cit. on pp. 153, 181, 182, 185).

[144] H. Delingette and N. Ayache. "Soft tissue modeling for surgery simulation". *Handbook of Numerical Analysis* 12 (2004), pp. 453–550. DOI: 10.1016/S1570-8659(03)12005-4 (cit. on p. 77).

[145] L. Depillis, K. Fister, W. Gu, C. Collins, M. Daub, D. Gross, M. Moore, and B. Preskill. "Mathematical model creation for cancer chemo-immunotherapy". *Comput. Math. Methods Med.* 10 (2009). DOI: 10.1080/17486700802216301 (cit. on p. 31).

[146] L. Depillis, W. Gu, and A. Radunskaya. "Mixed immunotherapy and chemotherapy of tumors: Modeling, applications and biological interpretations". *Journal of theoretical biology* 238 (2006), pp. 841–62. DOI: 10.1016/j.jtbi.2005.06.037 (cit. on p. 31).

[147] M. Destrade, Y. Du, J. Blackwell, N. Colgan, and V. Balbi. "Canceling the elastic Poynting effect with geometry". *Physical Review E* 107.5 (2023), p. L053001. DOI: 10.1103/PhysRevE.107.L053001 (cit. on p. 78).

[148] M. Destrade, G. Saccomandi, and I. Sgura. "Methodical fitting for mathematical models of rubber-like materials". *Proceedings of the Royal Society A: Mathematical, Physical and Engineering Sciences* 473.2198 (2017), p. 20160811. DOI: 10.1098/rspa.2016.0811 (cit. on p. 93).

[149] M. Destrade, M. Gilchrist, J. Murphyj, B. Rashid, and G. Saccomandi. "Extreme softness of brain matter in simple shear". *International Journal of Non-Linear Mechanics* 75 (2015), pp. 54–58. DOI: 10.1016/j.ijnonlinmec.2015.02.014 (cit. on pp. 15, 40, 78, 89).

[150] S. Di Stefano, M. Carfagna, M. M. Knodel, K. Hashlamoun, S. Federico, and A. Grillo. "Anelastic reorganisation of fibre-reinforced biological tissues". *Computing and Visualization in Science* 20.3–6 (2019), pp. 95–109. DOI: 10.1007/s00791-019-00313-1 (cit. on pp. 49, 63, 64).

[151] S. Di Stefano, A. Giammarini, C. Giverso, and A. Grillo. "An elasto-plastic biphasic model of the compression of multicellular aggregates: the influence of fluid on stress and deformation". *ZAMP - Zeitschrift für angewandte Mathematik und Physik* 73 (2022), p. 79. DOI: 10.1007/s00033-022-01692-1 (cit. on p. 49).

[152] S. Di Stefano, A. Ramírez-Torres, R. Penta, and A. Grillo. "Self-influenced growth through evolving material inhomogeneities". *International Journal of Non-Linear Mechanics* 106 (2018). DOI: 10.1016/j.ijnonlinmec.2018.08.003 (cit. on pp. 27, 153).

[153] A. Dicarlo and S. Quiligotti. "Growth and balance". *Mechanics Research Communications* 29 (2002), pp. 449–456. DOI: 10.1016/S0093-6413(02)00297-5 (cit. on p. 27).

[154] O. Diekmann, P.-E. Jabin, S. Mischler, and B. Perthame. "The dynamics of adaptation: An illuminating example and a Hamilton–Jacobi approach". *Theoretical Population Biology* 67.4 (2005), pp. 257–271. DOI: 10.1016/j.tpb.2004.12.003 (cit. on pp. 28, 151).

[155] M. Discacciati and A. Quarteroni. "Navier-Stokes/Darcy coupling: Modeling, analysis, and numerical approximation". *Revista Matemática Complutense* 22 (2009). DOI: 10.5209/rev_REMA.2009.v22.n2.16263 (cit. on p. 161).

[156] B. Donnelly and J. Medige. "Shear properties of human brain tissue". *Journal of biomechanical engineering* 119 (1997), pp. 423–32. DOI: 10.1115/1.2798289 (cit. on p. 15).

[157] C. S. Drapaca, S. Sivaloganathan, and G. Tenti. "Nonlinear constitutive laws in viscoelasticity". *Mathematics and Mechanics of Solids* 12.5 (2007), pp. 475–501. DOI: 10.1177/1081286506062450 (cit. on p. 79).

[158] S. E. Duenwald, R. Vanderby, and R. S. Lakes. "Viscoelastic relaxation and recovery of tendon". *Annals of Biomedical Engineering* 37 (2009), pp. 1131–1140. DOI: 10.1007/s10439-009-9687-0 (cit. on p. 79).

[159] S. Dumont, M. Serpilli, R. Rizzoni, and F. C. Lebon. "Numerical validation of multiphysic imperfect interfaces models". *Frontiers in Materials* 7 (2020), p. 158. DOI: 10.3389/fmats.2020.00158 (cit. on p. 153).

[160] A. Dzutsev, J. H. Badger, E. Perez-Chanona, S. Roy, R. Salcedo, C. K. Smith, and G. Trinchieri. "Microbes and cancer". *Annual Review of Immunology* 35 (2017), pp. 199–228. DOI: 10.1146/annurev-immunol-051116-052133 (cit. on p. 12).

[161] A. Edwards, E. Keggin, and P. Plowman. "The developing role for intensity-modulated radiation therapy (IMRT) in the non-surgical treatment of brain metastases". *The British journal of radiology* 83 (2009), pp. 133–6. DOI: 10.1259/bjr/28596848 (cit. on p. 18).

[162] E. Eggenweiler and I. Rybak. "Unsuitability of the Beavers–Joseph interface condition for filtration problems". *Journal of Fluid Mechanics* 892 (2020), A10. DOI: 10.1017/jfm.2020.194 (cit. on p. 161).

[163] W. Ehlers and G. Eipper. "Finite elastic deformations in liquid-saturated and empty porous solids". *Transport in Porous Media* 34 (1999), pp. 179–191. DOI: 10.1023/A:1006565509095 (cit. on p. 40).

[164] W. Ehlers, M. Morrison Rehm, P. Schröder, D. Stöhr, and A. Wagner. "Multiphasic modelling and computation of metastatic lung-cancer cell proliferation and atrophy in brain tissue based on experimental data". *Biomechanics and Modeling in Mechanobiology* 21.1 (2022), pp. 277–315. DOI: 10.1007/s10237-021-01535-4 (cit. on pp. 25, 27, 35).

[165] W. Ehlers and A. Wagner. "Multi-component modelling of human brain tissue: a contribution to the constitutive and computational description of deformation, flow and diffusion processes with application to the invasive drug-delivery problem". *Computer Methods in Biomechanics and Biomedical Engineering* 18.8 (2015), pp. 861–879. DOI: 10.1080/10255842.2013.853754 (cit. on pp. 25, 27).

[166] D. Eichberg, A. Shah, and M. Ivan. "Laser interstitial thermal therapy for "inoperable" gliomas". In: 2019, pp. 209–229. DOI: 10.1016/B978-0-12-813633-1.00015-3 (cit. on p. 18).

[167] A. Elazab, A. M. Anter, H. Bai, Q. Hu, Z. Hussain, D. Ni, T. Wang, and B. Lei. "An optimized generic cerebral tumor growth modeling framework by coupling biomechanical and diffusive models with treatment effects". *Applied Soft Computing* 80.C (2019), pp. 617–627. DOI: 10.1016/j.asoc.2019.04.034 (cit. on p. 25).

[168] B. Ellingson, H. Nguyen, A. Lai, R. Nechifor, O. Zaw, W. Pope, W. Yong, P. Nghiemphu, L. Liau, and T. Cloughesy. "Contrast-enhancing tumor growth dynamics of preoperative, treatment-naive human glioblastoma". *Cancer* 122 (2016), pp. 1718–1727. DOI: 10.1002/cncr.29957 (cit. on pp. 65, 149).

[169] C. Engwer, T. Hillen, M. Knappitsch, and C. Surulescu. "Glioma follow white matter tracts: A multiscale DTI-based model". *Journal of Mathematical Biology* 71 (2015), pp. 551–582. DOI: 10.1007/s00285-014-0822-7 (cit. on pp. 25, 26).

[170] C. Engwer, A. Hunt, and C. Surulescu. "Effective equations for anisotropic glioma spread with proliferation: A multiscale approach and comparisons with previous settings". *Mathematical Medicine and Biology* 33 (2016), pp. 435–459. DOI: 10.1093/imammb/dqv030 (cit. on pp. 25, 26).

[171] C. Engwer, M. Knappitsch, and C. Surulescu. "A multiscale model for glioma spread including cell-tissue interactions and proliferation". *Mathematical Biosciences & Engineering* 13.2 (2016), pp. 443–460. DOI: 10.3934/mbe.2015011 (cit. on pp. 25, 26).

[172] C. Engwer and M. Wenske. "Estimating the extent of glioblastoma invasion: Approximate stationalization of anisotropic advection–diffusion–reaction equations in the context of glioblastoma invasion". *Journal of Mathematical Biology* 82 (2021). DOI: 10.1007/s00285-021-01563-9 (cit. on pp. 25, 26).

[173] M. Esmaeili, A. L. Stensjøen, E. M. Berntsen, O. Solheim, and I. Reinertsen. "The direction of tumour growth in glioblastoma patients". *Scientific Reports* 8.1 (2018). DOI: 10.1038/s41598-018-19420-z (cit. on pp. 35, 41).

[174] M. Esteller. "Cancer epigenomics: DNA methylomes and histone-modification maps". *Nature reviews. Genetics* 8 (2007), pp. 286–98. DOI: 10.1038/nrg2005 (cit. on p. 12).

[175] F. Evans, M. Dittmer, A. Fuente, and D. Fitzgerald. "Protective and regenerative roles of T Cells in central nervous system disorders". *Frontiers in Immunology* 10 (2019), p. 2171. DOI: 10.3389/fimmu.2019.02171 (cit. on p. 106).

[176] L. Evans and P. Souganidis. "A PDE approach to geometric optics for certain semilinear parabolic equations". *Indiana University Mathematics Journal* 38.1 (1989), pp. 141–172 (cit. on p. 137).

[177] J. Falco et al. "In silico mathematical modelling for Glioblastoma: A critical review and a patient-specific case". *Journal of Clinical Medicine* 10 (2021), p. 2169. DOI: 10.3390/jcm10102169 (cit. on pp. 24, 25, 26).

[178] S. Federico, A. Grillo, G. La Rosa, G. Giaquinta, and W. Herzog. "A transversely isotropic, transversely homogeneous microstructural-statistical model of articular cartilage". *Journal of biomechanics* 38.10 (2005), pp. 2008–2018. DOI: 10.1016/j.jbiomech.2004.09.020 (cit. on p. 181).

[179] A. Fedorov et al. “3D Slicer as an image computing platform for the quantitative imaging network”. *Magnetic Resonance Imaging* 30 (2012), pp. 1323–41. DOI: 10.1016/j.mri.2012.05.001 (cit. on p. 45).

[180] Y. Feng, R. J. Okamoto, R. Namani, G. M. Genin, and P. V. Bayly. “Measurements of mechanical anisotropy in brain tissue and implications for transversely isotropic material models of white matter”. *Journal of the Mechanical Behavior of Biomedical Materials* 23 (2013), pp. 117–132. DOI: 10.1016/j.jmbbm.2013.04.007 (cit. on p. 102).

[181] G. Fiandaca, M. Delitala, and T. Lorenzi. “A mathematical study of the influence of hypoxia and acidity on the evolutionary dynamics of cancer”. *Bulletin of Mathematical Biology* 83 (2020). DOI: 10.1007/s11538-021-00914-3 (cit. on pp. 30, 133, 145, 146).

[182] R. A. Fisher. “The wave of advance of advantageous genes”. *Annals of Eugenics* 7.4 (1937), pp. 355–369. DOI: 10.1111/j.1469-1809.1937.tb02153.x (cit. on p. 29).

[183] W. H. Fleming and P. Souganidis. “PDE-viscosity solution approach to some problems of large deviations”. *Annali Della Scuola Normale Superiore Di Pisa-classe Di Scienze* 13 (1986), pp. 171–192 (cit. on p. 137).

[184] C. Flynn, A. J. Taberner, P. M. F. Nielsen, and S. Fels. “Simulating the three-dimensional deformation of *in vivo* facial skin”. *Journal of the Mechanical Behavior of Biomedical Materials* 28 (2013), pp. 484–494. DOI: 10.1016/j.jmbbm.2013.03.004 (cit. on p. 79).

[185] *FMRIB Software Library*. URL: https://fsl.fmrib.ox.ac.uk/fsl/fslwiki (cit. on pp. 46, 147).

[186] J. Folkman. “The vascularization of tumors”. *Scientific American* 234.5 (1976), pp. 58–73. DOI: 10.1038/scientificamerican0576-58 (cit. on p. 157).

[187] J. Folkman. “Tumor angiogenesis: therapeutic implications”. *The New England Journal of Medicine* 285.21 (1971), pp. 1182–1186. DOI: 10.1056/NEJM197111182852108 (cit. on p. 144).

[188] M. Fraldi and A. Carotenuto. “Cells competition in tumor growth poroelasticity”. *Journal of the Mechanics and Physics of Solids* 112 (2018), pp. 345–367. DOI: 10.1016/j.jmps.2017.12.015 (cit. on pp. 69, 71, 76).

[189] M. Fresnais, S. Turcan, D. Theile, J. Ungermann, Y. Abou Zeed, J. R. Lindner, M. Breitkopf, J. Burhenne, W. E. Haefeli, and R. Longuespée. “Approaching sites of action of temozolomide for pharmacological and clinical studies in Glioblastoma”. *Biomedicines* 10.1 (2022). DOI: 10.3390/biomedicines10010001 (cit. on p. 43).

[190] H. B. Frieboes, M. E. Edgerton, J. P. Fruehauf, D. Rose, L. K. Worrall, R. A. Gatenby, M. Ferrari, and V. Cristini. “Prediction of drug response in breast cancer using integrative experimental/computational modeling”. *Cancer Research* 69.10 (2010), pp. 4484–4492. DOI: 10.1158/0008-5472.CAN-08-3745 (cit. on p. 144).

[191] H. Frieboes, J. Lowengrub, S. Wise, X. Zheng, P. Macklin, E. Bearer, and V. Cristini. “Computer simulation of glioma growth and morphology”. *NeuroImage* 37 (2007), S59–S70. DOI: 10.1016/j.neuroimage.2007.03.008 (cit. on pp. 25, 62, 64).

[192] H. Friedman, T. Kerby, and H. Calvert. “Temozolomide and treatment of malignant glioma”. *Clinical Cancer Research* 6 (7 2000), pp. 2585–2597 (cit. on p. 62).

[193] M. H. Friedman. *Principles and models of biological transport*. New York, NY: Springer-Verlag, 2008 (cit. on p. 160).

[194] Z. B. Fülöp, A. Ramírez-Torres, and R. Penta. "Multiscale modelling of fluid transport in vascular tumours subjected to electrophoresis anticancer therapies". *Zeitschrift für angewandte Mathematik und Physik* 75.1 (2024), p. 9. DOI: 10.21203/rs.3.rs-3252285/v1 (cit. on p. 158).

[195] I. Fumagalli, M. Corti, N. Parolini, and P. Antonietti. "Polytopal discontinuous Galerkin discretization of brain multiphysics flow dynamics". *Journal of Computational Physics* 513 (2024), p. 113115. DOI: 10.1016/j.jcp.2024.113115 (cit. on p. 184).

[196] Y. Fung. *Biomechanics: mechanical properties of living tissues*. Springer Science and Business Media, 1993 (cit. on pp. 79, 81, 100).

[197] J. R. Funk, G. W. Hall, J. R. Crandall, and W. D. Pilkey. "Linear and quasi-linear viscoelastic characterization of ankle ligaments". *Journal of Biomechanical Engineering* 122.1 (2000), pp. 15–22. DOI: 10.1115/1.429623 (cit. on p. 79).

[198] J. Gallaher, J. Brown, and A. Anderson. "The impact of proliferation-migration tradeoffs on phenotypic evolution in cancer". *Scientific Reports* 9 (2019). DOI: 10.1038/s41598-019-39636-x (cit. on p. 17).

[199] E. S. Gamburg, W. F. Regine, R. A. Patchell, J. M. Strottmann, M. Mohiuddin, and A. B. Young. "The prognostic significance of midline shift at presentation on survival in patients with glioblastoma multiforme". *International Journal of Radiation Oncology, Biology, Physics* 48.5 (2000), pp. 1359–1362. DOI: 10.1016/s0360-3016(00)01410-3 (cit. on p. 16).

[200] J. Garcia and J. Smith. "A biphasic hyperelastic model for the analysis of fluid and mass transport in brain tissue". *Annals of Biomedical Engineering* 37.2 (2009), pp. 375–386. DOI: 10.1007/s10439-008-9610-0 (cit. on p. 49).

[201] A. Garo, M. Hrapko, J. A. W. Van Dommelen, and G. W. M. Peters. "Towards a reliable characterisation of the mechanical behaviour of brain tissue: the effects of post-mortem time and sample preparation". *Biorheology* 44.1 (2007), pp. 51–58. DOI: 10.1177/0006355X2007044001003 (cit. on p. 77).

[202] R. A. Gatenby and E. T. Gawlinski. "The glycolytic phenotype in carcinogenesis and tumor invasion: Insights through mathematical models". *Cancer Research* 63.14 (2003), pp. 3847–3854 (cit. on pp. 133, 144).

[203] R. A. Gatenby and R. Gillies. "Why do cancers have high aerobic glycolysis?" *Nature Reviews Cancer* 4 (2004), pp. 891–899. DOI: 10.1038/nrc1478 (cit. on p. 133).

[204] H. Gerhardt. "Simulation of vessel morphogenesis using cellular automata". *Organogenesis* 4 (2008), pp. 241–246. DOI: 10.4161/org.4.4.6978 (cit. on p. 32).

[205] P. Gerlee and A. Anderson. "An evolutionary hybrid cellular automaton model of solid tumour growth". *Journal of Theoretical Biology* 246 4 (2007), pp. 583–603. DOI: 10.1016/j.jtbi.2007.01.027 (cit. on p. 62).

[206] P. Gerlee and S. Nelander. "The impact of phenotypic switching on glioblastoma growth and invasion". *PLOS Computational Biology* 8 (2012). DOI: 10.1371/journal.pcbi.1002556 (cit. on p. 25).

[207] P. Gerlee and S. Nelander. "Travelling wave analysis of a mathematical model of glioblastoma growth". *Mathematical Biosciences* 276 (2016), pp. 75–81. DOI: 10.1016/j.mbs.2016.03.004 (cit. on p. 25).

[208] A. Giese, R. Bjerkvig, M. Berens, and M. Westphal. "Cost of migration: Invasion of malignant gliomas and implications for treatment". *Journal of Clinical Oncology* 21.8 (2003), pp. 1624–1636. DOI: 10.1200/JCO.2003.05.063 (cit. on p. 17).

[209] A. Giese, L. Kluwe, B. Laube, H. Meissner, M. E. Berens, and M. Westphal. "Migration of human glioma cells on myelin". *Neurosurgery* (1996), pp. 755–764. DOI: 10.1097/00006123-199604000-00026 (cit. on p. 35).

[210] A. Giese, L. Kluwe, B. Laube, H. Meissner, M. Berens, and M. Westphal. "Migration of human glioma cells on myelin". *Neurosurgery* (1996), pp. 755–764. DOI: 10.1097/00006123-199604000-00026 (cit. on p. 41).

[211] A. Giese, M. Loo, N. Tran, D. Haskett, S. Coons, and M. Berens. "Dichotomy of astrocytoma migration and proliferation". *International Journal of Cancer* 67 (1996), pp. 275–282. DOI: 10.1002/(SICI)1097-0215(19960717)67:2<275::AID-IJC20>3.0.CO;2-9 (cit. on p. 17).

[212] M. D. Gilchrist, B. Rashid, J. G. Murphy, and G. Saccomandi. "Quasi-static deformations of biological soft tissue". *Mathematics and Mechanics of Solids* 18.6 (2013), pp. 622–633. DOI: 10.1177/1081286513485770 (cit. on p. 90).

[213] R. Gillies, D. Verduzco, and R. Gatenby. "Evolutionary dynamic of carcinogenesis and why targeted therapy does not work". *Nature reviews. Cancer* 12 (2012), pp. 487–93. DOI: 10.1038/nrc3298 (cit. on p. 133).

[214] A. Girelli, G. Giantesio, A. Musesti, and R. Penta. "Effective governing equations for dual porosity Darcy–Brinkman systems subjected to inhomogeneous body forces and their application to the lymph node". *Proceedings of the Royal Society A* 479.2276 (2023), p. 20230137. DOI: 10.1098/rspa.2023.0137 (cit. on pp. 153, 161).

[215] A. Giudici, K. W. F. van der Laan, M. M. van der Bruggen, S. Parikh, E. Berends, S. Foulquier, T. Delhaas, K. D. Reesink, and B. Spronck. "Constituent-based quasi-linear viscoelasticity: a revised quasi-linear modelling framework to capture non-linear viscoelasticity in arteries". *Biomechanics and Modeling in Mechanobiology* 22.5 (2023), pp. 1607–1623. DOI: 10.1007/s10237-023-01711-8 (cit. on p. 79).

[216] C. Giverso and P. Ciarletta. "Tumour angiogenesis as a chemo-mechanical surface instability". *Scientific Reports* 6 (2016), p. 22610. DOI: 10.1038/srep22610 (cit. on p. 32).

[217] C. Giverso and P. Ciarletta. "On the morphological stability of multicellular tumour spheroids growing in porous media". *Eur. Phys. J. E Soft Matter* 39.10 (2016), p. 92. DOI: 10.1140/epje/i2016-16092-7 (cit. on pp. 157, 158).

[218] C. Giverso and L. Preziosi. "Influence of the mechanical properties of the necrotic core on the growth and remodelling of tumour spheroids". *International Journal of Non-Linear Mechanics* 108 (2019), pp. 20–32. DOI: 10.1016/j.ijnonlinmec.2018.10.005 (cit. on p. 71).

[219] C. Giverso, M. Scianna, and A. Grillo. "Growing avascular tumours as elasto-plastic bodies by the theory of evolving natural configurations". *Mechanics Research Communications* 68 (2015), pp. 31–39. DOI: 10.1016/j.mechrescom.2015.04.004 (cit. on pp. 27, 38, 39, 41, 71).

[220] C. Giverso, M. Verani, and P. Ciarletta. "Emerging morphologies in round bacterial colonies: comparing volumetric versus chemotactic expansion". *Biomechanics and Modeling in Mechanobiology* 15.3 (2016), pp. 643–661. DOI: 10.1007/s10237-015-0714-9 (cit. on p. 158).

[221] J. D. Gordan, J. A. Bertout, C.-J. Hu, J. A. Diehl, and M. C. Simon. "HIF-2α promotes hypoxic cell proliferation by enhancing c-Myc transcriptional activity". *Cancer Cell* 11.4 (2007), pp. 335–347. DOI: 10.1016/j.ccr.2007.02.006 (cit. on p. 145).

[222] A. Goriely, M. Geers, G. Holzapfel, J. Jayamohan, A. Jérusalem, S. Sivaloganathan, W. Squier, J. Dommelen, S. Waters, and E. Kuhl. "Mechanics of the brain: perspectives, challenges, and opportunities". *Biomechanics and modeling in mechanobiology* 14 (2015). DOI: 10.1007/s10237-015-0662-4 (cit. on p. 15).

[223] M. Green, L. E. Bilston, and R. Sinkus. "In vivo brain viscoelastic properties measured by magnetic resonance elastography". *NMR in Biomedicine* 21 (2008). DOI: 10.1002/nbm.1254 (cit. on p. 61).

[224] J. Greene, O. Lavi, M. Gottesman, and D. Levy. "The impact of cell density and mutations in a model of multidrug resistance in solid tumors". *Bulletin of mathematical biology* 76 (2014). DOI: 10.1007/s11538-014-9936-8 (cit. on p. 29).

[225] A. Greiner, N. Reiter, F. Paulsen, G. A. Holzapfel, P. Steinmann, E. Comellas, and S. Budday. "Poro-viscoelastic effects during biomechanical testing of human brain tissue". *Frontiers in Mechanical Engineering* 7 (2021), p. 708350. DOI: 10.3389/fmech.2021.708350 (cit. on p. 77).

[226] A. Grillo, A. Guaily, C. Giverso, and S. Federico. "Non-linear model for compression tests on articular cartilage". *Journal of Biomechanical Engineering* 137.7 (2015), p. 071004. DOI: 10.1115/1.4030310 (cit. on p. 181).

[227] A. Grillo, S. Stefano, and S. Federico. "Growth and remodelling from the perspective of Noether's Theorem". *Mechanics Research Communications* 97 (2019). DOI: 10.1016/j.mechrescom.2019.04.012 (cit. on p. 27).

[228] S. Grivennikov, F. Greten, and M. Karin. "Immunity, inflammation, and cancer". *Cell* 140 (2010), pp. 883–99. DOI: 10.1016/j.cell.2010.01.025 (cit. on p. 12).

[229] M. Groves, V. Puduvalli, K. Hess, K. Jaeckle, P. Peterson, W. Yung, and V. Levin. "Phase II trial of temozolomide plus the matrix metalloproteinase inhibitor, marimastat, in recurrent and progressive Glioblastoma Multiforme". *Journal of clinical oncology : official journal of the American Society of Clinical Oncology* 20 (2002), pp. 1383–8. DOI: 10.1200/JCO.20.5.1383 (cit. on p. 19).

[230] S. Gu et al. "Applying a patient-specific bio-mathematical model of glioma growth to develop virtual [18F]-FMISO-PET images". *Mathematical medicine and biology : a journal of the IMA* 29 (2011), pp. 31–48. DOI: 10.1093/imammb/dqr002 (cit. on pp. 106, 145).

[231] M. Gurtin, E. Fried, and L. Anand. *The Mechanics and Thermodynamics of Continua*. Cambridge University Press, 2010 (cit. on pp. 51, 52).

[232] D. Hanahan. "Hallmarks of cancer: New dimensions". *Cancer Discovery* 12 (2022), pp. 31–46. DOI: 10.1158/2159-8290.CD-21-1059 (cit. on pp. 11, 12).

[233] D. Hanahan and R. Weinberg. "Hallmarks of cancer: The next generation". *Cell* 144 (2011), pp. 646–74. DOI: 10.1016/j.cell.2011.02.013 (cit. on pp. 11, 144).

[234] D. Hanahan and R. Weinberg. "The hallmarks of cancer". *Cell* 100 (2000), pp. 57–70. DOI: 10.1016/S0092-8674(00)81683-9 (cit. on p. 11).

[235] S. Hang. "TetGen, a Delaunay-based quality tetrahedral mesh generator". *ACM Transactions on Mathematical Software* 41.2 (2015), pp. 1–36. DOI: 10.1145/2629697 (cit. on pp. 45, 99).

[236] C. Harkos, S. F. Svensson, K. E. Emblem, and T. Stylianopoulos. "Inducing biomechanical heterogeneity in brain tumor modeling by MR elastography: Effects on tumor growth, vascular density and delivery of therapeutics". *Cancers* 14 (2022), p. 884. DOI: 10.3390/cancers14040884 (cit. on pp. 27, 35, 50, 61).

[237] S. Harmansa, A. Erlich, C. Eloy, G. Zurlo, and T. Lecuit. "Growth anisotropy of the extracellular matrix shapes a developing organ". *Nature Communications* 14.1 (2023), p. 1220. DOI: 10.1038/s41467-023-36739-y (cit. on p. 181).

[238] L. Hathout, V. Patl, and P. Y. Wen. "A 3-dimensional DTI MRI-based model of GBM growth and response to radiation therapy". *International journal of oncology* 49 3 (2016), pp. 1081–1087. DOI: 10.3892/ijo.2016.3595 (cit. on p. 25).

[239] H. Hatzikirou, D. Basanta, M. Simon, K. Schaller, and A. Deutsch. "'Go or Grow': the key to the emergence of invasion in tumour progression?" *Mathematical medicine and biology : a journal of the IMA* 29 (2012), pp. 49–65. DOI: 10.1093/imammb/dqq011 (cit. on pp. 17, 25).

[240] H. Hatzikirou, A. Deutsch, C. Schaller, M. Simon, K. Swanson, N. Bellomo, and P. Maini. "Mathematical modelling of glioblastoma tumour development: A review". *Mathematical Models and Methods in Applied Sciences* 24 (2005), pp. 1779–1794. DOI: 10.1142/S0218202505000960 (cit. on p. 24).

[241] Y. He and B. Kaina. "Are there thresholds in Glioblastoma cell death responses triggered by temozolomide?" *International Journal of Molecular Sciences* 20.7 (2019), p. 1562. DOI: 10.3390/ijms20071562 (cit. on pp. 43, 62).

[242] H. Helisaz, E. Belanger, P. Black, M. Bacca, and M. Chiao. "Quantifying the impact of cancer on the viscoelastic properties of the prostate gland using a quasi-linear viscoelastic model". *Acta Biomaterialia* 173 (2024), pp. 184–198. DOI: 10.1016/j.actbio.2023.11.002 (cit. on p. 79).

[243] B. Helmink, M. Khan, A. Hermann, V. Gopalakrishnan, and J. Wargo. "The microbiome, cancer, and cancer therapy". *Nature Medicine* 25 (2019). DOI: 10.1038/s41591-019-0377-7 (cit. on p. 12).

[244] S. L. Hervey-Jumper and M. S. Berger. "Introduction: Surgical management of eloquent area tumors". *Neurosurgery* 87 (6 2020), pp. 1076–1077. DOI: 10.1093/neuros/nyaa358 (cit. on p. 19).

[245] T. Hillen and K. J. Painter. "A user's guide to PDE models for chemotaxis". *Journal of Mathematical Biology* 58.1 (2009), pp. 183–217. DOI: 10.1007/s00285-008-0201-3 (cit. on pp. 119, 158).

[246] L. Hlatky and E. L. Alpen. "Two-dimensional diffusion limited system for cell growth". *Cell Proliferation* 18.6 (1985), pp. 597–611. DOI: 10.1111/j.1365-2184.1985.tb00703.x (cit. on p. 145).

[247] R. Hoefflin et al. "Spatial niche formation but not malignant progression is a driving force for intratumoural heterogeneity". *Nature Communications* 7 (2016). DOI: 10.1038/ncomms11845 (cit. on p. 149).

[248] S. Hoehme et al. "Prediction and validation of cell alignment along microvessels as order principle to restore tissue architecture in liver regeneration". *Proceedings of the National Academy of Sciences* 107.23 (2010), pp. 10371–10376. DOI: 10.1073/pnas.0909374107 (cit. on p. 50).

[249] C. Hogea, C. Davatzikos, and G. Biros. "An image-driven parameter estimation problem for a reaction–diffusion glioma growth model with mass effects". *Journal of Mathematical Biology* 56 (2008), pp. 793–825. DOI: 10.1007/s00285-007-0139-x (cit. on pp. 25, 27).

[250] C. Holdsworth, D. Corwin, R. Stewart, R. Rockne, A. Trister, K. Swanson, and M. Phillips. "Adaptive IMRT using a multiobjective evolutionary algorithm integrated with a diffusion–invasion model of glioblastoma". *Physics in Medicine & Biology* 57.24 (2012), p. 8271. DOI: 10.1088/0031-9155/57/24/8271 (cit. on p. 27).

[251] M. H. Holmes. *Introduction to perturbation methods*. Vol. 20. Springer Science & Business Media, 1995. DOI: 10.1007/978-1-4612-5347-1 (cit. on pp. 155, 156).

[252] M. Holmes and V. Mow. "The nonlinear characteristics of soft gels and hydrated connective tissues in ultrafiltration". *Journal of Biomechanical Engineering* 23.11 (1990), pp. 1145–1156. DOI: 10.1016/0021-9290(90)90007-P (cit. on pp. 49, 63).

[253] G. A. Holzapfel. *Nonlinear Solid Mechanics: A Continuum Approach for Engineering*. John Wiley & Sons Ltd., 2000 (cit. on pp. 89, 90).

[254] T. J. Horgan and M. D. Gilchrist. "The creation of three-dimensional finite element models for simulating head impact biomechanics". *International Journal of Crashworthiness* 8.4 (2003), pp. 353–366. DOI: 10.1533/ijcr.2003.0243 (cit. on p. 100).

[255] D. Hormuth II, K. Al Feghali, A. Elliott, T. Yankeelov, and C. Chung. "Image-based personalization of computational models for predicting response of high-grade glioma to chemoradiation". *Scientific Reports* 11 (2021), p. 8520. DOI: 10.1038/s41598-021-87887-4 (cit. on pp. 27, 36, 47, 62, 75).

[256] D. Hormuth II, M. Fahrat, C. Christenson, B. Curl, C. Quarles, C. Chung, and T. Yankeelov. "Opportunities for improving brain cancer treatment outcomes through imaging-based mathematical modeling of the delivery of radiotherapy and immunotherapy". *Advanced Drug Delivery Reviews* 187 (2022), p. 114367. DOI: 10.1016/j.addr.2022.114367 (cit. on p. 36).

[257] D. Hormuth II, J. Weis, S. Barnes, M. Miga, V. Quaranta, and T. Yankeelov. "A mechanically coupled reaction–diffusion model that incorporates intra-tumoural heterogeneity to predict in vivo glioma growth". *Journal of the Royal Society Interface* 14 (2017), p. 20161010. DOI: 10.1098/rsif.2016.1010 (cit. on pp. 27, 36).

[258] U. Hornung. *Homogenization and porous media*. Vol. 6. Springer Science & Business Media, 1997. DOI: 10.1007/978-1-4612-1920-0 (cit. on p. 153).

[259] M. Hosseini–Farid, M. Ramzanpour, J. McLean, M. Ziejewski, and G. Karami. "A poro-hyper-viscoelastic rate-dependent constitutive modeling for the analysis of brain tissues". *Journal of the Mechanical Behavior of Biomedical Materials* 102 (2020), p. 103475. DOI: 10.1016/j.jmbbm.2019.103475 (cit. on p. 77).

[260] M. Hosseini–Farid, A. Rezaei, A. Eslaminejad, M. Ramzanpour, M. Ziejewski, and G. Karami. "Instantaneous and equilibrium responses of the brain tissue by stress relaxation and quasi-linear viscoelasticity theory". *Scientia Iranica* 26.4 (2019), pp. 2047–2056. DOI: 10.24200/sci.2019.21314 (cit. on p. 79).

[261] S. Huang. "Genetic and non-genetic instability in tumor progression: Link between the fitness landscape and the epigenetic landscape of cancer cells". *Cancer metastasis reviews* 32 (2013). DOI: 10.1007/s10555-013-9435-7 (cit. on p. 135).

[262] S. Huang. "Tumor progression: Chance and necessity in Darwinian and Lamarckian somatic (mutationless) evolution". *Progress in biophysics and molecular biology* 110 (2012), pp. 69–86. DOI: 10.1016/j.pbiomolbio.2012.05.001 (cit. on p. 12).

[263] A. Hunt and C. Surulescu. "A multiscale modeling approach to glioma invasion with therapy". *Vietnam Journal of Mathematics* 45 (2016), pp. 221–240. DOI: 10.1007/s10013-016-0223-x (cit. on pp. 25, 26, 27).

[264] J. M. Huyghe, D. H. Van Campen, T. Arts, and R. M. Heethaar. "The constitutive behaviour of passive heart muscle tissue: A quasi-linear viscoelastic formulation". *Journal of Biomechanics* 24.9 (1991), pp. 841–849. DOI: 10.1016/0021-9290(91)90309-b (cit. on p. 79).

[265] K. Iarosz, F. Borges, A. Batista, M. Baptista, R. Siqueira, R. Viana, and S. Lopes. "Mathematical model of brain tumour with glia-neuron interactions and chemotherapy treatment". *Journal of Theoretical Biology* 368 (2015), pp. 113–121. DOI: 10.1016/j.jtbi.2015.01.006 (cit. on pp. 25, 27).

[266] P.-E. Jabin and R. Schram. "Selection-Mutation dynamics with spatial dependence". *Journal de Mathématiques Pures et Appliquées* 176 (2016). DOI: 10.1016/j.matpur.2023.06.001 (cit. on pp. 28, 30).

[267] R. K. Jain, R. T. Tong, and L. L. Munn. "Effect of vascular normalization by antiangiogenic therapy on interstitial hypertension, peritumor edema, and lymphatic metastasis: Insights from a mathematical model". *Cancer Research* 67.6 (2007), pp. 2729–2735. DOI: 10.1158/0008-5472.CAN-06-4102 (cit. on p. 160).

[268] S. Jannesar, B. Nadler, and C. J. Sparrey. "The transverse isotropy of spinal cord white matter under dynamic load". *Journal of Biomechanical Engineering* 138.9 (2016), p. 091004. DOI: 10.1115/1.4034171 (cit. on p. 79).

[269] S. Jbabdi, E. Mandonnet, H. Duffau, L. Capelle, K. R. Swanson, M. Pélégrini-Issac, R. Guillevin, and H. Benali. "Simulation of anisotropic growth of low-grade gliomas using diffusion tensor imaging". *Magnetic Resonance in Medicine* 54.3 (2005), pp. 616–624. DOI: 10.1002/mrm.20625 (cit. on pp. 25, 26, 35, 41, 48, 126).

[270] M. Jenkinson, C. Beckmann, T. Behrens, M. Woolrich, and S. Smith. "FSL". *NeuroImage* 62.2 (2012), pp. 782–790. DOI: 10.1016/j.neuroimage.2011.09.015 (cit. on p. 46).

[271] S. Ji, M. Ghajari, H. Mao, R. H. Kraft, M. Hajiaghamemar, M. B. Panzer, R. Willinger, M. D. Gilchrist, S. Kleiven, and J. D. Stitzel. "Use of brain biomechanical models for monitoring impact exposure in contact sports". *Annals of Biomedical Engineering* 50.11 (2022), pp. 1389–1408. DOI: 10.1007/s10439-022-02999-w (cit. on p. 77).

[272] B.-J. Jin, A. Smith, and A. Verkman. "Spatial model of convective solute transport in brain extracellular space does not support a "glymphatic" mechanism". *The Journal of General Physiology* 148 (2016). DOI: 10.1085/jgp.201611684 (cit. on pp. 63, 64).

[273] I. Jones. "Low Reynolds number flow past a porous spherical shell". *Mathematical Proceedings of the Cambridge Philosophical Society* 73 (1973), pp. 231–238. DOI: 10.1017/S0305004100047642 (cit. on p. 161).

[274] S.-L. Jui, S. Zhang, W. Xiong, F. Yu, M. Fu, and D. Wang. "Brain MRI tumor segmentation with 3D intracranial structure deformation features". *IEEE Intelligent Systems* 31.2 (2016), pp. 66–76. DOI: 10.1109/MIS.2015.93 (cit. on p. 16).

[275] M. Kalli, C. Voutouri, A. Minia, V. Pliaka, C. Fotis, L. G. Alexopoulos, and T. Stylianopoulos. "Mechanical compression regulates brain cancer cell migration through MEK1/Erk1 pathway activation and GDF15 expression". *Frontiers in Oncology* 9 (2019), p. 992. DOI: 10.3389/fonc.2019.00992 (cit. on p. 16).

[276] W. Kang, L. Wang, and Y. Fan. "Viscoelastic response of gray matter and white matter brain tissues under creep and relaxation". *Journal of Biomechanics* 162 (2024), p. 111888. DOI: 10.1016/j.jbiomech.2023.111888 (cit. on p. 15).

[277] A. Kansal, S. Torquato, I. GR, E. Chiocca, and T. Deisboeck. "Simulated brain tumor growth dynamics using a three-dimensional cellular automaton". *Journal of theoretical biology* 203 (2000), pp. 367–82. DOI: 10.1006/jtbi.2000.2000 (cit. on p. 25).

[278] A. Karimi, M. Haghighatnama, A. Shojaei, M. Navidbakhsh, A. Motevalli Haghi, and S. J. Adnani Sadati. "Measurement of the viscoelastic mechanical properties of the skin tissue under uniaxial loading". *Proceedings of the Institution of Mechanical Engineers, Part L: Journal of Materials: Design and Applications* 230.2 (2016), pp. 418–425. DOI: 10.1177/1464420715575169 (cit. on p. 79).

[279] L. Kaufman, C. Brangwynne, K. Kasza, E. Filippidi, V. Gordon, T. Deisboeck, and D. Weitz. "Glioma expansion in collagen I matrices: Analyzing collagen concentration-dependent growth and motility patterns". *Biophysical Journal* 89.1 (2005), pp. 635–650. DOI: 10.1529/biophysj.105.061994 (cit. on pp. 35, 41).

[280] O. Kedem and A. Katchalsky. "Thermodynamic analysis of the permeability of biological membranes to non-electrolytes". *Biochimica et Biophysica Acta* 27 (1958), pp. 229–246. DOI: 10.1016/0006-3002(58)90330-5 (cit. on p. 160).

[281] E. F. Keller and L. A. Segel. "Model for chemotaxis". *Journal of Theoretical Biology* 30.2 (1971), pp. 225–234. DOI: 10.1016/0022-5193(71)90050-6 (cit. on pp. 158, 159).

[282] E. Khain, M. Katakowski, S. Hopkins, A. Szalad, X. Zheng, F. Jiang, and M. Chopp. "Collective behavior of brain tumor cells: The role of hypoxia". *Physical review. E, Statistical, nonlinear, and soft matter physics* 83 (2011), p. 031920. DOI: 10.1103/PhysRevE.83.031920 (cit. on p. 25).

[283] S. Khajanchi. "Modeling the dynamics of glioma-immune surveillance". *Chaos, Solitons & Fractals* 114 (2018), pp. 108–118. DOI: 10.1016/j.chaos.2018.06.028 (cit. on pp. 31, 104).

[284] S. Khajanchi and J. Nieto. "Spatiotemporal dynamics of a glioma immune interaction model". *Scientific Reports* 11 (2021), p. 22385. DOI: 10.1038/s41598-021-00985-1 (cit. on pp. 31, 104, 107).

[285] E. Khan, M. Lane, and O. Sagher. "Eloquent: history of a word's adoption into the neurosurgical lexicon". *Journal of Neurosurgery* 127 (6 2017), pp. 1461–1466. DOI: 10.3171/2017.3.JNS17659 (cit. on p. 19).

[286] J.-w. Kim and C. V. Dang. "Cancer's molecular sweet tooth and the Warburg effect." *Cancer research* 66 18 (2006), pp. 8927–30. DOI: 10.1158/0008-5472.CAN-06-1501 (cit. on p. 146).

[287] M. M. Kim, Y. Umemura, and D. Leung. "Bevacizumab and Glioblastoma: Past, present, and future directions". *The Cancer Journal* 24.4 (2018), pp. 180–186. DOI: 10.1097/ppo.0000000000000326 (cit. on p. 19).

[288] P. Kim and P. Lee. "Modeling protective anti-tumor immunity via preventative cancer vaccines using a hybrid agent-based and delay differential equation approach". *PLoS computational biology* 8 (2012), e1002742. DOI: 10.1371/journal.pcbi.1002742 (cit. on p. 31).

[289] Y. Kim, H. Jeon, and H. Othmer. "The role of the tumor microenvironment in glioblastoma: A mathematical model". *IEEE Transactions on Biomedical Engineering* 64 (2017), pp. 519–527. DOI: 10.1109/TBME.2016.2637828 (cit. on p. 25).

[290] Y. Kim, H. Kang, G. Powathil, H. Kim, D. Trucu, W. Lee, S. Lawler, and M. Chaplain. "Role of extracellular matrix and microenvironment in regulation of tumor growth and LAR-mediated invasion in glioblastoma". *PLOS ONE* 13 (2018), pp. 1–40. DOI: 10.1371/journal.pone.0204865 (cit. on p. 25).

[291] Y. Kim, G. Powathil, H. Kang, D. Trucu, H. Kim, S. Lawler, and M. Chaplain. "Strategies of eradicating glioma cells: A multi-scale mathematical model with MiR-451-AMPK-mTOR control". *PLOS ONE* 10 (2015), pp. 1–30. DOI: 10.1371/journal.pone.0114370 (cit. on p. 25).

[292] D. Kirschner, T. Jackson, and J. Arciero. "A mathematical model of tumour-immune evasion and siRNA treatment". *Discrete and Continuous Dynamical Systems-series B* 4 (2003), pp. 39–58. DOI: 10.3934/dcdsb.2004.4.39 (cit. on p. 31).

[293] D. Kirschner and J. Panetta. "Modeling immunotherapy of the tumor - Immune interaction". *Journal of mathematical biology* 37 (1998), pp. 235–52. DOI: 10.1007/s002850050127 (cit. on pp. 31, 103).

[294] T. Koch, K. Heck, N. Schröder, H. Class, and R. Helmig. "A new simulation framework for soil–root interaction, evaporation, root growth, and solute transport". *Vadose zone journal* 17.1 (2018), pp. 1–21. DOI: 10.2136/vzj2017.12.0210 (cit. on p. 154).

[295] K. Kono, Y. Inoue, K. Nakayama, M. Shakudo, M. Morino, K. Ohata, K. Wakasa, and R. Yamada. "The role of diffusion-weighted imaging in patients with brain tumors". *American Journal of Neuroradiology* 22.6 (2001), pp. 1081–1088 (cit. on p. 47).

[296] A. Konstorum, A. Vella, A. Adler, and R. Laubenbacher. "Addressing current challenges in cancer immunotherapy with mathematical and computational modeling". *Journal of The Royal Society Interface* 14 (2017). DOI: 10.1098/rsif.2017.0150 (cit. on pp. 31, 103).

[297] A. Kowald, J. Passos, and T. Kirkwood. "On the evolution of cellular senescence". *Aging Cell* 19 (2020). DOI: 10.1111/acel.13270 (cit. on p. 13).

[298] N. Kronik, Y. Kogan, V. Vainstein, and Z. Agur. "Improving alloreactive CTL immunotherapy for malignant gliomas using a simulation model of their interactive dynamics". *Cancer immunology, immunotherapy : CII* 57 (2008), pp. 425–39. DOI: 10.1007/s00262-007-0387-z (cit. on pp. 31, 104).

[299] W. Krumbein. "Measurement and geological significance of shape and roundness of sedimentary particles". *Journal of Sedimentary Research* 11.2 (1941), pp. 64–72. DOI: 10.1306/D42690F3-2B26-11D7-8648000102C1865D (cit. on p. 67).

[300] L. Kumosa, T. Routh, J. Lin, J. Lucisano, and D. Gough. "Permeability of subcutaneous tissues surrounding long-term implants to oxygen". *Biomaterials* 35 (2014). DOI: 10.1016/j.biomaterials.2014.05.012 (cit. on p. 145).

[301] P. Kunkel, U. Ulbricht, P. Bohlen, M. Brockmann, R. Fillbrandt, D. Stavrou, M. Westphal, and K. Lamszus. "Inhibition of glioma angiogenesis and growth in vivo by systemic treatment with a monoclonal antibody against vascular endothelial growth factor receptor-2". *Cancer research* 61 (2001), pp. 6624–8. DOI: 10.1158/1078-0432.CCR-04-2270 (cit. on p. 19).

[302] V. Kuznetsov, I. Makalkin, M. Taylor, and A. Perelson. "Nonlinear dynamics of immunogenic tumors: Parameter estimation and global bifurcation analysis". *Bulletin of mathematical biology* 56 (1994), pp. 295–321. DOI: 10.1007/BF02460644 (cit. on pp. 31, 103).

[303] S. Kyriacou, C. Davatzikos, S. Zinreich, and R. Bryan. "Nonlinear elastic registration of brain images with tumor pathology using a biomechanical model". *IEEE Transactions on Medical Imaging* 18 (1999), pp. 580–592. DOI: 10.1109/42.790458 (cit. on p. 25).

[304] S. Kyriacou, A. Mohamed, K. Miller, and S. Neff. "Brain mechanics for neurosurgery: Modeling issues". *Biomechanics and modeling in mechanobiology* 1 (2002), pp. 151–64. DOI: 10.1007/s10237-002-0013-0 (cit. on p. 16).

[305] K. Lamszus, P. Kunkel, and M. Westphal. "Invasion as limitation to anti-angiogenic glioma therapy". *Acta neurochirurgica. Supplement* 88 (2003), pp. 169–77. DOI: 10.1007/978-3-7091-6090-9_23 (cit. on p. 19).

[306] K.-J. Langen, N. Galldiks, E. Hattingen, and N. Shah. "Advances in neuro-oncology imaging". *Nature reviews. Neurology* 13 (2017). DOI: 10.1038/nrneurol.2017.44 (cit. on p. 22).

[307] A. Lattanzi, X. Yin, and C. Hrenya. "A fully-developed boundary condition for the random walk particle tracking method". *International Journal of Heat and Mass Transfer* 131 (2019), pp. 604–610. DOI: 10.1016/j.ijheatmasstransfer.2018.11.062 (cit. on p. 55).

[308] O. Lavi, J. Greene, D. Levy, and M. Gottesman. "The role of cell density and intratumoral heterogeneity in multidrug resistance". *Cancer research* 73 (2013). DOI: 10.1158/0008-5472.CAN-13-1768 (cit. on p. 29).

[309] T. Lazebnik, S. Yanetz, and S. Bunimovich-Mendrazitsky. "PDE modeling of bladder cancer treatment using BCG immunotherapy". In: 2022, pp. 119–129. DOI: 10.1007/978-981-16-6297-3_9 (cit. on pp. 31, 103).

[310] D. Le Bihan and M. Iima. "Diffusion Magnetic Resonance Imaging: What water tells us about biological tissues". *PLOS Biology* 13.7 (2015), pp. 1–13. DOI: 10.1371/journal.pbio.1002203 (cit. on pp. 62, 64).

[311] S. Lee and C. Schmitt. "The dynamic nature of senescence in cancer". *Nature Cell Biology* 21 (2019). DOI: 10.1038/s41556-018-0249-2 (cit. on p. 13).

[312] W. Lee, S. D. Lee, M. Y. Park, L. Foley, E. Purcell–Estabrook, H. Kim, and S. S. Yoo. "Functional and diffusion tensor magnetic resonance imaging of the sheep brain". *BMC Veterinary Research* 11 (2015), pp. 1–8. DOI: 10.1186/s12917-015-0581-8 (cit. on p. 102).

[313] J. Less, T. Skalak, E. Sevick, and R. Jain. "Microvascular architecture in a mammary carcinoma: branching patterns and vessel dimensions". *Cancer Research* 15.1 (1991), pp. 265–273 (cit. on p. 157).

[314] K. Letendre, E. Donnadieu, M. Moses, and J. Cannon. "Bringing statistics up to speed with data in analysis of lymphocyte motility". *PloS one* 10 (2015), e0126333. DOI: 10.1371/journal.pone.0126333 (cit. on p. 119).

[315] T. Lewin, P. Maini, E. Moros, H. Enderling, and H. Byrne. "The evolution of tumour composition during fractionated radiotherapy: Implications for outcome". *Bulletin of Mathematical Biology* 80 (2018). DOI: 10.1007/s11538-018-0391-9 (cit. on pp. 151, 185).

[316] M. V. Liberti and J. W. Locasale. "The Warburg effect: How does it benefit cancer cells?" *Trends in Biochemical Sciences* 41.3 (2016), pp. 211–218. DOI: https://doi.org/10.1016/j.tibs.2015.12.001 (cit. on p. 146).

[317] R. Lilley, A. Reynaud, P. D. Docherty, N. Smith, and N. Kabaliuk. "Rheological experimentation to investigate history dependent viscoelastic properties of *ex-vivo* ovine brain tissue". *IFAC-PapersOnLine* 53.2 (2020), pp. 16275–16280. DOI: 10.1016/j.ifacol.2020.12.623 (cit. on p. 102).

[318] L. Liotta, G. Saidel, and J. Kleinerman. "Diffusion model of tumor vascularization". *Bulletin of Mathematical Biology* 39 (1977), pp. 117–128. DOI: 10.1007/BF02463043 (cit. on p. 32).

[319] J. Lipkova, B. Menze, B. Wiestler, P. Koumoutsakos, and J. Lowengrub. "Modeling glioma progression, mass-effect, and intracranial pressure in patient anatomy". *Journal of The Royal Society Interface* 19 (2022). DOI: 10.1098/rsif.2021.0922 (cit. on p. 25).

[320] J. Lipková et al. "Personalized radiotherapy design for Glioblastoma: Integrating mathematical tumor models, multimodal scans, and bayesian inference". *IEEE Transactions on Medical Imaging* 38.8 (2019), pp. 1875–1884. DOI: 10.1109/TMI.2019.2902044 (cit. on p. 75).

[321] J. Liu, D. Hormuth II, T. Davis, J. Yang, M. McKenna, A. Jarrett, H. Enderling, A. Brock, and T. Yankeelov. "A time resolved experimental-mathematical model for predicting the response of glioma cells to single-dose radiation therapy". *Integrative Biology* 13.7 (2021), pp. 167–183. DOI: 10.1093/intbio/zyab010 (cit. on p. 27).

[322] M. C. Lloyd, J. J. Cunningham, M. M. Bui, R. J. Gillies, J. S. Brown, and R. A. Gatenby. "Darwinian dynamics of intratumoral heterogeneity: Not solely random mutations but also variable environmental selection forces". *Cancer Research* 76.11 (2016), pp. 3136–3144. DOI: 10.1158/0008-5472.CAN-15-2962 (cit. on p. 149).

[323] R. Löber-Handwerker, K. Döring, C. Bock, V. Rohde, and V. Malinova. "Defining the impact of adjuvant treatment on the prognosis of patients with inoperable glioblastoma undergoing biopsy-only: Does the survival benefit outweigh the treatment effort?" *Neurosurgical Review* 45 (2022), pp. 2339–2347. DOI: 10.21203/rs.3.rs-1167838/v1 (cit. on pp. 16, 19).

[324] A. Logg, K. Mardal, and G. Wells. *Automated solution of differential equations by the Finite Element Method*. Springer, 2012 (cit. on pp. 63, 95).

[325] T. Lorenzi, F. Macfarlane, and C. Villa. "Discrete and continuum models for the evolutionary and spatial dynamics of cancer: A very short introduction through two case studies". In: 2020, pp. 359–380. DOI: 10.1007/978-3-030-46306-9_22 (cit. on p. 29).

[326] T. Lorenzi, R. Chisholm, and J. Clairambault. "Tracking the evolution of cancer cell populations through the mathematical lens of phenotype-structured equations". *Biology Direct* 11 (2016), p. 43. DOI: 10.1186/s13062-016-0143-4 (cit. on p. 29).

[327] T. Lorenzi, R. Chisholm, L. Desvillettes, and B. Hughes. "Dissecting the dynamics of epigenetic changes in phenotype-structured populations exposed to fluctuating environments". *Journal of theoretical biology* 386 (2015). DOI: 10.1016/j.jtbi.2015.08.031 (cit. on p. 29).

[328] T. Lorenzi and K. Painter. "Trade-offs between chemotaxis and proliferation shape the phenotypic structuring of invading waves". *International Journal of Non-Linear Mechanics* (2021). DOI: 10.1016/j.ijnonlinmec.2021.103885 (cit. on p. 133).

[329] T. Lorenzi, B. Perthame, and X. Ruan. "Invasion fronts and adaptive dynamics in a model for the growth of cell populations with heterogeneous mobility". *European Journal of Applied Mathematics* 33 (2021), pp. 1–18. DOI: 10.1017/S0956792521000218 (cit. on pp. 30, 133).

[330] T. Lorenzi, C. Venkataraman, A. Lorz, and M. Chaplain. "The role of spatial variations of abiotic factors in mediating intratumour phenotypic heterogeneity". *Journal of Theoretical Biology* 451 (2018), pp. 101–110. DOI: 10.1016/j.jtbi.2018.05.002 (cit. on pp. 30, 133, 145).

[331] A. Lorz, T. Lorenzi, J. Clairambault, A. Escargueil, and B. Perthame. "Modeling the effects of space structure and combination therapies on phenotypic heterogeneity and drug resistance in solid tumors". *Bulletin of mathematical biology* 77 (2015). DOI: 10.1007/s11538-014-0046-4 (cit. on p. 30).

[332] A. Lorz, T. Lorenzi, M. Hochberg, J. Clairambault, and B. Perthame. "Populational adaptive evolution, chemotherapeutic resistance and multiple anti-cancer therapies". *ESAIM Mathematical Modelling and Numerical Analysis* 47 (2012). DOI: 10.1051/m2an/2012031 (cit. on p. 29).

[333] A. Lorz, S. Mirrahimi, and B. Perthame. "Dirac mass dynamics in multidimensional nonlocal parabolic equations". *Communications in Partial Differential Equations* 36 (2010). DOI: 10.1080/03605302.2010.538784 (cit. on p. 28).

[334] E. Lou et al. "Phase II trial of upfront bevacizumab and temozolomide for unresectable or multifocal glioblastoma". *Cancer Medicine* 2.2 (2013), pp. 185–195. DOI: https://doi.org/10.1002/cam4.58 (cit. on p. 19).

[335] D. Louis et al. "The 2021 WHO classification of tumors of the central nervous system: A summary". *Neuro-Oncology* 23 (2021). DOI: 10.1093/neuonc/noab106 (cit. on pp. 13, 14).

[336] S. W. Lowe, E. Cepero, and G. Evan. "Intrinsic tumour suppression". *Nature* 432.7015 (2004), pp. 307–315. DOI: 10.1038/nature03098 (cit. on p. 11).

[337] V. Lubarda. "Constitutive theories based on the multiplicative decomposition of deformation gradient: Thermoelasticity, elastoplasticity, and biomechanics". *Applied Mechanics Reviews* 57 (2004). DOI: 10.1115/1.1591000 (cit. on p. 27).

[338] G. Lucci, A. Agosti, P. Ciarletta, and C. Giverso. "Coupling solid and fluid stresses with brain tumour growth and white matter tract deformations in a neuroimaging-informed model". *Biomech. Model. Mechanobiol.* 21 (2022), pp. 1483–1509. DOI: 10.1007/s10237-022-01602-4 (cit. on pp. 25, 27, 28, 35, 36, 41, 42, 47, 48, 49, 61, 62, 64, 65, 69, 151, 159).

[339] D. Łydżba. "Micromechanical analysis of saturated porous media with local mass exchange phenomenon". In: *Applied Micromechanics of Porous Materials*. Springer, 2005, pp. 57–81. DOI: 10.1007/3-211-38046-9_2 (cit. on p. 153).

[340] J. MacLaurin, J. Chapman, G. Jones, and T. Roose. "The buckling of capillaries in solid tumours". *Proceedings of the Royal Society A* 468 (2012), pp. 4123–4145. DOI: 10.1098/rspa.2012.0418 (cit. on p. 27).

[341] D. B. MacManus, M. Maillet, S. O'Gorman, B. Pierrat, J. G. Murphy, and M. D. Gilchrist. "Sex-and age-specific mechanical properties of liver tissue under dynamic loading conditions". *Journal of the Mechanical Behavior of Biomedical Materials* 99 (2019), pp. 240–246. DOI: 10.1016/j.jmbbm.2019.07.028 (cit. on p. 79).

[342] D. B. MacManus, B. Pierrat, J. G. Murphy, and M. D. Gilchrist. "Region and species dependent mechanical properties of adolescent and young adult brain tissue". *Scientific Reports* 7.1 (2017), p. 13729. DOI: 10.1038/s41598-017-13727-z (cit. on p. 77).

[343] S. Madhusoodanan, M. Ting, T. Farah, and U. Ugur. "Psychiatric aspects of brain tumors: A review". *World Journal of Psychiatry* 5 (2015), pp. 273–285. DOI: 10.5498/wjp.v5.i3.273 (cit. on p. 16).

[344] K. Mahasa, R. Ouifki, A. Eladdadi, and L. Depillis. "Mathematical model of tumor-immune surveillance". *Journal of Theoretical Biology* 404 (2016). DOI: 10.1016/j.jtbi.2016.06.012 (cit. on p. 31).

[345] A. W. Mahdiyasa, D. J. Large, M. Icardi, and B. P. Muljadi. "MPeat2D–A fully coupled mechanical-ecohydrological model of peatland development in two dimensions". *EGUsphere* 2023 (2023), pp. 1–31. DOI: 10.5194/esurf-12-929-2024 (cit. on pp. 154, 181).

[346] A. Mansour, A. Trefi, M. Mansour, A. Shekho, and S. Salloum. "The complexities of treating brain and spinal cord tumors: a review of current approaches". *Annals of Medicine & Surgery* 85 (2023). DOI: 10.1097/MS9.0000000000001213 (cit. on p. 18).

[347] Y. Mansury and T. Deisboeck. "The impact of "search precision" in an agent-based tumor model". *Journal of Theoretical Biology* 224 (2003), pp. 325–37. DOI: 10.1016/S0022-5193(03)00169-3 (cit. on p. 25).

[348] Y. Mansury, T. Deisboeck, and E. Micheli-Tzanakou. "Modeling tumors as complex biosystems: An agent-based approach". In: 2006, pp. 573–602. DOI: 10.1007/978-0-387-33532-2_25 (cit. on p. 25).

[349] Y. Mansury, M. Kimura, J. Lobo, and T. Deisboeck. "Emerging patterns in tumor systems: Simulating the dynamics of multicellular clusters with an agent-based spatial agglomeration model". *Journal of Theoretical Biology* 219 (2002), pp. 343–370. DOI: 10.1006/jtbi.2002.3131 (cit. on p. 25).

[350] H. Marcus, V. Vakharia, S. Ourselin, J. Duncan, M. Tisdall, and K. Aquilina. "Robot-assisted stereotactic brain biopsy: Systematic review and bibliometric analysis". *Child's Nervous System* 34 (2018), pp. 1–11. DOI: 10.1007/s00381-018-3821-y (cit. on p. 18).

[351] S. Marino, I. Hogue, C. Ray, and D. Kirschner. "A methodology for performing global uncertainty and sensitivity analysis in systems biology". *Journal of Theoretical Biology* 254 (2008), pp. 178–196. DOI: 10.1016/j.jtbi.2008.04.011 (cit. on p. 120).

[352] A. Martínez-González, G. Calvo, L. Pérez Romasanta, and V. Pérez-García. "Hypoxic cell waves around necrotic cores in glioblastoma: A biomathematical model and its therapeutic implications". *Bulletin of mathematical biology* 74 (2012). DOI: 10.1007/s11538-012-9786-1 (cit. on p. 16).

[353] A. Marusyk, V. Almendro, and K. Polyak. "Intra-tumour heterogeneity: a looking glass for cancer?" *Nature reviews. Cancer* 12 (2012), pp. 323–34. DOI: 10.1038/nrc3261 (cit. on p. 133).

[354] P. Mascheroni, M. Carfagna, A. Grillo, D. Boso, and B. Schrefler. "An avascular tumor growth model based on porous media mechanics and evolving natural states". *Mathematics and Mechanics of Solids* 23.4 (2018), pp. 686–712. DOI: 10.1177/1081286517711217 (cit. on pp. 27, 41).

[355] P. Mascheroni, R. Penta, and J. Merodio. "The impact of vascular volume fraction and compressibility of the interstitial matrix on vascularised poroelastic tissues". *Biomechanics and Modeling in Mechanobiology* 22.6 (2023), pp. 1901–1917. DOI: 10.21203/rs.3.rs-2773443/v1 (cit. on p. 76).

[356] P. Mascheroni, S. Savvopoulos, J. C. L. Alfonso, M. Meyer-Hermann, and H. Hatzikirou. "Improving personalized tumor growth predictions using a Bayesian combination of mechanistic modeling and machine learning". *Communications medicine* 1.1 (2021), p. 19. DOI: 10.1038/s43856-021-00020-4 (cit. on p. 182).

[357] P. Mascheroni, C. Stigliano, M. Carfagna, D. Boso, L. Preziosi, P. Decuzzi, and B. Schrefler. "Predicting the growth of glioblastoma multiforme spheroids using a multiphase porous media model". *Biomechanics and Modeling in Mechanobiology* 15 (2016), pp. 1215–1228. DOI: 10.1007/s10237-015-0755-0 (cit. on pp. 25, 27, 42, 63).

[358] A. Matzavinos, M. Chaplain, and V. Kuznetsov. "Mathematical modelling of the spatio-temporal response of cytotoxic T-lymphocytes to a solid tumour". *Mathematical medicine and biology : a journal of the IMA* 21 (2004), pp. 1–34 (cit. on pp. 31, 107).

[359] S. R. McDougall, A. R. A. Anderson, M. A. J. Chaplain, and J. A. Sherratt. "Mathematical modelling of flow through vascular networks: Implications for tumour-induced angiogenesis and chemotherapy strategies". *Bulletin of Mathematical Biology* 64.4 (2002), pp. 673–702. DOI: 10.1006/bulm.2002.0293 (cit. on p. 32).

[360] C. C. Mei and B. Vernescu. *Homogenization methods for multiscale mechanics*. Singapore: World scientific, 2010. DOI: 10.1142/7427 (cit. on pp. 153, 155).

[361] A. Menichetti, D. B. MacManus, M. D. Gilchrist, B. Depreitere, J. Vander Sloten, and N. Famaey. "Regional characterization of the dynamic mechanical properties of human brain tissue by microindentation". *International Journal of Engineering Science* 155 (2020), p. 103355. DOI: 10.1016/j.ijengsci.2020.103355 (cit. on p. 77).

[362] L. Mihai, S. Budday, G. Holzapfel, E. Kuhl, and A. Goriely. "A family of hyperelastic models for human brain tissue". *Journal of the Mechanics and Physics of Solids* 106 (2017), pp. 60–79. DOI: 10.1016/j.jmps.2017.05.015 (cit. on p. 40).

[363] F. Milde, M. Bergdorf, and P. Koumoutsakos. "A hybrid model for three-dimensional simulations of sprouting angiogenesis". *Biophysical Journal* 95 (2008), pp. 3146–3160. DOI: 10.1529/biophysj.108.134932 (cit. on p. 32).

[364] K. Miller. "Constitutive model of brain tissue suitable for finite element analysis of surgical procedures". *Journal of Biomechanics* 32.5 (1999), pp. 531–537. DOI: 10.1016/S0021-9290(99)00010-X (cit. on p. 15).

[365] K. Miller and K. Chinzei. "Constitutive modelling of brain tissue: Experiment and theory". *Journal of Biomechanics* 30.11 (1997), pp. 1115–1121. DOI: 10.1016/S0021-9290(97)00092-4 (cit. on p. 15).

[366] K. Miller, K. Chinzei, G. Orssengo, and P. Bednarz. "Mechanical properties of brain tissue in-vivo: experiment and computer simulation". *Journal of Biomechanics* 33.11 (2000), pp. 1369–1376. DOI: 10.1016/S0021-9290(00)00120-2 (cit. on p. 15).

[367] L. Miller and R. Penta. "Investigating the effects of microstructural changes induced by myocardial infarction on the elastic parameters of the heart". *Biomechanics and Modeling in Mechanobiology* 22.3 (2023), pp. 1019–1033. DOI: 10.1007/s10237-023-01698-2 (cit. on p. 153).

[368] Y. Miroshnikova et al. "Tissue mechanics promote IDH1-dependent HIF1 α - tenascin C feedback to regulate glioblastoma aggression". *Nature Cell Biology* 18 (2016). DOI: 10.1038/ncb3429 (cit. on pp. 61, 64).

[369] S. Mirrahimi and B. Perthame. "Asymptotic analysis of a selection model with space". *Journal de Mathématiques Pures et Appliquées* 104 (2015). DOI: 10.1016/j.matpur.2015.07.006 (cit. on p. 30).

[370] S. Mischler, L. Desvillettes, P.-E. Jabin, and G. Raoul. "On selection dynamics for continuous structured populations". *Communications in mathematical sciences* 6 (2008). DOI: 10.4310/CMS.2008.v6.n3.a10 (cit. on p. 28).

[371] M. Mooney. "A theory of large elastic deformation". *Journal of Applied Physics* 11.9 (1940), pp. 582–592. DOI: 10.1063/1.1712836 (cit. on p. 89).

[372] O. Morrison, M. Destrade, and B. B. Tripathi. "An atlas of the heterogeneous viscoelastic brain with local power-law attenuation synthesised using Prony-series". *Acta Biomaterialia* 169 (2023), pp. 66–87. DOI: 10.1016/j.actbio.2023.07.040 (cit. on p. 89).

[373] H. Motallebzadeh, M. Charlebois, and W. R. J. Funnell. "A non-linear viscoelastic model for the tympanic membrane". *The Journal of the Acoustical Society of America* 134.6 (2013), pp. 4427–4434. DOI: 10.1121/1.4828831 (cit. on p. 79).

[374] C. T. Motz, V. Kabat, T. Saxena, R. V. Bellamkonda, and C. Zhu. "Neuromechanobiology: An expanding field driven by the force of greater focus". *Advanced Healthcare Materials* 19.10 (2021), e2100102. DOI: 10.1002/adhm.202100102 (cit. on p. 16).

[375] E. Nader et al. "Blood rheology: Key parameters, impact on blood flow, role in sickle cell disease and effects of exercise". *Frontiers in physiology* 10 (2019), p. 1329 (cit. on p. 159).

[376] S. P. A. Narayan, J. M. Krishnan, A. P. Deshpande, and K. R. Rajagopal. "Nonlinear viscoelastic response of asphalt binders: An experimental study of the relaxation of torque and normal force in torsion". *Mechanics Research Communications* 43 (2012), pp. 66–74. DOI: 10.1016/j.mechrescom.2012.02.012 (cit. on pp. 78, 85, 86).

[377] S. Nasseri, L. E. Bilston, and N. Phan–Thien. "Viscoelastic properties of pig kidney in shear, experimental results and modelling". *Rheologica Acta* 41.1 (2002), pp. 180–192. DOI: 10.1007/s003970200017 (cit. on p. 79).

[378] O. Nave. "A mathematical model for treatment using chemo-immunotherapy". *Heliyon* 8 (2022), e09288. DOI: 10.1016/j.heliyon.2022.e09288 (cit. on p. 31).

[379] M. L. Neal et al. "Discriminating survival outcomes in patients with Glioblastoma using a simulation-based, patient-specific response metric". *PLOS ONE* 8.1 (2013), pp. 1–7. DOI: 10.1371/journal.pone.0051951 (cit. on p. 75).

[380] H. Nia, M. Datta, G. Seano, S. Zhang, W. Ho, S. Roberge, and P. Huang. "In vivo compression and imaging in mouse brain to measure the effects of solid stress". *Nature Protocols* 15.8 (2020), pp. 2321–2340. DOI: 10.1038/s41596-020-0328-2 (cit. on p. 27).

[381] H. Nia et al. "Solid stress and elastic energy as measures of tumour mechanopathology". *Nature Biomedical Engineering* 1 (2017). DOI: 10.1038/s41551-016-0004 (cit. on pp. 27, 61, 69).

[382] R. D. O'Dea, M. Nelson, A. El Haj, S. L. Waters, and H. M. Byrne. "A multiscale analysis of nutrient transport and biological tissue growth in vitro". *Mathematical Medicine and Biology: A Journal of the IMA* 32.3 (2015), pp. 345–366. DOI: 10.1093/imammb/dqu015 (cit. on p. 153).

[383] R. W. Ogden. *Non-Linear Elastic Deformations*. Dover Publications, 1997 (cit. on pp. 89, 90).

[384] R. Ogden and R. Hill. "Large deformation isotropic elasticity - on the correlation of theory and experiment for incompressible rubberlike solids". *Proceedings of the Royal Society A* 326.1567 (1972), pp. 565–584. DOI: 10.1098/rspa.1972.0026 (cit. on p. 39).

[385] K. Onwudiwe, J. Najera, S. Siri, and M. Datta. "Do tumor mechanical stresses promote cancer immune escape?" *Cells* 11.23 (2022), p. 3840. DOI: 10.3390/cells11233840 (cit. on p. 16).

[386] M. Orme and M. Chaplain. "A mathematical model of the first steps of tumour related angiogenesis: capillary sprout formation and secondary branching". *IMA Journal of Mathematics Applied in Medicine and Biology* 13 (1996), pp. 73–98. DOI: 10.1093/imammb/13.2.73 (cit. on p. 32).

[387] A. Padhani and L. Ollivier. "The RECIST criteria: implications for diagnostic radiologists". *The British Journal of Radiology* 74 (2001), pp. 983–986. DOI: 10.1259/bjr.74.887.740983 (cit. on p. 74).

[388] K. Painter and T. Hillen. "Mathematical modelling of glioma growth: The use of Diffusion Tensor Imaging (DTI) data to predict the anisotropic pathways of cancer invasion". *Journal of Theoretical Biology* 323 (2013), pp. 25–39. DOI: 10.1016/j.jtbi.2013.01.014 (cit. on pp. 25, 26).

[389] A. Palladini et al. "In silico modeling and in vivo efficacy of cancer-preventive vaccinations". *Cancer research* 70 (2010), pp. 7755–63. DOI: 10.1158/0008-5472.CAN-10-0701 (cit. on p. 31).

[390] G. Palmieri et al. "Fluorescence-guided surgery for high-grade gliomas: State of the art and new perspectives". *Technology in cancer research & treatment* 20 (2021), p. 15330338211021605. DOI: 10.1177/15330338211021605 (cit. on p. 18).

[391] G. Papanicolau, A. Bensoussan, and J.-L. Lions. *Asymptotic analysis for periodic structures*. Elsevier, 1978 (cit. on pp. 153, 155).

[392] F. Pappalardo, P.-L. Lollini, F. Castiglione, and S. Motta. "Modeling and simulation of cancer immunoprevention vaccine". *Bioinformatics* 21.12 (2005), pp. 2891–2897. DOI: 10.1093/bioinformatics/bti426 (cit. on p. 31).

[393] *ParaView*. URL: https://www.paraview.org/ (cit. on p. 99).

[394] O. Pasternak, N. Sochen, Y. Gur, N. Intrator, and Y. Assaf. "Free water elimination and mapping from diffusion MRI". *Magnetic Resonance in Medicine* 62.3 (2009), pp. 717–730. DOI: 10.1002/mrm.22055 (cit. on p. 46).

[395] I. Peña-Pino and C. Chen. "Stereotactic radiosurgery as treatment for brain metastases: An update". *Asian Journal of Neurosurgery* 18 (2023). DOI: 10.1055/s-0043-1769754 (cit. on p. 18).

[396] R. Penta, K. Raum, Q. Grimal, S. Schrof, and A. Gerisch. "Can a continuous mineral foam explain the stiffening of aged bone tissue? A micromechanical approach to mineral fusion in musculoskeletal tissues". *Bioinspiration & biomimetics* 11.3 (2016), p. 035004. DOI: 10.1088/1748-3190/11/3/035004 (cit. on p. 153).

[397] R. Penta, D. Ambrosi, and A. Quarteroni. "Multiscale homogenization for fluid and drug transport in vascularized malignant tissues". *Mathematical Models and Methods in Applied Sciences* 25 (2014), pp. 79–108. DOI: 10.1142/S0218202515500037 (cit. on pp. 32, 153, 156, 159, 160, 161, 162, 163).

[398] R. Penta and A. Gerisch. "An introduction to asymptotic homogenization". In: *Multiscale models in mechano and tumor biology: Modeling, homogenization, and applications*. Springer. 2017, pp. 1–26. DOI: 10.1007/978-3-319-73371-5_1 (cit. on pp. 153, 155).

[399] R. Penta and J. Merodio. "Homogenized modeling for vascularized poroelastic materials". *Meccanica* 52 (2017). DOI: 10.1007/s11012-017-0625-1 (cit. on pp. 153, 156, 161, 162, 163, 182, 185).

[400] R. Penta, A. Ramírez-Torres, J. Merodio, and R. Rodríguez-Ramos. "Effective governing equations for heterogenous porous media subject to inhomogeneous body forces". *Mathematics in Engineering* 3.4 (2021), pp. 1–17. DOI: 10.3934/mine.2021033PreviousArticleNextArticle (cit. on p. 156).

[401] K. Perktold, M. Prosi, and P. Zunino. "Mathematical models of mass transfer in the vascular walls". In: *Cardiovascular mathematics: Modeling and simulation of the circulatory system*. Ed. by L. Formaggia, A. Quarteroni, and A. Veneziani. Springer Milan, 2009, pp. 243–278. DOI: 10.1007/978-88-470-1152-6_7 (cit. on p. 160).

[402] B. Perthame. *Transport Equations in Biology*. Frontiers in Mathematics. Birkhäuser Basel, 2006. DOI: 10.1007/978-3-7643-7842-4 (cit. on pp. 28, 158).

[403] B. Perthame and G. Barles. "Dirac concentrations in Lotka-Volterra parabolic PDEs". *Indiana University Mathematics Journal* 57 (2007). DOI: 10.1512/iumj.2008.57.3398 (cit. on pp. 28, 136).

[404] G. J. Pettet, C. P. Please, M. J. Tindall, and D. L. S. McElwain. "The migration of cells in multicell tumor spheroids". *Bulletin of Mathematical Biology* 63.2 (2001), pp. 231–257. DOI: 10.1007/BF02459487 (cit. on p. 144).

[405] S. Pinheiro, F. Bueno Lemos, H. Marques, M. Luz, L. Silva, C. Santos, K. Evangelista, M. Calmon, M. Loureiro, and F. Melo. "Immunotherapy in glioblastoma treatment: Current state and future prospects". *World Journal of Clinical Oncology* 14 (2023), pp. 138–159. DOI: 10.5306/wjco.v14.i4.138 (cit. on pp. 19, 103, 116).

[406] M. Piotrowska, M. Bodnar, and U. Foryś. "Tractable model of malignant gliomas immunotherapy with discrete time delays". *Mathematical Population Studies* 21 (2014). DOI: 10.1080/08898480.2013.804690 (cit. on p. 31).

[407] M. Pless and U. Weinberg. "Tumor treating fields: Concept, evidence and future". *Expert opinion on investigational drugs* 20 (2011), pp. 1099–106. DOI: 10.1517/13543784.2011.583236 (cit. on p. 19).

[408] K. Polyak and R. Weinberg. "Transitions between epithelial and mesenchymal states: Acquisition of malignant and stem cell traits". *Nature reviews. Cancer* 9 (2009), pp. 265–73. DOI: 10.1038/nrc2620 (cit. on p. 12).

[409] C. Pouchol, J. Clairambault, A. Lorz, and E. Trélat. "Asymptotic analysis and optimal control of an integro-differential system modelling healthy and cancer cells exposed to chemotherapy". *Journal de Mathématiques Pures et Appliquées* 116 (2016). DOI: 10.1016/j.matpur.2017.10.007 (cit. on p. 29).

[410] G. Powathil, M. Kohandel, S. Sivaloganathan, A. Oza, and M. Milosevic. "Mathematical modeling of brain tumors: effects of radiotherapy and chemotherapy". *Physics in Medicine & Biology* 52.11 (2007), pp. 3291–3306. DOI: 10.1088/0031-9155/52/11/023 (cit. on pp. 27, 43, 62, 64).

[411] J. H. Poynting. "On pressure perpendicular to the shear planes in finite pure shears, and on the lengthening of loaded wires when twisted". *Proceedings of the Royal Society of London. Series A, Containing Papers of a Mathematical and Physical Character* 82.557 (1909), pp. 546–559. DOI: 10.1098/rspa.1909.0059 (cit. on p. 78).

[412] M. Preul, Y. Kuang, E. Kostelich, W. Ramey, E. Rutter, and N. Martirosyan. "Mathematically modeling the biological properties of gliomas: A review". *Mathematical Biosciences and Engineering* 12 (2015), pp. 879–905. DOI: 10.3934/mbe.2015.12.879 (cit. on p. 24).

[413] T. Prevost, A. Balakrishnan, S. Suresh, and S. Socrate. "Biomechanics of brain tissue". *Acta Biomaterialia* 7.1 (2011), pp. 83–95. DOI: 10.1016/j.actbio.2010.06.035 (cit. on pp. 61, 64).

[414] L. Preziosi and A. Tosin. "Multiphase and multiscale trends in cancer modelling". *Mathematical Modelling of Natural Phenomena* 4 (2009), pp. 1–11. DOI: 10.1051/mmnp/20094301 (cit. on p. 27).

[415] S. Prokopiou, E. Moros, J. Poleszczuk, J. Caudell, J. Torres-Roca, K. Latifi, J. Lee, R. Myerson, L. Harrison, and H. Enderling. "A proliferation saturation index to predict radiation response and personalize radiotherapy fractionation". *Radiation Oncology* 10 (2015). DOI: 10.1186/s13014-015-0465-x (cit. on pp. 151, 185).

[416] R Core Team. *Documentation for TukeyHSD*. Version 4.4.2. URL: https://www.rdocumentation.org/packages/stats/versions/3.6.2/topics/TukeyHSD (cit. on p. 100).

[417] K. Rajagopal. "Multiple configurations in continuum mechanics". *Reports of the institute for computational and applied mechanics* 6 (1995) (cit. on p. 27).

[418] K. Rajagopal and L. Tao. *Mechanics of Mixtures*. World Scientific, 1995. DOI: 10.1142/2197 (cit. on p. 36).

[419] A. Ramírez-Torres, R. Rodríguez-Ramos, F. J. Sabina, C. García-Reimbert, R. Penta, J. Merodio, R. Guinovart-Díaz, J. Bravo-Castillero, A. Conci, and L. Preziosi. "The role of malignant tissue on the thermal distribution of cancerous breast". *Journal of theoretical biology* 426 (2017), pp. 152–161. DOI: 10.1016/j.jtbi.2017.05.031 (cit. on p. 153).

[420] B. Rashid, M. Destrade, and M. D. Gilchrist. "Influence of preservation temperature on the measured mechanical properties of brain tissue". *Journal of Biomechanics* 46.7 (2013), pp. 1276–1281. DOI: 10.1016/j.jbiomech.2013.02.014 (cit. on p. 77).

[421] B. Rashid, M. Destrade, and M. D. Gilchrist. "Inhomogeneous deformation of brain tissue during tension tests". *Computational Materials Science* 64 (2012), pp. 295–300. DOI: 10.1016/j.commatsci.2012.05.030 (cit. on p. 78).

[422] B. Rashid, M. Destrade, and M. D. Gilchrist. "Temperature effects on brain tissue in compression". *Journal of the Mechanical Behavior of Biomedical Materials* 14 (2012), pp. 113–118. DOI: 10.1016/j.jmbbm.2012.04.005 (cit. on pp. 77, 78).

[423] B. Rashid, M. Destrade, and M. D. Gilchrist. "Mechanical characterization of brain tissue in compression at dynamic strain rates". *Journal of the Mechanical Behavior of Biomedical Materials* 10 (2012), pp. 23–38. DOI: 10.1016/j.jmbbm.2012.01.022 (cit. on pp. 15, 78, 79, 83, 89).

[424] B. Rashid, M. Destrade, and M. D. Gilchrist. "Mechanical characterization of brain tissue in simple shear at dynamic strain rates". *Journal of the Mechanical Behavior of Biomedical Materials* 28 (2013), pp. 71–85. DOI: 10.1016/j.jmbbm.2013.07.017 (cit. on pp. 15, 78, 79, 83, 89).

[425] B. Rashid, M. Destrade, and M. D. Gilchrist. "Mechanical characterization of brain tissue in tension at dynamic strain rates". *Journal of the Mechanical Behavior of Biomedical Materials* 33 (2014), pp. 43–54. DOI: 10.1016/j.jmbbm.2012.07.015 (cit. on pp. 15, 78, 79, 83, 89, 102).

[426] D. Reardon et al. "A review of VEGF/VEGFR-targeted therapeutics for recurrent glioblastoma". *Journal of the National Comprehensive Cancer Network : JNCCN* 9 (2011), pp. 414–27. DOI: 10.6004/jnccn.2011.0038 (cit. on p. 19).

[427] M. Righi and V. Balbi. "Foundations of viscoelasticity and application to soft tissue mechanics". In: 2021, pp. 71–103. DOI: 10.1007/978-3-030-88084-2_3 (cit. on pp. 78, 79, 81, 85, 87, 89, 91, 93).

[428] R. S. Rivlin. "Large elastic deformations of isotropic materials IV. Further developments of the general theory". *Philosophical Transactions of the Royal Society of London. Series A, Mathematical and Physical Sciences* 241.835 (1948), pp. 379–397. DOI: 10.1098/rsta.1948.0024 (cit. on p. 89).

[429] R. S. Rivlin. "Large elastic deformations of isotropic materials VI. Further results in the theory of torsion, shear and flexure". *Philosophical Transactions of the Royal Society of London. Series A, Mathematical and Physical Sciences* 242.845 (1949), pp. 173–195. DOI: 10.1098/rsta.1949.0009 (cit. on p. 78).

[430] R. Rockne, E. Alvord Jr., J. Rockhill, and K. Swanson. "A mathematical model for brain tumor response to radiation therapy". *Journal of Mathematical Biology* 58 (2009), pp. 561–578. DOI: 10.1007/s00285-008-0219-6 (cit. on pp. 25, 27, 43, 62, 64, 72, 74).

[431] R. C. Rockne et al. "A patient-specific computational model of hypoxia-modulated radiation resistance in glioblastoma using 18F-FMISO-PET". *Journal of The Royal Society Interface* 12.103 (2015), p. 20141174. DOI: 10.1098/rsif.2014.1174 (cit. on p. 27).

[432] R. Rockne, J. Rockhill, M. Mrugala, A. Spence, I. Kalet, K. Hendrickson, A. Lai, T. Cloughesy, E. Alvord Jr., and K. Swanson. "Predicting the efficacy of radiotherapy in individual glioblastoma patients in vivo: A mathematical modeling approach". *Physics in Medicine and Biology* 55 (2010), pp. 3271–85. DOI: 10.1088/0031-9155/55/12/001 (cit. on pp. 27, 62, 64, 74).

[433] L. Rong, N. Li, and Z. Zhang. "Emerging therapies for glioblastoma: current state and future directions". *Journal of Experimental & Clinical Cancer Research* 41 (2022). DOI: 10.1186/s13046-022-02349-7 (cit. on pp. 20, 103).

[434] W. Roos, L. Batista, S. Naumann, W. Wick, M. Weller, C. Menck, and B. Kaina. "Apoptosis in malignant glioma cells triggered by the temozolomide-induced DNA lesion O6-methylguanine". *Oncogene* 26.2 (2007), pp. 186–197. DOI: 10.1038/sj.onc.1209785 (cit. on pp. 43, 62).

[435] T. Roose and M. A. Swartz. "Multiscale modeling of lymphatic drainage from tissues using homogenization theory". *Journal of biomechanics* 45.1 (2012), pp. 107–115. DOI: 10.1016/j.jbiomech.2011.09.015 (cit. on p. 153).

[436] J. Rubenstein, J. Kim, T. Ozawa, M. Zhang, M. Westphal, D. Deen, and M. Shuman. "Anti-VEGF antibody treatment of glioblastoma prolongs survival but results in increased vascular cooption". *Neoplasia (New York, N.Y.)* 2 (2000), pp. 306–14. DOI: 10.1038/sj.neo.7900102 (cit. on p. 19).

[437] A. Rycman, S. McLachlin, and D. S. Cronin. "A hyper-viscoelastic continuum-level finite element model of the spinal cord assessed for transverse indentation and impact loading". *Frontiers in Bioengineering and Biotechnology* 9 (2021), p. 693120. DOI: 10.3389/fbioe.2021.693120 (cit. on p. 79).

[438] P. Saffman. "On the boundary condition at the surface of porous medium". *Studies in Applied Mathematics* 50 (1971). DOI: 10.1002/sapm197150293 (cit. on p. 161).

[439] D. Sahoo, C. Deck, and R. Willinger. "Development and validation of an advanced anisotropic visco-hyperelastic human brain FE model". *Journal of the Mechanical Behavior of Biomedical Materials* 33 (2014), pp. 24–42. DOI: 10.1016/j.jmbbm.2013.08.022 (cit. on p. 79).

[440] L. Sander and T. Deisboeck. "Growth patterns of microscopic brain tumors". *Physical review. E, Statistical, nonlinear, and soft matter physics* 66 (2002). DOI: 10.1103/PhysRevE.66.051901 (cit. on p. 25).

[441] S. Scialò. "A five field formulation for flow simulations in porous media with fractures and barriers via an optimization based domain decomposition method". *Finite Elements in Analysis and Design* 238 (2024), p. 104204. DOI: 10.1016/j.finel.2024.104204 (cit. on p. 154).

[442] M. Scianna and L. Preziosi. "Multiscale developments of the Cellular Potts Model". *Multiscale Modeling & Simulation* 10 (2012). DOI: 10.1137/100812951 (cit. on p. 28).

[443] G. Seano et al. "Solid stress in brain tumours causes neuronal loss and neurological dysfunction and can be reversed by lithium". *Nature Biomedical Engineering* 3 (2019), pp. 230–245. DOI: 10.1038/s41551-018-0334-7 (cit. on pp. 16, 24, 27, 69).

[444] T. W. Secomb, J. P. Alberding, R. Hsu, M. W. Dewhirst, and A. R. Pries. "Angiogenesis: An adaptive dynamic biological patterning problem". *PLoS Computational Biology* 9.3 (2013), e1002983. DOI: 10.1371/journal.pcbi.1002983 (cit. on p. 32).

[445] F. Şeker, N. Pınarbaşı-Değirmenci, I. Solaroglu, and T. Bagci Onder. "Tumor cell infiltration into the brain in Glioblastoma: From mechanisms to clinical perspectives". *Cancers* 14 (2022), p. 443. DOI: 10.3390/cancers14020443 (cit. on p. 17).

[446] N. S. Selyutina, I. I. Argatov, and G. S. Mishuris. "On application of Fung's quasi-linear viscoelastic model to modeling of impact experiment for articular cartilage". *Mechanics Research Communications* 67 (2015), pp. 24–30. DOI: 10.1016/j.mechrescom.2015.04.003 (cit. on p. 79).

[447] J. W. Shay and W. E. Wright. "Role of telomeres and telomerase in cancer". *Seminars in Cancer Biology* 21.6 (2011), pp. 349–353. DOI: 10.1016/j.semcancer.2011.10.001 (cit. on p. 11).

[448] T. Shearer, W. J. Parnell, B. Lynch, H. R. C. Screen, and I. David Abrahams. "A recruitment model of tendon viscoelasticity that incorporates fibril creep and explains strain-dependent relaxation". *Journal of Biomechanical Engineering* 142.7 (2020). DOI: 10.1115/1.4045662 (cit. on p. 79).

[449] C. J. Sherr and F. McCormick. "The RB and p53 pathways in cancer". *Cancer Cell* 2.2 (2002), pp. 103–112. DOI: 10.1016/S1535-6108(02)00102-2 (cit. on p. 11).

[450] R. J. Shipley, A. F. Smith, P. W. Sweeney, A. R. Pries, and T. W. Secomb. "A hybrid discrete–continuum approach for modelling microcirculatory blood flow". *Mathematical medicine and biology: a journal of the IMA* 37.1 (2020), pp. 40–57. DOI: 10.1093/imammb/dqz006 (cit. on p. 161).

[451] R. Shipley and S. Chapman. "Multiscale modelling of fluid and drug transport in vascular tumours". *Bulletin of mathematical biology* 72 (2010), pp. 1464–91. DOI: 10.1007/s11538-010-9504-9 (cit. on pp. 32, 153, 161).

[452] R. L. Siegel, A. N. Giaquinto, and A. Jemal. "Cancer statistics". *CA: A Cancer Journal for Clinicians* 74.1 (2024), pp. 12–49. DOI: 10.3322/caac.21820 (cit. on p. 13).

[453] G. Sinclair, H. Benmakhlouf, H. Martin, M. Brigui, M. Maeurer, and E. Dodoo. "The role of radiosurgery in the acute management of fourth ventricle compression due to brain metastases". *Surgical Neurology International* 9 (2018), p. 112. DOI: 10.4103/sni.sni_387_17 (cit. on p. 16).

[454] S. Sivaloganathan, M. Statsna, G. Tenti, and J. Drake. "Biomechanics of the brain: A theoretical and numerical study of Biot's equations of consolidation theory with deformation-dependent permeability". *International Journal of Non-Linear Mechanics* 40 (2005), pp. 1149–1159. DOI: 10.1016/j.ijnonlinmec.2005.04.004 (cit. on p. 49).

[455] E. D. Sneed and R. L. Folk. "Pebbles in the lower Colorado river, Texas a study in particle morphogenesis". *Journal of Geology* 66.2 (1958), pp. 114–150. DOI: 10.1086/626490 (cit. on p. 67).

[456] I. Sobey and B. Wirth. "Effect of non-linear permeability in a spherically symmetric model of hydrocephalus". *Mathematical Medicine and Biology* 23 (2006), pp. 339–361. DOI: 10.1093/imammb/dql015 (cit. on p. 49).

[457] R. Springhetti and N. S. Selyutina. "Viscoelastic modeling of articular cartilage under impact loading". *Meccanica* 53.3 (2018), pp. 519–530. DOI: 10.1007/s11012-017-0717-y (cit. on p. 79).

[458] R. Stace, T. Stiehl, M. Chaplain, A. Marciniak-Czochra, and T. Lorenzi. "Discrete and continuum phenotype-structured models for the evolution of cancer cell populations under chemotherapy". *Mathematical Modelling of Natural Phenomena* 15 (2020), p. 14. DOI: 10.1051/mmnp/2019027 (cit. on p. 29).

[459] T. Steed, J. Treiber, M. Brandel, K. Patel, A. Dale, B. Carter, and C. Chen. "Quantification of glioblastoma mass effect by lateral ventricle displacement". *Scientific Reports* 8 (2018). DOI: 10.1038/s41598-018-21147-w (cit. on pp. 16, 24, 27, 67, 68).

[460] P. Steeg. "Angiogenesis inhibitors: motivators of metastasis?" *Nature medicine* 9 (2003), pp. 822–3. DOI: 10.1038/nm0703-822 (cit. on p. 19).

[461] A. Stensjøen, O. Solheim, K. Kvistad, A. Håberg, Ø. Salvesen, and E. Berntsen. "Growth dynamics of untreated glioblastomas in vivo". *Neuro-oncology* 17 (2015), pp. 1402–1411. DOI: 10.1093/neuonc/nov029 (cit. on pp. 65, 149).

[462] A. Stephanou, S. McDougall, A. Anderson, and M. Chaplain. "Mathematical modelling of the influence of blood rheological properties upon adaptative tumour-induced angiogenesis". *Mathematical and Computer Modelling* 44 (2006), pp. 96–123. DOI: 10.1016/j.mcm.2004.07.021 (cit. on p. 32).

[463] A. Stephanou, S. R. McDougall, A. R. A. Anderson, and M. A. J. Chaplain. "Mathematical modelling of flow in 2D and 3D vascular networks: Applications to anti-angiogenic and chemotherapeutic drug strategies". *Mathematical and Computer Modelling* 41.10 (2005), pp. 1137–1156. DOI: 10.1016/j.mcm.2005.05.008 (cit. on p. 32).

[464] D. C. Stewart, A. Rubiano, K. Dyson, and C. S. Simmons. "Mechanical characterization of human brain tumors from patients and comparison to potential surgical phantoms". *PLOS ONE* 12 (2017), pp. 1–19. DOI: 10.1371/journal.pone.0177561 (cit. on pp. 61, 64).

[465] C. Stokes and D. Lauffenburger. "Analysis of the roles of microvessel endothelial cell random motility and chemotaxis in angiogenesis". *Journal of Theoretical Biology* 152 (1991), pp. 377–403. DOI: 10.1016/S0022-5193(05)80349-8 (cit. on p. 32).

[466] R. Stupp et al. "Effects of radiotherapy with concomitant and adjuvant temozolomide versus radiotherapy alone on survival in glioblastoma in a randomised phase III study: 5-year analysis of the EORTC-NCIC trial". *The Lancet Oncology* 10.5 (2009), pp. 459–466. DOI: 10.1016/s1470-2045(09)70025-7 (cit. on pp. 18, 19).

[467] R. Stupp et al. "Radiotherapy plus Concomitant and Adjuvant Temozolomide for Glioblastoma". *New England Journal of Medicine* 352.10 (2005), pp. 987–996. DOI: 10.1056/NEJMoa043330 (cit. on pp. 18, 19, 42, 62).

[468] T. Stylianopoulos, J. Martin, M. Snuderl, F. Mperkis, S. Jain, and R. Jain. "Coevolution of solid stress and interstitial fluid pressure in tumors during progression: Implications for vascular collapse". *Cancer Research* 73 (2013), pp. 3833–3841. DOI: 10.1158/0008-5472.CAN-12-4521 (cit. on pp. 69, 71).

[469] T. Stylianopoulos et al. "Causes, consequences, and remedies for growth-inducedsolid stress in murine and human tumors". *PNAS* 109.38 (2012), pp. 15101–15108. DOI: 10.1073/pnas.1213353109 (cit. on pp. 61, 69).

[470] L. Su, M. Wang, J. Yin, F. Ti, J. Yang, C. Ma, S. Liu, and T. J. Lu. "Distinguishing poroelasticity and viscoelasticity of brain tissue with time scale". *Acta Biomaterialia* 155 (2023), pp. 423–435. DOI: 10.1016/j.actbio.2022.11.009 (cit. on p. 77).

[471] S. Suddin, F. Adi-Kusumo, L. Aryati, and G. Gunardi. "Reaction-diffusion on a spatial mathematical model of cancer immunotherapy with effector cells and IL-2 compounds' interactions". *International Journal of Differential Equations* 2021 (2021), pp. 1–10. DOI: 10.1155/2021/5535447 (cit. on p. 31).

[472] X. Sun and Q. Yu. "Intra-tumor heterogeneity of cancer cells and its implications for cancer treatment". *Acta Pharmacologica Sinica* 36 (2015), pp. 1–10. DOI: 10.1038/aps.2015.92 (cit. on p. 133).

[473] S. N. Sundaresh, J. D. Finan, B. S. Elkin, A. V. Basilio, G. M. McKhann, and B. Morrison III. "Region-Dependent Viscoelastic Properties of Human Brain Tissue Under Large Deformations". *Annals of Biomedical Engineering* 50.11 (2022), pp. 1452–1460. DOI: 10.1007/s10439-022-02910-7 (cit. on p. 79).

[474] S. N. Sundaresh, J. D. Finan, B. S. Elkin, C. Lee, J. Xiao, and B. Morrison III. "Viscoelastic characterization of porcine brain tissue mechanical properties under indentation loading". *Brain Multiphysics* 2 (2021), p. 100041. DOI: 10.1016/j.brain.2021.100041 (cit. on pp. 79, 102).

[475] G. J. Sunderland, M. D. Jenkinson, and R. Zakaria. "Surgical management of posterior fossa metastases". *Journal of Neuro-Oncology* 130 (2016), pp. 535–542. DOI: 10.1007/s11060-016-2254-2 (cit. on p. 16).

[476] R. M. Sutherland. "Cell and environment interactions in tumor microregions: The multicell spheroid model". *Science* 240.4849 (1988), pp. 177–184. DOI: 10.1126/science.240.4849.177 (cit. on p. 144).

[477] S. Suveges, K. Hossain-Ibrahim, Steele, J. Douglas, R. Eftimie, and D. Trucu. "Mathematical modelling of glioblastomas invasion within the brain: A 3D multiscale moving-boundary approach". *Mathematics* 9 (2021), p. 2214. DOI: 10.3390/math9182214 (cit. on p. 25).

[478] S. Svensson et al. "Decreased tissue stiffness in glioblastoma by MR Elastography is associated with increased cerebral blood flow". *European Journal of Radiology* 147 (2021), p. 110136. DOI: 10.1016/j.ejrad.2021.110136 (cit. on p. 61).

[479] A. Swan, T. Hillen, J. Bowman, and A. Murtha. "A patient-specific anisotropic diffusion model for brain tumour spread". *Bulletin of Mathematical Biology* 80 (2017), pp. 1259–1291. DOI: 10.1007/s11538-017-0271-8 (cit. on pp. 25, 26, 71).

[480] K. Swanson, E. Alvord Jr., and J. Murray. "A quantitative model for differential motility of gliomas in grey and white matter". *Cell Proliferation* 33 (2000), pp. 317–29. DOI: 10.1046/j.1365-2184.2000.00177.x (cit. on pp. 25, 26, 116, 125, 127, 145).

[481] K. Swanson, E. Alvord Jr., and J. Murray. "Quantifying efficacy of chemotherapy of brain tumors with homogeneous and heterogeneous drug delivery". *Acta biotheoretica* 50 (2002), pp. 223–37. DOI: 10.1023/A:1022644031905 (cit. on pp. 25, 26).

[482] K. Swanson, E. Alvord Jr., and J. Murray. "Virtual brain tumours (gliomas) enhance the reality of medical imaging and highlight inadequacies of current therapy". *British Journal of Cancer* 86 (2002), pp. 14–8. DOI: 10.1038/sj.bjc.6600021 (cit. on pp. 25, 26, 106, 107, 116, 124, 125, 127).

[483] K. Swanson, E. Alvord Jr., and J. Murray. "Virtual resection of gliomas: Effect of extent of resection on recurrence". *Mathematical and Computer Modelling* 37.11 (2003), pp. 1177–1190. DOI: 10.1016/S0895-7177(03)00129-8 (cit. on pp. 25, 26).

[484] K. Swanson, C. Bridge, J. Murray, and E. Alvord Jr. "Virtual and real brain tumors: using mathematical modeling to quantify glioma growth and invasion". *Journal of the Neurological Sciences* 216 (2004), pp. 1–10. DOI: 10.1016/j.jns.2003.06.001 (cit. on pp. 25, 26).

[485] K. Swanson, R. Rockne, J. Claridge, M. Chaplain, E. Alvord, and A. Anderson. "Quantifying the role of angiogenesis in malignant progression of gliomas: In silico modeling integrates imaging and histology". *Cancer Research* 71 (2011), pp. 7366–75. DOI: 10.1158/0008-5472.CAN-11-1399 (cit. on p. 25).

[486] M. Taffetani, C. De Falco, R. Penta, D. Ambrosi, and P. Ciarletta. "Biomechanical modelling in nanomedicine: multiscale approaches and future challenges". *Archive of Applied Mechanics* 84 (2014), pp. 1627–1645. DOI: 10.1007/s00419-014-0864-8 (cit. on p. 153).

[487] E. G. Takhounts, J. R. Crandall, and K. Darvish. "On the importance of nonlinearity of brain tissue under large deformations". *Stapp Car Crash Journal* 47 (2003), pp. 107–134. DOI: 10.4271/2003-22-0005 (cit. on p. 102).

[488] M. Al-Tameemi, M. Chaplain, and A. D'Onofrio. "Evasion of tumours from the control of the immune system: Consequences of brief encounters". *Biology direct* 7 (2012), p. 31. DOI: 10.1186/1745-6150-7-31 (cit. on p. 31).

[489] M. Tanaka, W. Debinski, and I. Puri. "Hybrid mathematical model of glioma progression". *Cell Proliferation* 42 (2009), pp. 637–46. DOI: 10.1111/j.1365-2184.2009.00631.x (cit. on pp. 25, 62).

[490] X. Tang. "A brief review: The application of mathematical modeling in cancer immunotherapy". *Theoretical and Natural Science* 9 (2023), pp. 174–179. DOI: 10.54254/2753-8818/9/20240738 (cit. on pp. 31, 103).

[491] M. Tektonidis, H. Hatzikirou, A. Chauviere, M. Simon, K. Schaller, and A. Deutsch. "Identification of intrinsic in vitro cellular mechanisms for glioma invasion". *Journal of theoretical biology* 287 (2011), pp. 131–47. DOI: 10.1016/j.jtbi.2011.07.012 (cit. on p. 25).

[492] *TetGen*. URL: https://wias-berlin.de/software/tetgen/ (cit. on pp. 45, 99, 123, 147).

[493] *The Vascular Modeling Toolkit*. 2017. URL: https://www.vmtk.org/ (cit. on pp. 45, 46, 147).

[494] P. Tracqui, G. Cruywagen, D. Woodward, G. Bartoo, J. Murray, and E. Alvord Jr. "A mathematical model of glioma growth: The effect of chemotherapy on spatio-temporal growth". *Cell Proliferation* 28.1 (1995), pp. 17–31. DOI: 10.1111/j.1365-2184.1995.tb00036.x (cit. on pp. 25, 26).

[495] B. Tysnes and R. Mahesparan. "Biological mechanisms of glioma invasion and potential therapeutic targets". *Journal of Neuro-Oncology* 53.2 (2001), pp. 129–147. DOI: 10.1023/A:1012249216117 (cit. on p. 35).

[496] N. Upadhyay and A. Waldman. "Conventional MRI evaluation of gliomas". *The British journal of radiology* 84 Spec No 2 (2011), S107–11. DOI: 10.1259/bjr/65711810 (cit. on p. 22).

[497] P. Vaupel, O. Thews, and M. Hoeckel. "Treatment resistance of solid tumors". *Medical oncology (Northwood, London, England)* 18 (2001), pp. 243–59. DOI: 10.1385/MO:18:4:243 (cit. on p. 17).

[498] M. Vidotto, A. Bernardini, M. Trovatelli, E. De Momi, and D. Dini. "On the microstructural origin of brain white matterhydraulic permeability". *PNAS* 118.36 (2021). DOI: 10.1073/pnas.2105328118 (cit. on pp. 48, 63).

[499] M. Vidotto, D. Botnariuc, E. De Momi, and D. Dini. "A computational fuid dynamics approach to determine white matter permeability". *Biomechanics and Modeling in Mechanobiology* 18 (2019), pp. 1111–1122. DOI: 10.1007/s10237-019-01131-7 (cit. on p. 63).

[500] G. Vilanova, I. Colominas, and H. Gomez. "A mathematical model of tumour angiogenesis: growth, regression and regrowth". *Journal of The Royal Society Interface* 14 (2017), p. 20160918. DOI: 10.1098/rsif.2016.0918 (cit. on p. 32).

[501] G. Vilanova, I. Colominas, and H. Gomez. "Capillary networks in tumor angiogenesis: from discrete endothelial cells to phase-field averaged descriptions via isogeometric analysis". *International Journal for Numerical Methods in Biomedical Engineering* 29 (2013), pp. 1015–1037. DOI: 10.1002/cnm.2576 (cit. on p. 32).

[502] G. Vilanova, I. Colominas, and H. Gomez. "Computational modeling of tumor-induced angiogenesis". *Archives of Computational Methods in Engineering* 24 (2017). DOI: 10.1007/s11831-016-9199-7 (cit. on p. 32).

[503] C. Villa, M. A. Chaplain, and T. Lorenzi. "Modeling the emergence of phenotypic heterogeneity in vascularized tumors". *SIAM Journal on Applied Mathematics* 81.2 (2021), pp. 434–453. DOI: 10.1137/19M1293971 (cit. on pp. 30, 133, 145).

[504] B. Wang, J. Kohli, and M. Demaria. "Senescent cells in cancer therapy: friends or foes?" *Trends in Cancer* 6 (2020). DOI: 10.1016/j.trecan.2020.05.004 (cit. on p. 13).

[505] C. Wang et al. "Prognostic significance of growth kinetics in newly diagnosed Glioblastomas revealed by combining serial imaging with a novel biomathematical model". *Cancer Research* 69 (2009), pp. 9133–9140. DOI: 10.1158/0008-5472.CAN-08-3863 (cit. on pp. 65, 149).

[506] C. Wang et al. "Effect of neoadjuvant iodine-125 brachytherapy upon resection of glioma". *BMC Cancer* 22 (2022). DOI: 10.1186/s12885-022-09504-5 (cit. on p. 23).

[507] J. Wang, Z. Huang, S. Lo, W. Yuh, and N. Mayr. "A generalized linear-quadratic model for radiosurgery, stereotactic body radiation therapy, and high dose rate brachytherapy". *Science Translational Medicine* 2.39 (2010), 39ra48. DOI: 10.1126/scitranslmed.3000864 (cit. on p. 43).

[508] X. Wang, R. June, and D. Pierce. "A 3-D constitutive model for finite element analyses of agarose with a range of gel concentrations". *Journal of the Mechanical Behavior of Biomedical Materials* 114 (2021). DOI: 10.1016/j.jmbbm.2020.104150 (cit. on p. 49).

[509] O. Warburg. "On the origin of cancer cells". *Science* 123.3191 (1956), pp. 309–314 (cit. on pp. 12, 17, 133, 144, 146).

[510] M. Weller et al. "European Association for Neuro-Oncology (EANO) guideline on the diagnosis and treatment of adult astrocytic and oligodendroglial gliomas". *The Lancet Oncology* 18 (2017). DOI: 10.1016/S1470-2045(17)30194-8 (cit. on p. 19).

[511] D. Wells, L. Knapp, D. Brockmann, W. Kath, and J. Leonard. "Spatial and functional heterogeneities shape collective behavior of tumor-immune networks". *PLoS Comput Biol* 11 (2015). DOI: 10.1371/journal.pcbi.1004181 (cit. on pp. 31, 103).

[512] M. Welter, K. Bartha, and H. Rieger. "Emergent vascular network inhomogeneities and resulting blood flow patterns in a growing tumor". *Journal of Theoretical Biology* 250.2 (2008), pp. 257–280. DOI: 10.1016/j.jtbi.2007.09.015 (cit. on p. 32).

[513] M. Welter, K. Bartha, and H. Rieger. "Interstitial fluid flow and drug delivery in vascularized tumors: a computational model". *PLoS ONE* 8.8 (2013). DOI: 10.1371/journal.pone.0070395 (cit. on p. 32).

[514] A. Wineman. "Nonlinear Viscoelastic Solids—A Review". *Mathematics and Mechanics of Solids* 14.3 (2009), pp. 300–366. DOI: 10.1177/1081286509103660 (cit. on p. 79).

[515] A. Winer, S. Adams, and P. Mignatti. "Matrix metalloproteinase inhibitors in cancer therapy: Turning past failures into future successes". *Molecular Cancer Therapeutics* 17 (2018). DOI: 10.1158/1535-7163.MCT-17-0646 (cit. on p. 19).

[516] D. Wodarz. "Computational modeling approaches to studying the dynamics of oncolytic viruses". *Mathematical biosciences and engineering : MBE* 10 (2013), pp. 939–57. DOI: 10.3934/mbe.2013.10.939 (cit. on p. 31).

[517] D. Woodward, J. Cook, P. Tracqui, G. Cruywagen, J. Murray, and E. Alvord Jr. "A mathematical model of glioma growth: The effect of extent of surgical resection". *Cell Proliferation* 29.6 (1996), pp. 269–288. DOI: 10.1111/j.1365-2184.1996.tb01580.x (cit. on pp. 25, 26).

[518] G. Woodward, G. Dunn, E. Nance, J. Hanes, and H. Brem. "Emerging insights into barriers to effective brain tumor therapeutics". *Frontiers in Oncology* 4 (2014), p. 126. DOI: 10.3389/fonc.2014.00126 (cit. on p. 19).

[519] K. Xiao, S. Ho, and A. E. Hassanien. "Brain magnetic resonance image lateral ventricles deformation analysis and tumor prediction". *Malaysian Journal of Computer Science* 20 (2007). DOI: 10.22452/mjcs.vol20no2.2 (cit. on pp. 16, 68).

[520] L. Xiulan and A. Friedman. "Combination therapy of cancer with cancer vaccine and immune checkpoint inhibitors: A mathematical model". *PLOS ONE* 12 (2017). DOI: 10.1371/journal.pone.0178479 (cit. on p. 31).

[521] S. Yan, D. Jia, Y. Yu, L. Wang, Y. Qiu, and Q. Wan. "Novel strategies for parameter fitting procedure of the Ogden hyperfoam model under shear condition". *European Journal of Mechanics A / Solids* 86 (2021), p. 104154 (cit. on p. 78).

[522] W. Yang, T. C. Fung, K. S. Chian, and C. K. Chong. "Investigations of the viscoelasticity of esophageal tissue using incremental stress-relaxation test and cyclic extension test". *Journal of Mechanics in Medicine and Biology* 6.03 (2006), pp. 261–272. DOI: 10.1142/S0219519406001984 (cit. on p. 79).

[523] J. Yu, N. Manouchehri, S. Yamamoto, B. K. Kwon, and T. R. Oxland. "Mechanical properties of spinal cord grey matter and white matter in confined compression". *Journal of the Mechanical Behavior of Biomedical Materials* 112 (2020), p. 104044. DOI: 10.1016/j.jmbbm.2020.104044 (cit. on p. 79).

[524] M. Yu and D. Quail. "Immunotherapy for glioblastoma: Current progress and challenges". *Frontiers in Immunology* 12 (2021). DOI: 10.3389/fimmu.2021.676301 (cit. on p. 21).

[525] S. Yuan, R. J. Norgard, and B. Z. Stanger. "Cellular plasticity in cancer". *Cancer Discovery* 9.7 (2019), pp. 837–851. DOI: 10.1158/2159-8290.CD-19-0015 (cit. on p. 12).

[526] W. Zhan, F. Rodrigues y Baena, and D. Dini. "Effect of tissue permeability and drug diffusion anisotropy on convection-enhanced delivery". *Drug Delivery* 26.1 (2019), pp. 773–781. DOI: 10.1080/10717544.2019.1639844 (cit. on p. 49).

[527] L. Zhang, C. Strouthos, Z. Wang, and T. Deisboeck. "Simulating brain tumor heterogeneity with a multiscale agent-based model: Linking molecular signatures, phenotypes and expansion rate". *Mathematical and Computer Modelling* 49.1 (2009), pp. 307–319. DOI: 10.1016/j.mcm.2008.05.011 (cit. on p. 25).

[528] X. Zhang, M. Fryknäs, E. Hernlund, W. Fayad, A. De Milito, M. H. Olofsson, V. Gogvadze, L. Dang, S. Påhlman, L. A. K. Schughart, et al. "Induction of mitochondrial dysfunction as a strategy for targeting tumour cells in metabolically compromised microenvironments". *Nature communications* 5.1 (2014), p. 3295. DOI: 10.1038/ncomms4295 (cit. on p. 149).

[529] Z. H. Zhang, M. X. Pan, J. T. Cai, J. D. Weiland, and K. Chen. "Viscoelastic properties of the posterior eye of normal subjects, patients with age-related macular degeneration, and pigs". *Journal of Biomedical Materials Research Part A* 106.8 (2018), pp. 2151–2157. DOI: 10.1002/jbm.a.36417 (cit. on p. 79).